Transactions of the ASME®

FLUIDS ENGINEERING DIVISION
Technical Editor
DEMETRI P. TELIONIS (1999)
Executive Secretary
PAT WHITE (1999)
Assistants to the Editor
N. W. SCHAEFFLER
J. E. POWELL
Calendar Editor
M. F. ACKERSON

Associate Technical Editors
P. R. BANDYOPADHYAY (1997)
S. BANERJEE (1999)
P. W. BEARMAN (1998)
M. N. DHAUBHADEL (1999)
J. EATON (1999)
J. A. C. HUMPHREY (1997)
F. HUSSAIN (1998)
J. KATZ (1998)
C. MERKLE (2000)
B. SCHIAVELLO (1999)
O. SIMONIN (1998)
P. M. SOCKOL (1998)
M. SOMMERFELD (1999)
M. S. TRIANTAFYLLOU (1998)

BOARD ON COMMUNICATIONS
Chairman and Vice-President
R. MATES

OFFICERS OF THE ASME
President, **KEITH B. THAYER**
Exec. Director
D. L. BELDEN
Treasurer
J. A. MASON

PUBLISHING STAFF
Managing Director, Engineering
CHARLES W. BEARDSLEY
Director, Technical Publishing
PHILIP DI VIETRO
Managing Editor, Technical Publishing
CYNTHIA B. CLARK
Managing Editor, Transactions
CORNELIA MONAHAN
Production Assistant
MARISOL ANDINO

Transactions of the ASME, Journal of Fluids Engineering (ISSN 0098-2202) is published quarterly (Mar., June, Sept., Dec.) for $195.00 per year by The American Society of Mechanical Engineers, 345 East 47th Street, New York, NY 10017. Periodicals postage paid at New York, NY and additional mailing offices. POSTMASTER: Send address changes to Transactions of the ASME, Journal of Fluids Engineering, c/o THE AMERICAN SOCIETY OF MECHANICAL ENGINEERS, 22 Law Drive, Box 2300, Fairfield, NJ 07007-2300.

CHANGES OF ADDRESS must be received at Society headquarters seven weeks before they are to be effective. Please send old label and new address.

PRICES: To members, $40.00, annually; to nonmembers, $195.00. Add $40.00 for postage to countries outside the United States and Canada.

INDEXED by Applied Mechanics Reviews and Engineering Information, Inc. Canadian Goods & Services Tax Registration #126148048.

Journal of Fluids Engineering

Published Quarterly by The American Society of Mechanical Engineers

VOLUME 120 • NUMBER 1 • MARCH 1998

(Contents continued on p. 159)

This journal is printed on acid-free paper, which exceeds the ANSI Z39.48-1992 specification for permanence of paper and library materials. ♾™

♻ 85% recycled content, including 10% post-consumer fibers.

(Contents continued)

Technical Briefs

Announcements and Special Notices

STEPHEN J. KLINE
1922–1997

A TRIBUTE TO STEPHEN J. KLINE
1922–1997

Clarence J. and Patricia R. Woodward Professor Emeritus of Mechanical Engineering and of Values, Technology, Science and Society at Stanford University, Honorary Fellow of ASME, Member of National Academy of Engineering

Here, in the words of many of Steve Kline's friends, students and colleagues, is a testimony to the character and accomplishments of an energetic and fertile life devoted to unraveling the most difficult and important issues of fluid phenomena, as well as to clarifying philosophical issues at the intersection of technology and society and the conceptual foundations of multidisciplinary thinking. Steve also believed in the obligation of professionals to contribute to the education and leadership of their profession. He was instrumental in forming the ASME Fluids Engineering Division; for many years he served on its boards and committees and as a JFE Associate Editor. Always he stressed fundamentals, critical thinking and the interdependence of research and practice. Here we shall focus for JFE on his contributions to fluid mechanics research and teaching.

Steve Kline had relentless curiosity, a powerful character and drive. "Since I was very young I have had two characteristics which pushed me toward and helped me in a career in science and engineering," Kline once wrote, "I have an intense curiosity about how things work and primary interest in problems which are largely unsolved and important to humans and to the advancement of science and technology."

At M.I.T., Steve studied under Ascher Shapiro, who said "Steve was an outstanding graduate student in the Department of Mechanical Engineering at M.I.T. His doctoral thesis was on friction in the entry region of a tube, with emphasis on the effects of cooling of the tube walls on the friction coefficient and on boundary-layer transition in the developing boundary layer."

Steve's first research triumph was to unravel the century-old confusion over the behavior of simple (but critical) diffusers for kinetic energy recovery from fast flows. Before Steve's work, extensive data in the literature was confusingly contradictive. Design rules were vague; the key parameters were not known. He, and his students, first looked to see how nature did in fact behave. As Bob Showalter said: "Steve Kline wanted pictures, whenever he could get them. Images were part of his thinking. Steve liked abstractions all right, but he wanted abstractions that connected, in step-by-step graphical and pictorial detail, to things that he could see. I hope Steve is remembered for that special, careful, disciplined way of thinking."

After he saw the picture, he generalized his observations with a map of the characteristic regimes of diffuser behavior. He recognized, for the first time, that diffusers were most efficient when on the verge of the transitory stall regime. He brought permanent order to understanding of a key element of all efficient fluid systems and machines. And this order permits the modern CFD analysis of diffusers—which Steve and his students pursued to his end. Johnston reviews the fundamentals of these contributions and some recent Stanford results in an article that appears in this issue of JFE.

The second major stream of Steve's research, the structure of turbulent flows, commenced early and also occupied his genius until his end. Bob Showalter explains that "Steve had a hard won, vivid sense of the boundary between where he understood and where he didn't. This gave him unusually clear judgments about what problems needed to be attacked, and what problems were ripe for attack. These were judgments that he could explain and justify to others. Some of those judgments made a difference." "The fluids profession owes a debt to Steve's forceful temperament, as well as his intellect. The conventional wisdom was dominant that turbulence was statistical. Forceful men said that flows were so complicated that you could 'see anything you wanted in them.' These people said that cause and structure ceased when flows became turbulent. Some statistical models described some data very well. They seemed closed and complete, and sterile." Here Steve Kline made a great contribution. As Chuck Smith says: "If Steve Kline is remembered for nothing else, it should be as the father of the concept of coherent turbulent structure. In 1955, Steve, working with his students on diffuser flows, noticed that when dye was injected along the surface of the diffuser it collected into low-speed streaks. Convincing themselves that this was not an anomaly of their flow system, this led Steve and his students to launch a series of detailed studies which gave rise to the classic concept of coherent turbulent structure, including the identification of rapid ejections of energetic fluid, termed 'bursts', as the offspring of the low-speed streaks, and the stimulus for energy exchange in near-wall turbulence. It turns out that others had observed these types of streak patterns earlier, but Steve was the one that had the insight to recognize the importance of this discovery, and to pursue systematic investigation."

"I should note," Smith continued, "that it was very difficult to get the initial papers on this basic discovery published, since this flew in the face of the paradigm of statistical turbulence modeling. It took 12 years from the first observation to the publication of the definitive paper in the *Journal of Fluid Mechanics* in 1967. Whenever one reads a modern paper on wall turbulence, it will usually cite this initial 1967 paper as the start of our recognition of turbulence as comprised of three-dimensional, time-dependent, but coherent behavior. While we will continue to argue over what comprises this coherency of turbulence, and struggle for a rational explanation of how all the structures of turbulence are generated and interrelated, eventually we will be able to sort through the myriad complexities of turbulence. And we will do it standing on the shoulders of Stephen J. Kline. I am saddened that he won't be here to enjoy that time."

Peter Runstadler was one of those students who remembers "one summer afternoon, while I was working as a research assistant trying to select a good doctoral thesis topic, Steve and I were using dye to visualize the flow through diffusers in a water table. We were injecting dye through a syringe to look at the flow that developed along the diffuser walls during the onset of transitory stall. It was the first time that either of us had used this approach to visualize the flow in the transitory stall regime. We became fascinated by the 'streaks' that developed very near to the wall and the fact that no where did we really see a laminar sub-layer. Steve immediately recognized the importance of the phenomenon and suggested that I might want to structure my thesis around this 'streaky structure'. Of course this was the start of a long series of studies at Stanford on the structure of the turbulent boundary layer. Steve continued to champion work in this area for many years. His use of flow visualization techniques coupled with analysis, to understand fundamental yet complex fluid flow regimes, he taught to many engineers. It stands as one among his many contributions to the engineering community."

Not only was Steve deeply concerned with the science of turbulent flows, but as concerned with improving the tools of engineers who must deal with them. A classic example of his approach was to organize the Turbulent Boundary Layer "Olympics" at Stanford in 1968 which, according to ASME,

was "a land-mark in the development of boundary layer technology." Howard Emmons explains: "I believe the most important technical and historically significant contribution of Stephen J. Kline was his conception of, organization of, and operation of two one-week symposia on the analysis of turbulent flows. Turbulent flows are still today not fully understood but practicing engineers must work with them. There are many approximate methods; integral, ekg, Reynolds stresses, etc. Steve devised a procedure to determine their relative merits. He, with help of colleagues, spent a year carefully studying all available experimental results on turbulent incompressible flows. From these, twenty of the most accurate were selected; boundary layers, flows behind a step, flows in front of a step, etc. Flow geometry and inlet flow conditions were carefully described together with the variables to be used in presenting the graphical results. There was no hint of the correct numerical results."

"Anyone with a turbulence model was then invited to attend the symposium, if they used their method to compute all twenty problems and presented the results at the meeting. Steve chose a panel of about five people to analyze all methods and close the conference with their analysis. The result showed that all methods were acceptable for some problems but that NO method was good for all problems. However, this conference helped to weed out the poorest methods."

Steve's intense interest in making pictures of phenomena impelled a fruitful engagement with the National Committee for Fluid Mechanics Films, lead by Ascher Shapiro, who said of Steve: "He was one of the most committed and hard-working members of that project, which created teaching films still in use today. Steve was the author and principal of one of the films, *Flow Visualization,* which won an international award, and has been widely known and influential."

Not only was Steve Kline a great contributor to fluids science and engineering; he was a great teacher, with hundreds of undergraduate and masters students under his tutelage and some 30 Ph.D. thesis students he mentored. Steve Robinson describes well Steve as a teacher and mentor: "The last time I saw Steve was on August 6, the day before my first flight into space. I thought his illness might prevent a trip to Florida, but I learned one last time that it doesn't pay to underestimate Steve Kline's strength of conviction. Sure enough, he was there in the Florida heat, and the day before launch, I was able to see my closest friends and family, including Steve and Naomi, but only while outside and separated by a 20-foot buffer because of medical quarantine. As everyone called across their greetings and good luck wishes, I leaned over to hear what Steve had to say—he asked, 'what Mach number do you get to?'. It was just Steve being his unique self, and as I stood there with my friend and mentor in front of me, and the space shuttle on the launch pad behind me, I was glad for that 20-foot separation so that everyone couldn't see the tears in my eyes."

Robinson continues "Steve's combination of intellect, curiosity, broad knowledge, and vision gave him a clarity of thought that was unmatched. As his student, I was always amazed by how quickly he could assimilate what my research turned up into this big picture of the natural world. When I completed what I optimistically thought was the final version of my doctoral dissertation, I figured I would have a week or so to rest while he reviewed it. To my great dismay, he called the very next afternoon to say he had a few comments. In fact, he had read every word of my 475-page thesis overnight, and had used that trademark green pen of his to write between very 5th line or so. And worst of all, most of his 'comments' were in fact insightful questions suggesting further research."

"Steve was constantly fascinated by human interactions, and his warmth and humor drew people in," said Robinson. "He had a way of making his students feel that he was a colleague as well as mentor, and knew the importance of honoring his students by learning from them himself. He was also committed to self-improvement. Everyone here knows that Steve didn't always remember to say goodbye at the end of a telephone conversation; to him, the interaction continued in thought after the talking was done, so signing off didn't always occur to him. Once, while I was working with him at this home office, I noticed a little yellow sticky note on his telephone. He had written on it, 'SAY GOODBYE'." "Steve Kline's wisdom has touched us all, and his energy, ideas, and high standards live on in each of us. In this way, I think Steve has taught us still one more thing: If you work from the heart as he did, and your contributions are far-reaching and permanent as his were, your spirit lives on and you don't have to say goodbye."

While beyond and above the scope of this tribute to Steve's technical and teaching career, his philosophical thinking, concepts and writings cannot go unmentioned. Jan Schnittger summarizes: "he covered several more disciplines than most of us ever hope to do. His exposé of the human sciences in relation to natural sciences and engineering and the controversies in between them is most worthwhile. In his book, Conceptual Foundations for Multidisciplinary Thinking, (Stanford Press 1995), there is a wonderful summary of immense value not least for 'practical' people. Kline laid bare a large number of 'phony' battles between members of different disciplines, thanks to him we now have tools to dissolve most of these controversies."

Robert McGinn, who with Steve, Walter Vincenti and others, created the renown Stanford program in Science, Technology and Society and who chairs now that program said "Kline's most important single contribution is his model for technological innovation. Kline felt that the dominant linear or 'assembly line' model for research and development, with its assumption that investment in basic research will automatically be transformed into new technology, was not only simplistic, but actually harmful. So he developed what he called the "chain-link" model of innovation, which has been widely adopted in a number of disciplines both in the United States and abroad."

All we who knew Steve well were impressed with his clear vision into the most complex of subjects, with his genius at bringing order out of complexity and his persistence. Bob Showalter described Steve well "Steve was not a man of religious faith, but he was a man of intense intellectual faith. Steve believed that reality was there, even if it was unseen. He believed the world was understandable in the end. Steve believed that by looking hard at problems, representing them more and more sharply, more and more starkly, and checking and rechecking logic and evidence, breakthroughs would be possible." Showalter concluded with memorial for us all: "If you would remember Steve Kline, look at your problems a little more sharply. Stare at them a little longer. Do more cross-checking. Make sure that what you see and what you say about it fit tightly. Worry more. Be a little more ready than you might otherwise be to discard an idea related to your problem, and try again. Keep at it. Sometimes you may gain new and important insights, as he did. That would be Steve Kline's best memorial."

Compiled by Bob Dean, founding editor of JFE, from many contributions and with assistance from Jim Johnston

Journal of Fluids Engineering

Editorial

In every March issue we publish the technical editor's report on the operation of this Journal. This year, we celebrate the life and accomplishments of Steve Kline, one of the distinguished members of the ASME fluids engineering community and we launch electronic publishing, perhaps the most exciting venture in archival publishing. Steve Kline was instrumental in organizing the Fluids Engineering Division and launching the *Journal of Fluids Engineering*. It is most appropriate that the lead article in this issue is a memorial authored by Robert Dean, the first technical editor of JFE. This editorial is devoted almost exclusively to electronic publishing.

The *Journal of Fluids Engineering* was chosen among all ASME Transactions to go electronic first. This is a pilot project, which will be followed in a few years by all the other journals. The paper version of the Journal will continue to be published and distributed to all its subscribers. All four issues in 1998, starting with the present, will appear on the World Wide Web free of charge. From 1999 and on, the electronic version of the Journal will be available only to its subscribers. The *Journal of Fluids Engineering On-Line* will be on the Web at the end of March, at which time the December, 1997 issue and March, 1998 issue will be posted. The on-line version of the *Journal of Fluids Engineering* will contain all elements provided in the print version: abstracts will be fully searchable and full articles will be provided in PDF format. JFE On-Line will be accessed through ASMENET at http://www.asme.org/pubs/journals/fluideng/fluideng.html.

An electronic supplement of JFE has actually been available since 1995. So far, in the electronic JFE we provided our readers with digital data to accompany selected papers. These data were deposited in the JFE Data Bank and are still available at the old Web Site of JFE (http://scholar.lib.vt.edu/ejournals/JFE/jfe.html). The electronic space was also available for the publication of figures in color, video, lengthy derivation, lengthy descriptions of experimental rigs, computer code listings etc.

Very little will change in our mode of operation, at least for a year or two. Papers will conform to the same publication guidelines and will be set in type but also be prepared for the electronic medium by ASME. The printed version of a paper will appear on paper, with the existing limitations in length and the same material will appear in the electronic medium. Authors will have the options to offer for editing and archiving supplements to their work which will appear only in the electronic JFE. The printed version of a paper will include very short passages informing the readers that in the electronic JFE they can find more material, like more figures, digital data and appendices.

The electronic JFE will include search mechanisms. Readers will be able to search by authors' names, titles, topics, key words etc. We have actually already compiled our author index dating back to 1988, which for the time being is still available in the old Web site of the Journal. Authors are alerted to the fact that abstracts now take even greater significance. Some readers may look only at an abstract in the electronic form before they decide to read the entire paper. Moreover, the search engine that will match key words with papers will search only the abstracts. Authors should therefore make sure that their abstracts contain all of the significant key words that essentially define the content of their paper and are free from complex formulas.

The leadership of the Fluids Engineering Division has welcomed the power of electronically communicating scientific information. The final versions of papers for the FED summer conferences are submitted electronically and the conference proceedings are available only on CD-ROM. With the leadership of Edwin Rood, the Division organized a forum during the November 1997 IMECE on Electronic Review and Publishing. At that forum, the following possible mode of electronic review and publishing was proposed. A paper submitted to the Journal is assigned to an associate editor by the Technical Editor but also, with the consent of the authors it is posted for discussion and criticism on the Web. This will be a special site, clearly identified as part of the electronic JFE. Ideas, results, and new findings are therefore clearly attributed to the authors at this stage and can be referenced by other investigators. Simultaneously, anonymous reviewers are invited by the associate editor to offer their criticism of the posted paper in a parallel, secure, password-protected environment. The paper is revised accordingly and posted again on the Web. The paper thus matures and eventually is accepted by the editors for publication in the Journal.

An Ad Hoc Committee was appointed by the Fluids Engineering Division to explore and test such an approach to electronic review and publishing. A pilot project was launched which has already tested informally the technical aspects of the electronic discussion. In the next step of this project a few papers submitted to JFE will be posted with the consent of the authors for open review and discussion. The readers are invited to participate in this project by posting their comments. The Committee will report to the Division at the Summer 1998 and the IMECE 1998 conferences. A forum on this topic will be again held at the IMECE 1998.

Another experiment will be carried out by the Editorial Board of this Journal. This experiment is intimately connected with the electronic reviewing and publishing discussed earlier, but will be carried out independently of the other two projects. Authors will have the option of submitting their papers electronically. "Snail mail," including internal collection from the sender's and distribution in the receiver's institution often takes four to eight days. In case of mailing abroad, this period may be as long as twelve or fifteen days. Considering the fact that a paper may require five mailings just for the first phase of the review process, namely (1) author to Technical Editor, (2) Technical Editor to associate editor, (3) associate editor to reviewers, (4) reviewers to associate editor, (5) associate editor to author and Technical Editor, electronic submission and mailing may save more than a month of the reviewing process. With target times of two to at most three months from submission to

the first communication of reviews with the authors, cutting four to six weeks is considerable.

This procedure will be optional for authors, editors and reviewers. The Editorial Board cannot guarantee that all mailings will be electronic, but papers submitted electronically will be accepted for consideration. Authors are also requested to submit a transmittal letter and a single copy of their contribution on paper. Papers should be submitted electronically only as Word files. Further information and tools will be made available for such electronic transmission of journal papers in the JFE On-Line.

This editorial will be posted for discussion. The readers are welcome to post their comments electronically. Again, visit the ASMENET at http://www.asme.org/pubs/journals/fluideng/fluideng.html to post your comments, or e-mail your comments directly to Cynthia Clark at clarkc@asme.org.

For all the other topics which are often included in this editorial we may postpone discussion but we should offer some acknowledgments. In this issue, we again list the names of reviewers who worked on our papers during the previous year. We sincerely appreciate their contribution. We also acknowledge the valuable contributions of the associate editors whose tenure expired this year. These are: Promode R. Bandyopadhyay, Francese Giralt, and Joseph A. C. Humphrey, in the area of Fluid Mechanics; and Munir M. Sindir in the area of Computational Fluid Dynamics. A friend of this Journal who has acted on many occasions as a guest editor for the column of unanswered questions is Dr. Lloyd Trefethen. Our thanks to him are long overdue. Finally, we would like to thank Philip Di Vietro (Director, Technical Publishing—ASME) and Cynthia B. Clark (Managing Editor, Technical Publishing—ASME) who have worked hard to make the electronic publishing of this Journal possible and will continue working on refining the process.

The Technical Editor

Review: Diffuser Design and Performance Analysis by a Unified Integral Method

(Data Bank Contribution)*

J. P. Johnston
Professor Emeritus,
Department of Mechanical Engineering,
Stanford University,
Stanford, CA 94305-3030

A computational tool, called a Unified Integral Method (UIM) is reviewed. The method is used for preliminary design and performance analysis of simple diffusers with thin inlet boundary layers and subsonic flow in their inviscid core regions. The assumptions needed for application of a UIM are not very restrictive in many practical cases: straight diffusers with thin, turbulent inlet boundary layers and subsonic, irrotational core flows. The method provides designers with useful results including pressure recovery, location of separation and stalled regions, and exit plane profiles which may be used to evaluate total pressure loss and various flow distortion indices. Besides reviewing some basic concepts concerning stall and separation, describing the basis of the method and some details for making the UIM work, actual cases where it was tested versus data are discussed. In addition, UIM results are compared to results obtained by a RANS method run in a well known duct flow solver for a subsonic diffuser where data are also available. In another case, its output and data were compared to results from a CFD code typical of the many design codes in use in industry today. In both cases, the UIM results were as good, or better than those from the higher level methods, and the UIM is much simpler and easier to use as a design tool.

1 Introduction

A diffuser is a duct where the flow velocity decreases and the static pressure increases as the fluid moves from inlet to outlet. Aircraft and jet engines contain diffusers for a variety of purposes. Examples are (*i*) the inlet diffuser ahead of a gas turbine engine combustor which slows and compresses the air discharged from the final stage of the compressor, (*ii*) the engine inlet diffuser which slows the air delivered to the inlet face of the compressor or fan, and (*iii*) the exhaust diffuser for a gas turbine in a stationary power plant. In all cases, maximum recovery of static pressure without substantial loss of integrated total pressure must be achieved in order to obtain good performance.

When the inlet flow speed is supersonic, a diffuser is usually designed to apply oblique or normal shocks to slow the flow to subsonic speed. This shock region is followed downstream by a subsonic portion. On supersonic aircraft, for example, a substantial fraction of the total compression must be achieved with low losses in the subsonic region. In addition, the flow at the diffuser exit plane must not exhibit more than a minimum level of flow distortion to assure good compressor performance.

Diffusers without shocks, but which contain regions of transonic and subsonic flow, are of concern in this paper. Furthermore, diffusers of interest here have straight axes, and typically, at inlet, have relatively thin wall boundary layers and a large central *core zone.* With a straight axis, the core zone flow may be modeled as inviscid and one-dimensional. The need to keep diffusers compact (short) and at the same time achieve high performance places great demands on the designer who must specify the wall shape of the diffuser. For example, most aircraft inlet diffusers are straight and as short as possible to save on weight.

The designer, in the preliminary phases of work, needs tools for rapid assessment of diffuser performance for a wide variety of possible geometric and inlet flow conditions. Many simple tools are available, but most will only give rough or partial answers. In the case of straight diffusers of rectangular, conical and annular cross section, design charts and other simple methods, based on experimental data bases, are available as individual papers and in collections of correlated data, see lists 1 and 2 in the Appendix. These sources allow the designer to avoid massive flow separation (stall) and to estimate static pressure recovery and mean total pressure loss. However, in some cases, the older data do not give as much detail as a designer requires. For example, exit plane velocity profiles are not furnished, and hence the simple methods are of little value in assessment of total pressure loss, and inflow distortion factors in the case of axial flow compressors for jet engines.

The *goal* of this paper is to review the basis for a unified integral method (UIM) applicable to analysis of internal (duct) flows. Among other things, the UIM that can be used to refine and extend the results of the design charts. This UIM is rapid, relatively simple, quite robust, and provides a rational method for extrapolation and interpolation of the known features of diffuser flow and performance. It is a computational tool constructed to satisfy the basic integral forms of the conservation laws for mass and momentum. It is also empirical in that it relies on correlations of experimental data obtained in various labs over many years. For example, auxiliary relations for boundary layer mass entrainment, and wall/wake laws, developed to describe velocity profiles up to and beyond detachment (separation) are utilized.

The UIM techniques developed at Stanford permit stable computation into regions downstream of detachment (separation). This was only possible once a good physical understanding of the zone of turbulent boundary layer separation was obtained, see Kline et al. (1983), Sandborn and Kline (1961),

* Data have been deposited to the JFE Data Bank. To access the file for the paper, see instructions on p. 232 of this issue.

Contributed by the Fluids Engineering Division for publication in the JOURNAL OF FLUIDS ENGINEERING. Manuscript received by the Fluids Engineering Division September 2, 1997; revised manuscript received October 28, 1997. Associate Technical Editor: D. P. Telionis.

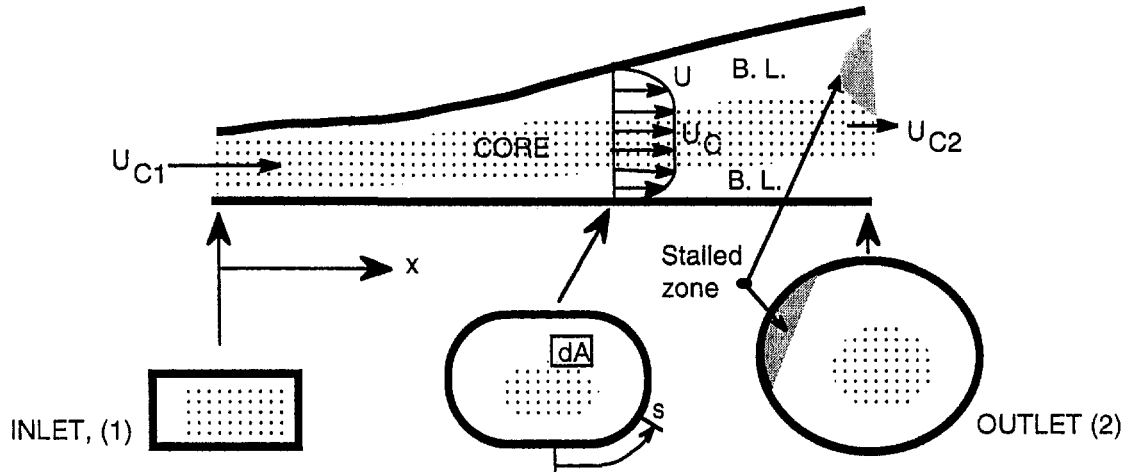

Fig. 1 Sketch of a straight diffuser with change of cross section shape from inlet to outlet

and Simpson (1981). These UIM methods are fairly comprehensive and have been thoroughly tested by various users. This review concentrates on a particular UIM developed at Stanford University. The references cited should be examined in detail by potential users, because we can only outline the basic features of the method here.

Around 1980, more advanced methods of computing turbulent shear flows started to emerge as useful tools (Kline et al., 1982). Most of these methods are devised to solve the Reynolds Average Navier Stokes (RANS) equations in ducts with specified inlet and outlet boundary conditions. They all require modeling of the turbulent Reynolds stresses, and the k-epsilon model is the most popular turbulence model in industrial use today. RANS codes suitable for duct flows are commercially available, and others are obtainable, e.g., (*i*) NPARC2d supported by NASA Lewis Labs and (*ii*) INS2d (incompressible flow) from Ames Research Center. Questions which are addressed later in this paper are: *why,* and *when* should diffuser designers consider the use of the simpler UIM if "superior, more modern" methods are available?

2 Separation (Detachment) and Stall in Simple, Straight Diffusers

If diffuser flow behaved as well as subsonic nozzle flow, simple boundary layer methods applied iteratively in conjunction with inviscid flow solvers would suffice. However, boundary layers in diffusers are subject to strong adverse pressure gradients, and although turbulent, these layers often detach from the diffuser walls in a *process* called separation, which may in some cases be followed downstream by rather massive regions of reversed flow which are generally referred to as *zones of stall,* see Fig. 1. As a consequence of rapid boundary layer growth and the formation of stall zones, the boundary layers and the core regions interact strongly; it is said that the through flow in the diffuser passage undergoes a substantial *blockage* effect. Under such circumstance, simple boundary layer methods which interact iteratively with the core flow solution fail to converge near the beginning of the region of separation, and downstream continuation to the solution fails.

For turbulent boundary layers, separation is a process which may be spread over some physical distance, depending on many factors, but strength of the pressure gradient is the primary factor. In abrupt diffusers, like sudden area expansions or wide angle cones, strong initial pressure gradients cause separation to occur over a very short distance very close to the inlet plane, and stall zones (full stall or jet flow, see below) may fill a large fraction the available downstream cross section. A stall zone contains reverse and forward flow regions that can "block" a portion of the diffuser area and prevent the through flow from decelerating as intended. This effect, referred to as flow *blockage,* is also important in diffusers with smoothly faired walls where boundary layers get thick and badly distorted in regions of rapid rate of area increase.

The flow blockage plays a role almost as important as wall geometry in the performance of a diffuser. Blockage, expressed as an area, Ab, is the portion of the cross-sectional area, A, of a duct which is displaced by all the wall boundary layers (unseparated or stalled). The fractional blockage, B, is the ratio of Ab to A, at any axial station along the duct. B_1, the blockage at the diffuser inlet plane has been found to be a critical performance determinant. The distribution of cross sectional area $A(x)$, see Fig. 1, is the primary determinant of the distribution of pressure gradient along the diffuser walls. $Ab(x)$ and $B(x)$ grow downstream faster than $A(x)$ and cause reduction of the pressure gradient along the diffuser walls. Therefore, $Ab(x)$ must be known or predicted if turbulent boundary layer separation is to be understood and predicted.

Diffusers designed for high effectiveness in pressure recovery, low loss of mean stagnation pressure, and low levels of flow distortion at outlet must spread the pressure rise out over a significant distance from inlet to exit to prevent massive stall. High performance diffusers may be designed using different performance and geometric constraints. For example, diffuser pressure recovery is often maximized for a fixed value of the ratio of axial length to inlet width, N/W_1. In many practical cases, for planar (two-dimensional, constant depth) diffusers designed to such an optimum condition, N/W_1 falls in the range 5 to 15, and the overall area ratio, $AR = W_2/W_1$, falls between 2 and 4; the *shaded* area in Fig. 2. It is seen that a diffuser in this area of the map may contain some regions of separated flow if its optimized geometry falls inside a stalled zone, a very common situation.

Thus, for high performance diffusers, turbulent separation is observed over a detachment region which starts upstream of the exit and extends downstream of the exit plane into a tailpipe if one is extended from the exit plane (not shown in Fig. 1). Onset of detachment is defined as a point on the wall called incipient detachment, **id**, where unsteady backflow occurs near the wall about one percent of the time. Downstream, by one or more boundary layer thicknesses, the average wall-shear stress may drop to zero, a point of full detachment, **d**. Here, the fluid layers adjacent to the wall move up and downstream in equal amounts, statistically. Stall, which may develop downstream of **d**, is generally quite unsteady and sometimes consists of large eddies which appear and disappear with rather low frequency compared to any normal turbulence frequencies. This is the

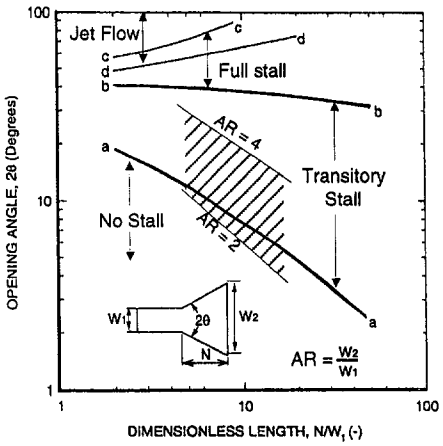

Fig. 2 Planar diffuser flow regime map

phenomenon referred to a *transitory stall.* These processes and concepts are discussed in many of the papers in List 1 of the Appendix. Also, see Kline et al. (1983), Sajben and Liau (1995), and Simpson (1981), a source which reviews turbulent boundary layer separation processes.

The flow regimes and pressure recoveries in simple, straightwalled diffusers with planar, conical, and annular cross sections have been studied in considerable detail and four flow regimes denoted: (*i*) no appreciable stall, (*ii*) transitory stall in corners and on one diverging wall, (*iii*) full stall on one wall with detachment close to the inlet, and (*iv*) jet flow with full stall on all walls. It was found that the geometries that demark the onset of regimes (*i*) and (*ii*) are relatively unaffected by B_1 for small inlet blockage ($B_1 < 0.05$), high Reynolds number, Re_1 ($=Uc_1W_1/\nu$) $> 10^4$ to 10^5, and subsonic Mach number, M_1. Figure 2 illustrates the flow regime dividing lines for the case of planar diffusers of high inlet aspect ratio; diffusers with two straight diverging walls and two parallel walls set far apart compared to W_1, the inlet spacing of the diverging walls. This figure is one form of the chart derived originally using flow visualization in the early work by Kline and his Stanford group.

The shaded region in Fig. 2 illustrates an area where performance optimized diffusers are frequently found. These geometries overlap the transitory stall regime, and contain stalled zones which extend downstream beyond their outlet planes. Even though the flow regime dividing lines (e.g., line *a-a*) are rather insensitive to inlet conditions over certain ranges of B_1, Re_1, and M_1 the performance, measured as pressure recovery, is not. In fact, once the geometry of the diffuser is set, then significant reductions of pressure recovery and increased losses of total pressure may occur with increase of B_1 even for the lowest possible inlet blockages. Prediction of such effects is important in practice.

3 Basis for a Unified Integral Method (UIM)

3.1 Theoretical Basis. All UIMs are founded on the solution of a set of first order differential equations. The equations are formulated from the law of conservation of mass for the total flow through the diffuser and the linear momentum theorem for the boundary layers. The Stanford UIM also uses equations for the rates of entrainment of core fluid into the boundary layers as auxiliary information, and a form of the Coles wall/wake equations for velocity profiles which permits back flow near the wall in a separated zone.

Figure 1 illustrates the physical situation where a zone of inviscid flow, the core, extends from inlet plane (1) to outlet or exit plane (2). A boundary layer zone, which may contain a stalled zone (region containing steady or transitory back flow), surrounds the core zone. Wall shape along x and cross section shape may vary from (1) to (2). For the diffuser in Fig. 1, three cross sections are illustrated. Each section may have a different shape and an area, A, which increases as x increases downstream. A velocity profile is sketched to illustrate the core and boundary layer regions. The core flow is assumed to be irrotational for the nearly straight diffusers considered here, and thus the core zone's velocity, U_c, pressure, p_c, and density, ρ_c, are constant across the core at each section. This one-dimensional assumption for the core may be relaxed, but the analysis and the computation then become much more complex, and the gains in programming and computation time with respect of the use of a RANS method may be questioned.

Conservation of mass for the case where no fluid is injected or removed through the walls requires that the *mass flow rate through each section be identical.* The mass flow rate, m, through a section of area A is:

$$m = \text{constant} = \rho_c U_c Ae = \rho_c U_c (A - Ab) \tag{1}$$

Ae is the "effective" area which will pass the mass flow at core density and velocity. The section area is the sum, of effective and blocked area, e.g., $A = Ae + Ab$. Blocked area, or blockage area is a generalization, for internal flows, of the concept of boundary layer displacement thickness used in external aerodynamics.

Ab plays a vital role in the UIM, one which cannot be ignored as is the displacement thickness in a low order computation of pressure forces on an airfoil in free flight. Sovran and Klomp (1967) showed that the inlet blockage ratio, $B_1 = (Ab/A)_1$, was the most important determinant of diffuser performance, next to diffuser geometry itself. This observation has proven true for almost all straight geometries as long as the inlet Reynolds number is high enough to obtain turbulent boundary layers and the inlet Mach number is subsonic. To illustrate the importance of blockage, differentiate Eq. (1) and note that $dm = 0$.

$$\frac{dU_c}{U_c} = -\frac{dA - dAb}{(A - Ab)} - \frac{d\rho_c}{\rho_c} \tag{2}$$

This shows that rapid downstream growth of blocked area reduces the ability of the increasing physical area (subsonic case) to diffuse the core zone, i.e., to reduce U_c.

The static pressure increase along the diffuser is also affected. This is seen using Euler's inviscid dynamic equation along a streamline in the core zone.

$$dp + \rho_c U_c dU_c = 0 \tag{3}$$

According to the boundary layer approximation, the static pressure at a given x-station is constant across both the core and the boundary layers; consequently, subscript c need not be appended to p as $p = p_c$. When Eqs. (2) and (3) are combined, one obtains

$$dp = \frac{\rho_c U_c^2}{(A - Ab)}(dA - dAb) - U_c^2 d\rho_c \tag{4}$$

which shows that the expected increase in pressure as a result of increase of section area is reduced by growth of the blocked area.

Two of equations (2, 3, 4) are physically independent, first order equations that could be solved in a marching code, starting with given conditions at diffuser inlet, to obtain the dependent unknowns (p, U_c, ρ_c, and Ab) as functions of distance x. Since the core zone is assumed inviscid and isentropic, a thermodynamic property relationship can be used to relate p and ρ_c (simple perfect gas, $p/\rho_c^{\gamma} = \text{constant}$). However, at this level there are only *three* physically independent equations for *four* unknowns.

The linear momentum theorem for steady flow through a control volume dx long, Fig. 3, is also used in the UIM. The basic theorem, along the x-axis is:

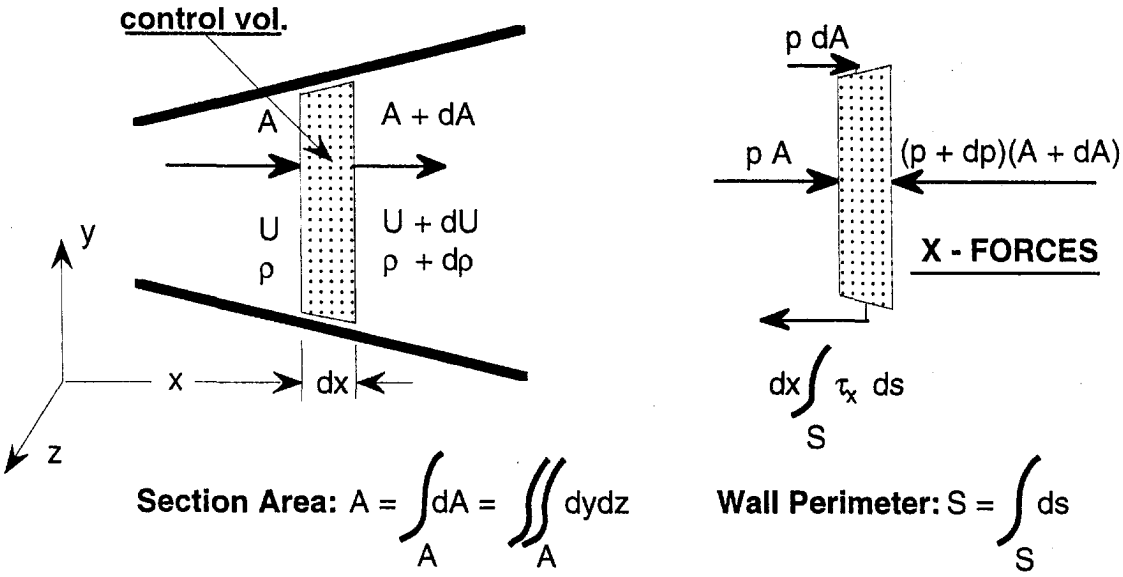

Fig. 3 Control volume, flows, and forces for a diffuser with a straight axis

$$\Sigma F_x = \int_{A+dA} U_x(\rho U_x dA) - \int_A U_x(\rho U_x dA)$$

The sum of forces consists of the pressure forces and the wall shear stress forces on the control volume as shown on the right side of Fig. 3. In our case $U_x = U$, and, after employing some manipulation using Eqs. (2), (3), (4), another physically independent equation for static pressure change with x is obtained (Sovran and Klomp, 1967, pp. 305–306):

$$Abdp = d(\rho_c U_c^2 A\theta) - dx \int_S \tau_w ds \tag{5}$$

The right-hand term is the net retarding force of the wall shear stresses integrated around the perimeter, S, at a given x-station. The term is generally positive so that wall shear contributes directly to loss of static pressure increase, as long as the flow at the wall is forward. However, in regions of reverse flow (stall zones) the wall stress is negative, and can reduce this component of loss. The main term involves a second integral parameter, the "momentum" loss area, $A\theta$. Just as the blocked area is related to a displacement thickness, so $A\theta$ is related to a boundary layer momentum thickness, θ, Eq. (8*b*). If local velocity and density profiles are available these areas are obtainable from:

$$Ab = \int_A \left(1 - \frac{\rho U}{\rho_c U_c}\right) dA \tag{6a}$$

$$A\theta = \int_A \left(1 - \frac{U}{U_c}\right) \frac{\rho U}{\rho_c U_c} dA \tag{6b}$$

As is generally the case with integral methods, the addition of one independent equation increases the number of unknowns. Here, Eq. (5) requires new information as $A\theta$ and wall stress, τ_w, are both added unknown variables.

The equations established above are not the ones actually employed in computations. For example, full area integrals, see Eqs. 6(*a*) and 6(*b*) have not been employed to date, but rather variations in boundary layer around the periphery have been accounted for in segments or *elements*. In practical cases it would be rare for a diffuser to have complete flow symmetry at inlet, hence asymmetry should be permitted so its effects may be studied by parametric variation.

The total blocked area may be written as a sum of n elements, Ab_i, each the product of spanwise length, S_i, and the boundary layer displacement thickness, δ_i^*, for the element.

$$Ab = \sum_{i=1}^{n} Ab_i = \sum_{i=1}^{n} S_i \delta_i^* \tag{7}$$

where the total peripheral distance around the diffuser wall at an x-station is

$$S = \sum_{i=1}^{n} S_i$$

Also, for a given element ($i = 1$ to n) the momentum loss area is $A\theta_i = S_i\theta_i$. The blocked area integral across the element's boundary layer gives

$$\delta_i^* = \delta_i \int_0^1 \left(1 - \frac{\rho U}{\rho_c U_c}\right)_i d\left(\frac{y}{\delta_i}\right) \tag{8a}$$

where y is distance normal to a wall. The momentum loss area employs the momentum thickness;

$$\theta_i = \delta_i \int_0^1 \left(1 - \frac{\rho U}{\rho_c U_c}\right)_i \left(\frac{\rho U}{\rho_c U_c}\right)_i d\left(\frac{y}{\delta_i}\right) \tag{8b}$$

To be precise, δ_i^* and θ_i should be weighted integrals to account for variation in spanwise width of an element between $y = 0$ and δ_i. For diffusers with flat walls this is not a problem, but it might lead to small errors in the case of diffusers with transversely curved walls such as conical and annular cases. This correction, which is not used in any known UIMs, is hardly justified because of potentially larger errors from other assumptions and approximations. The relationship between the blockage area and the two-dimensional displacement thickness, δ^*, is carefully discussed by Sovran and Klomp (1967) on p. 298.

The momentum equation, (5), combined with (3) to eliminate dp, is written for each element where the wall shear force integral is also segmented into n elements.

$$\frac{dU_c}{U_c} + \frac{d(\rho_c U_c^2 S_i \theta_i)}{\rho_c U_c^2 S_i \delta_i^*} - \frac{dx}{\delta_i^*} \frac{\tau_{wi}}{\rho_c U_c^2} = 0 \tag{9}$$

Sets of equations are thus obtained for the n parallel elements

representing flow along spanwise slices of the boundary layer. Note however, that core region variables such as U_c are common to each element. Each of the n elements may have different initial conditions at the diffuser inlet, a situation which allows one to model real inlet conditions more effectively. In practice, UIM computer programs that have up to four separate elements are known to exist (Paynter, 1997), but there is no fundamental limit on n.

Finally, the blockage area is obtained by summation from Eq. (7), and then used in Eq. (1) or Eq. (2) to form a single equation that conserves total mass flow in the set of equations for the fundamental unknowns: U_c, ρ_c, θ_i, δ_i^*, and τ_{wi}. If the fluid is a perfect gas the core Mach number, M_c, will replace U_c and the density is obtained from an isentropic relationship as a function of the ratio of specific heats, γ, M_c, and M_{c1}, the value at diffuser inlet. Other, auxiliary equations are added as required.

In the UIM developed at Stanford, another physically independent relation was introduced, the entrainment equation, an expression for the rate at which flow is transferred from the core into the boundary layers. The two-dimensional definition of the dimensionless entrainment function gives a relationship for each of the n elements of the boundary layer;

$$E_i = \frac{1}{\rho_c U_c S_i} \frac{d}{dx} [\rho_c U_c S_i (\delta_i - \delta_i^*)] \qquad (10)$$

Equation (10) is formulated so that it reduces exactly to the local rate of mass entrained for (i) two-dimensional boundary layer flow (S_i = constant), and (ii) circumferentially uniform axisymetric flow ($S_i = 2\pi R$ where R is the radius of the wall). The parameter E_i must be determined for each element by appropriate empirical correlations, see Section (3.4).

3.2 Computational Basis. Having the equations and correlations is not enough however. The equations are first order, and in theory, for a given diffuser geometry, may be solved by marching, step-by-step downstream from specified initial conditions at the diffuser inlet. A simple Runga-Kutta marching algorithm may be employed.

(i) Because of the regions of flow reversal, velocity profiles must be accurately modeled by equations that admit reverse flow (Kuhn and Nielsen, 1971), but which do not require a priori knowledge of the inflow from the outlet plane of the diffuser. The Navier-Stokes equations, using RANS for example, require such boundary information for their solution. This is one the difficulties in employing them for separated internal (duct) flows, especially when the separated zone extends downstream of the last computational station.

(ii) An entrainment rate correlation for E which is suitable for both attached and separated flows also needs to be employed.

(iii) In the 1970's it became clear, after many failures, that all iterative marching algorithms fail at some point. Boundary-layer separation, with flow reversal, occurs ahead of the outlet for diffusers of optimum pressure recovery. The rapidly increasing blockage in the separation region, near and downstream of incipient detachment (**id**) requires one to solve the equation set *simultaneously* not iteratively (Ghose and Kline, 1978). The rapid growth of the boundary layer near **id** causes the core region and the boundary layers to be *strongly* coupled, not weakly interacting. Weak interaction methods are satisfactory for nozzle flows or unstalled airfoil cases where boundary layer computation follows a previous computation of outer, inviscid flow. In nozzles, where boundary layers remain thin, one or more cycles of iteration to account for the displacement or blockage effects of the boundary layer generally suffice. Iterative marching methods which cyclically solve the boundary-layer equations in a diffuser after the inviscid core is calculated (by applying a core pressure gradient from an upstream computational step) always diverge near detachment (Childs, 1981). *Simultaneous solution means that the equations for the principal dependent variables are treated as implicit at each x-station.* Thus all variables advance downstream at the same time.

(iv) Even using simultaneous (strong) interaction, two-dimensional separation may still lead to mathematical singularities in the equations near detachment points. Various methods (tricks) of jumping across a detachment singularity were devised (Bardina et al., 1981, Ghose and Kline, 1978) to allow the physically approximate, integral marching equations to give smooth and stable results when compared to the empirical data. In the most recent version of the method (Childs and Ferziger, 1983), the issue of such singularities was essentially resolved. They showed, by analysis of the singularities in the equation set, that a strong singularity occurs near separation, between incipient (**id**) and full detachment (**d**), when the equations are solved by simultaneous (strong) interaction for the case where the boundary layer is treated as a *single element* (e.g., a planar diffuser with identical boundary layers on opposite, diverging walls at inlet). However, when the layers were slightly asymmetric at inlet, the singularity may be avoided by changing to a solution method they called a *weak-strong* interaction scheme. The first boundary layer to approach detachment would be treated by simultaneous (strong) interaction with the core, but the other elements, the ones which are initially thinner, would be computed by a weak interaction method. Here, local core flow pressure gradient is extrapolated and imposed on the non separating elements at each x-station, and then several iterations of the strong and weak solutions are used for closure. Hence, one boundary-layer element separates and the others recover in the regions of reduced pressure gradient downstream of detachment. This change to a weak-strong method proved stable in practice, and the results modeled observed physical behavior.

3.3 Velocity and Density (Temperature) Profiles. Attempts to obtain completely general profiles of U and ρ are futile. The developers of UIMs utilized the best information available at the time, and there have been no advances in integral methods in the intervening period to make one want to suggest any basic improvements.

Only perfect gases were studied in cases where density varies across a profile. Since boundary layer analysis is employed, pressure is constant at the core value for each x-station. Thus, $\rho T = \rho_c T_c$, and the Crocco temperature profile is used to compute T and ρ once the velocity profile is known.

$$\frac{\rho_c}{\rho} = \frac{T}{T_c} = 1 + r\frac{(\gamma - 1)}{1} M_c^2 \left(1 - \left(\frac{U}{U_c}\right)^2\right) \qquad (11)$$

T_c, ρ_c, and M_c are computed at each station with 1-D, isentropic, perfect gas relations which are valid in the core region. The recovery factor is often taken as $\mathbf{r} = 1$, but for adiabatic surfaces $\mathbf{r} = 0.89$, typically. Since subsonic diffuser calculations are made at Mach numbers less than unity, either value is accurate enough.

The velocity profiles, $U(y)$, are more complex, but fortunately the Coles wall-wake law possesses the required feature that it can represent a turbulent profile with a zone of reversed flow next to the wall. A form of this "law" useful for both incompressible fluids and compressible gases applies the Coles-Van Driest formulation to give:

$$\frac{U^*}{U_c} = \frac{U_c^*}{U_c} + \mathbf{V}_\mathbf{T} \ln\left(\frac{y}{\delta}\right) - \mathbf{V}_\mathbf{B} \cos^2\left(\frac{\pi}{2}\frac{y}{\delta}\right) \qquad (12)$$

Here, $U^* = U$ for incompressible flow, and suitable correlations of existing data were developed to evaluate the velocity ratio, U/U_c, from U^*/U_c when the flow is transonic and subsonic, (Childs and Ferziger, 1983).

The wall shear velocity, $U\tau$ ($=\sqrt{\tau_w/\rho}$), and the wall stress parameter, $\mathbf{V}_\mathbf{T}$ ($=U\tau/\kappa U_c$), are assigned negative values when

the flow is separated and reversed near the wall. The wake parameter, $\mathbf{V_B}$ ($=2\Pi\mathbf{V_T}$), is positive except in flows with strong favorable pressure gradients which is not a concern in diffusers. The wall shear stress coefficients, needed in Eq. (9), also have $\pm$ sign as they are related to $\mathbf{V_T}$ by

$$\frac{C_f}{2} = \frac{\tau_W}{\rho_e U_e^2} = \kappa^2 \mathbf{V_T} |\mathbf{V_T}| \qquad (13)$$

Boundary layer detachment, **d**, is indicated where $C_f = \tau_W = \mathbf{V_T} = 0$ and the sign changes from positive to negative.

Given: U_e^*/U_e, $\mathbf{V_T}$ or C_f, $\mathbf{V_B}$, the wall law constants ($\kappa = 0.41$, $C = 5$), and the density ratio ρ/ρ_e from Eq. (11), the velocity profile in Eq. (12) may be used to find δ^*/δ and θ/δ by integration on y/δ from 0 to 1. $\mathbf{V_B}$ is not an independent parameter in the UIM method where δ and U_e *or* M_e are used as running variables. It is obtained as a function of U_e^*/U_e, $\mathbf{V_T}$ and Re_δ ($=\delta U_e/\nu$) when the original wall/wake law ($U/U_\tau = f(yU_\tau/\nu)$ is evaluated at the edge of the boundary layer, $y = \delta$. For compressible flows, numerical integration must be employed because of the complexity introduced by Eq. (11) for the density, but for incompressible flow some investigators utilized closed form solutions to evaluate the parameters (e.g., Bardina et al., 1981).

3.4 Parametric Correlations. Besides the variables and parameters already introduced, different versions of the UIM have employed various other quantities either directly or indirectly in various empirically based correlations. A short list includes: $H = \delta^*/\theta$, the boundary layer shape factor; $h = 1 - H^{-1}$, another shape factor; $\Lambda = \delta^*/\delta$, the so called boundary layer blockage, and the ratio, θ/δ.

When the profiles are integrated to obtain δ^* and θ, from Eqs. (8*a*, *b*), one obtains relations represented functionally by:

$$F_1(\Lambda, \mathbf{V_T}, \mathrm{Re}_\delta, M_e) = 0$$

and

$$F_2(\theta/\delta^*, \mathbf{V_T}, \mathrm{Re}_\delta, M_e) = 0$$

In the compressible case, these equations may be expressed algebraically, to give $\mathbf{V_T}$ and h directly, but not if the flow is compressible. The functional forms of the correlations needed in the computation are

$$\mathbf{V_T} = F_3(\Lambda, \mathrm{Re}_\delta, M_e)$$

which gives the skin friction needed in the momentum integral equations by use of Eq. (13), and, by combination of the previous functions and definitions, a function for the shape factor,

$$h = (1 - \theta/\delta^*) = F_4(\Lambda, \mathrm{Re}_\delta, M_e)$$

This shows that one may use Λ in place of θ as a primary running variable in the momentum integral equations, a change found useful by the developers of the methods. The other running variables are δ *or* δ^* and M_e for compressible flow *or* U_e for incompressible flow.

Figures 4(*a*) and 4(*b*) are plots of functions F_3 and F_4 for a useful range of Mach numbers and Reynolds numbers. The curves are in good agreement with experimental results, as illustrated in Fig. 5, drawn from various incompressible cases. As full detachment, **d**, is approached, all the correlation lines tend to collapse on a single line at $\Lambda \approx 0.5$ and $h \approx 1.5$; or $H \approx 4.0$. Incipient detachment, **id**, occurs at $\Lambda \approx 0.42$ where $h \approx 0.63$ and $H \approx 2.7$. In a recent paper, Sajben and Liao (1995), offer further insight on the use of these values for detachment criteria.

For flows in the separated region downstream of detachment, the wake part of the wall/wake law becomes inaccurate. Childs and Ferziger (1983) proposed an ad hoc modification to replace F_4 and used it successfully in computations which went beyond

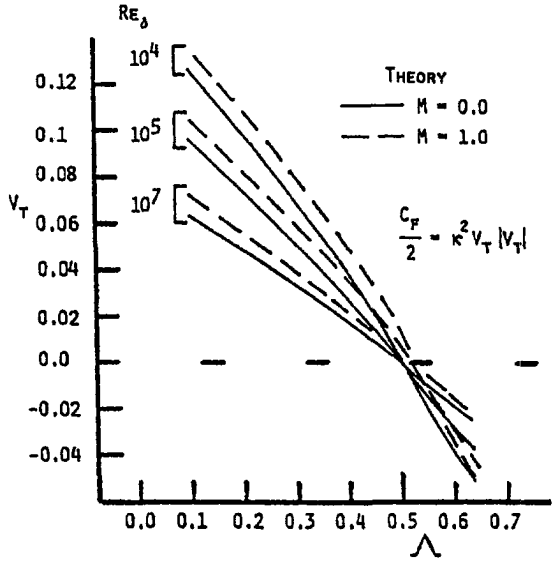

Fig. 4(*a*) Function F_3 for V_T or skin friction (Childs and Ferziger, 1983). Copyright © 1983 AIAA-Reprinted with permission.

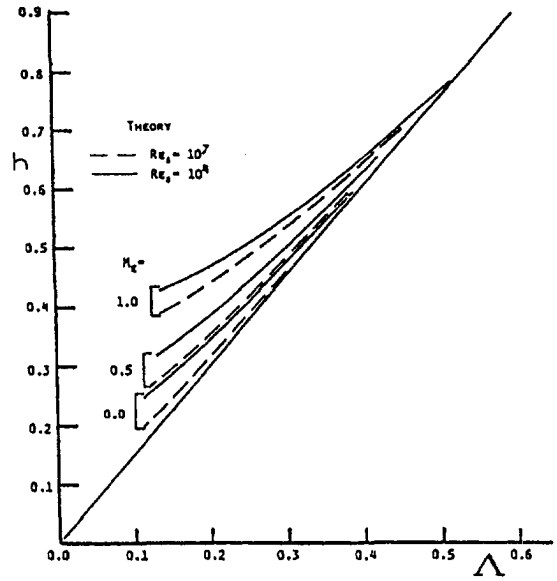

Fig. 4(*b*) Function F_4 for shape factor h (Childs and Ferziger, 1983). Copyright © 1983 AIAA-Reprinted with permission.

full detachment. Here, for $\Lambda > 0.53$ the function below was substituted for F_4.

$$h = 1.0 - 0.213 \exp(-7.049(\Lambda - 0.53)) \qquad (14)$$

Equation (14) smoothly continues the incompressible function from $\Lambda = 0.53$ out to the point where $\Lambda = 1$, $h = 1$. Its authors point out that Eq. (14) is only an "educated guess" which improves certain computed results.

It remains to consider the correlations needed for E in the entrainment integral equation, Eq. (10). Entrainment into the turbulent boundary layers is obtained by use of the correlation due to Bradshaw et al. (1964). Under *equilibrium* conditions (very slow variation along the streamwise direction) this correlation relates local entrainment to the maximum value of the turbulent shear stress at an x-station,

$$E_{eq} = 10 \frac{\tau_{max}}{\rho_e U_e^2} \qquad (15)$$

τ_{max} is obtained by use of an eddy viscosity method based on,

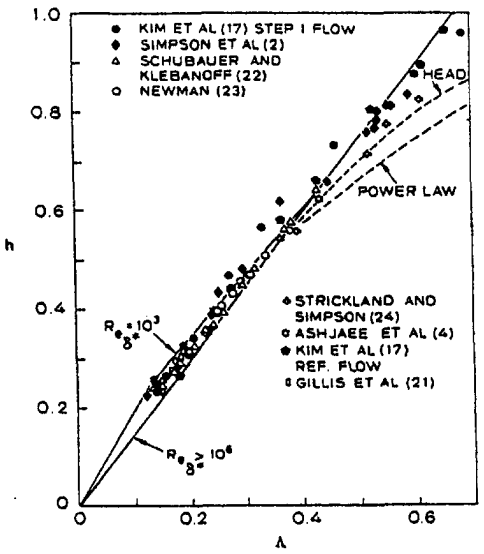

Fig. 5 h versus Λ, incompressible flow data (Kline et al., 1982)

$\nu_{\text{turb}} = KU_c\delta^*$, and an estimate of the mean shear, dU/dy, at the location of maximum stress.

The larger turbulent eddies in the middle and outer parts of the boundary layer which cause the majority of the entrainment may not develop downstream at equilibrium values, especially in a rapidly developing diffuser flow. Hence, a first-order lag equation is used to model the lag effect for each element,

$$\frac{dE_i}{dx} = \frac{\lambda_i}{\delta_i}(E_{i\text{eq}} - E_i) \tag{16}$$

The lag parameter, λ_i, is small for attached flow, but becomes larger for separated flow, an effect accounted for by use of an empirical function of the shape factor Λ. This function is based on numerical experiments tuned to a few experimental cases, Fig. 6 in Childs and Ferziger (1983).

4 UIM Results Compared to Data

4.1 Some Incompressible Flow Cases. The earliest results obtained by a UIM were those by Ghose and Kline (1978) followed by Bardina et al. (1981) for incompressible flow in straight walled planar and conical diffusers. Their work was later generalized to include straight walled annular diffusers (Shimora and Ferziger, 1983). Data from various sources were utilized in comparative computations. The principal dependent variables presented as a result of the computations were distributions of pressure recovery coefficient,[1] $Cp(x)$, with distance, x, along walls,

$$Cp(x) = \frac{p(x) - p_1}{\frac{1}{2}\rho_{c1}U_{c1}^2} = 1 - \left(\frac{U_c(x)}{U_{c1}}\right)^2 \tag{17}$$

and the overall recovery coefficient, Cp, where $p(x) = p_2$ and $U_c(x) = U_{c2}$. They demonstrated that the method could generate reasonably accurate results, including the location of separation when the flow entered the regime of transitory stall. Simplified correlations for Λ, h and E were devised for these incompressible methods to reduce early computational difficulties.

The first example is shown in Fig. 6, a flow regime map for planar diffusers. Line a-a, the onset of the regime of transitory stall, is located with fair accuracy for shorter diffusers ($N/W_1 < 12$) by two computed detachment criteria, $\Lambda = 0.42$ for **id** and $\Lambda = 0.5$ for **d**. The results are less satisfactory for longer diffusers, those with low values of opening angle, $2\theta < 6$ deg. This may be because, upstream of detachment, the real boundary layers merged in the core and thus invalidate the assumption of an inviscid core zone. The flow visualization data used to establish the regime dividing lines also suffer larger uncertainty in this region.

To demonstrate that the method works for other cross sectional shapes, Lyrio (1981) computed a conical diffuser case with low inlet blockage. The results are demonstrated in Fig. 7 where pressure recovery coefficient, Cp, and skin friction coefficient, Cf, are plotted versus distance, x/R_1, along the

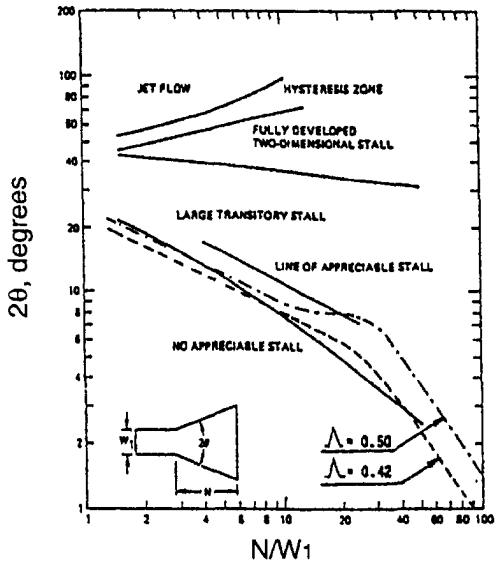

Fig. 6 UIM predictions of line a-a (Lyrio, 1981)

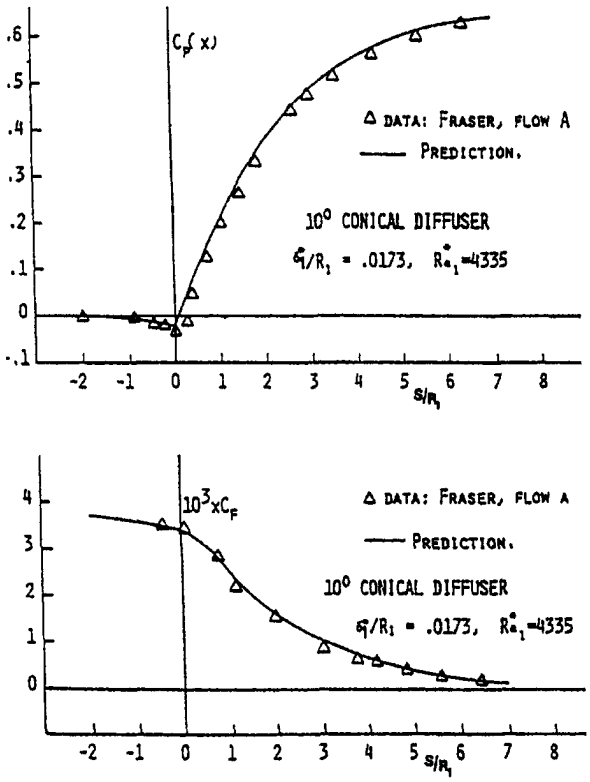

Fig. 7 UIM prediction of a conical diffuser (Lyrio, 1981)

[1] The definition is general, but the right-hand term is only valid for incompressible flow. For a perfect gas, $\rho_{c1}U_{c1}^2 = \gamma p_1 M_{c1}^2$, but for compressible flow it is more common to use $(Pc - p_1)$ where Pc is the core region stagnation pressure.

diffuser axis from upstream of the inlet to exit at $x/R_1 = N/R_1 = 7$. Here, the results are very satisfactory as in similar cases where there is no detachment upstream of the exit plane.

Another interesting incompressible test case, is comprised of two planar diffusers of different opening angles but with the same overall area ratio ($W_1/W_2 = 4$) and inlet aspect ratio ($b/W_1 = 4$) Yamazato and Irabu (1987). The diffusers had $2\theta = 10$ deg. with $N/W_1 = 17.1$ and $2\theta = 12$ deg. with $N/W_1 = 14.3$, respectively. Both are separated just upstream of exit, both have identical inlet conditions (thin turbulent boundary layers and uniform low turbulence cores) at a Reynolds number, $W_1U_{c1}/\nu = 1.4 \times 10^5$. Mean velocity profiles and wall shear stresses were measured at a number of x-stations. This case is similar to two cases by Ashjaee (1980), but here a constant area, square, $7.5 \times W_2$ long, duct is included downstream of the diffuser exit. This "tailpipe" is long enough so that the stalled region reattaches upstream of the tailpipe's exit plane. At the exit, the mean velocity profile approaches uniformity.

The authors of this experiment applied two methods, (i) a Stanford UIM (Lyrio 1981) and (ii) a modification which improves the prediction, especially in the tailpipe. The modification adds equations for computing the end-wall boundary layers, layers not considered in the original methods except by Ashjaee (1980) who showed that their inclusion only made small improvements in his diffusers which had no tailpips. The data and computed results for the more severely separated 12 deg. diffuser are illustrated in Fig. 8(a, b, c, d). The UIM (Lyrio) ignores end-wall layers, produces major errors, especially near the diffuser exit plane and in the tailpipe. End-wall blockage retards the development of separation in the diffuser a little, and the prediction shows a substantial improvement in exit plane recovery both with respect to the data and the Lyrio method, which fails to produce correct trends in the tailpipe. The new results, when compared to the max. and mean values of the velocity profiles (Fig. 8(d), UN versus x/W_1), look much better by the end of the tailpipe, but are worse in the diffuser than the Lyrio method. There are several reasons for this, but the most likely is that complex 3-D flow distortions inside the diffuser caused the max. velocity in the mean profiles to be high relative to the mean core flow speed at the measurement stations in the stalled region. The proper comparison should be against $Cp(x)$ along the diffuser and tailpipe, but the authors failed to provide the static pressure distributions in their paper.

Comparisons to the data from Ashjaee's diffusers are shown below for the most recent version of the Stanford UIM (Childs and Ferziger, 1983), developed for subsonic flow. Figure 9(a) shows the overall pressure recovery versus opening angle where the entrainment correlation of Eq. (14) was used when $\Lambda > 0.53$. In the original method, the core tends to accelerate (static pressure drops) in the separated region where high entrainment causes the blocked area to grow too fast. This was prevented artificially by holding the core velocity constant in the region of excess entrainment until the correlations indicated that E had dropped enough to permit further diffusion. The flat regions on the local pressure recovery curves of Fig. 9(b) are locations where this artificial "fix" to the entrainment correlation occurs. In both figures, use of Eq. (14) improves agreement with overall and local pressure recovery. The worst results are at 2θ of 20 and 24 deg's., opening angles where detachment, **id** and **d**, occur near the inlet of the diffuser, conditions close to Full Stall, line b-b in Fig. 2.

A comparison was also made to the distributions of skin friction, $C_f(s)$, along the walls of the Ashjaee diffuser of $2\theta = 10$ deg which is stalled on one diverging wall (**d** occurs at $x/W_1 \approx 7.5$) but unstalled on the other. The weak-strong interaction scheme was utilized, so the boundary layers on opposite diverging walls are computed separately, and the UIM only predicts separation on one wall. The results, Fig. 10, show that the UIM is providing a good representation of the data for this variable, except close to detachment where detachment is predicted

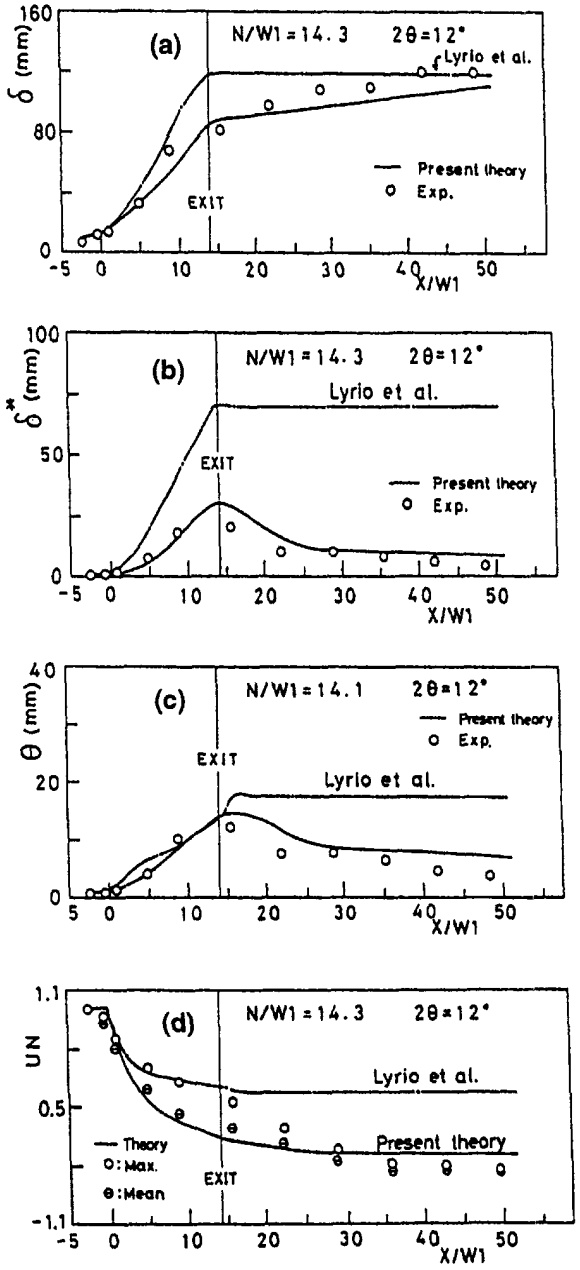

Fig. 8 UIM predictions for a planar diffuser with constant area tailpipe which starts at EXIT (Yamazato and Irabu, 1987)

slightly too soon, at $s/W_1 \approx 5$. Another computation, Rothe et al. (1997), of the location of separation in the 10 deg diffuser used the UIM of Lyrio (1981) with symmetric boundary layers and found **d** at $s/W_1 \approx 7$.

These differences are not very significant, and differences in overall, and local pressure recovery for all the UIM computations of unseparated, and lightly separated diffusers in this data set are within ±10 percent of measured values. Hence, for such simple diffusers with low inlet blockage, turbulent inlet boundary layers, and low inlet Mach numbers one may conclude that the UIM is adequate as a performance predictor unless the diffuser is near full stall, a design condition generally avoided if possible.

4.2 Subsonic Compressible Flow in a Planar Diffuser. The compressible UIM method has barely been examined, let alone tested, in the case of diffusers with subsonic, but high inlet Mach numbers. There is very little detailed experimental

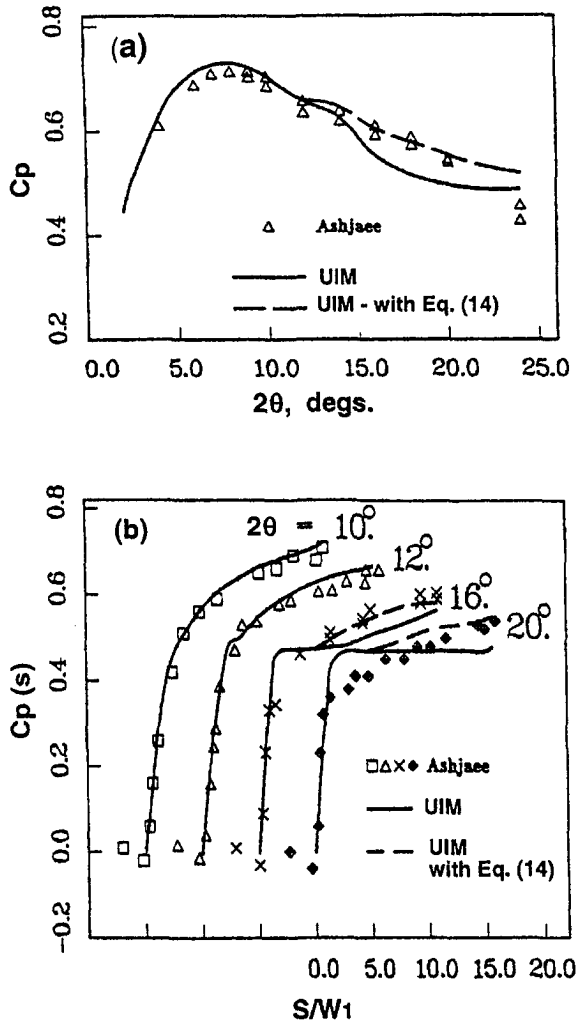

Fig. 9 UIM predictions for a family of planar diffusers of fixed N/W_1 (Childs and Ferziger, 1983). Copyright © 1983 AIAA-Reprinted with permission.

data against which one may compare the computations. The results of Sajben et al. (1977) for a planar diffuser of high inlet aspect ratio were a test case used by Childs and Ferziger (1983).

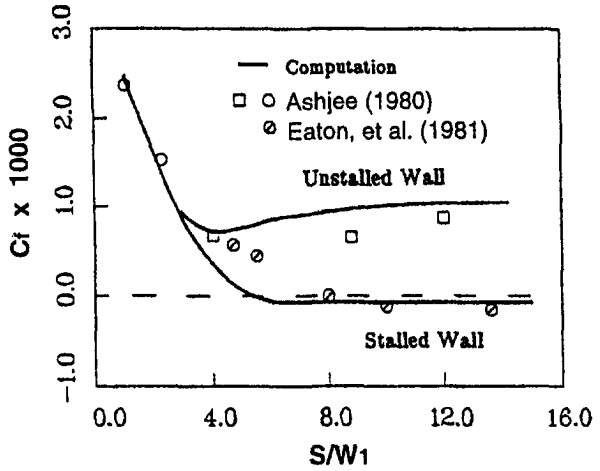

Fig. 10 UIM prediction of skin friction versus distance, s, along walls of a 10 deg. diffuser (Childs and Ferziger, 1983). Copyright © 1983 AIAA-Reprinted with permission.

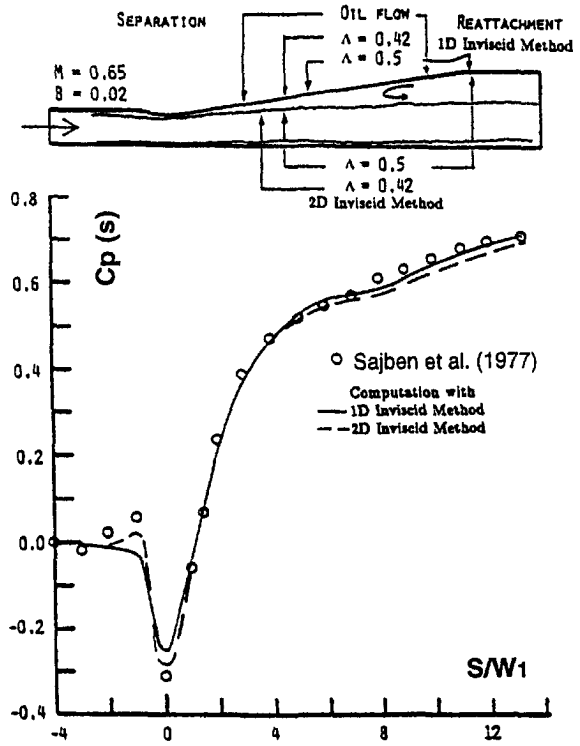

Fig. 11 UIM applied to compressible flow in an asymmetric diffuser (Childs and Ferziger, 1983). Copyright © 1983 AIAA-Reprinted with permission.

This diffuser was asymmetric with one flat wall, $\theta = 0$, and the other set at $\theta = 8.8$ degrees. Also, $N/W_1 = 10$. Inlet conditions were: $M_{c1} = 0.65$ and $B_1 = 0.02$, a low total blockage at inlet. Although the inlet boundary layers were not completely specified, the computation was rather insensitive to the initial values of Λ_1 because of the local acceleration in the throat ahead of the beginning of the diffusing region at $x/W_1 = 0$, see throat in sketch at top of Fig. 11.

In the original work (Childs, 1981) a special integral, two-dimensional solver for the core region that could account for mild wall curvature was developed. This improvement gave a better approximation to the effects of local acceleration and deceleration near the wall at the inlet to the diffuser. Figure 11 shows some results where static pressure recovery is plotted versus x/W_1. A compressible recovery coefficient used here is

$$Cp(s) = \frac{p(s) - p_1}{(P_c - p_1)} \tag{18}$$

where P_c is the core region stagnation pressure and s is distance along a wall starting at the throat.

The two-dimensional core method improves the pressure distribution in the region of the inlet, but has little effect on the overall recovery, at the exit plane. The predicted locations of **id** and **d** are changed somewhat, as shown on the sketch, but one doubts that the extra programming effort to implement the two-dimensional improvement is warranted if only overall results are needed for design purposes.

5 UIM Results Compared to Higher-Order Methods

There are two studies where higher order methods using RANS have been applied to calculate diffuser flows with thin inlet boundary layers, and results compared both to data and to results computed by a UIM. In one case (Rothe et al., 1997), the incompressible diffuser flows of Ashjaee (1980) were used, and in the other (Mayer and Kneeling, 1992) the subsonic diffuser flow of Sajben et al. (1977) was computed.

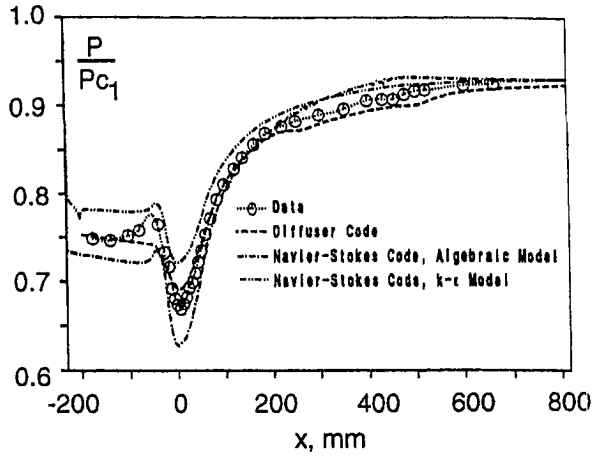

Fig. 12 Wall pressure profiles from a RANS method and a UIM, "Diffuser Code," Mayer and Kneeling (1992). Data from Sajben et al. (1977).

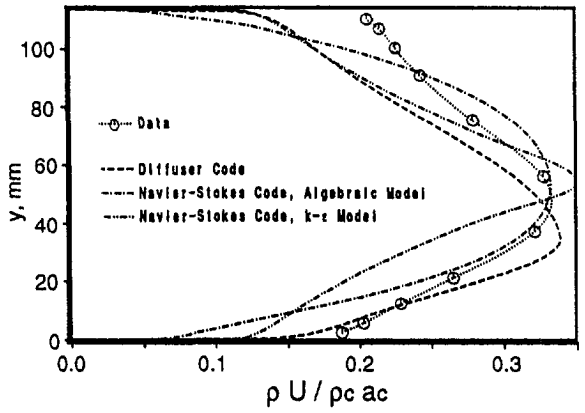

Fig. 13 Mass flux profiles compared at diffuser exit, Mayer and Kneeling (1992). Data from Sajben et al. (1977).

The latter case, described briefly in Section (4.2), will be presented first. This diffuser had an inlet Mach number of 0.65 and was observed to barely reach a detached condition on one wall. A UIM adapted from Childs and Ferziger (1983) and two RANS computations were used in addition to a boundary layer computation which won't be discussed here. One RANS computation used an algebraic turbulent stress model based on a modified Baldwin-Lomax method, and the other used a k-ϵ model. The UIM was carried out on a work station, and computations were completed in seconds. The RANS computations were performed on a CRAY with the PARC code and a tested grid generation scheme. Grid points were closely spaced near the walls so that there were at least two points in the laminar sublayers and approximately 25 grid points across the boundary layers. With a maximum grid-cell aspect ratio (cell length to height) of about 400, a grid containing 46,800 points (60 cross-stream and 780 streamwise) was generated. Detailed descriptions of the methods are available in Mayer and Kneeling (1992), but it is useful to note that the authors claim that; "The convergence properties of the Navier-Stokes code was disappointing; many CPU hours and iterations were required to reduce the residual by an order of magnitude."

Figure 12 shows the ratio of static pressure to central core stagnation pressure at inlet (upstream plenum) versus distance down the wall (x = 0 at the throat). The UIM without wall curvature correction was used so that the bump in wall static pressure just ahead of the throat is not predicted (see solid line in Fig. 11). Nevertheless, the UIM gives as good a prediction as either RANS computation. Both RANS computations suffered problems which prevented accurate matching of the pressure at the upstream state and downstream state at the same time.

Next, a mean, mass-flux-averaged velocity profile is compared to the predictions at the exit in Fig. 13. The UIM method predicted boundary layer merger ahead of this station, and hence the results are not strictly accurate at the diffuser exit plane. In all cases, the predictions fail to capture this level of detail accurately, although the maximum values for all but the RANS using the k-ϵ model are in close agreement with the data. Similar profiles are obtained when total pressure profiles are plotted. These profiles, when integrated to obtain area-averaged stagnation pressure recoveries at the diffuser exit are found to agree with each other within 1 percent. Unfortunately, data on this variable are not available, but all the results, including the UIM, appear to be adequate for diffuser design.

The skin friction coefficient, C_f, is plotted versus distance, x, in Fig. 14. This variable was not measured, and the computed results are in poor agreement with each other. Only the UIM computation predicted detachment with **d** at $x \approx 210$ mm and a reattachment downstream at $x \approx 540$ mm. The data for this case indicated little or no detachment, but this data was based on oil-film flow visualization, a useful method but one which is open to a wide latitude of interpretation in the low speed regions near the wall of a detached turbulent boundary layer. The RANS computation which used the algebraic model agrees with the UIM downstream of the throat, but not at in the inlet region, upstream of the throat. The computation with the k-ϵ model seems to match the C_f profile of the UIM in the upstream regions. But, it behaves very strangely downstream of $x \approx 100$ mm. It was thought that the k-ϵ models produce higher than acceptable shear stresses in adverse pressure gradients and thus tend to delay detachment to a downstream location. However, in this case, the strongest pressure gradients are upstream of $x \approx 100$ mm where the model appears to produce reasonable behavior. At this time the reasons for these strange effects are not understood.

Rothe et al. (1997) used a CFD code (FLUENT^{TM}, Version 4.23) for a particularly difficult task, "assessment" of flow predictability in a *family* of stalling diffuser flows, those of Ashjee (1980). This code is typical of many CFD codes used in industry today for design and flow analysis, and hence the results of this work are, by implication, rather generic. Such codes are *not* research tools like the RANS methods discussed above, and many engineers depend on them for guidance in day-to-day design tasks. An assessment of their capabilities is thus useful. In Rothe's work, not only were CFD results on pressure recovery and detachment location compared to data, they also were compared to results from a UIM (Shimomura and Ferziger, 1983).

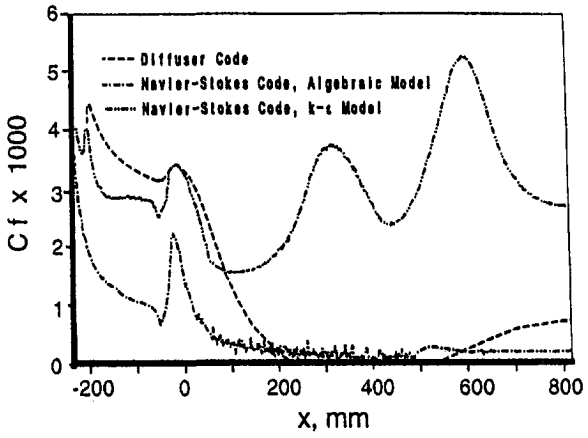

Fig. 14 Skin friction distributions, Mayer and Kneeling (1992)

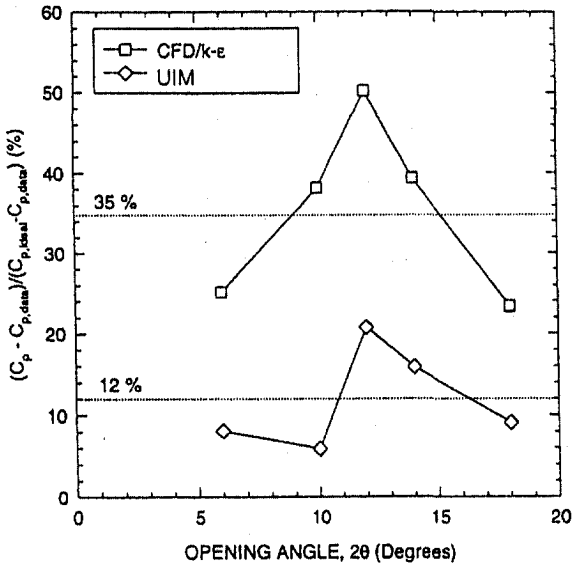

Fig. 15 Deviation (%) of predicted *Cp*'s with respect to the data for a family of planar diffusers, Rothe et al. (1997). $C_{p,data}$ from Ashjee (1980).

The CFD method used 160 streamwise cells by 58 in the cross-stream direction as a base case. Grid independence of the solutions was checked by doubling and then halving the number of cells in selected cases. Turbulence was modeled by an established k-ϵ model and by a more recent k-ϵ-RNG model. In this class of commercially available codes, the first near-wall cell models the shear stress by use of a turbulent "log-law," a fact that appears to be the weak point of this CFD method. The wall matching condition does not represent the physics of separating turbulent boundary layers downstream of the **id** condition on smoothly faired walls.

Five cases of planar diffusers were computed; the one at $2\theta = 6$ deg was fully attached, but the other four cases (10, 12, 14, and 18 deg) had detachment along one wall, upstream of the exit. The deviations of the overall pressure coefficients with respect to the data are plotted versus 2θ in Fig. 15, and the locations of the detachment points are shown in Fig. 16.

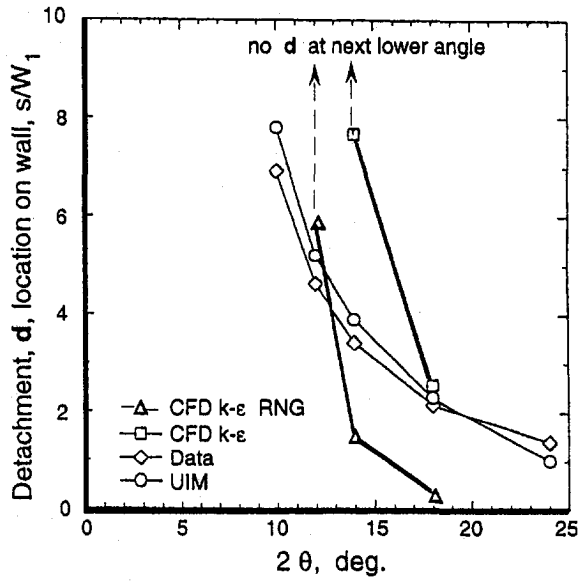

Fig. 16 Comparison of detachment locations for a family of planar diffusers, Rothe et al. (1997). Detachment data from Ashjee (1980).

The CFD k-ϵ model predicted recovery, Cp, to be 25 to 50 percent higher than the data where the error was measured in percent of the difference between the ideal and measured values, $Cp_i - Cp$. Note, $Cp_i = [1 - (W_1/W_2)^2]$, in planar diffusers with incompressible flow. The results for the CFD k-ϵ-RNG model were similar. On the other hand, the UIM predictions are in better agreement with the measurements as shown in Fig. 15.

The differences are made even clearer in Fig. 16. Here, the two turbulence models give rather different results, but they both have a similar trend; a very rapid change of detachment point location with change of diffuser opening angle, 2θ. Conversely, the trends and locations of the data are very close to those predicted with the UIM. On this basis alone, one would have to conclude that the UIM is the more accurate method. However, remember that the UIM has, in a sense, been "tuned" by use of special empirical functions and prior knowledge of the physics of turbulent detachment. The UIM has many inherent limitations which the CFD, or more advanced RANS methods do not. The reasons for the large errors in the CFD are likely to reside in both the turbulence modeling, and, as noted above, in the wall matching conditions which do not represent the physics of turbulent wall-layers in detaching and detached flow, see Rothe et al. (1997) for detailed discussion of this point.

6 Data Bank Contribution

The data of Ashjaee (1980) used in almost all implementations of the UIM, is suggested as a test case for several reasons. (*i*) It provides cases obtained under carefully controlled geometric and inlet conditions. (*ii*) The cases include a wide variety of geometries (2θ varied at fixed N/W_1) which cover both stalled and unstalled flow regimes, and (*iii*) detailed velocity profiles and skin friction are given at one opening angle ($2\theta = 10$ deg) in the Transitory Stall regime. Low frequency, "transitory" fluctuations in the stalled regimes were minimized, and despite symmetry of the geometry and inlet conditions, detachment occurred on one of the two diverging walls.

This set of planar diffusers had symmetrically opened side wall angles, set at $\pm\theta$ about the center plane. It had fixed $N/W_1 = 15$; inlet aspect ratio $b/W_1 = 4$; a uniform, low turbulence core, and thin, two-dimensional, turbulent boundary layers which were nearly identical on all four walls at inlet. Due to the large inlet aspect ratio, end-wall boundary layers may be ignored and the diffuser flow assumed to be fully two-dimensional, but, as shown by Ashjaee and Johnston (1980), the inclusion of end-wall effects improves the computed results a little. For a 2D computation, the upstream conditions to use are: inlet blockage, $2\delta_1^*/W_1 = 0.027$, $\Lambda_1 = 0.114$, and $\mathrm{Re}_1 = W_1 U_{c1}/\nu = 2.2 \times 10^5$. These conditions apply just ahead of the diffuser, at $x/W_1 = -1.15$, the inlet station where $Cp = 0$.

The full geometry is described in Ashjee (1980). The inlet region is shown in Fig. 2 of Ashjee and Johnston (1980) where $x = 0$ at the intersection of an inlet duct wall and a deflected side wall. A short, parallel walled duct was also used downstream of each diffuser, starting at $s/W_1 = 15$ (s is measured along a surface, x is axial distance along center plane). The parallel inlet and outlet duct walls were connected to the side walls with short flexible joints of length $0.375 * W_1$. They may be modeled as circular arcs, tangent to duct and side wall at each end of the joint.

$Cp(x)$ and x-locations of the detachment lines are tabulated in the data files for 12 different opening angles: $2\theta = 4$, 6, 7, 8, 9, 10, 12, 14, 16, 18, 20, and 24 degrees. Velocity profiles measured at interior x-stations for the case of $2\theta = 10$ deg., a case with mild separation having **d** at $x/W_1 \approx 8$, are provided in Ashjaee (1980), but only the integral parameters are tabulated in the data files that accompany this paper.

7 Concluding Remarks

The UIM is a method for using boundary layer integral equations in diffuser flows where flow separation may be a dominant feature. The method produces reasonably accurate results, the most useful of which include the pressure recovery, the location of boundary layer detachment, and velocity profiles at the exit plane.

In summary, the method applies to diffusers with nearly straight axes, simple wall shapes, variable cross-sectional shape along the axis (e.g., change from rectangular to circular or oval is feasible), and certain inlet conditions. Short inlet ducts and, under some circumstances, tailpipes may be included in the computation. The appropriate inlet conditions are (*i*) thin inlet boundary layers (total blockage, $B_1 < 0.05$), (*ii*) nearly uniform, low turbulence core flow, (*iii*) subsonic core flow (maybe as high as, $M_{c1} < 1$, but this limit has yet to be tested), and (*iv*) inlet Reynolds number high enough so the boundary layers are turbulent. Although these may seem like rather restrictive conditions, they apply for many practical diffuser designs.

The design "friendliness" and utility of the method, when applied under proper conditions, is an issue which has been alluded to above. When a UIM is written as part of a properly tested and robust code which doesn't crash for physical or mathematical reasons (see remarks concerning stability, and use of simultaneous and weak-strong solution of the equation set), it can be a very "friendly" design tool. Many solutions involving changes of diffuser geometry and changes of inlet conditions may be produced quickly, often in a matter of minutes. In fact, a good UIM code may be used to supplement and extrapolate existing performance correlations and design charts, as well as provide a basis for design charts in cases not already studied experimentally.

Finally, when tested against current RANS methods applicable to duct flows, and against a code typical of many widely used industrial CFD methods, the UIM has been demonstrated to produce results which are equal or better in accuracy of prediction of the performance parameters of greatest value in the usual course of diffuser design. In all cases where valid comparisons have been made, the UIM seems to hold the edge as a practical, efficient, and physically realistic method when preliminary analysis of an engineering design problem is required. Higher-order methods will eventually achieve their potential as practical design tools. Such codes are applicable to a wider range of cases and conditions (e.g. curved walls, thick inlet layers, high core turbulence, supersonic inlet flow, etc.). However, for a designer to overlook a simple tool like the UIM may be an expensive mistake.

Acknowledgments

This paper is dedicated to my colleague and friend, Prof. Emeritus Stephen J. Kline, who passed away in October, 1997. Steve conceived of and led our diffuser research (Internal Flow Program) from its start in 1959 until the mid-1980's when it concluded.

I also gratefully acknowledge Prof. J. H. Ferziger who made substantial contributions to the diffuser program in the 1970's. The many graduate students, who produced the bulk of the results, are also recognized for their efforts.

External support, professional and monetary, at first came from General Electric Corp. who were soon joined by General Motors Research Labs. I need to thank two individuals who were especially important to me: Dr. G. Sovran, General Motors Research Labs, and Dr. L. Smith, General Electric Aircraft Gas Turbines. Government support came primarily from the Air Force Office of Scientific Research and later from the Office of Naval Research (Project Squid) in the last several years of the program.

Finally, Dr. G. Paynter of Boeing encouraged me to prepare the original version of this paper, and arranged with Boeing Corp. to transfer their UIM code, an improved version of the original code by Childs (1981), for my use.

APPENDIX

A Brief Bibliography

This very brief bibliography lists a number of the basic publications that resulted from research, starting in the 1950's, which put subsonic diffuser design on a sound, scientific basis.

List 1—Individual Papers on Diffuser Design

Ashjaee, J., and Johnston, J. P., 1980, "Subsonic Turbulent Flow in Plane Wall Diffusers: Peak Pressure Recovery and Transitory Stall," ASME JOURNAL OF FLUIDS ENGINEERING, Vol. 102, pp. 275–282.

Carlson, J. J., Johnston, J. P., and Sagi, C. J., 1967, "Effects of Wall Shape on Flow Regimes and Performance in Straight Two-Dimensional Diffusers," ASME *Journal of Basic Engineering,* Vol. 89, pp. 151–160.

Fox, R. W., and Kline, S. J., 1962, "Flow Regime Data and Design Method for Curved Subsonic Diffusers," ASME *Journal of Basic Engineering,* Vol. 84, pp. 303–316.

Hoffman, J. A., 1981, "Effects of Free-Stream Turbulence on Diffuser Performance," ASME JOURNAL OF FLUIDS ENGINEERING, Vol. 103, pp. 385–390.

Howard, J. H. G., Henseler, H. J., and Thornton-Trump, A. B., 1967, "Performance and Flow Regimes for Annular Diffusers," ASME Paper No. 67-WA/FE-21.

Kline, S. J., Abbott, D. E., and Fox, R. W., 1959, "Optimum Design of Straight-Walled Diffusers," ASME *Journal of Basic Engineering,* Vol. 81(D), pp. 321–330.

McDonald, A. T., and Fox, R. L., 1966, "An Experimental Investigation of Incompressible Flow in Conical Diffusers," *International Journal of Mechanical Science,* Vol. 8, No. 2, pp. 81–90.

McMillan, O. J., and Johnston, J. P., 1973, "Performance of Low-Aspect-Ratio Diffusers with Fully Developed Turbulent Inlet Flows, Parts I and II," ASME *Journal of Basic Engineering,* Vol. 95, pp. 385–400.

Powars, C. A., and Johnston, J. P., 1969, "Effects of Aspect Ratio on the Performance of Straight-Walled, Two-Dimensional Diffuser," ASME *Journal of Basic Engineering,* Vol. 91(D), pp. 549–551.

Reid, E. G., 1953, "Performance Characteristics of Plane-Wall Two-Dimensional Diffusers," NACA TN-2888, Feb.

Reneau, L. R., Johnston, J. P., and Kline, S. J., 1967, "Performance and Design of Straight, Two-Dimensional Diffusers," ASME *Journal of Basic Engineering,* Vol. 89, pp. 141–150.

Rothe, P. H. and J. P. Johnston, 1976, "Effects of System Rotation on the Performance of Two-Dimensional Diffusers," ASME JOURNAL OF FLUIDS ENGINEERING, Vol. 98, pp. 422–430.

Runstadler, P. W., Jr., and Dean, R. C., Jr., 1969, "Straight Channel Diffuser Performance at High Inlet Mach Numbers," ASME *Journal of Basic Engineering,* Vol. 91, pp. 397–422.

Sagi, C. J., and Johnston, J. P., 1967, "The Design and Performance of Two-Dimensional Curved Diffusers," ASME *Journal of Basic Engineering,* Vol. 89, pp. 715–731.

Sovran, G., and Klomp, E. D., 1967, "Experimentally Determined Optimum Geometries for Rectilinear Diffusers with Rectangular, Conical, or Annular Cross-Section," *Fluid Mechanics of Internal Flow,* G. Sovran, ed., Elsevier Publishing, New York, pp. 270–319.

Springer, H., 1959, "Experimental Investigation of Straight and Curved Diffusers," Mittelung Nr. 27 aus dem Institut. fur Aerodynamik an den ETH, Zürich.

Wolf, S., and Johnston, J. P., 1969, "Effects of Nonuniform Inlet Velocity Profiles on Flow Regime and Performance in Two-Dimensional Diffusers," ASME *Journal of Basic Engineering,* Vol. 91, pp. 462–474.

Yamazato, E., 1968/75, "Performance of Wide-Angle Two-Dimensional Diffusers," *Bulletin of the Science and Engineering Division,* University of the Ryukyus, Issue #1 (1968), Issue #3 (1970), Issue #5 (1972), Issue #6 (1973), Issue #8 (1975), Japan.

List 2—Collections of Correlated Data

Idelchik, I. E., 1986, *Handbook of Hydraulic Resistance,* 2nd ed., Revised and Augmented, Hemisphere Publishing Corp., New York, Washington, Philadelphia, London, ISBN 0-89116-284-4.

Japikse, D., 1984, *Turbomachinery Diffuser Design Technology,* DTS-1, Concepts ETI, Inc., Box 643, Norwich, VT 05055

Miller, D. S., 1978, *Internal Flow Systems,* Vol. 5 in the BHRA Fluids Engineering Series, British Hydromechanics Research Association Fluid Engineering 1978, ISBN 0 900983 78 7.

Runstadler, P. W., F. X. Dolan, and R. C. Dean, Jr., 1975, *Diffuser Data Book,* TN-186, Creare Inc., P.O. Box 71, Hanover, NH 03755.

References

Ashjaee, J., 1980, "Subsonic Turbulent Flow in Plane-Wall Diffusers; Pressure Recovery and Transitory Stall," Ph.D. dissertation, Dept. of Mechanical Engineering, Stanford University.

Ashjaee, J., and Johnston, J. P., 1980, "Subsonic Turbulent Flow in Plane Wall Diffusers: Peak Pressure Recovery and Transitory Stall," ASME JOURNAL OF FLUIDS ENGINEERING, Vol. 102, pp. 275–282.

Bardina, J. G., Lyrio, A., Kline, S. J., Ferziger, J., and Johnston, J. P., 1981, "A Prediction Method for Planar Diffuser Flows," ASME JOURNAL OF FLUIDS ENGINEERING, Vol. 103, 1981, pp. 315–321.

Bradshaw, P., Ferris, D. H., and Atwell, N. P., 1964, "Calculation of the Turbulent Boundary Layer Using the Turbulent Energy Equation," *Journal of Fluid Mechanics,* Vol. 9, Part 4, pp. 591–625.

Childs, R. E., 1981, "A Computational Method for Subsonic Compressible Flow in Diffusers," Ph.D. dissertation, Dept. of Mechanical Engineering, Stanford University, Stanford, CA.

Childs, R. E., and Ferziger, J. H., 1983, "A Computational Method for Subsonic Compressible Flow in Diffusers," Paper 83-0505, AIAA 21st Aerospace Sciences Meeting, Reno, NV, Jan. 10–13, 1983.

Eaton, J. K., Westphal, R. V., and Johnston, J. P., 1981, "Two New Instruments for Flow Direction and Skin Friction Measurements in Separated Flow," *Flow its Measurement and Control in Science and Industry,* Vol. 2, W. W. Durgin, ed., Instrument Society of America, ISBN 0-87664-511-2, pp. 77–90.

Fraser, J. P., 1958, "Study of an Incompressible Turbulent Boundary Layer in a Conical Diffuser," *Proceedings ASCE, Journal of Hydraulic Division,* Vol. 84, p. 1684.

Ghose, S., and Kline, S. J., 1978, "The Computation of Optimum Pressure Recovery in Two-Dimensional Diffusers," ASME JOURNAL OF FLUIDS ENGINEERING, Vol. 100, pp. 419–426.

Kline, S. J., Bardina, J. G., and Strawn, R. C., 1983, "Correlation of the Detachment of Two-Dimensional Turbulent Boundary Layers," *AIAA Journal,* Vol. 21, No. 1, pp. 68–73.

Kline, S. J., Cantwell, B. J., and Lilley, G. M., 1982. *Proceedings of the 1980–81 AFOSR-HTTM-Stanford Conference on Complex Turbulent Flows,* Vols. I, II, and III, Dept. of Mechanical Engineering, Stanford University, Stanford, CA.

Kuhn, G. D. and Nielsen, J. N., 1971, "An Analytic Method for Calculating Turbulent Separated Flows Due to Adverse Pressure Gradients," Report No: TR NEAR-1-PU, Project Squid, U. S Office of Naval Research.

Lyrio, A. A., 1981, "An Integral Method for the Computation of Steady and Unsteady Turbulent Boundary Layer Flows, Including the Transitory Stall Regime in Diffusers," Ph.D. dissertation, Dept. of Mechanical Engineering, Stanford University.

Mayer, D. W., and Kneeling, W., 1992, "Evaluation of Two Flow Analyses for Subsonic Diffuser Design," AIAA Paper 92-0273, 30th Aerospace Sciences Meeting, Reno, NV, Jan. 6–9.

Paynter, G., (1997), private communication.

Rothe, P. H., Barry, J. J., Johnston, J. P., and Pulliam, T., 1997, "CFD Assessment With Diffuser Data," Paper: FEDSM-3026, ASME Fluids Engineering Division Summer Meeting, June 22–26.

Sajben, M. and Liao, Y., 1995, "Criterion for the Detachment of Laminar and Turbulent Boundary Layers," *AIAA Journal,* Vol. 33, No. 11, pp. 2114–2119.

Sajben, M. C., Kroutil, J. C., and Chen, C. P., 1977, "A High Speed Schlieren Investigation of High Speed Diffuser Flows with Dynamic Distortion," Paper MDRL-77-17, McDonnell-Douglas Research Laboratory, St. Louis, MO, 1977.

Sandborn, V. A., and Kline, S. J., 1961, "Flow Models in Boundary Layer Stall Inception," ASME *Journal of Basic Engineering,* Vol. 83, pp. 317–327.

Shimomura, I., and Ferziger, J. H., 1983, "A Program for Prediction of Diffuser Performance in the Unstalled and Stalled Flow Regimes," Report PD-28, Thermosciences Div., Dept. of Mechanical Engineering, Stanford University.

Simpson, R. L., 1981, "Review of Turbulent Flow Separation," ASME JOURNAL OF FLUIDS ENGINEERING, Vol. 103, pp. 520–581.

Sovran, G., and Klomp, E. D., 1967, "Experimentally Determined Optimum Geometries for Rectilinear Diffusers with Rectangular, Conical, or Annular Cross-Section," *Fluid Mechanics of Internal Flow,* G. Sovran, ed., Elsevier Publishing Co., New York, pp. 270–319.

Yamazato, E. and Irabu, K., 1987, "A Prediction for Two-Dimensional Diffuser Flows," Bulletin Faculty of Engineering, University of the Ryukyus, Japan, No. 34.

The Systematic Uncertainty of Laboratory Flow Calibrations[1]

D. R. Keyser
Vice-President, Performance Test Codes,
Naval Air Warfare Center, Aircraft Division,
Patuxent River, MD 20670-1906
Fellow ASME

There are two axioms applicable to this paper: the first is that no flowmeter can be more accurate than the laboratory which calibrated it; the second that no uncalibrated flowmeter can be more accurate than a like one that is calibrated in a recognized standards laboratory. The fundamental systematic uncertainty in flow measurement is that inherited from the flow calibration laboratory. This paper focuses on ascertaining this fundamental systematic uncertainty by deriving from the published instances of interlaboratory comparisons a value in which one may be 95 percent confident. For water flow measurements, this value turns out to be ±0.28 percent, and for liquid hydrocarbon fuels it is ±0.77 percent. Cold water calibrations are the most accurate.

Introduction

What is the systematic uncertainty of a typical flow calibration laboratory? This question is of acute interest to Performance Test Codes because this bias is difficult to estimate, and it is often a major component of the uncertainty of any flow measurement. In the majority of Performance Test Codes, flow must be measured very accurately because it bears directly on the test result, the uncertainty of which is of prime importance in determining the quality, and acceptability, of the test. This paper answers the question by reviewing the literature of flow measurement to find those instances in which back-to-back comparisons are made between laboratories by using some flowmeter as a transfer standard.

A flowmeter can be no more accurate than the laboratory that calibrated it. This self-evident statement takes on real meaning only when a value of uncertainty can be assigned to it. Unlike many other physical quantities, flow measurement is not a single measurand which can be traced to an international standard. Flow calibration laboratories are systems of instruments and apparatus. The component instrumentation should be traceable to an international standard, and in principle their uncertainties can be known, combined, and propagated to the resulting calibration. However, the apparatus, installation, and plant are unique to each laboratory and these inherent differences lead to other systematic uncertainties which are not traceable.

To estimate the systematic uncertainty of a flow laboratory, it is most realistic to do this using direct comparisons of the calibration results for the same flowmeter, which is agreed to be the transfer standard, because all of the laboratory's procedures and apparatus are included and evaluated. If more than two laboratories are involved in such intercomparisons, it is called a round-robin test.

Unfortunately there are not many publications entitled "Laboratory Intercomparisons of Calibrations using the Xmeter." Rather, these data are buried in one or two paragraphs within a paper in which the subject is some other major concern of flow measurement technology, and such data are used to bolster the main thesis of the paper. These data are scarce, and much reading had to be done to find what is reported here.

An assumption implicit in reporting these results is that if the laboratories involved are aware that their calibrations will be compared to the others, they will put forth their best effort.

Published Laboratory Intercomparisons

It is standard practice to use 95 percent confidence limits for estimating all uncertainties, first in Performance Test Codes, and now internationally as well. Certainly there are times when the systematic uncertainty from a flow calibration laboratory is much smaller than the values quoted herein; in fact 95 percent of the time it should be. The practical problem is that the user never knows when that is happening. Conversely, one time out of twenty, one should expect a larger uncertainty to occur. In the statistical treatment of these data concerning interlaboratory comparisons, one can never be sure which one is closer to the truth—that is why the uncertainties must be reported as ± values. Where only a few data were presented, the maximum deviation was recorded. Where there were sufficient data to calculate a reliable variance, this was done assuming the data were absolute values to determine the mean to which was added the product of the standard deviation of the sample with Student's t for 90 percent confidence limits. The 90 percent confidence limit was chosen because we have a one-sided distribution. We are not interested in that part of the distribution smaller than the mean; we are interested only in excluding the upper 5 percent of the uncertainty data.

Cold Water Calibrations. Bean, Beitler, and Sprenkle (1941), three of the Old Masters of flow measurement, made the first statement I could find; it is now outdated, but it did establish the baseline from which later improvements were made in flow measurement technology: "However, between the results reported by different laboratories on tests of the same nozzle, the differences were as much as 1 per cent to 1.5 per cent, even when the same sections of pipe had been used. As a rule, the differences were higher at low Reynolds numbers than at the high. Therefore, the authors suggest that, in the use of these nozzle coefficients, a tolerance (i.e. the probable range of uncertainty) of ±0.75 percent be allowed at Reynolds' numbers R_d of 500,000 and over, with 3-inch pipe and larger."

Wyler and Benedict (1974) published the results of calibration comparisons between throat and pipe wall tap nozzles in which three laboratories were used. Figure 5, *opere citato,* shows that the difference in the means of the calibration data between lab 1 and lab 3 is about 0.28 percent, while that from lab 2 lies between them. Spencer and Neale (1974) reported results of calibrations of flange-tapped, 0.5β orifices, at The National Engineering Lab in Scotland and Alden Research Lab in Massachusetts in which the difference between the fitted calibration curves of the same orifice is about 0.25 percent. These tests were conducted in 8-inch pipe, and two other orifice sizes were also tested: 0.3 and 0.8 β. The differences for the 0.3β were the same as those for the 0.5β, but for the 0.8β orifice, the difference was closer to 0.5 percent. These calibration data

[1] The opinions expressed in this paper are the author's and shall not be construed as those of the U.S. Navy nor of the Naval Establishment at Large.

Contributed by the Fluids Engineering Division for publication in the JOURNAL OF FLUIDS ENGINEERING. Manuscript received by the Fluids Engineering Division April 22, 1997; revised manuscript received October 28, 1997. Associate Technical Editor: D. P. Telionis.

Table 1 Difference between the calibration curves and the PTC-6 reference curve for the condensate flow section

	Tap 1	Tap 2	Tap 3	Tap 4
Alden Lab (1981)	+0.17%	−0.12%	−0.16%	0.04%
G.E. Co. (1969)	−0.08%	−0.14%	−0.16%	−0.13%
Δ	0.25%	0.02%	0.0%	0.17%

are plotted and shown in Keyser (1996), the source paper to which the reader is directed for more detail.

Albert et al. (1982) reported differences between the PTC-6 reference curve for ASME throat tap nozzles and calibrations of each of four sets of taps of one such nozzle and its PTC-6 flow section calibrated first at the General Electric laboratory in 1969 and again in 1981 at Alden Research Laboratory (ARL). (Since the ± is relative to the reference curve, values of opposite sign are additive in determining the systematic difference between the laboratories). Their results are presented in Table 1.

Further data for another such nozzle were received from T. M. Brown (1995) for these two laboratories. These data are presented in Table 2, and the differences are those reported at a Reynolds' number of 3,000,000, which is in the middle of the calibration range where the data overlap.

Taking a philosophical point of view, many regard a systematic uncertainty of this sort as fixed for the duration of the test; however, over the longer term it is thought to vary slowly over a period of days, weeks, or months. Therefore, over the long run, it also appears quasi-random with statistical variance. This comparison is between only two of the many acceptable laboratories which specialize in cold water calibrations at relatively high Reynolds' numbers. If we so attempt to estimate the probable range of this systematic uncertainty to the 95% confidence level (which is the accepted practice for other random uncertainties), the conservative test engineer would use a value of ±0.29 percent systematic uncertainty based on Tables 1 and 2, which was calculated by adding to the mean of all those deviations the product of their standard deviation with Student's t for 90 percent confidence.

A Study of Inter-Laboratory Comparisons of Calibrations of 10 Orifice Plates was reported by Levie et al. (1978) using an original 10-in. pipe section and a complete set of orifice plates which was discovered preserved since last used in a series of calibration tests in 1952–54 at Refugio, TX to establish orifice coefficients for natural gas. "The laboratories are described and the test data (well over 1200 tests were made) summarized. Agreement between the mean values obtained were within ±0.3%; differences are attributed mainly to variations in the flow distribution into the test assembly but also to uncertainties in the absolute measurement of the flowrate and pressure difference." Four laboratories were used in the following order: Daniel Industries, Foxboro Co., National Engineering Laboratory (Glasgow, UK), and Central Electricity Generating Board Hydraulic Calibration Centre (UK). "To facilitate a comparison analysis it was then decided to ignore any dependence (on Re) and assess on the basis of mean values only within the flowrate range common to all laboratories." Table 3 is a summary of these comparisons:

Brunkalla (1985) reported the calibrations of an 8 in. and 12 in. throat tap nozzle, each with four differential pressure taps,

Table 2 Comparison of ASME flow nozzle calibrations coefficient of discharge

	Tap 1	Tap 2
Alden R.L. (1992)	0.9960	0.9960
G.E. (1969)	0.9954	0.9962
Δ %	0.06	−0.02

Table 3 Summary of comparison of discharge coefficients for all labs

Labs compared	Δ of Mean C_d %	Number of calibrations compared
FOX-DAN	+0.28	20
FOX-NEL	+0.25	15
FOX-CEGB	+0.18	6
DAN-NEL	−0.26	25
DAN-CEGB	−0.18	8
CEGB-NEL	+0.15	11

at the Badger Meter Co. laboratory and then at ARL. Using a statistical treatment similar to that comparing the GE and ARL calibrations, we have 8 calibration curves for two sizes of identical nozzles between the two labs. These data are presented in Table 4.

These data are the differences between the means of all coefficients obtained from both laboratories for Reynolds' numbers above 200,000. It was stated that the BMI lab was limited to Re < 800,000, but apparently all the data, including that above 800,000 was used from ARL. The data in Table 4 are all means, and given their variance it is estimated that the expected systematic uncertainty between the labs at 95 percent confidence is ±0.284 percent.

Cotton and Westcott (1960) included in their discussion two instances of laboratory intercomparisons: "These same two nozzles were also calibrated at the University of Pennsylvania. The results are shown in Figs. 7 and 8 along with the theoretical curve and the results from the Turbine-Generator Development Laboratory. The extrapolated curve from the University of Pennsylvania calibration is about 0.15 per cent lower than the calibration curve obtained in the Turbine-Generatory Development Laboratory." (This is the aforementioned GE lab.) Next they showed: "Fig. 9 shows a comparison of results of one nozzle calibrated at three different laboratories." These laboratories were at Ohio State University, Worcester Polytechnic Institute, and the University of Pennsylvania. Again all four sets of taps were calibrated. In the range where the data overlapped (400,000 < Re < 1,200,000), frequently there were differences between the laboratories of about 0.3 to 0.4 percent for calibration points at the same Reynolds' number. Of course in this region higher variations are often observed because of the varying conditions for the inception of boundary layer transitions. In addition, it was reported that "The repeatability of three calibrations of the same nozzle at the University of Pennsylvania at different times is illustrated in Fig. 10. The extrapolated curves are at the most different from the theoretical curve by 0.2 per cent. In the laminar region there is considerable deviation, but here again this has not been a matter of great concern." These latter data, while not an interlaboratory comparison, may illustrate the magnitude of the effect of moving the calibrated flow section from the laboratory to the test site and reinstalling it in nearly identical piping.

Clay et al. (1981) reported that: "As a general principle, it is considered that it is neither possible nor desirable to quote a

Table 4 Summary of differences in discharge coefficients, ARL-BMI

Nozzle size in.	Tap #	Δ, %
8	1	−0.03
8	2	+0.01
8	3	+0.22
8	4	+0.09
12	1	−0.02
12	2	−0.08
12	3	−0.22
12	4	−0.07

best measurement capability for a flow calibration laboratory which is independent of the device being calibrated. At the same time, the quoted calibration results should, at the 95 per cent confidence level, be within a specified uncertainty band relative to the average results obtained by calibrating the same device at all 'approved' high accuracy laboratories either nationally or internationally." . . . "Reliance on static traceability chains to the national standards of mass, length, time, etc., alone in assessing the overall uncertainty of a laboratory flow calibration facility can result in significant under-estimates. . . . Dynamic traceability carried out under operating conditions supplements such static studies and exposes fresh sources of systematic and random uncertainties." . . . . "Even when a laboratory has been accredited with a specific uncertainty level, the problem arises of determining the additional installation uncertainties applicable to particular flow transducers." They reported intercomparison results between three laboratories in the U.K.: "In 1977, a turbine metering package consisting of a 150 mm (6 in.) nominal bore meter mounted with 15D straight length of pipe upstream and 5D downstream (with a tube bundle type flow straightener mounted at the inlet end of the upstream pipe) was circulated around three laboratories: NEL, CEGB, and Automatic Oil Tools Systems (AOT). . . . Briefly, the NEL and CEGB laboratories use the weight/time system with a diverter, and the AOT laboratory employs a large unidirectional meter prover." In this round robin, the meter was calibrated first at AOT and then returned there for recalibration before sending it out to the third laboratory. This method provided positive assurance that the bearing friction had not changed and the meter was functioning the same. They found that the difference between the calibration curves of the three amounted to 0.13 percent, using this meter assembly. Without this piping assembly, their experience showed a systematic uncertainty of ±0.25 percent, using the meter alone. Indeed the systematic uncertainties between laboratories for different kinds of meters were somewhat higher, probably caused by varying sensitivities to the different dynamic flow conditions between the labs. In their experience and judgement, they stated a value of ±0.3 percent even using the aforementioned piping arrangement, for vortex meters, magnetic meters, and orifice plates of $b > 0.5$.—and about double that if the integral piping were not used.

Turbine Meters and Hydrocarbon Liquid Calibrations. In my experience, whenever a fluid other than air or water is used, the systematic uncertainty increases at least in part because of the higher uncertainty of the properties of the calibrating fluid. Mattingly (1988) reported the results of intercomparisons of 13 laboratories whose business it is to calibrate fuel flow meters for performance testing of gas turbines. "Thermodynamic state properties are required to specify component conditions and fluid properties; rate measurements of materials (fuel and oxidizer) are critical to accurate engine assessment" . . . "To estimate the systematic error for a flow measurement laboratory, it is most realistic to do this using round robin testing results because all of the lab's routine procedures can be incorporated and evaluated."

The transfer standard meter run in these tests consisted of two turbine meters in tandem. In this way if any damage occurred to one meter or its bearing friction were to increase, comparison with the other meter would expose the change. In this situation, a test in the initiating laboratory can be followed in succession by tests in a large number of laboratories without the necessity of returning the meter run to the initiating laboratory until the round of testing is complete. In this series 20 calibrations were made in each laboratory at each of two flows (0.5 and 1.7 gpm nominal) for each meter in each upstream and downstream position. The 20 meter factors were averaged for each test for use in the intercomparison. The Reynolds number for the low flow was about 3700; that for the high was about 12,800; the liquid used was a standardized kerosene, MIL-C-7024 B-II. In the round robin were three government standards labs, five DoD labs, and five industrial labs. The data of interest here are summarized in Table 5.

Table 5 Tandem turbine meters calibrated in kerosene

Labs compared	Δ, %
Low flow:	
F-G	0.76
F-I	0.42
C-H	0.63
F-I	0.50
High flow:	
F-H	0.58
F-H	0.55
F-H	0.65
F-H	0.57

While it may be observed and objected that labs F and H appear too frequently, the data show that if either were discarded from the sample, the difference would be reduced only by 0.05 percent. Arguing against discarding any data, Dr. Mattingly has stated that both labs F and H are among the most highly regarded in the business. Since one can never know which lab may hold the truth, the absolute value of the maximum difference provides the logical starting point. The average value from Table 5 is ±0.58 percent, and to be 95 percent sure the systematic uncertainty is covered in the case of turbine flow meters calibrated for liquid hydrocarbon fuels, it is recommended that the value ±0.77 percent be used, based on the statistical distribution shown in Table 5.

Mass Flow Meter Calibrations. The measurement of mass flow directly, as with a Coriolis type meter, is inherently less accurate than is the measurement of volumetric flow. Conceptually this statement can be understood easily by the fact that, not only does one have to measure the volumetric flow as discussed above, but one must also simultaneously *measure* the fluid density while it is flowing. Consequently there are two major uncertainties, flow and density, which must be combined. In direct mass flow measurement, the sensitivity to this uncertainty is unity, while in differential pressure meters, it is $\frac{1}{2}$. Furthermore, in order to measure mass flow directly with a meter, it is necessary to add energy in some form to the flowing fluid. Measuring this rate of energy influx is such an additional source of uncertainty. Of course if this uncertainty is proved to be negligible relative to the other sources, then the two may give equivalent levels of accuracy.

Benedict and Wyler (1979) published the intercomparison of six identical mass flowmeters between two identical calibration stands: "The calibrations were repeated many times, thus the contribution of flow stand precision in the results was negligible. The per cent differences between the two flow stands for the calibrations of the six flowmeters are shown in in Table 6 for three flow rates." These are reprinted in Table 6.

Each of these values in Table 6 are differences in means of a large number of individual calibrations. Therefore there was

Table 6 Percent difference between mass flow stands

Flowmeter	Flow 1	Flow 2	Flow 3
1	−0.02	+0.01	+0.14
2	−0.12	+0.06	+0.08
3	−0.55	−0.99	1.02
4	−0.9	−0.89	1.02
5	−0.9	−0.3	0.66
6	−0.67	−0.86	−1.4
Averages =	−0.53	−0.49	0.66

a high degree of certainty that there was a systematic difference between the two flow stands—which is one of the great benefits of such intercomparisons. The average difference in Table 6 is −0.56 percent, and because of the scatter in the data, the 95 percent confidence value for the systematic uncertainty between the stands is −1.41 percent (using Student's t for 90 percent, because this is a one-sided estimate). The weigh scales were recalibrated, and one was found to be off by 0.59 percent, which contributed the majority of the bias. Correcting the data for that effect brought the average difference down to +0.028 percent. Now a true two-sided 95 percent confidence limit could be calculated, and it was found to be ±1.05 percent, which is the estimated systematic uncertainty between these two mass flow stands following recalibration.

Summary

The fundamental systematic uncertainty in every flow measurement is that inherited from the flow calibration laboratories. The only case in which this is the only systematic uncertainty to be applied to a flowmeter is when the entire flow metering assembly, from the flow conditioner and the recommended lengths of straight upstream and downstream piping for the meter *plus* the readout transducers (differential pressure transducers or blade-passing counters, for example) is moved intact from the laboratory to the plant test site. If anything were to be changed, such as the readout devices, the laboratory's systematic uncertainty must be augmented by that of the new readout device as well. We have found three classes of accuracy in the literature, the least accurate being flow calibrations of direct mass flow meters, the next being liquid hydrocarbon calibrations, and the most accurate being cold water calibrations. It should be obvious to even the casual reader that systematic uncertainties for *un*calibrated flow metering assemblies must be greater than those found and presented here.

Table 7 summarizes the results as described above for the water calibrations.

The modal and median values from Table 7 are both ±0.28 percent, indicating that the distribution is probably Guassian. The mean value is ±0.27 percent if we disregard the old data from 1941 and the data for the 0.8 β orifice plates (use of such high β differential pressure devices is not recommended in the Codes and Standards). A value of ±0.28 percent for the systematic uncertainty component charged to the laboratory calibration is recommended for water flow.

The interlaboratory comparisons for liquid hydrocarbon fuels in general, but most particularly those measured with turbine meters, cover 13 laboratories, which makes a good sample and provides pretty good reliability for the estimate of the systematic uncertainty. A value of ±0.77 percent is recommended in these instances.

Table 7 Water flow lab systematic uncertainties

Year	Bias, %	Authors
1991	0.06	Brown, T.
1981	0.13	Clay et al., metering section
1974	0.24	Spencer and Neale,
1981	0.25	Clay et al., meter only
1975	0.28	Benedict and Wyler.
1978	0.28	Levie, Clay, Miller, Spencer, and Upp,
1985	0.284	Brunkalla, R.
1982	0.29	Albert, Summer, and Halmi, and Brown
1960	0.4	Cotton and Westcott,
1974	0.5	Spencer and Neale,
1941	0.75	Bean, Beitler, and Sprenkle

There wasn't much data found regarding mass flowmeter calibrations. The small sample size and one intercomparison between two facilities doesn't provide a great deal of reliability for the recommended estimate of ±1.05 percent systematic uncertainty.

References

Albert, P. G., Sumner, W. J., and Halmi, D., "A Primary Flow Section for Use with the Alternative ASME Acceptance Test," ASME paper 82-JPGC-PTC-4.

Bean, H. S., Beitler, S. R., and Sprenkle, R. E., 1941, "Discharge Coefficients of Long-Radius Nozzles When Used With Pipe-Wall Pressure Taps," *Trans.* ASME, pp. 439–445.

Benedict, R. P., and Wyler, J. S., 1979, "Engineering Statistics—with Particular Reference to Performance Test Code Work," ASME *Journal of Engineering for Power.*

Brown, T. M. "Comparison of ASME Flow Nozzle Calibrations," Private Correspondence.

Brunkalla, R. 1985, "Effects of Fabrication Technique on the Discharge Coefficient of a Throat Tap Nozzle" ASME Paper 85-JPGC-PTC-3.

Cotton, K. C., and Westcott, J. C., 1960, "Throat Tap Nozzles used for Accurate Flow Measurements," ASME *Journal of Engineering for Power,* Oct., pp. 247–263.

Clay, C. A. E., Griffiths, C., and Spencer, E. A., 1981, "Improving the Confidence in Hydraulic Laboratory Calibrations," *Flow, Its Measurement and Control in Science and Industry,* Vol. 2, Durgin. W. W., ed. Instrument Society of America, Research Triangle Park, NC 27709, pp. 789–808.

Keyser, D. R., 1996, "How Accurate are Flow Calibrations Anyway?" *Proceedings of the 1996 International Joint Power Generation Conference,* PWR Vol. 30, Vol. 2, ASME H01077, pp. 131–138.

Levie, S. A., Clay, C. A. E., Miller R. W., Spencer, E. A., and Upp, I. 1978, *Flow Measurement of Fluids,* Dijstelbergen, H. H. and Spencer, E. A. eds., North-Holland Publisher, pp. 253–265.

Mattingly, G. E., 1988, "A Round Robin Flow Measurement Testing Program Using Hydrocarbon Liquids: Results for First Phase Testing," Sept., NISTIR 88-4013, Department of Commerce, National Institute of Standards and Technology, Gaithersburg, MD 20899.

Spencer, A., and Neale, L. 1974, "The Reliability of Test Data from Flow Measurement Calibration Laboratories," Flow, Its Measurement and Control in Science and Industry, *Flow Benchmarks: Principles,* Dowdell, R. B. ed.. Instrument Society of America, Pittsburgh, PA., pp. 1255–1266.

Wyler, J., and Benedict, R. P., 1974, "Comparisons between Throat and Pipe Wall Tap Nozzles," ASME Paper 74-WA/FM-3.

D. Maynes
Assistant Professor,
Department of Mechanical Engineering,
Brigham Young University,
Provo, UT 84602

J. Klewicki
Associate Professor.

P. McMurtry
Associate Professor.

Department of Mechanical Engineering,
University of Utah,
SLC, UT 84112

Time Resolved Torque of Three-Dimensional Rotating Bluff Bodies in a Cylindrical Tank

Torque measurements have been made on rotating three-dimensional bluff bodies in a cylindrical container from start-up to mean flow steady state. The flow is observed to pass through three distinct temporal regimes in the transient process. These regimes include a build-up period where the torque remains approximately constant, a decay period where the torque decreases, and a mean steady state where the mean torque remains at a constant level. Effects of body geometry, rotation rate, acceleration rate, and fluid height in the tank are quantified. The torque coefficient during the build-up and mean steady-state regimes is shown to be a function of Reynolds number and body geometry. A time scale marking the beginning of the decay period is presented in terms of the problem parameters. Over the range of parameters studied, the build-up, decay, and mean steady-state regimes are completely specified by the Reynolds number, geometric parameters, and decay time scale.

1 Introduction

The rotating flow field inside of a contained tank has received much attention since the early efforts of Couette (Couette, 1890 and Taylor, 1923). In 1936 Taylor performed his famous torque measurements with rotating cylinders (Taylor, 1936) which described the Reynolds number range over which stable flow existed and the transition to turbulence. Since these early efforts many investigators have focused on the Taylor-Couette flow problem and an exhaustive review is given by Andereck and Hayot (1992).

Several investigators have focused on the spin-up and spin-down of a fluid in a circular cylinder under laminar flow conditions (Wedemeyer, 1964; Greenspan and Howard, 1963; and Weidman, 1976). It has been shown that for spin-up (Greenspan and Howard, 1963) the flow consists of three distinct phases; the formation of an Ekman boundary layer, secondary flow, and the viscous decay of small residual oscillations. The secondary flow accounts for the advective transport of angular momentum from the walls to the interior. For spin-down to rest the flow always experiences a centrifugal instability, which ultimately disrupts the interior fluid motion (Taylor, 1936).

The flow past bluff bodies has also long been of interest to fluid dynamicists. Voluminous data has been collected on drag coefficients for arbitrarily shaped bluff bodies in a uniform flow. The separated flow past, and forces on, circular cylinders for example has received much attention (Deffenbaugh, 1976, Sarpkaya, 1966). At moderate to high Re, the flow past bluff bodies results in periodic vortex shedding on the leeside of the body. Rotating bluff body flows in a contained tank, however, are fundamentally different from rotating cylinders and uniform flows past bluff bodies because the body rotates in its own wake. At virtually all Reynolds number the flow field is separated, turbulent, three dimensional, and unsteady.

The most widely investigated flow field of this type is the flow induced by a rotating impeller in stirred mixing tanks. Numerous researchers have addressed this type of flow field with emphasis on the effects of impellers of different geometries on the flow field characteristics (Gunkel and Weber, 1975; Rushton et al., 1950; Rutherford et al., 1996). Most of the literature addressing stirred tank reactors, however, focuses on geometric ratios of the impeller radius, r_i, to tank radius, R, of 0.33–0.50 and impeller blade height, h_i, to tank height, H, of 0.05–0.07. A review of the literature also indicates that the transient evolution from a quiescent fluid to mean flow steady state has been largely unexplored. (Hereafter steady state refers to the mean flow steady-state condition.) The present work focuses on the evolution of the hydrodynamic torque from start-up to steady state and for a range of bluff body sizes with body height to tank height ratio, h/H, much larger than those explored for stirred tank reactors. The investigation was conducted by measuring the hydrodynamic torque on rotating bluff bodies from start-up to steady state. Experiments were conducted which quantified the effects of body size, rotation parameters, body vertical position, and liquid level in a cylindrical tank.

2 Experimental Techniques and Setup

2.1 Experimental Setup. Experiments were conducted in a 1 m^3 cylindrical tank located in the Physical Fluid Dynamics laboratory at the University of Utah. The facility is 152.4 centimeters tall and 91.44 centimeters in diameter. The liquid used for the investigation was distilled water at 20°C. The characteristic length of the tank is the tank radius R. A motor is located directly above the tank and connects to a shaft which is fixed to the bluff bodies. The motor is computer controlled via an indexer. Five bluff bodies were used in the investigation. All were square in cross section with various heights, h. The characteristic length, L, of the bluff bodies is taken to be the length from body center to a corner in a horizontal plane or $L = F(2)^{1/2}$ where F is the length of the body face as shown in Fig. 1. The nondimensional sizes of the bluff bodies used were $L^* = L/R = 0.15, 0.23, 0.31, 0.39, 0.7$ with the corresponding h to R ratio (body height over radius), $h^* = h/R = 1.05, 1.05, 0.48, 1.05, 0.72$.

2.2 Measurement of the Hydrodynamic Torque. The hydrodynamic torque is characteristic of the pressure and viscous forces exerted on the body by the fluid. The pressure forces, which dominate the hydrodynamic drag, result due to the separated flow along the body faces. As such, torque is also a good indicator of different physical regimes in the transient process. Although the measurement of the torque does not pro-

Contributed by the Fluids Engineering Division for publication in the JOURNAL OF FLUIDS ENGINEERING. Manuscript received by the Fluids Engineering Division November 5, 1996; revised manuscript received October 15, 1997. Associate Technical Editor: F. Giralt.

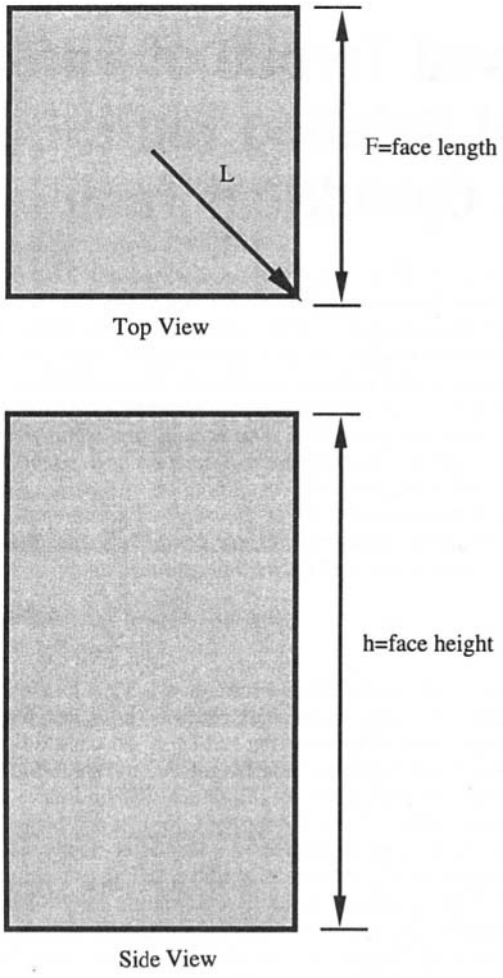

Fig. 1 Schematic of a typical bluff body with dimensions labeled. *h* is body height, *F* is length of the body face, and *L* is the distance in a horizontal plane from body center to a corner.

vide a detailed description of the velocity and/or vorticity fields, it does a provide important insight into the integral behavior of the flow field. Two Key Transducer torque meters were used in the investigation. The output from the transducers is a voltage signal with values between −5 and 5 volts and are accurate to within ±0.05 percent of full scale. The voltage output is proportional to the measured torque where full scale corresponds to 22.6 N-m and 0.706 N-m for the two transducers, respectively. The value of the measured torque varies more than three orders of magnitude from 0.011 N-m with $L^* = 0.15$ and $\mathrm{Re} = 9.42 \times 10^3$ to 48 N-m with $L^* = 0.70$ and $\mathrm{Re} = 5.7 \times 10^5$. The signal from the torque meter is connected to a IOtech 16-bit A/D converter interfaced to a workstation. Figure 2 shows a schematic of the tank, bluff body, motor, torque meter, PC motor controller, and the data acquisition equipment.

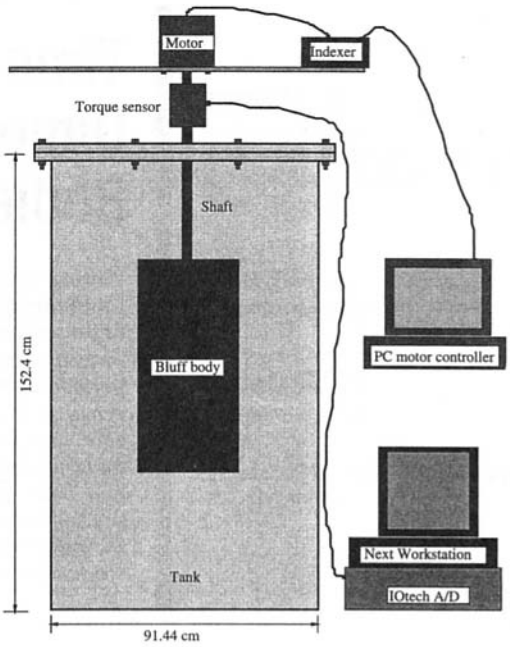

Fig. 2 Schematic of experimental facility, typical bluff body, motor and controller and data acquisition equipment

2.3 Nondimensional Parameters. The transient torque can be written as a function of nine geometric and rotational parameters in addition to the fluid properties;

$$T = F(L, h, R, H, \omega, \alpha, \rho, \nu, t) \tag{1}$$

A dimensional analysis reduces the number of independent parameters to six, the torque coefficient, C_m, can be written as a function of these independent parameters as follows;

$$C_m = F(\mathrm{Re}, t^*, \quad h^*, \quad L^*, \quad H^*, \quad \alpha^*) \tag{2}$$

$$C_m = \frac{T}{\frac{1}{2}\rho V^2 SL}, \quad \mathrm{Re} = \frac{\omega L^2}{\nu}, \quad S = Lh \tag{3}$$

$$V = \omega(t)L, \quad L^* = \frac{L}{R} \tag{4}$$

$$h^* = \frac{h}{R}, \quad H^* = \frac{H}{R}, \quad \alpha^* = \frac{\alpha}{\omega^2} \tag{5}$$

$$t^* = \tfrac{1}{2}\alpha t^2 \quad \text{if} \quad t < t_o \text{ where } t_o = \frac{\omega}{\alpha}$$

$$t^* = \omega(t - t_o) + \tfrac{1}{2}\alpha t_o^2 \quad \text{if} \quad t \geq t_o \tag{6}$$

The Reynolds number appears as the rotation rate times L^2 divided by ν, and t^* is the number of revolutions the body has

Nomenclature

C_m = torque coefficient ($T/(1/2rV^2SL)$)
F = length of body facd (cm)
h = body height (cm)
h^* = nondimensional body height (h/R)
H = fluid height in tank (cm)
H^* = nondimensional fluid height (H/R)
L = characteristic body length ($\sqrt{2}(F/2)$), (cm)
L^* = nondimensional body length (L/R)
R = tank radius (cm)
Re = Reynolds number (wL^2/ν)
S = characteristic body area (hL)
t^* = nondimensional time (t^* = revolutions)
$\tau = (t^*(L^{*2})(h/H)$
T = torque (N-m)
V = characteristic velocity (ωL, cm/s)
α = angular acceleration ($1/s^2$)
ω = angular rotation rate (1/s)
ν = kinematic viscosity (m^2/s)
ρ = fluid density (kg/m^3)

Table 1 Nondimensional parameter ranges investigated

Re	$L^* = L/R$	$H^* = H/R$	$h^* = h/R$	$\alpha^* = \alpha/\omega^2$
6300–62800	.15	3.33	1.05	.25–25
14100–141400	.23	3.33, 2.66, 2.11, 1.66	1.055	.0025–250
25100–251200	.31	3.33	0.48	.25–25
39300–292500	.39	3.33, 2.66, 2.11, 1.66	1.055	.0025–250
31800–572600	.7	3.33	0.72	1.–25

traveled. C_m is equal to the torque normalized by the dynamic pressure multiplied by the characteristic area, S, and length, L. L^*, h^*, and H^* are geometric parameters and represent the tank and body geometries and α^* is the normalized angular acceleration. The properties, ρ and ν were obtained for water at 20°C.

2.3 Experimental Procedure. Experiments were conducted over a range of nondimensional parameters for each of the five bluff bodies. Baseline experiments were run with the tank completely filled. This condition results in the development of a boundary layer on the top surface of the tank. The bluff bodies were positioned such that their uppermost surfaces were 46 cm below the top of the tank. The effects on the torque were quantified for different geometry and rotation parameters by varying the independent nondimensional parameters. Ranges of the nondimensional parameters investigated for each body are listed in Table 1. Experiments were conducted over as large as Reynolds number range as possible within the limits of the motor capability and the range of the torque transducers. This results in data sets wherein the Reynolds number range is not the same for the five different bodies. Experiments were thus performed with significant overlap in the Reynolds number so that comparisons can be made between the different bodies at similar Re.

All of the experiments were conducted in the following manner. The fluid was allowed to come to rest prior to initiation of rotation. Motion was initiated and the data acquisition system was triggered by the rotational motor drive. Rotation continued until the mean flow steady-state condition was maintained long enough to reliably quantify the mean flow steady-state torque.

For each set of data, the resulting torque is a combination of the hydrodynamic torque, torque required to overcome inertia in the ramp up to constant ω, and torque required to overcome friction in the shaft bearings. For all cases presented the torque to overcome inertia is small—only of concern in the acceleration region. This is because the inertia of the bodies is small and high accelerations were not used. For the highest α and largest body used the torque required to overcome inertia was only about 1 percent of the maximum torque in the acceleration period. The bearing friction torque was quantified by measuring the torque with the tank empty. These measurements were very repeatable with different sizes of bodies mounted to the shaft. It was found, as expected, that the friction torque was only a function of rotational velocity. The value of this torque increases from 0.002 N-m at $\omega = 0.2$ rps to 0.006 N-m at $\omega = 2.0$ rps. and the magnitude was in all cases very small compared to the hydrodynamic torque.

3 Results

3.1 Body Size and Rotation Rate Effects. Figure 3 shows the transient hydrodynamic torque plotted versus time at Re = 1.25×10^4, 2.83×10^4, 4.40×10^4, 6.28×10^4, and at $L^* = 0.15$. The data are plotted on log coordinates in this figure and most figures presented because the data typically span over two orders of magnitude on at least one axis. Constant ω is reached at early times, $(O(1)s)$ for all cases, and the point

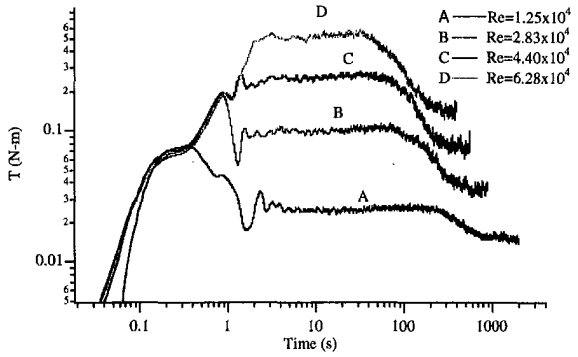

Fig. 3 Torque (N-m) versus time for $L^* = 0.15$, $h^* = 1.05$, $H^* = 3.33$ and at four Re. $\alpha = 1.0$ rps^2 for all cases.

at which acceleration ceases is characterized by a peak in the torque followed by a slight decrease. Once constant ω is reached the torque remains approximately constant for some time. We call this time of constant torque the build-up regime. As can be seen, the duration of the build-up regime depends upon the Reynolds number. At the end of the build-up regime the torque starts to decay, called the decay regime, until the flow field reaches steady state. At this time the torque levels off to a minimum value with some fluctuation induced due to the turbulent nature of the flow field. As Re increases, the value of the torque increases at all points along the curve. After the decay regime this increase is from about .015 N-m at Re = 1.25×10^4 to about 0.15 at Re = 6.28×10^4. Additionally, the difference in the magnitude of the torque in the build-up regime to that at steady state increases from about 0.01 at Re = 1.25×10^4 to about 0.4 at Re = 6.28×10^4 and the rate of decay increases with increasing Re. As is evident from Fig. 3, the time when decay begins decreases for increasing ω.

Figure 4 displays C_m versus t^* (recall t^* = number of revolutions) for the same data of Fig. 3. Note that the value of C_m in the build up regime is approximately the same for the four sets of data at about 0.55. In the steady-state regime, however, the magnitude of C_m decreases with increasing Re. Also, the point at which decay begins is approximately the same t^* for all rotation rates. This value is approximately 65 revolutions and suggests that for fixed L^*, ω^{-1} is the appropriate time scale for normalization.

Only results from $L^* = 0.15$ are shown in Figs. 3 and 4, however, this behavior is exhibited in a similar fashion by all our data for the different L^*. Figure 5 displays C_m versus t^* data for each of the five bodies employed and at Re = 3.14×10^4, 7.07×10^5, 1.25×10^5, 1.96×10^5, and 2.54×10^5. The value of C_m in the build-up regime varies from about 0.55 for $L^* = 0.15$ to about 0.90 for $L^* = 0.70$. This increase is

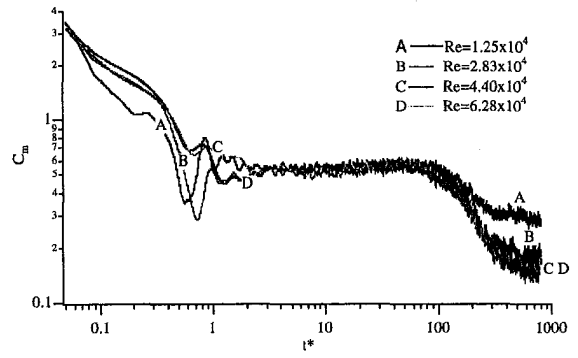

Fig. 4 C_m versus t^* for $L^* = 0.15$, $h^* = 1.05$, $H^* = 3.33$ and at four Re. $\alpha = 1.0$ rps^2 for all cases.

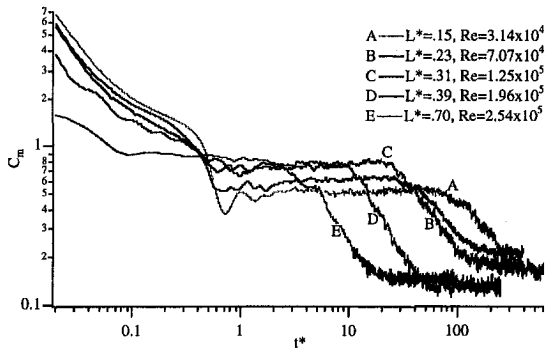

Fig. 5 C_m **versus** t^* **for** $L^* = 0.15, 0.23, 0.31, 0.39$, **and 0.70,** $h^* = 1.05, 1.05, 0.48, 1.05$, **and 0.70,** $H^* = 3.33$ **and at five Re.** $\alpha = 1.0$ **rps**^{2} **for all cases.**

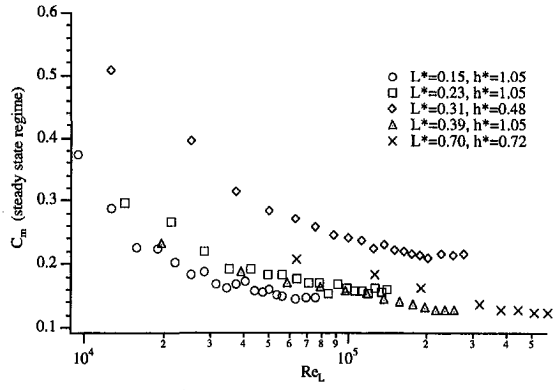

Fig. 7 Mean steady-state value of C_m **versus Re for** $L^* = 0.15, 0.23, 0.31, 0.39$, **and 0.7 and** $h^* = 1.05, 1.05, 0.48, 1.05$ **and 0.70**

not a function of L^* only as is shown by the $L^* = 0.31$ and $L^* = 0.39$ cases. C_m in the build-up regime is very similar for both of these cases although L^* varies by a factor of 1.25 and h^* varies by a factor of 2. Over the entire Re range investigated for each L^*, the value of C_m in the build-up regime is very similar to the respective values shown in Fig. 5. For each L^* the decay regime begins at a different value of t^*. The t^* where the decay regime begins, however, remains constant if L^* is held constant but Re changes. The t^* when decay begins for each body is noted from Fig. 5 to be about 65 for $L^* = 0.15$, 30 for $L^* = 0.23$, 25 for $L^* = 0.31$, 10 for $L^* = 0.39$, and 2.5 for $L^* = 0.7$.

Experiments were conducted over the range $9.0 \times 10^3 \leq \text{Re} \leq 6.0 \times 10^5$ to quantify the behavior of C_m with Re in the build up and steady-state regimes. These results are presented in Figs. 6 and 7 where C_m is plotted versus Re. Figure 6 plots C_m from the build-up regime versus Re for the five L^* whereas Fig. 7 plots C_m for the steady-state regime over the same Re range. It is evident from Fig. 6 that for fixed L^* the magnitude of C_m in the build-up regime remains approximately constant over the Re ranges investigated. Similar behavior is observed for a cylinder or sphere in cross flow where the drag coefficient, C_d, remains relatively constant over a wide range of Re and suggests that the body induced wake structure does not change significantly. Note also that the magnitude of C_m in this regime is a function of both L^* and h^*. Conversely, it appears from Fig. 7 that in the steady-state regime C_m depends strongly upon h^* but shows only slight variations for different L^*. These C_m data exhibit a decrease in magnitude as Re increases for all five L^*. The importance of this data is that given a Reynolds number in the range investigated, C_m can be closely estimated for both the build up and steady-state regimes over the range of L^* and h^* presented in Figs. 6 and 7. Variations in C_m at steady state cannot be assessed from Fig. 7. This will require data over a larger Re range.

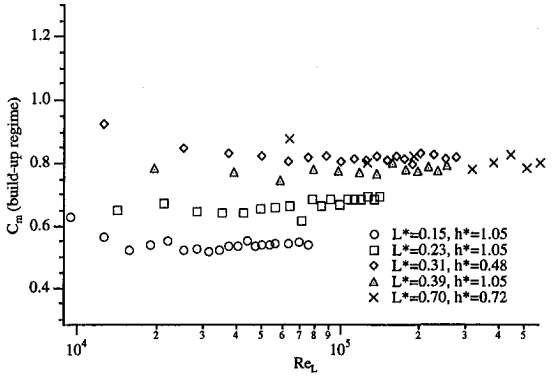

Fig. 6 Build-up regime value of C_m **versus Re for** $L^* = 0.15, 0.23, 0.31, 0.39$, **and 0.7 and** $h^* = 1.05, 1.05, 0.48, 1.05$ **and 0.70**

3.2 Discussion and Nondimensional Time Scaling. A physical description of the evolving flow field from the torque measurements and flow visualization studies is postulated. Prior to start-up the entire flow field is at rest and thus has zero momentum. As the body is brought into motion vortices are shed from the corners of the body creating a wake or separated regions next to the body faces and momentum is transferred to the fluid from the body. As the fluid near the body gains momentum, or velocity, this fluid convects radially outward due to an unbalance in the centrifugal force. These turbulent motions act to transport fluid with momentum greater in magnitude than zero away from the body and replace it with fluid exhibiting zero or low magnitude momentum. Thus, the magnitude of the torque in the build-up regime remains constant in the mean because the body is always acting upon low magnitude (close to zero) momentum fluid. Consequently, the structure of the separated regions near the body remain similar for the duration of the build-up regime.

At the time when decay begins the entire fluid volume has been affected by the rotating body and thus the momentum of all of the fluid in the tank has increased. Thus the force exerted by the fluid on the rotating body decreases and results in a decaying torque magnitude with time. As energy continues to be added to the fluid in the tank volume a point is gradually reached (the end of the decay regime) when production, energy input, is balanced by viscous dissipation. At this time the torque remains at a constant mean value corresponding to the steady-state regime.

A nondimensional time scale, which results in the merging of the data for all L^*, H^*, and h^* in a temporal sense, is

$$\tau = t^* \frac{L^{*2}h^*}{H^*} \quad \text{or} \quad \tau = t^* \frac{L^2 h}{R^2 H} \tag{7}$$

This normalization contains the three-nondimensional geometric parameters L^*, h^*, and H^* and nondimensional time t^*. C_m plotted versus τ is presented in Fig. 8 for the five L^*, five Re, and three h^*. Physically $(L^{*2})(h^*/H^*)$ is the ratio of body volume to tank or liquid volume. The nondimensional time scale, τ, also represents an order of magnitude ratio of the total kinetic energy added to the flow by the body rotation, $(\omega L)^2 L^2 h \omega t$, and the kinetic energy of the entire flow field when steady state is attained, $(\omega L)^2 R^2 H$. The value of τ is about 0.5 when C_m starts to decay and is about 3.0 when steady state is attained. These values are consistent for all our data. This time scaling, along with the C_m versus Re relationships shown in Figs. 6 and 7 provide a general relationship of C_m from $\tau = 0.01$ to steady state for $9.0 \times 10^3 \leq \text{Re} \leq 6.0 \times 10^5$ and over the L^* and h^* parameters investigated.

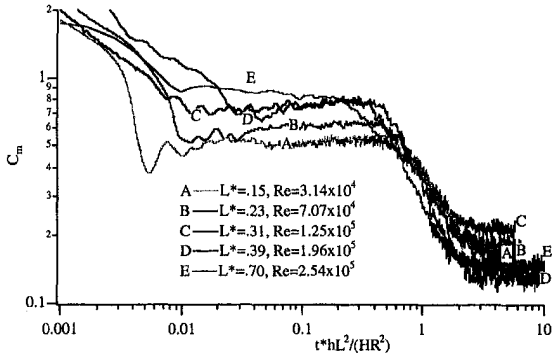

Fig. 8 C_m versus τ for $L^* = 0.15$, 0.23, 0.31, 0.39, and 0.7, $h^* = 1.05$, 1.05, 0.48, 1.05, and 0.70, $H^* = 3.33$ and at five Re. $\alpha = 1.0$ rps^2 for all cases

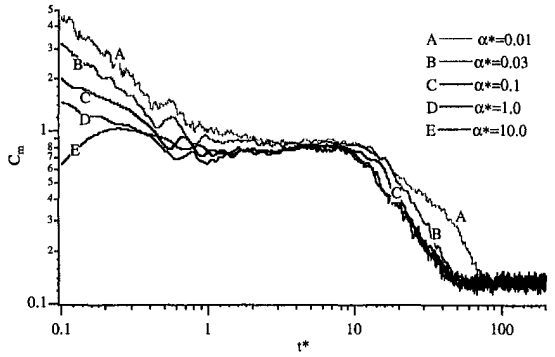

Fig. 10 C_m versus t^* for $L^* = 0.39$, $h^* = 1.05$, $H^* = 3.33$, Re $= 1.96 \times 10^5$ and five α^*

3.3 Acceleration Effects. For α of order one and greater, constant ω is attained quickly relative to the flow field evolution. The effects of α less than one were quantified by varying α while holding ω constant for three different ω and for all L^*. Because the results are qualitatively similar for different ω and L^*, only data for the $L^* = 0.39$ and Re $= 1.25 \times 10^5$ case are presented. Figure 9 plots torque versus time for $\alpha^* = 0.01$, 0.03, 0.1, 1.0, and 10.0. For $\alpha^* = 10.0$ and 1.0 the behavior is described in Section 3.1. The torque reaches a value of about 9 N-m and stays constant until it starts to decay after about 10 seconds. As α^* decreases so also does the duration that the torque remains at a constant value. Note that for $\alpha^* = 0.1$ the torque attains a magnitude of about 9 N-m at about 12 seconds and then the decay starts immediately. For $\alpha^* = .03$ and .01 the torque never reaches this level prior to decay. At $\alpha^* = 0.03$ the maximum value is about 7 N-m and is attained at 33 seconds. For $\alpha^* = 0.01$ the maximum torque is about 3 N-m and is reached in 100 seconds. When T is normalized by body size and $\omega(t)$ to give C_m, the behavior of C_m versus t^* displays interesting differences for low α^*. This normalization is shown in Fig. 10. The magnitude of C_m is about 0.8 for all cases up to $t^* \approx 10$. Above $t^* \approx 10$ C_m begins to decay. The decay is similar for $\alpha^* = 0.1$, 1.0, and 10.0. The point at which decay begins, however, shifts to slightly greater t^* as α^* decreases below 0.1. The decay of the torque curves for $\alpha^* = 0.03$ and 0.01 is significantly different than for the other cases. Although C_m appears to start to decay at $t^* \approx 10$ for all cases it does not reach its steady-state value until $t^* \approx 80$ for $\alpha^* = 0.01$. Conversely, steady state was reached at $t^* \approx 40$ for each of the other four cases. Additionally, the rate of decay does not remain constant but changes during the decay regime for both $\alpha = 0.03$ and 0.01. The reason for this can be determined from Fig. 9. As noted above, for low α^* (0.01, 0.03) the torque does not reach the same magnitude as for the cases with $\alpha^* = 10.0$, 1.0 and 0.1. Thus, the body is still accelerating at the t^* when the entire flow field has been affected by the rotating body. Consequently, the magnitude of the torque decreases because fluid with increasing momentum acts on the body, but increases at a faster rate because the body is still accelerating. When acceleration ceases, the magnitude of the measured torque quickly decreases. Thus there are regions with different decay slopes on Fig. 10 for the low α^* cases.

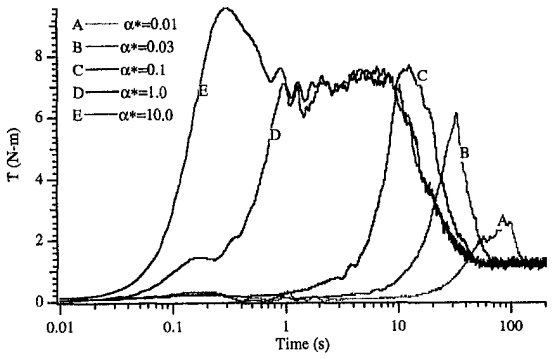

Fig. 9 Torque versus time for $L^* = 0.39$, $h^* = 1.05$, $H^* = 3.33$, Re $= 1.96 \times 10^5$ and five α^*

It was previously noted that decay began for all cases at $\tau \approx 0.5$ where $\tau = t^*L^{*2}h^*/H^*$ for $\alpha^* = 1.0$. During the acceleration period $t^* = \frac{1}{2}\alpha t^2$ and the time when acceleration ceases is ω/α. Substituting ω/α for t and thus $\frac{1}{2}\alpha(\omega/\alpha)^2$ for t^* into the expression for τ, Eq. (8) is obtained.

$$\frac{L^{*2}h^*}{\alpha^* H^*} = 1.0 \tag{8}$$

If the left-hand side of Eq. (8) is greater than or equal to one the rate of decay will initially be slower than if this quantity is less than one. In other terms, if $\alpha^* \geq L^{*2}h^*/H^*$ (case A) than decay will begin at $\tau \approx 0.5$, the rate of decay will exhibit one slope, and steady state will be attained at $\tau \approx 3.0$. For $\alpha^* \leq L^{*2}h^*/H^*$ (case B) two decay slopes will be exhibited and steady state will be attained at $\tau > 3.0$. For $L^* = 0.39$ and Re $= 1.25 \times 10^5$, the minimum α^* for case A is 0.048. Note that from Fig. 10 the two data sets with $\alpha^* < 0.048$ all exhibit behavior similar to case B. All of our data support this observation. For $L^* = 0.23$ and $h^* = 1.05$ the minimum α^* for case A is 0.017. Data for this L^* and h^* indeed show that for $\alpha^* > 0.017$ the data exhibits case A behavior. Furthermore, the individual data sets of C_m versus t^* cannot be distinguished from the others. At $\alpha^* = 0.01$ the $L^* = 0.23$ data show only a slight variation from the case A behavior.

3.3 Liquid Level and Body Position Effects. The effect of liquid height on the torque was characterized by successively lowering the water level in the tank. These levels resulted in the free surface occurring at 5.08 cm, 30.48 cm, 55.88 and 76.2 cm below the top of the tank. Figure 11 presents data quantifying the effects of water height on C_m. The data in Fig. 11 is C_m versus t^*h^*/H^* with $L^* = 0.39$ and at the four water levels listed above. The horizontal axis is simply the nondimensional time, τ, without the L^{*2} factor. This is justified because L^* is the same for all data of Fig. 11. The Re and α^* are the same for all cases presented and are 1.96×10^5 and 1.0, respectively. Reynolds numbers of Re $= 9.8 \times 10^4$, 2.94×10^5 and $\alpha^* = 0.01$, 0.03, and 0.1 were also investigated with the differences in the results showing similar behavior as the results of Sections 3.1 and 3.2. Experiments showing similar behavior were also conducted with $L^* = 0.23$ over the parameter ranges shown in Table 1. As H^* decreases, the t^*h^*/H^* when C_m starts to decay is the same for all cases. The rate of decay is approximately the same for all cases.

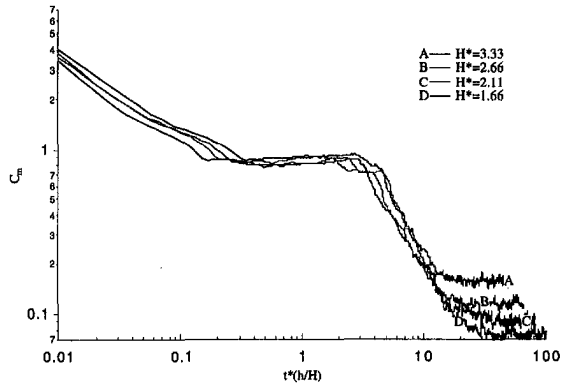

Fig. 11 C_m **versus** t^*h^*/H^* **for** $L^* = 0.39$, $h^* = 1.05$, $\alpha^* = 1.0$, Re $= 1.96 \times 10^5$ **and at four** H^*

When steady state is attained, the magnitudes of C_m for the four different cases are markedly different and are proportional to the tank water level, H. For $L^* = 0.39$ C_m is about 0.075 at $H^* = 1.66$, 0.1 at $H^* = 2.11$, 0.12 at $H^* = 2.66$ and 0.15 for $H^* = 3.33$. The same trend exists for the $L^* = 0.23$ data. Also note from Fig. 11 that the value of t^*h^*/H^* when steady state is attained increases with decreasing water level indicating different steady state conditions are attained. The case of $H^* = 3.33$ corresponds to the tank being completely filled so that a boundary layer exists on the upper surface. For a few cases the water level was dropped so that the effects of the free surface, if any, would be evident. Thus, experiments were also conducted with $H^* = 3.22$. The data corresponding to $H^* = 3.22$ were very similar to the $H^* = 3.33$ data. Differences in the two sets of data were indistinguishable.

At each H^* the location of the bluff body was adjusted to different vertical, Z, positions to quantify the effects of body position relative to the tank top and bottom for the transient process. These positions were 28.3, 38.4, 48.6, and 58.8 cm below the fluid surface with $H^* = 2.66$. For all of the data collected, adjusting the vertical position of the body had a negligible effect, both temporally and in magnitude, on the measured transient torque.

4 Conclusions

Torque data have been collected for rotating bluff bodies in a cylindrical tank. These data indicate that three distinct temporal regimes exist in the curves of C_m versus t^* during the transient process. These regimes are a build-up regime, where C_m remains relatively constant, a decay regime, and a mean flow steady-state regime. A nondimensional time scale, τ, was defined based upon the rotational and geometric parameters. Plotting the C_m data versus τ caused the data to decay at a fixed value regardless of L^*, h^*, or H^*. This time scale contains the ratio of body volume to tank volume. In general, for τ about 0.5, the decay of C_m begins, and continues until τ about 3.0 at which point the flow has reached steady state. The value of C_m is a function only of L^* and h^* in the build-up regime where it approaches a value between 0.5 and 1.0, and is a function of Re, L^*, h^*, and H^* at steady state. At steady state the value of C_m is proportional to the height of the water in the tank. Varying the z-position of the body inside the tank had no distinguishable effect upon the torque throughout the entire transient process. The effects of acceleration were investigated and it was observed that for α^* greater than $L^{*2}h^*/H^*$, the mean flow steady state was attained at $\tau \approx 3.0$. If α^* was decreased below $L^{*2}h^*/H^*$, the t^* when steady state was attained increased above 3.0. During the build-up regime and at steady state, the magnitude of C_m does not depend upon α^*.

Acknowledgment

This work was funded by Lawrence Livermore National Laboratory under contract #B301530.

References

Andereck, C. D., and Hayot, F., 1992, *Ordered and Turbulent Patterns in Taylor-Couette Flow,* Plenum Press, New York.

Couette, M., 1890, "Etudes Sur le Frottment des Liquides," *Annales de Chimie et de Physique,* Ser VI, Vol. 21, pp. 433–510.

Deffenbaugh, F. D., 1976, "Time Development of the Flow About an Impulsively Started Cylinder," *AIAA Journal,* Vol. 14, pp. 908–913.

Greenspan, H. P., and Howard, L. N., 1963, "On a Time-Dependent Motion of a Rotating Fluid," *Journal of Fluid Mechanics,* Vol. 17, Part 3, pp. 385–404.

Gunkel, A. A., and Weber, M. E., 1975, "Flow Phenomena in Stirred Tanks," *AIChE Journal,* Vol. 21, No. 5, pp. 931–949.

Rushton, J. H., Costich, E. W. and Everett, H. J., 1950, "Power Characteristics of Mixing Impellers Part II," *Chemical Engineering Progresses,* Vol. 46, No. 8, pp. 467–477.

Rutherford, K., Mahmoudi, M. S., Lee, K. C., and Yianneskis, M., 1996, "The Influence of Rushton Impeller Blade and Disk Thickness on the Mixing Characteristics of Stirred Vessels," *Transactions of the Institution of Chemical Engineers,* Vol. 74, Part A, pp. 369–378.

Sarpkaya, T., 1966, "Separated Flow About Lifting Bodies and Impulsive Flow About Cylinders," *AIAA Journal,* Vol. 4, pp. 414–420.

Taylor, G. I., 1923, "Stability of a Viscous Liquid Contained Between Two Rotating Cylinders," *Philosophical Transactions of the Royal Society,* Series A223, p. 289.

Taylor, G. I., 1936 "Fluid Friction Between Rotating Cylinders I. Torque Measurements," *Proceedings of the Royal Society,* London, Series A, Vol. 157, p. 494.

Wedemeyer, E. H., 1964, "The Unsteady Flow Within a Spinning Cylinder," *Journal of Fluid Mechanics,* Vol. 20, Part 3, pp. 383–399.

Weidman, P. D., 1976, "On the Spin-up and Spin-down of a Rotating Fluid. Part 1," *Journal of Fluid Mechanics,* Vol. 77, pp. 685–708.

Direct Measurements of Turbulent Boundary Layer Wall Pressure Wavenumber-Frequency Spectra

B. M. Abraham
Mechanical Engineer.
Mem. ASME

W. L. Keith
Mechanical Engineer.
Mem. ASME

Submarine Sonar Department,
Naval Undersea Warfare Center
Division Newport,
Newport, RI 02841-1708

Direct measurements of streamwise wavenumber-frequency spectra of turbulent wall pressure fluctuations were made in an acoustically quiet water tunnel. A linear array of evenly spaced flush mounted pressure sensors was used to measure the wall pressure field at 48 streamwise locations. This array provided over 24 dB of resolution (sidelobe rejection) in the wavenumber domain, leading to an accurate estimate of the "convective ridge" and part of the subconvective and low wavenumber portions of the spectrum at discrete frequencies. Boundary layer parameters, including the mean wall shear stress, boundary layer thickness, displacement thickness, and momentum thickness, were derived from mean streamwise velocity measurements for $8100 < R_\theta < 16{,}700$. Time and length scales derived from these parameters were used to nondimensionalize the measured spectra. The effectiveness of different scalings for nondimensionalizing the low and convective wavenumber regions at discrete frequencies was evaluated.

Introduction

The fluctuating wall pressure field beneath a turbulent boundary layer is the primary source of structural excitation and associated radiated noise for aircraft and marine vehicles and acoustic arrays of microphones or hydrophones. Estimates of the spectral levels at low and also higher wavenumbers are required in the structural design of vehicles. The low wavenumber levels are important since structural resonances often occur at low wavenumbers and acoustic signals are usually received at a relatively low wavenumber compared to the convective turbulent energy. However, the higher convective wavenumbers also need to be resolved since this is where the greatest levels of turbulent energy exist. The wavenumber-frequency spectrum is often used to characterize the stationary aspects of the turbulent boundary layer wall pressure. Two-point measurements have been used to infer the wavenumber-frequency characteristics of the wall pressure from the cross-spectrum. Even though such measurements have been valuable in modeling efforts, they often lack the spatial resolution needed to resolve the wavenumber-frequency spectrum. One exception is the investigation of Panton and Robert (1994) which had excellent spatial resolution for a flat plate turbulent boundary layer in air. They also recommended a wavenumber-phase velocity scaling for the wavenumber-frequency spectrum, unlike the current investigation which seeks to non-dimensionalize and scale the spectrum at a fixed frequency as a function of wavenumber.

Few direct measurements of wavenumber-frequency spectra have been made in experimental facilities. Wills (1970) measured two-point wall pressure cross-spectra in a wind tunnel and then used a spatial Fourier transform to obtain an estimate of the wavenumber-frequency spectrum. Both streamwise and spanwise spectra were presented. Wills' estimate of the wavenumber-frequency spectrum was limited to the region in wavenumber near the convective ridge. The limitations were primarily due to phase matching of the electronics and acoustic contamination in the test section. A comparison of Wills' streamwise wavenumber-frequency data with the present and other investigations is given later. Wills also introduced the wavenumber/phase velocity representation of the wall pressure data. Blake and Chase (1971) measured the wavenumber-frequency spectrum at fixed wavenumbers using common and alternating phase arrays of four microphones in a wind tunnel. The frequency spectra from the array outputs showed a definite peak where the convective ridge occurred. Acoustic noise in the duct test section and sidelobe performance of the spatial filters were limiting factors.

Sherman et al. (1990) obtained wave-vector frequency estimates of the wall pressure using two sets of 11 by 11 hydrophone arrays (fixed spacing) mounted to a buoyant test vehicle in water. Despite the small number of sensors in either the streamwise or spanwise direction, the convective ridge energy was resolved at lower frequencies, although there was some contamination from the vibration of the test vehicle. Sherman et al. did not measure or estimate the boundary layer parameters for the three speeds used in that experiment. Farabee and Geib (1991) used a phased array of six pressure sensors to measure the wavenumber-frequency spectrum of wall pressure at fixed wavenumbers in a wind tunnel. The low number of sensors limited the sidelobe rejection of the wavenumber filters. Karangelen et al. (1991) estimated the wavenumber-frequency spectrum by transforming the cross-spectrum through curve-fitting the coherence and phase (for a flat plate turbulent boundary layer in air). The resulting estimates of the wavenumber-frequency spectra were very sensitive to the values of the phase near zero separation. This may explain why the low-wavenumber levels are predicted to be higher than the Corcos model and other experiments.

Manoha (1991) performed a direct measurement of the wavenumber frequency spectrum of wall pressure over a cylindrical body using 32 transducers in air. Although the array in Manoha's experiment was carefully calibrated, the measurements were limited at low wavenumber by background facility noise. Herbert and Leehey (1992) estimated the streamwise and spanwise wavenumber-frequency spectrum by transforming their cross-spectral measurements from a wind tunnel with and with-

Contributed by the Fluids Engineering Division for publication in the JOURNAL OF FLUIDS ENGINEERING. Manuscript received by the Fluids Engineering Division July 15, 1996; revised manuscript received September 11, 1997. Associate Technical Editor: F. Hussain.

out a boundary layer manipulator (consisting of honeycomb sections) in place. There was significant acoustic noise in the baseline data which prevented conclusions to be drawn regarding low wavenumber levels, but the convective ridge levels were resolved.

The simulations given by Choi and Moin (1990) have shown spectra which agreed with other numerical results in the convective ridge region, but have higher levels at lower wavenumbers. As a result, extrapolation of such low Reynolds number simulations ($R_\theta \approx 280$) to much higher Reynolds number flows typical of hydrodynamic or aerospace applications is not possible.

Panton and Robert (1994) transformed the cross-spectrum of wall pressure data from a wind tunnel to obtain the wavenumber-frequency spectrum as was done by Wills (1970). They deduced that the asymmetrical shape in streamwise wavenumber of the wavenumber-frequency spectrum was due to the spatial character of the convection velocity. Using the Corcos (1963) model, Keith and Abraham (1997) showed quantitatively how this spatial variation in the measured convection velocity has a significant effect on the wavenumber-frequency spectrum at low wavenumbers. They attributed the overprediction of low wavenumber levels using the Corcos model, as discussed by Smol'yakov and Tkachenko (1983), to this effect. Chase (1987) has proposed a model which more accurately predicts the subconvective low wavenumber levels. Recently, Manoha (1996) has directly measured the streamwise wavenumber-frequency spectrum of the wall pressure in a flat plate boundary layer in water. He used an array of 32 flush mounted sensors and compared his results to several semi-empirical models.

The objective of the current investigation is the direct measurement of the streamwise wavenumber frequency spectrum $\Phi(k_x, \omega)$ of wall pressure fluctuations beneath an equilibrium turbulent boundary layer using an array of equally spaced sensors. By covering a range of Reynolds numbers, the scaling laws for the spectra are determined from the measured boundary layer length and time scales. The direct measurement method will yield the same estimate of the wavenumber-frequency spectrum as that from transforming two-point cross-spectrum measurements. However, the direct method has advantages in that sensors do not need to be moved and any alignment errors are essentially constant. The use of pressurized water as a working fluid severely limits the use of a moving second sensor in the test section. Additionally the direct measurement method would be needed for a nonstationary flow, such as an accelerating flow, because pressure data is required from many locations at the same absolute time for estimation of the wavenumber-frequency spectrum.

Facility Description and Experimental Configuration

The experiments were conducted in the Quiet Water Tunnel Facility at the Naval Undersea Warfare Center Detachment, New London, CT (now located in Newport, RI). A flow schematic of the water tunnel is shown in Fig. 1. The water tunnel was designed with acoustic isolation provided by rubber hoses between the major components to minimize transmission of acoustic energy and vibration. A heat exchanger allows the water temperature to be held constant during data acquisition. The speed is controlled by a fluid clutch and centrifugal pump. The centerline streamwise mean velocity is held constant within 0.015 m/s using a closed-loop control system.

The interior of the rectangular test section is 210.82 cm long, 30.48 cm wide, and increases in height linearly from 10.16 cm at the inlet to 11.20 cm at the exit. This divergence in height compensates for the boundary layer growth on the tunnel walls, such that the dynamic head and static pressure over the length of the test section is constant within 1 percent. The boundary layers grow over the length of the test section but never interact. Measurements of the cross spectrum between sensors measured on opposite walls (Keith and Barclay, 1993) of the test section revealed no coherent energy from the turbulent wall pressure fluctuations.

Immediately upstream of the rectangular test section is a 76.2 cm diameter plenum chamber. This middle plenum chamber

Nomenclature

d = wall pressure sensor diameter (m)
f = frequency (Hz)
C_w = spatial/temporal window bandwidth correction
$G(\xi, \tau)$ = cross-correlation function (Pa^2)
$H(k_x, k_z)$ = normalized wavevector response of circular sensor
$H_a(k_x)$ = normalized array wavenumber response
J_1 = Bessel function of the first kind and first order
k_x, k_z = streamwise, spanwise wavenumber, (rad/m)
$k_c = \omega/u_c$ = convective wavenumber (rad/m)
$p(x, z, t)$ = fluctuating wall pressure (Pa)
$r = d/2$ = circular wall pressure sensor radius (m)
$R_\theta = U_o\theta/\nu$ = momentum thickness Reynolds number
t = time (s)
$\bar{u}$ = mean streamwise velocity (m/s)
u_c = convection velocity (m/s)
$u_\tau = \sqrt{\tau_w/\rho}$ = friction velocity (m/s)
$u^+ = \bar{u}/u_\tau$ = mean streamwise velocity scaled with u_τ
U_o = free-stream velocity (m/s)
$w(y/\delta)$ = wake function
$W(x, t)$ = spatial/temporal window function
x, y, z = streamwise, wall normal, spanwise spatial coordinates (m)
$y^+ = yu_\tau/\nu$ = distance from wall scaled with ν/u_τ
δ = boundary layer thickness (m)
δ^* = displacement thickness (m)
θ = momentum thickness (m)
$\gamma(\xi, \omega)$ = coherence function
λ = wavelength (m)
ν = kinematic viscosity (m^2/s)
ξ, η = streamwise, spanwise separation (m)
ρ = fluid density (kg/m^3)
$\tau_w = \rho u_\tau^2$ = mean wall shear stress (Pa)
$\Phi(\omega) = \Phi(f)/2\pi$ = single sided autospectrum of wall pressure ($Pa^2/(rad/s)$)
$\Phi(k_x, \omega)$ = double sided streamwise wavenumber-frequency spectrum of wall pressure ($Pa^2/[(rad/s) \times (rad/m)]$)
$\Phi(k_x, k_z, \omega)$ = double sided wavevector-frequency spectrum of wall pressure ($Pa^2/[(rad/s) \times (rad^2/m^2)]$)
$\omega = 2\pi f$ = radian frequency (rad/s)
$p(\omega) = (1/2\pi) \times \int_{-\infty}^{+\infty} p(\tau)e^{-i\omega\tau}d\tau$ = forward Fourier transform

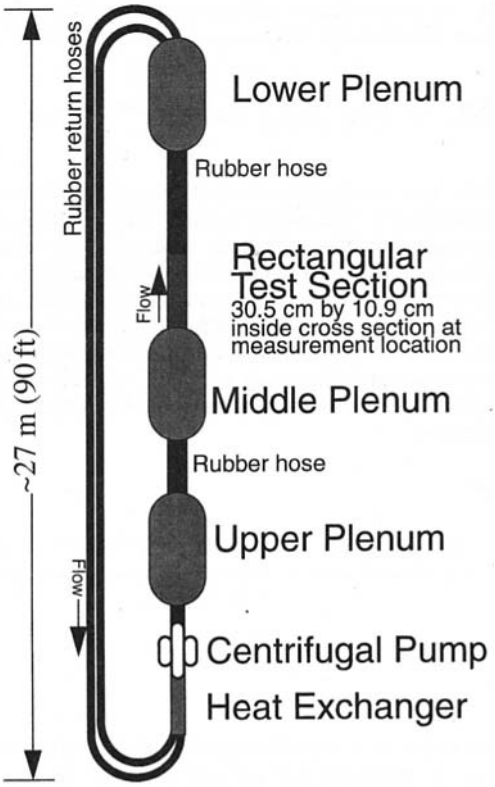

Fig. 1 Quiet water tunnel facility schematic

consists of an inlet diffuser section, followed by a 0.95 cm cell aluminum honeycomb section 45.72 cm in length. The flow converges from the plenum into the rectangular test section through a nozzle with an area contraction ratio of 8.2 (rectangular to rectangular transition). A detailed description of these components is given by Keith et al. (1991). Previous investigations of turbulent wall pressure fluctuations made in the rectangular test section are given by Keith and Barclay (1993), Keith and Bennett (1991), and Keith (1989).

Following Blake and Chase (1971), Smol'yakov and Tkachenko (1983), Farabee and Geib (1991), and Manoha (1991), the wavenumber filter consisted of a linear array of 48 circular pressure sensors which was mounted in the spanwise center of the top wall of the test section. The leading edge of the array was 163 cm (56.2 δ at 6.1 m/s speed) downstream of the inlet of the test section. The turbulent boundary layer on each wall was fully developed for the range of R_θ covered in the experiment.

As detailed in Fig. 2, the sensors were equally spaced at a streamwise increment, Δx, of 4.22 mm (0.166 in.). Each sensor consisted of a small, air-filled hollow cylinder of lead zirconate

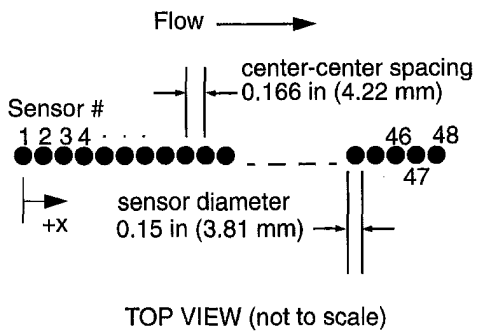

Fig. 2 Design of wall pressure sensor array

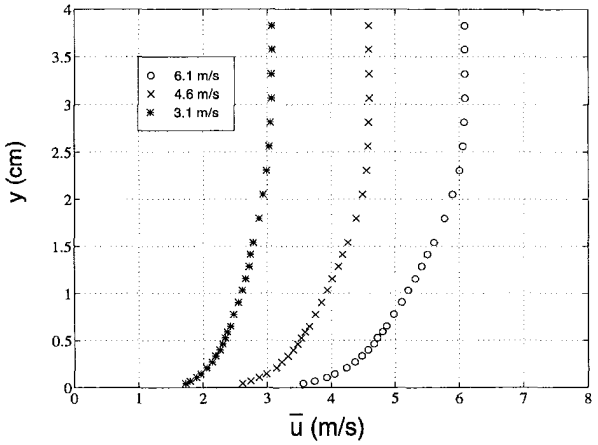

Fig. 3 Measured streamwise velocity profiles

titanate (PZT) piezo-electric ceramic of outer diameter 2.54 mm and length 8.64 mm. Each cylinder had small epoxy endcaps. The nominal sensitivity and capacitance were −221.3 dB//1 V/μPa and 1800 pF, respectively. The sensors were encapsulated in Hexcel Uralite 3130 urethane and mounted in a 5.08 cm thick stainless-steel plate such that the main axis of the sensor cylinder was perpendicular to the flow direction and one end of the cylinder was flush with the wall. The effective sensor diameter was 3.81 mm (0.15 in.), which was the diameter of the holes in which the sensors were mounted. The main response of the piezoelectric cylinder is through radial strain. The pressure acting on the end of the cylinder is transmitted through the urethane to the cylinder. To first order, the sensor responds to the pressure over the flush-end of the cylinder such that it is essentially uniformly sensitive. A nonuniform sensitivity (e.g., tapering off near the radial edges of the sensor) will exhibit itself in the sensor response at higher wavenumber ($\lambda < d$ or $k_x > 2\pi/d$). This is not a critical issue in this investigation because the array only resolves wavenumber components for $-\pi/\Delta x < k_x < \pi/\Delta x$ (or $\lambda > 2\Delta x$). Generally, the sensor spacing, Δx, is always greater than the sensor diameter, d.

Each sensor in the array was calibrated in air using an acoustic method. A speaker mounted to a short section of PVC tube (21.9 cm diameter and 10.2 cm length) was mounted on the surface of the steel disk holding the array with a reference microphone (Bruel and Kjaer model 8103) placed at the center of the array. The pressure field on the surface of the array was essentially uniform below the 970 Hz dipole resonance of the speaker. A Hewlett Packard model 3562A dual channel spectrum analyzer was used to measure the transfer function between the outputs of the reference and test hydrophones. A broadband random signal was used as input to an amplifier for the speaker. The magnitude and phase of the transfer function between the reference and test hydrophone were measured for each pressure sensor in the array. The calibrations were used to convert the measured voltage units (V) to fluctuating pressure (Pa) for the wavenumber-frequency processing. The channel to channel voltage sensitivities were within ±2 dB and ±3 deg phase. The mean calibration was −221 dB//1 V/μPa and 0 deg phase.

The mean streamwise velocity profile, $\bar{u}(y)$, was measured using a pitot tube of diameter 0.889 mm connected to a manual traverse. Figure 3 shows the velocity profiles in dimensional units for free-stream speeds of 6.1, 4.6, and 3.1 m/s. The mean wall-shear stress, τ_w, and equivalently, the friction velocity, u_τ, were estimated by fitting the velocity profiles to the log-law model of Coles and Hirst (White, 1991):

$$u^+ = \frac{1}{0.41} \ln y^+ + 5.0. \quad (1)$$

Figure 4 shows the velocity profiles scaled with inner variables.

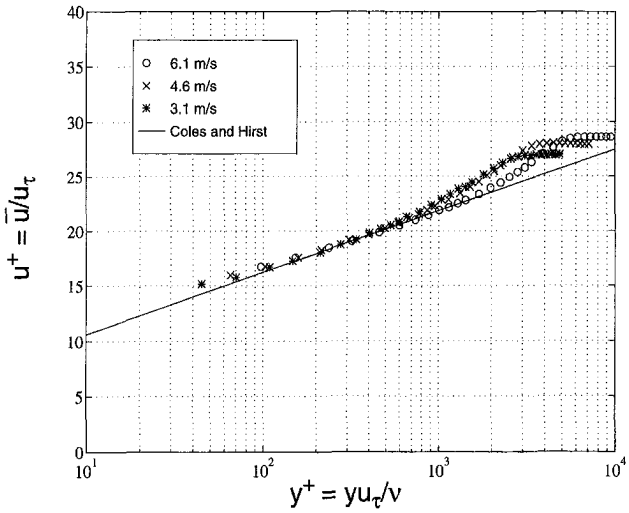

Fig. 4 Streamwise velocity profiles scaled on inner variables

The velocity profiles display the classic wake region for an equilibrium flow near the outer part of the boundary layer which occurs at higher y^+ for higher R_θ. The minor deviation from the log-law at $y^+ < 100$ is believed to be from near-wall fluid acceleration due to the presence of the pitot tube. This effect is not from area averaging by the pitot tube. The theoretical average streamwise velocity predicted by integrating (1) over a circular area corresponding to the face of the pitot probe is slightly less than that predicted by (1) at the center of the probe. The probe diameter is 89, 130, and 194 ν/u_τ for the 3.1, 4.6, and 6.1 m/s speeds, respectively.

The displacement and momentum thicknesses were obtained by integrating the mean streamwise velocity profile directly following White (1991). The boundary layer thickness was determined using Cole's (1956) velocity defect law given by,

$$\frac{U_o - \bar{u}}{u_\tau} = -2.5 \ln\left(\frac{y}{\delta}\right) + 1.38\left[2 - w\left(\frac{y}{\delta}\right)\right], \quad (2)$$

where w is the wake function, as given by Coles (1956). Using the previously estimated values for u_τ, a value for δ was determined which satisfied (2) for each data point in the outer region of the boundary layer. These values were then averaged to determine the final value for δ, which was used in the subsequent scaling of the spectra.

The resulting boundary layer parameters are given in Table 1 for the three Reynolds numbers used in the experiment. The results for u_τ/U_o are very close to those predicted by Coles (1953) for an "ideal" turbulent boundary layer. The changes in ν over the range of Reynolds numbers investigated were due to slight variations in the water temperature from day to day. The 95 percent confidence limits for U_o, δ, δ^*, θ, and u_τ are 1, 5, 4.5, 4.5, and 1.3 percent, respectively.

Signal Processing

The wavenumber-frequency spectrum, $\Phi(k_x, \omega)$ is defined as the space-time Fourier transform of the cross-correlation function $G(\xi, \tau)$. Assuming a stationary, homogeneous field, the streamwise wavenumber-frequency spectrum is given by,

$$\Phi(k_x, \omega) = \frac{1}{(2\pi)^2} \int_{-\infty-\infty}^{+\infty+\infty} G(\xi, \tau) e^{-i(k_x\xi + \omega\tau)} d\xi d\tau. \quad (3)$$

In practice, the wavenumber-frequency spectrum can be estimated from discrete space-time records of the wall pressure by ensemble averaging the magnitude squared of the space-time Discrete Fourier Transform (DFT). This method gives an estimate of the power level in discrete wavenumber and frequency "bins." Because the data are limited in both spatial and temporal extent, window functions are used to suppress sidelobes in the wavenumber and frequency domains, respectively. In this investigation, the two-sided wavenumber-frequency spectrum is estimated as,

$$\Phi_m(k_x, \omega) = \frac{\left\langle \left| \sum_{n=1}^{N} \sum_{m=1}^{M} W(x_m, t_n) p_m(x_m, t_n) e^{-i(k_x x_m + \omega t_n)} \Delta x \Delta t \right|^2 \right\rangle}{(2\pi)^2 NMC_w}, \quad (4)$$

where:

$\langle\rangle$ denotes expected value (through ensemble averaging),

p_m = measured wall pressure at sensor m,

$x_m = (m-1)\Delta x$,

$t_n = (n-1)\Delta t$,

$W(x_m, t_n) = W_x(x_m) W_t(t_n)$,

$W_t(t_n) = 1 - \cos^2\left[\frac{(n-1)\pi}{(N-1)}\right]$ = Hanning window,

$W_x(x_m)$ = spatial window (or array shading function),

$C_w = \frac{1}{NM} \sum_{n=1}^{N} \sum_{m=1}^{M} W^2(x_m, t_n)$ = window constant. (5)

Note that there are M sensors (typically 48) and N time points (typically 1024). The spatial or array shading function $W_x(x_m)$ was determined using the method of Sherrill and Streit (1987) for arrays with failed elements. The 10th element in the 48 channel array malfunctioned, so its weight value was set to zero. The resulting shading provided theoretical sidelobe levels of −34.5 dB in the wavenumber domain and a "main lobe" width of $0.165/\Delta x$ (39.1 rad/m for the array described in the preceding section) based on the 3 dB down point of the wavenumber filter. The data records for each speed consisted of 250 averages of 1024 temporal points for each of the 48 channels. The Hanning window provided a first sidelobe level of −31.4 dB in the frequency domain. The wavenumber-frequency spectrum was calculated at 144 values of the streamwise wavenumber (through zero padding in the FFT algorithm) for data smoothing, but this does not increase the resolution of the wavenumber filter. The random error in the wavenumber-frequency spectrum (Capon and Goodman, 1970) estimated with 250 averages is approximately 6.3 percent or 0.27 dB.

Because the wavenumber-frequency spectrum was estimated using finite-sized sensors, the measured spectrum was somewhat attenuated compared to the true spectrum due to area averaging of short wavelength disturbances or equivalently filtering of high wavenumber energy. The temporal response of the sensors was assumed to be instantaneous because the sensor fundamental resonance was at approximately 80 kHz whereas the measured turbulent energy was limited (by the electronic noise floor of the sensor preamplifiers) to frequencies of 3 kHz or less at the highest speed of 6.1 m/s.

The normalized response of a uniformly sensitive circular sensor is given as,

Table 1 Boundary layer parameters

U_o (m/s)	ν (m²/s)	δ (mm)	δ^* (mm)	θ (mm)	R_θ	u_τ/U_o	$R^* = u_\tau\delta/\nu$
3.1	1.13×10^{-6}	37.1	4.04	2.97	8,100	0.370	3,770
4.6	1.12×10^{-6}	30.0	3.56	2.62	10,700	0.0357	4,400
6.1	9.75×10^{-7}	29.0	3.58	2.67	16,700	0.0350	6,350

$$H(k_x, k_z) = \frac{2J_1(Kr)}{Kr} \tag{6}$$

where $K = \sqrt{k_x^2 + k_z^2}$. The sensor will attenuate the wavevector frequency spectrum $\Phi(k_x, k_z, \omega)$ over a range of the k_x and k_z wavenumbers. Attenuation of the true spectrum will become more severe as the convective ridge energy moves to higher streamwise wavenumbers and becomes broader in both streamwise and spanwise wavenumber with increasing frequency. The measured frequency autospectrum will be,

$$\Phi_m(\omega) = \int_{-\infty}^{+\infty}\int_{-\infty}^{+\infty} \Phi(k_x, k_z, \omega)|H(k_x, k_z)|^2 dk_z dk_x, \tag{7}$$

where $\Phi(k_x, k_z, \omega)$ is assumed to be the true or unattenuated wavevector-frequency spectrum. The streamwise wavenumber-frequency spectrum, as measured by an array of sensors aligned in the streamwise direction, is,

$$\Phi_m(k_x, \omega) = \int_{-\infty}^{+\infty}\int_{-\infty}^{+\infty} \Phi(k_x, k_z, \omega)|H(k_x, k_z)|^2 \times |H_a(k_{xx} - k_x)|^2 dk_z dk_{xx}, \tag{8}$$

where H_a is the normalized streamwise wavenumber response of an array of point sensors which repeats for $k_x\Delta x = \ldots, -3\pi, -\pi, \pi, 3\pi, \ldots$, etc. The wavenumber response is normalized such that:

$$\int_{-\pi/\Delta x}^{+\pi/\Delta x} H_a(k_x) dk_x = 1. \tag{9}$$

Aliasing in the frequency domain was eliminated by use of analog low-pass filters and therefore did not affect the above estimates of $\Phi_m(k_x, \omega)$. There is no spatial equivalent to this filtering to prevent aliasing in the wavenumber domain. Energy which occurs within the Nyquist wavenumber band ($-\pi/\Delta x < k_x < \pi/\Delta x$) will be resolved by the array. From the high wavenumber characteristics of the sensor response function (5) one can see that the sensor itself will act somewhat as a low-pass wavenumber filter, but energy may still alias into the resolved wavenumber domain. Energy which occurs at streamwise wavenumbers outside this range will be aliased back into the resolved wavenumber domain. For example, energy which occurs at $k_x = -1.2\pi/\Delta x$ will appear as energy at $k_x = +0.8\pi/\Delta x$, but will still be subject to the attenuation characteristics of the sensor at $k_x = 1.2\pi/\Delta x$. One technique to minimize wavenumber aliasing is to spatially over-sample and only use lower portions of the resolved wavenumber-frequency spectra. This method was used numerically by Chang et al. (1994) to improve performance of a Large Eddy Simulation (LES).

The wall pressure data were acquired using analog and digital electronics. The transducers were connected to Precision Filters, Inc., model 600-SE-40 40 dB preamplifiers. The preamplifier outputs were filtered by two banks of Precision Filters Inc. Model 6624-L-LP1-1ACG low-pass filters set at $f_s/2.5$ to prevent aliasing in the frequency domain. Here f_s is the sample frequency (2000 Hz for the 6.1 and 4.6 m/s speeds and 1000 Hz for the 3.1 m/s speed). The 48 channels were digitized using three sets of Iotech, Inc., Model ADC488/16A 16 channel, 16 bit analog to digital converters. The data were transferred across a General Purpose Interface Bus (GPIB) to a SUN Microsystems, Inc., SPARCstation 2 computer, which was used to post-process the data.

The input referred noise floor of the preamplifiers was approximately -61.5 dB//1 Pa^2/Hz (single-sided spectrum level). The system was configured such that none of the measured wavenumber-frequency spectral data were limited by electronic noise except by 60 Hz and narrow-band, harmonic, line noise. The line noise is common to all the preamplifiers, so it appears as a zero-wavenumber component in the wavenumber-frequency spectrum. The autospectrum levels were not limited by electronic noise, but were limited by acoustic noise from the pump at frequencies below 30 Hz.

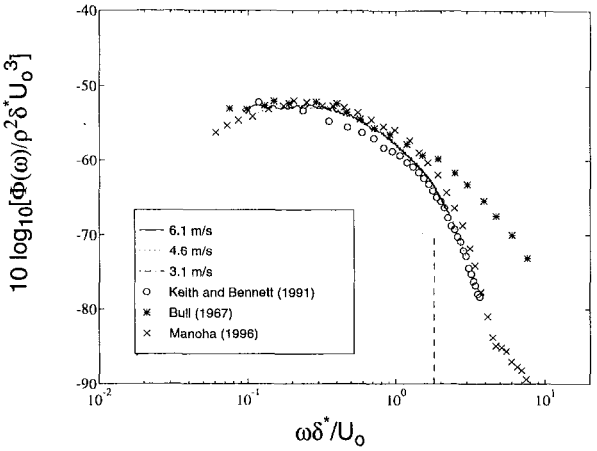

Fig. 5(*a*) Uncorrected for finite sensor size

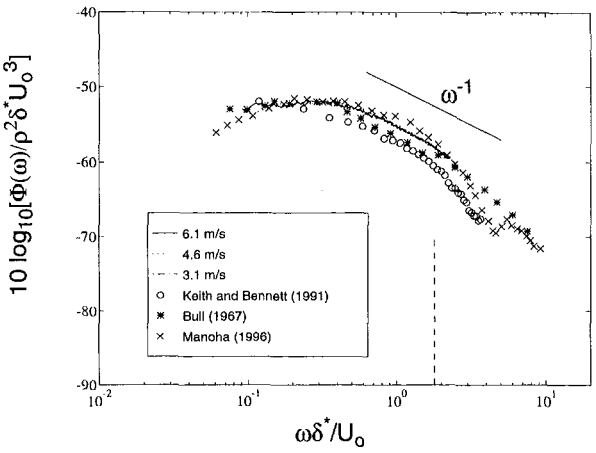

Fig. 5(*b*) Corrected for finite sensor size

Fig. 5 Measured wall pressure spectra (dashed line is frequency at which spectra for current investigation are attenuated 3 dB or more)

Array Measurement Results and Analysis

The single-sided frequency autospectra $\Phi(\omega)$ from the investigation are shown in Fig. 5(*a*). The spectra are scaled with the "outer" variables of Keith et al. (1992) and are uncorrected for sensor size effects. Shown for comparison are the spectra measured by Keith and Bennett (1991) at an R_θ of 13,400, by Bull (1967) at an R_θ of 19,500, and that by Manoha (1996) at an R_θ of 29,100. Keith and Bennett measured equilibrium wall pressure and wall shear spectra in the same facility as the current investigation but on the lower wall and with a smaller boundary layer (18.8 mm). The current measurements scale well with Bull's and Manoha's data for $\omega\delta^*/U_o < 1$. Above this frequency, the measurements diverge due to the different sensor sizes used in the investigation. The ratios of d/δ^* for Bull (1967), Keith and Bennett (1991), Manoha (1996), and the current investigation (3.1, 4.6, and 6.1 m/s) are 0.195, 0.89, 1.0, 0.94, 1.07, and 1.06, respectively. Bull's data are shown for reference because Chase (1987) used Bull's spectral data for the empirical coefficients that govern the spectral levels as a function of frequency in his wavevector-frequency model of the wall pressure. The measured spectra show a maximum at approximately $0.2 < \omega\delta^*/U_o < 0.25$ ($49 < \omega\delta/u_\tau < 61$ for

U_o = 4.6 m/s). This supports Farabee and Casarella's (1991) measurements where the spectral peak occurred at $\omega\delta/u_\tau \cong 50$.

Over the range of R_θ used in this investigation (8,100 to 16,700), and the range of frequencies shown in Fig. 5(*a*) ($0.09 < \omega\delta^*/U_o < 3$), scalings using outer variables (e.g., that shown in Fig. 5(*a*)) and using mixed variables (e.g., $\omega\delta/u_\tau$ versus $\Phi(\omega)u_\tau/\tau_w^2\delta$) both provide an excellent collapse of the data (within ±0.6 dB). Using inner variables (e.g., $\omega\nu/u_\tau^2$ versus $\Phi(\omega)u_\tau^2/\tau_w^2\nu$), the spectra scale within ±1 dB for $0.02 < \omega\nu/u_\tau^2 < 0.2$. Following the results of Farabee and Casarella (1991), in view of the frequency range covered by the current investigation ($60 < \omega\delta/u_\tau < 740$), the energy in the wall pressure spectra is dominated by the "mid" and "overlap" regions. Therefore, one would expect the "mixed" scaling (termed "outer" by Farabee and Casarella (1991) to work well and the "inner" scaling to work only for $\omega\nu/u_\tau^2 > 100/(u_\tau\delta/\nu)$, (0.022 for R_θ of 10,700). The ω^{-1} character of the overlap (or "universal") range (Bradshaw, 1967) is shown in Fig. 5(*b*).

As given by Eq. (7), the measured wall pressure spectrum is attenuated according to the response of the sensor and the characteristics of the "true" wavevector spectrum. The frequency above which the measured frequency autospectrum was estimated to be attenuated 3 dB or more is 230, 348, and 446 Hz for free-stream velocities of 3.1, 4.6, and 6.1 m/s, respectively. These frequencies are noted in nondimensional form ($\omega\delta^*/U_o \approx 1.8$) on Fig. 5(*a*). Figure 5(*b*) shows the spectra corrected using the results of Corcos (1963). As shown, the data display a good collapse (±2 dB) when the corrections for finite sensor size are included.

The measured coherence scaled with the similarity variable $\omega\xi/u_c$ is shown in Figs. 6(*a*) and 6(*b*). The Corcos exponential decay model [$\gamma(\xi, \omega) = \exp(-0.125|\omega\xi/u_c|)$] is shown for reference. Figure 6(*a*) shows the coherence as a function of frequency at fixed streamwise spacings while Fig. 6(*b*) shows the coherence at fixed frequencies as a function of sensor spacing. Farabee and Casarella (1991) found that for $\omega\delta/u_\tau > 30$, the similarity scaling of the Corcos model effectively collapsed their measured coherence. In this investigation, the similarity scaling worked for $\omega\delta/u_\tau > 110$. Additionally, the failure of the Corcos model at low frequencies for increasing streamwise sensor spacing is shown in Fig. 6(*a*). These results are very similar to the results of Farabee and Casarella (1991) and the DNS results of Choi and Moin (1990) (as calculated by Abraham and Keith, 1995) and serve to verify the character of the turbulent boundary layer wall pressure field.

Estimates of the streamwise wavenumber-frequency spectrum were attenuated from the streamwise and spanwise wavenumber characteristics of the sensor. The attenuation in the streamwise wavenumber is zero for $k_x = 0$ and a maximum of 2.3 dB at the Nyquist wavenumber $\pm\pi/\Delta x = \pm 745$ rad/m as estimated by (6). Most of the attenuations occurs from the finite spanwise sensor size. The wavenumber-frequency spectrum data have not been corrected for sensor size effects because these corrections are minimal (e.g., <2.3 dB) for the frequencies at which the wavenumber-frequency spectrum is resolved. In the resolved streamwise wavenumber range, one can obtain a first order estimate of the attenuation by estimating the autospectral corrections suggested by Corcos (1963).

Despite the apparently large sensor diameter based on the viscous length scale (d^+ = 390, 560, 830 wall units for the 3.1, 4.6 and 6.1 m/s speeds, respectively) due to the fact that the working fluid is water, the wavenumber-frequency spectrum is not significantly attenuated in the resolved wavenumber range. Because turbulence does not have a single defining length scale, using the sensor size based on viscous units does not uniquely quantify how much attenuation of the wall pressure occurs due to finite sensor size. Corcos found that the defining parameter was $\omega r/U_c$ where r is the sensor radius and U_c is the convection

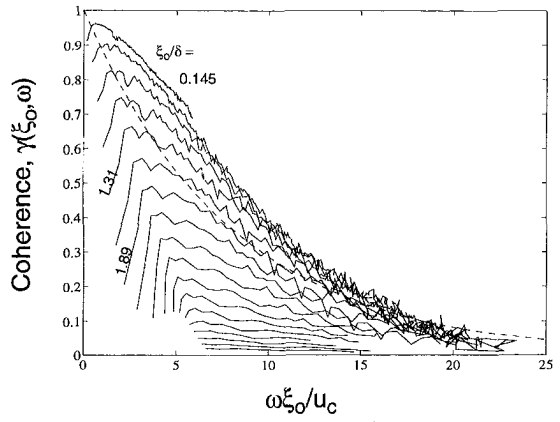

Fig. 6(*a*) With fixed streamwise sensor spacings (ξ_o/δ = 0.145 to 5.09 in increments of 0.291). Dashed line is exp(−0.125|$\omega\xi_o/U_c$|)

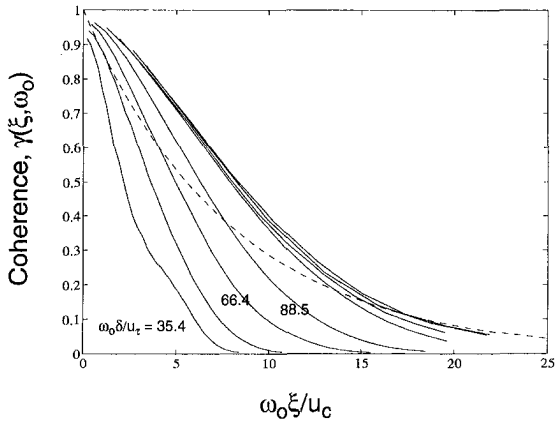

Fig. 6(*b*) With fixed frequencies ($\omega_o\delta/u_\tau$ = 35.4, 44.3, 66.4, 88.5, 177, 266, 354, and 443). Dashed line is exp(−0.125|$\omega_o\xi/U_c$|)

Fig. 6 Streamwise coherence as a function of cross-spectral phase at U_o = 6.1 m/s

velocity. The quantity ω/U_c is also the convective wavenumber, k_c. The corresponding convective wavelength is then $\lambda_c = 2\pi/k_c = 2\pi U_c/\omega$. Thus at low frequency, the convective wavelengths become large enough so that negligible attenuation of the wall pressure occurs. The direct, simultaneous, array measurement method used by the current investigation automatically limits the array to resolution of wavelengths of $2\Delta x$ (where Δx is the sensor spacing) or greater. If the wavenumber-frequency spectrum is estimated by transforming the cross-spectrum, then this limit must be externally imposed. Curve-fitting, smoothing, and interpolation of the cross-spectral data can mislead one to believe that the resolved wavelength (and wavenumber) range is greater than can physically be realized.

The streamwise wavenumber-frequency spectra measured at free-stream velocities of 6.1, 4.6, and 3.1 m/s are shown in Figs. 7, 8, and 9, respectively. The spectra are given in dimensional units and are double-sided in both frequency and wavenumber such that the integral of the spectrum over all wavenumber and frequency (positive and negative) yields the measured mean square fluctuating wall pressure. The same scales in wavenumber and frequency are retained in the figures to facilitate comparisons. Data below 30 Hz are not shown because they were limited by acoustic noise from the centrifugal pump. The acoustic noise is limited to a wavenumber band ($-\omega/c < k_x < \omega/c$) where c is the speed of sound in water (approximately 1500 m/s). Because the width of the wavenumber filter is approximately 39 rad/m, all of the acoustic energy within the measured frequency range (0–600 Hz) will appear as if it occurred at 0 rad/m. The highest levels of energy occur along the

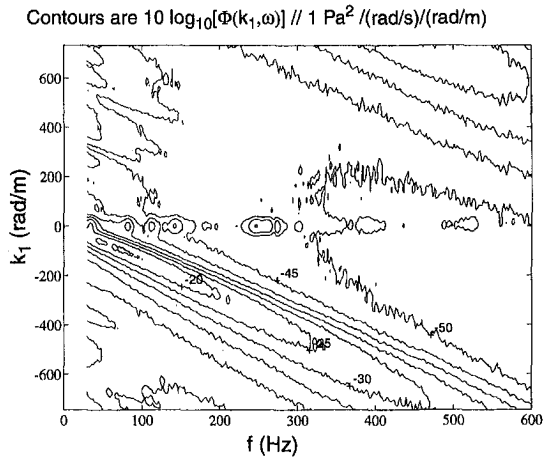

Fig. 7 Measured wavenumber-frequency spectrum at 6.1 m/s velocity

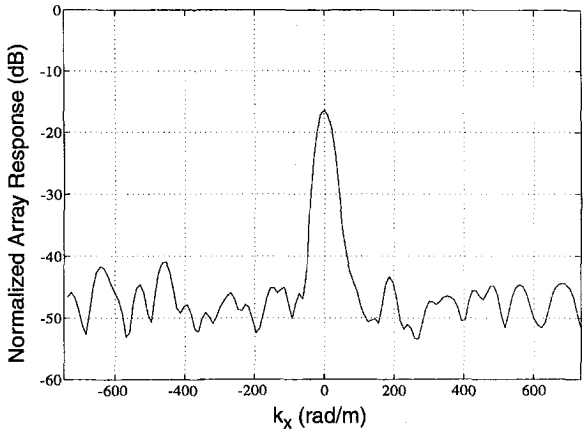

Fig. 10 Normalized array response inferred from low-frequency pump acoustic-noise

"convective ridge" which extends from approximately −40 rad/m at 30 Hz to −745 rad/m at 500 Hz in Fig. 7. The width of the ridge increases with frequency which is consistent with the Corcos (Smol'yakov and Tkachenko, 1983) and Chase (1987) spectral models and the results of Wills (1970), Choi and Moin (1990), Karangelen et al. (1991), Manoha (1991), Herbert and Leehey (1992), Panton and Robert (1994), Manoha (1996), and Abraham and Keith (1996). The noise seen at zero wavenumber is from both electronic noise and low level acoustic noise from the pump. This noise is completely limited to the wavenumber bin at 0 rad/m. There are frequency bands, however, that do not appear to be limited by this noise (e.g., between 180 and 240 Hz in Fig. 7).

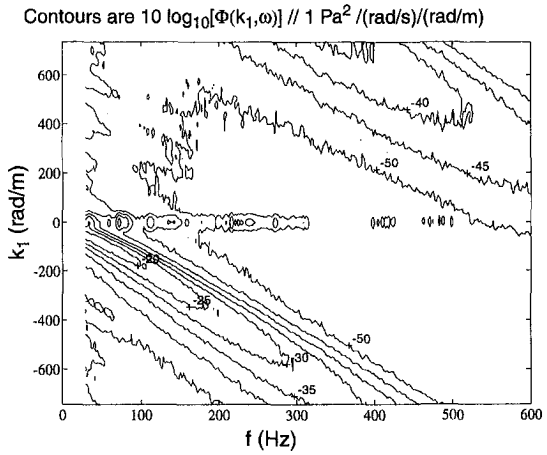

Fig. 8 Measured wavenumber-frequency spectrum at 4.6 m/s velocity

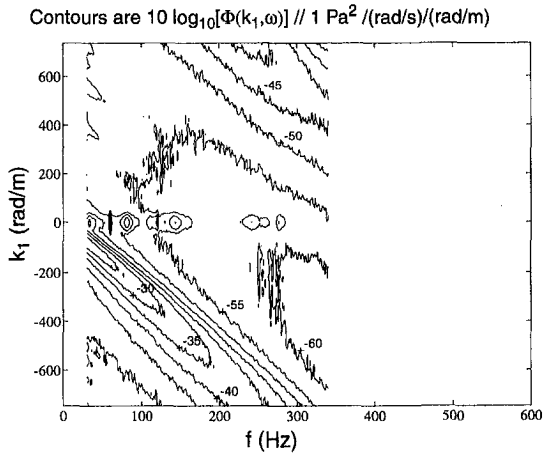

Fig. 9 Measured wavenumber-frequency spectrum at 3.1 m/s velocity

The measured data are limited at some wavenumbers by sidelobe leakage from energy in the convective ridge region ($k_x \approx k_c$) into other wavenumbers where there is significantly less energy. To provide a guideline as to which wavenumber bands are not limited by sidelobe levels, the Chase (1987) model of the wavevector-frequency spectrum, was used with the array response to predict the levels shown in Figs. 7, 8, and 9. Figure 10 shows the normalized response of the array to the pump acoustic noise between 5 and 15 Hz. This is an array response in the sense that the dominant energy source occurs at a fixed wavenumber (~0 rad/m), and the array is "steered" through digital signal processing to the other wavenumbers shown in Fig. 10. The acoustic levels are at least 20 dB higher than the convective ridge levels and both sources of energy occur at approximately $k_x = 0$. The array response shows that the sidelobe levels were between approximately 24.4 to 38.5 dB below the main lobe level. This response function, H_a, was convolved with Chase's wavevector-frequency model (10) to give an estimate of the measured streamwise wavenumber-frequency spectrum using (8), which also takes into account the sensor response. Chase's (1987) model for incompressible flow is used as the "true" wavevector-frequency spectrum and is expressed as,

$$\Phi(k_x, k_z, \omega) = \frac{\rho^2 u_\tau^3}{[K_+^2 + (b\delta)^{-2}]^{5/2}} \times \left\{ C_T K^2 \left[\frac{K_+^2 + (b\delta)^{-2}}{K^2 + (b\delta)^{-2}} \right] + C_M k_x^2 \right\}, \quad (10)$$

where,

$$K^2 = k_x^2 + k_z^2$$

$$K_+^2 = \frac{(\omega - u_c k_x)^2}{(h u_\tau)^2} + K^2$$

The empirical constants were set at $h = 3$, $b = 0.75$, $C_T = 0.014/\mathrm{h}$, and $C_M = 0.466/\mathrm{h}$. The convection velocity u_c was determined from the location in streamwise wavenumber of the peak of the convective ridge ($k_x = k_c$) such that,

$$u_c = -\omega/k_c, \quad (11)$$

which is the phase velocity if the convective energy were modeled as a traveling wave.

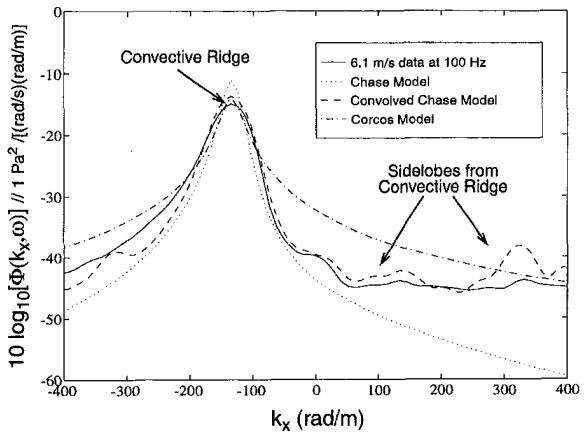

Fig. 11 Measured wavenumber-frequency spectrum compared with chase and corcos models

The Corcos model of the streamwise wavenumber frequency spectrum is derived by Fourier transforming Corcos' (1963) model of the wall pressure cross-spectrum from the spatial to the wavenumber domain. It is stated as,

$$\Phi(k_x, \omega) = \frac{\alpha\Phi(\omega)}{\pi k_c\left[\alpha^2 + \left(\frac{k_x}{k_c} - 1\right)^2\right]} \tag{12}$$

where α is the constant in Corcos' (1963) exponential decay model of the cross spectrum and k_c is negative.

Figure 11 shows the measured streamwise wavenumber-frequency spectrum for $U_o = 6.1$ m/s at a frequency of 100 Hz. Shown for comparison are the aforementioned Chase and Corcos models. The levels predicted by (7) are shown as the Chase convolved model. Also shown is the spectrum predicted by the Chase model with no sensor or array filtering. This streamwise wavenumber-frequency spectrum was obtained by numerically integrating (10) over spanwise wavenumber, k_z. The Corcos model is shown with a decay constant α of -0.125 and has an autospectrum magnitude $\Phi(\omega)$ equal to the measured data.

The first point to note in Fig. 11 is that there are regions within the resolved wavenumber range ($-745 < k_x < 745$ rad/m) where the measured data appear to be limited by sidelobe leakage. These regions are approximately $k_x > 0$ and $k_x < -400$ for this particular frequency and speed. Therefore the "valid" measurement region includes the convective ($k_x \sim k_c$), part of the superconvective ($k_x < k_c$), and part of the subconvective ($k_x > k_c$) regions. The fact that the levels predicted by (8) with (10) and the data in Fig. 10 agree with the measured levels at wavenumbers far removed from the convective ridge indicate that some data were limited by the filtering performance of the array response shown in Fig. 10.

Second, there are marked differences between the measured spectrum and the Corcos model. The Corcos model is symmetric about k_c whereas the measured spectrum show higher levels just above k_c (superconvective) and significantly lower levels (up to 10 dB) at subconvective wavenumbers. Manoha (1991) also note this discrepancy. Panton and Robert (1994) argued that the effect must be from the spatial character of the convection velocity. Keith and Abraham (1997) showed quantitatively that this "skew" effect in streamwise wavenumber could be produced by introducing a convection velocity which varies with ξ into the Corcos (1963) model of the cross spectrum before it is Fourier transformed into streamwise wavenumber. Chang et al. (1994) noted subconvective levels from numerical simulations of fully developed channel flow that were 10 to 25 dB lower than those predicted by the Corcos model. The measured spectrum agrees extremely well with Chase's model in the convective and subconvective regions. However, at superconvective wavenumbers, the measured data are up to 5 dB higher than the Chase model in the range where sidelobe leakage does not limit the measurement.

The convection or phase velocity u_c is often a required parameter in models of the wavenumber-frequency spectrum or for the estimation of sensor size effects. The convection velocities were estimated as a function of frequency using (11) for the three R_θ used in the investigation and are shown in Fig. 12 scaled with the outer variables δ^* and U_o. The convection velocity data extends to a higher frequency than the spectral data because it can be extracted from the location of the convective ridge even after it has aliased in the wavenumber domain. This is done in the exact same fashion as one "unwraps" the phase of a two-point measurement in the frequency domain to determine convection velocity with a fixed spacing. This velocity and frequency scaling and another using δ as a length scale provided an excellent collapse of the measured convection velocities. For $\omega\delta^*/U_o > 2.5$, the convection velocity is constant at $u_c/U_o \approx 0.67$. The data show a slight low-frequency "roll down" of the convection velocity which Farabee and Casarella (1991) attributed to near-wall turbulence that had a more severe decay at low convective wavenumber than energy at higher frequencies (and wavenumbers).

Figure 13 shows the convection velocity scaled with u_τ and the frequency scaled with δ and u_τ. This scaling does not scale u_c as effectively as the outer scaling over the measured range of R_θ. The changes in u_τ/U_o introduce a Reynolds number effect (described by Coles, 1953) into the scaling which does not track with the measured data. The convection velocities were also scaled with inner variables using u_τ and ν as shown in Fig. 14. This scaling provided a good collapse of the data, with slightly more scatter than with the outer scaling. The convection velocity approaches a limit of $u_c/u_\tau \approx 17.5$ for $\omega\nu/u_\tau^2 > 0.14$.

Constant frequency "cuts" of the wavenumber-frequency spectrum from the three different speeds were scaled using the measured boundary layer parameters in Table 1. There was a range of nondimensional frequencies over which the measured wavenumber-frequency spectra from the different R_θ could be compared. The upper frequency is the frequency at which the convective wavenumber, k_c, equals the Nyquist wavenumber ($\pm\pi/\Delta x = \pm 745$ rad/m). The lower frequency limit was 30 Hz due to the pump acoustic noise. Table 2 shows these frequency limits in dimensional and nondimensional form.

The wavenumber-frequency spectra from the three R_θ measurements were compared at fixed nondimensional frequencies. The frequency range from Table 2, which overlaps the three different Reynolds numbers, is $0.25 < \omega\delta^*/U_o < 1.8$, $60.9 <$

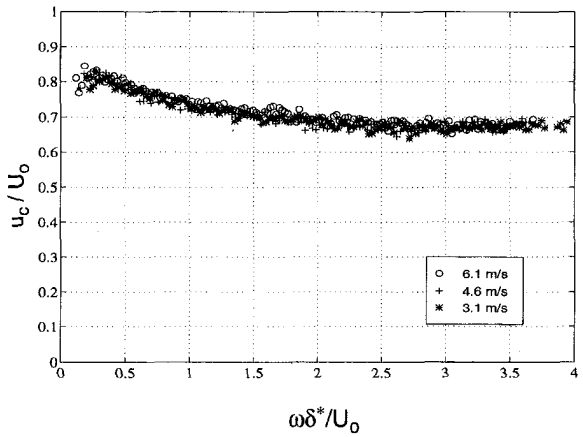

Fig. 12 Measured convection velocity from wavenumber-frequency spectra scaled with outer variables

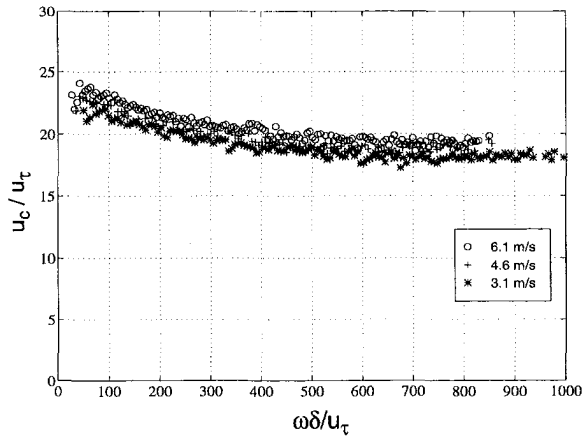

Fig. 13 Measured convection velocity from wavenumber-frequency spectra scaled with mixed variables

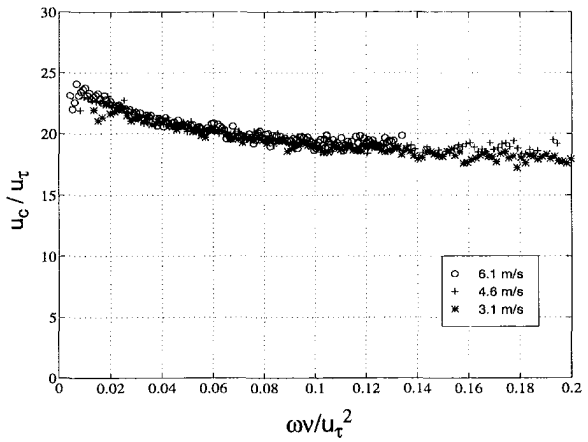

Fig. 14 Measured convection velocity from wavenumber-frequency spectra scaled with inner variables

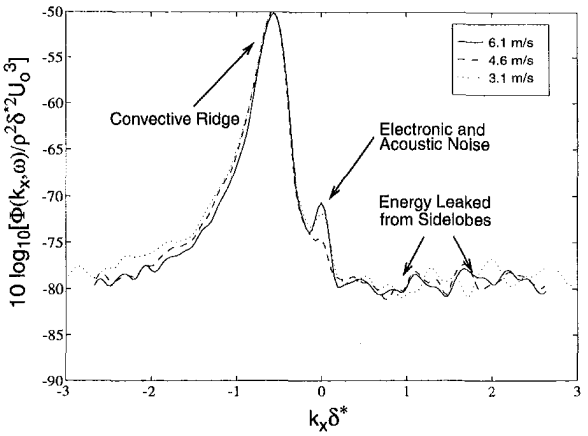

Fig. 15 Scaled wavenumber-frequency spectra at frequency $\omega\delta^*/U_o$ = 0.453

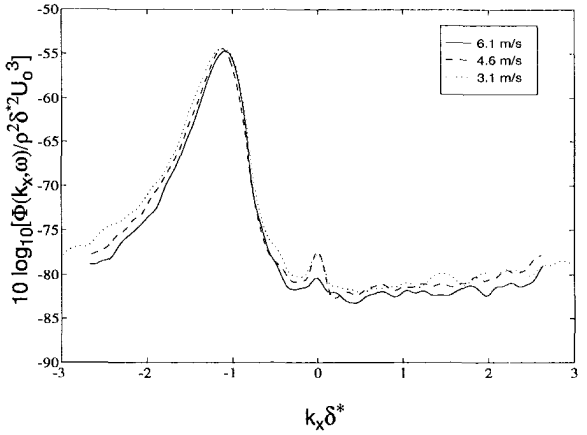

Fig. 16 Scaled wavenumber-frequency spectra at frequency $\omega\delta^*/U_o$ = 0.828

$\omega\delta/u_\tau < 421$, and $0.016 < \omega\nu/u_\tau^2 < 0.067$. This range is in the upper part of the "mid" and the lower part of the "overlap" frequency ranges defined by Farabee and Casarella (1991), so one would expect the frequency autospectrum to scale using (δ, u_τ) or $(\nu/u_\tau, u_\tau)$. The following definitions for "outer," "mixed 1," "mixed 2," and "inner" variable scalings, respectively, were considered:

$$k_x\delta^* \text{ versus } \Phi(k_x, \omega)/\rho^2\delta^{*2}U_o^3 \tag{13}$$

$$k_x\delta \text{ versus } \Phi(k_x, \omega)u_\tau/\tau_w^2\delta^2 \tag{14}$$

$$k_x\delta^* \text{ versus } \Phi(k_x, \omega)U_o/\tau_w^2\delta^{*2} \tag{15}$$

$$k_x\nu/u_\tau \text{ versus } \Phi(k_x, \omega)u_\tau^3/\tau_w^2\nu^2. \tag{16}$$

Figures 15, 16, and 17 show the wavenumber-frequency spectrum scaled with (13) at frequencies $\omega\delta^*/U_o$ of 0.453, 0.828, and 1.58, respectively. As seen in the figures, this scaling provided an excellent collapse of the measured spectrum over the entire resolved range of wavenumber. The fact that the suspected sidelobe-limited regions also scale with the boundary layer parameters support the assumption that energy is "leaking" in from the energy in the convective ridge region.

Note that a nondimensionalization of the streamwise wavenumber using the convective wavenumber, k_c, at each frequency was not needed to effectively collapse the spectra from the different Reynolds numbers, although in general there will be

Table 2 Frequency ranges for comparison of wavenumber-frequency spectra with unaliased convective ridge

Speed (m/s)	f (Hz) (min, max)	$\omega\delta^*/U_o$ (min, max)	$\omega\delta/u_\tau$ (min, max)	$\omega\nu/u_\tau^2$ (min, max)
3.1	30, 245	0.25, 2.0	60.9, 498	0.016, 0.13
4.6	30, 367	0.15, 1.8	34.5, 421	0.0079, 0.096
6.1	30, 496	0.11, 1.8	25.6, 424	0.004, 0.067

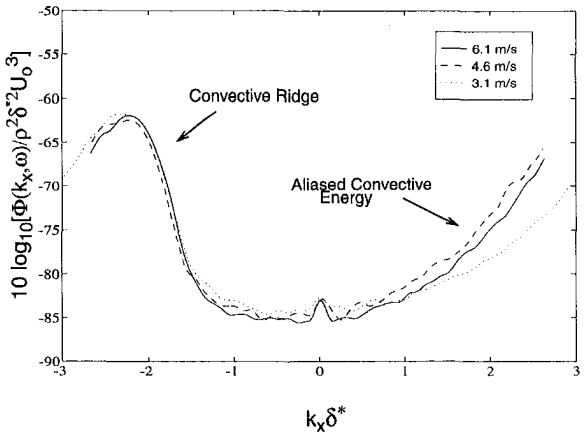

Fig. 17 Scaled wavenumber-frequency spectra at frequency $\omega\delta^*/U_o$ = 1.58

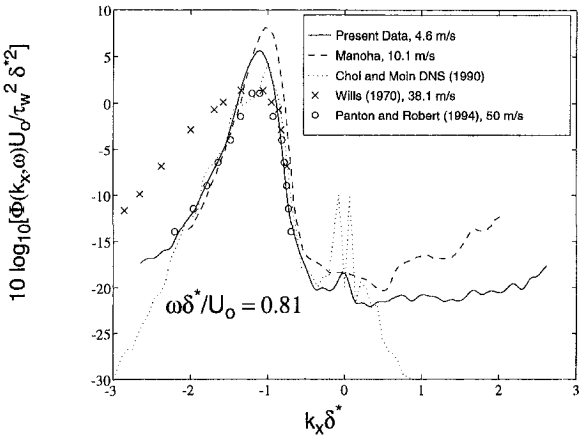

Fig. 18 Comparison of measured wavenumber-frequency spectrum with experiments and numerical simulation

some dispersion as shown in the scaled convection velocities in Figs. 12–14 (recall that u_c was determined from k_c via (11)). It is of interest that the different regions of the wavenumber-frequency spectrum (subconvective, convective, and superconvective) all scale well over the different Reynolds numbers. An important result is that scaling laws for the frequency autospectrum (the integral of $\Phi(k_x, \omega)$ in k_x) can also be used for the wavenumber-frequency spectrum with an added appropriate length scale for nondimensionalization (e.g., δ^*, δ or ν/u_τ).

The scalings given by (14)–(16) also very effectively collapsed the measured wavenumber-frequency spectra, with no significant differences compared to the results shown in Figs. 15–17. The convection velocity scalings in Figs. 12 and 14 corresponding to the wavenumber-frequency scalings in (13), (15), and (16) are evidence that the location of the convective ridge will scale properly ($k_c\delta^* = (\omega\delta^*/U_o)(U_o/u_c)$ or $k_c\nu/u_\tau = (\omega\nu/u_\tau^2)(u_\tau/u_c)$) as long as the nondimensional frequency ($\omega\delta^*/U_o$ or $\omega\nu/u_\tau^2$) is the same for the data at different R_θ.

Keith et al. (1992) showed that scaling the wall pressure autospectrum with τ_w, δ^* and u_τ/U_o (i.e., $\omega\delta^*/U_o$ versus $\Phi(\omega)U_o/\tau_w^2\delta^*$) provided a good overall collapse for experimental measurements in the range $1{,}400 < R_\theta < 75{,}000$. For the low Reynolds number ($R_\theta = 285$), DNS results of Choi and Moin (1990), the autospectrum also scaled well with the experimental results for $\omega\delta^*/U_o < 1$. Therefore the scaling given by (15) should scale the wavenumber-frequency spectrum over the widest R_θ range for $\omega\delta^*/U_o < 1$.

Figure 18 shows a comparison at $\omega\delta^*/U_o = 0.81$ of the measured wavenumber-frequency spectrum at $U_o = 4.6$ m/s ($R_\theta = 10{,}700$) with the experimental results of Manoha (1996) with $R_\theta = 46{,}600$, and the numerical (DNS) results of Choi and Moin (1990) with $R_\theta = 285$. Also shown are the results of Wills (1970) with $R_\theta \approx 8{,}400$ and Panton and Robert (1994) with $R_\theta \approx 12{,}000$. Since Wills' data was normalized, it was scaled such that the integral in wavenumber matched the autospectrum level of the present investigation at $\omega\delta^*/U_o = 0.81$. The agreement between all the experimental investigations and the DNS is remarkable especially in the sub-convective region. Agreement is also excellent in the superconvective region for the data of Choi and Moin (1990), Panton and Robert (1994), Manoha (1996), and the present investigation. It is not clear why levels estimated by Wills in the super-convective region are higher than the other data sets but it could be from the instrumentation available at the time. The DNS results do not agree well with any of the other data sets at low wavenumber due to numerical instabilities noted by Choi and Moin (1990). Again, a wavenumber normalization was not needed. However, the collapse of the data in Fig. 18 is even better if k_x/k_c is used instead of $k_x\delta^*$. The levels estimated by Choi and Moin (1990), Manoha (1996), and the present investigation at $-kc$ (positive wavenumber) are 24-35 dB lower than the convective ridge levels. This attributes to the effective accuracy of the spatial filters used by the investigation. Wills (1970) noted a spectral level only 7 dB below the convective level due to phase mismatch of his electronics.

From Fig. 18, the ratio of the convective ridge spectral level to the "low" wavenumber levels near $k_x = 0$ are approximately −23 to −26 dB. The results of Manoha (1996) and the present investigation are limited by sidelobe leakage for spectral levels 26 dB or more below the convective ridge levels. The DNS results appear to be limited near $k_x = 0$ by numerical instability. Spectral levels 15–17 dB below the convective ridge and levels for positive wavenumbers were not given in the contour plots by Wills (1970) and Panton and Robert (1994). It is unclear whether the DNS levels for $k_x \gg k_c$ (i.e., the positive wavenumber range) can be considered "true" spectral levels at this time. A longer array aperture (total) length would increase the wavenumber resolution (smaller wavenumber "bin") and give a better estimate of the subconvective energy. The sensor spacing must be held constant, however, to maintain the current unaliased measurement range. In the current investigation, the array length was limited by the mechanical aspects of the facility and the sensor spacing was limited by the outer diameter of the wall pressure sensor.

Array measurements at lower and higher frequencies and Reynolds numbers than those covered in this investigation are needed further to verify the appropriate scaling laws. The frequency autospectrum scalings given by Farabee and Casarella (1991) and Keith et al. (1992) can be used as a guideline in scaling the wavenumber-frequency spectrum with appropriate length scales added for the wavenumber. A higher resolution direct measurement of the wavevector-frequency spectrum for a hydrodynamic turbulent boundary layer is not feasible at the current time due to instrumentation costs and technology. Numerical simulations (Choi and Moin, 1990, Chang et al., 1994), however, have already provided an estimate of the wavevector-frequency spectrum at low Reynolds numbers. If scaling issues can be resolved between the low and practical higher Reynolds numbers (i.e. for $\omega\delta^*/U_o > 1$ with the scaling of Eq. (15)), then the numerical results can be extrapolated with more confidence and therefore confirm or suggest modification of the available empirical models of the wavevector-frequency spectrum.

Conclusions

Direct measurements of the streamwise wavenumber-frequency spectrum of turbulent boundary layer wall pressure fluctuations using an array of 48 flush-mounted sensors were performed. The array was mounted in a water tunnel beneath a fully developed boundary layer and measurements were made for $8100 < R_\theta < 16{,}700$. The measurements effectively described the wavenumber and frequency content of the energy in the wall pressure over specified limits in both wavenumber and frequency. Aliasing effects in the wavenumber domain at a fixed frequency were determined to be a limiting factor for measurements made at wavenumbers far from the convective wavenumber where the spectrum level was at least 26–28 dB or lower than the convective ridge levels. However, measurement of the convective ridge and associate sub- and superconvective spectral levels within this dynamic range had adequate resolution.

The convection or phase velocity was extracted from the wavenumber-frequency spectrum and nondimensionalized with various scalings. Scalings using "outer" variables (δ^* or δ and U_o) and inner variables (ν and u_τ) gave the most effective collapse of the measured phase velocity. The wavenumber-frequency spectrum was also nondimensionalized with several scalings and compared at fixed nondimensional frequencies.

The frequency range for comparison was limited to that where energy contributions to the wall pressure are from both the "log-law" and "inner" parts of the boundary layer, and scalings using "outer," (e.g., δ^* and U_o) "mixed," (e.g., δ and u_τ or δ^*, τ_w, and u_τ/U_o) and "inner" (e.g. ν and u_τ) variables all were very efficient. The scalings provided an excellent collapse of the spectrum over all resolved wavenumbers for the Reynolds number range covered in this experiment ($8100 < R_\theta < 16{,}700$). Nondimensionalizing the wavenumber-frequency spectrum as $\Phi(k_x, \omega) U_o/\tau_w^2 \delta^{*2}$ provided a good overall scaling for $285 < R_\theta < 46{,}600$ and $\omega\delta^*/U_o < 1$.

Array measurements at higher and lower Reynolds numbers and at lower and higher frequencies will provide additional information useful in describing the behavior of the wavenumber-frequency spectrum and in developing appropriate scaling laws. Then existing models of the wavenumber-frequency spectrum can be improved or validated and be more useful in the modeling of the response of structures beneath turbulent boundary layers.

Acknowledgments

The authors express their appreciation to Mr. James Powers and Mr. Patrick Monahan of the Naval Undersea Warfare Center, Division Newport, for the design and construction, respectively, of the wall pressure sensors used in this investigation. In addition, the authors gratefully acknowledge the support of the Independent Research Program at the Naval Undersea Warfare Center Division Newport, Dr. Stuart Dickinson, program manager.

References

Abraham, B. M., and Keith, W. L., 1995, "Analysis of the Wall Pressure Field from a Numerical Simulation of Turbulent Channel Flow," *Proceedings of the ASME Symposium on Flow Noise Modeling, Measurement, and Control,* Noise Control and Acoustics Vol. 19, pp. 55–65.

Abraham, B. M., and Keith, W. L., 1996, "Direct Measurements of Turbulent Boundary Layer Wall Pressure Wavenumber-Frequency Spectra," *Proceedings of the ASME Symposium on Vehicle Flow/Structure Noises,* Noise Control and Acoustics Vol. 22, pp. 177–187.

Blake, W. K., and Chase, D. M., 1971, "Wavenumber-Frequency Spectra of Turbulent Boundary Layer Pressure Measured by Microphone Arrays," *Journal of the Acoustical Society of America,* Vol. 49, No. 3, Part 2, pp. 862–876.

Bradshaw, P., 1967, "Inactive Motion and Pressure Fluctuations in Turbulent Boundary Layers," *Journal of Fluid Mechanics,* Vol. 30, pp. 241–258.

Bull, M. K., 1967, "Wall-Pressure Fluctuations Associated with Subsonic Turbulent Boundary Layer Flow," *Journal of Fluid Mechanics,* Vol. 28, No. 4, pp. 719–754.

Capon, J., and Goodman, N. R., 1970, "Probability Distributions for Estimators of the Frequency-Wavenumber Spectrum," *Proceedings of the IEEE,* Vol. 58, No. 10, pp. 1785–1786.

Chang, P. A., Abraham, B. M., Piomelli, U., 1994, "Wavenumber-Frequency Characteristics of Wall Pressure Fluctuations Computed using Turbulence Simulations," *Proceedings of the ASME Symposium on Active Control of Vibration and Noise,* Design Engineering Vol. 75, pp. 229–224.

Chase, D. M., 1987, "The Character of the Turbulent Wall Pressure Spectrum at Subconvective Wavenumbers and a Suggested Comprehensive Model," *Journal of Sound and Vibration,* Vol. 112, No. 1, pp. 125–147.

Choi, H., and Moin, P., 1990, "On the Space-Time Characteristics of Wall-Pressure Fluctuations," *Physics of Fluids A,* Vol. 2, No. 8, pp. 1450–1460.

Coles, D., 1953, "Measurements in the Boundary Layer on a Smooth Flat Plate in Supersonic Flow, Pt. 1, The Problem of the Turbulent Boundary Layer," Report No. 20-69, Jet Propulsion Laboratory, California Institute of Technology, Pasadena, CA.

Coles, D., 1956, "The Law of the Wake in the Turbulent Boundary Layer," *Journal of Fluid Mechanics,* Vol. 1, pp. 191–226.

Corcos, G. M., 1963, "Resolution of Pressure in Turbulence," *Journal of the Acoustical Society of America,* Vol. 35, No. 2, pp. 192–199.

Farabee, T. M., and Casarella, M. J., 1991, "Spectral Features of Wall Pressure Fluctuations Beneath Turbulent Boundary Layers," *Physics of Fluids A,* Vol. 3, No. 10, pp. 2410–2420.

Farabee, T. M., and Geib, F. E., 1991, "Measurements of Boundary Layer Pressure Fluctuations at Low Wavenumbers on Smooth and Rough Walls," *Proceedings of the ASME Symposium on Flow Noise Modeling, Measurement, and Control,* Noise Control and Acoustics Vol. 11, pp. 55–68.

Herbert, K., and Leehey, P., 1992, "Wall Pressure Spectrum in a Flat Plate Turbulent Boundary Layer and Downstream of a Turbulent Boundary Layer Manipulator," *Proceedings of the ASME Symposium on Flow-Induced Vibration and Noise, Flow-Structure and Flow-Sound Interactions,* Noise Control and Acoustics Vol. 13, pp. 147–163.

Karangelen, C. C., Casarella, M. J., and Farabee, T. M., 1991, *Proceedings of the ASME Symposium on Flow Noise Modeling, Measurement, and Control,* Noise Control and Acoustics, Vol. 11, pp. 37–44.

Keith, W. L., 1989, "Spectral Measurements of Pressure Fluctuations on Riblets," *American Institute of Aeronautics and Astronautics Journal,* Vol. 27, No. 12, pp. 1822–1824.

Keith, W. L., and Abraham, B. M., 1997, "Effects of Convection and Decay of Turbulence on the Wall Pressure Wavenumber-Frequency Spectrum," ASME JOURNAL OF FLUIDS ENGINEERING, Vol. 119, pp. 50–55.

Keith, W. L., and Barclay, J. J., 1993, "Effects of a Large Eddy Breakup Device on the Fluctuating Wall Pressure Field," ASME JOURNAL OF FLUIDS ENGINEERING, Vol. 115, No. 3, pp. 389–397.

Keith, W. L., and Bennett, J. C., 1991, "Low-Frequency Spectra of the Wall Shear Stress and Wall Pressure in A Turbulent Boundary Layer," *American Institute of Aeronautics and Astronautics Journal,* Vol. 29, No. 4, pp. 526–530.

Keith, W. L., Bennett, J. C., and Barclay, J. J., 1991, "Hydroacoustic Research at the Quiet Water Tunnel Facility of the Naval Underwater Systems Center," *Proceedings of the ASME Symposium on Hydroacoustic Facilities,* Noise Control and Acoustics Vol. 10, pp. 43–54.

Keith, W. L., Hurdis, D. A., and Abraham, B. M., 1992, "A Comparison of Turbulent Boundary Layer Wall Pressure Spectra," ASME JOURNAL OF FLUIDS ENGINEERING, Vol. 114, No. 3, pp. 338–347.

Manoha, E., 1991, "Wall Pressure Wavenumber-Frequency Spectrum Beneath a Turbulent Boundary Layer Measured with Transducers Calibrated with an Acoustical Method," *Proceedings of the ASME Symposium on Flow Noise Modeling, Measurement, and Control,* Noise Control and Acoustics Vol. 11, pp. 21–35.

Manoha, E., 1996, "The Wavenumber-Frequency Spectrum of the Wall Pressure Fluctuations beneath a Turbulent Boundary Layer," *Proceedings of the AIAA Aeroacoustics Conference,* May 6–8, State College, PA, American Institute of Aeronautics and Astronautics, AIAA Paper 96–1758.

Panton, R. L., and Robert, G., 1994, "The Wavenumber-Phase Velocity Representation for the Turbulent Wall-Pressure Spectrum," ASME JOURNAL OF FLUIDS ENGINEERING, Vol. 116, pp. 477–483.

Sherman, C. H., Ko, S. H., and Buehler, B. G., 1990, "Measurement of the turbulent boundary layer wave-vector spectrum," *Journal of the Acoustical Society of America,* Vol. 88, No. 1, pp. 386–390.

Sherrill, M. S., and Streit, R. L., 1987, "In Situ Optimal Reshading of Arrays with Failed Elements," *IEEE Journal of Oceanic Engineering,* Vol. OE-12, No. 1, pp. 155–162.

Smol'yakov and Tkachenko, 1983, *The Measurement of Turbulent Fluctuations,* Springer-Verlag, New York, pp. 178–190.

White, F. M., 1991, *Viscous Fluid Flow,* McGraw-Hill, New York, pp. 411–420.

Wills, J. A. B., 1970, "Measurements of the Wave-Number/Phase Velocity Spectrum of Wall Pressure Beneath a Turbulent Boundary Layer," *Journal of Fluid Mechanics,* Vol. 45, Part 1, pp. 65–90.

S. Parneix
Post-Doctoral Fellow,
Center for Turbulence Research,
Stanford University,
Stanford CA, 94305-3030

D. Laurence
Senior Research Engineer,
Electricité de France, DER,
Laboratoire National d'Hydraulique,
6 quai Watier, 78400 Chatou, France

P. A. Durbin
Professor,
Mechanical Engineering,
Stanford University,
Stanford CA, 94305-3030

A Procedure for Using DNS Databases

A second moment closure (SMC) computation is compared in detail with the direct numerical simulation (DNS) data of Le et al. (1997) for the backstep flow at Re = 5100 in an attempt to understand why the intensity of the backflow and, consequently, the friction coefficient in the recirculation bubble are under-estimated. The data show that this recirculation bubble is far from being laminar except in the very near wall layer. A novel "differential a priori" procedure was used, in which the full transport equation for one isolated component of the Reynolds stress tensor was solved using DNS data as input. Conclusions are then different from what would have been deduced by comparing a full simulation to a DNS. In particular, the ϵ-equation, usually blamed for faults in model predictions, has been found to give excellent results in this case. In fact, the main problem comes from the $\overline{uv}$-equation which predicts a too high turbulent force. A modification, by including the gradients of mean flow in the transport model, has then been attempted and has cured 50 percent of the backflow discrepancy.

1 Introduction

A commonly given motive for direct numerical simulation (DNS) of turbulent flow is to provide data that might be of value to modelers. However, in the case of nonhomogeneous turbulence, only the one-dimensional data from fully-developed channel flow has received wide-spread use (Rodi and Mansour, 1993). That data set has lived up to promise, but simulations of more complex geometries have not proved as useful.

The geometrical simplicity of channel flow does not permit one to assess many of the essential properties of turbulence models. On a mathematical level, the single-point moment equations are ordinary differential equations in channel flow; on a physical level, the phenomenon of flow separation is not addressed by this case.

The manner in which DNS data has been utilized by modelers also has not exploited its potential. The standard "assessment" of a pressure-strain model has consisted of plugging DNS data into the algebraic formulas of the model, then comparing the result to other DNS data. This is not a proper assessment of a transport closure model: the model is phrased as a set of partial differential equations and boundary conditions, not as an algebraic formula, so the plug-in exercise can be misleading. Moreover, one important problem with such a technique is that, even if a "perfect" equation is found for every term of the global budgets (which means that the modeled equation fits perfectly with the DNS data), the general convergence of the global system has not been included in the study, and the resulting model can be numerically unstable. Such terms like dissipation or transport of Reynolds stresses may also be not well enough resolved, even by recent DNS, for an accurate and complete analysis term by term. It is more sensible to treat DNS data as conventional experimental data and simply compare it to *solutions* of the model.

In this paper, we propose an intermediate level of testing: the differential nature of the model is respected, but the DNS data is plugged into the model. Our motivation is to isolate individual aspects of the closure. For instance, if the mean flow and the Reynolds stresses are given by DNS data, does the $k - \epsilon$ system of the Second Moment Closure equations (which is, of course, different from the classical $k - \epsilon$ model) predict k and ϵ correctly? The ϵ-equation is commonly blamed for faults in model predictions: can this be substantiated by isolating that equation from other closure assumptions? In fact, when we isolated the ϵ-equation by utilizing DNS data from the Le et al. (1997) simulation of flow over a backward facing step, we found the ϵ-equation to do an admirable job. The results presented herein do not confirm the conventional wisdom.

To the best of our knowledge, only Hanjalic (1994) has previously used a preliminary version of the present method. Hanjalic did not actually describe the method or its significance; however, the caption of his Fig. 13 indicates that the ϵ-equation was solved using the Reynolds stresses $\overline{u_i u_j}$ and the mean velocity U from the DNS of a channel flow. In essence this embodies the idea of differential a priori testing: test the model by using DNS data fields, but still solve a full transport equation for the turbulence statistics. The present paper presents the first comprehensive, two-dimensional use of this technique. We have used a RANS code to obtain solutions to the turbulence transport equations.

2 Methodology

An "a priori" test is one in which a model is assessed outside of its full predictive context. The objective of a priori testing is to remove ambiguities or inaccuracies that occur in solutions of the full set of equations. These include numerical errors and inaccuracies in terms additional to those being tested. Numerical inaccuracy motivates a priori tests of LES subgrid closures; modeling inaccuracy motivates the present application to RANS closure.

All a priori testing suffers the danger of not judging the true mathematical role of the model. A model for the redistribution term of the Reynolds-stress transport equation is a formula to be used in a set of parabolic partial differential equations. It should be judged by its effect on the dependent variable, $\overline{u_i u_j}$, of those equations. This entails solving the transport model. To isolate the turbulence model, the mean flow field can be taken from a DNS data base; we will use the backstep simulation data of Le et al. (1997). Furthermore, each component of the transport equations can be isolated by prescribing the other components of $\overline{u_i u_j}$ via DNS fields. The isolated component must be solved in full.

Our method is to solve the partial differential equations of the turbulence model numerically, with certain fields prescribed

Contributed by the Fluids Engineering Division for publication in the JOURNAL OF FLUIDS ENGINEERING. Manuscript received by the Fluids Engineering Division January 22, 1997; revised manuscript received May 27, 1997. Associate Technical Editor: P. M. Sockol.

by DNS data. In general, the distribution of grid points for a DNS is not optimal for RANS, so we have interpolated the DNS fields onto a RANS grid; bilinear interpolation was used. The 770 × 194 DNS grid of Le et al. was uniform in x and stretched in y. The RANS grid is nonuniform in both directions and consisted of 120 × 120 cells, refined near the walls and around the corner of the step. It covered the region $x/h = -3$ to 30 and $y/h = 0$ to 6, $x = 0$ being the location of the sudden expansion, h being the step height and $y = 6h$ being the center of the channel. All RANS computations were performed with a general geometry, finite difference code developed by Rogers and Kwak (1990). The spatial discretization of convective terms was via a third-order, upwind biased scheme; diffusion terms were central differenced. Solutions were checked for grid-independence on a grid twice finer in both directions: the results were graphically indistinguishable from those presented herein. Inlet profiles of mean velocities, Reynolds stresses and dissipation were also taken from the DNS and imposed as the inlet conditions of all the following computations.

This new a priori method can be applied to the k and ϵ equations, which are a subset of the full Second Moment Closure equations (see the Appendix for the complete SMC model):

$$U_i^{\mathrm{DNS}}\partial_i k = \mathcal{P}^{\mathrm{DNS}} - \epsilon + \partial_i(\nu + \nu_{T_{ij}})\partial_j k$$

$$U_i^{\mathrm{DNS}}\partial_i \epsilon = \frac{C'_{\epsilon_1}\mathcal{P}^{\mathrm{DNS}} - C_{\epsilon_2}\epsilon}{T} + \partial_i(\nu + \nu_{T_{ij}})\partial_j \epsilon \qquad (1)$$

with $\nu_{T_{ij}} = C_\mu T \overline{u_i u_j}^{\mathrm{DNS}}$ and boundary conditions $k = \partial_n k = 0$ on no-slip walls. The production term uses the exact definition

$$\mathcal{P}^{\mathrm{DNS}} = -\overline{u_i u_j}^{\mathrm{DNS}}\partial_j U_i^{\mathrm{DNS}}. \qquad (2)$$

The turbulence time-scale

$$T = \sqrt{\frac{k^2}{\epsilon^2} + 36\frac{\nu}{\epsilon}}$$

involves the dependent variables, so it was computed as part of the a priori test. The terms in (1) with "DNS" superscript are ensemble averaged DNS fields that were interpolated onto the RANS grid; k and ϵ were obtained by solving these equations.

3 Full Computations

In addition to the a priori tests, a full SMC, RANS computation was performed. The full computation shows some areas in which improvements to the model are desired. The SSG redistribution model (Speziale et al., 1991) was used in conjunction with the elliptic relaxation method for treating wall effects (Durbin, 1993; Wizman et al., 1996), see the Appendix. The specifics of the modeling are not crucial here; our results are likely to be representative of the class of SMC's based on the general quasi-linear form, (A.5). The model constants were originally calibrated using DNS and experimental data for channel flow, zero pressure gradient boundary layers (Durbin, 1993) and homogeneous flows (Speziale et al., 1991). That model was directly applied to the backstep flow, without further modification. All the equations and constants used for this computation can be found in the Appendix.

Figure 1 shows the predicted streamlines compared to the DNS data. One can observe that the reattachment length is very well predicted and a secondary bubble is found. The flow seems to have a correct behavior near the reattachment point: it does not show the anomalous streamline pattern that has been found in other computations (Hanjalic, 1996, with the SSG pressure-strain model). Because of these previous results, we did a careful grid refinement study to verify that the present solution does not contain the spurious streamline pattern near reattachment

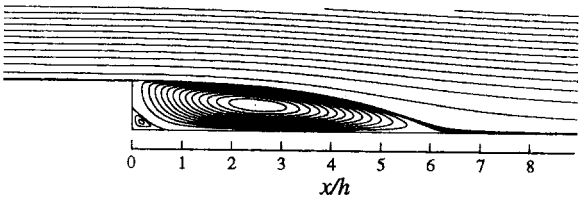

Fig. 1(*a*) Streamlines, second moment closure

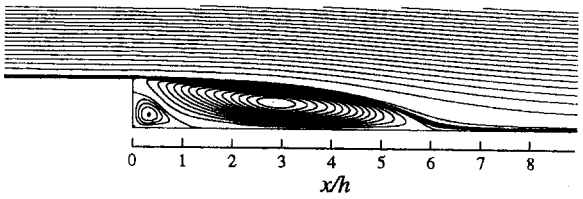

Fig. 1(*b*) Streamlines, DNS

that Hanjalic obtained. The elliptic relaxation method might be the source of the improvement.

However, the size of the secondary, corner bubble is much smaller in the computation than in the data. This defect seems to be linked to an under-prediction of the maximum friction coefficient in the backflow (Fig. 2(*a*)). By looking to the profiles of the streamwise mean velocity (Fig. 2(*b*)), one can observe that the overall features of the mean flow are reproduced, but the intensity of the backflow is missed by almost a factor of 2 at $x/h = 4$. Note that this specific problem seems to be common to every existing second moment closure (SMC) model, whatever near-wall formulation is used (low-Reynolds number, wall function or elliptic relaxation). Also, as with all existing turbulence models, including eddy viscosity models, the recovery after reattachment is too slow. The friction coefficient distribution shows similar discrepancies (too slow near-wall flow) both upstream and downstream the reattachment point, but we do not know if these two problems (too slow backflow and too slow recovery) are linked.

Figure 3 presents profiles of the computed normal component of the mean velocity V. The V-profiles at $x/h = 0.1$ and 2 confirm the distribution of the friction coefficient: the intensity of the two bubbles is severly under-estimated. By looking at the profiles before reattachment, one can observe that V is also under-estimated in the shear layer by about 15 percent. In fact, all the problems can be linked together by noting that more entrainment in the shear layer would lead to a more intense main recirculation, leading to a bigger and more intense secondary bubble. However, a modification of the backflow would also change the pressure distribution and thereby influence the velocity distribution in the shear layer.

4 A Priori Tests

A standard way of analyzing a DNS database consists in using the full DNS data to compute the distribution of some important variables, like the turbulent Reynolds number—$\mathrm{Re}_t = k^2/(\nu\epsilon)$—in order to understand the main physical features of the flow or to get new ideas for modeling. Figure 4, showing Re_t and the budget of the U-momentum equation in the middle of the recirculation ($x/h = 4$), presents an example of such a study. In their experiments, Jovic and Driver (1995) found that the minimum of C_f follows a "laminar-like" law: $C_{f_{min}} = -0.19\mathrm{Re}_h^{-0.5}$ for Reynolds numbers between 5000 and 50,000. However, Re_t, which represents about ten times the ratio between the turbulent viscosity and the molecular viscosity, is in the range 200–800 in the whole domain, including the bubble (of course, it goes to 0 at the wall). Clearly the flow is fully turbulent; the $\mathrm{Re}_h^{-0.5}$ fit does not imply a laminar recirculation

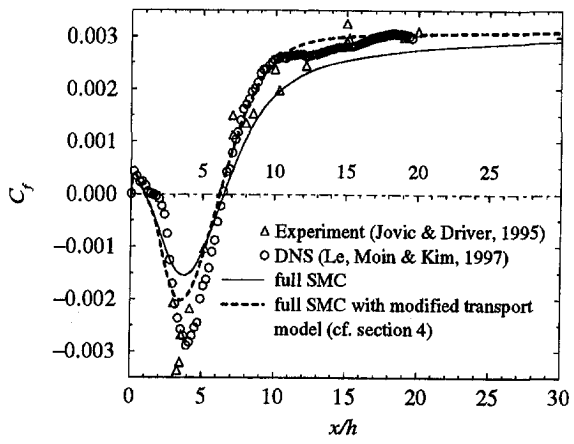

Fig. 2(*a*) Friction coefficient

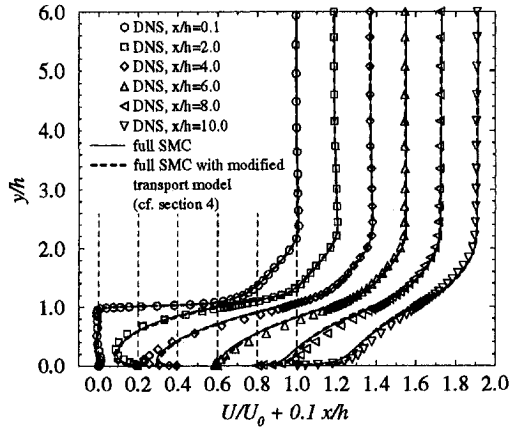

Fig. 2(*b*) *U* profiles

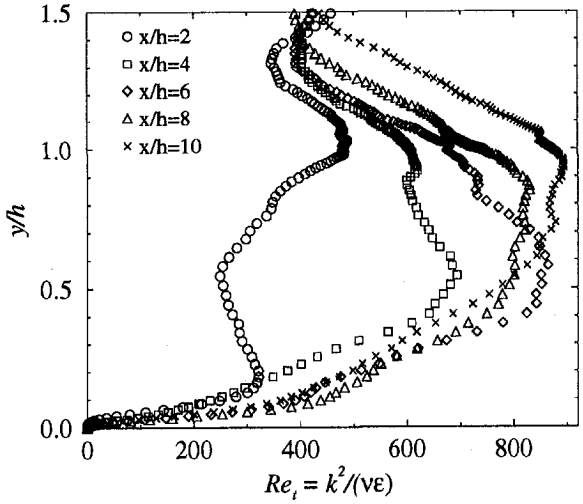

Fig. 4(*a*) DNS Re_t profiles

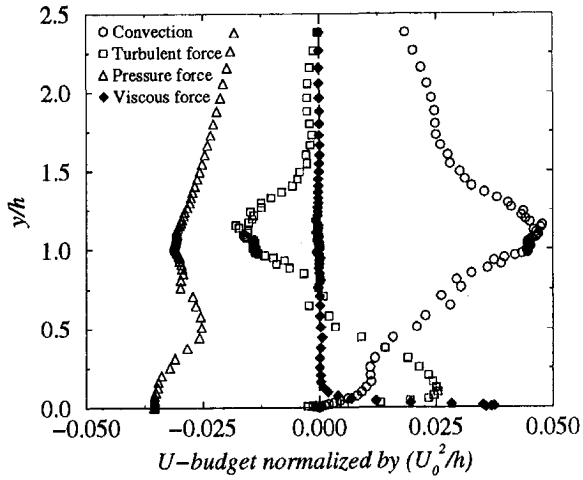

Fig. 4(*b*) *U*-momentum budget at station $x/h = 4$ (middle of the recirculation)

bubble. If one is still not completely sure of the turbulent nature of this recirculation, it becomes obvious by looking at the U-momentum budget (Fig. 4(b)): at station $x/h = 4$, the Reynolds stress gradients dominate the viscous force in the whole bubble, except very near the wall, well below the maximum of the reverse flow.

It is possible to go further in the investigation of a DNS database: in the present case by utilizing the full DNS statistical fields to assess closure models. An overall comparison between full RANS computations and a priori tests explains why an analysis using only the full computation may lead to erroneous conclusions. For example, the known dependence of shear layer growth on the ϵ-equation has lead to shortcomings of the full predictions being blamed on that equation. To judge the truth of this accusation, one might perform a parametric study on the model constants (we did so, and our efforts in that direction did not suggest that the ϵ model was the culprit). The a priori method provides a more refined test.

Figures 5 and 6 show a full RANS computation and an a priori "$k - \epsilon$" subsystem computation side by side (again, this is not the $k - \epsilon$ model, but the k and ϵ equations coming from the SMC model). It can be seen (Figs. 5(b) and 6(b)) that when the correct mean flow convection velocity and production rate are given via DNS, the $k - \epsilon$ equations of the Second Moment Closure give good predictions. When we solved the ϵ-equation separately, with k given by DNS fields (Eq. (1)), results very similar to Figs. 6 were found (cf. Fig. 7(a)).

This is an interesting test because the dissipation ϵ is usually considered as the weak point of any turbulence model. In fact, the derivation of the ϵ-equation relies mainly on intuition, so most of the shortcomings of turbulence models were thought to be in this equation—and most of the modifications of turbulence models were done to it. In this study, we used the "primitive" ϵ-equation, derived by Hanjalic and Launder (1972) with only two small modifications: ϵ/k has been replaced by the

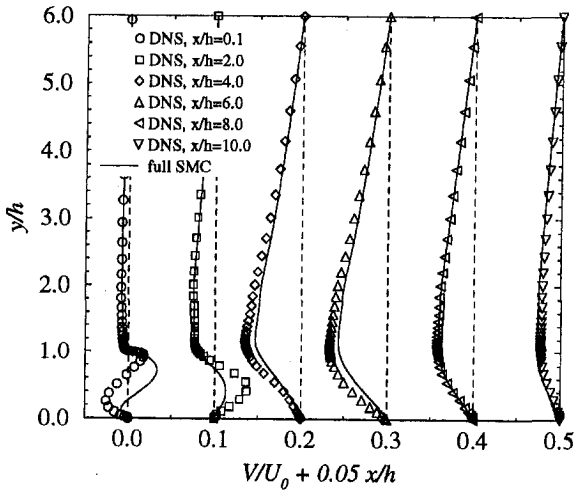

Fig. 3 *V* profiles

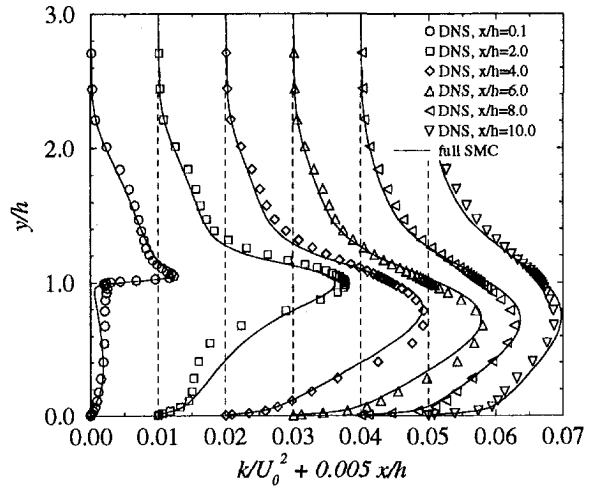

Fig. 5(*a*) *k* profiles, full computation

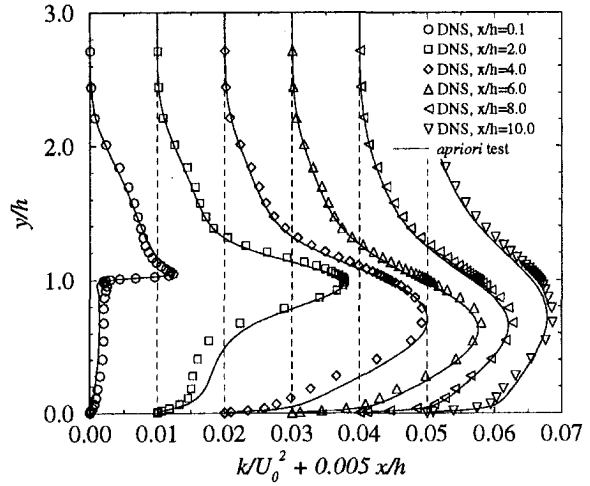

Fig. 5(*b*) *k* profiles, a priori test

inverse of the time scale $1/T$ (Durbin, 1993), and an extra-production term was included into C_{ϵ_1} to take into account the anisotropic wall effect (Parneix et al., 1996). In Eq. (1)

$$C'_{\epsilon_1} = C_{\epsilon_1}\left(1 + \tfrac{1}{30}\sqrt{\mathcal{P}_k/\mathcal{P}}\right) \qquad (3)$$

where $\mathcal{P}_k = 0.09(k^2/\epsilon)|S|^2$ is the production term that appears in the $k-\epsilon$ model and $\mathcal{P}$ is the exact Reynolds-stress production ($\mathcal{P} = -\overline{u_i u_k}\partial_k U_i$). This term is a generalization of the formulation $C'_{\epsilon_1} = C_{\epsilon_1}(1+\frac{1}{30}\sqrt{k/v^2})$, introduced by Durbin and Laurence (1996). It increases the production of ϵ in the near-wall region, thus decreasing the peak of the turbulent kinetic energy. The term $C'_{\epsilon_1} = C_{\epsilon_1} + a_1\mathcal{P}/\epsilon$ has sometimes been used for this same purpose, but the present method is more computationally stable in complex configurations.

When we fixed all the other variables at their DNS values (including k) and solved this equation, the results were surprisingly good, especially in the recirculation and in the recovery regions (cf. Fig. 7(a)). It is interesting to see whether the extra-term introduced in Eq. (3) has a strong influence or not on these results. Figure 7(b) presents the k-profiles computed through an a priori test (k ans ϵ were solved together) without this extra-production term $\mathcal{P}_k/\mathcal{P}$ in the ϵ-equation. The turbulent kinetic energy is then increased in the boundary layer, upstream from the step; this over-estimation is diffused in the shear-layer and in the recirculation by turbulent transport (higher levels than with the extra-term active, compare to Fig. 5(b)). Also, the peak of k, which starts to appear near the wall in the downstream recovery region seems to be over-estimated. Overall the influence is quite small and only affects the near-wall region. Indeed, when ϵ is solved alone with k interpolated from the DNS, the ϵ profiles do not show any major difference with or without the extra-term of (3).

Given these results, it is difficult to believe that only a modification of the ϵ-equation will cure all the problems, and especially the under-prediction of the backflow and rate of recovery. Although it is true that the reattachment length is sensitive to the difference $(C_{\epsilon_2} - C_{\epsilon_1})$, the origin of this seems to lie in the shear layer, where the dependence of the growth rate on $(C_{\epsilon_2} - C_{\epsilon_1})$ is well known. This a priori test is consistent with the fact that several corrections (e.g., Iacovides and Launder, 1995; Rodi and Mansour, 1993), introduced into the classical ϵ-equation, or modifications of the model constants, did not show any significant improvement of the backflow intensity in our full SMC computations. Since ϵ is thought not to be responsible for the backflow and recovery discrepancy, we come back to other modeled terms; first to the transport model.

We tested this model by the new a priori technique. If just the k equation is solved, with DNS data for ϵ, then the only modeled term is the turbulent transport (see Eq. (1)). Solving just the k-equation gave results similar to those presented in Fig. 5(b). Surprisingly, the behavior of the transport model is excellent in this case (backstep at low Reynolds number). In fact, the only discrepancy that has been found concerns the secondary recirculation ($x/h = 0.1$ and 2) where a severe over-

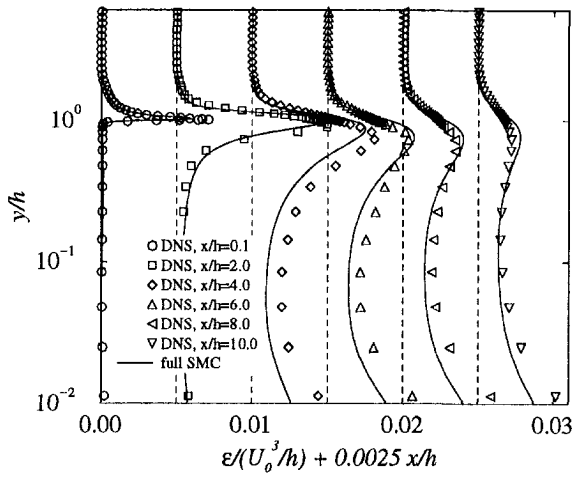

Fig. 6(*a*) ϵ profiles, full computation

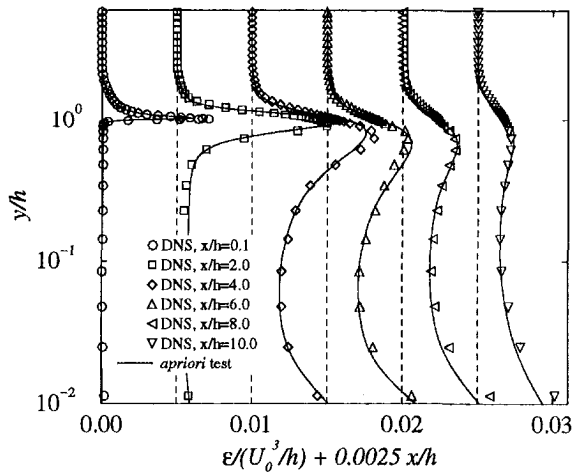

Fig. 6(*b*) ϵ profiles, a priori test

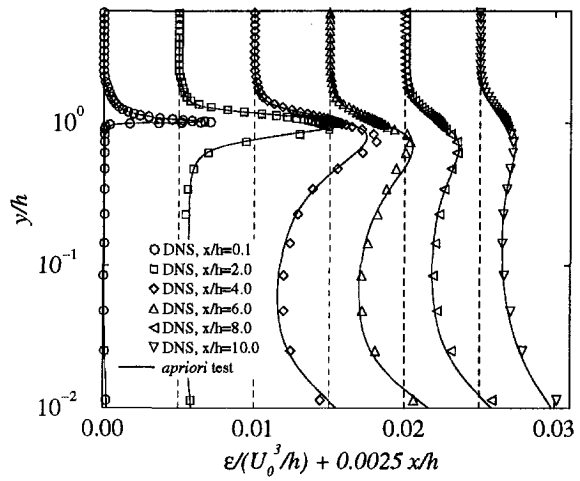

Fig. 7(*a*) ϵ **a priori profiles with** U^{DNS}, k^{DNS}, $\overline{u_i u_j}^{DNS}$ **and Eq. (3)**

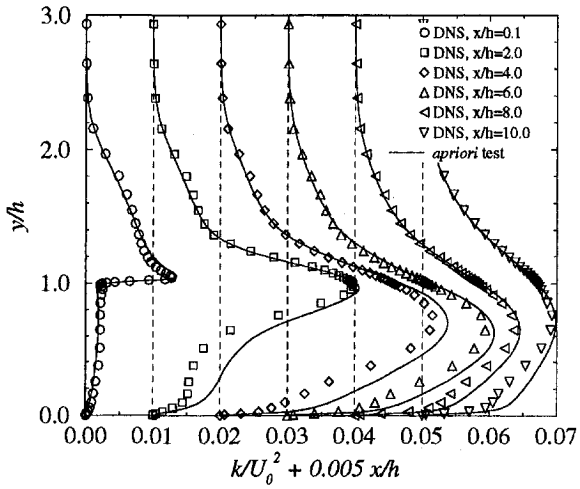

Fig. 7(*b*) *k* **a priori profiles without the extra-production term in Eq. (3)**

prediction has been obtained. The full computation presented in the previous section used $C_\mu = 0.22$; this behavior in the secondary recirculation is not improved by modifying C_μ. Hence, the usual gradient transport formula performs very well in the shear layer but over-predicts the turbulence in the near-wall region, especially in the secondary recirculation region. We tried to improve the Daly-Harlow model by including a dependence on gradients of the mean flow, but even when more accurate *k*-profiles in the secondary bubble were obtained by the a priori test, the full computation did not show any improvement in the C_f distribution.

In conclusion, these results lead us to believe that both the *k* and ϵ equations of the Second Moment Closure approach represent the physics of the flow quite well (at least in this case) and that the backflow and recovery problems come from other equations of the model, i.e., the Reynolds-stress transport equations.

The same kind of a priori test was repeated for each $\overline{u_i u_j}$-equation and its associated elliptic relaxation operator for the pressure-strain correlation. We have already explained the interest in doing such tests: the full RANS computation does not isolate faults in the modeling. Indeed, the $\overline{uv}$-profiles obtained through the full computation seem to be quite good whereas the a priori test (with $\overline{u^2}$, $\overline{v^2}$, U, V, k and ϵ fixed to their DNS value) shows an over-prediction of the gradient—$\partial_y \overline{uv}$ near the wall (Fig. 8). This erroneous gradient has a crucial influence on mean flow prediction.

The corresponding results for $\overline{v^2}$ are portrayed in Fig. 9. The computation of $\overline{u^2}$ will not be shown, but the levels of agreement to data are similar to Fig. 9. In both cases the a priori solution is much better than was found for $\overline{uv}$. Also, Fig. 9 shows again the interest of this a priori testing technique. The full computation predicts a sever under-estimation of $\overline{v^2}$ in the whole domain, and especially in the recirculation. One might think that the $\overline{v^2}$-equation needs to be improved, whereas the a priori test shows that once all the other variables are well predicted, there is no need of modifications at all.

The mean momentum budgets show that the dominant turbulent forces are $-\partial_y \overline{uv}$ and $-\partial_y \overline{v^2}$. These terms, computed with the a priori tests, are shown in Figure 10. The normal stress gradient, $\partial_y \overline{v^2}$ (Fig. 10(*a*)), which appears in the *V*-equation, has a peculiar behavior at the corner of the step ($x = 0.1$, $y = 1$), but this deficiency seems to stay local and to have little influence on the rest of the domain; the kink that is observed here has not been transported downstream ($x/h \geq 2$). With the exception of this problem, $\overline{v^2}$ is accurately predicted. The only other discrepancy can be found near the wall before the reattachment point, at $x/h = 4$ and 6. This should not directly affect the mean flow because at this location the flow is nearly parallel to the wall, $V = 0$.

Figure 10(*b*) shows the a priori turbulent force acting in the *U*-momentum equation. At locations $x/h = 4$, 6 and 8 and $y < 0.15$, this force is over-predicted by almost a factor of 2. These locations are near the reattachement point. In the backflow re-

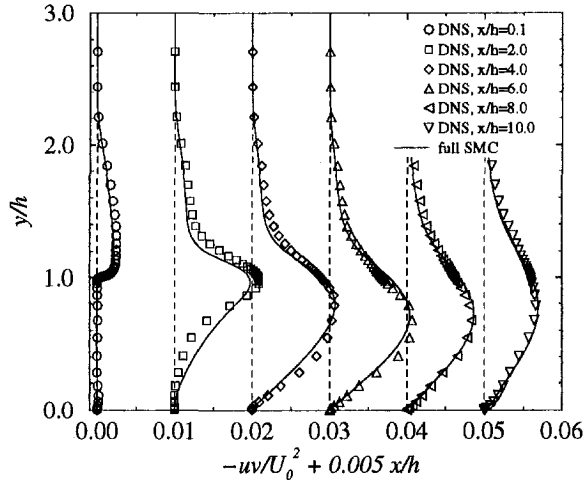

Fig. 8(*a*) $-\overline{uv}$ **profiles, full computation**

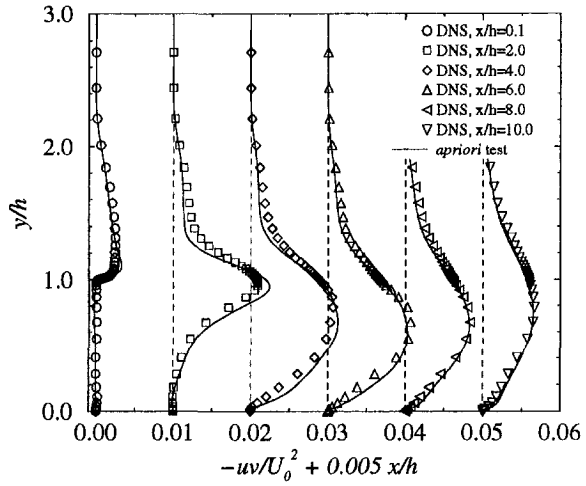

Fig. 8(*b*) $-\overline{uv}$ **profiles, a priori test**

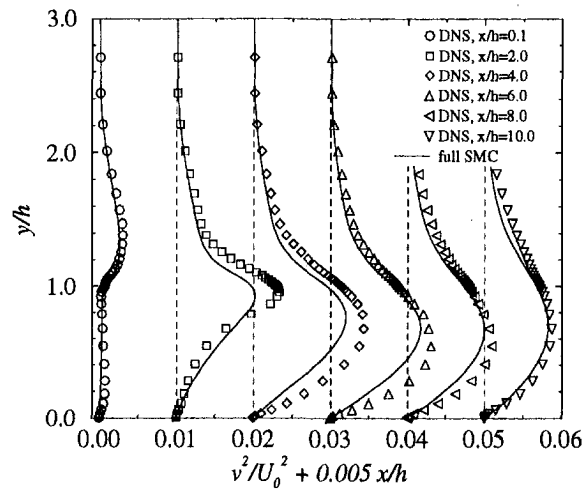

Fig. 9(*a*) $\overline{v^2}$ profiles, full computation

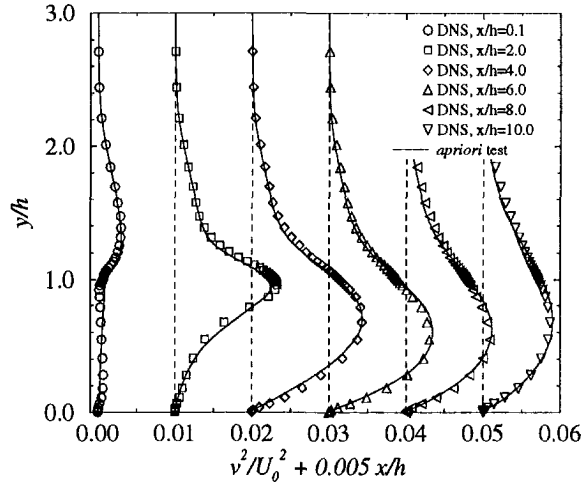

Fig. 9(*b*) $\overline{v^2}$ profiles, a priori test

gion U is negative and the turbulent force, $-\partial_y \overline{uv}$, acts to slow down the flow. Thus the over-prediction by a factor of 2 could explain the severe under-prediction of backflow we obtained with the full SMC computation. We should remark that this a priori test was performed with $\epsilon_{12}^{\mathrm{DNS}}$; this shows that anisotropy of the dissipation tensor has little effect. It does not seem that a model of dissipation anisotropy is warranted (in fact, we performed computations with one such model, but the results were similar to those presented herein).

A parametric study on the constants of the SSG pressure-strain model was performed: whatever the modifications attempted, the a priori test on the $\overline{uv}$-equation still showed an over-prediction of $-\partial_y \overline{uv}$ in the backflow region. These various tests led to the sentiment that this time the transport model might be in fault.

Hanjalic and Launder (1972) arrived at their gradient transport expression by neglecting the convection, diffusion and production terms in the third moment transport equation. Daly and Harlow (1970) only retained terms involving $\partial_l \overline{u_i u_j}$ in the $\overline{u_i u_j u_l}$ equation, with other terms acommodated by modifying the constant C_μ. The appendix uses the simpler, Daly-Harlow, form (computations were done also with the Hanjalic-Launder form, but we get similar results, i.e., the turbulent force stayed twice too high in the backflow region). We tried to modify this transport model by introducing a dependence on the gradient of mean flow:

$$T_{ij} = T_{ij}^{DH} - \frac{3}{4}\frac{\partial}{\partial x_k}\left\{ (C_\mu T)^2 P_{il} \frac{\partial \overline{u_j u_k}}{\partial x_l} + (C_\mu T)^2 P_{jl} \frac{\partial \overline{u_i u_k}}{\partial x_l} \right\} \quad (4)$$

P_{ij} is the production of $\overline{u_i u_j}$ and T_{ij}^{DH} is the classical Daly-Harlow model (cf. Appendix).

Figure 10 includes the results obtained with this new model. An improvement in the prediction of both $-\partial_y \overline{uv}$ (decrease of the over-prediction of the turbulent force in the backflow) and $-\partial_y v^2$ in the near-wall backflow region can be seen, without significant modifications to the profiles in the rest of the domain. When this new model was implemented into the whole set of equations (keeping the Daly-Harlow model for ϵ since it has given excellent results), a significant improvement in the C_f distribution was obtained (Fig. 2(*a*)). This shows that the a priori tests and the subsequent analysis are consistent with the full SMC computation. The discrepancy of the minimum friction coefficient was reduced by 50 percent without any damage to the recirculation length prediction. Such an improvement was not obtained with other modifications including additive terms in the ϵ-equation, changes of the pressure-strain model and parametric variations of the model constants. Even though the profiles of $\overline{uv}$ in the recovery were not affected by this new model during the a priori test, the improvement in the backflow region improved the friction coefficient and the U-profiles in the recovery as well (Fig. 2(*b*)).

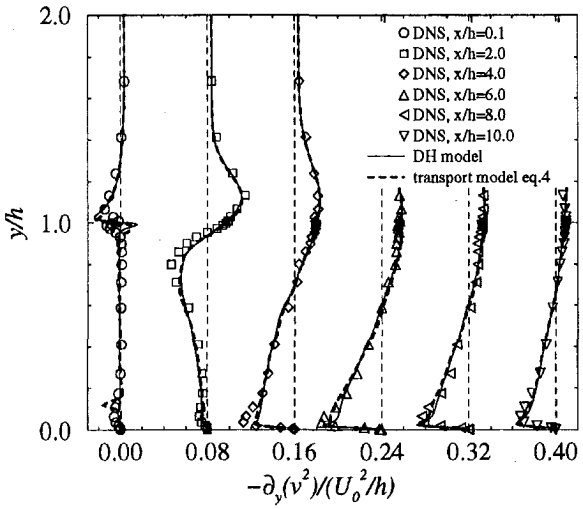

Fig. 10(*a*) A priori Reynolds force $-\partial_y \overline{v^2}$ profiles

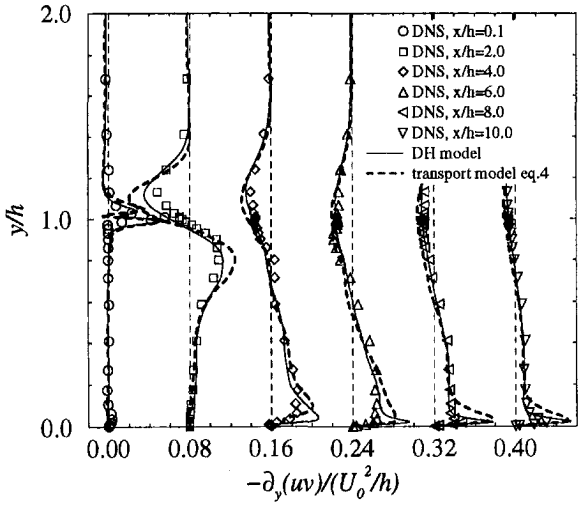

Fig. 10(*b*) A priori Reynolds force $-\partial_y \overline{uv}$ profiles

The maximum backflow is still under-predicted and needs some cure. In fact, this new model only affects the near-wall region of the flow, which becomes thinner at higher Reynolds number. We tried the new transport model in high-Re case, where the recovery discrepancy was more pronounced. Once again, the friction coefficient distribution, which shows a similar relative under-prediction by a factor of 2 of the minimum peak, was improved by 50 percent in the backflow, but this improvement could no longer be seen in the U-profiles and the solution still showed a too slow recovery.

Over all, the present results explain the interest in using this new a priori testing technique to study the solution properties of RANS models. The new transport model illustrated how shortcomings that are identified might generate ideas for improving turbulence models.

5 Conclusion

A full Second Moment Closure computation has been carried out for evaluating the turbulent flow over a backward-facing step at low Reynolds number (Re = 5,100). The model, including elliptic relaxation of pressure-strain for taking into account the non-local effects of pressure near to walls, has previously been calibrated solely with channel flow and zero pressure gradient turbulent boundary layer data at various Reynolds numbers; it has been directly applied to the backstep without any modification. The results show a very good prediction of the recirculation length, but an under-prediction of the backflow by a factor of 2. The recovery has been seen also to be too slow.

An analysis of the corresponding DNS database proved that the main bubble is definitely turbulent, even at this low Reynolds number. A new technique of a priori testing with DNS data has been developed; it consists, basically, in evaluating the accuracy of each equation of the model by solving one variable while fixing all the others to their DNS values. It came out that both Daly-Harlow transport model for k, and the ϵ-equation do surprisingly well, to the contrary of what is generally thought in the literature.

In fact, the main problem comes from the $\overline{uv}$-equation, which gives an over-prediction of the turbulent force $(-\partial_y \overline{uv})$, which is acting as slowing down the backflow, by a factor of 2 in the middle of the recirculation. We attempted a modification of the transport Daly-Harlow model, by including terms involving the gradient of mean flow. Both a priori tests and full computation showed an improvement of the near-wall behavior of the model; 50 percent of the $C_{f_{min}}$ discrepancy in the backflow has been cured without deteriorating the excellent prediction of the recirculation length.

Acknowledgments

S.P. thanks Electricité de France for their financial support; P.D. acknowledges support from the Office of Naval Research, Dr. L. P. Purtell, program manager.

References

Daly, B., and Harlow, F., 1970, "Transport Equations in Turbulence," *Physics of Fluids,* Vol. 13, No. 11, pp. 2634–2649.

Durbin, P., 1993, "A Reynolds-Stress Model for Near-Wall Turbulence," *Journal of Fluid Mechanics,* Vol. 249, pp. 465–498.

Durbin, P. A., and Laurence, D., 1996, "Nonlocal Effects in Single Point Closure," Turbulence Research Associates-96 meeting, Seoul Korea.

Hanjalic, K., and Launder, B. E., 1972, "A Reynolds Stress Model of Turbulence and Its Application to Thin Shear Flows," *Journal of Fluid Mechanics,* Vol. 52, pp. 609–638.

Hanjalic, K., 1994, "Advanced Turbulence Closure Models: A View of Current Status and Future Prospects," *International Journal of Heat and Fluid Flow,* Vol. 15, No. 3, pp. 178–203.

Hanjalic, K., 1996, "Some Resolved and Unresolved Issues in Modeling Non Equilibrium and Unsteady Turbulent Flows," *Engineering Turbulence Modeling and Measurements,* W. Rodi and G. Bergeles, eds., Elsevier Publ, Vol. 3, pp. 3–18.

Iacovides, H., and Launder, B. E., 1995, "Computational Fluid Dynamics Applied to Internal Gas-Turbine Blade Cooling: A Review," *International Journal of Heat and Fluid Flow,* Vol. 16, pp. 454–470.

Jovic, S., and Driver, D., 1995, "Reynolds Number Effect on the Skin Friction in Separated Flows Behind a Backward-Facing Step," *Experiments in Fluids,* Vol. 18.

Le, H., Moin, P., and Kim, J., 1997, "Direct Numerical Simulation of Turbulent Flow Over a Backward-Facing Step," *Journal of Fluid Mechanics,* Vol. 330, pp. 349–374.

Parneix, S., Laurence, D., and Durbin, P., 1996, "Second moment closure analysis of the backstep flow database," *Proceedings of the CTR 1996 Summer Program,* Stanford University, Vol. 6, pp. 47–62.

Rodi, W., and Mansour, N. N., 1993, "Low Reynolds Number $k-\epsilon$ Modeling With the Aid of Direct Simulation Data," *Journal of Fluid Mechanics,* Vol. 250, pp. 509–529.

Rogers, S. E., and Kwak, D., 1990, "Upwind Differencing Scheme for the Time-Accurate Incompressible Navier-Stokes Equations," *AIAA Journal,* Vol. 28, pp. 253–262.

Speziale, C. G., Sarkar, S., and Gatski, T. B., 1991, "Modeling the Pressure-Strain Correlation of Turbulence: An Invariant Dynamical Systems Approach," *Journal of Fluid Mechanics,* Vol. 227, pp. 245–272.

Wizman, V., Laurence, D., Durbin, P. A., Demuren, A. O., and M. Kanniche, 1996, "Modeling Near Wall Effects in Second Moment Closures by Elliptic Relaxation," *International Journal of Heat and Fluid Flow,* 17, 255–266.

APPENDIX

Second Moment Closure With Elliptic Relaxation

The Reynolds stress transport equation is written as:

$$D_t\overline{u_iu_j} = P_{ij} + \wp_{ij} - \overline{u_iu_j}\frac{\epsilon}{k} + T_{ij} + \nu\nabla^2\overline{u_iu_j} \qquad (A.1)$$

with

$$P_{ij} = -\overline{u_iu_k}\partial_k U_j - \overline{u_ju_k}\partial_k U_i$$

$$\wp_{ij} = -\overline{u_i\partial_j p} - \overline{u_j\partial_i p} - \left(\epsilon_{ij} - \overline{u_iu_j}\frac{\epsilon}{k}\right) + \tfrac{2}{3}\overline{u_k\partial_k p}\,\delta_{ij}$$

$$T_{ij} = -\partial_k(\overline{u_ku_iu_j} + \tfrac{2}{3}\overline{u_kp}\,\delta_{ij}) \qquad (A.2)$$

The term $\wp_{ij}$ differs from the usual pressure-strain ϕ_{ij} since it includes a deviatoric dissipation tensor in the form

$$\wp_{ij} = \phi_{ij} - \left(\epsilon_{ij} - \overline{u_iu_j}\frac{\epsilon}{k}\right) \qquad (A.3)$$

The following neutral formulation for the elliptic relaxation is now invoked (Durbin and Laurence, 1996):

$$f_{ij} - L^2\nabla^2 f_{ij} = \frac{L\wp^h_{ij}}{k} \qquad (A.4)$$

with $\wp_{ij} \equiv kf_{ij}/L$. For homogeneous turbulence $\wp_{ij}$ in Eq. (A.4) reduces to $\wp^h_{ij}$, for which any standard redistribution model ϕ^h_{ij} can be used. The SSG rapid model is

$$\wp^h_{ij_{rapid}} = -C_2 dev(P_{ij}) - C_3 dev(D_{ij}) - C_s kS_{ij} \qquad (A.5)$$

where "dev" denotes the deviatoric operator: $dev(P_{ij}) = P_{ij} - \frac{1}{3}P_{kk}\delta_{ij}$ The coefficients are:

$$C_2 = 0.4125;\ C_3 = 0.2125;\ C_s = \tfrac{1}{30} + 0.65\sqrt{A_2} \qquad (A.6)$$

The slow term is of the form

$$\wp^h_{ij_{slow}} = -[C_1 a_{ij} + C_1' dev(a_{ik}a_{kj})]\frac{k}{T} \qquad (A.7)$$

with

$$a_{ij} = dev(\overline{u_iu_j})/k \quad \text{and} \quad A_2 = a_{ij}a_{ij}. \qquad (A.8)$$

The model coefficients are

$$C_1 + 1 = \left[1.7 + 0.9 \frac{\mathcal{P}}{\epsilon} \right], \; C_1' = -1.05. \qquad \text{(A.9)}$$

The time scale, T, is defined as:

$$T = \sqrt{\frac{k^2}{\epsilon^2} + 36 \frac{\nu}{\epsilon}} \qquad \text{(A.10)}$$

The length scale L also is prevented from going to zero at the wall by using the Kolmogorov scale as a lower bound:

$$L = C_L \sqrt{\frac{k^3}{\epsilon^2} + C_\eta^2 \frac{\nu^{3/2}}{\epsilon^{1/2}}} \qquad \text{(A.11)}$$

Lastly, the Daly-Harlow expression for the turbulent diffusion is used:

$$T_{ij} = \partial_l (C_\mu \overline{u_l u_m} T \partial_m \overline{u_i u_j}) \qquad \text{(A.12)}$$

The remaining constants used in our computations are:

$$C_\mu = 0.22, \; \sigma_\epsilon = 1.5, \; C_L = 0.1, \; C_\eta = 230,$$

$$C_{\epsilon_1} = 1.44, \; C_{\epsilon_2} = 1.83 \qquad \text{(A.13)}$$

Turbulence in Compressible Mixing Layers

Foluso Ladeinde
Professor.

Wei Liu
Researcher.

Edward E. O'Brien
Professor.

Department of Mechanical Engineering,
SUNY at Stony Brook,
Stony Brook, NY 11794-2300

The direct numerical simulation (DNS) of two-dimensional compressible turbulent mixing layers is reported in this paper for convective Mach numbers M_c = 0.5, 0.8 and 1.0. All scales of flow are resolved with a 256^2 grid, although results are also obtained for 64^2, 96^2 and 128^2 grids for the purpose of determining the effective accuracy and grid-independence of our calculations. The effect of Mach number is also reported for all the Reynolds stress tensor components and for the "shear" components of the anisotropy tensor, the dissipation tensor, pressure-strain, and the triple correlation tensor. The short-time behaviors of some of these quantities are similar to those reported by Sarkar (1995) for homogeneous shear flow, in spite of the differences in the problem type and initial and boundary conditions. The relative magnitudes and signs of the unclosed terms in the Reynolds stress equations provide information on those that have to be retained for turbulence modeling as well as the sense of their contribution.

1 Introduction

Turbulence mixing layers represent a prototype of the mixing that takes place during combustion in some propulsion systems. Because this phenomenon occurs at high speed, the effect of compressibility has been studied (Sandham and Reynolds, 1991). The reference just cited also contains much of the relevant fluid dynamical work on compressible mixing layers, to which the reader should refer.

The goal in our work is to acquire a detailed understanding of compressible mixing layers with an emphasis on results that may eventually lead to affordable Reynolds stress models for engineering calculations (see Ladeinde, 1995). Therefore, a significant portion of this paper is devoted to investigation of the intensity of second moment terms in the evolution equations for the Reynolds stress tensor, with a particular emphasis on the unclosed terms in the equations. Previous work on compressible mixing layers does not address this issue.

The results reported in this paper are based on the direct numerical simulation of compressible turbulence. The numerical procedures and the validation of our computer program will be presented, together with the results on the magnitudes of some of the second moments and the effect of Mach number.

2 Mathematical Formulation

The pertinent equations are those that govern the conservation of mass, momentum and thermodynamic energy under compressible conditions. Further, each nondimensional variable is decomposed as follows, taking velocity u_i as an example:

$$u_i = \bar{u}_i + u_i'.$$

Here, an overline represents a Reynolds-averaged quantity whereas a superscripted prime denotes fluctuations. The governing equations are solved in the nondimensional form, with the free-stream velocity $\bar{u}_\infty = \bar{u}|_{y\to\infty}$ taken as the velocity scale and the vorticity thickness δ_ω as length scale, which is defined as

$$\delta_\omega = \frac{\Delta U_\infty}{\left|\dfrac{d(\overline{\rho u}/\bar{\rho})}{dy}\right|_{y=0}},$$

where ΔU_∞ is the velocity difference across the layer, i.e., $\Delta U_\infty = \bar{u}|_{y\to\infty} - \bar{u}|_{y\to-\infty}$. The mean velocity profile in all cases is given by:

$$\bar{u} = \tanh(2y).$$

The initial mean temperature profile is calculated using the Crocco-Busemann relation, and assuming unity Prandtl number:

$$\bar{T} = 1 + M_c^2 \frac{(\gamma - 1)}{2}(1 - \bar{u}^2),$$

where γ is the ratio of specific heats and M_c is the free-stream Mach number (or convective Mach number), defined as

$$M_c = \frac{\Delta U_\infty}{c_\infty}.$$

The quantity c_∞ is the free-stream sound speed. Uniform pressure is assumed for the initial mean flow ($\bar{p}_0 = 1$) and the mean density profile is obtained from:

$$\bar{\rho}_0 = \frac{\bar{\rho}_0 \bar{T}_0}{\gamma M_c^2}.$$

Superimposed on the mean velocity profile are disturbances of the form

$$u' = A_m \frac{yL}{10\pi} \sin\left(\frac{2\pi x}{L_x}\right) e^{-(y^2/10)}, \quad (1)$$

$$v' = A_m \cos\left(\frac{2\pi x}{L_x}\right) e^{-(y^2/10)}, \quad (2)$$

where the amplitude A_m is chosen to be 0.05, following Sandham and Yee (1989) and L_x is the length of the domain in x-direction. The computational domain is $(x, y) \in (0, 20) \times (-50, 50)$. The velocity perturbation in the y-direction is made to resemble the eigenfunction from the linear theory, while that for the streamwise component is chosen so that the entire disturbance is divergence-free.

Four different meshes, 64^2, 96^2, 128^2 and 256^2, are chosen for our calculations. For each mesh, a constant grid size distribution is employed in the streamwise direction, i.e., constant Δx, while, in the cross stream, the grid points are unequally spaced, with mesh concentration near the center of the layer ($y = 0$), to cover the region dominated by large scale structures. The mesh generation routine is described in detail by Drummond

Contributed by the Fluids Engineering Division for publication in the JOURNAL OF FLUIDS ENGINEERING. Manuscript received by the Fluids Engineering Division November 21, 1996; revised manuscript received October 15, 1997. Associate Technical Editor: M. M. Sindir.

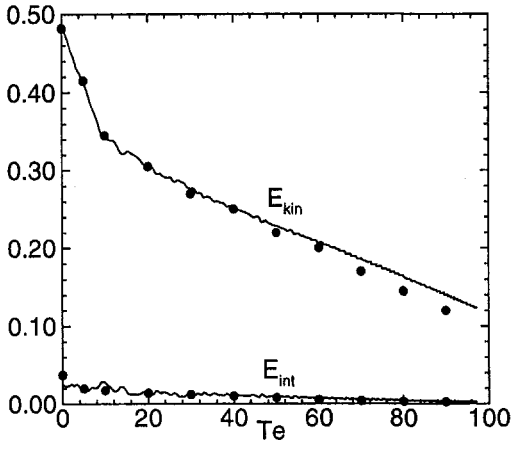

Fig. 1 Characteristics of the SV/PS (M_s = 0.5) Simulation. Results from our work (lines) are compared with the pseudospectral calculations by Ghosh and Matthaeus (1992) (dots). E_{kin} is total kinetic energy, E_{int} is total internal energy and T_e is eddy turn over time.

(1988). A periodic boundary condition is imposed in the x-direction. For the y-boundaries, a zero velocity gradient condition is imposed as a simpler but an acceptable alternative to the NSCBC conditions (Poinsot and Lele, 1992).

Each term of the evolution equations for the Reynolds stress tensor $\overline{\rho u_i'' u_j''}$ has been computed for the purpose of examining the intensity of turbulence in mixing layers. The goal here is to investigate the magnitudes of the unclosed terms in the equations and guide the modeling of these terms. The exact transport equation for the Reynold stress tensor is (Sarkar et al., 1991)

$$\underbrace{\frac{\partial}{\partial t}(\widetilde{\rho u_i'' u_j''})}_{1} + \underbrace{\frac{\partial}{\partial x_k}(\overline{\rho} \widetilde{u_i'' u_j''} \tilde{u}_k)}_{2} = \underbrace{\mathbf{P}_{ij}}_{3} + \underbrace{\pi_{ij}}_{4} - \underbrace{\mathbf{T}_{ijk,k}}_{5} - \underbrace{\overline{\rho}\epsilon_{ij}}_{6} + \underbrace{\frac{2}{3}\overline{p'\theta}\delta_{ij}}_{7} + \underbrace{(-u_i''\overline{p}_{,j} - \overline{u_j''}\overline{p}_{,i})}_{\text{Remaining Term1}} + \underbrace{(\overline{u_i''}\overline{\sigma}_{jk,k} + \overline{u_j''}\overline{\sigma}_{ik,k})}_{\text{Remaining Term2}}, \quad (3)$$

where

$$\mathbf{P}_{ij} = -\overline{\rho}(\widetilde{u_i'' u_k''}\tilde{u}_{j,k} + \widetilde{u_j'' u_k''}\tilde{u}_{i,k}),$$

$$\pi_{ij} = \overline{p'u_{i,j}'} + \overline{p'u_{j,i}'} - \tfrac{2}{3}\overline{p'\theta}\delta_{ij},$$

$$\mathbf{T}_{ijk} = \overline{\rho}\widetilde{u_i'' u_j'' u_k''} + (\overline{p'u_i'}\delta_{jk} + \overline{p'u_j'}\delta_{ik}) - (\overline{u_i'\sigma_{jk}'} + \overline{u_j'\sigma_{ik}'}),$$

$$\overline{\rho}\epsilon_{ij} = \overline{\sigma_{ik}'u_{j,k}'} + \overline{\sigma_{jk}'u_{i,k}'},$$

$$\theta = u_{k,k}',$$

σ_{ij} is the viscous stress:

$$\sigma_{ij} = \mu(u_{i,j} + u_{j,i} - \tfrac{2}{3}u_{k,k}\delta_{ij}).$$

In Eq. (3), $\mathbf{P}_{ij}$ is the production, π_{ij} the deviatoric part of the pressure-strain correlation, $\mathbf{T}_{ijk}$ the diffusive transport, ϵ_{ij} the turbulent dissipation rate tensor and $\overline{p'\theta}$ the pressure-dilatation correlation. The symbol tilde, "~", on a variable indicates Favre-averaging defined, for any variable ϕ, as

$$\tilde{\phi} = \frac{\overline{\rho\phi}}{\overline{\rho}}.$$

All terms are calculated at position $y = 0$ at different times. In a modeling framework, the terms 4 to 7, Remaining Term1 and Remaining Term2 in (3) are unclosed and therefore need to be modeled.

3 Numerical Method

A high-order finite difference-based ENO (Essentially Non-Oscillatory) scheme is used for the direct numerical simulation (DNS) of compressible turbulence, details of which are available in Ladeinde et al. (1996). The procedure can be expressed in the operational form:

$$u(x_j, t_{n+1}) = E(\tau)\cdot R(\hat{f}(u(x_j, t_n)); \tau), \quad (4)$$

where $E(\cdot)$ is an operator representing the advancement of the solution in time from level n to $n+1$, $\tau = t_{n+1} - t_n$ and $R(\cdot)$ is the reconstruction of the numerical flux, $\hat{f}$, which is of the form:

$$\hat{f}_{j+1/2}(u(x_j, t_n); \tau) = \sum_{k=0}^{md} c(i-j, k)\cdot f[i, k], \quad (5)$$

where md is the order of the procedure, c is a high-order interpolation coefficient, i is the left most point in the stencil used to approximate $\hat{f}_{j+(1/2)}$, and $f[i, k]$ is the undivided difference of the flux term.

A third-order explicit Runge-Kutta TVD scheme is used for the time advancement of the operator $E(\cdot)$ in Eq. (4). The primary dependent variables (ρ, u, v, E) were obtained directly from the ENO simulation. The pressures and temperatures were calculated as follows

$$p = (\gamma - 1)[E - \tfrac{1}{2}\rho(u^2 + v^2 + w^2)],$$

$$T = \frac{\gamma M_c^2 p}{\rho}.$$

4 Results

The computer program used for the present simulations has been validated for the kinds of calculations reported here. One of the validation exercises is reported in Ladeinde et al. (1995) and pertains to the DNS of the two-dimensional compressible turbulence problem investigated by Ghosh and Matthaeus (1992), who used the pseudospectral method. Four types of initial conditions were investigated. Figures 1 and 2 show the comparisons for the SV/PS initial condition case at M_s = 0.5 (see Ladeinde et al., 1995 for notations and details). In Fig. 1,

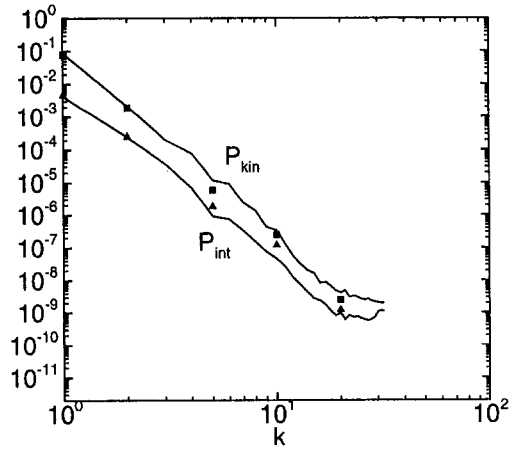

Fig. 2 Characteristics of the SV/PS (M_s = 0.5) Simulation. Results from our work (lines) are compared with the pseudospectral calculations by Ghosh and Matthaeus (1992) at $T_e \cong 20.5$. The circular and triangular symbols denote the results for of Ghosh and Matthaeus for P_{kin} and P_{int}, respectively. P_{kin} is kinetic energy spectrum, P_{int} is internal energy spectrum and T_e is eddy turn over time, and k is wavenumber.

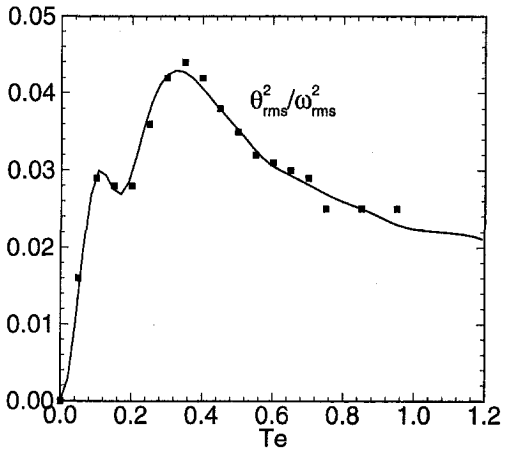

Fig. 3 Comparison of $\theta^2_{rms}/\omega^2_{rms}$ with the results in Lee et al. (1991) for eddy shocklets in three-dimensional decaying compressible turbulence. θ and ω are fluctuating dilatation and vorticity, respectively. Mach numbers, Ma, of 0.65 and 1.65 were compared, with comparable agreement. Figure shows the comparison for Ma = 0.65. T_e is eddy turn over time.

the time evolution of E_{int} (average internal energy) and E_{kin} (average kinetic energy) are shown. Figure 2 shows the spectra of the internal energy and the kinetic energy, as functions of the wavenumber. The excellent agreement between the two sets of calculations is apparent.

Another test to which our program was subjected consists of the reproduction of the results presented by Lee et al. (1991) for the eddy shocklets in decaying compressible turbulence. The conditions in Lee et al. were used except for the numerical procedure which, in Lee et al., is based on the compact Padé approximant scheme. Figures 3 shows the comparison of the ratio $\theta_{\text{rms}}/\omega_{\text{rms}}$ (where θ is fluctuating dilatation and ω is fluctuating vorticity) with the results reported by Lee et al. Good agreement is apparent. Comparisons were also made for the skewness and flatness (not shown), also with good agreement.

The simulation of the two-dimensional compressible turbulent mixing layers, on which our study of the turbulence moment equations is based, uses the same conditions as in Sandham and Yee (1989). Figure 4 shows the evolution of vorticity thickness δ_ω at M_c = 0.8, Re = 400 for different meshes. The same quantity calculated by Sandham and Yee with the TVD method and the McCormack method is also shown in Fig. 4 for comparison purposes. The vorticity, density, and pressure fields are

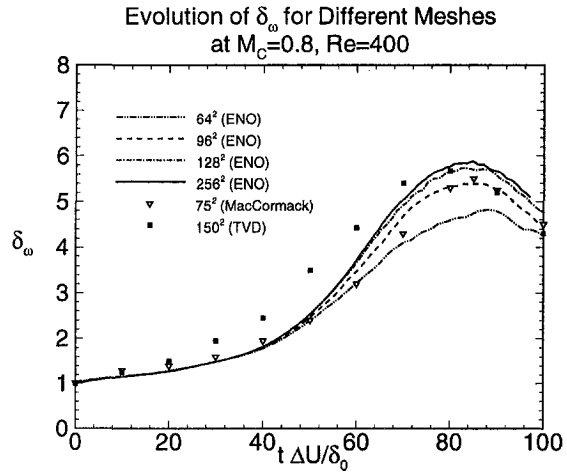

Fig. 4 Evolution of the vorticity thickness δ_ω at M_c = 0.8, Re = 400 for different meshes: present work (lines), Sandham and Yee (1989) (symbols)

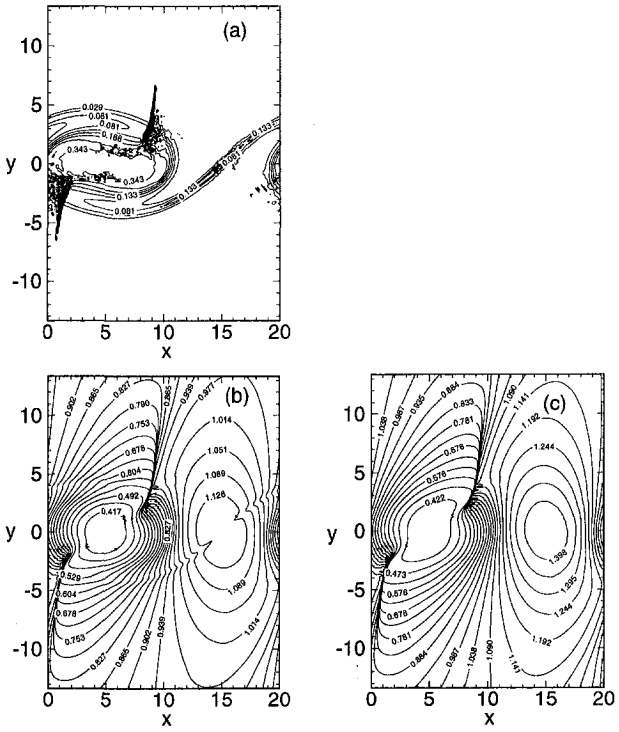

Fig. 5 Contour maps from the present work: (*a*) vorticity field, (*b*) density field, and (*c*) pressure field

shown in Fig. 5, which shows identical distribution to those reported by Sandham and Yee (1989) (not shown). The vortex rollup can be observed, as can the precision with which the local shock is captured. Some comments are in order for the oscillations in the density field of Fig. 5(*b*) as there exists at least two reasons to suggest why the oscillations might be physical. First, our numerical procedure is constructed to avoid such oscillations that are numerical in nature (Shu et al., 1989). For another, we have not observed the same oscillation with the pressure distribution (Fig. 5(*c*)), which on the basis of the similarity of the two fields, evidently requires the same computational challenge as the density field calculation.

It is important that numerical procedures be able to exhibit grid independence, if the results they provide are to be of any use. Grid independence of our code was investigated for the case M_c = 0.8, Re = 400 (see Fig. 4). The asymptotic behavior of our calculation can be observed: the curves become closer together as the grid is refined, such that the results are almost identical for 128^2 and 256^2. This kind of result generates confidence in the calculations. The results with MacCormack (75^2 mesh) and TVD (150^2 mesh) methods, which were carried out by Sandham and Yee (1989), are also presented in the same figure.

Our computer program has also been put through an accuracy study to determine the actual spatial accuracy of the schemes. The same grids shown in Fig. 4 are used for this study, whereby errors are measured assuming the results for 256^2 are "exact." The procedure for obtaining accuracy consists of the assumption that the error, E_i, for a grid denoted by "i," can be written as $E_i = \alpha \cdot \Delta_i^\beta$, where the further assumption is made that the constants α and β are the same for all grids. This error is defined as

$$E_i \equiv \bar{\delta}_{256} - \bar{\delta}_i,$$

where

$$\bar{\delta}_i \equiv \frac{1}{t}\int_0^t \delta_\omega^i \cdot dt,$$

which is a time-average of the vorticity thickness δ_ω. The con-

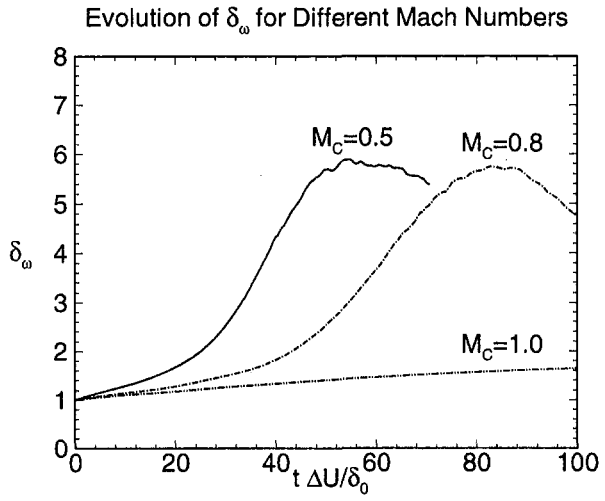

Fig. 6 Evolution of vorticity thickness δ_ω for different Mach numbers

stants α and β are determined using 64^2, 96^2, and 128^2 grid, via the least-square method. The result is

$$E_i \simeq 176.42 \cdot \Delta_i^{3.24},$$

which shows that the order of accuracy of our 2D ENO code is approximately third (Δ_i^3).

The validated computer program has been used to generate the mixing layer results shown in Figs. 6 through 10. Figure 6 shows the vorticity thickness (δ_ω) for three Mach numbers 0.5, 0.8 and 1.0 using the initial conditions described earlier in this paper. The Reynolds number is 400 for all cases. The well-known result of thinner layer thickness with increasing Mach number is reproduced in our calculation. In general, we observe an initial period of slow, linear growth and a much faster nonlin-

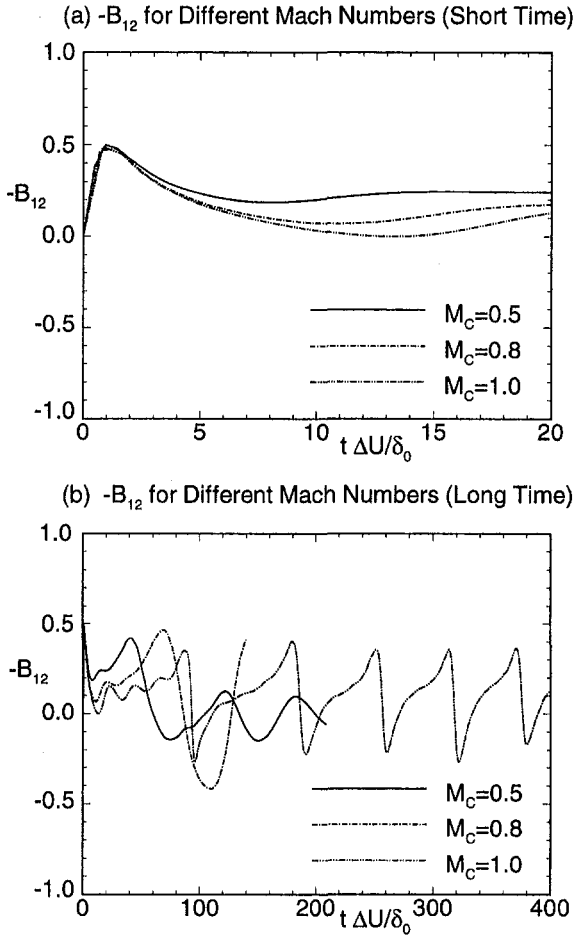

Fig. 7 Evolution of $-B_{12}$ for different Mach numbers: (*a*) short time, (*b*) long time

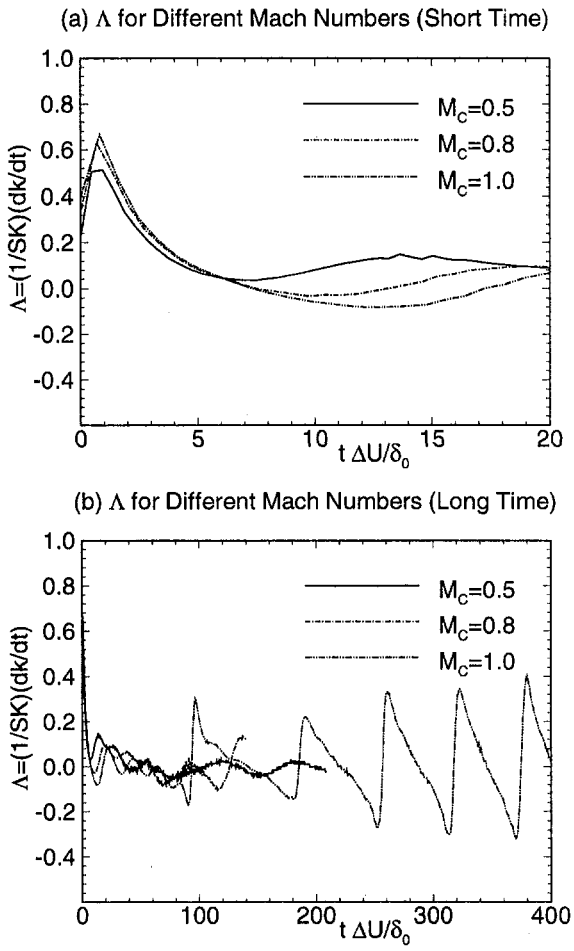

Fig. 8 Evolution of $\Lambda = (1/SK)(dK/dt)$ for different Mach numbers: (*a*) short time, (*b*) long time

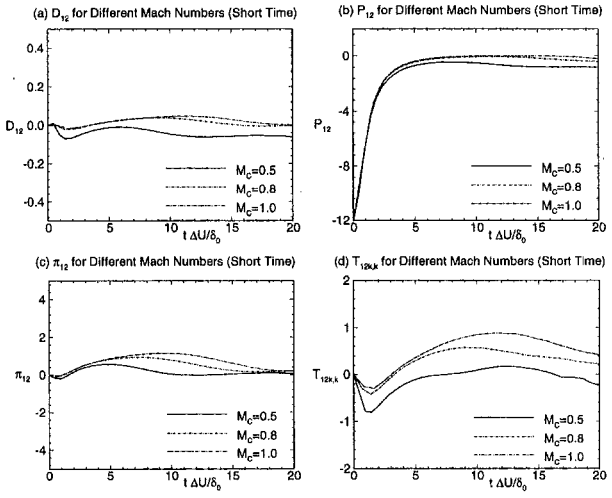

Fig. 9 Evolution of the "shear" components: (*a*) dissipation, D_{12}, (*b*) production, P_{12}, (*c*) pressure-strain, π_{12}, (*d*) transport, $T_{12k,k}$. Results are shown for short time.

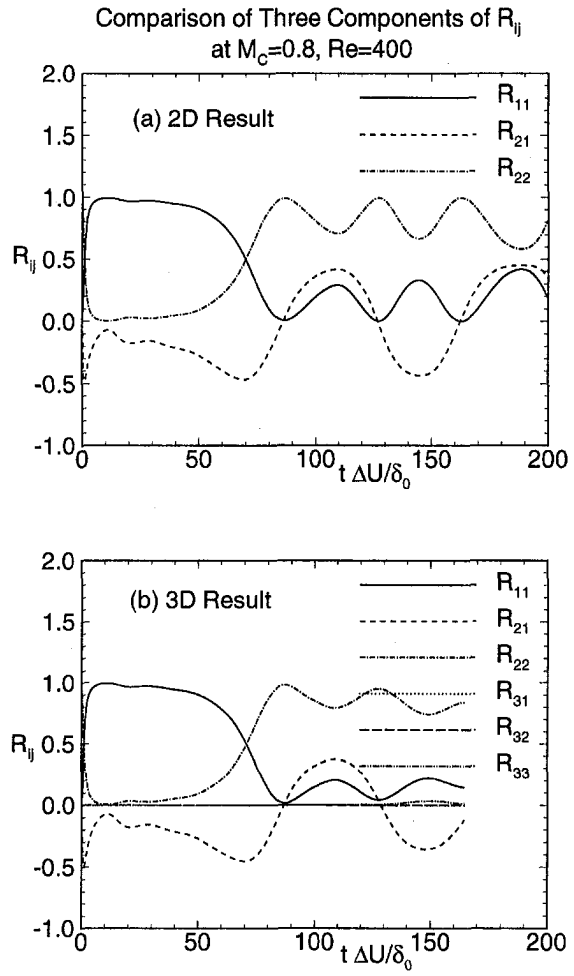

Fig. 10 Comparison of the components of Reynolds stress tensor $R_{ij} = \widetilde{u_i''u_j''}/2K$ for M_c = 0.8, Re = 400: (*a*) 2D results, (*b*) 3D results

ear growth at a later time, which are also consistent with those reported by Sandham and Reynolds (1991). For the case M_c = 0.5, no shocks were found in the flow field. However, for M_c = 0.8, local shock waves were generated during the development of vortex rollup. This phenomenon was also observed for the Mach numbers beyond 0.8.

A study of the evolution of the anisotropic tensor $B_{ij} = \widetilde{u_i''u_j''}/2K - (1/3)\delta_{ij}$ (here $K = (1/2)\widetilde{u_k''u_k''}$) shows that, at short time $0 < t' < 20$ ($t' = t \cdot \Delta U_\infty/\delta_0$), there is a systematic decrease in the quantity $-B_{12}$ with increasing Mach number (Fig. 7(*a*)). This might have already been implied by Sarkar (1995), who reported similar behavior for homogeneous shear flow. During the same time period, other quantities develop in a consistent pattern. The value of $\Lambda = (1/SK)(dK/dt)$, which describes the instantaneous temporal growth rate of K, tends to be higher for lower Mach numbers (Fig. 8(*a*)) (S is the shear rate, here defined as $S = (\partial\tilde{u}/\partial y)_{y=0}$). Note that these results are consistent with those reported for homogeneous shear flow by Sarkar (1995), despite the differences in the initial conditions and problem setup. However, we observed that, at long time in the case of mixing layers, the behaviors do not show any consistent pattern. Each quantity shows a wavy evolution pattern, with larger amplitudes for increasing Mach number. The "shear" component B_{12} seems to approach a zero mean value at long time, although the oscillation is stronger for the higher Mach number cases (Fig. 7(*b*)). Similar observations were made for Λ (Fig. 8(*b*)).

Other terms in the Reynolds stress transport equation (3) are also studied. The magnitude of pressure-dilatation $(\overline{p'\theta})$, as well as terms [2], [Remaining Term1] and [Remaining Term2] in (3) are all insignificant for all Mach number cases. Discussed here are the "shear" components of four tensors including dissipation (D_{ij}), production (P_{ij}), pressure-strain (π_{ij}), and transport ($T_{ijk,k}$). For convenience, these quantities are rescaled by SK with S and K defined as above. At short time, all four quantities (D_{12}, P_{12}, π_{12} and $T_{12k,k}$) show a similar variation with Mach number. That is, their magnitudes increase with increasing Mach number (Fig. 9(*a*), (*b*), (*c*) and (*d*)). The comparison of the three components of the Reynolds stress tensor $R_{ij} = \widetilde{u_i''u_j''}/2K$ for M_c = 0.8, Re = 400 shows that the R_{11} component dominates at early time, after which it decreases in magnitude and begins to oscillate. The other components, R_{12} and R_{22}, are significant in magnitude at later time, although with a large oscillation. R_{12} is negative for most of the time while other components are positive (Fig. 10(*a*)).

5 Discussion

It can be observed from our procedure that extra efforts were made to produce high quality calculations and to characterize the effective accuracy of our numerical procedures, which was found to be approximately $O(\Delta^3)$. Based on the grid convergence study, as well as some elementary scaling analysis (not shown), it would seem that the 128^2 grid is sufficient to resolve the necessary DNS scales, although most of the results have been generated with 256^2 grid. Evidently, higher parameter values may dictate different grid requirements.

The first interesting observation from the present study is the similar profile at early time for the kinetic energy growth rate Λ and the anisotropy tensor B_{ij} with quantities reported by Sarkar (1995) for the homogeneous shear flow. Initial and boundary conditions are different for these two problems so that, on the surface, there are few reasons to expect similar results. It would seem that the nature of shear and the definitions of these two quantities (Λ and B_{ij}) are such as to nullify the effects of initial and boundary conditions. However, at long time, when nonlinearity is stronger, the behaviors in the case of mixing layers show no consistent pattern. The literature does not report on the long time behavior in the homogeneous shear layer case, so that no comparisons can be made.

Although the calculations presented in this paper are two-dimensional, they might still be relevant to the physical engineering problem which is evidently three-dimensional (Moser and Rogers, 1993). To support this suggestion, we carried out a preliminary calculation of several three-dimensional mixing layers and compared some of the fields with the two-dimensional results, using similar initial conditions. For example, Fig. 10(*b*) is the Reynolds stress tensor obtained from the three-dimensional case. The short-time behavior clearly shows some agreement with the two-dimensional case. We point out that the two-dimensional initial conditions may not be appropriate for the three-dimensional simulations, from a mode excitation stand point. However, it is still true that the oblique shock waves, which are the optimal initial perturbation for the three-dimensional case, may not represent the physical engineering mixing layers. Thus, the comparison just discussed for two-dimensional and three-dimensional cases might be relevant.

The temporal oscillations in R_{ij} (Fig. 10(*a*)), as well as in Λ and B_{ij}, after the initial transient seems to be related to the vortex structure in the physical, spatial mixing layers. Equivalence between the temporal and physical mixing layers is assumed via the Taylor's hypothesis, which, for our setup, takes the form:

$$2\frac{\partial}{\partial t_e} = U_\infty \frac{\partial}{\partial x}$$

where $t_e = (\Delta U_\infty/\delta_0)t'$, with t' as the dimensional time.

Taking the case $M_c = 0.8$ as an example (Fig. 10(a)), the period of the oscillation of R_{11} is approximately 40 along the t_e axis, which corresponds to a traveling distance of 20 in space ($U_\infty = 1$). The latter is also equal to the size of our computational domain in which only one vortex is contained. Therefore, the temporal oscillations in some of these variables are related to the repetition of the domain under the assumption of periodicity in space.

To examine the validity of this explanation, we carried out a test in which two vortices were forced into the same size of computational domain. We observed that the flow contains two cells (not shown) at short time ($0 < t_e < 50$), but that the two cells coalesced into a single cell at a later time ($t_e > 100$). At short time, when two cells were present, the period of the oscillations reduced to approximately 20 in time t_e, corresponding to a streamwise spatial distance of 10, which is consistent with Taylor's hypothesis. When the two cells coalesced, the period in time t_e becomes 40, which is the same as that for the regular calculations with one vortex. Therefore, the explanation put forward above appears tenable.

Finally, the relevance of the second moment calculations to engineering may not be obvious. However, the results in this paper do show that, because of small magnitudes, modeling efforts do not need to place much emphasis on the pressure dilatation, the convective transport of Reynolds stress by the mean flow, the term [2] and the "remaining" terms in Eq. (3). Specific numerical details of the various second moment terms are useful in order-of-magnitude analysis for turbulence model development. For example, models must recognize that R_{12} is negative, for applications within the ranges of the parameters reported in this paper. The reader may also appreciate that the temporal histories provided for the various turbulence quantities in Figs. (7) through (10) are, in fact, statements about the variation of these quantities along the streamwise direction. Obviously, this is useful turbulence model data.

Acknowledgments

This work was supported by the National Science Foundation under grant no. CTS 9626413, which we gratefully acknowledge.

References

Drummond, J. P., 1988, "A Two-Dimensional Numerical Simulation of a Supersonic, Chemically Reacting Mixing Layer," NASA TM 4055, Langley Research Center, Hampton, VA.

Ghosh, S., and Matthaeus, W. H., 1992, "Low Mach Number Two-Dimensional Hydrodynamic Turbulence: Energy Budgets and Density Fluctuations in a Polytropic Fluid," *Physics of Fluids,* Vol. A4, No. 1, pp. 148–164.

Ladeinde, F., 1995, "Supersonic Flux-Split Procedure for Second Moments of Turbulence," *AIAA Journal,* Vol. 33, No. 7, pp. 1185–1195.

Ladeinde, F., O'Brien, E. E., and Cai, X. D., 1996, "A Parallelized ENO Procedure for Direct Numerical Simulation of Compressible Turbulence," *Journal of Scientific Computing,* Vol. 11, No. 3, pp. 215–241.

Ladeinde, F., O'Brien, E. E., Cai, X., and Liu, W., 1995, "Advection by Polytropic Compressible Turbulence," *Physics of Fluids,* Vol. 7, No. 11, pp. 2848–2857.

Lee, S., Lele, S. K., and Moin, P., 1991, "Eddy Shocklets in Decaying Compressible Turbulence," *Physics of Fluids,* Vol. A3, No. 4, pp. 657–664.

Moser, R. D., and Rogers, M. M., 1993, "The Three-Dimensional Evolution of a Plane Mixing Layer: Pairing and Transition to Turbulence," *Journal of Fluid Mechanics,* Vol. 247, pp. 275–320.

Poinsot, T. J., and Lele, S. K., 1992, "Boundary Conditions for Direct Simulations of Compressible Viscous Flows," *Journal of Computational Physics,* Vol. 101, pp. 104–129.

Sandham, N. D., and Reynolds, W. C., 1991, "Three-Dimensional Simulations of Large Eddies in the Compressible Mixing Layer," *Journal of Fluid Mechanics,* Vol. 224, pp. 133–158.

Sandham, N. D., and Yee, H. C., 1989, "A Numerical Study of a Class of TVD Schemes for Compressible Mixing Layers," NASA TM 102194, Ames Research Center, Moffett Field, CA.

Sarkar, S., 1995, "The Stabilizing Effect of Compressibility in Turbulent Shear Flow," *Journal of Fluid Mechanics,* Vol. 282, pp. 163–186.

Sarkar, S., Erlebacher, G., Hussaini, M. Y., and Kreiss, H. O., 1991, "The Analysis and Modelling of Dilatational Terms in Compressible Turbulence," *Journal of Fluid Mechanics,* Vol. 227, pp. 473–493.

Shu, C.-W., and Osher, S., 1989, "Efficient Implementation of Essentially Non-Oscillatory Shock Capturing Schemes II," *Journal of Computational Physics,* Vol. 83, pp. 32–78.

R. R. Parchen
Eindhoven University of Technology,
Faculty of Applied Physics,
Fluid Dynamics Laboratory,
P.O. Box 513,
NL 5600 MB, Eindhoven,
The Netherlands;
CURRENT ADDRESS: TNO Institute of
Applied Physics,
PO Box 155,
NL 2600 AD, Delft,
The Netherlands

W. Steenbergen
Eindhoven University of Technology,
Faculty of Applied Physics,
Fluid Dynamics Laboratory,
P.O. Box 513,
NL 5600 MB, Eindhoven,
The Netherlands;
CURRENT ADDRESS: University of Twente,
Faculty of Applied Physics,
Applied Optics Group,
P.O. Box 217,
NL 7500 AE Enschede,
The Netherlands

An Experimental and Numerical Study of Turbulent Swirling Pipe Flows[1]

Both experimental and numerical studies have been performed aimed at the description of the decay of swirl in turbulent pipe flows. Emphasis is put on the effect of the initial velocity distribution on the rate of decay. The experiments show that, even far downstream of the swirl generator, the decay of the integral amount of angular momentum depends on the initial velocity distribution. This suggests that the description of the decay in terms of the widely suggested single exponential, function, is not sufficient. The calculations are based on (i) a standard $k - \epsilon$ model and (ii) models based on an algebraic transport model for the turbulent stresses. It appears that in a weakly swirling pipe flow, second-order models reduce to simple modifications of the standard $k - \epsilon$ model. While the standard $k - \epsilon$ model predicts a decay largely insensitive to the initial velocity distribution, the modified versions of the $k - \epsilon$ model, the ASM and the RSM, predict a strong sensitivity to the initial velocity distribution. Nevertheless, the standard $k - \epsilon$ model seems to predict the rate of decay of the swirl better than the second-order models. It is concluded that the corrections for the streamline curvature introduced by the second-order closures, largely overestimate the effect of rotation on the radial exchange of angular momentum.

Introduction

In the last decades the use of gaseous fuels has grown sharply. Consequently, the importance of accurate flow measurements of large amounts of gas has been a major interest of all gas transport companies. Research (e.g., Mattingly et al., 1988) has shown that the accuracy of two standard techniques for flow metering, orifices and turbine meters, may suffer from disturbances in the flow. A disturbance that is known for its slow decay and for its large effect on the two above-mentioned metering techniques is swirl. Swirl may be generated when the flow passes two consecutive out-of-plane bends. This configuration is likely to occur near gas-metering stations. In the case of swirl the present standards for the arrangements of flow-metering devices do not guarantee the accurary required (0.3 percent of the total flow). To overcome this "installation effect", different strategies may be followed:

- in-situ calibration;
- flow straighteners;
- more length of straight pipe upstream of the metering device.

For economical reasons, in-situ calibration is not possible. Flow straighteners introduce undesirable pressure losses and new disturbances. For the third option knowledge is required of the rate of deacy of the swirl.

The aim of this study is to formulate simple correlation formula for the decay of swirl with the purpose to improve the design of gas-metering stations.

Swirling Pipe Flows

The character of flows relevant to transport systems for natural gas is different from the character of swirling flows encountered in other engineering environments, such as industrial burners or cyclones. The intensity of the swirl, generated by out-of-plane bends, is rather low, and since the decay of swirl is a slow process, the length of the domain of interest is large, $L/D = \mathcal{O}(100)$. Evidently, at least in parts of the domain "parabolization" is a valid approximation, and a numerical analysis may take advantage of the simplifications implied in this approach.

The amount of literature aiming at a detailed description of the relaxation of swirl in pipes is limited. Most complete experimental studies are the hot-wire experiments of Kitoh (1991), Algifri et al. (1987), the electrochemical-probe measurements of Itoh et al. (1980), and an extensive set measurements of NIST (Mattingly et al., 1988).

However, even for the mean velocity components, a common trend in the reported experiments is not always obvious. Kitoh (1991) and Algifri et al. (1987) observe a "three-region" character of the circumferential velocity distribution: a core that rotates like a solid-body; an outer region resembling a free-vortex flow; and a wall region showing a sharp decrease of the circumferential velocity. Furthermore, their results show a retarded axial flow near the pipe axis or even flow reversal. On the other hand, Mattingly et al. (1988) report a solid-body rotation extending over the complete pipe cross-section and a uniform axial velocity distribution. The lack of agreement in the main characteristics of the flow suggests that several different flow regimes may exist.

The amount of studies aimed at the prediction of swirling pipe flows is also small. Kreith and Sonju (1965) describe an analytical approach based on a constant eddy-viscosity. Kobayashi and Yoda (1987) give a description on the basis of a $k - \epsilon$ model, with modified coefficients. However, according to the present general opinion (see for example Launder, 1989) eddy-viscosity based turbulence closures are less suited for the description of swirling flows. Nevertheless, the prediction method of Kreith and Sonju (1965) for swirling flows similar to those occurring in transport systems for natural gas, leads to a fairly accurate prediction of the decay.

In the present study, the modeling is based on the second-order closure schemes. However, the simplicity of the geometry

[1] Correspondence to: J. Voskamp, Eindhoven University of Technology, Faculty of Applied Physics, Fluid Dynamics Laboratory, PO Box 513, NL 5600 MB, Eindhoven, The Netherlands

Contributed by the Fluids Engineering Division for publication in the JOURNAL OF FLUIDS ENGINEERING. Manuscript received by the Fluids Engineering Division May 28, 1994; revised manuscript received November 3, 1997. Associate Technical Editor: D. Stock. The long delay with publication of this paper is due to the difficulties encountered by the editorial board.

under consideration and the slow axial development of the flow allow substantial simplifications.

Turbulence Modeling in Swirling Pipe Flow

The Effect of Swirl on the Reynolds-Stress Tensor. To evaluate the most important effects of swirl on the Reynolds stresses, it is advantageous to consider a slightly simplified flow. Instead of a slowly developing flow, we assume that the axial development of the flow may be neglected. In this "frozen-flow" configuration the convection terms for the Reynolds stresses follow directly from the curvature terms in the Reynolds-stress transport equations in a cylindrical coordinate system, provided that the cross-flow-plane distributions of the Reynolds stresses possess a cylindrical symmetry. Because of the assumption of a frozen flow, an algebraic formulation of the Reynolds-stress equations is considered. As pointed out by Fu et al. (1988), the "standard" ASM model by Rodi (1976) ignores the stress transport due to swirl. Since these transport terms are algebraic in the Reynolds-stresses, they are retained in the following treatment.

For the radial distribution of the axial and circumferential velocity component, the $\overline{vw}$ and $\overline{uv}$ components of the Reynolds stress tensor are dominant. It appears, that for these Reynolds stress components, simple closed-form solutions of the algebraic equations are feasible. If all curvature terms in the transport equations for the stresses are neglected, the closed-form expressions for $\overline{vw}$ and $\overline{uv}$, based on the "rapid-part" approximation due to Naot et al. (1970) and the "return-to-isotropy" approximation due to Rotta (1951) reduce to

$$\overline{vw}_0 = -\frac{2}{3}\varphi_1\varphi_2\frac{k^2}{\epsilon}\left(\frac{\partial W}{\partial r} - \frac{W}{r}\right) \quad \text{and}$$

$$\overline{uv}_0 = -\frac{2}{3}\varphi_1\varphi_2\frac{k^2}{\epsilon}\frac{\partial U}{\partial r} \tag{1}$$

with,

$$\varphi_1 = \frac{1 - C_2}{C_1 + P/\epsilon - 1} \quad \text{and} \quad \varphi_2 = \frac{C_1 + C_2 P/\epsilon - 1}{C_1 + P/\epsilon - 1}$$

k, the turbulent kinetic energy,
ϵ, the rate of dissipation of the turbulent kinetic energy,
P, the production of turbulent kinetic energy, and
C_1, C_2 the coefficients for the "return to isotropy" and "rapid part" approximation, respectively. Here we consider the "standard" pressure-strain coefficient set proposed by Launder et al. (1975) and the set, optimized for flows with swirl, proposed by Gibson and Younis (1986).

The corresponding expressions including the curvature terms are,

$$\overline{vw}_1 = \frac{\overline{vw}_0}{1 + \mathrm{Ri}_{\overline{vw}}} \quad \text{and}$$

$$\overline{uv}_1 = \overline{uv}_0\frac{1 + \mathrm{Ri}_{\overline{uv}}}{(1 + \mathrm{Ri}_{\overline{vw}}/4)(1 + \mathrm{Ri}_{\overline{vw}})}, \tag{2}$$

with

$$\mathrm{Ri}_{\overline{vw}} = 4\frac{k^2}{\epsilon^2}(\varphi_1 + \varphi_3)\frac{W}{r}\left(\varphi_1\frac{\partial W}{\partial r} + \varphi_3\frac{W}{r}\right),$$

$$\mathrm{Ri}_{\overline{uv}} = \frac{k^2}{\epsilon^2}(\varphi_1 + \varphi_3)\frac{W}{r}\left(\varphi_1\frac{\partial W}{\partial r} + (3\varphi_1 + \varphi_3)\frac{W}{r}\right)$$

and

$$\varphi_3 = \frac{1}{C_1 + P/\epsilon - 1}.$$

An alternative approximation for the "rapid part" is the rotation-rate invariant approximation due to Fu et al. (1987). It appears that the expressions for $\overline{vw}$ and $\overline{uv}$ based on this approximation are almost identical to expressions based on the approximation due to Naot et al. (1970). Only the value for φ_3 is different:

$$\varphi_3 = \frac{1 - C_2}{C_1 + P/\epsilon - 1}.$$

Equations (2) show that, due to the curvature terms, the radial exchange of momentum can either be increased or decreased. For example, the radial exchange of angular momentum is reduced for velocity distributions obeying

$$\frac{\partial}{\partial r}(r^\alpha W) > 0 \quad \text{where}$$

$$\alpha = 1/(1 - C_2) \text{ (Naot et al.)} \quad \text{and} \quad \alpha \doteq 1 \text{ (Fu et al.)}$$

while in the opposite case it will be increased. It appears that, in parts of the cross-section, the predicted distribution of W scales with $r^{-\alpha/2}$, indicating that the flow is not free of axially directed vorticity here, see Fig. 1 (bottom).

Furthermore, comparison of Eqs. (1) and (2) suggests that for a slowly developing pipe flow with moderate swirl the classical $k - \epsilon$ model may be modified to incorporate effects of swirl, i.e.,

$$\overline{vw} = \frac{\overline{vw}_{k-\epsilon}}{1 + \mathrm{Ri}_{\overline{vw}}} \quad \text{and} \quad \overline{uv} = \overline{uv}_{k-\epsilon}\frac{1 + \mathrm{Ri}_{\overline{uv}}}{(1 + \mathrm{Ri}_{\overline{vw}}/4)(1 + \mathrm{Ri}_{\overline{vw}})}.$$

Indeed, Parchen (1993) shows that results obtained using a full ASM and an elliptic representation of the flow equations are almost identical to results obtained employing a parabolic representation of the equations and a modified $k - \epsilon$ model. Calculations of Chen (1992) employing a Reynolds-stress model indicate that for the case of a pipe flow with low and moderate swirl, also these results are in agreement with the modified $k - \epsilon$ model results (e.g., differences in the predicted axial velocity are less than 5 percent). The results presented here are obtained with the modified $k - \epsilon$ model and a parabolized system of equations. The modified model will be referred to as M$k - \epsilon$.

Nomenclature

C_1, C_2 = coefficients for pressure strain correlation
D = pipe diameter
k = turbulent kinetic energy
P = turbulent kinetic energy production
r, x = radial and axial position
R = pipe radius
Ri = Richardson number
S = swirl number
S_{int} = swirl number obtained from velocity distribution
S_τ = swirl number obtained from wall shear stress
U, V, W = axial, radial and circumferential velocity
U_{av} = axial velocity averaged over pipe cross section
$\overline{u^2}, \overline{v^2}\ldots$ = Reynolds stresses
β = coefficient in exponential decay function
ϵ = dissipation of turbulent kinetic energy
$\tau_{\varphi,\mathrm{wall}}$ = tangential component of wall shear stress
ν = kinematic viscosity

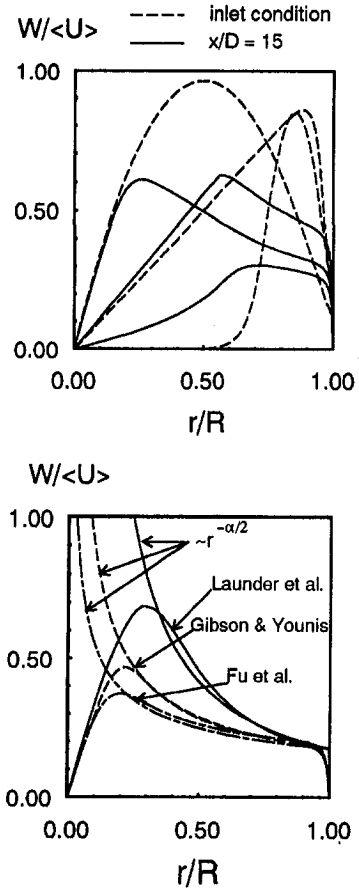

Fig. 1 Some typical distributions of the circumferential velocity component, $Re_D = 10^5$, $U_{inlet}/U_{av} = 1.0$; top: The effect of the initial condition on the circumferential velocity W. (Gibson and Younis pressure-strain coefficients); bottom: The effect of the pressure-strain model on the circumferential velocity W. ($W_{inlet}/U_{av} = 1.0$).

Decay of Swirl. A suitable measure to describe the decay of the swirl in pipe flows, is the total axial flux of angular momentum,

$$S = 2\pi \int_0^R U(rW)rdr \Big/ (\pi R^3 U_{av}^2). \tag{3}$$

The axial development of S is described by,

$$\frac{\partial S}{\partial x'} = -\tau_{\varphi,\text{wall}}/(U_{av}^2), \quad \text{with} \quad x' = x/D \quad \text{and}$$

$$\tau_{\varphi,\text{wall}} = \nu\left(\frac{\partial W}{\partial r} - \frac{W}{r}\right)_{\text{wall}} \tag{4}$$

As Eq. (4) indicates, the decay of S is determined by the wall shear stress only.

Some Typical Results. Some typical results obtained with the $Mk - \epsilon$ model are shown in Figs. 1. The most important features predicted by the calculations (see also Parchen, 1993) are:

- for a turbulent pipe flow with moderate swirl without recirculation, predictions obtained using a full ASM and predictions using the above presented $Mk - \epsilon$ model are equivalent;
- for the largest part of the pipe cross-section the radial exchange of momentum is suppressed by the swirl;
- for moderate to high swirl intensities, the distribution of the circumferential velocity component may be divided into three regions:
  - — a "frozen" core region, where the shape of the distribution of W is determined by the initial condition, see Fig. 1 (top);
  - — an intermediate region, where the shape of the distribution of W is determined by the specific form of the pressure-strain interaction approximation, see Fig. 1 (bottom));
  - — a wall region, where the flow approximately conforms to a logarithmic velocity distribution;
- the decay of the total flux of angular momentum strongly depends on the initial velocity distributions. The sensitivity to the form of the pressure-strain approximation is weaker;
- for low levels of swirl, the algebraic stress expressions reduce to the conventional Boussinesq approximation.

Description of the Experiments

Flow Apparatus. In most experiments that are described in literature, the methods applied for the generation of swirl are similar. This results in initial velocity distributions with small variation, the circumferential velocity distribution exhibiting a "three region" character, and the axial velocity distribution exhibiting retarded flow, or even flow reversal, near the center of the pipe. The aim of the experiments presented here is to study the decay of swirl at essentially different initial conditions.

The experiments are conducted in a closed-loop pipe system, containing water as the flowing medium. The pipe has an inner diameter of $\phi 70$ mm, and has a total length of 20 m. The pipe has a typical wall roughness $k/D = 1 * 10^{-5}$, which may be regarded as hydraulically smooth for the Reynolds number applied. The pipe system contains an electromagnetic flowmeter which is positioned at the end of the test pipe.

Swirl Generator. An impression of the swirl generator is given in Fig. 2. The fluid is accelerated in the tangential direction by means of a series of adjustable vanes, which are arranged in a circular pattern. The initial velocity distribution can be changed by removing the dot-hatched part of the streamline body. This allows fluid to flow through the center of the streamline body, which will change the radial distribution of angular and axial momentum.

Experimental Equipment. The instantaneous velocities are measured using a laser-Doppler velocimeter (LDV). It is a two-component reference-beam system, manufactured by Dantec. The Doppler signals are processed by Dantec frequency

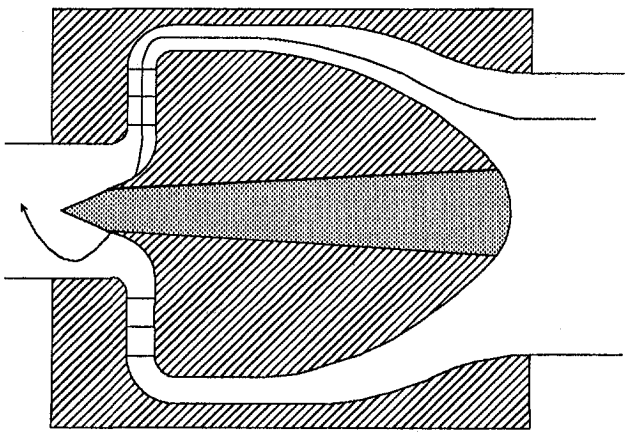

Fig. 2 The swirl generator. For the creation of different initial velocity distributions, the dot-hatched part can be removed

trackers. These trackers have been calibrated to take their nonlinear response into account.

Since most swirling flows develop into a nonaxisymmetric state, velocity measurements need to resolve all three components of the velocity vector. This can be realized by combining results from measurements with the optical system aligned at two different angles. By taking measurements at three different angles, also the complete Reynolds stress tensor is measured.

For a detailed description of the laser Doppler system and its operation, and of the measurement section, the reader is referred to Steenbergen and Stouthart (1993) and Steenbergen (1996).

Experimental Program

All experiments are conducted at a Reynolds number $U_{av}D/\nu = 50000$. At each location, 8000 samples are taken at a frequency of 200 Hz.

Starting with two different initial velocity distributions the decay of the swirl is studied. In one series of experiments, the swirl generator will be operated in the configuration depicted in Fig. 2. All fluid enters the pipe through the annular channel around the streamline body. This configuration resembles those applied by Kitoh (1991) and Algifri et al. (1987). This first type of flow will be referred to as the "concentrated vortex"-flow.

In the other series of experiments, the swirl will be generated with the center part of the streamline body (the dot-hatched part in Fig. 2) removed. Thus, nonrotating fluid is injected near the center of the pipe. This type of flow will be referred to as the "distributed vortex"-flow.

Results of the Experiments

The "Concentrated Vortex"

Mean Velocities. For the concentrated vortex, the mean velocities are given in Fig. 3. As far as the mean velocities are concerned, it appears that the distributions found in the present experiment are comparable to the distributions found by Kitoh (1991) and Alfigri et al. (1987). Near the symmetry axis, the axial component of the vorticity remains constant until $x/D = 36$. Only in the annular region outside the vicinity of the symmetry axis, the azimuthal velocity decreases in downstream direction. Until $x/D = 36$ the axial velocity distribution exhibits flow reversal near the symmetry axis. For $x/D \geq 50$, also in the vicinity of the symmetry axis the azimuthal velocity decreases. Simultaneously, the axial velocity rapidly increases in this region. This event coincides with the development of asymmetry in the flow field. Now, gradually the flow adopts a "solid body" pattern. Even in the long term, the asymmetry does not disappear.

Reynolds Stresses. The Reynolds normal stresses are given in Fig. 4. For $x/D \leq 50$, the normal stresses exhibit an increasing maximum near the center of the pipe for the major part of the decay stretch. It is worthwhile to note, that for x/D between 22.3 and 49.4, the increase in the cross-plane normal stresses v^2 and w^2 is not exhibited in the axial normal stress u^2. The levels of v^2 and w^2 are approximately equal.

The "Distributed Vortex"

Mean Velocities. The mean velocities are given in Fig. 5. In this flow, there is no recirculaton area. Contrary to the concentrated vortex flow, decay affects the flow field in the entire cross-section. At $x/D = 43.4$, the flow has adopted a solid body state of rotation. For $35.9 \leq x/D \leq 69.8$, the axial velocity distribution is remarkably flat.

Reynolds Stresses. The Reynolds normal stresses are given in Fig. 6. They show the same behavior as in the concentrated vortex flow, viz. a maximum level of the normal stresses in the central region, however, with a level of $\overline{u^2}$ which does not keep pace with v^2 and w^2.

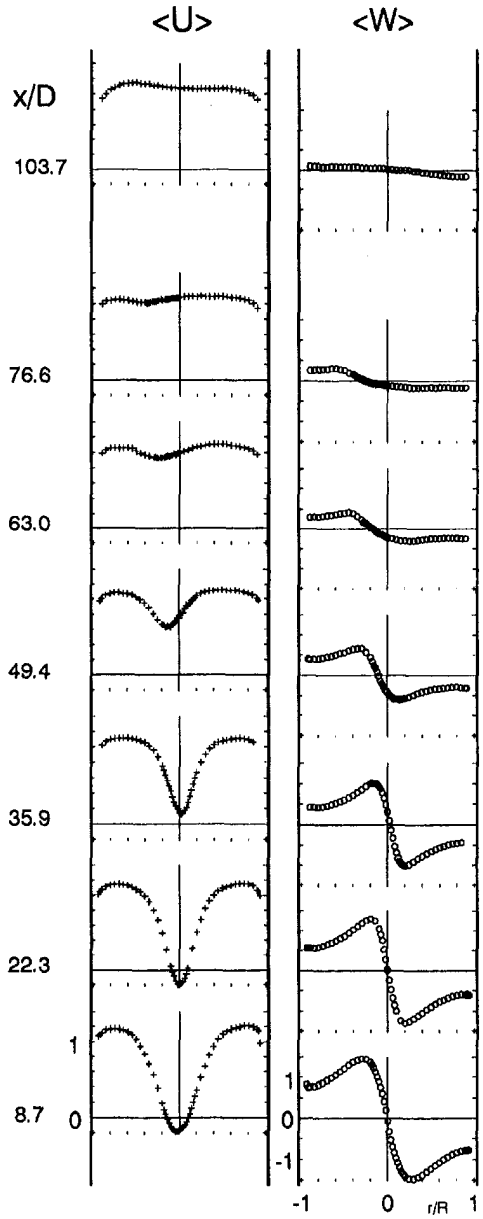

Fig. 3 The radial distributions of the axial (left) and azimuthal (right) mean velocities (±1 percent), for the "concentrated vortex"

Discussion

The behavior of the concentrated vortex flow suggests, that initially there is a strongly reduced amount of transfer of momentum from the central region to the surrounding annulus. Further downstream a region occurs with larger momentum transfer, although even at $x/D = 76.6$ a remainder of the vortex core can be observed. The development of the distributed vortex flow suggests, that there is an increased radial transfer of momentum: this results in a solid body rotation and a very flat axial velocity distribution.

Swirl Decay. The integral amount of swirl is given by the swirl number, defined in Eq. (3). Because the integrand of Eq. (3) depends on r^2, the flow in the vicinity of the wall has a relatively large contribution to the swirl number. Since we lack data from this part of the flow, the swirl number estimate de-

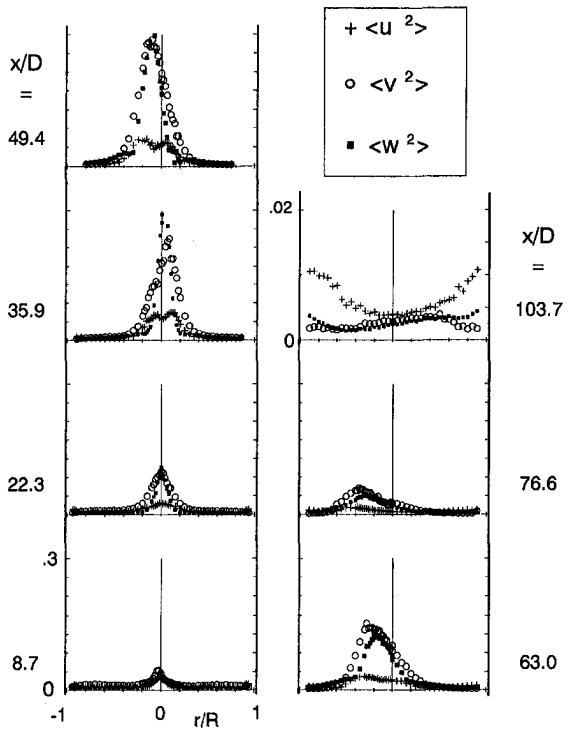

Fig. 4 The radial distributions of the components of the Reynolds-stress tensor (±10 percent) for the "concentrated vortex"

pends on the assumption concerning the velocity distribution in the wall region. Here the swirl numbers are given for (i) linear interpolation between the wall and the last measurement point ($r/R = 0.9$ for the distributed vortex, and $r/R = 0.94$ for the "concentrated vortex") and (ii) for the assumption that both U and W in the wall region are equal to the values measured in the near wall measurement point. Linear interpolation will lead to an underestimation of the swirl number, while the unphysical assumption of a constant velocity will certainly result in an overestimation. Therefore, the estimated swirl numbers can be regarded as the boundaries of an interval that certainly contains the correct value. The development of the swirl number is given in Fig. 7 for both types of swirl and for both interpolation procedures. The results have been matched with exponential functions $S = S_0 \exp(-\beta x/D)$. The average of the values of β for both interpolation procedures is also given in Fig. 7. It appears that for the entire decay process, the rate of decay of the distributed vortex exceeds that of the concentrated vortex by approximately 20 percent. This is also true for that part of the concentrated vortex for which $S \geq 0.4$. The difference between swirl numbers according to both interpolation procedures is approximately a constant fraction of the local value (parallel lines in semi-logarithmic plot). Hence, the estimation of the rate of decay, and therefore the conclusion regarding the differences in decay rates, is not invalidated by the absence of near wall data.

Measurement Accuracy

The accuracy of the determination of the decay rate has already been treated, and it appears that our conclusion regarding the differences in decay rate holds under large assumed variations of the unresolved part of the flow.

Nevertheless, it is useful to estimate the overall accuracy of the presented velocity distributions. The velocities have been nondimensionalized with the bulk velocity based on the flow meter reading, which has an accuracy of 0.1 percent (as found by calibration). The error in the mean velocities is mainly determined by the nonlinearity of the frequency trackers. Since the trackers are calibrated, this effect is almost removed. The bias that remains is caused by the error in the representation of the calibration results, tracker drift during operation, and by errors in the determination of the crossing angles of the laser beams. The overall error is estimated by integrating the axial velocity profile measured in fully developed pipe flow. The resulting flow estimate agrees within 1 percent with the flow meter result. This leads to an uncertainty of 1 percent in the mean velocities, and 2 percent additional error in the swirl number estimate. Therefore, the error due to the unresolved wall region is much larger than any other systematic error.

An impression of the uncertainty in the Reynolds stresses is obtained by comparison with fully developed pipe flow data obtained by hot-wire experiments by Lawn (1971). Our normal stresses are approximately 10 percent lower than those measured by Lawn. A more severe test is the comparison of the measured distributions of $\overline{vw}$ with the value of the tangential wall shear stress, given by Eq. (4). The distribution of $\overline{vw}$, measured at $x/D = 8.7$ in the "concentrated vortex" at $x/D =$

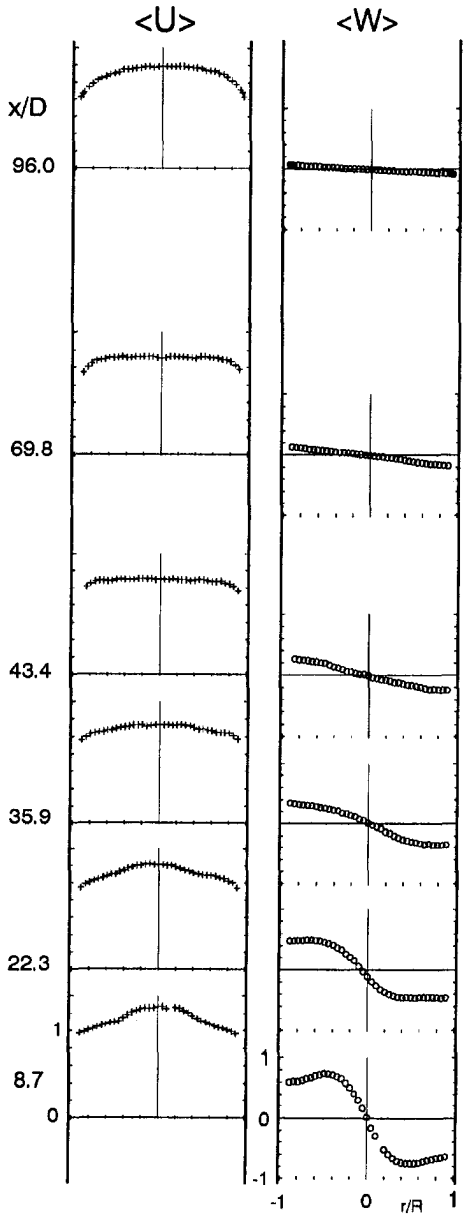

Fig. 5 The radial distributions of the axial (left) and azimuthal (right) mean velocities (±1 percent), for the "distributed vortex"

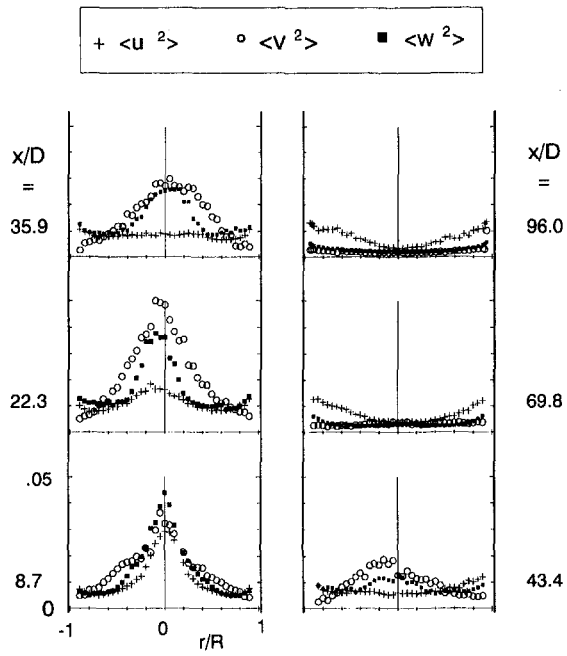

Fig. 6 The radial distributions of the components of the Reynolds-stress tensor (±10 percent) for the "distributed vortex" experiment

8.7, is given in Fig. 8, together with estimates of $\tau_{\varphi,\text{wall}}$ based on the exponential fits given in Fig. 7 for both interpolation procedures. Taking into account the uncertainty in the swirl number estimate, the measured values of $\overline{vw}$ are accurate within 10 percent.

Predictions

Results obtained with the $k-\epsilon$ model and the M$k-\epsilon$ model will be shown. For the $k-\epsilon$ model, the low-Reynolds version according to Chien (1982) is used.

Numerical Technique. The predictions are based on the parabolized versions of the transport equations. The discretization is carried out with a finite difference scheme, employing three-point discretization formula. The resulting three-diagonal matrices are solved with the Thomas algorithm, see Fletcher (1991). For the forward step, nonlinear terms are treated explicitly, while linear terms are treated implicitly. A nonuniform grid is defined between the wall and the pipe center, employing 100 or 200 grid points.

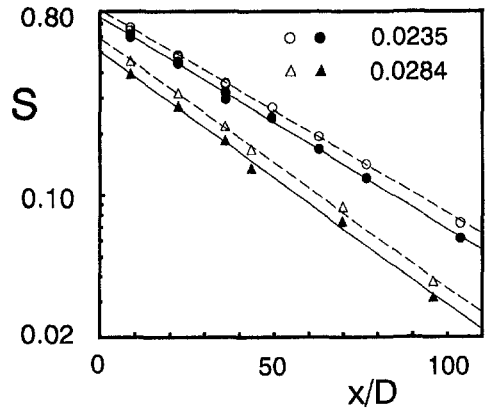

Fig. 7 Swirl numbers versus axial distance. ▲, △: "distributed vortex"; ●, ○: concentrated vortex. Open symbols: linear interpolation in wall region. Numbers: average β-values for both interpolation procedures.

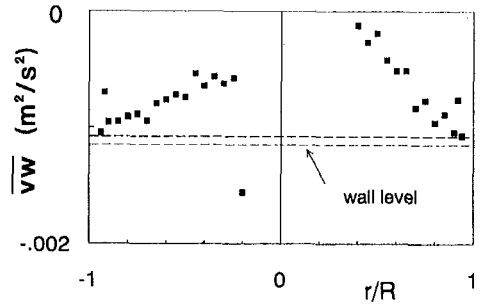

Fig. 8 Comparison of $\overline{vw}$-distribution with the wall shear stress based on momentum balance for the "concentrated vortex" at $x/D = 8.7$

For the mean velocities, the measured distributions for U and W are employed. Between the wall and the first measurement point, initial conditions have been obtained with a $\frac{1}{8}$ power law for both U and W. Between measurement points, linear interpolation was used. The initial conditions for k and ϵ where obtained from a short run of the $k-\epsilon$ model with a solid body rotation and a flat axial velocity distribution. The predictions appeared to be quite insensitive to the exact choice of initial distributions for k and ϵ.

The forward integration step is limited by the partly explicit treatment. Another limitation is the presence of strong source terms in the very first stage of the calculation, due to the application of a low-Reynolds model. The initial step size was $0.5*10^{-4}\,R$, gradually increasing to $0.1\,R$.

Computational Results. Because the predictions are based on the parabolized equations of motion, only comparisons are possible for the distributed vortex because there no recirculation occurs. The results of measurements and predictions employing the $k-\epsilon$ model and the M$k-\epsilon$ model are given in Fig. 9.

The $k-\epsilon$ model predicts a rapid evolution of the swirl toward a solid body rotation, which is a well known feature of the $k-\epsilon$ model. In contrast, the M$k-\epsilon$ model fixes the rate of rotation in the vicinity of the pipe center on a constant level, while in the same region the axial velocity is increased more and more. The radial extent of the region of constant momentum is reduced during the decay. It is obvious, that the prediction by the M$k-\epsilon$ model is beyond reality. In fact, this model mimics the behavior in the early decay stage of the concentrated vortex flow. The $k-\epsilon$ model is wrong in its prediction of a rapid evolution to a "solid body"-rotation, however in the longer term a solid body rotation is being observed. Therefore, it must be concluded that the predictions of the $k-\epsilon$ model are much more realistic than that of the M$k-\epsilon$ model. This also holds true for the swirl number, which is given in Fig. 10. The predicted rates of decay are too low, the difference being 18 percent for the $k-\epsilon$ model, and 34 percent for the M$k-\epsilon$ model.

Numerical Accuracy. The details of the numerical procedure are already given. An overall impression of the numerical accuracy is obtained by evaluation of the momentum balance. Since the swirl number S is related to the tangential wall shear stress by Eq. (4), S can be obtained in two ways: by integration of the predicted velocity distributions (S_{int}), and by solving Eq. (4) using the predicted values of the wall shear stress (S_τ). The difference $\Delta S = S_{int} - S_\tau$ is a combination of the error in estimating the wall shear stress, and the errors present in the velocity distributions. It can be shown, that at position $x' = x/D$, ΔS is

$$\Delta S = \int_0^R (U\Delta W + W\Delta U) r^2 dr - \int_0^{x'} \Delta\tau_{\varphi,\text{wall}} dx \quad (5)$$

with ΔU, ΔW, and $\Delta\tau_{\varphi,\text{wall}}$ the differences between the numeri-

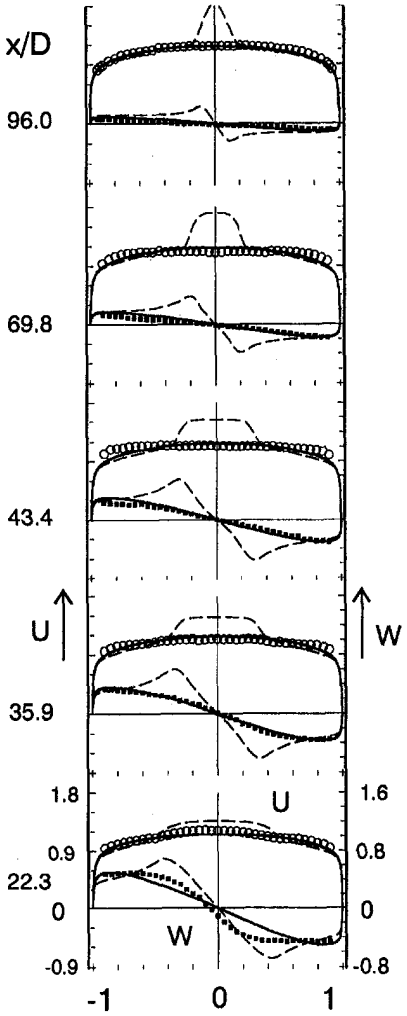

Fig. 9 Predictions of the "distributed vortex"-flow. — $k-\epsilon$; --- M$k-\epsilon$

cal solution and the unknown exact solution. S_{int}, S_τ and ΔS are given in Fig. 11, for the $k-\epsilon$ model and the M$k-\epsilon$ model, for the standard (coarse) grid, and a fine grid containing 200 grid points, where especially the grid density in the wall region has been increased. For S_{int} the decay rate β with the $k-\epsilon$ model is 0.02305 in the fine grid against 0.02304 in the coarse grid. For the M$k-\epsilon$ model, $\beta = 0.01908$ in the fine grid against 0.01869 in the coarse grid. This means, that the trends given

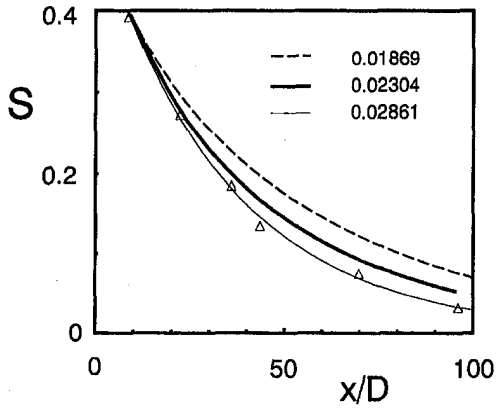

Fig. 10 Measured and predicted swirl numbers of the "distributed vortex"-flow and the decay rates. β. —△— exp; — $k-\epsilon$; --- M$k-\epsilon$.

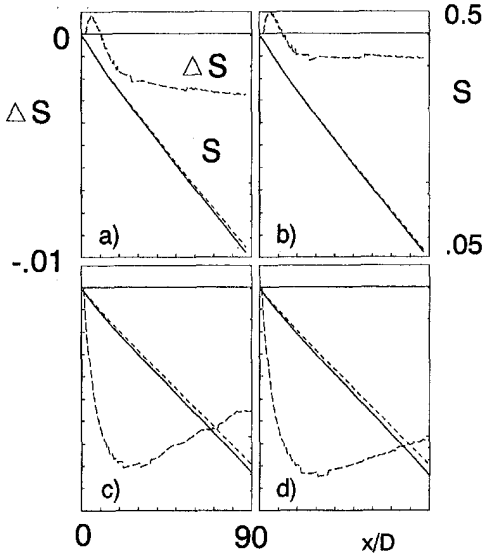

Fig. 11 S_{int} (—) S_{tau} (---) and ΔS (– – –) for: (a) $k-\epsilon$, coarse grid, (b) $k-\epsilon$, fine grid, (c) M$k-\epsilon$, coarse grid, (d) M$k-\epsilon$, fine grid

in Fig. 10 are not affected by the choice of the grid. For the $k-\epsilon$ model, the fine grid results in a reduction of ΔS except in the early stage of the computation, whereas for the M$k-\epsilon$ model grid refinement does not have the desired effect. This suggests that for the M$k-\epsilon$ predictions the streamwise stepsize is the major source of error.

Conclusions

To study swirling turbulent pipe flows, experiments and computations have been carried out. The computations are based on an ASM-model in which the curvature terms in the Reynolds stress transport equations have been retained. The computations predict a decrease of the radial exchange of momentum over a large part of the pipe cross section. The swirl decay is predicted to be strongly dependent on the initial velocity distributions. The applied pressure-strain model is of less importance for the decay.

The experiments also show the importance of the initial condition for the swirl decay. Variations of 16 percent for the rate of swirl decay have been observed between two different initial velocity distributions. The strength of the "memory effect" depends on the initial condition, and is stronger for a concentrated vorticity than for a distributed vorticity. Also, the memory effect that is observed in the experiments is weaker than suggested by the computations.

Comparison of measured and predicted velocity distributions shows that, in spite of its shortcomings in rotating flows, the $k-\epsilon$ model gives results which are much more realistic than that of the ASM model. In the swirling flow that has been studied, the effect of rotation is only small, and the flow behaves more or less like a thin shear flow.

Acknowledgments

The authors are indebted to Johan Stouthart for his indispensable contributions during the realization of the experiments, and to Jan Voskamp for his encouraging background support. This research was sponsored by NV Nederlandse Gasunie, NAM, and Ruhrgas.

References

Algifri, A. H., Bhardwaj, R. K., and Rao, Y. V. N., 1987, "Prediction of the Decay Process in Turbulent Swirl Flow," *Proceeding of the Institution of Mechanical Engineers,* Vol. 201, pp. 279–283.

Chen, Q., 1992, Private Communication, Lab. Aero and Hydrodynamics, Dep. of Eng. and Maritime Techn., Delft University of Technology.

Chien, K. Y., 1982, "Predictions of Channel and Boundary-Layer Flows with a Low-Reynolds-Number Turbulence Model," *AIAA Journal,* Vol. 20, pp. 33–38.

Fletcher, C. A. J., 1991, *Computational Techniques for Fluid Dynamics 1: Fundamental and General Techniques,* Springer-Verlag.

Fu, S., Huang, P., Launder, B., and Leschziner, M. A. 1988, "A Comparison of Algebraic and Differential Second Moment Closures for Axisymmetric Turbulent Shear Flows with and Without Swirl," ASME JOURNAL OF FLUIDS ENGINEERING, Vol. 110, pp. 216–221.

Fu, S., Launder, B. E., and Leschziner, M. A., 1987, "Modelling Strongly Swirling Recirculating Jet Flow with Reynolds-Stress Transport Closures," *Proceedings of the 6th Symposium on Turbulent Shear Flows.*

Gibson, M. M., and Younis, A. B., 1986, "Calculation of Swirling Jets with a Reynolds-stress Closure," *Physics of Fluids,* Vol. 29, pp. 38–48.

Ito, S., Ogawa, K., and Kuroda, C., 1980, "Turbulent Swirling Flow in a Circular Pipe," *Journal Chemical Engineering Japan,* Vol. 13, pp. 6–10.

Kitoh, O., 1991, "Experimental Study of Turbulent Swirling Flow in a Straight Pipe," *Journal of Fluid Mechanics,* Vol. 225, pp. 445–479.

Kobayashi, T., and Yoda, M., 1987, "Modified $k - \epsilon$ Model for Swirling Flow in a Straight Pipe," *JSME International Journal,* Vol. 30(259), pp. 66–71.

Kreith, F., and Sonju, O. K., 1965, "The Decay of a Turbulent Swirl in a Pipe," *Journal of Fluid Mechanics,* Vol. 22, pp. 257–271.

Launder, B. E., 1989, "Phenomenological Modelling: Present, ... and Future?" J. L. Lumley, ed., *Whither Turbulence? Turbulence at the Crossroads,* 439–485. Springer-Verlag.

Launder, B. E., Reece, G. J., and Rodi, W., 1975, "Progress in the Development of a Reynolds-stress Turbulence Closure," *Journal of Fluid Mechanics,* Vol. 68, pp. 537–577.

Lawn, C., 1971, "The Determination of the Rate of Dissipation in Turbulent Pipe Flow," *Journal of Fluid Mechanics,* Vol. 48, pp. 477–505.

Mattingly, G. E., and Yeh, T. T., 1988, "NBS' Industry-Government Consortium Research Program on Flowmeter Installation Effects," Summary Report July–Dec. 1987, National Bureau of Standards, Gaithersburg.

Naot, D., Shavit, A., and Wolfstein, M., 1970, "Interactions Between Components of the Turbulent Velocity Correlation Tensor," *Israel Journal of Technology,* Vol. 8, pp. 259–269.

Parchen, R. R., 1993, "Decay of Swirl in Turbulent Pipe Flows," PhD thesis, Eindhoven University of Technology, Laboratory for Fluid Dynamics and Heat Transfer, Eindhoven, The Netherlands.

Rodi, W., 1976, "A New Algebraic Relation for Calculation of the Reynolds Stresses," *Zeitschrift für Angewandte Mathematik und Mechanik,* Vol. 56, pp. 219–221.

Rotta, J. C., 1951, "Statistische Theorie nichthomogener Turbulenz," *Zeitschrift für Physik,* Vol. 129, pp. 547–572.

Steenbergen, W., and Stouthart, J., 1993, "Three-Dimensional Laser Doppler Experiments with a Two-Dimensional System in a Turbulent Pipe Flow," *Laser Anemometry: Advances and Applications,* Proceedings of the Fifth International Conference, J. M. Bessem et al., eds., *SPIE Proceedings,* Vol. 2052, pp. 729–736.

Steenbergen, W., 1996, "Reduction of Beam Refraction in Optical Pipe Flow Experiments by Use of Sheet-Fabricated Pipe Walls," *Experiments in Fluids,* Vol. 22, pp. 165–173.

Analytical Model of a Side-Heated Free Convection Loop Placed in a Transverse Magnetic Field

Nesreen Ghaddar
Associate Professor,
American University of Beirut,
Faculty of Engineering and Architecture,
850 Third Ave, New York, NY 10022

The hydrodynamic characteristics of a buoyancy-driven convection loop containing an electrically-conducting fluid in a transverse magnetic field are investigated analytically using a one-dimensional model. One side of the loop is isothermally heated and the other side isothermally cooled, and the upper and lower sections are insulated. The model which is based on the use of the Hartmann Plane-Poiseuille flow solution for estimating loop shear stress, predicts the flow velocity and the induced current of the magnetohydrodynamic generator in terms of the flow and geometric parameters. The study covers ranges of Grashof number, Gr, from 10^2 to 10^6, the Hartmann number, Ha, from 0 to 20, the Prandtl number, Pr, from .003 to 7, and loop height to thickness ratio, L/d, from 10 to 50. It is shown that at low Prandtl numbers, Pr $\ll$ 1, there exists an optimal Hartmann number, Ha_{opt}, that maximizes the induced electric current. This Ha_{opt} depends weakly on the Grashof number. The side-heated loop performance is also compared with the bottom heated loop model of Ghaddar, (1997a). It is found that at a low Prandtl number, side heated loop induces the higher velocity whereas at high Prandtl numbers the bottom heated loop induces higher velocity.

1 Introduction

Laminar natural convection flow in closed loops has been studied by many investigators since it has considerable number of practical applications in the design of thermal energy systems, including thermosyphonic solar applications and nuclear technologies. When a transverse magnetic field is applied to an electrically conducting fluid in the loop, convective hydrodynamic motion is damped and an electric current is induced. Such a system has two principal applications: the first is in energy systems or industrial processes that require control of flow destabilisation or prohibition of motion; the second interest lies in the possible use of the system for electricity generation.

In previous works, the dynamics of the flow in a single loop has been investigated by Creveling et al. (1975) who studied the dynamics of the thermosyphonic flow in a single circular loop system with the lower half heated and the upper half cooled using one-dimensional analysis and they verified their model with experimental observations. They derived the steady-state solutions for both laminar and turbulent flow in terms of flow and geometric parameters and accurately predicted the unstable intermediate region by superimposing small disturbances upon the steady state solution and solving the linearized dynamic equations using the approach of Welander (1967). Recently, Ghaddar (1997, 1997a, b) has studied thermosyphonic closed loops that are heated from the bottom in a transverse magnetic field using both a one-dimensional analytical model and a two-dimensional spectral element numerical model. The analytical model of Ghaddar (1997a) predicted values of induced flow velocity and induced current which compared favorably with the numerical model of Ghaddar (1997b). Erhard et al. (1989) and Davis and Roppo (1987) investigated double-loop systems, heated from below, where two circular loops were coupled by a heat exchanger for a side coupling location. Their experiments and mathematical models confirmed the existence of a subcritical parameter range that alternatively exhibits steady as well as time dependent behavior. No work has been reported so far on the effect of a transverse magnetic field for motion control in such loops.

Related work reported in literature has concentrated on buoyancy driven convection in enclosures with the use of a transverse magnetic field to damp hydrodynamic motion, particularly related to the manufacturing of crystals (Vives and Perry 1987; Vasseur et al., 1995; and Hart, 1983). Garandet et al. (1992) proposed an analytical solution to the equations of magnetohydrodynamics that can be used for the core flow in 2-D shallow cavities (Horizontal Bridgman configuration). Their model was verified by Alchaar et al. (1995) who solved the same equations numerically for a wide range of Grashof, Hartmann, and Prandtl numbers.

In this work, an analytical one-dimensional solution based on parallel flow approximation of the side-heated loop convection in presence of a transverse magnetic field is developed. The model is based on expression of shear stress at the walls in terms of the Hartmann Plane-Poiseuille flow solution. The range of validity of the approximate solution is discussed. The optimisation of the system parameters for maximisation of the induced electric current is investigated. The side-heated system behavior and performance are also compared with the bottom heated loop solution of Ghaddar (1997a) to predict which configuration induces higher circulation velocities and hence higher induced current.

2 Problem Statement

The essential features of the thermosyphonic closed loop are shown in Fig. 1. The loop has a height $2L$, an internal channel half width d. The upper and lower connecting portions of the vertical channel are semi-circular each of height l. The Boussinesq fluid contained in the loop is electrically conducting with an electrical conductivity σ, and a coefficient of thermal

Contributed by the Fluids Engineering Division for publication in the JOURNAL OF FLUIDS ENGINEERING. Manuscript received by the Fluids Engineering Division January 8, 1997; revised manuscript received August 4, 1997. Associate Technical Editor: M. S. Cramer.

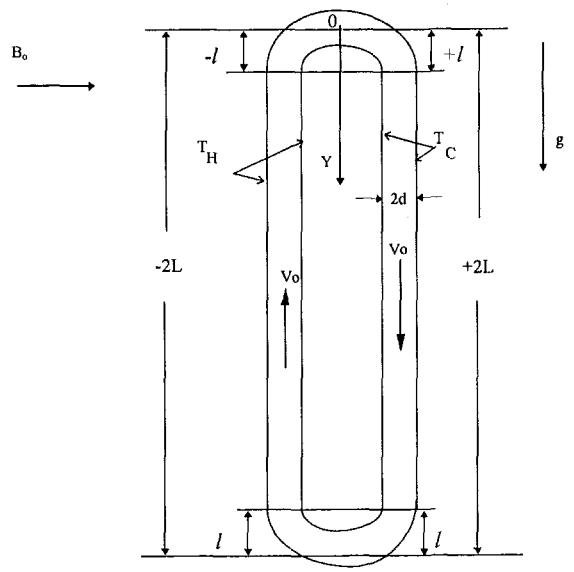

Fig. 1 The essential features of the thermosyphonic side-heated closed loop

expansion β. The magnetic field B_o is applied perpendicular to gravity in the x-direction. The thermophysical properties of the fluid at a reference temperature T_o are assumed to be constant except for the density ρ which is related to temperature according to $\rho = \rho_o(1 - \beta(T - T_o))$. The right side of the loop wall is isothermally heated to T_H, the left side isothermally cooled to T_C where T_C taken as the reference temperature. The connecting regions of the loop of radius $2l$ are insulated.

Assuming the channel width of the loop to be much smaller than its length $2L$, i.e., $2d \ll 2L$, the one-dimensional model of the flow and heat transfer model can be used with sufficient accuracy (Welander, 1967). To simplify the coordinate system, circular ends at the top and bottom parts of the loop are considered to be straight and the origin of the y-axis is placed at the top of the loop, parallel to the flow direction as it moves down with gravity along the cold side from 0 to $+2L$, and against gravity along the hot side from $-2L$ to 0, with motion being clockwise. Axial heat conduction and viscous heating are neglected and the steady conservation equations are written in terms of the cross-sectionally averaged velocity V_o and bulk temperature T_b:

$$\text{continuity:} \quad V_o = \text{constant} \tag{1}$$

$$\text{momentum:} \quad 0 = -\frac{\partial p}{\partial y} + \rho g - \sigma V_o B_o^2 - \frac{\tau}{d}, \tag{2}$$

energy in the isothermal regions $-2L + l \le y \le -l$ and $l \le y \le 2L - l$:

$$\rho_o C\left[V_o \frac{\partial T_b}{\partial y}\right] = \frac{h}{2d}\{T_w - T_b(y)\} + \sigma V_o^2 B_o^2, \tag{3a}$$

and energy in the insulated regions $-l \le y \le +l$ and $2L - l \le y \ge -2L + l$:

$$\rho_o C\left[V_o \frac{\partial T_b}{\partial y}\right] = \sigma V_o^2 B_o^2, \tag{3b}$$

where g is the gravitational acceleration, p is the pressure, τ is the shear stress, h is the convective heat transfer coefficient in the channel, $\sigma B_o^2 V_o^2$ is the Joulean heating term, and T_w is the loop wall temperature in the isothermal regions defined by:

$$T_w = T_H \quad \text{for} \quad -2L + l \le y \le -l \tag{4a}$$

$$T_w = T_C \quad \text{for} \quad l \le y \le 2L - l \tag{4b}$$

Equations (1)–(3) are solved for steady-state conditions in the next section.

3 Analytical Steady-State Solution

3.1 Hartmann-Plane Poiseuille Flow Model. Steady-state conditions indicate that the mass flux ρV_o is constant along the loop. So the energy transfer Eq. (3a) can be solved for the bulk temperature distribution. It is preferable to express the bulk temperature in dimensionless form using $\theta_b = (T_b - T_C)/(T_H - T_C)$, along the loop in terms of the dimensionless induced velocity:

$$\theta_b = \begin{cases} 1 + Ae^{-my/d} + \dfrac{\text{Ha}^2\ \text{Ec Pr}}{4\ \text{Nu}} & \text{for} \quad -2L + l \le y \le -l \\ Be^{-my/d} + \dfrac{\text{Ha}^2\ \text{Ec Pr}}{4\ \text{Nu}} & \text{for} \quad +l \le y \le 2L - l \end{cases} \tag{5a}$$

where the dimensionless parameter m is a form of Stanton number given by:

$$m = h/(2\rho C V_o) = \text{Nu}/2\ \text{Re Pr} \tag{6}$$

The other parameters appearing in Eqs. (5) and (6) are the Reynolds number based on the induced velocity, $\text{Re} = V_o d/\nu$; the Nusselt number, $\text{Nu} = hd/k$; the Prandtl number, $\text{Pr} = \nu/\alpha$; the Eckert number, $\text{Ec} = Vo^2/C\Delta T$; the temperature difference between hot and the cold side walls, $\Delta T = T_H - T_C$; and the Hartmann number, $\text{Ha} = B_o d(\sigma/\rho_o\nu)^{1/2}$. The square of the Hartmann number represents the ratio of the Lorentz force from the induced current to the viscous force. [For comparison, the quantity $(\sigma/\rho_o\nu)^{1/2}$ for liquid mercury (Pr $\approx$ .02) is about 2.7×10^5 while for sea water (Pr $\approx$ 7) it is about 65.]

Solution of equation (3b) in the insulated sections gives a linearly increasing bulk temperature due to Joulean heating in each segment. Therefore, imposing the continuity condition of bulk temperature in those segments:

$$\theta_b(l) = \theta_b(-l) + 2\ \text{Ha}^2\ \text{Ec}(l/d)/\text{Re} \tag{7a}$$

$$\theta_b(-2L + l) = \theta_b(2L - l) + 2\ \text{Ha}^2\ \text{Ec}(l/d)/\text{Re} \tag{7b}$$

leads to expressions for the parameters A and B of Eq. (5) given by:

$$A = \frac{[1 - e^{-2m(\text{L}-l)/d}]}{[e^{-m(2L-3l)/d} - e^{m(2L-l)/d}]} - \frac{2\ \text{Ha}^2\ \text{Ec}(l/d)}{\text{Re}} \frac{[1 + e^{-2m(L-l)/d}]}{[e^{-m(2L-3l)/d} - e^{m(2L-l)/d}]} \tag{8a}$$

$$B = Ae^{2ml/d} + \left[1 + \frac{2\ \text{Ha}^2\ \text{Ec}(l/d)}{\text{Re}}\right] e^{ml/d} \tag{8b}$$

In this development it is assumed that the heat transfer coefficient, and hence Nusselt number, is constant throughout the loop. This assumption is valid for small values of Reynolds number. For moderate values of Reynolds, the heat transfer is generally improved with Nu varying as $\text{Nu} = 0.77\ \text{Re}^{0.4}$ in the laminar flow regime according to experimental work of Gau et al. (1992), on flow in heated vertical channels.

The momentum Eq. (2) integrated around the loop gives:

$$4\frac{\tau L}{d} + 4\sigma V_o B_o^2 L = \rho_o g \beta \Delta T \left[+ \int_{-2L}^{-2L+l} \theta b dy + \int_{-2L+l}^{-l} \theta_b dy + \int_{-l}^{0} \theta_b dy - \int_{0}^{l} \theta_b dy - \int_{l}^{2L-l} \theta_b dy - \int_{2L-l}^{2L} \theta_b dy \right] \quad (9)$$

which shows balance between buoyancy, Lorentz force, and friction where pressure variations in the loop are only due to gravity. The negative and positive signs of the buoyant terms are related to gravity direction which is positive for the upward going flow and negative for the downward going flow. In each integral segment, the respective bulk temperature are used the isothermal region and the insulated region. Figure 2 shows the dimensionless bulk temperature distribution, θ_b, along the loop at $L/d = 20$, $l/d = 2$, Ha = l, Ec = 0 for (a) Re = 50, at various Prandtl numbers and for (b) Pr = 1 at various values of Reynolds numbers. The maximum temperature difference ($\theta_b - \theta_w$), and hence the maximum rate of heat transfer occurs as the upward moving hot fluid enters the cold segment at the top ($y = l$) and as the down moving cooled fluid is entering the hot section from below at $y = (-2L + l)$. The areas under the θ_b distribution curve in the different thermal segments (two isothermal and four insulated) represent the six integrals appearing in the RHS of Eq. (9).

The flow in the channel is assumed fully developed and the solution of Hartmann (1937) for MHD plane-Poiseuille flow with a transverse magnetic field is used to correlate the walls shear stress force to the mean flow velocity V_o by:

$$\tau = \frac{\mu V_o}{d} \mathrm{Ha}^2 \frac{\tanh(\mathrm{Ha})}{\mathrm{Ha} - \tanh(\mathrm{Ha})} \quad (10)$$

The wall shear stress is based on Hartmann solution which applies for a zero thickness wall, or for a nonconducting wall.

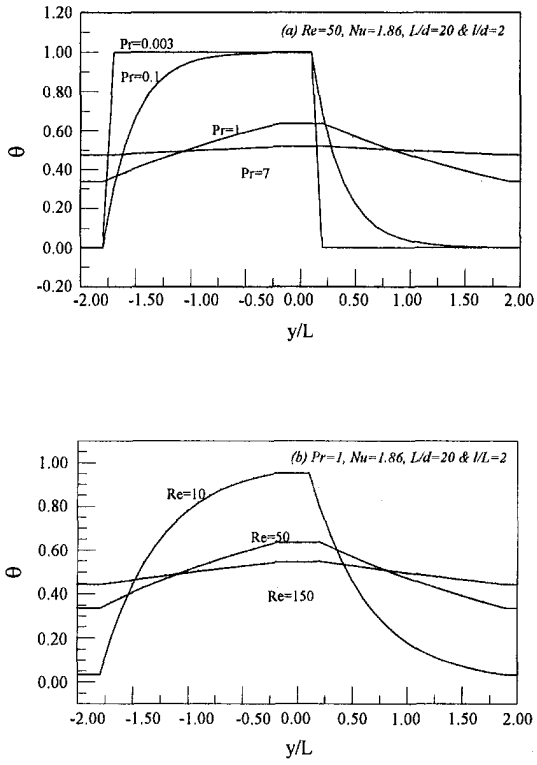

Fig. 2(a–b) The dimensionless bulk temperature distribution, $\theta_b = (T_b - T_c)/(T_H - T_c)$ along the loop for $L/d = 20$, $l/L = 0.1$, Ha = 1 for (a) Re = 50, Pr = 0.02, 1 and 5 and for (b) Pr = 1 and Re = 10, 50 and 150

Hartmann solution for a finite wall channel is well-known, but has not been considered in this work but can be easily done in future work. Using the value of τ in (10) and evaluating the integral of the buoyancy term using the temperature distribution obtained in Eq. (5), reduces Eq. (8) to the following:

$$\frac{4\mu V_o \mathrm{Ha}^2 \tanh \mathrm{Ha}}{d^2(\mathrm{Ha} - \tanh \mathrm{Ha})} + 4\sigma V_o B_o^2 = \rho_o g \beta \Delta T \left[\frac{-A}{m(L/d)} (e^{ml/d} - e^{m2L-l)/d}) + \frac{B}{m(L/d)} (e^{-m(2L-l)/d} - e^{-ml/d}) + 2\left(1 - \frac{l}{L}\right) \right] \quad (11)$$

Equation (11) gives a correlation between the induced flow velocity V_o and the other flow and geometric parameters in the system and can then be reduced to the following non-dimensional correlation:

$$\mathrm{Gr} = \frac{4\,\mathrm{Re}\,\mathrm{Ha}^2 \left[1 + \dfrac{\tanh \mathrm{Ha}}{\mathrm{Ha} - \tanh \mathrm{Ha}}\right]}{2(1 - l/L) - \dfrac{4\,\mathrm{Re}\,\mathrm{Pr}[F]}{(L/d)\mathrm{Nu}}} \quad (12a)$$

where Gr is the Grashof number, $\mathrm{Gr} = g\beta\Delta T d^3/\nu^2$, the parameter F is defined as,

$$F = -\tfrac{1}{2}[A(e^{ml/d} - e^{m(2L-l)/d}) + B(e^{-ml/d} - e^{-m(2L-l)/d})] \quad (12b)$$

and A and B are the dimensionless terms defined in equation 8. Note that in the solution there is no restriction on the relative size, l/L, of the insulated region to the isothermal regions. The general solution contained in Eqs. (12) is valid for all values of Prandtl, Grashof and nonzero Hartmann numbers in the laminar range with $d \ll L$ to ensure parallel flow assumptions.

The value of the F parameter of Eq. (12b) is bounded between zero and one, i.e., $0 \le F \le 1$, for all values of flow parameters as can be seen from Fig. 3. The boundedness of F comes from the integral of the buoyancy term of Eq. (9), where the integrated area under θ_b would in the extreme reach a value of $2(L - l)$. At high Prandtl and Reynolds numbers, $F \to 0$, but the term $[F\{4\,\mathrm{Pr}\,\mathrm{Re}/\mathrm{Nu}(L/d)]$ in the denominator of Eq. (12a) remains significant. At very low Prandtl numbers ($\mathrm{Pr} \ll 1$) and low to moderate Reynolds numbers, the parameter F approaches unity ($F \to 1$) which simplifies Eq. (12a) so that Re may be expressed as:

$$\mathrm{Re} = \frac{2(1 - l/L)\mathrm{Gr}}{4\,\mathrm{Ha}^2 + \dfrac{4\,\mathrm{Ha}^2 \tanh \mathrm{Ha}}{\mathrm{Ha} - \tanh \mathrm{Ha}} + \dfrac{4\,\mathrm{Pr}\,\mathrm{Gr}}{\mathrm{Nu}(L/d)}} \quad \text{for} \quad \mathrm{Pr} \ll 1 \quad (13)$$

At very low Prandtl numbers when $\mathrm{Re}\,\mathrm{Pr} \ll 1$, the model given by Eq. (13) may become less accurate due to the initial assumption of negligible streamwise diffusion. The parameter F appearing in the solution is directly related to the area integrals under the bulk temperature distribution curve with their respective signs. (see Eq. (9)). The reason this parameter approaches a value of unity for low Prandtl fluids is because the bulk temperature follows in this case, very closely the imposed wall temperatures and contributes to a higher fraction of the nominal density difference $\rho_H - \rho_C$ on both sides of the loop to drive the motion.

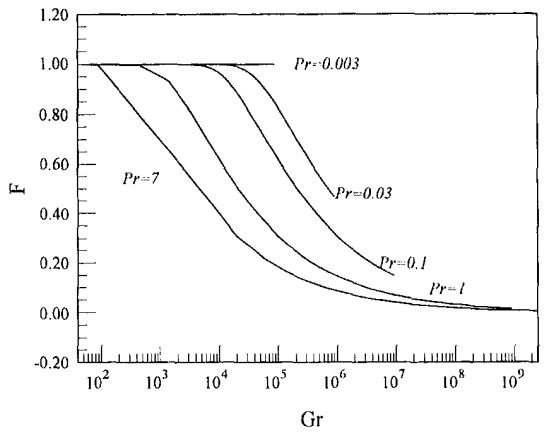

Fig. 3 A plot of the *F* parameter as a function of Grashof number for $L/d = 20$, $l/L = .1$, Ha = 5 and Nu = 1.86 at various Prandtl numbers

The induced electric current j in the direction perpendicular to the plane of the magnetic field and flow velocity, is defined as:

$$j = \sigma(V_o\hat{y} \times B_o\hat{x}) = \text{Re Ha}\left(\frac{v}{d^2}\sqrt{\sigma\mu}\right)\hat{z} \qquad (14)$$

At low Prandtl numbers, Pr $\ll$ 1, the induced electric current can be explicitly derived using Eq. (13) in terms of given system parameters as:

$$j = \left(\frac{v}{d^2}\sqrt{\sigma\mu}\right)\left[\frac{2(1 - l/L)\ \text{Gr Ha}}{4\ \text{Ha}^2 + \dfrac{4\ \text{Ha}^2 \tanh \text{Ha}}{\text{Ha} - \tanh \text{Ha}} + \dfrac{4\ \text{Pr Gr}}{\text{Nu}(L/d)}}\right]$$

for Pr $\ll$ 1 (15)

In the discussion of the flow behaviour associated with the proposed 1-D solution, the physics of the flow will be described under various flow conditions and geometric parameters. Also the presented solution can be extended to treat finite channels, but in this case the walls of the channel in the direction perpendicular to the flow must be non-conducting and the shear stress need to be modified to account for the aspect ratio of the channel (Branover, 1978).

3.2 Friction Factor Model Solution and the Limiting Case of Zero Hartmann Number. The special case of Ha $\simeq$ 0, can be derived from the developed solutions in Eqs. (12) through (15) by taking the limit of the solution of the shear stress in Eq. (10) as Ha $\to$ 0 which gives a value of $\tau = 3\mu V_o/d$ which is the same as the value that would be obtained from plane channel flow with zero magnetic field. For comparison purposes, the Ha = 0 case is solved in this section using the using the friction factor to define the shear stress rather than the Hartmann-Poiseuille flow value of shear. The governing equations of mass momentum and energy transfer (1) to (4) of the free-convection loop are now solved using the same procedure of the previous Section 3.1, but using the limiting friction factor model. The shear stress force term in Eq. (9) is now expressed as $\tau = f\rho V_o^2/2$, where $f = 6/\text{Re}_d$ is the friction factor for laminar fully developed flow in a plane channel.

The bulk temperature distribution of the friction factor model in the domain is exactly the same as that obtained in Eq. (5) but the heat source term due to the induced current by B_o has been removed. Substituting $\tau = f\rho V_o^2/2$ into Eq. (9) and performing the necessary algebra will lead to an expression for Gr in terms of the flow parameters as:

$$\text{Gr} = \frac{\text{Re}(12 + 4\ \text{Ha}^2]}{2 - \dfrac{2l}{L} - \dfrac{4\ \text{Re Pr}[F]}{(L/d)\text{Nu}}} \quad \text{"friction factor model"} \qquad (16)$$

which applies to the natural convection loop. At very low Prandtl number ($F \to 1$), the Reynolds number can be obtained explicitly as:

$$\text{Re} = \frac{2(1 - l/L)\text{Gr}}{12 + 4\ \text{Ha}^2 + \dfrac{4\ \text{Pr Gr}}{\text{Nu}(L/d)}}$$

friction factor model for Pr $\ll$ 1 (17)

The associated induced electric current for low Prandtl number is then given by:

$$j_f = \left(\frac{\nu}{d_H^2}\sqrt{\sigma\mu}\right)\ \frac{2(1 - l/L)\ \text{Gr Ha}}{12 + 4\ \text{Ha}^2 + \dfrac{4\ \text{Pr Gr}}{\text{Nu}(L/d_H)}}$$

friction factor model Pr $\ll$ 1 (18)

where j_f represents the induced electric current based on the friction factor model. The free convection solution obtained in (16) and (18) for the case of zero magnetic field strength, Ha = 0, will represent the upper bound on values of the induced velocity at various Grashof numbers for the Hartmann-Poiseuille model.

4 Results and Discussion

The one-dimensional analysis of the thermosyphonic loop problem has previously been tested against experimental results

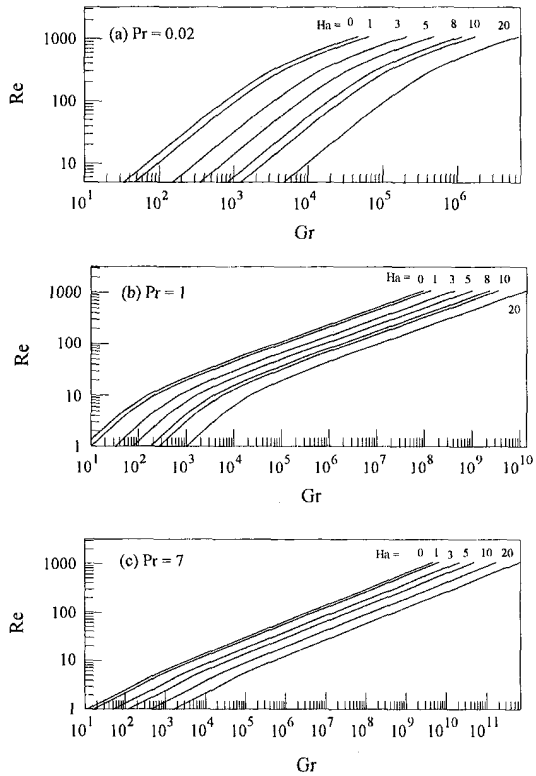

Fig. 4(*a–c*) The variation of Reynolds number, Re, as a function of Grashof number, Gr, at Nu = 1.86, $L/d = 20$, $l/d = 2$ and various values of Hartmann number at (*a*) Pr = 0.02, (*b*) Pr = 1 and (*c*) Pr = 7

by Creveling et al. (1975), but for zero transverse magnetic field and for a circular configuration with bottom isothermal heating and top constant heat flux cooling of the loop. Comparisons have been made only for the friction factor model that gave the solution of Ha = 0 case by Ghaddar (1997a). The analytical solution of Ha = 0 reported by Ghaddar (1997a) for bottom heated loop was found to be consistent with published data of Creveling et al. (1975) particularly in the low Reynolds number range.

In the following sections, the 1-D proposed Hartmann-Poiseuille solution of the laminar steady flow in the thermosyphonic loop will be presented, the system behavior discussed and the induced electric current will be optimised. The Eckert number Ec is taken as zero throughout the analysis since expected induced current is too small to cause significant warming of the fluid in the loop. Comparisons will also be made with the bottom heated thermosyphonic loop.

4.1 Hartmann-Poiseuille Flow Model Results. Figure 4 shows the variation of Reynolds number, Re, as a function of Grashof number, Gr, as obtained in Eq. (12) at Nu = 1.86, L/d = 20, l/d = 2 and various values of Hartmann number, Ha, for (a) Pr = 0.02 (b) Pr = 1 and (c) Pr = 7. It is clear that as the magnetic field strength is increased, a higher driving buoyancy force is needed to attain the same circulation velocity. In the limit as Hartmann number becomes high, the flow Reynolds number at fixed Grashof number follows an $(Ha)^{-2}$ power law. At zero magnetic field, Ha = 0, the friction factor model solution obtained in Eq. (16) is also seen in Fig. 4 and the induced velocity is the highest at fixed Grashof number and nonzero Hartmann numbers. The MHD Hartmann-Poiseuille model for the free convection loop represents the system behavior more accurately than the friction factor model for large Hartmann numbers flows because it takes into account the changes in velocity gradients at the wall surface due to the presence of the magnetic field.

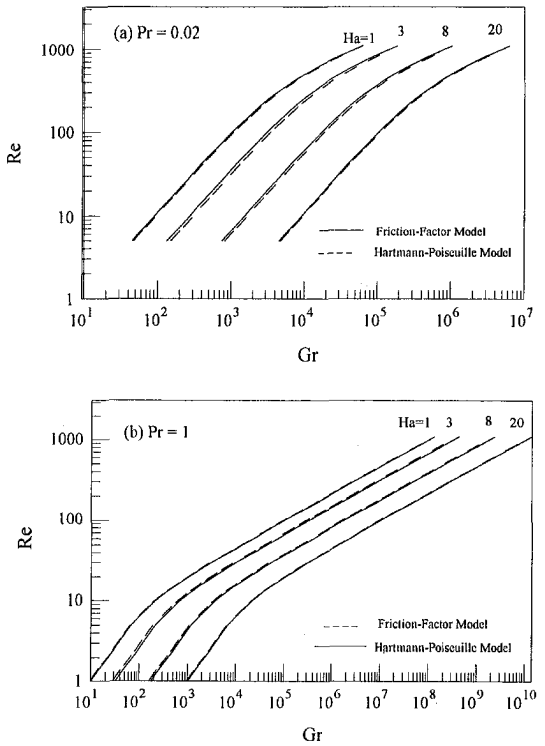

Fig. 5(a–b) The variation of Reynolds number with Grashof number in both models at various Hartmann numbers at (a) Pr = 0.02 and (b) Pr = 1 for Nu = 1.86, L/d = 20 and l/L = 0.1

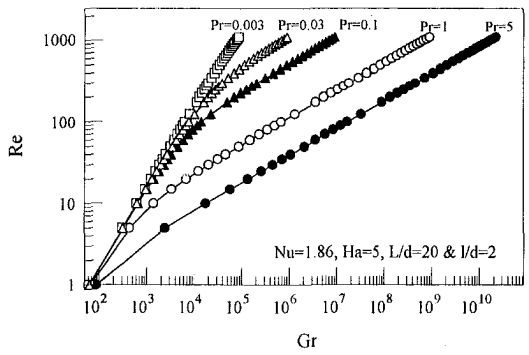

Fig. 6(a) Reynolds number is plotted against Grashof number for L/d = 20, l/d = 2, Ha = 5 and various values of Pr = 0.003, 0.03, 0.1, 1 and 5

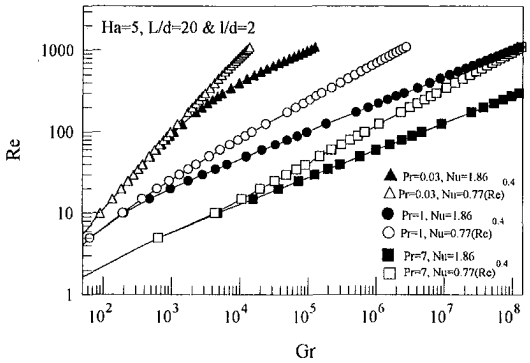

Fig. 6(b) Reynolds number is plotted against Grashof number for L/d = 20, l/d = 2, Ha = 1 and Nu = 1.86 and for Nu = 0.77 $(Re)^{0.4}$ at various Prandtl numbers

Figure 5 shows the variation of Reynolds number with Grashof number in both models at various Hartmann numbers at (a) Pr = 1 and (b) Pr = 0.02 for Nu = 1.86, L/d = 20 and l/d = 2. Both models give a similar result for the induced flow Reynolds number at low Ha, but as Hartmann is increased the percentage difference in the solution reaches values of not more than five percent for Ha < 20. The difference between both models is hardly noticed in Fig. 5, where a logarithmic scale is being used.

The effect of Prandtl number on the flow is shown in Fig. 6(a), where Reynolds number is plotted against Grashof number for L/d = 20, l/d = 2, Ha = 5 and various values of Pr = 0.02, 0.2, 1, and 7. The flow is strongly dependent on Pr and the smaller the Prandtl number, the lower is the required Grashof number (buoyancy term) to maintain the same flow rate. This indicates that mercury may perform better than water in such loops. The 1-D model has used the constant Nusselt number of the fully developed flow in plane channels. Since the flow is driven by buoyancy, it is interesting to explore the effect of dependence of Nu on Re on the solution in the high Grashof number range. The correlation of Gau et al. (1992), based on measurements of heat transfer in heated *vertical channels,* is used ($Nu/Re^{0.4}$ = 0.77) in the solution. Gau et al. (1992) correlation is valid for laminar flow with Reynolds number ranging from 100 to 4000 and Grashof number from 30 to 4×10^7 which is well within the range of the present study. The result is shown in Fig. 6(b) where Re number is plotted against Grashof number at fixed Prandtl numbers, for both fixed and variable Nusselt numbers. A higher Nusselt number induces a higher flow circulation, particularly in the high Re-Gr range, while at low Gr there is hardly any effect on the flow.

The geometric parameters that directly affect the flow velocity are the loop height, L, and the surface area ratio of the unheated region to the heated region represented by the ratio

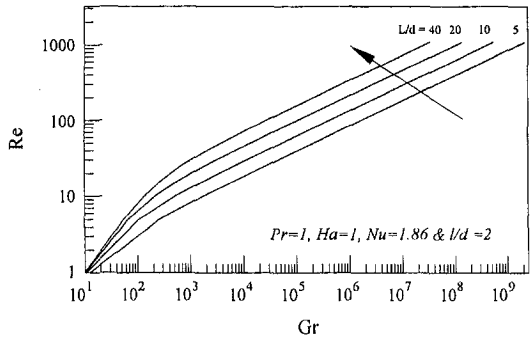

Fig. 7(*a*) The variation Reynolds number versus Grashof number at Ha = 1, Pr = 1, *l*/*L* = 0.1 for various values of *L*/*d* in the range from 5 to 40

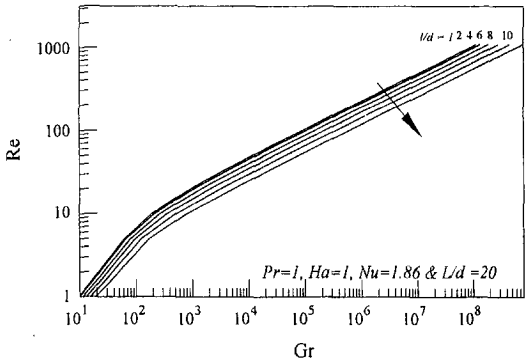

Fig. 7(*b*) The variation of Reynolds number versus Grashof number at Ha = 1, Pr = 1, *L*/*d* = 20 for various values of *l*/*L* in the range from 0.05 to 0.5

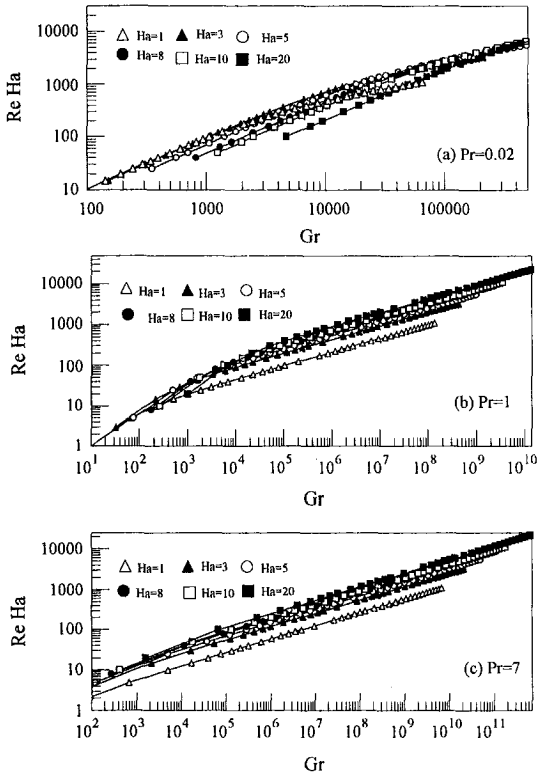

Fig. 8(*a–c*) The dimensionless induced electric current parameter $jd^2/\{\nu(\sigma\mu)^{1/2}\}$ as a function of Grashof number for (*a*) Pr = 0.02, (*b*) Pr = 1 and (*c*) Pr = 7 at *L*/*d* = 20, *l*/*L* = 0.1 and Nu = 1.86

l/*L*. Figure 7(*a*) shows the variation of Reynolds number versus Grashof number at Ha = 1, Pr = 1, *l*/*d* = 2 for various values of *L*/*d* in the range from 5 to 40: the longer the loop, the larger the induced flow velocity. Figure 7(*b*) shows the variation of Reynolds number versus Grashof number at Ha = 1, Pr = 1, *L*/*d* = 20 for various values of *l*/*L* in the range from 0.05 to 0.5. Increasing the insulated region's length minimally reduces the induced velocity.

The product of the Reynolds and Hartmann numbers is related to the induced current directly by Re Ha = $jd^2/\{\nu(\sigma\mu)^{1/2}\}$. Figure 8 shows the dimensionless induced electric current parameter $jd^2/\{\nu(\sigma\mu)^{1/2}\}$ as a function of Grashof number for (*a*) Pr = 0.02, (*b*) Pr = 1, and (*c*) Pr = 7 at *L*/*d* = 20, *l*/*d* = 2, and Nu = 1.86. At fixed Hartmann number, the induced current increases with increasing Grashof number due to increased buoyancy force which affects the flow directly.

At low Prandtl numbers, the induced electric current parameter $jd^2/\{\nu(\sigma\mu)^{1/2}\}$ is explicitly correlated to Grashof and Hartmann numbers (see Eq. (15)); it is given in Fig. 9 as a function of Hartmann number at various Grashof numbers for Pr = 0.02. It is evident that there is an optimal Hartmann number that maximises the induced electric current. The logarithmic scale used in Fig. 9 smooths out the sharp peaks of induced electric current where for example at Gr = 5000, the peak value of Re Ha is equal to 434.75 at Ha_{opt} = 2.2 compared to 326 at Ha = 1 and Re Ha = 331.06 at Ha = 5. So about 30 percent increase in induced current at Ha_{opt} = 2.2 over values observed at Ha = 1 and 5 for Pr = 0.02. It is also noticeable that as Grashof number increases, the optimal Hartmann number increases. This behavior is contrary to that case when the loop is heated from the bottom: the optimal Hartmann number becomes smaller as the Grashof number is increased, as reported by Ghaddar (1997a).

The optimal Hartmann number can be found by differentiating Eq. (15) with respect to Ha and equating the result to zero. This gives after algebraic manipulations, the following relation for Ha_{opt}:

$$0 = -4\,Ha_{opt}^4\,Nu\,L/d + Gr\,Ha_{opt}^2\,Pr - 4\,Ha_{opt}^4\,Nu(L/d)\,\sec h^2(Ha_{opt}) + 2\,Gr\,Ha_{opt}\,Pr\tanh(Ha_{opt}) + Gr\,Pr\tanh^2(Ha_{opt}) + 2\,Ha_{opt}^3\,Nu(L/d)\tanh(Ha_{opt}) \quad (19)$$

The roots of Eq. (19) for optimal Hartmann number can then be found for given values of Gr, Pr, Nu, and *L*/*d*. We can derive a simpler equation to estimate the optimal Hartmann number if we use the friction factor model: the simpler expression of the

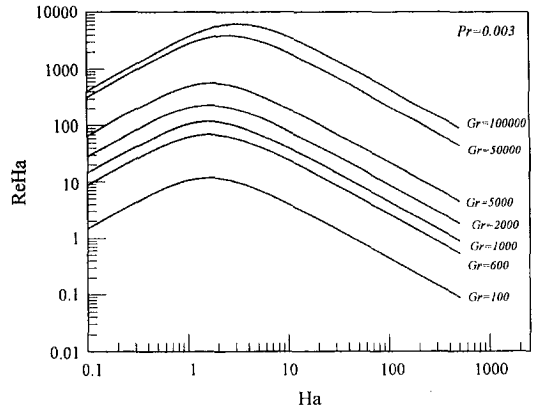

Fig. 9 The dimensionless induced electric current parameter $jd^2/\{\nu(\sigma\mu)^{1/2}\}$ as a function of Hartmann number at various Grashof numbers for Pr = 0.02, *L*/*d* = 20, *l*/*L* = 0.1 and Nu = 1.86

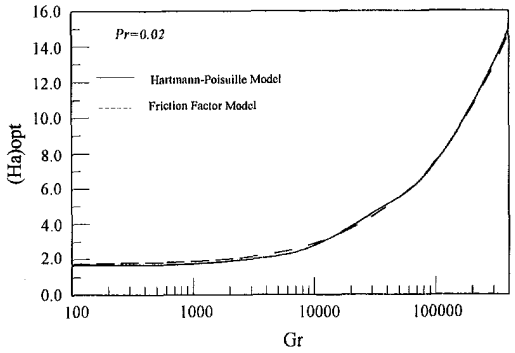

Fig. 10 A plot of optimal Hartmann number versus Grashof number using both the friction factor model and the Hartmann-Poiseuille model

induced electric current of Eq. (18), based on the friction factor model can be differentiated and then the derivative equated to zero. This gives a closed-form relation for the optimal Hartmann number for maximum induced current as a function of the system parameters given by:

$$(\mathrm{Ha}_{\mathrm{opt}})_f = \sqrt{3 + \frac{\mathrm{Gr\ Pr}}{\mathrm{Nu}(L/d)}}. \quad \text{for} \quad \mathrm{Pr} \ll 1 \qquad (20)$$

where subscript f refers to the friction factor model. A comparison is now made between the Hartmann-Poiseuille model using Eq. (19) and the friction factor model using Eq. (20). Figure 10 shows a plot of optimal Hartmann number versus Grashof number using both the friction factor model and the Hartmann-Poiseuille model for Nu = 1.86, L/d = 20 and Pr = 0.02. The friction factor model over predicts $\mathrm{Ha}_{\mathrm{opt}}$ by 1–2 percent as compared to the more accurate Hartmann-Poiseuille Flow model.

In the laminar range of the induced steady flow, the presence of $\mathrm{Ha}_{\mathrm{opt}}$ is significant in terms of improving the system efficiency of conversion from thermal to electrical energy in the presence of a low strength magnetic field. The heat transfer carried from the heat source (right section of the loop) to the heat sink (cold left section of the loop) is given by:

$$Q_L = 2h\Delta T \int_l^{2L-l} \theta_b dy. \qquad (21)$$

Using the expression for $T_b(y)$ of Eq. (5b) and integrating Eq. (21) gives the rate of heat transport to the cold portion of the loop in dimensionless form as:

$$\Gamma = \frac{Q_L}{2Lh\Delta T}$$

$$= \left(\frac{B\ \mathrm{Re\ Pr}}{\mathrm{Nu}(L/d)} [e^{-m(2L-l)/d} - e^{-ml/d}] + \frac{4\ \mathrm{Ha}^2\ \mathrm{Ec\ Pr}}{\mathrm{Nu}} \right], \qquad (22)$$

where B is given in Eq. (8b). The dimensionless heat flux, Γ, defined in Eq. (22) is a function of all the system parameters: Pr, Nu, L/d, l/d and Re, where Re depends on Gr and Ha. In Fig. 11, the dimensionless heat flux, Γ, is plotted as a function of Gr number at L/d = 20, l/L = 0.1, Nu = 1.86, Ec = 0 for different values of (a) Prandtl numbers at Ha = 1 and (b) Hartmann numbers at Pr = 1. As the Prandtl number is increased the heat transfer parameter Γ increases for a fixed Grashof number. The rate of heat transfer in presence of a magnetic

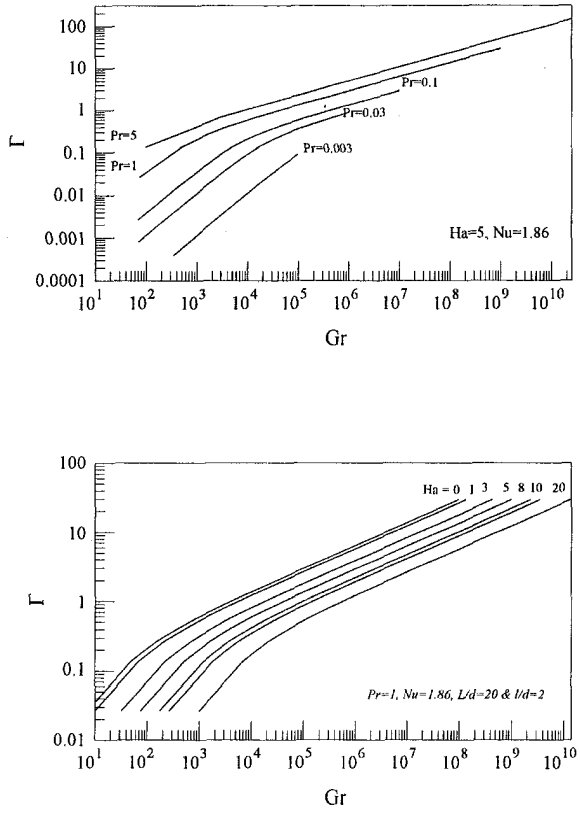

Fig. 11(a–b) The heat transfer parameter, Γ, plotted as a function of Gr number for (a) various Prandtl numbers and for (b) different values of Hartmann number at L/d = 20, l/d = 0.1, Nu = 1.86

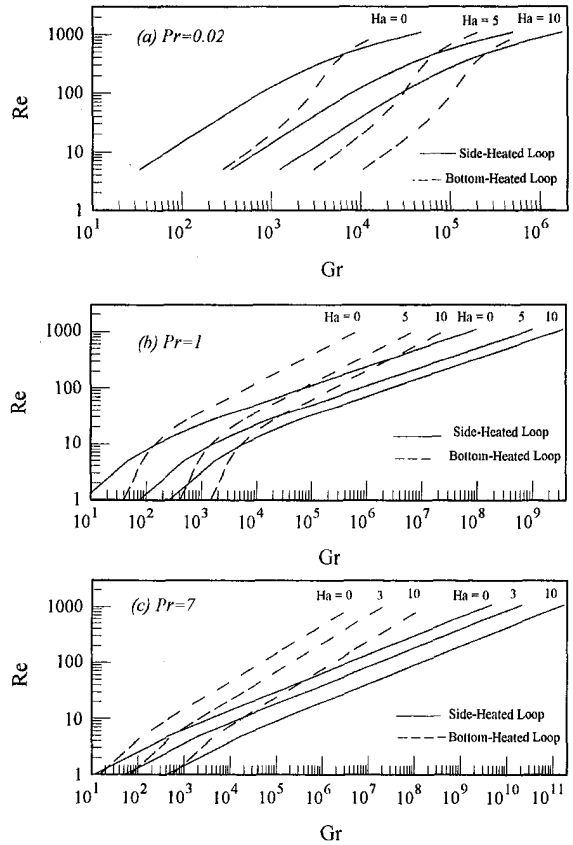

Fig. 12 The induced circulation Reynolds number for both the side-heated and the bottom-heated loops, as a function of Grashof number at various Hartmann numbers for (a) Pr = 0.02, (b) Pr = 1 and (c) Pr = 7 with Nu = 1.86, L/d = 20 and l/d = 2

field decreases with increased Ha, at fixed Gr unlike the induced electric current dependence.

4.2 Comparison Between Side-Heated and Bottom-Heated Thermosyphonic Loops. Induced natural circulation in the closed loop is generally expected to depend on the location of heating in the loop. The buoyant driving force comes from the difference in density between the upward-moving fluid and the downward moving fluid. It would be of interest to compare the effect of changing thermal boundary conditions on the extent of the induced motion. The results for a side-heated loop as presented in this work can be compared with the correlation obtained by Ghaddar (1997a) for a bottom-heated loop with lower part of loop walls heated isothermally to TH, the upper part cooled isothermally to TC and the middle part insulated. The bottom heated correlation was given by:

$$\mathrm{Gr} = \frac{4\ \mathrm{Re}\ \mathrm{Ha}^2 \left[1 + \dfrac{\tanh \mathrm{Ha}}{\mathrm{Ha} - \tanh \mathrm{Ha}}\right]}{\dfrac{2l}{L}[S] + \dfrac{4\ \mathrm{Re}\ \mathrm{Pr}[K]}{(L/d)\mathrm{Nu}}} \tag{23}$$

where K and S are numerical bounded parameters between zero and unity depending on the area integrals of the temperature distribution curve and are given in the work of Ghaddar (1997a). Figure 12 shows the induced circulation Reynolds number for both the side-heated and the bottom-heated loops, as a function of Grashof number at various Hartmann numbers for (a) Pr = 0.02, (b) Pr = 1, and (c) Pr = 7 with Nu = 1.86, L/d = 20, and l/d = 2. It is interesting to note that the bottom-heated loop induces higher circulation velocities at fixed Grashof number for Pr = 7. At Pr = 1 the side-heated loop induces higher circulation at Reynolds numbers below 20 and at Pr = 0.02, the side-heated loop induces higher circulation at Reynolds numbers below 700. The difference in behaviour is related to the net integrated area in each thermal region of the loop under the bulk temperature distribution curve of Fig. 2 and the sign of the area integral depending if the flow is with gravity or against gravity (see Eq. (9) for the sign). For a side-heated loop, the insulated regions do not contribute to the final buoyant force since they cancel each other out. For a bottom heated-loop, the difference in temperature of the insulated regions is a major contributor to the buoyant force particularly at low Pr where the bulk flow temperature very closely follows the wall temperature.

The problem with the bottom-heated loops is that they are unstable according to the work of Creveling et al. (1975). The flow exhibits a highly oscillatory behavior in the intermediate region between laminar and turbulent flows where the flow becomes time dependent. Introducing side heating into a dominantly bottom-heated loop has a profound effect onto the stability of both steady solutions as demonstrated by Ehrhard and Muelleur (1990). In a steady stable laminar thermosyphonic loop flow, bottom-heating induces higher circulation for low Prandtl number fluids than side heating.

Conclusions

A theoretical analysis was carried out with a one-dimensional approach to derive the hydrodynamic model of a buoyancy-driven electrically-conducting fluid in a vertical side-heated loop placed in a transverse magnetic field. The closed-form solution of the flow velocity is used to predict the induced electric current of the system. According to the solution there exist an optimal strength of the magnetic field that depends on the system flow and geometric parameters to maximise the induced electric current. At high Grashof number only a low strength magnetic field is required to achieve a significant induced electric current.

Future work will address the conversion efficiency of thermal to electrical energy of the described magneto hydrodynamic generator and will include experimental verification of the results.

Acknowledgment

The author greatly acknowledges the support of the University Research Board of the American University of Beirut. Also, discussions with Mr. Shawki Fattal have been of great help.

References

Alchaar S., Vasseur P., and Bilgen E., 1995, "Natural Convection Heat Transfer in a Rectangular Enclosure with a Transverse Magnetic Field," ASME *Journal of Heat Transfer,* Vol. 117, pp. 668–673.

Branover, H., 1978, *Magneto Hydrodynamic Flow in Ducts,* Wiley, New York, Chapter 4, pp. 74–85.

Cramer K. R. and Pai S., 1973, *Magneto Hydrodynamics for Engineers and Applied Physics,* McGraw-Hill, New York, Chapter 4, pp. 114.

Creveling, H. F., De Paz J. F., Baladi J. Y., and Schoenhals R. J., 1979, "Stability Characteristics of a Single-Phase Free Convection Loop," *Journal of Fluid Mechanics,* Vol. 67, part 1, pp. 65–84.

Davis, S. H. and Roppo M. N., 1987, "Coupled Lorenz Oscillators," *Physica D,* Vol. 24, pp. 226–242.

Ehrhard P., Karcher Ch., and Muller U., 1989, "Dynamical Behaviour of Natural Convection in a Double Loop System," *Experimental Heat Transfer,* Vol. 2, pp. 13–26.

Ehrhard P., and Muelleur M., 1990, "Dynamical Behaviour of Natural Convection in a Single Phase Loop," *Journal of Fluid Mechanics,* Vol. 217, pp. 487–509.

Garandet J. P., Alboussieri T., and Moreau T., 1992, "Buoyancy Driven Convection in a Rectangular Enclosure with a Transverse Magnetic Field," *International Journal of Heat & Mass Transfer,* Vol. 35, No. 4, pp. 741–748.

Gau, C, Yih, A., And Aung, W., 1992, "Measurements of Heat Transfer and Flow Structure in Heated Vertical Channels," AIAA *Journal of Thermophysics and Heat Transfer,* Vol. 6, No. 4, pp. 707–712.

Ghaddar N., 1997a, "Analytical Model of Induced Electric Current from free-Convection Loop Placed in a Transverse Magnetic Field," *International Journal of Heat and Mass Transfer,* in press.

Ghaddar, N., 1997b, "Numerical Simulation of a Vertical Thermosyphonic Loop placed in a Transverse Magnetic Field," *Numerical Heat Transfer,* in press.

Hart, J. E., 1983, "Low Prandtl number Convection Between Differentially Heated End Walls," *International Journal of Heat Mass Transfer,* Vol. 26, pp. 1069–1074.

Hartmann J., 1937, "Hg-Dynamics in a Homogeneous Magnetic Field," Part I, *Kgl. Danske Videnskab. Selskab, Mat.-Fys. Medd.,* Vol. 15, No. 6.

Welander P., 1967, "On the Oscillatory Instability of a Differentially Heated Fluid Loop" *Journal of Fluid Mechanics,* Vol. 29, pp. 17–30.

Vasseur P., Hasnaoui M., Belgen E., and Robillard L., 1995, "Natural Convection in an Inclined Fluid Layer with a Transverse Magnetic Field: Analogy with a Porous Medium," ASME *Journal of Heat Transfer,* Vol. 117, PP. 121–129.

Vives C., and Perry C., 1987, "Effects of Magnetically Damped Convection During the Controlled Solidification of Metals and Alloys," *International Journal of Heat & Mass Transfer,* Vol. 30, pp. 479–496.

The Steady Horizontal Flow of a Wall Jet Into a Large-Width Cavity

K. O. Homan
Assistant Professor,
Department of Mechanical Engineering,
University of Nebraska-Lincoln,
Lincoln, NE 68588

S. L. Soo
Professor Emeritus,
Department of Mechanical and
Industrial Engineering,
University of Illinois at Urbana-Champaign,
Urbana, IL 61801

This paper treats the steady flow of a wall jet into a large-width cavity for which the primary axis is normal to the direction of the jet inflow. Numerical solutions of the two-dimensional Navier-Stokes equations are computed for inlet Reynolds numbers of 10 to 50 and tank width to inlet height ratios of 16 to 128. The length and velocity scales of the wall jet boundary layer exhibit close agreement with the classic wall jet similarity solution and published experimental data but the width of the region for which the comparison proves to be favorable has a limited extent. This departure from a self-similar evolution of the wall jet is shown to result from the finite domain width and its influence on the large recirculation cell located immediately above the wall jet boundary layer.

Introduction

Single fluid thermal storage devices have been used extensively in solar thermal systems and in chilled water cooling systems. The most common designs depend on thermal stratification to separate the "hot" and "cold" fluid during the various stages of operation. Although the physical scales and characteristic temperature differentials are significantly different for the solar and cooling applications of thermal-storage devices, the basic designs are very similar. In both applications, the cooler fluid with the maximum density enters the tank through an inlet near the bottom and flows across the floor of the tank, while warmer, lighter fluid is removed through an outlet at the top of the tank. Visual observations of the flow early in this filling process show the inlet fluid spreading along the floor of the tank as a density current and being turned upward by the tank wall opposite the inlet (Baines et al., 1983; Yoo et al., 1987). As the filling process progresses, the thermocline moves vertically through the tank and away from the inlet. Thus, during the late stages of the filling process, the temperature field is locally uniform in the near inlet region and the importance of gravitational effects on the jet flowfield disappears. The near-inlet flowfield is therefore well described by the isothermal flow of a wall jet into a large width cavity.

In this paper, we focus on the wall jet boundary layer and the relationship of its characteristics to a finite cavity width. These interactions are unique to the chosen configuration and are not captured in the self-similar boundary-layer description of a wall jet since it is primarily applicable to wall jets issuing along an infinitely long wall. We present numerical solutions of the Navier-Stokes equations for the steady laminar flow of a two-dimensional wall jet into a large width cavity. The height of the cavity is chosen to be sufficiently large that the inlet flow is decoupled from the presence of the thermocline and the outlet flow. The wall jet appearing in the present flow configuration is compared both to the similarity solution of Glauert (1956) and to published experimental data (Bajura and Szewczyk, 1970). The flowfield is computed for a range of Reynolds numbers and a sufficiently wide range of width to inlet ratios to reveal distinct types of interactions between the inlet flow and the opposite wall.

Contributed by the Fluids Engineering Division for publication in the JOURNAL OF FLUIDS ENGINEERING. Manuscript received by the Fluids Engineering Division May 31, 1996; revised manuscript received August 4, 1997. Associate Technical Editor: M. M. Sindir.

Problem Formulation

Assumptions and Governing Equations. The two-dimensional geometry is shown in Fig. 1. The characteristic length, velocity and time are the inlet height l, the area-averaged inlet velocity $\bar{u}_o$, and $l/\bar{u}_o$, respectively. The dimensionless vorticity-streamfunction equations for an unsteady two-dimensional flow are

$$\frac{\partial \omega}{\partial t} = -\nabla\bullet(\mathbf{u}\omega) + \frac{1}{\mathrm{Re}}\nabla^2\omega \qquad (1a)$$

$$\nabla^2\psi = -\omega \qquad (1b)$$

for $0 \le x \le X$ and $0 \le y \le Y$, where $X \equiv W/l$ and $Y \equiv H/l$. The quantities W and H are the dimensional width and height of the domain as indicated in Fig. 1. The stream function, ψ, and vorticity, ω, are related to the x and y components of velocity by $u = \psi_y$, $v = -\psi_x$, and $\omega = v_x - u_y$.

The steady boundary conditions applied at the inlet, $x = 0$, for $0 \le y \le 1$, are $u = 6y(1 - y)$ and $v = 0$. The conditions applied along the outflow boundary, $0 < x < X$, $y = Y$, are $\psi_{yy} = 0$ and $\omega_y = 0$ (Roache, 1970). Along the remaining boundaries, the steady conditions are $\psi = 0$ and $\psi_y = 0$ at $y = 0$, $\psi = 0$ and $\psi_x = 0$ at $x = X$, and $\psi = 1$ and $\psi_x = 0$ at $x = 0$. The initial conditions are $\psi = \omega = 0$.

Numerical Method. The steady-state solution was obtained by a time-marching technique as suggested by the inclusion of the time derivative in Eq. (1a). The governing equations were discretized on a grid with uniform spacing h in both coordinate directions. The temporal integration was based on the Alternating Direction Implicit (ADI) scheme of Briley and McDonald (1980) applied to both the convection and diffusion operators. The Crank-Nicolson time differencing scheme was used. Spatial derivatives were discretized using second-order accurate central differences for both first and second order derivatives. The velocities in the convective term are lagged one time step. For Eq. (1a), the accuracy of this numerical scheme is first-order in time and second-order in space. The Poisson equation for the stream function, Eq. (1b), is also discretized using second-order central differences. The equation is solved at each time step using a W-cycle based Full Multigrid Correction Scheme (Stuben and Trottenberg, 1982).

The distribution of the deviation from hydrostatic pressure, p, was computed by line integration of the vector momentum equation relative to a datum located at $(0, Y)$. The integration

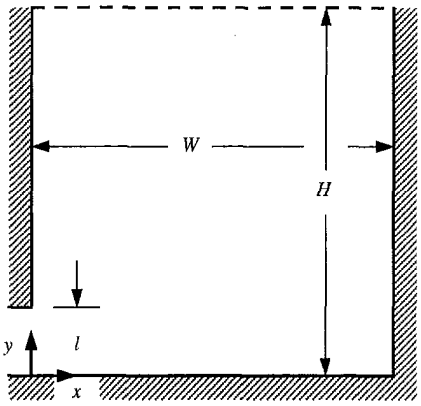

Fig. 1 Schematic of the geometry and coordinate system

paths were chosen so as to avoid regions of large gradient, especially those located along the lower portion of the $x = 0$ boundary.

The criteria used to determine whether the solution had reached the steady-state was that the maximum of $|\omega^{n+1} - \omega^n|/\Delta t$ over the domain interior be less than or equal to 5.0×10^{-3}. The time step, Δt, was limited by a diffusion-type condition imposed by the explicit treatment of the boundary vorticity (Roache, 1976) and the need for diagonal dominance in the ADI coordinate sweeps.

The level of grid convergence was gauged by the estimated solution error and the magnitude of $\nabla^2\psi + \omega$ integrated over the domain. The estimate of global solution error, e, was based upon Richardson extrapolation (Ferziger, 1993; Roache, 1993). For grid sizes of $\frac{1}{4} \geq h \geq \frac{1}{16}$, the maximum of $e(\psi)$ was of the order 10^{-2}; the maximums for the vorticity solution were approximately one order of magnitude larger. For grid sizes $h = \frac{1}{8}$ and $\frac{1}{16}$, the error reduction of the streamfunction was about 3.9, indicating the solution was achieving the error reduction expected of a second-order scheme. For the grid sizes $h = \frac{1}{8}$ and $\frac{1}{16}$, the area integral of the Poisson equation was satisfied to within the order of 10^{-2} for the range of Reynolds numbers computed in the present study. Grid sizes of at least $\frac{1}{8}$ were used for all of the solutions presented in this paper, except as noted.

The outflow boundary conditions do not enforce a fully-developed profile at the outlet, although for large Y/X, the profiles do approach this condition. However, our results show that even the most sensitive structures of the flow, such as the reattachment point, are not significantly affected by a less than fully developed profile at the outflow boundary. For the solutions presented in this paper, the ratio of Y/X was at least 1 for Re $= 10$ and at least 2 for Re ≥ 20.

Laminar Plane Wall Jet. The similarity solution (Glauert, 1956) for the laminar plane wall jet proceeds from the assumption that the pressure field is uniform, the wall jet is sufficiently slender and that the appropriate boundary conditions are $\tilde{u} = \tilde{v} = 0$ at $\tilde{y} = 0$ and $\tilde{u} \to 0$ as $\tilde{y} \to \infty$. Glauert showed that a similarity solution can be obtained in terms of a shape function, f, when the quantity termed the flux of exterior momentum flux,

$$\tilde{F} = \int_0^\infty \tilde{u} \left\{ \int_{\tilde{y}}^\infty \tilde{u}^2 \, d\tilde{y} \right\} d\tilde{y}, \tag{2}$$

is conserved. Note however, in terms of the boundary layer coordinate, the thickness of the boundary layer extends to infinity. Consistent with previous experimental studies of free jet and wall jet flows (Bajura and Szewczyk, 1970; Sato and Sakao, 1964), we define a finite boundary-layer thickness by rescaling the boundary layer coordinate and velocity shape function so that the velocity attains a value equal to $\frac{1}{2}$ at a height of unity. The rescaled velocity shape function is therefore $g' \equiv f'/f'_{\max}$ and the rescaled boundary layer coordinate, $\hat{\eta}$, is defined as $g'(\hat{\eta} = 1) = \frac{1}{2}$. With these definitions, the variation of the dimensionless velocity maximum and boundary layer height as a function of horizontal position is then predicted by the similarity solution to be:

$$U \equiv \tilde{U}/\bar{u}_o \cong 0.535 \left(\frac{\Gamma \, \mathrm{Re}}{x} \right)^{1/2} \tag{3a}$$

$$\delta \equiv \tilde{\delta}/l \cong 5.68 \left[\frac{1}{\Gamma} \left(\frac{x}{\mathrm{Re}} \right)^3 \right]^{1/4} \tag{3b}$$

where, as before, $\mathrm{Re} \equiv \bar{u}_o l/\nu$. The dimensionless flux of outer momentum flux, Γ, is

$$\Gamma \equiv U^3 \delta^2 \kappa \cong 0.867 \, \tilde{F}/(\bar{u}_o^3 \, l^2) \tag{4}$$

where

$$\kappa \equiv \int_0^1 g' \left\{ \int_{\hat{\eta}}^1 g'^2 \, d\hat{\eta} \right\} d\hat{\eta} \tag{5}$$

for the finite boundary layer height.

Solutions and Results

Boundary Layer Characteristics. Although comparison of the local velocity profile, m_i', with the theoretical shape profile, g', is straightforward, comparison of the δ and U data with their theoretically predicted variation, Eqs. (3*a*) and (3*b*), is much less straightforward. The comparison is complicated by the fact that Γ is not known a priori and that the actual wall jet originates from an inlet of finite height. As for the free jet, the problem is that real jets exit from a finite height inlet with a velocity profile that is not a simple stretching of the similarity profile. The traditional way to resolve this dilemma, for both free jets and wall jets, is to introduce a so-called virtual origin and to assume that $\Gamma = \Gamma(x = 0)$. The virtual origin can then be interpreted as the point from which the self-similar region would appear to originate if the boundary layer height could be extrapolated back to zero thickness. The modified form of the similarity solution is then

$$U = c \left(\frac{\Gamma \, \mathrm{Re}}{x + x_o} \right)^{1/2}, \tag{6a}$$

$$\delta = c \left[\frac{1}{\Gamma} \left(\frac{x + x_o}{\mathrm{Re}} \right)^3 \right]^{1/4}. \tag{6b}$$

Practical use of this result requires not only an assumed value for Γ, but also correlations for x_o. Typically, correlations based on Eqs. (6) use the multiplicative constant c and the virtual origin x_o as free parameters.

The growth of the boundary layer height and the decay of the velocity maximum are shown in Fig. 2 with solid lines for the case in which $\mathrm{Re} = 50$ and $W/l = 32$. Also shown, with dotted lines, are curve fits of the δ and U data to Eqs. (6) for the horizontal region in which $|m_i' - g'| \leq 0.025$ over the vertical interval $0 \leq \eta \leq 1$. This definition gives the beginning and end of the similarity region for the case as $x_b = 1.31$ and $x_e = 10.6$, respectively. Both of the curve fits follow the data very closely for most of the region shown in Fig. 2. Within this boundary layer region, κ has a nearly constant value equal to

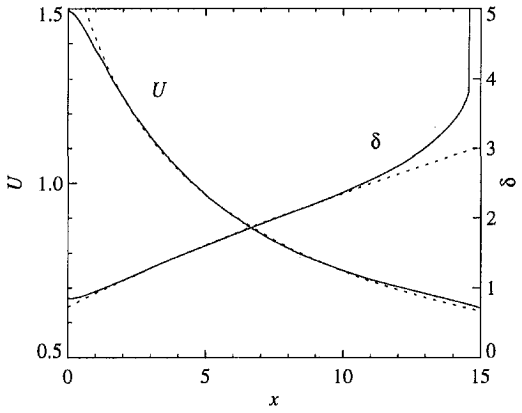

Fig. 2 Velocity maximum decay and boundary layer growth for the case of Re = 50 and $W/l = 32$

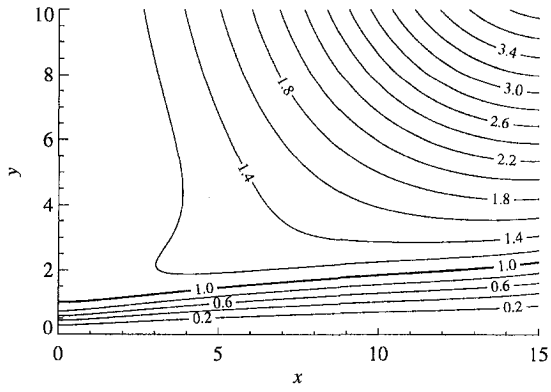

Fig. 4 Contours of stream function in the near inlet region for the case of Re = 50 and $W/l = 32$

approximately 90% of the inlet value, $\kappa_o = 0.232$. The dimensionless flux of exterior momentum flux, Γ, is hardly constant though, even for the portion of the region which appears to be indistinguishable from the similarity predictions for δ and U. Most likely, this results from the fact that Γ depends in turn on the quantities U, δ and κ, and therefore shows the accumulation of their individual differences from the similarity solution. The average of Γ over the boundary layer region is about 84% of the inlet value, $\Gamma_o = 0.571$.

Unscaled profiles of horizontal velocity component are shown in Fig. 3. In the figure, the asterisks show the location of the boundary layer edge. This figure emphasizes an extreme growth in the boundary layer height near $x = 15$, visible also in Fig. 2. The explanation for this sudden growth in the boundary layer height is the presence of a recirculation cell partially visible in a plot of streamlines near the inlet, shown in Fig. 4. For the classical wall-jet problem, the flow remains horizontal, but in the present problem the flow must turn to exit at the top of the domain. As we will discuss later, the turning results in a strong recirculation cell directly above the wall jet. With the wall at $x = 32$, the center of this recirculation cell is at $x_c = 15.7$. The vortex center is taken as the location, (x_c, y_c), at which the streamfunction is a maximum within the vortex. Below its center, the recirculation cell involves relatively large positive horizontal velocities, so that the definition of the wall-jet boundary at $u(x, y = \delta) = U(x)/2$ leads to points in the recirculation cell. Hence the sudden change in the boundary layer height. Although the location of the recirculation does not have as drastic an effect on the velocity maximum decay, the departure from the similarity prediction is increasingly noticeable as the vortex center is approached and then passed.

The horizontal variation of pressure, $p(x, y)$, in the near inlet region is shown in Fig. 5. The two profiles located within the boundary layer, $y = 0.5$ and 2.0, are nearly the same magnitude indicating both vertical and horizontal gradients are small as assumed in the boundary layer theory. The large gradients located right near the inlet are evident in the $y = 0.5$ profile for the region $x < 1$. However, even those gradients are smaller than the depression produced by the recirculation cell. The profile at $y = 10$, for example, even though it lies below the vortex center, shows clearly the strength of this low pressure region.

The location of the vortex center relative to the boundary layer region is shown in Table 1 for each of the cases computed in the present study. The end of the boundary layer region, x_e, follows the movement of the vortex center quite closely. For Re = 10, $x_e > x_c$ although the total length of the boundary layer region is quite small at this low Reynolds number. Since the slenderness of the boundary layer scales according to $\delta/x \sim (xF\,\mathrm{Re}^3)^{-1/4}$, the requirement that $\delta/x \ll 1$ is hardly satisfied at this low of a Reynolds number. At the higher Reynolds numbers, x_e is seen to be always less than x_c and roughly proportional to it.

The beginning of the boundary layer region, or alternatively, the length of the adjustment region, is seen to be inversely proportional to Reynolds number and basically independent of the vortex center location. The possible exceptions, those for the largest domain size at Reynolds numbers equal to 20 and 50, are most likely due to the relatively larger grid size ($h = \frac{1}{4}$). The diminishing width of the adjustment region is also evident in the outer momentum flux data, summarized in Table 2. The average of the outer momentum flux in the boundary layer

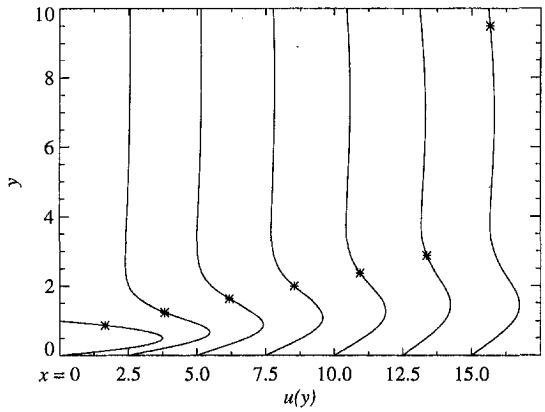

Fig. 3 Velocity profiles in the boundary layer region for the case of Re = 50 and $W/l = 32$

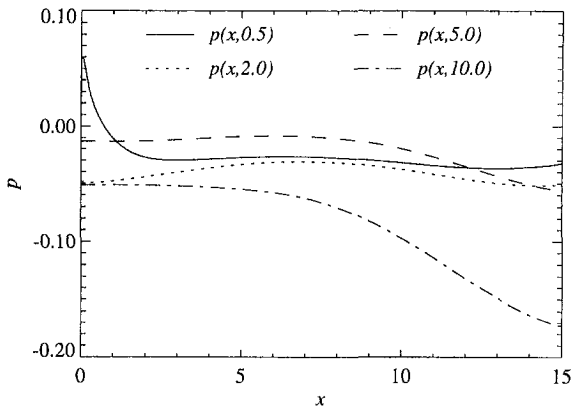

Fig. 5 Horizontal pressure profiles in the boundary layer region for the case of Re = 50 and $W/l = 32$

Table 1 Location of the wall jet boundary layer and the associated recirculation region

	W/l	x_b	x_e	x_c	y_c	y_r
Re = 10	16	4.75	5.38	3.0	5.5	13.0
	32	5.13	6.13	3.5	6.3	15.9
	64	5.13	6.38	3.5	6.3	17.0
	128	6.0	6.75	3.8	6.5	17.6
Re = 20	16	2.25	5.25	7.0	12.3	23.5
	32	2.38	10.0	14.0	15.3	35.5
	64	2.38	12.1	18.6	17.3	57.9
	128	5.25	12.0	19.5	17.5	73.8
Re = 50	16	1.31	3.44	7.1	12.1	22.5
	32	1.31	10.6	15.7	13.6	39.7
	64	1.63	13.9	21.8	15.6	68.1

region, $\bar{\Gamma}$, shows a clear increase with Reynolds number and appears to be steadily approaching the inlet value of 0.571. This trend was also observed by Chanaud and Powell (1962) in an experimental study of a plane free jet. Their results showed that the similarity solution, when based on the inlet jet momentum, provided a steadily improving approximation of the experimental velocity maximum decay as the Reynolds number was increased from 15 to 68.

Also shown in Table 2 are the data for the proportionality constants and virtual origin of Eqs. (6). The trend of the virtual origin is to increase with Reynolds number as noted by other researchers (Bajura and Szewczyk, 1970; Sato and Sakao, 1964). At a Reynolds number of 10, the virtual origin determined by the correlations for δ and U differ considerably, but at higher Reynolds numbers, the gap closes. Presumably, this is one more indication of the tenuous comparison of Re = 10 results to the similarity solution. The multiplicative constants are, for all of the Reynolds numbers shown, very close to those predicted by the similarity solution in Eq. (3). The published correlations of Bajura and Szewczyk (1970) and Gorla and Jeng (1972) for the virtual origin and the multiplicative constant c as a function of Reynolds number correspond well to the trends shown in Table 2. Even though their correlations are based on data for Reynolds numbers of over 200, our results predict x_o and c to the same order of magnitude as estimated by their correlations.

Role of Recirculation Cell and Finite-Width Domain. Already in the previous section, even with attention focused on the relatively small boundary layer region, the importance of the large scale flowfield characteristics began to emerge. In this section these characteristics are examined in greater detail and their relationship to the overall geometry explored.

In Fig. 6, a plot of pressure and stream function contours for the case Re = 20 and W/l = 16 is shown. For this case, the wall jet appears to be strongly constrained by the righthand wall. There is a significant high pressure region in the lower

Table 2 Curve fit of the boundary layer growth and velocity maximum decay in the wall jet boundary layer

			δ		U	
	W/l	$\bar{\Gamma}$	c	x_o	c	x_o
Re = 10	16	0.0826	4.74	−0.977	0.431	−2.99
	32	0.0863	4.85	−1.09	0.441	−3.13
	64	0.0866	4.86	−1.103	0.444	−3.15
	128	0.0766	4.69	−1.16	0.432	−3.74
Re = 20	16	0.366	5.62	0.305	0.519	0.0284
	32	0.352	5.52	0.208	0.537	0.0536
	64	0.348	5.43	0.268	0.541	0.0433
	128	0.323	5.48	−0.094	0.543	−0.203
Re = 50	16	0.494	5.43	2.81	0.539	2.65
	32	0.478	5.50	2.62	0.541	2.50
	64	0.467	5.46	2.62	0.544	2.48

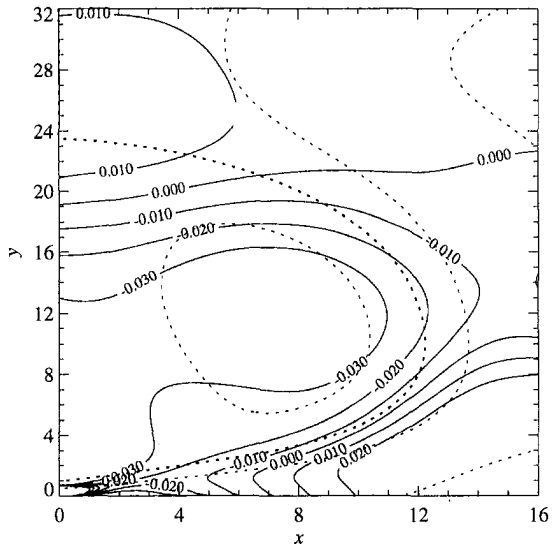

Fig. 6 Pressure contours (solid lines) overlayed with stream function contours, ψ = (0, 0.5, 1.0, 1.5), for the case of Re = 20, W/l = 16 and H/W = 4

right hand corner and another on the left hand wall in the area surrounding the reattachment point. In this case, the separating streamline meets the wall at nearly a 90 degree angle. An additional separation bubble is also evident higher up on the opposite wall. The low pressure region coinciding with the primary recirculation cell is quite pronounced, generating a pressure differential larger than either the corner stagnation or reattachment region. Figure 7 shows the horizontal variation of pressure for vertical locations corresponding approximately to the inlet location, the center of the recirculation region, the reattachment region and the developing region. The figure illustrates clearly the high pressure region in the lower right corner and the low pressure region produced by the recirculation region. The pressure profile at y = 24 shows a fairly strong gradient driving the flow away from the left wall. At y = 60, there is still a gradient driving flow toward the right wall although its strength has diminished and the flow profile is nearly fully developed.

An interesting contrast emerges as the width of the domain is increased by a factor of four. Figure 8 shows pressure and stream function contours similar to Fig. 6. In this case, the largest pressure gradients by far are those associated with the recirculation cell excepting those near the inlet. Relative to the pressure gradients associated with the primary vortex, the

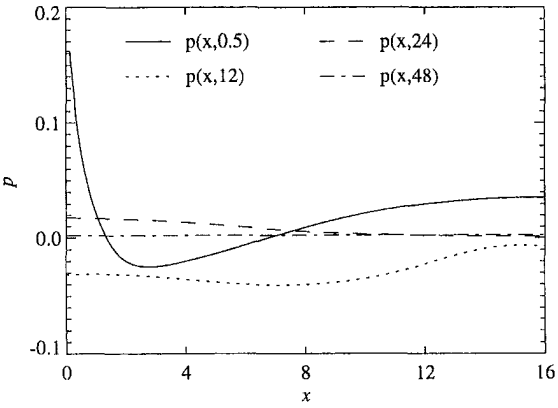

Fig. 7 Horizontal pressure profiles for the case of Re = 20, W/l = 16, and H/W = 4

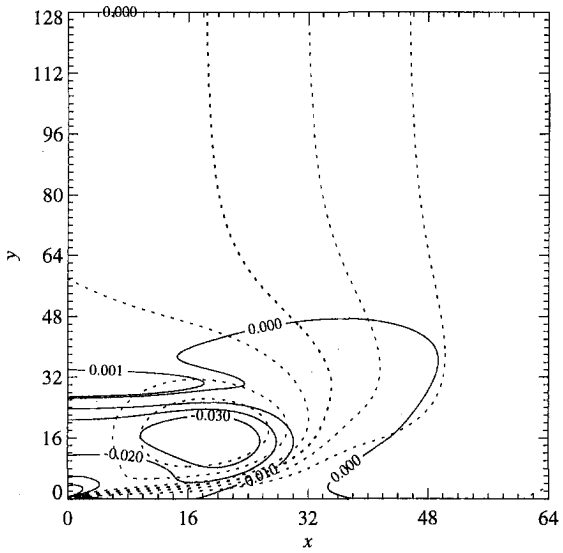

Fig. 8 Pressure contours (solid lines) overlayed with stream function contours (dotted lines, $\psi = \{0, 0.25, 0.5, 1.0, 1.5, 2.0\}$) for the case of Re = 20, $W/l = 64$, $H/W = 2$, $h = \frac{1}{8}$

lower right hand corner and the reattachment region exhibit only small pressure variations. The primary separation bubble is much smaller than the width of the tank and does not appear to be directly constrained by it. A noteworthy feature indicative of the different flow behavior is the shape of the stream function contour $\psi = 0.25$. Along the lower right side of the recirculation region the streamlines follow its curvature. However, as the streamlines reach a vertical position about even with the vortex center, the streamlines spread apart and move toward the right wall. These adjustments appear to be a direct result of the constraints imposed by the outflow location, i.e., that in a sufficiently tall cavity the flow must eventually reach a symmetric fully-developed vertical velocity profile. In contrast to the small width case where the right wall and the low pressure bubble both conspired to turn the flow towards the left wall, in the large width case the Coanda effect produced by the low pressure bubble is offset by the width of the domain. The tendency of the flow to impinge on the left wall then diminishes. The pressure distribution is again dominated by the pressure gradients associated with the recirculation region excepting those in the immediate area of the inlet. Interestingly, the pressure gradients are still adjusting the flow profile at $y = 60$, for example, since $p_x(32, 60) = -4.8 \times 10^{-6}$. Further evidence of the overall adjustment is the angle which the separation streamline forms with the left wall at reattachment. In this case, the angle is much less than 90 degrees, closer to 45 degrees, and its location on the left wall is much higher than in the $W/l = 16$ case.

Finally, Table 1 presents the basic features of the recirculation region attached to the left wall for each of the cases computed in this study. A correlation for the location of the vortex center in plane free jets, $x_c = 1.71 \exp(\mathrm{Re}^2/175)$, was presented by Zauner (1985) based in part on visualizations of axisymmetric jets. For Reynolds numbers of 10 and 20, that correlation predicts $x_c = 2.5$ and 13.9, respectively, which compares quite well with those shown in Table 1. The strength of the recirculation cell, as gauged by the stream function maximum, is nearly constant over the range of domain widths simulated for Re = 10. In addition, the reattachment point and location of the stream function maximum are also nearly constant for this same Reynolds number. At Re = 20, the $W/l = 16$ case shows the recirculation cell being constrained by the width of the channel since for $W/l \geq 32$ the value of the stream function maximum and its location remain fairly constant. The location of the reattachment point shows less sign of leveling off though, again signaling its dependence on the large scale features of the flowfield. Similar observations hold true for the case of Re = 50 although, as to be expected, the strength of the recirculation region increases. Overall, the strength of the vortex seems to depend primarily on the Reynolds number provided the horizontal width of the cell is not directly constrained by the domain width. The vertical size of the recirculation region, as gauged by the reattachment point y_r, appears much more sensitive to the domain width and the sharpness of the turning which it dictates. Presumably, the reattachment of the separation streamline to the $x = 0$ boundary is only guaranteed because, in the present study, the height of the simulated domain was very large.

Conclusions

The classic similarity description of a slender wall jet issuing into a semi-infinite domain predicts a growth of the boundary layer width according to $(x/\mathrm{Re})^{3/4}$ and a decay of the velocity maximum at a rate of $(x/\mathrm{Re})^{-1/2}$. The growth of the boundary layer is supported by a recirculation cell located immediately above the boundary layer region. For the horizontal flow of a wall jet into a finite width domain, numerical solutions of the two-dimensional Navier-Stokes equations show substantial agreement with the similarity solution within the wall jet boundary layer. However, the extent of the region for which the comparison can be considered favorable is directly limited by the imposed domain width and its effect on the horizontal scale of the recirculation cell. Already at domain width to inlet height ratios of 32, the horizontal scale of the recirculation cell is nearly constant for Reynolds numbers less than 50. For the finite width domain, the end of the boundary layer region corresponds closely to the location of the recirculation cell center. The recirculation cell, and the low pressure region it produces, are of sufficient strength to turn the wall jet in a manner similar to that associated with the Coanda effect. The turning of the flow to a direction aligned with the tank axis forces a closure of the recirculation cell along the vertical wall immediately above the inlet. The vertical scale of this closed recirculation cell appearing immediately above the jet inlet is comparable to the domain width, even at domain width to inlet height ratios of 128.

Acknowledgments

This research was supported by the US Army Construction Engineering Research Laboratories of Champaign, IL through the AT23-EB-ESO Program. Computing time on the SGI Challenge has been provided by a grant from the National Center for Supercomputing Applications (NCSA) of Urbana, IL. The helpful discussions provided by Professor John S. Walker are gratefully acknowledged.

References

Baines, W. D., Martin, W. W., and Smith, D. M., 1983, "Development of Stratification in a Rectangular Tank by Horizontal Inflow," ASME JOURNAL OF FLUIDS ENGINEERING, Vol. 105, pp. 59–64.

Bajura, R. A., and Szewczyk, A. A., 1970, "Experimental Investigation of a Laminar Two-Dimensional Plane Wall Jet," *Physics of Fluids,* Vol. 13, p. 1653.

Briley, W. R., and McDonald, H., 1980, "On the Structure and Use of Linearized Block Implicit Schemes," *Journal of Computational Physics,* Vol. 34, p. 54.

Chanaud, R. C., and Powell, A., 1962, "Experiments Concerning the Sound-Sensitive Jet," *The Journal of the Acoustical Society of America,* Vol. 34, p. 907.

Ferziger, J. H., 1993, "Estimation and Reduction of Numerical Error," *Quantification of Uncertainty in Computational Fluid Dynamics,* Vol. 158 of ASME FED, p. 1.

Glauert, M. B., 1956, "The Wall Jet," *Journal of Fluid Mechanics,* Vol. 1, p. 625.

Gorla, R. S. R., and Jeng, D. R., 1972, "Laminar Plane Wall Jet," *Proc. 12th Midwestern Mechanics Conference: Developments in Mechanics,* Vol. 6, p. 137.

Roache, P. J., 1970, "Sufficiency Conditions for a Commonly Used Downstream Boundary Condition on Stream Function," *Journal of Computational Physics,* Vol. 6, 317.

Roache, P. J., 1976, *Computational Fluid Dynamics,* Hermosa Publishers, Albuquerque, NM.

Roache, P. J., 1993, "A Method for Uniform Reporting of Grid Refinement Studies," *Quantification of Uncertainty in Computational Fluid Dynamics,* Vol. 158 of ASME FED, p. 109.

Sato, H., and Sakao, F., 1964, "An Experimental Investigation of the Instability of a Two-Dimensional Jet at Low Reynolds Numbers," *Journal of Fluid Mechanics,* Vol. 20, 22.

Stuben, K., and Trottenberg, U., 1982, "Multigrid Methods: Fundamental Algorithms, Model Problem Analysis and Applications," *Lecture Notes in Mathematics,* Vol. 960, p. 1, Springer-Verlag.

Yoo, J., Wildin, M. W., and Truman, C. R., 1987, "Traveling, Velocity of Thermally Driven Two-Dimensional Gravity Currents," *Natural Circulation,* Vol. 61 of ASME FED, p. 319.

Zauner, E., 1985, "Visualization of the Viscous Flow Induced by a Round Jet," *Journal of Fluid Mechanics,* Vol. 154, 111.

R. Martinuzzi
Assistant Professor,
Department of Mechanical and
Material Engineering.

A. M. Zaghloul
Research Associate,
Department of Civil and
Environmental Engineering.

W. Al-Qaraguli
Senior Undergraduate Student,
Department of Civil and
Environmental Engineering.

R. E. Baddour
Professor,
Department of Civil and
Environmental Engineering.

The University of Western Ontario,
London, Ontario, N6A 5B9

Turbulence Structure of Plane Surface-Jets in a Weak Coflowing Stream for Different Initial Wake Conditions

Plane turbulent surface-jets, in the presence of a weak coflowing ambient current, were experimentally investigated using a single-component Laser Doppler Velocimeter. This study is concerned with the influence on the turbulent mixing characteristics of the relative speed ratio, U_a', and the wake generated behind the plate separating the jet from the ambient stream at the exit. Data were analyzed for similarity characteristics, surface speed decay, jet growth rate, jet momentum flux, jet volume flux, and turbulence decay. An integral analysis of the governing equations was also conducted to examine the turbulent entrainment properties of the surface jets.

1 Introduction

Interest in turbulent surface-jets has been motivated by a need to better understand the interaction between the free surface and the jet structure. These flow processes are important from both fundamental and applied perspectives. For example, sonar signatures from ship wakes or surface wave patterns resulting from shallow current are strongly dependent on such interactions. Environmental flows are also a relevant class of such studies. The pollutant transport downstream of discharges in rivers, lakes, and oceans is governed in the near field by the turbulent mixing properties of surface-jets. The difficulty of these problems is further compounded by the presence of both an ambient stream and an initial wake. While some studies of pure surface plane jets have been reported, there have been no experimental studies explicitly treating two-dimensional surface-jets in the presence of an imposed weak irrotational coflowing ambient current. The purpose of this paper is to study the structure of a simple basic model for such flows: a plane turbulent surface-jet in the presence of both an irrotational coflowing stream and a momentum deficit due to a wake at the initial region of the jet.

The case of the free turbulent jet is a classical problem (Schlichting, 1979) for which a similarity solution exits downstream of the initial entry region. Application of the similarity condition in an unbounded, stagnant domain implies that the momentum flux, **J**, is a conserved quantity. However, an extensive review of literature data by Ramaprian and Chandrasekhara (1985) shows that measurements of **J** in many plane-jet experiments lead to conflicting conclusions. While some reports indicate that **J** increases with streamwise distance from the inlet, others suggest a decreasing trend. Schneider (1985) and Kotsovinos (1978) provide analytical arguments, supported by experimental data, that **J** should decrease with axial distance for a jet in a stagnant medium. These analyses are based on the observation that in a bounded medium, the induced return flow, albeit small, contributes to a reduction in the total jet momentum. As a result, while the growth rate remains linear, the centerline velocity decays somewhat more quickly than predicted with the classical theory.

The implications of the aforementioned studies for this analysis are unclear. The present case differs from the classical problem in three important respects. First, the presence of an imposed coflowing ambient current should tend to overshadow and possibly eliminate the appearance of an induced return flow. For example Bradbury (1965), Bradbury and Riley (1967) as well as Anwar and Weller (1969) report that the structure of a plane jet in a coflowing stream changes from that of a self-preserving jet in the near field to a self-preserving wake in the far field. Sherman (1990) indicated that a general similarity solution for a submerged coflowing jet can only exist as limiting cases for which the ambient stream is either zero or of the same order as the surface speed.

The second major difference is that the present flow is bounded by a free surface, which tends to suppress turbulent fluctuations and limit vertical transport by large scale motion. Experimental investigations of plane surface-jets in stagnant surroundings by Chu and Vanvari (1976), Rajaratnam and Humphries (1984) and Swean et al. (1989) show that the surface-jet exhibits some of the characteristics of wall jets previously studied by Schwarz and Cosart (1961) and Irwin (1973). In the latter case, it was found that a nearly self-preserving jet could be obtained only by controlling the streamwise pressure gradient. It is expected that the surface-jet will exhibit qualities of both the free jet and the wall-bounded jet where, unlike the latter, the pressure gradient is not a free parameter but is fixed by the free surface. A study of the turbulent structure of a plane surface-jet in a weak co-current was recently conducted investigating the effect of the ambient current (Zaghloul et al., 1995). This study shows that the surface-jet does display a self-preserving character for the velocity profiles and turbulent quantities. The near and far field jet structures are different and the near field is much shorter than in a plane submerged jet in a cocurrent.

The third major difference between the present case and that of the classical jet is the presence of a wake in the initial, or

Contributed by the Fluids Engineering Division for publication in the JOURNAL OF FLUIDS ENGINEERING. Manuscript received by the Fluids Engineering Division February 20, 1996; revised manuscript received October 1, 1997. Associate Technical Editor: M. Triantafyllou.

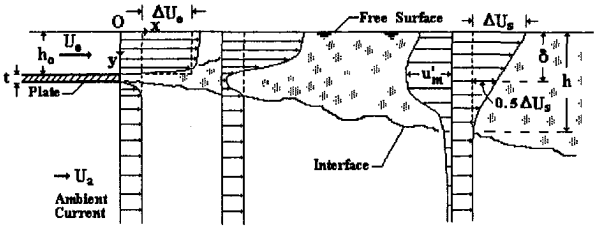

Fig. 1 Schematic representation of the surface-jet geometry and nomenclature

entry region, of the jet. This initial wake is due to the plate separating the jet and the ambient stream. Cimbala and Park (1990) experimentally investigated the structure of four different turbulent, two-dimensional wakes. A controlled jet was forced through a slit at the trailing edge of an airfoil in a stream. It was reported that the downstream flow exhibited either a wake-like or a jet-like structure depending on whether the initial forced jet momentum was less or greater than the momentum deficit of the wake at the trailing edge. The momentum as a function of the downstream location for the jet-like case was not reported.

This study examines the effect of a wake at the initial region, between the jet and the ambient current, on the development, growth, similarity properties and turbulence structure of a plane surface-jet with a weak cocurrent.

2 Experimental Rig

The experiments were conducted in an open water channel 15 cm wide, 28 cm deep with a 1.6 m long test section. The flow empties into a large holding basin and the pressure gradient in the working section was negligible. A 45 cm long plate separating the jet from the ambient stream was located in a large, upstream settling chamber and extended 15 cm into the test section. The surface-jet and the associated nomenclature are shown schematically in Fig. 1. A thin and a thick plate (1 mm and 10 mm thickness, respectively), spanning the entire channel width, were separately used to obtain a small and a large wake, respectively. The plates, mounted below the free surface, and a downstream weir were used to fix the depth of the jet at $h_o = 8$ mm. The average speed of the jet in excess to that of the ambient stream ($\Delta U_o = U_o - U_a$) and the ambient current speed, U_a, were controlled to obtain relative speed ratios, $U_a' = U_a/(\Delta U_o)$, of 0.12 and 0.16 for the thin (1 mm) plate, and 0.12 and 0.17 for the thick (10 mm) plate. The Reynolds number of the jet, $\mathrm{Re}_o = (U_o D_o)/\nu$, calculated at the trailing edge of the plate based on the hydraulic diameter, D_o, was approximately 5000. The jet flow was subcritical, and the Froude number, $F_o = U_o/\sqrt{gh_o}$, was approximately 0.55. No disturbances of the free surface could be detected visually. The laser beam aimed along the surface did not show any deflections. Table 1 is a summary of the experimental conditions.

Velocity measurements were made using a single-component, He-Ne Laser Doppler Velocimeter (LDV) operated in forward scatter mode. The sending lens had a focal length of 350 mm and the resulting measuring volume was 1.5 mm long and 160 μm in diameter. The receiving optic consisted of a lens assembly (numerical aperture 0.07) and a 100 μm core diameter fiber optic connected to a photomultiplier. A Bragg cell with electronic downmixer was used. The selected frequency shift (50 kHz) was at least twice the maximum Doppler frequency observed in the jet as recommended in Edwards (1987) to handle angle bias.

For velocity measurements, the counter was set in single measurement per burst mode. The Doppler frequency was estimated over 16 cycles/burst using a 1 percent validation criterion for the 5/8 comparator. Arrival time averaging (Sample and Hold technique with trapezoid interpolation, see Edwards, 1987) was used to calculate the first and second statistical moments. Between 30,000 to 60,000 LDV-events were collected for each measurement point. Natural suspension particles were sufficient to obtain average validated data rates of $N = 150$–200 Hz in the ambient stream. In the jet, data rates typically ranged from $N = 300$–600 Hz to 150–300 Hz at locations 20 h_o and $70h_o$ downstream of the plate edge, respectively. The smallest Taylor time microscales, T_λ, was estimated from the autocorrelation function to range from 0.01 s to 0.05 s at locations 20 h_o and 70 h_o, respectively. These values are similar to those obtained by dividing the length microscale for a plane jet (Bradbury, 1965) with the local streamwise velocity. The resulting data density were found to be sufficiently high with respect to the criterion $NT_\lambda > 5$.

Error estimates for the data presented in Figs. 2 to 9 are based on 95 percent confidence level as proposed by Abernathy et al. (1985). The uncertainty in the position was in the streamwise direction ± 1 mm and ± 0.25 mm in the vertical, relative to the free surface. The uncertainty in the determining the jet half-width was estimated to be of order of 2 to 4 percent based on repeatability and comparison to visualization results. The resulting uncertainty for y/δ is ± 7 percent at $x/h_o = 0$ and ± 2.5 percent at $x/h_o = 50$. The uncertainty for the velocity and fluctuation measurements was estimated assuming a contribution due to the cumulative effects of the electronic components (resolution, oscillator stability, etc.) and due to the stochastic nature of the process. Randomly selected profiles were repeated to verify data consistency. It is estimated that the absolute uncertainty of the estimate for the mean streamwise velocity component is of the order of 0.015 U_s (1.5 percent of the local maximum velocity U_s) in the high flow region ($y/\delta < 0.6$); and increases toward the edges to about 0.02 U_s. Note, however, that in terms of local velocity the uncertainty is about 4 percent at $y/\delta \approx 1$ and 7 percent at $y/\delta \approx 2$). The uncertainty for the derived quantities, such as momentum fluxes, was calculated according to Doeblin (1975). These estimates are included in the figure captions.

The effect of surfactants on the velocity profile was not investigated, but this is expected to be small since the jet is planar. The effect of lateral spreading is negligible (Anthony and Willmarth, 1992) compared to circular jets and a streamwise layer could not be detected (Madnia and Bernal, 1994)

Small concentrations of fluorescein dye were used for edge detection and thus to estimate the average location of the turbulent boundary. A video camera with Red Green Blue (RGB) output was connected to a colour frame grabber mounted on a 486 computer. A vertical sheet of light 3 mm thick was introduced in the centre plane of the testing channel to illuminate the fluorescent dye present in the jet. A series of video images of the jet were digitally recorded and analyzed for light intensity

Table 1 Summary of test conditions for thin (1 mm) and thick (10 mm) plates ($h_o = 8$ mm, $T \cong 20$°C)

Plate thickness	U_a'	Re_o	F_o	U_a mm/s	ΔU_o mm/s	Q_o mm^2/s
1 mm	0.12	4800	0.53	18.5	168	1340
1 mm	0.16	5200	0.56	25.0	157	1440
10 mm	0.12	5100	0.57	18.5	160	1430
10 mm	0.17	5200	0.55	26.0	154	1440

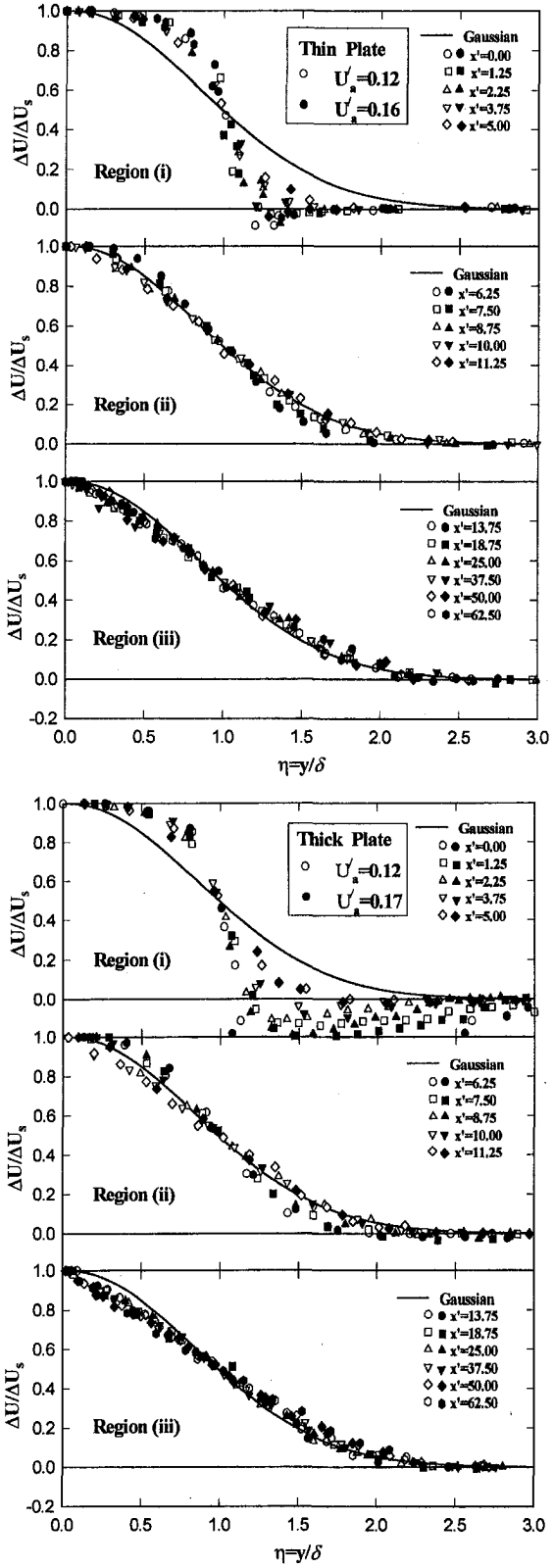

Fig. 2 Normalized velocity distribution normal to the free surface at different downstream locations. Solid line is Gaussian distribution included for comparison. Uncertainty estimate $\Delta U_s \rightarrow \approx \pm 1.5$ percent; $\Delta U \rightarrow \approx \pm 0.02$ percent. (*a*) Thin plate (small wake); (*b*) thick plate (large wake)

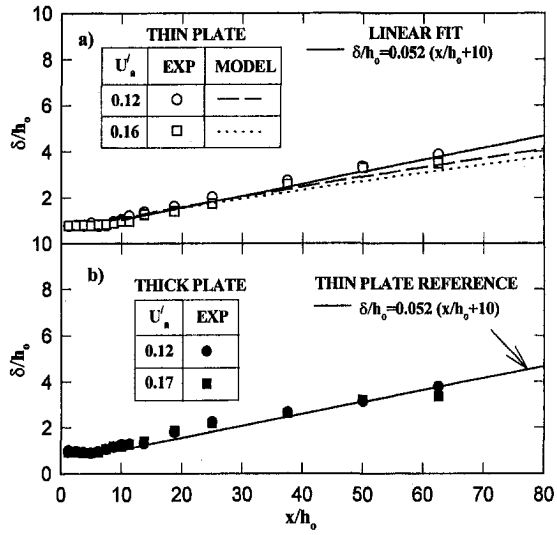

Fig. 3 Relative jet thickness, δ/h_o versus x/h_o for (*a*) thin plate; (*b*) thick plate. (Uncertainty $\delta/h_o = \pm 2$–4 percent).

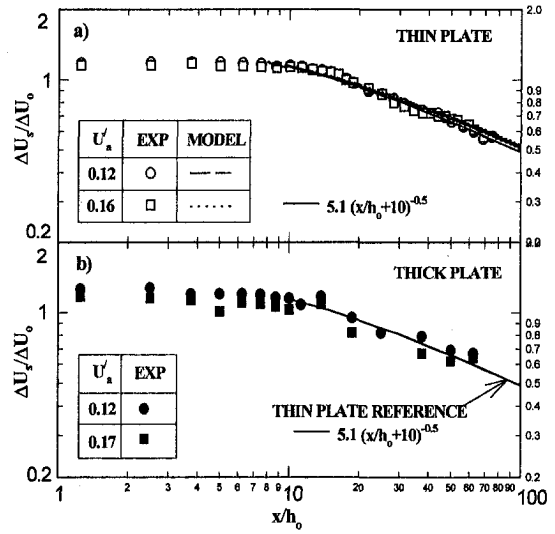

Fig. 4 Surface velocity, $\Delta U_s/\Delta U_o$, versus x/h_o for (*a*) thin plate; (*b*) thick plate

with computer imaging software (Zaghloul, 1996). Two hundred frames were recorded over a 12 minute period to estimate the average depth of the turbulent interface. This information was used to support the length scale calculations derived from the velocity profiles.

3 Results

The streamwise mean velocity, U, as a function of the vertical distance from the free surface, y, is shown in Fig. 2(a–b) at various streamwise locations, $x' = x/h_o$, downstream of the plate trailing edge for four different cases. The velocity profiles are presented in the form $\Delta U/\Delta U_s$ versus y/δ where: $\Delta U = U - U_a$; $\Delta U_s = U_s - U_a$; U_s is the maximum local velocity which occurs at the free surface and δ is the local jet thickness defined at the point $\Delta U/\Delta U_s = 0.5$. The ratio of the jet depth obtained using the visualization experiments, h, to the width, δ, calculated using the point $\Delta U/\Delta U_s = 0.5$ was constant ($h/\delta \approx 2.2$) within experimental uncertainty of ± 4 percent. Hence, without loss of generality, the width of the jet is defined using the latter criterion, as commonly used in the classical jet analysis.

In Fig. 2, the solid line representing a Gaussian distribution is included for comparison purposes. Three distinct regions can

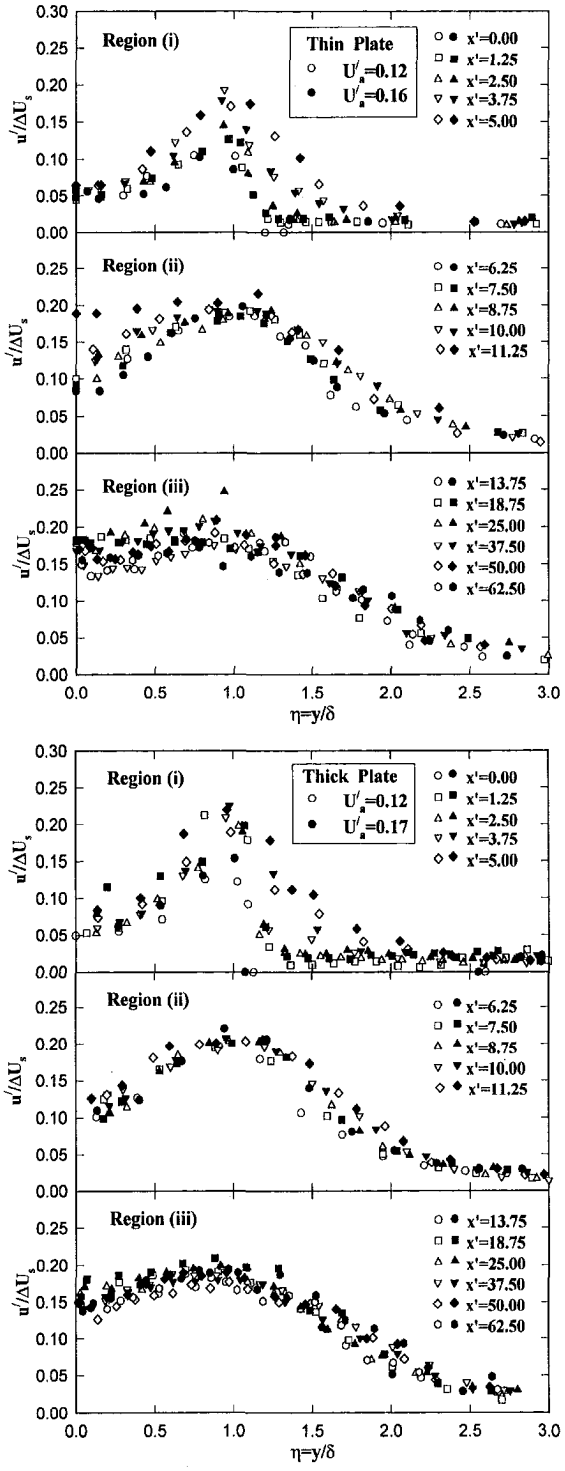

Fig. 5 Normalized rms, u', distribution normal to the free surface at different downstream locations (Uncertainty estimates for $\Delta U_s \rightarrow \approx \pm 1.5$ percent; $u' \rightarrow \approx \pm 0.08$ percent). (*a*) Thin plate (small wake); (*b*) thick plate (large wake)

be identified: (*i*) an initial development region, $x/h_o < 5$, for which the jet is not self-similar and is characterized by a top-hat profile near the surface and a wake velocity defect directly downstream of the plate trailing edge; (*ii*) an intermediate region for which the velocity profiles are well approximated by a Gaussian velocity distribution; and (*iii*) a terminal, self-similar region characterized by an almost linear velocity distribution. In the latter region, the profiles are closer to the mixing layer distribution than to those for a wake flow, which is probably

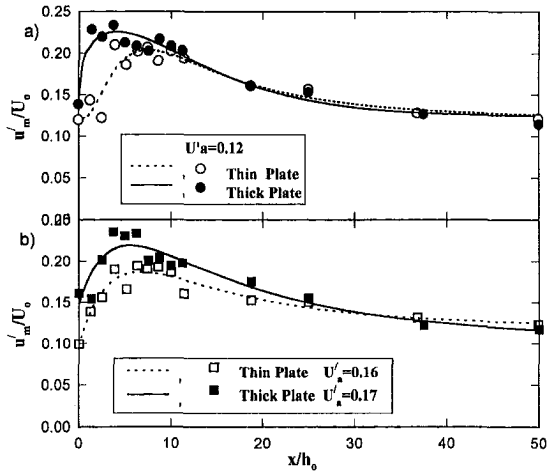

Fig. 6 Maximum rms fluctuation u'_m/U_o versus x/h_o (Uncertainty $u'_m/U_o = \pm 8$ percent)

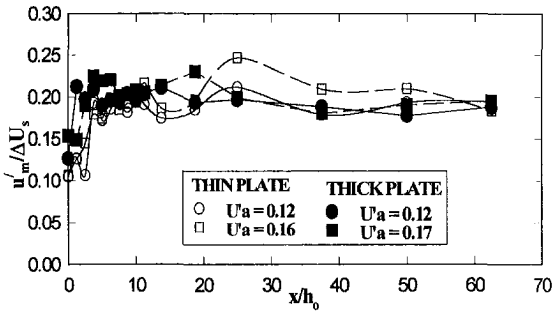

Fig. 7 Maximum rms velocity, $u'_m/\Delta U_s$, versus x/h_o

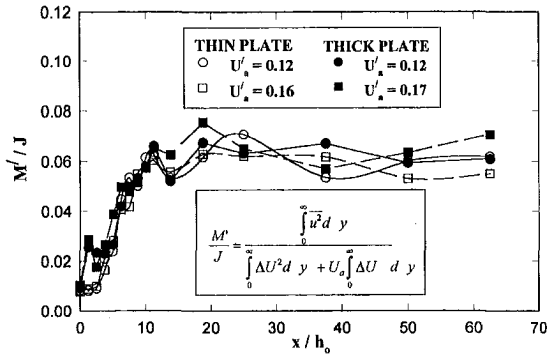

Fig. 8 Turbulent momentum flux distribution as a function of the downstream location (Uncertainty $M'/J = \pm 16$ percent)

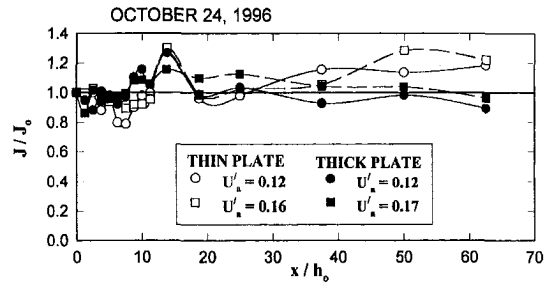

Fig. 9 Jet momentum flux, J/J_o versus X/h_o (Uncertainty $J/J_o \rightarrow \pm 9$ percent)

due to the influence of the free surface. The self-similar region appears to exist without a rigorous control of the pressure gradient, unlike the case for the wall jet (Irwin, 1973). The intermediate region observed does not satisfy the criteria for self-similarity and should be interpreted as a transition region.

The growth of the surface-jets, quantified by δ/h_o, as a function of the streamwise location, x/h_o, is shown in Fig. 3(a–b). For the thin plates, the growth of the jet is essentially linear in regions (ii) and (iii). The slope ($d\delta/dx \cong 0.052$) is comparable to that for the outer shear layer of a wall jet in a stagnant surrounding ($d\delta/dx = 0.0678$, Schwarz and Cosart, 1961) and is quite different than for the free jet ($d\delta/dx = 0.109$, Bradbury, 1965) suggesting again that the free-surface acts to suppress the growth of large scale motion as in the case of the wall jet. For the thick plate, the growth rate is initially larger than for the thin plate. This is likely due to the wake near the exit. Further downstream, however, the growth rate associated with the thick plate appears smaller when compared with the thin plate. In general, for the thin plate, the growth rate decreases slightly with increasing U_a'. For the thicker plate the larger wake dominates the jet development and the effect of U_a' on the growth of δ is minimal. Also, the growth of the jet deviates from the linear distribution far downstream of the jet exit.

Assuming a linear development for δ of the form $A(x - x_o)$, the value for x_o was estimated and then used to approximate the decay of the surface velocity, ΔU_s, in the form $B(x - x_o)^n$. As is shown in Fig. 4(a, b), a curve with exponent $n = -\frac{1}{2}$ correlates well with the measured velocity data. These observations suggest further that a similarity solution exists which closely matches the behaviour predicted with the classical theory. Furthermore, the decay exponent of the surface velocity suggests that for the surface-jet with weak co-current, the momentum flux is nearly conserved.

The vertical profiles of rms velocity u' at various downstream location from the jet outlet are shown in Fig. 5 for all four cases studied. It can be observed that the turbulence field exhibits similarity in the terminal region when Normalized with ΔU_s

The distinguishing characteristics for the three flow regions of the surface-jet are easily observed in the results obtained for the maximum velocity fluctuations (rms velocities) as a function of the streamwise location, x/h_o, as shown in Fig. 6. Region (i) is characterized by a rapid increase in the maximum rms velocity fluctuations, u_m'. The transition region ($6 < x/h_o < 12$) coincides with the area where u_m' is close to its maximum. In this region, u_m' is slowly changing indicating a region of near equilibrium in the turbulence energy balance, that is, the local rate of turbulence production is very nearly completely offset by the local rate of dissipation. Under these conditions, it is expected that the turbulent length scales are independent of the jet boundaries and constant throughout the jet. It is also noted that in this region the surface velocity and the jet width are very nearly constant. Hence, the turbulent or eddy viscosity should be independent of x and y, which is a situation similar to that for the circular jet, for which the velocity distribution is closely approximated by a Gaussian profile (Schlichting, 1979). It is also noted that these conditions are only approximately satisfied so that the jet is not truly self-similar in region (ii). The terminal self-similarity region corresponds to the region of decay for u_m'.

The self-similar character of the turbulent field is further supported by the data shown in Fig. 7, where $u_m'/\Delta U_s$ vs. x/h_o is shown. This ratio approaches a constant value downstream of region (ii), indicating that both the mean and turbulent fields scale with the surface velocity. It is further observed that the turbulent momentum flux, M', scales directly with the jet momentum, $\mathbf{J}$ (see Fig. 8). These two results support the hypothesis that the turbulence energy balance also scales with the ΔU_s and δ. It thus follows that the difference of the turbulence production and dissipation rates must scale with, $(\Delta U_s)^3/\delta$, which is a sufficient condition for the jet to be truly self-preserving.

For a small initial wake and constant ambient stream velocity, U_a, the momentum flux defined as

$$J = \int_0^\infty (\Delta U)^2 dy + U_a \int_0^\infty \Delta U dy \qquad (1)$$

is expected to remain constant along the jet (see Eq. (5) for $dU_a/dx = 0$). The longitudinal variations of $\mathbf{J}$ as determined from the experimental data is shown in Fig. 9. For the case of the thin plate (small wake), there is a net momentum gain which approaches 1.2 $\mathbf{J_o}$, where $\mathbf{J_o}$ is the initial jet momentum at the plate end. These results are consistent with those of Hussain and Clark (1977) and Ramaprian and Chandrasekhara (1985) who attribute the momentum increase and entrainment of surrounding fluid to the presence of a negative pressure gradient inside the jet. For the thicker plate, the momentum deficit of the resulting larger wake clearly affects the momentum flux further downstream, which is less than for the thinner wake. The reduction of the momentum flux may explain why the linear growth region for the 10 mm plate is shorter than for the 1 mm plate.

The slower growth of the jets with larger wakes in the far field region is not expected to result from bottom effects. Swean et al. (1984) investigated the behavior of a two-dimensional turbulent surface-jet in a channel of limited depth. Jet confinement was observed to decrease the growth rate of the length scale and increase the decay rate of the velocity scale. Similarity of the mean velocity-profile was still observed. Jet momentum appeared to have been lost due to momentum exchange with the return flow underneath the issuing surface-jet. In the present study, it is noted that the velocity decay (Fig. 4) is not affected by the initial wake and that, although $\mathbf{J}$ is less than for the thin plate, the momentum is essentially conserved. Furthermore, the jet width, δ, is actually smaller than for the thin plate case in the far field.

As noted in Fig. 3(a), for the case of the thin plate, the growth rate of δ increases as U_a' decreases. This behavior is observed as a slightly earlier on-set of the linear region. The turbulence level is higher for smaller values of U_a' (see Fig. 6), which is consistent with the a more rapid spreading of the jet since the higher turbulence levels imply stronger mixing. The increase in turbulence levels is a result of a higher local production rate. For the jet flow, the main contribution to the turbulence production term is the shear rate. A decline of U_a' corresponds, by definition, to higher initial shearing and thus increased turbulence.

For the thicker plate, the wake near the exit dominates the development of the jet. In region (i), the presence of the strong recirculation zone tends to increase the local turbulence levels (see Fig. 6). As a consequence, the initial mixing and spreading of the jet is greater for the thick plate as is seen in Fig. 3(c, d). On the other hand, the wake effectively separates the jet and ambient current streams so that the growth of the jet is not sensitive to U_a' as can be seen in Fig. 3(b).

The properties of the regions described above relate to the wake produced behind the plate at the jet exit. For the large wake (thicker plate), the initial development region is shorter, the decay of turbulence faster (see Fig. 6) and the slope of the velocity distribution in the terminal region smaller (i.e., the profiles are flatter) than for the thin plate. In comparison, for the small wake (thin plate) the velocity distribution maintains a nearly Gaussian character for longer distances (see Fig. 2(a) and 2(c)), further supporting the argument that the development of the self-similar region is related to the dominant scales of turbulence, which are directly related to the rate at which the turbulence energy is dissipated.

4 Integral Analysis

The time-averaged two-dimensional continuity and momentum equations governing the development of a turbulent jet in a coflowing stream reduce to (Townsend, 1966):

$$\frac{\partial U}{\partial x} + \frac{\partial V}{\partial y} = 0 \tag{2}$$

$$U\frac{\partial U}{\partial x} + V\frac{\partial U}{\partial y} = -\frac{\partial}{\partial x}(\overline{u^2} - \overline{v^2}) - \frac{\partial}{\partial y}\overline{uv} \tag{3}$$

where $U(x, y) = U_a(x) + \Delta U(x, y)$ is the mean velocity in the x-direction, $V(x, y)$ the mean velocity in the y-direction, and u, v are instantaneous turbulent fluctuations of U and V, respectively. The overbar designates a time-averaged quantity. It is assumed that the ambient stream velocity U_a is only a function of x. Integrating Eqs. (2) and (3) in the direction y, we obtain:

$$\frac{d}{dx}\left(\int_0^\infty \Delta U^2 dy + U_a\int_0^\infty \Delta U dy + \int_0^\infty (\overline{u^2} - \overline{v^2})dy\right) = -\frac{dU_a}{dx}\int_0^\infty \Delta U dy \tag{4}$$

Since the turbulent fluxes in Eq. (4) are one order of magnitude smaller than the mean fluxes, the integral equation governing the development of the surface-jet in a current can be approximated by

$$\frac{dJ}{dx} = \frac{d}{dx}(M + U_a Q) = -Q\frac{dU_a}{dx} \tag{5}$$

where $M = \int \Delta U^2 dy$ and $Q = \int \Delta U dy$ are the excess momentum and volume fluxes, respectively. Equation (5) relates the change in momentum of the jet to the gradient of the stream velocity outside the jet. According to Eq. (5), a positive gradient dU_a/dx is expected to decrease the momentum flux, J, while a negative gradient is likely to increase J. The streamwise variation of J, for the jets with thin and thick plates at the exit is shown in Fig. 9. These results indicate a gain of momentum of about 20 percent between $x/h_o = 20$ and 60 for the case of the thin plate. This finding is consistent with the decrease of ambient current speed measured along the jet. The observed increase in momentum flux is also in agreement with Schneider (1985) who argued that the momentum of the entrained fluid from the coflowing ambient stream is off-setting the momentum loss observed in jets in stagnant surroundings. For the thick plate, however, the jet is gradually loosing momentum due to the presence of a stronger initial wake which appears to be extracting momentum from the jet flow.

For a self-similar solution of the form:

$$U(x, y) = U_a + \Delta U_s f\left(\frac{y}{\delta(x)}\right) \tag{6}$$

one obtains that Q and M relate to the local scales ΔU_s and δ according to:

$$Q = I_u \Delta U_s \delta;\ M = I_{uu}\Delta U_s^2\,\delta \tag{7}$$

in which $I_u = \int f d\eta$ and $I_{uu} = \int f^2 d\eta$ are constant shape parameters, and $\eta = y/\delta$. The entire system of equations is closed by invoking the entrainment hypothesis by Morton et al. (1956):

$$\frac{d}{dx}(Q + U_a h) = \alpha_j \Delta U_s \tag{8}$$

which quantifies the mass transfer of ambient fluid into the jet. The entrainment coefficient, α_j, may generally vary with the speed and turbulence of the co-flowing stream and may also be affected by the wake near the exit. The average depth of the jet boundary, as determined from flow visualization studies, was $h = 2.2\delta$.

In this study the entrainment coefficient, α_j, as defined in Eq. (8), was typically 0.035. The data suggested, however, that α_j increases with U_a' for both thick and thin plates. The effect of the initial wake was also found to reduce the magnitude of the entrainment coefficient. This finding is probably due to the observed loss of momentum and the more rapid decay in the turbulence fluctuations.

Numerical predictions obtained with the assumptions that J = constant and $\alpha_j = 0.035$ are compared with the experimental data in Fig. 3(*a*) and Fig. 4(*a*). Agreement for the thin plate is only satisfactory in the near field, suggesting a need for more advanced models which consider the longitudinal variations of both J and α_j.

5 Concluding Remarks

The effect of a wake near the exit on the turbulence structure and entrainment characteristics of a plane surface-jet in a weak coflowing stream was investigated. The measurements showed an increase in turbulence intensity in the wake region and entrainment was enhanced in the recirculation region. Further downstream, the effect of the wake was to reduce both the jet excess momentum and entrainment of ambient fluid. It is also observed that the growth rate of the jet decreases and becomes less dependent on the ambient current as the wake size increases. Unlike the wall jet (Irwin, 1973), the surface-jet in a weak coflowing stream exhibited a self-preserving character without imposing a controlled pressure gradient.

Acknowledgments

This work was supported with grants from the Natural Sciences and Engineering Research Council of Canada. The authors would like to thank an anonymous reviewer for comments and guidance related to the velocity bias estimations and corrections.

References

Abernathy, R. B., Benedict, R. P., and Dowdell, R. B., 1985, "ASME Measurement Uncertainty," ASME JOURNAL OF FLUIDS ENGINEERING, Vol. 107, pp. 161–164.

Anthony, D. G., and Willmarth, W. W., 1992, "Turbulence Measurements in a Round Jet Beneath a Free Surface," *Journal of Fluid Mechanics*, Vol. 243, pp. 699–720.

Anwar, H. O., and Weller, J. A., 1969, "A Thin Rectangular Jet Discharging into a Slow-Moving Stream," *Water Power*, pp. 214–219.

Bradbury, J. L. S., 1965, "The structure of a self-preserving turbulent plane jet," *Journal of Fluid Mechanics*, Vol. 23, p. 31–34.

Bradbury, J. L. S., and Riley, J., 1967, "The Spreading of a Turbulent Plane Jet Issuing into a Parallel Moving Airstream," *Journal of Fluid Mechanics*, Vol. 27, pp. 381–394.

Chu, V. H., and Baddour, R. E., 1984, "Turbulent Gravity Stratified Shear Flows," *Journal of Fluid Mechanics*, Vol. 138, p. 353–370.

Chu, V. H., and Vanvari, M. R., 1976, "Experimental Study of Turbulent Stratified Flows," *Journal of Hydraulic Engineering*, ASCE, Vol. 102, p. 691–706.

Cimbala, J. M., and Park, W. J., 1990, "An Experimental Investigation of the Turbulent Structure in a Two-Dimensional Momentumless Wake," *Journal of Fluid Mechanics*, Vol. 213, p. 479–509.

Doeblin, O. E., 1975, *Measurements Systems, Application and Design*, McGraw-Hill, New York.

Edwards, R. V., 1987, "Report of the Special Panel on Statistical Particle Bias Problems in Laser Anemometry," ASME JOURNAL OF FLUIDS ENGINEERING, Vol. 109, pp. 89–93.

Irwin, H. P. A. H., 1973, "Measurements in a Self-Preserving Plane Wall Jet in a Positive Pressure Gradient," *Journal of Fluid Mechanics*, Vol. 61, pp. 33–63.

Kotsovinos, N. E., 1978, "A Note on the Conservation of the Axial Momentum of a Turbulent Jet," *Journal of Fluid Mechanics*, Vol. 87, p. 55–63.

Madnia, C. K., and Bernal, L. P., 1994, "Interaction of a Turbulent Round Jet with the Free Surface," *Journal of Fluid Mechanics*, Vol. pp. 305–332.

Morton, B. R., Taylor, G. I., and Turner, J. S., 1956, "Turbulent Gravitational Convection From Maintained and Instantaneous Sources," *Proceedings of the Royal Society of London*, Vol. A235, pp. 1–23.

Rajaratnam, N., and Humphries, J. A., 1984, "Turbulent Non-Buoyant Surface Jets," *Journal of Hydraulic Research,* IAHR, Vol. 22, pp. 103–114.

Ramaprian, B. R., and Chandrasekhara, M. S., 1985, "LDA Measurement in Plane Turbulent Jets," ASME JOURNAL OF FLUIDS ENGINEERING, Vol. 107, pp. 264–271.

Schlichting, H., 1979, *Boundary Layer Theory,* McGraw-Hill, New York.

Schneider, W., 1985, "Decay of Momentum Flux in Submerged Jet," *Journal of Fluid Mechanics,* Vol. 154, pp. 91–110.

Schwarz, W. H., and Cosart, W. P., 1961, "The Two-Dimensional Turbulent Wall-Jet," *Journal of Fluid Mechanics,* Vol. 10, pp. 481–495.

Sherman, F. S., 1990, *Viscous Flow,* McGraw-Hill, New York.

Swean, T. F., Ramberg, S. E., Plesniak, M. W., and Stewart, M. B., 1989, "Turbulent Surface Jet in Channel of Limited Depth," *Journal of Hydraulic Engineering,* ASCE, Vol. 115, pp. 1587–1606.

Townsend, A. A., 1976, *The Structure of Turbulent Shear Flows,* Cambridge University Press.

Zaghloul, A. M., Martinuzzi, R., and Baddour, R. E., 1995, "Turbulence Structure of Plane Surface Jet in a Current," *Proceedings, 10th Engineering Mechanics Conference,* ASCE, Boulder, CO, pp. 1006–1009.

Zaghloul, A. M., 1996, "Turbulence Structure of Plane Surface Jet in a Current," Ph.D dissertation, The University of Western Ontario, London, Ontario, Canada.

ERRATA

"Experimental Measurement in a Centrifugal Pump Impeller," A. C. Bwalya and M. W. Johnson, published in the *Journal of Fluids Engineering,* Vol. 118, pp. 692–697.

In a discussion on the above paper by Dr. Y. N. Chen, published in the September 1997 issue of the *Journal of Fluids Engineering,* Vol. 119, p. 729, Fig. 23 was omitted from the discussion. The figure appears below.

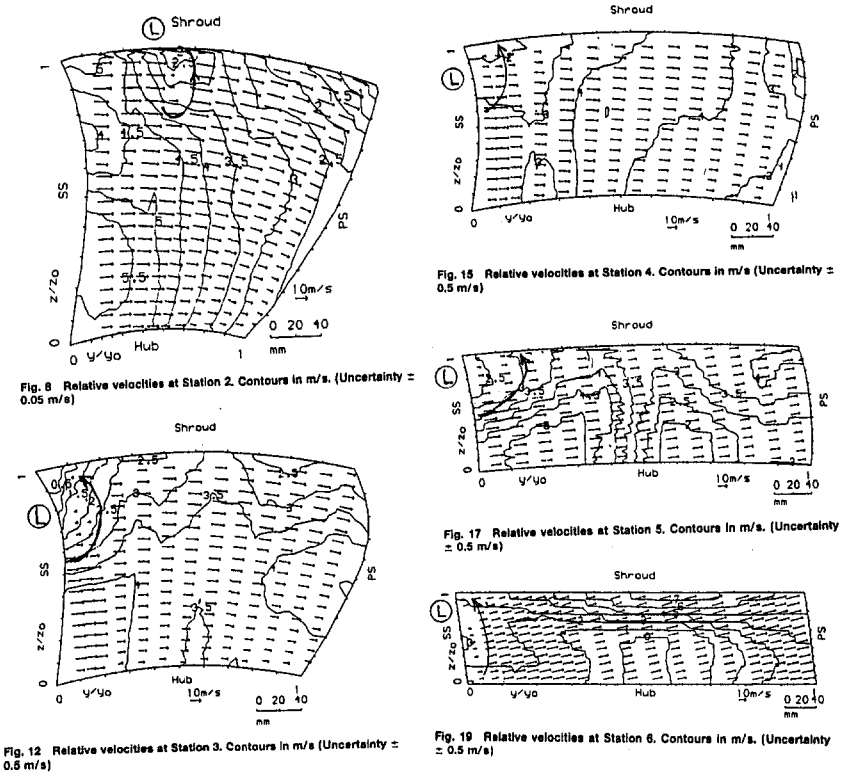

Fig. 8 Relative velocities at Station 2. Contours in m/s. (Uncertainty ± 0.05 m/s)

Fig. 15 Relative velocities at Station 4. Contours in m/s (Uncertainty ± 0.5 m/s)

Fig. 17 Relative velocities at Station 5. Contours in m/s. (Uncertainty ± 0.5 m/s)

Fig. 12 Relative velocities at Station 3. Contours in m/s (Uncertainty ± 0.5 m/s)

Fig. 19 Relative velocities at Station 6. Contours in m/s. (Uncertainty ± 0.5 m/s)

Fig. 23

B. Majumdar
Senior Lecturer.

Ratan Mohan
Assistant Professor.

S. N. Singh
Professor.

D. P. Agrawal
Professor.

Departments of Applied Mechanics and Mechanical Engineering,
Indian Institute of Technology, Delhi,
New Delhi—110 016, India

Experimental Study of Flow in a High Aspect Ratio 90 Deg Curved Diffuser

Measurements for developing turbulent flow in a high aspect ratio ($AS = 6$), small area ratio ($AR = 2$), 90 deg curved diffuser have been made. Mean velocities, static and total pressures, and turbulence intensities were measured using a three-hole pressure probe and a hot-wire probe. Flow visualization studies were also made using a tuft probe. Experiments show that, except for a very small zone near the exit, there is no flow reversal in any part of the diffuser. Streamwise bulk flow is seen to shift toward the concave wall side in the downstream half of the diffuser, under the influence of centrifugal force. One pair of counter-rotating vortical motion was identified at 30 deg turn, which break into more pairs (at least two) of counter-rotating vortices in the downstream. The z-plane velocity profiles show a nearly 2-D flow in the initial part of the diffuser but subsequently the flow becomes increasingly 3-D. A static pressure recovery coefficient of 51 percent was achieved.

Introduction

Diffusers are encountered in various engineering applications such as aircraft intakes, turbomachinery passages, diffusing bends of piping systems, etc. Often the flow passage is curved, giving rise to secondary flows and three-dimensional effects. The objectives in diffuser design are the determination of pressure recovery, losses, and uniformity of flow at exit. While these performance characteristics can be obtained directly from experiments (e.g., the early experimental work of Fox and Kline (1962) and Sagi and Johnston (1967) on curved diffusers), in recent years there is an impetus to determine these computationally, particularly because of the great enhancement in computer capabilities. A reliable flow prediction code gives much more facility in studying alternative designs. However, in the development/validation stage of a code detailed flow data is required. Recent experimental studies have therefore tended to focus on the single diffuser to obtain high-quality data and establish the flow structure in the curved diffuser. Here it may be added that data on curved ducts is equally useful, as the flow there has generic similarity to that in a curved diffuser.

Detailed measurements of the streamwise and secondary velocities, wall static pressures, and turbulence intensities for low speed turbulent flow in a 40 deg turn C-diffuser of $AS = 1.5$, $AR = 1.5$, and $L/W_1 = 3$ have been made by McMillan (1982). Rojas et al. (1983a) used Laser Doppler Anemometry (LDA) for measurement of flow variables in laminar and turbulent flows in S-shaped and C-shaped diffusers ($AR = 1.5$, $\Delta\beta = 45$ deg). The three components of velocity, wall pressure distribution and, in the turbulent case, the $u'v'$ cross-correlation were measured. The experimental pressure recoveries in the diffusers were also measured. For curved ducts, Humphrey et al. (1981) have made detailed measurements of the longitudinal and radial components of the mean velocity, turbulence intensities, and components of the Reynolds stress tensor for turbulent flow ($\mathrm{Re} = 40{,}000$) in a square-sectioned ($AS = 1$) 90 deg turn duct using LDA. Taylor et al. (1982) have also made similar measurements for 3-D developing laminar and turbulent flow in a 90 deg curved duct, again of $AS = 1$. Chang et al. (1983) measured streamwise and radial velocities in a square sectioned duct, but of 180 deg turn. Flow in ducts of rectangular cross sections with a high aspect ratio, however, have not been studied very much. Recently, Kim and Patel (1994) made extensive measurements of the mean velocity and Reynolds stress components in developing turbulent flow in a 90 deg turn curved duct of $AS = 6$ using five hole pressure probe and hot wire anemometry.

One of the main features of flow in curved channels is the presence of centrifugal force (because of curvature) which gives rise to the radial pressure gradient and consequently pressure-driven secondary motion. Curvature also affects turbulence structure (i.e., the Reynolds stresses) and hence the stress-driven secondary flows. However, the latter are usually much smaller and may not be observable, unless the masking effect of the pressure driven secondary flows is somehow isolated. The use of a high aspect ratio for the channel is relevant in this context, as the effect of the pressure driven secondary flows may be confined to the top and bottom walls and a nearly 2-D flow obtained in the central region. The 2-D profiles would be more useful for studying the effect of curvature on turbulence and its modeling. Earlier attempts to study the effect of curvature on two-dimensional turbulent boundary layers have been made by Smits et al. (1979), Gillis and Johnston (1983), Hoffman et al. (1985), and Muck et al. (1985). However, detailed measurements clearly establishing the extent of 2-D flow in a high aspect ratio ($AS = 6$) curved duct have been made only recently by Kim and Patel (1994). They obtained an essentially 2-D flow in the mid 70 percent of the duct. In the present study also we have aimed to achieve a predominantly 2-D flow in the center plane region of a curved diffuser. Coincidentally (since the diffuser was fabricated two years ago), an inlet aspect ratio of 6 has been used in this work too. It was decided to study a diffuser because there are generally fewer studies on diffusers and those studied (McMillan, 1982; Rojas et al., 1983) employed much smaller inlet aspect ratios ($AS = 1, 1.5$). A 90 deg turn was chosen to observe the flow development over a reasonably strong and prolonged curvature. Finally, a low area ratio ($AR = 2$) was taken to have separation-free flow, otherwise accurate flow measurement becomes difficult. In the measurements, a three hole pressure probe was used for the mean velocities and static and total pressures and a hot wire anemometer for the turbulence intensities.

Apparatus and Experimental Procedure

An outline of the experimental setup along with the geometrical details, is shown in Fig. 1(a). The setup consists of a

Contributed by the Fluids Engineering Division for publication in the JOURNAL OF FLUIDS ENGINEERING. Manuscript received by the Fluids Engineering Division July 25, 1994; revised manuscript received October 15, 1997. Associate Technical Editor: D. E. Stock.

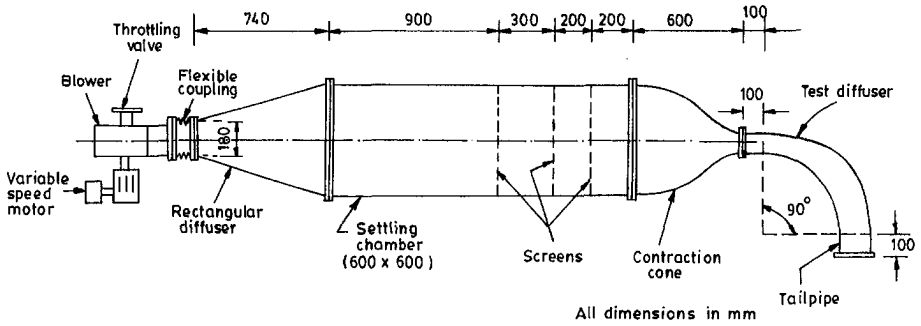

Fig. 1(*a*) Experimental setup

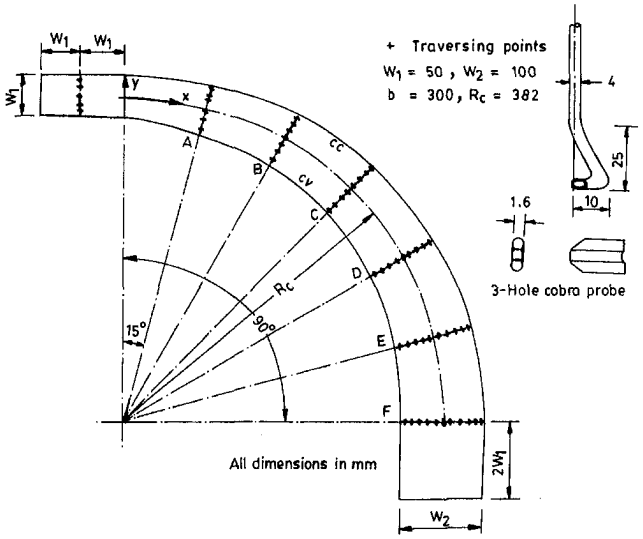

Fig. 1(*b*) Test section details

single stage centrifugal blower, a rectangular diffuser, settling chamber, contraction cone, and the test diffuser. The details of the test diffuser and location of the measuring sections are shown in a plan view in Fig. 1(*b*), which also shows the arrangement of the curvilinear coordinate system. The x-axis is in the longitudinal direction, i.e., along the diffuser centerline and the y-axis is perpendicular to it i.e., the transverse direction. The test diffuser ($AR = 2.0$, $\Delta\beta = 90$ deg) with circular centerline of length 0.6 m was designed based on the method of Fox and Kline (1962). The inlet width is 0.05 m and the inlet height 0.3 m, giving an aspect ratio of 6. The mean radius of curvature of the diffuser, R_c, is 0.382 m. The radius ratio, R_c/D_h, is thus 4.5. The four walls of the diffuser were made of transparent "Plexiglas" to facilitate flow visualization studies. Wall static pressure taps with 0.003 m O.D. are provided at equal intervals on both the curved walls as well as on the bottom wall. Constant area straight channels of 0.10 m length are attached at the inlet and exit of the diffuser to get well-defined flow at the inlet and outlet.

Experiments were carried out with air as the test fluid. The inlet average free-stream velocity was maintained at approximately 40 m/s. For the present diffuser geometry, this corresponds to a Reynolds number, Re, of 2.2×10^5 (based on the diffuser inlet hydraulic diameter), a Dean number, De, of 73700, and an inlet dynamic pressure of 926.4 Nm^{-2}.

The following types of measurements, along with the flow visualization studies with a tuft probe, have been taken in the present investigation: (i) wall static pressure on the diffuser walls, (ii) mean velocity and static and total pressure profiles at the inlet section, and (iii) detailed survey of the mean velocity, static and total pressures of the entire cross-section at six streamwise sections at 15 deg intervals (Fig. 1(*b*)). As seen in Fig. 1(*b*), the 7 Sections I, A, B, C, D, E, and F have 5, 6, 7, 8, 9, 10, and 11 traversing locations, respectively. The transverse position of these locations are implicit in Fig. 2 at the plotted points, where r^* gives the distance from the convex wall normalized by the width of the section. At each traversing location the number of reading stations in the z-(vertical)-direc-

Nomenclature

a, W_1 = width of the diffuser at inlet
AR = area ratio (W_2/W_1)
AS = aspect ratio (b/W_1)
b = depth of the diffuser
C_{pr} = coefficient of static pressure recovery
cc = concave
cv = convex
De = Dean's number
D_h = hydraulic diameter [$2ab/(a + b)$]
l = distance from the diffuser inlet (along the centerline)
L = centerline length of the diffuser
p_s = wall static pressure
r^* = radial distance from the convex wall at a given section, normalized by the width of the section
R_c = mean radius of curvature
Re = Reynolds number ($\rho UD_h/\mu$)
U_{avi} = average inlet velocity
U = mean streamwise velocity
W_2 = width of the diffuser at exit
$\Delta\beta$ = angle of turn
ξ = coefficient of total pressure loss

Table 1 Uncertainties in the experimental variables

Experimental variable	Estimated uncertainty: Low velocity range (<3 m/s)	Estimated uncertainty: High velocity range (>3 m/s)
Mean velocity (U)	±15%	±2%
Static/total pressure	±2%	±0.2%
Dynamic pressure	±2%	±0.2%
Flow angle	±0.5°	±0.5°
C_{Pr}	±3.5%	±0.2%
u_{rms}	±25%	±5%

tion were fixed at 35. The number of traverse locations and the vertical stations at a given section were decided keeping in mind the dimensions of the probe and the diffuser width at the section. No measurements were possible within 15 mm of the top surface of the diffuser because of the nature of the probe construction. However, the bottom wall could be reached to within a distance of 0.8 mm.

All measurements were made with the help of a calibrated 3-hole cobra probe in null mode. The probe could be rotated and aligned to the direction of flow within an accuracy of ±0.5 deg. In null mode, the central tube reads the total pressure and then static pressure can be evaluated from the calibration graph. The blockage effect due to the probe at the measuring points is minimized by the cobra shape of the probe itself (Fig. 1(b)). The pressures sensed by the 3-hole probe were read on a Betz optical micromanometer having a least count of ±0.1 mm of water column. Turbulence intensity was measured using a normal hot wire probe by aligning the probe direction to the mean flow at any given point, making use of the flow angle obtained from the three hole probe. The output from the hot wire anemometer was in volts and the least count was 0.1 mV for RMS voltage.

The uncertainties in the measured flow variables were estimated following the guidelines of Kline and McClintock (1953). The primary measurands are only the height of the water column and the angle. Since only single sample measurements were made, the least count value was assigned to the precision limit. The bias limit was set to zero, as there were no systemetic errors due to calibration or instrument zero errors. The uncertainties in the resultant variables, i.e., the mean velocity, pressure, etc., were evaluated from the procedure given in the above guideline and are presented in Table 1.

It may be observed in Table 1 that the uncertainty levels for U and C_{pr} in the low velocity range are somewhat high. However, less than 3 m/s conditions exist in only a very small fraction of the diffuser space (near the walls).

Results and Discussion

Flow Visualization. Flow visualization observations revealed only a very small pocket of separation on the convex wall, just near the diffuser exit. Otherwise, the flow in the diffuser is seen to be separation free. Secondary flows were also observed, particularly in the downstream region of the diffuser (approximately 45 deg onwards). Also, flow in the top half of the diffuser is seen to be relatively more unsteady.

Mean Velocity. The flow pattern in the diffuser, characterized by the velocity distribution, is presented in Figs. 2–5. With reference to these figures, the details of the flow development in the present diffuser are discussed in the following.

First, the straight channel between the contraction cone and the diffuser is quite short ($2W_1$). The flow at the diffuser entry is therefore still developing and the boundary layers are thin. Thin boundary layers on the curved walls lead to potential-flow-like situation in which the flow is seen to accelerate on the convex wall side, to balance the slower flow on the concave wall side as a result of higher pressure (due to centrifugal forces) there. The migration of the flow to the convex wall side is clearly seen from the velocity profile at Section A, Fig. 2. There appears to be some effect even upstream on the inlet velocity profile (Section I). Although an outward movement of the peak is seen, the bulk flow stays nearer to the convex wall almost until Section D. Ultimately the bulk flow also shifts to the concave wall side.

Next, the velocity profiles in the vertical plane are shown in Fig. 3. These profiles give an indication of the extent of two-dimensionality of the flow. Excluding the top and bottom wall regions, the flow may be regarded two-dimensional in the middle 70 percent of the diffuser only upto the 15 deg turn (Section A) at best. At 30 deg turn (Section B), the traverse location closest to the convex wall shows significant departure from uniformity so that 2-D flow can no longer be claimed. The distortion of profiles on the convex wall side increases progressively as can be seen for Sections C–F. At Section F the two negative values in the first profile mark the reverse flow zone on the convex wall. These velocity values were measured by turning the probe backwards, as the probe had flexibility of rotation by 360 deg. While more discussion on velocity redistribution follows, Fig. 3 clearly establishes that not much of the flow in the present diffuser is two-dimensional, somewhat disappointing to the starting objective. Since Kim and Patel (1994) did obtain an essentially 2-D flow in the mid 70 percent of their duct, one is led to conclude that the aspect ratio should have remained at least 6 at the exit of the present diffuser too, i.e., an inlet aspect ratio of about 12 should have been employed.

The normalized (by the inlet average velocity) longitudinal and transverse velocity contours in Figs. 4 and 5 also present the development of flow in the diffuser. As measurements have not been made near the top wall of the diffuser, a mirror image of the bottom wall values has been used in drawing the contours. The movement of bulk flow along the convex wall for almost up to Section D (noted earlier with respect to Fig. 2, Sections A–D), can be seen again in Fig. 4(a–d) for most of the height of the diffuser. Basically, there are several competing mechanisms which affect flow redistribution in the diffuser, namely,— potential-like flow, asymmetric-area expansion driven flow, pressure-driven secondary flow, stress-driven secondary flow, and growing boundary layers. At a given location in the diffuser, one or more of these may dominate, complement or counter each other to give the resultant flow. Figure 5 presents the transverse velocity contours and is useful for observing the secondary motions. It may be seen from this figure that the overall strength of the secondary flows is not large, the maximum in the diffuser being about 6 percent of the mean inlet velocity. Generally, higher transverse velocity maxima have

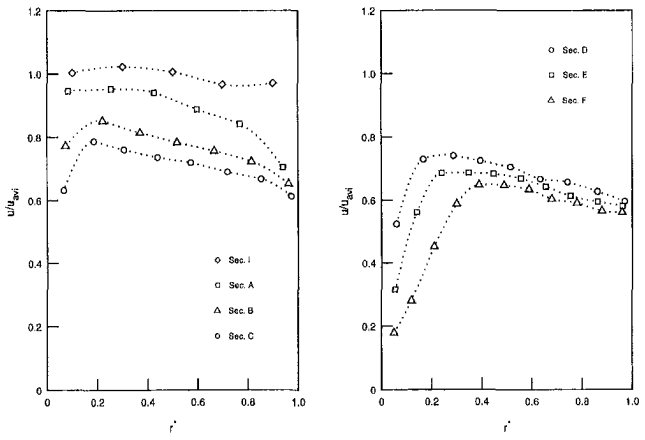

Fig. 2 Mid-plane streamwise velocity profiles (r^* = 0, convex wall; r^* = 1, concave wall)

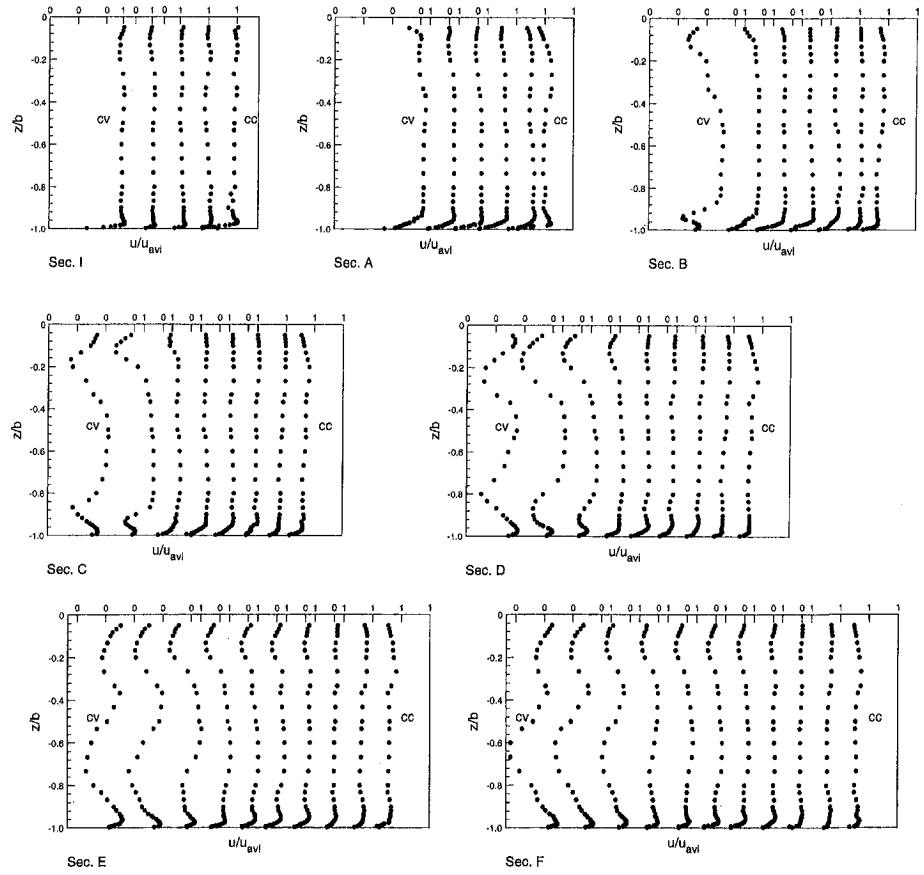

Fig. 3 Velocity profiles in the vertical plane

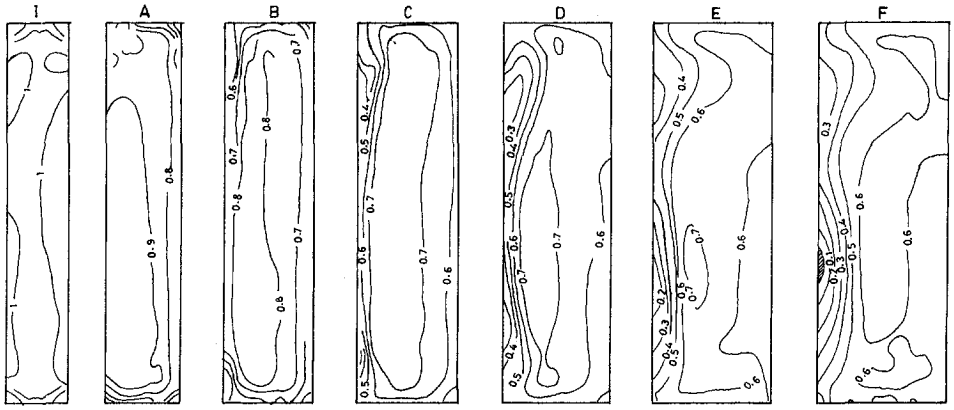

Fig. 4 Longitudinal velocity contours at Sections I–F (left edge = convex wall, right edge = concave wall)

been reported in literature, about 15–30 percent of the mean inlet velocity (Humphrey et al., 1981; Taylor et al., 1982; McMillan, 1982; Rojas et al., 1983b). A major reason for this is the low inlet aspect ratio of these ducts/diffusers—1, 1, 1.5, and 1, respectively, compared to 6 in the present case. Also, with the exception of Rojas et al. (1983b), the radius ratios in the above studies are smaller (i.e., stronger curvature) at 2.3, 2.3, and 3.6 as against 4.5 in ours; Rojas et al. used 7.0.

Coming to specific sections, at Section A the pressure-driven secondary flow is still not large enough and the potential-like flow and the asymmetric area expansion cause the movement of the fluid towards the convex wall. This may be seen as the heavy arrows directed to the convex wall in Fig. 5(*a*). However, in this figure, as well as to a larger extent in Fig. 5(*b* and *c*), flow movement to concave wall is also seen as a result of the pressure-driven secondary flows gaining in strength. Pressure-driven secondary flows are set up in curved channels because of an imbalance between the centrifugal force and the radial pressure gradient. Fluid from the concave wall is transported to the convex wall along the top and bottom walls and, to maintain continuity, a corresponding amount of fluid moves in the reverse direction in the region away from the top and bottom walls. Thus "longitudinal" vortices are generated at the top and bottom walls, that may grow in size, give rise to more vortices and may completely engulf the cross section in the downstream region of the channel. The pressure-driven secondary flows are an order of magnitude larger than the stress-driven secondary flows and completely mask the velocity variations due to the latter.

The vortices can be seen in Fig. 5 although, probably because of some disturbance at the inlet, the cross-flow development

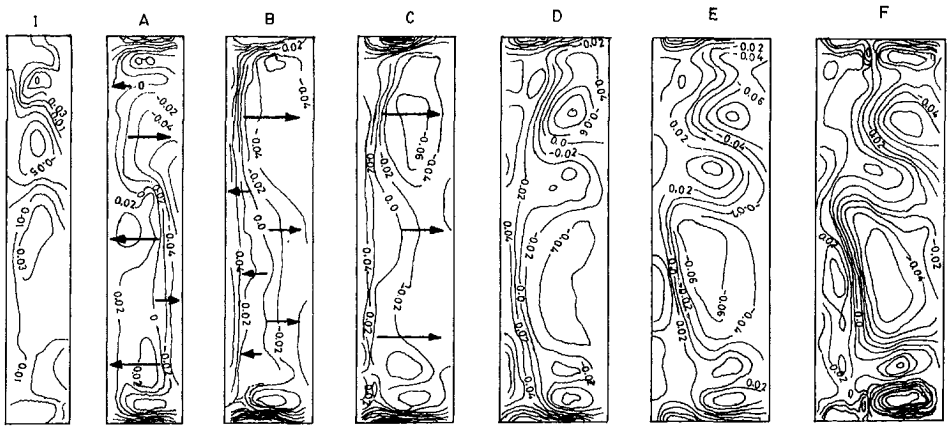

Fig. 5 Transverse velocity contours at Sections I–F (left edge = convex wall, right edge = concave wall)

has not occurred in a well-defined, symmetrical way. By the time flow reaches the exit, several irregular shaped vortices are in evidence in Fig. 5(*e* and *f*). Vortical motion has, of course, been observed in earlier experiments also (McMillan, 1982; Taylor et al., 1982; Rojas et al., 1983b; Hille et al., 1985) and have also been predicted from numerical calculations (Ghia et al., 1987; Hur et al., 1990). Hur et al. have shown the increase in the number of vortices in pairs, 2, 4, 6, etc., as the aspect ratio of the channel is increased. In the experimental observations of McMillan, the apparent centroids of the secondary motions move toward the convex wall as flow goes downstream and the intensity also increases. As more and more low momentum fluid accumulates near the convex wall, it helps to thicken the boundary layer on this wall and to shift the bulk fluid flow to the concave wall, occupying approximately 70–75 percent of the outlet area of the diffuser, as can be seen in Fig. 2(*f*) and 4(*f*). A very small separation pocket (thatched area in Fig. 4(*f*)), on the convex wall at the exit of the diffuser is also observed.

Although the movements of the vortices and their centroids have not come out very clearly from either Figs. 4 or 5, the wall pressure distributions shown in Fig. 6 clearly demonstrate the movement of flow along the walls. The pressure distribution on the concave wall (Fig. 6(*a*)) at any section up to 45 deg turn shows the pressure to be higher in the center and lower toward the parallel walls, highlighting the flow movement from the center toward the parallel walls along the concave wall. For the same section the pressure distribution on the convex wall (Fig. 6(*b*)) shows movement of flow in the reverse direction, i.e., from the parallel walls to the center. The movement of flow on the bottom wall is seen to be from the concave to convex wall (Fig. 6(*c*)), and hence the flow in the middle has to be from the convex to concave wall which is very clearly observed. From the preceding discussion it is clear that one pair of vortical motion does exist up to 45 deg turn, which form two or more pairs further downstream depending on the extent of turn. This observation is fully supported by the wall pressure distribution.

The magnitude of the average velocity at different sections decreases in proportion to the area expansion but is higher than the theoretical value by about 4–5 percent. However, at the diffuser exit the discrepancy is much more, $0.58U_{avi}$ as compared to the theoretical value of $0.5U_{avi}$. The reason for this could be the presence of the small separation pocket at the exit section, with subsequent errors in the evaluation of the section average velocity. Such lack of satisfaction of the continuity equation observed experimentally has also been reported by Rojas et al. (1983b) in their investigations of flow in S-shaped diffusers.

Pressure Recovery. The variation of average static pressure recovery and total pressure loss along the length of the diffuser is shown in Fig. 7. It shows the exit pressure recovery to be about 51 percent while the total pressure loss is 15.8 percent. For a comparison, Sagi and Johnston's (1967) measured C_{pr} value in a 90 deg curved diffuser of $AR = 2$ and $L/W_1 = 10$ is 45% for a circular-arc design. Extrapolation of their curve to $L/W_1 = 12$ (which is the length of our diffuser) would give a slightly higher C_{pr} value of about 48 percent. The wall pressure distribution (Fig. 6) also depicts a pressure recovery close to 50% which is in good agreement with the overall pressure recovery.

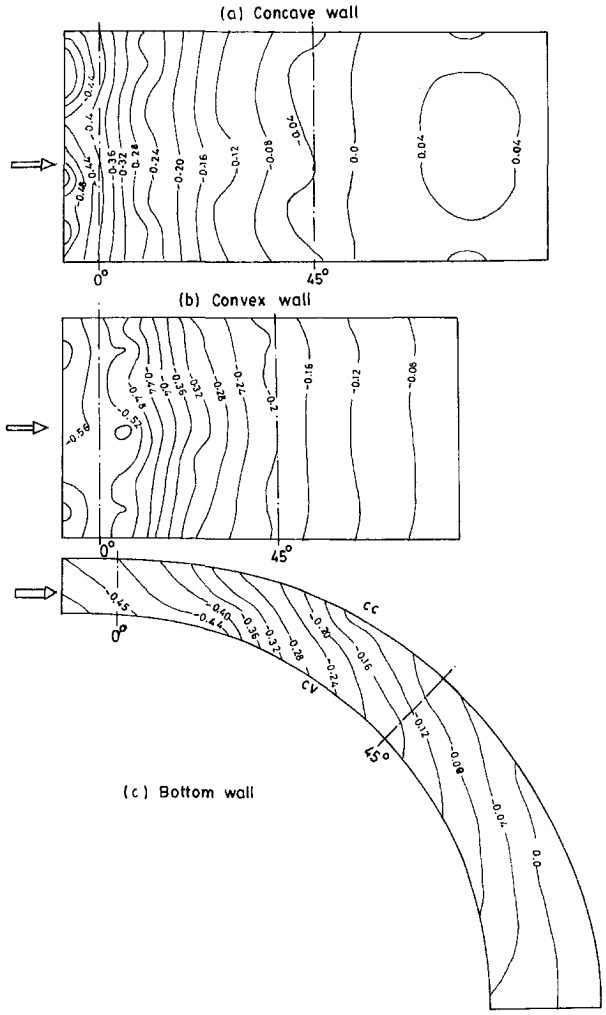

Fig. 6 Wall static pressure contours

Turbulence Intensity. The results of turbulence intensity measurements are shown in Fig. 8, Sections I–F. The normalized turbulence intensity, u_{rms}/u_{avi}, has been plotted at 5 or 6 transverse locations for each section. At the inlet Section I, a uniform turbulence intensity of 3–4 percent is observed all across, except near the bottom wall where it is higher at 12–13 percent. Though not measured, it would be similarly high at the top wall.

At 15 deg turn (Section A), the profiles show an increase in the turbulence intensities along the curved walls, going up to 13 percent near the concave wall and up to 10 percent near the convex wall. The increase in turbulence intensities along the four walls is expected due to the growth of the boundary layer shear layer. The intensity of shear layer is greater close to the concave wall as flow tries to retain its flow direction and hence a higher turbulence intensity is seen there. As the flow moves down (Section B–C), the distortion of the turbulence intensity profiles close to the concave wall reduces somewhat (maximum value 7 percent in Section C) due to the bulk movement of the flow toward this wall and self-imposed favorable pressure gradient by the flow as it does not follow the geometrical turn. On the other hand, an increase in intensity along the convex wall and in the central region can be seen. This is because of flow development against the adverse pressure gradient along the convex wall and hence the higher shear levels. Figure 8(d–f) show a further increase in turbulence intensity along the convex wall, as high as 16 percent at Section D.

The higher turbulence intensity levels near the convex wall and the central region at the downstream sections only serves to reaffirm the existence of more disturbed flow in this part of the diffuser, as already observed from the velocity profile results. By contrast, the flow along the concave wall has stabilized somewhat near the exit.

Conclusions

Detailed flow velocity, pressure, and turbulence intensity measurements have been made in a 90 deg turn curved diffuser of inlet aspect ratio 6 and area ratio 2. The following specific features are observed:

(i) No separation is observed in the diffuser except for a very small pocket of separation on the convex wall just at the exit of the diffuser.

(ii) The wall static pressure increases continuously on both the convex and concave walls as a result of diffusion.

(iii) Secondary flows observed are not very strong (maximum 6 percent of the inlet mean velocity). Counter-rotating vortices are observed from 30 deg turn of the diffuser.

(iv) The pressure recovery and total pressure loss coefficients are 51 and 15.8 percent, respectively.

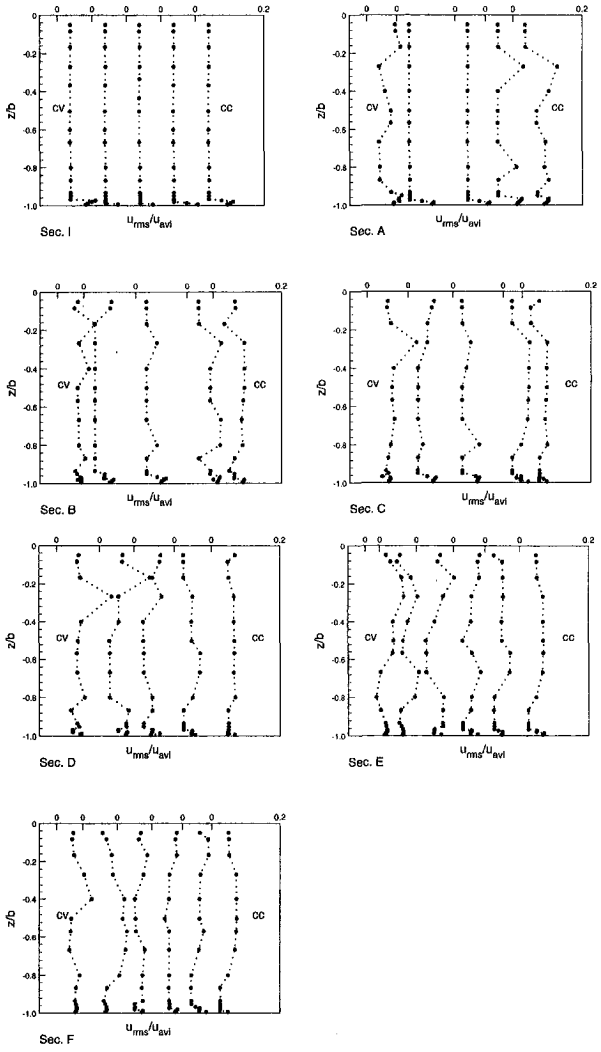

Fig. 8 Turbulence intensity profiles

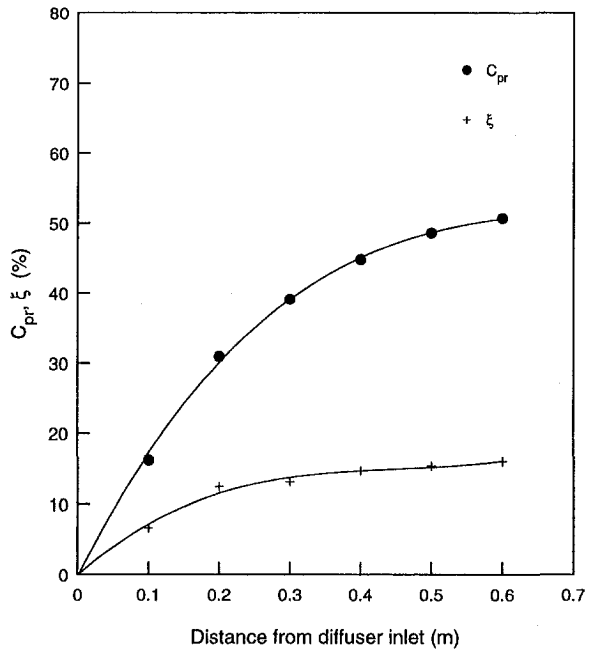

Fig. 7 Static pressure recovery and total pressure loss coefficients

It is seen from the present study that in a small area ratio (AR = 2) curved diffuser with reasonably high aspect ratio (AS = 6), the flow is not two-dimensional. Starting from the initial one-third of the diffuser length, the flow thereafter is clearly three-dimensional. In view of the studies of Kim and Patel (1994), a different combination of diffuser geometry and flow conditions (e.g., a still higher inlet aspect ratio and/or lower inlet velocities) would seem to be required for a nominally two-dimensional flow in the diffuser.

References

Chang, S. M., Humphrey, J. A. C., Johnson, R. W., and Launder, B. M., 1983, "Turbulent Momentum and Heat Transport in Flow through a 180° Bend of Square Cross-Section," *Proceedings of the 4th Symposium on Turbulent Shear Flows,* Karlsruhe, Germany.

Fox, R. W., and Kline, S. J., 1962, "Flow Regimes in Curved Subsonic Diffusers," ASME *Journal of Basic Engineering,* Series D, Vol. 84, pp. 303–316.

Ghia, K. N., Ghia, U., and Shin, C. T., 1987, "Study of Fully Developed Incompressible Flow in Curved Ducts, Using a Multi-Grid Technique," ASME JOURNAL OF FLUIDS ENGINEERING, Vol. 109, pp. 226–236.

Gillis, J. C., and Johnston, J. P., 1983, "Turbulent Boundary Layer Flow and Structure on a Convex Wall and its Redevelopment on a Flat Wall," *Journal of Fluid Mechanics,* Vol. 135, pp. 123–153.

Hille, P., Vehrenkamp, R., and Schulz-Dubois, E. O., 1985, "The Development and Structure of Primary and Secondary Flow in a Curved Square Duct," *Journal of Fluid Mechanics,* Vol. 151, pp. 219–241.

Hoffman, P. H., Muck, K. C., and Bradshaw, P., 1985, "The Effect of Concave Surface Curvature on Turbulent Boundary Layers," *Journal of Fluid Mechanics,* Vol. 161, pp. 371–403.

Humphrey, J. A. C., Whitelaw, J. H., and Yee, G., 1981, "Turbulent Flow in a Square Duct with Strong Curvature," *Journal of Fluid Mechanics,* Vol. 103, pp. 443–463.

Hur, N., Thangam, S., and Speziale, C. G., 1990, "Numerical Study of Turbulent Secondary Flows in Curved Ducts," ASME JOURNAL OF FLUIDS ENGINEERING, Vol. 112, p. 205.

Kim, W. J., and Patel, V. C., 1994, "Origin and Decay of Longitudinal Vortices in Developing Flow in a Curved Rectangular Duct," ASME JOURNAL OF FLUIDS ENGINEERING, Vol. 116, pp. 45–52.

Kline, S. J., and McClintock, F. A., 1953, "Describing Uncertainties in Single Sample Experiments," *Mechanical Engineering,* Vol. 74, pp. 3–8.

McMillan, O. J., 1982, "Mean-Flow Measurements of the Flow Field Diffusing Bend," NASA Contractor Report 3634.

Muck, K. C., Hoffman, P. H., and Bradshaw, P., 1985, "The Effect of Convex Surface Curvature on Turbulent Boundary Layers," *Journal of Fluid Mechanics,* Vol. 161, pp. 347–369.

Rojas, J., Whitelaw, J. H., and Yianneskis, M., 1983a, "Flow in Sigmoid Diffusers of Moderate Curvature," Imperial College of Science & Technology, London (Dept. of Mechanical Engineering) Report No. FS/83/21.

Rojas, J., Whitelaw, J. H., and Yianneskis, M., 1983b, "Developing Flow in *S*-Shaped Diffusers," Imperial College of Science & Technology, London (Dept. of Mechanical Engineering) Report No. FS/83/28.

Sagi, C. J., and Johnston, J. P., 1967, "The Design and Performance of 2-D Curved Diffusers," ASME *Journal of Basic Engineering,* Series D, Vol. 89, pp. 715–731.

Smits, A. J., Young, S. T. B., and Bradshaw, P., 1979, "The Effect of Short Regions of High Surface Curvature on Turbulent Boundary Layers," *Journal of Fluid Mechanics,* Vol. 94, pp. 209–242.

Taylor, A. M. K. P., Whitelaw, J. H., and Yianneskis, M., 1982, "Curved Ducts With Strong Secondary Motion: Velocity Measurements of Developing Laminar and Turbulent Flow," ASME JOURNAL OF FLUIDS ENGINEERING, Vol. 104, pp. 350–359.

Eduardo Blanco-Marigorta
Associate Professor.

Rafael Ballesteros-Tajadura
Associate Professor.

Carlos Santolaria
Professor.

Universidad de Oviedo,
Departamento de Energía,
Campus de Viesques,
33271 Gijón, Spain

Angular Range and Uncertainty Analysis of Nonorthogonal Crossed Hot Wire Probes

Crossed hot wire probes are widely used for measuring two-dimensional flows. Many applications in fluid mechanics like turbomachinery require an angular range as large as possible and a reasonable uncertainty in both direction and velocity values. The classic design places the wires orthogonally, while an angle between the probe wires allows a wider angular range to be obtained. The paper shows an experimental and a theoretical study of the response of this kind of probes, by analyzing the dependence of the calibration procedure and uncertainties of flow angle and velocity with the angle between the wires.

1 Introduction

Hot wire anemometry is one of the most practical and widely used techniques for fluid flow measurements. Depending on the application a particular hot wire probe geometry must be chosen. For example, crossed hot wires are the typical choice if the flow is two-dimensional.

In the classic design, the two wires are placed orthogonally. As a result, only the flows whose direction are included in a quadrant defined by the wires can be measured. If the flow direction has a range greater than 90 deg, ambiguous results are obtained, because the probe's behavior is the same as in the other quadrants (Lomas, 1986; Merati et al., 1984).

Moreover, due to deviations from the theoretical response characteristics, the distortion produced by the wire supports and the manufacturing faults (Strohl et al., 1973; Wygnanski et al., 1978), the useful range is somewhat smaller.

In the study of some fluid-dynamics phenomena, like the flow at the outlet plane of an axial compressor or the rotating stall flow in axial fans or compressors, it is necessary to have as large as possible an angular range, because of the sudden and wide changes of the flow direction.

In order to achieve as wide as possible an angular range, three probes have been designed and built. The chosen angle between the wires are 90, 120, and 135 deg. These probes have been subjected to a direct calibration procedure. This study permitted a comparison of the behaviour of the 90 deg probe with the other ones. An uncertainty analysis of the flow direction and velocity supplied by the probes has been carried out.

In parallel, an analytical study of the behaviour of non-orthogonal probes, assuming a theoretical law for the effective velocities has been carried out. In this way, the relation between the calibration coefficients and the direction and velocity uncertainties with the direction of the incident flow has been worked out, using the angle between the wires as a parameter.

Finally, measurements at the outlet of a jet flow fan from the absolute frame are presented. They have been made using one of the probes, which is able to capture the great changes in the absolute flow angle due to the blade wakes.

2 Angular Calibration and Uncertainty Analysis

A direct calibration procedure was selected. It is possible to derive two calibration coefficients to represent flow angle and velocity magnitude changes. The variation of these coefficients within the range of the probe is established through an angular calibration and the resulting curves were used instead of the response equations. In this way, geometrical effects can be directly taken into account (Mathioudakis, 1985).

Previously to the angular calibration, the relation between the effective velocity of each wire and the voltage supplied by the anemometer had to be obtained, including an air temperature correction factor.

During the calibration procedure, a sweep was made along different angular positions with an interval of 2.5 deg and, with the effective velocities, an angular coefficient **Acf** is defined as:

$$\mathbf{Acf} = \frac{\mathbf{Ue}_1}{\mathbf{Ue}_2} \tag{1}$$

and also a velocity coefficient **Ucf**:

$$\mathbf{Ucf} = \frac{\mathbf{U}}{\mathbf{Ru}} \tag{2}$$

where **U** is the real velocity of the flow and **Ru** is defined as follows:

$$\mathbf{Ru} = \sqrt{\mathbf{Ue}_1^2 + \mathbf{Ue}_2^2} \tag{3}$$

During measurements, the probe provided a set of values for the two effective velocities. From these velocities the **Acf** coefficient was calculated and from the relation between this coefficient and the flow angle, the flow direction was obtained.

Once the flow angle was obtained, the **Ucf** coefficient could be calculated from the curve expressed in Eq. (2). This coefficient permitted us to obtain the absolute value of the velocity:

$$\mathbf{U} = \mathbf{Ucf}\ \mathbf{Ru} \tag{4}$$

The flow angle and velocity uncertainties (**Unc**) have been evaluated following the method proposed by Kline and McClintock (1953).

According to the definition of **Acf**, this is only a function of the flow angle, i.e., $\mathbf{Acf} = \mathbf{f}(\alpha)$. So, the flow angle uncertainty is obtained using the following expression:

$$\mathbf{Unc}^2(\alpha) = \left(\frac{d\alpha}{d\mathbf{Acf}}\right)^2 \mathbf{Unc}^2(\mathbf{Acf}) \tag{5}$$

The uncertainty of **Acf**, as a function of the effective velocities, is obtained applying the same method to the Eq. (1):

Contributed by the Fluids Engineering Division for publication in the JOURNAL OF FLUIDS ENGINEERING. Manuscript received by the Fluids Engineering Division July 5, 1994; revised manuscript received October 9, 1997. Associate Technical Editor: D. E. Stock.

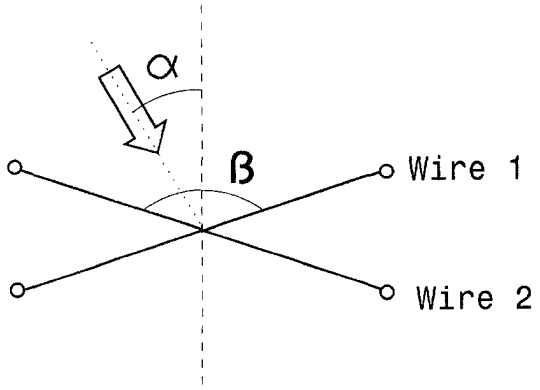

Fig. 1 Angle reference of the wires

$$\mathbf{Unc}^2(\mathbf{Acf}) = \frac{\mathbf{Unc}^2(\mathbf{Ue}_1)}{\mathbf{Ue}_2^2} + \frac{\mathbf{Ue}_1^2}{\mathbf{Ue}_2^4}\mathbf{Unc}^2(\mathbf{Ue}_2) \tag{6}$$

which can be rewritten in the following way:

$$\mathbf{Unc}^2(\mathbf{Acf}) = \mathbf{Acf}^2\left(\frac{\mathbf{Unc}^2(\mathbf{Ue}_1)}{\mathbf{Ue}_1^2} + \frac{\mathbf{Unc}^2(\mathbf{Ue}_2)}{\mathbf{Ue}_2^2}\right) \tag{7}$$

In a similar way, the relative uncertainty of the velocity is obtained starting from the definition of **Ucf** in Eq. (2), using the following expression:

$$\frac{\mathbf{Unc}^2(\mathbf{U})}{\mathbf{U}^2} = \frac{\mathbf{Unc}^2(\mathbf{Ru})}{\mathbf{Ru}^2} + \frac{\mathbf{Unc}^2(\mathbf{Ucf})}{\mathbf{Ucf}^2} \tag{8}$$

The uncertainty of **Ru** is evaluated as a function of the effective velocities applying the method to Eq. (3), and the following expression is obtained:

$$\mathbf{Unc}^2(\mathbf{Ru}) = \frac{\mathbf{Ue}_1^3}{\mathbf{Ru}}\frac{\mathbf{Unc}^2(\mathbf{Ue}_1)}{\mathbf{Ue}_1^2} + \frac{\mathbf{Ue}_2^3}{\mathbf{Ru}}\frac{\mathbf{Unc}^2(\mathbf{Ue}_2)}{\mathbf{Ue}_2^2} \tag{9}$$

and the uncertainty of **Ucf** is calculated as a function of the angular uncertainty using the derivative of the velocity coefficient with respect to the flow angle:

$$\mathbf{Unc}^2(\mathbf{Ucf}) = \left(\frac{d\mathbf{Ucf}}{d\alpha}\right)^2 \mathbf{Unc}^2(\alpha) \tag{10}$$

3 Theoretical Uncertainty for Different Angles

Figure 1 shows the wire configuration in a general case and the references chosen for the angles. In the theoretical study, the probe is subject to a certain flow velocity, and the effective velocities of the wires are obtained using the following expressions:

$$\mathbf{Ue}_1 = \mathbf{U}\cos\left(\frac{\pi}{2} - \frac{\beta}{2} - \alpha\right) \tag{11}$$

$$\mathbf{Ue}_2 = \mathbf{U}\cos\left(\frac{\pi}{2} - \frac{\beta}{2} + \alpha\right) \tag{12}$$

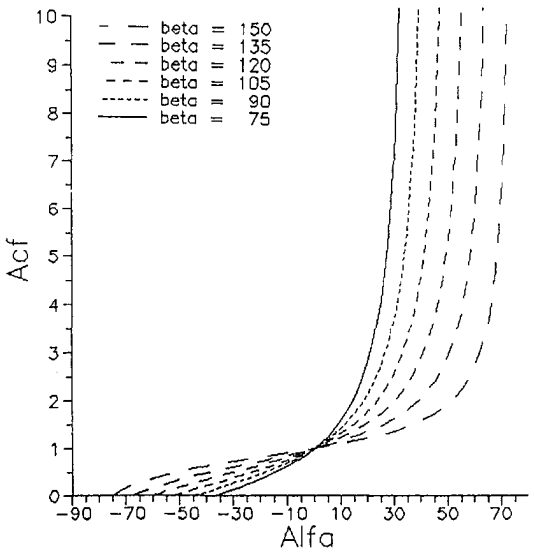

Fig. 2 Theoretical angular coefficient

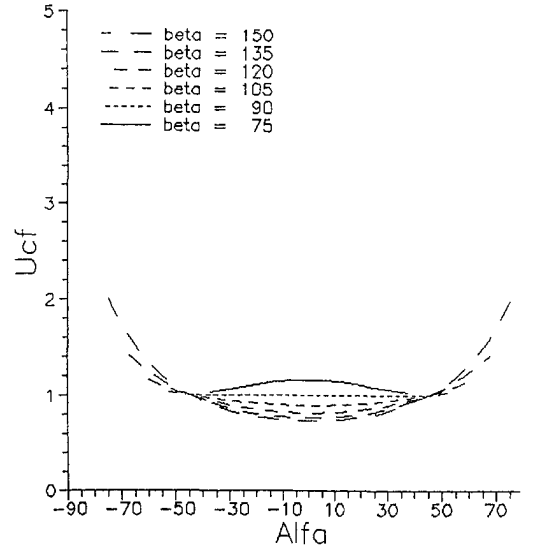

Fig. 3 Theoretical velocity coefficient

The useful angular range will be the one in which double values or deformations did not appear in the relation between the coefficients and the flow angle.

In this theoretical study, the following angles between the wires (β) have been considered: 75, 90, 105, 120, 135, and 150 deg. For each one, the relation between the angular coefficient **Acf** and the velocity coefficient **Ucf** as a function of the flow angle was obtained, by making an angular sweep of α between $-\beta/2$ and $+\beta/2$. Figures 2 and 3 show these relations.

It can be seen that in the selected range of α defined by the wires double values are not obtained, and then this angle

Nomenclature

Acf = angular coefficient
Ru = defined in Eq. (3)
U = flow velocity
Ucf = velocity coefficient
Ue = effective velocity
α = flow angle
β = angle between the wires

Subscripts

1 = Wire 1
2 = Wire 2

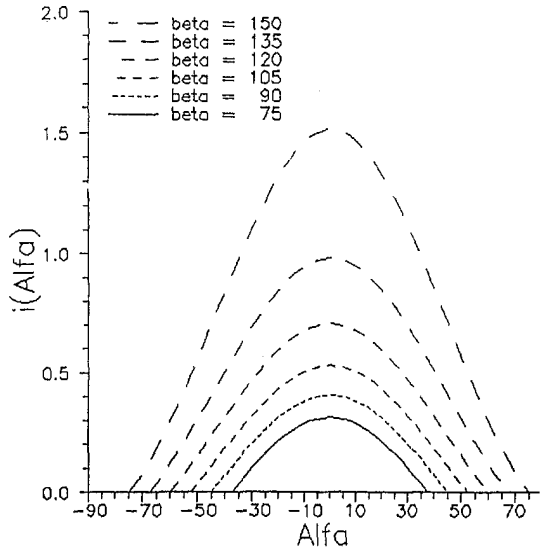

Fig. 4 Theoretical angle uncertainty

coincides, theoretically, with the useful angular range. It can also be observed that the coefficient **Acf** reaches zero or infinite towards the angular range edges, because one of the effective velocities becomes zero. Figure 3 shows that, if β is 90 deg, there is no need for a velocity correction, because **Ucf** = 1. This coefficient is greater than 1 if β decreases and it is lower than 1 if β increases. In any case, the values of **Ucf** are close to 1 except if β is bigger than 135 deg.

Flow angle and velocity uncertainties have been also evaluated, applying the method described above. As in the experimental work, the relative uncertainty of the effective velocity measurements was taken as equal to 1% with odds 20 to 1 (Mathioudakis, 1985). This fact allows us to compare both results.

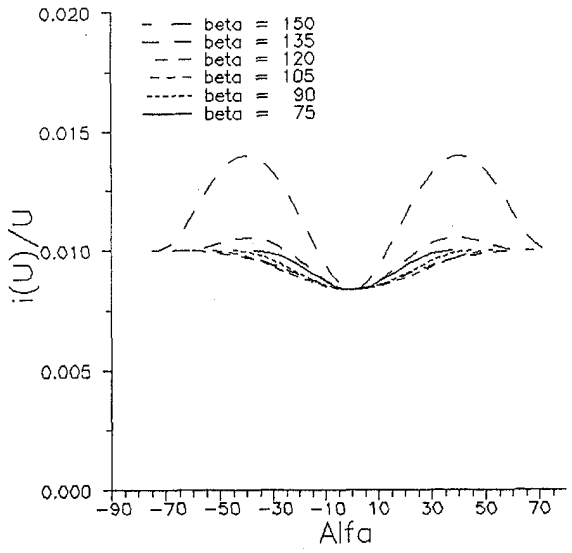

Fig. 5 Theoretical velocity uncertainty

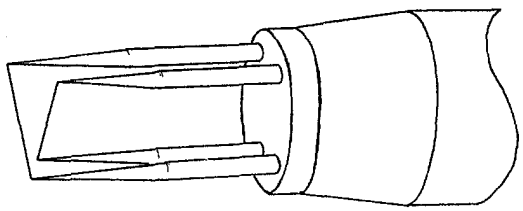

Fig. 6 Probe sketch

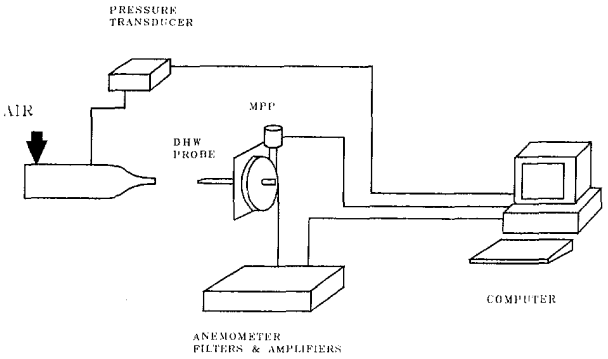

Fig. 7 Calibration setup

Figure 4 shows the relation between the flow angle uncertainty and β. It can be observed that this uncertainty reaches a maximum in the middle of the angular range (α = 0 deg) and decreases towards the edges. This variation is related to the derivative of the coefficient **Acf** with respect to α, already shown in figure 2. The flow angle uncertainty clearly increases with an increase of β. For example, for α = 0 deg, the angular uncertainties are 0.40 deg for β = 90 deg, 0.70 deg for β = 120 deg and 1.51 deg for β = 150 deg.

Figure 5 shows the relative uncertainty in the measurement of the flow velocity as a function of the flow angle. It can be shown that this uncertainty reaches a minimum in the middle of the angular range, increasing towards the edges. Its value is around 1%. If β is greater than β = 135 deg, the uncertainty increases substantially as we move away from the middle of the angular range.

4 Probe Design and Calibration System

Three probes were built. The selected β angles are 90, 120, and 135 deg. Figure 6 shows a sketch of the probe. The piece supporting the needles has a diameter of 4 mm. The wires are in a plane perpendicular to the support axis. The wires' length

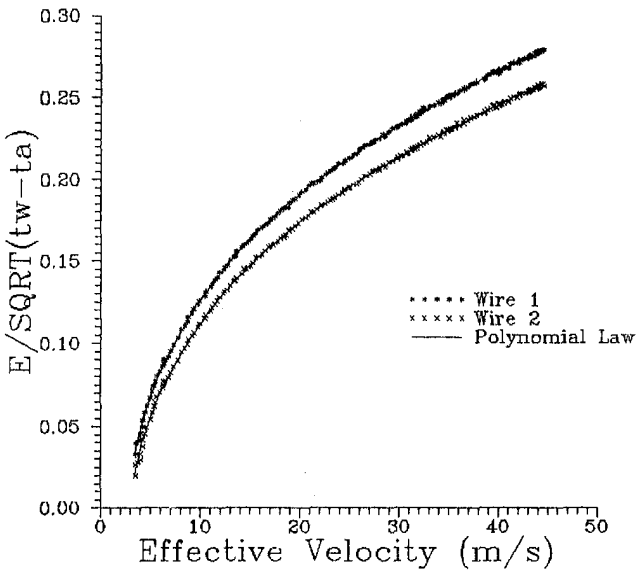

Fig. 8 Effective velocity calibration

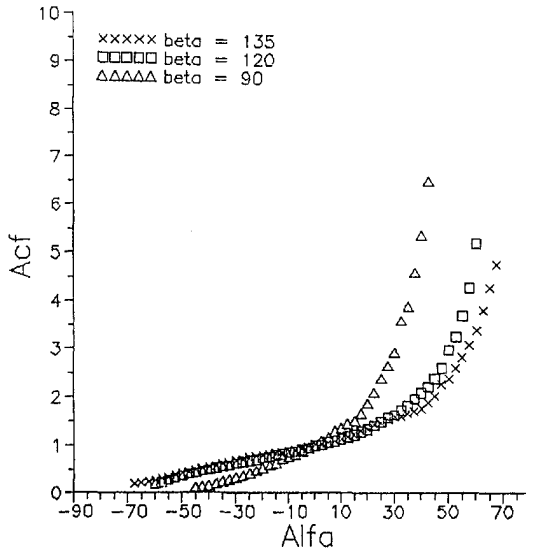

Fig. 9 Angular coefficient

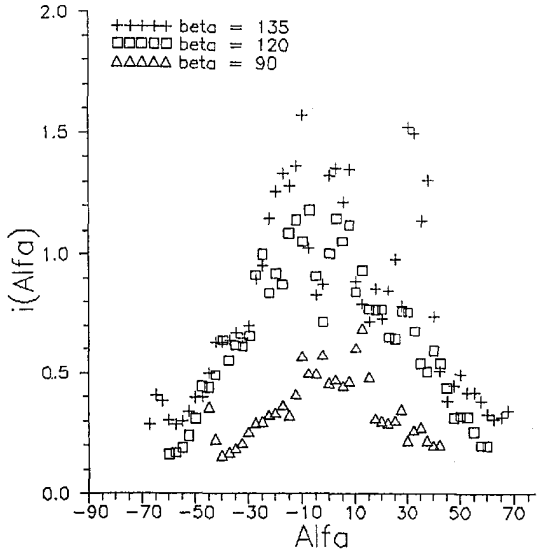

Fig. 11 Angular uncertainty

is 2 mm and their diameter is 5μm and therefore, their aspect ratio is 400. The distance between the wires is about 1 mm.

The calibration facility and set-up are shown in figure 7. The main elements are the nozzle, the positioning system and the computer. Air is supplied by a compressor at 7 bar. Two regulating valves allow the flow velocity at the nozzle outlet to be fixed. The pressure in the settling chamber previous to the nozzle is measured by using a differential pressure transducer.

The probe support is manoeuvred with a step-by-step motor. The motor reduction is 70:1 allowing an angle positioning with a precision greater than 0.1 deg.

The anemometer output voltages, after conditioning (filtered and amplified), are sent to an acquisition card placed in the computer together with the settling chamber pressure. The pressure is transformed into velocity and all the values are stored. A series of computer codes make this acquisition for the effective velocities and the angular calibration in a very short time with a large number of points, in order to decrease the uncertainty.

5 Experimental Results

Figure 8 shows the effective velocity calibration. A fifth-order polynomial is used instead of the classic King's law because a better fit is achieved.

Flow angle and velocity coefficients, for the three probes tested, are plotted in figures 9 and 10. Both are very similar to the theoretical coefficients shown above. Figure 9 indicates that the angular range is equal to β, that is, there are no double values. The **Acf** values do not tend neither to zero nor to infinity because none of the effective velocities reaches zero at the edges.

Figures 11 and 12 show the flow angle and velocity uncertainties. The dispersion of the points is due to the slight fluctuations in the slope of **Acf** and **Ucf** inherent in the direct calibration method. Nevertheless, the trends are very similar to the theoretical ones. Flow angle uncertainties are higher in the central zone and decrease at the edges. The maximum values are about 0.75 deg for the β = 90 deg probe, 1.25 deg for the β = 120 deg and 1.6 deg for the β = 135 deg one. Maximum uncertainty of 1.35 percent is obtained for the velocity. Its value does not change very much with β although the dispersion does.

Some measurements have been performed in an axial jet fan with the β = 120 deg probe. Figure 13 represents the absolute velocity and the absolute flow angle measured with respect to the axial direction. The probe has been placed near the rotor

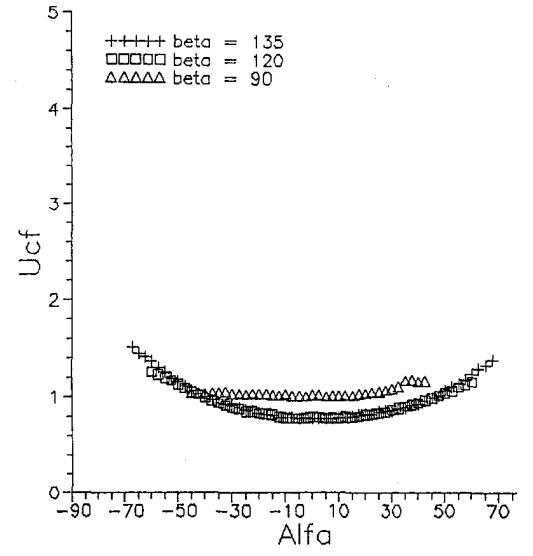

Fig. 10 Velocity coefficient

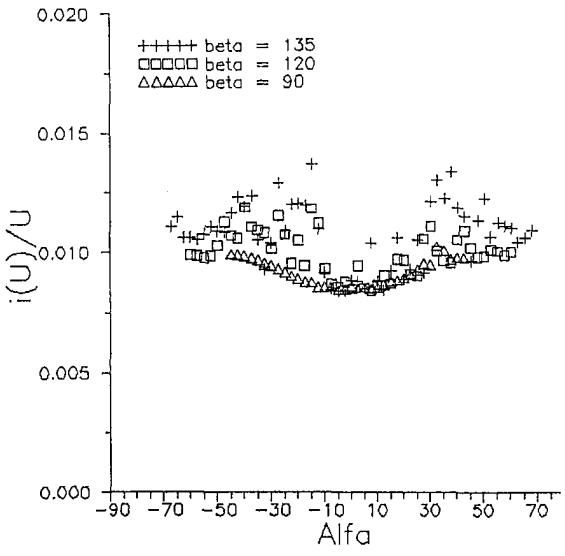

Fig. 12 Velocity uncertainty

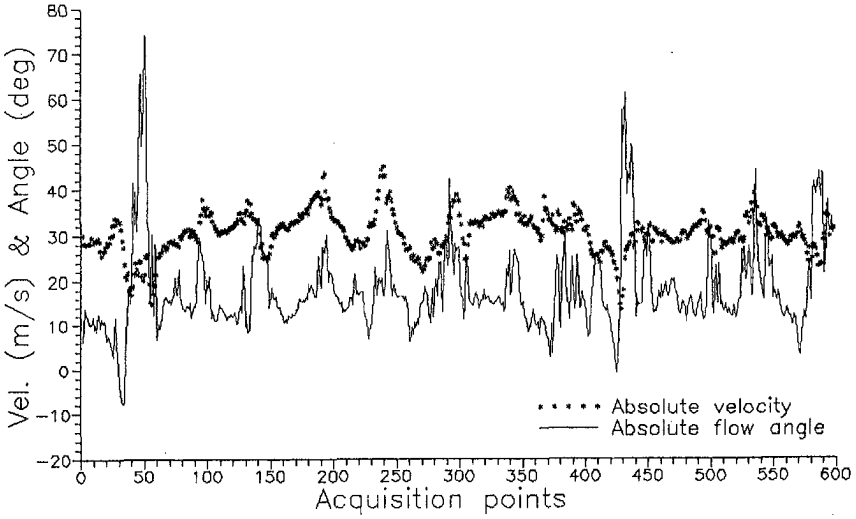

Fig. 13 Measurement at the rotor tip of a jet fan

tip and at 8 cm downstream from the blade axis. 400 points have been acquired for each rotor revolution. It can be seen that the flow angle and the absolute velocity change abruptly in the blade wakes.

6 Conclusions

A theoretical study of both response and uncertainty for non-orthogonal crossed hot wire probes has been made. It shows that it is possible to achieve angular ranges greater than 90 deg. The flow angle uncertainty increases with the angle β between the wires but it is kept within reasonable limits up to 135 deg. With β angles lower than 90 deg the uncertainty is even less than that obtained with classic probes. Velocity uncertainty is invariable for the β values considered.

Three probes with different angles between the wires were built. The direct calibration method used shows that it is possible to take measurements all along the probe range. The analysis gives maximum angle uncertainties of 0.75, 1.25, and 1.6 deg, respectively. The velocity uncertainty is always less than 1.35 percent.

This work shows that, if necessary, a substantial increase of flow angular range can be achieved without increasing uncertainty.

References

Kline, S. J., McClintock, F. A., 1953, "Describing Uncertainties in Single Sample Experiments," *Mechanical Engineering,* Jan., pp. 3–8.

Lomas, C. G., 1986, *Fundamentals of Hot Wire Anemometry,* Cambridge University Press, Cambridge, pp. 22–28.

Mathioudakis, C., 1985, "Rotating Stall in Axial Flow Compressors," Ph.D. thesis, Katholieke Universiteit Leuven, Leuven, pp. 145–158.

Merati, P., Adrian, R. J., 1984, "Directional Sensitivity of Single and Multiple Sensor Probes," *TSI Quarterly,* Vol. X, Issue 2, pp. 3–12.

Strohl, A., Comte-Bellot, G., 1973, "Aerodynamic Effects Due to Configuration of X-Wire Anemometers," ASME *Journal of Applied Mechanics,* Vol. 40, pp. 661–666.

Wygnanski, I., Ho, C., 1978, "Note on the Prong Configuration of an X-Array Hot Wire Probe," *Rev. Sci. Instrumentation,* Vol. 49, pp. 865–866.

Application of Neural Networks and Fuzzy Logic to the Calibration of the Seven-Hole Probe

O. K. Rediniotis
Assistant Professor,
Aerospace Engineering Department,
Texas A&M University,
College Station, TX 77843

G. Chrysanthakopoulos
Research Assistant,
Electrical Engineering Department,
Virginia Polytechnic Institute
and State University,
Blacksburg, VA 24061

The theory and techniques of Artificial Neural Networks (ANN) and Fuzzy Logic Systems (FLS) are applied toward the formulation of accurate and wide-range calibration methods for such flow-diagnostics instruments as multi-hole probes. Besides introducing new calibration techniques, part of the work's objective is to: (a) apply fuzzy-logic methods to identify systems whose behavior is described in a "crisp" rather than a "linguistic" framework and (b) compare the two approaches, i.e., neural network versus fuzzy logic approach, and their potential as universal approximators. For the ANN approach, several network configurations were tried. A Multi-Layer Perceptron with a 2-node input layer, a 4-node output layer and a 7-node hidden/middle layer, performed the best. For the FLS approach, a system with center average defuzzifier, product-inference rule, singleton fuzzifier, and Gaussian membership functions was employed. The Fuzzy Logic System seemed to outperform the Neural Network/Multi-Layer Perceptron.

Introduction—Background

Artificial Neural Networks. After a somewhat dormant period in the 1970s, the scientific community has exhibited an increasing interest in the development and implementation of artificial neural networks (ANN) in practical problems. The reawakening of this interest is due to the discovery of a powerful training algorithm, the backpropagation algorithm. The algorithm, in its earliest form, was first introduced by Werbos (1974) and was later refined by McClelland and Rumelhart (1986).

An artificial neural network could be viewed as a feedforward "black box" which can "learn" to simulate a system, a function or a process, through training. Let $\mathbf{x}$ and $\mathbf{F}(\mathbf{x})$ be the input and output vectors, respectively, of the system we want to simulate. If the function $\mathbf{F}$ is not explicitly known or is too complicated and N input-output pairs $(\mathbf{x}, \mathbf{F}(\mathbf{x}))_i$, $i = 1, \ldots, N$ are numerically known, then the ANN idea becomes particularly attractive. During the training, the ANN "black box" is presented with the training pairs $(\mathbf{x}, \mathbf{F}(\mathbf{x}))_i$ and its internal parameters (weights) are adjusted by the training algorithm. This procedure results in the "encoding" of the properties of function $\mathbf{F}$ in the different parts of the ANN. If, after the training is completed, the ANN is presented with an input $\mathbf{x}$, not belonging to the N training pairs, it will simulate the function $\mathbf{F}$ and will produce an output $\mathbf{F}'(\mathbf{x})$. The error, which is the difference $(\mathbf{F}(\mathbf{x}) - \mathbf{F}'(\mathbf{x}))$ between the actual and the predicted output values, is an indication of how successful the training was. ANNs have been shown to successfully model a wide diversity of systems and processes, including vortex dynamics principles (Schreck et al., 1993; Schreck and Faller, 1995), flight test data estimators (McMillen et al., 1995) and control of transition to turbulence (Fan et al., 1995).

Fuzzy Logic Systems. An even more recently developed field in mathematics, the theory of fuzzy sets and the logic stemming from it, have been attracting an increasing number of fans, sometimes at the expense of ANN. Although, traditionally, fuzzy logic has been viewed as a technique for representing imprecise, ambiguous and vague information, nothing prevents it from successfully dealing with concrete, quantitative and precise data. In fact, the Universal Approximation Theorem stated in a later section, ensures that fuzzy logic systems are capable of uniformly approximating any nonlinear function to any degree of accuracy.

Seven-Hole Probe Calibration. The seven-hole probe is a simple instrument from a fabrication standpoint. Seven pressure ports are axisymmetrically arranged on a hemispherical or conical tip, with each port communicating through tubing to a pressure measurement device. By measuring the seven pressures at the probe tip ports and through the use of proper probe calibration methods, the seven-hole probe can measure the three velocity components and the static pressure in a flowfield at the location of its tip. Its calibration techniques can be fairly elaborate, depending on the level of the desired accuracy, and will be the topic of this work. The reader can find details on conventional fabrication and calibration approaches in Rediniotis (1992).

Figure 1 shows the probe coordinate system and the angles defining the probe orientation with respect to the local flow velocity vector $\mathbf{V}$. The flow over the seven-hole probe can typically be divided into two flow regimes; low-angle and high-angle regime. The low-angle flow regime is defined as the cone angle (θ) range for which the pressure registered by hole #1 (central hole), is the highest among the seven measured pressures. In Fig. 2, this regime is identified as domain 1. This figure is a schematic representation of all possible probe orientations, in terms of pitch and yaw angles (α, β). It should be noted here that there is a one-to-one correspondence between the pairs (α, β) and (θ, ϕ), defined by the following relations:

$$\cos\theta = \cos\alpha \cos\beta$$
$$\sin\theta \cos\phi = \sin\beta \qquad (1)$$

Each domain in Fig. 2 is identified by a number indicating the hole that senses the highest pressure for all the possible probe orientations in that domain. For high-angle flows the highest

Contributed by the Fluids Engineering Division for publication in the JOURNAL OF FLUIDS ENGINEERING. Manuscript received by the Fluids Engineering Division May 3, 1996; revised manuscript received October 9, 1997. Associate Technical Editor: D. E. Stock.

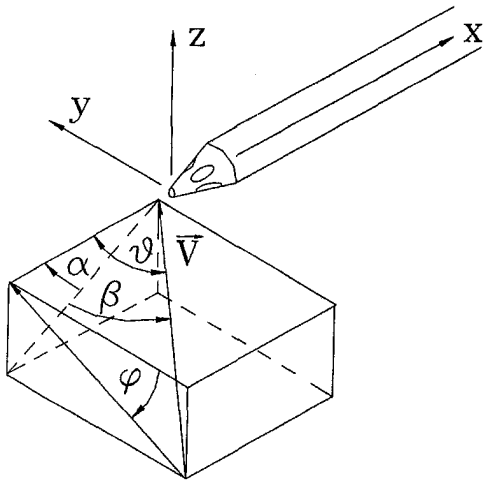

Fig. 1 Flow-angle and probe-coordinate-system definition

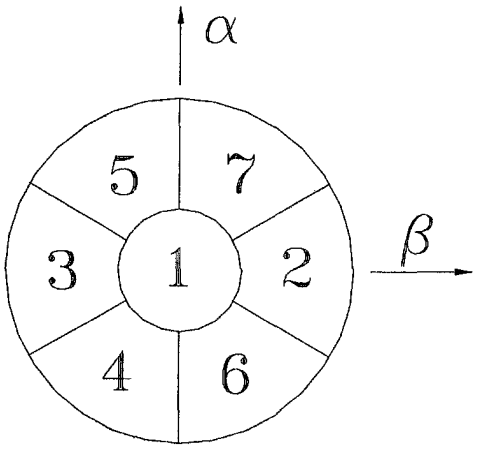

Fig. 2 Probe orientation/calibration domains

pressure occurs in one of the peripheral holes 2 through 7. A detailed description of the above can be found in Rediniotis et al. (1993).

At every measurement location in a flow-mapping experiment the local velocity vector can be fully characterized by four variables. In the low-angle regime the four variables are: pitch angle α, yaw angle β, total pressure coefficient A_t, and static pressure coefficient A_s. In the high-angle regime the four variables are: cone angle θ, roll angle ϕ, A_t, and A_s. While the two flow angles determine the orientation of the velocity vector, the combination of the two coefficients, A_t and A_s, yields the velocity magnitude. The above variables (output or dependent variables) need to be determined as functions of the seven measured pressures or equivalently, two non-dimensional pressure coefficients formed from these pressures: B_c, B_r, (input or independent variables). For example, for the low-angle regime, the following functional relationships have to be determined:

$$\alpha = \alpha(B_c, B_r), \quad \beta = \beta(B_c, B_r), \quad A_t = A_t(B_c, B_r), \quad A_s = A_s(B_c, B_r) \tag{2}$$

Similar relationship have to be determined for the high-angle regime. The definitions of the input and output variables are:

Low-Angle Regime (domain 1):

Input (Independent) Variables:

$$B_c = \frac{1}{\sqrt{3}} \frac{(P_4 + P_6 - P_5 - P_7)}{Q'}$$

$$B_r = \frac{2}{3} \frac{(P_2 - P_3)}{Q'} + \frac{1}{3} \frac{(P_7 + P_6 - P_4 - P_5)}{Q'} \tag{3}$$

where

$$Q' = P_1 - \frac{(P_2 + P_3 + P_4 + P_5 + P_6 + P_7)}{6}$$

Output (Dependent) Variables:

$$\alpha, \quad \beta, \quad A_t = \frac{P_1 - P_t}{Q'}, \quad A_s = \frac{P_1 - P_s}{Q'} \tag{4}$$

High-Angle Regimes (domains 2 through 7).

Input Variables:

$$B_c = \frac{P_i - P_1}{Q'}, \quad B_r = \frac{P_i^+ - P_i^-}{Q'} \tag{5}$$

Nomenclature

$\mathbf{x}$ = system input vector or input linguistic variable vector: $\mathbf{x} = (x_1, \ldots, x_n)^T$

y, $\mathbf{F}(\mathbf{x})$ = system output vector

N = number of ANN training data pairs

θ = cone angle (deg), as defined in Fig. 1

ϕ = roll angle (deg), as defined in Fig. 1

α = pitch angle (deg), as defined in Fig. 1

β = yaw angle (deg), as defined in Fig. 1

m = total number of calibration data points

P_i = pressure sensed by the ith hole of the seven-hole probe

P_t, P_s = local total and static pressure, respectively

$\mathbf{V}$ = local velocity vector/calibrator exit velocity

B_c, B_r = nondimensional pressure coefficients, formed from the seven pressures P_i

Q' = seven-hole probe pseudo-dynamic pressure

A_t, A_s = total and static pressure coefficient, respectively

$\mathbf{W}_i$ = ANN weight matrix at the end of the ith epoch

μ = ANN learning rate

ξ = ANN sum-squared error

$S(\mathbf{x})$ = FLS output

$R^{(l)}$ = lth fuzzy rule

M = total number of fuzzy rules

F_i^l = input fuzzy sets corresponding to the lth fuzzy rule, $i = 1, \ldots, n$

n = number of antecedents (input variables)

k = number of consequents (output variables)

G^l = output fuzzy set corresponding to the lth fuzzy rule

$\underline{\mathbf{x}}^l$ = vector of input fuzzy set centers, corresponding to the lth fuzzy rule: $\underline{\mathbf{x}}^l = (\underline{x}_1^l, \ldots, \underline{x}_n^l)^T$

$\underline{y}^l$ = output fuzzy set center, corresponding to the lth fuzzy rule

σ_i^l, a_i^l = parameters of Gaussian membership function for the ith input fuzzy set and the lth fuzzy rule

U = universe of discourse, $U \in R^n$

$H(\mathbf{x})$ = real and continuous function on a compact set $U \in R^n$

where $Q' = P_i - ((P_i^+ + P_i^-)/2)$, with P_i being the highest detected pressure and P_i^+, P_i^- being the pressures of the peripheral holes adjacent to hole i and on either side of it. Referring to Fig. 2, P_i^+ is adjacent to P_i in the clockwise direction and P_i^- in the counter-clockwise direction.

Output Variables:

$$\theta, \quad \phi, \quad A_t = \frac{P_i - P_t}{Q'}, \quad A_s = \frac{P_i - P_s}{Q'} \tag{6}$$

In the past, most seven-hole probe calibration methods have been based on polynomial interpolation and approximation techniques (Zilliac, 1989; Rediniotis, 1992; Rediniotis et al., 1993). For example, the functions in (2) are assumed to be polynomials of two independent variables. The coefficients of these polynomials are determined by using the probe calibration data. Such techniques suffer from the following inherent inadequacy. Polynomial interpolators of order higher than 3 are often ill-behaved in between the calibration points. Third-order, two-independent-variable polynomials (which are typically used for the calibration of each of the seven domains of Fig. 2) have 10 unknown coefficients, thus requiring 10 calibration points to determine them. Only 10 calibration points per domain, however, might be insufficient to produce the desired calibration accuracy. Since, as it is described below, the calibration process is fully automated and fast, the acquisition of more calibration points does not present a problem. The problem stems from the polynomial interpolator's inability to make use of more calibration points.

The techniques proposed herein do not have this limitation. They can accommodate and take advantage of as much calibration data as it is available. Moreover, in the case of the neural network approach, significant calibration data compression is achieved. For example, the algorithm can encode a 60 Kilobyte calibration data file, elegantly reducing it to a 6 Kilobyte data file that contains information about the network architectures as well as the weight and bias values. Once this network file is generated, data reduction is achieved very fast by accessing only that mere 6 Kilobyte data file.

The remaining of the paper first discusses the instrumentation used in this work and then presents the results of the application of the proposed techniques to the seven-hole probe calibration. Two different types of universal approximators were used. Type I were Multi-Layer Perceptrons, trained using the backpropagation algorithm and type II were Fuzzy Logic Systems. Conclusions from the present work are discussed last.

Instrumentation

The seven-hole probe employed in this study was fabricated in-house. Seven 0.028 in. O.D. steel hypodermic tubes were fitted into a 0.109 in. O.D. steel tube. The spaces between the tubes were filled with 0.009 in. steel wire and epoxy. Finally, one end of the probe was machined into a 60 deg-included-angle cone.

One of the setups employed in the calibration of the seven-hole probe was a jet calibrator, consisting of a settling chamber, a 25:1 contraction section and a 2 × 2 in. jet exit nozzle, and was supplied with compressed air. The probe was mounted such that its tip was right at the exit plane of the nozzle and centered with respect to it. Two stepper motors could vary the probe orientation with respect to the jet axis, i.e. they could vary the flow angles θ and ϕ within the ranges [0, 80 deg] and [−180, 180 deg], respectively, thus covering a wide-range calibration domain. At all probe orientations the probe tip location was kept the same. The jet velocity at the exit of the nozzle could be varied between 4 ft/s and 270 ft/s. However, a smaller velocity range was utilized for calibration and testing (20 ft/s to 90 ft/s). The calibration process was fully automated. The stepper-motor assembly positioned the probe according to a user-defined array of desired probe orientations (θ_i, ϕ_i), $i = 1, \ldots, m$. For each orientation, the data-acquisition system collected the data, i.e., eight pressure values. Seven of them were the probe tip pressures P_i, $i = 1, \ldots, 7$. The eighth was the pressure at the settling chamber of the calibrator. From this eight pressure and the known settling chamber and nozzle exit cross areas, the exit jet velocity V could be calculated by using Bernoulli's equation.

A 16-transducer Electronic Pressure Scanner (ESP) from PSI, Inc. with a full scale of +/− 10 inH_2O was employed to measure pressure. The ESP Pressure Scanner was interfaced with a laboratory computer and was calibrated on-line. The system was developed by Rediniotis (1994) and consisted of an ESP interface/data-acquisition board PDA-3101 (31 KHz max sampling rate) and an ACCUPRES computer-controlled, on-line pressure calibrator. Alternatively, the probe positioning system (stepper-motor assemblies) and the data-acquisition system could be installed in the test section of an open-circuit tunnel with a 2′ × 2′ test section and a velocity range between 10 ft/s and 50 ft/s.

To be able to assess the accuracy of the calibration techniques, test data were also collected by positioning the probe at several known orientations, $(\alpha_{test}, \beta_{test})$, or $(\theta_{test}, \phi_{test})$, none of them coincident with any of the orientations used for calibration, $(\alpha_{cal}, \beta_{cal})$ or $(\theta_{cal}, \phi_{cal})$, and by collecting the eight pressures. These pressures were fed into the calibration routines and a predicted pair $(\alpha_{pred}, \beta_{pred})$ or $(\theta_{pred}, \phi_{pred})$ was calculated. The difference between the two pairs $(\alpha_{test}, \beta_{test})$ and $(\alpha_{pred}, \beta_{pred})$ or $(\theta_{test}, \phi_{test})$ and $(\theta_{pred}, \phi_{pred})$ is a measure of the calibration accuracy.

Neural Network Approach

A total of approximately 1400 calibration points (200 points for each of the domains of Fig. 2) were acquired and used to train the ANNs. Seven separate ANNs were trained, one for each of the seven major calibration sectors. The basic network architecture is illustrated in Fig. 3. Each ANN has two inputs which are the two non-dimensional pressure coefficients, B_c, B_r. Each ANN has four outputs: the two flow angles, i.e., cone and roll (θ, ϕ) for the high-angle sectors or pitch and yaw (α, β) for the low-angle sector, the total pressure coefficient A_t and the static pressure coefficient A_s.

Although by no means exhaustively, we experimented with several neural network configurations including varying the number and size of hidden layers, delays and activation functions. The network that worked the best was the Multi-Layer Perceptron (MLP) described below. The MLP system had a 2-node input layer, a 4-node output layer and a 7-node hidden/middle layer. To train the network the backpropagation algorithm was used with a momentum coefficient and adaptive learning rate. The learning rate μ is defined in the following equation:

$$\mathbf{W}_{i+1} = \mathbf{W}_i - \mu \nabla \xi(\mathbf{W}_i) \tag{7}$$

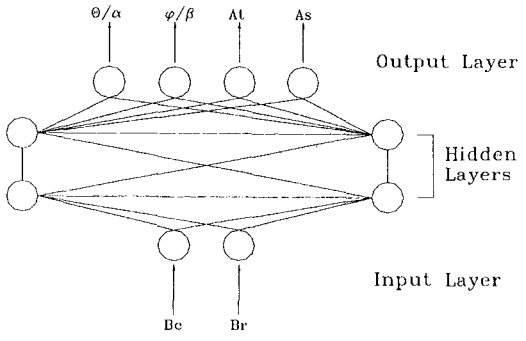

Fig. 3 The ANN architecture employed

Briefly, the training proceeds as follows. For each training vector (B_c, B_r, α, β, A_t, A_s) the network is presented with, it first uses the most recent values of its weights to calculate the outputs from the inputs of the training vector. It then calculates the difference between these calculated outputs and the actual outputs of the training vector. The backpropagation algorithm then determines which nodes of the network have contributed to this difference (error), and to what degree, and accordingly adjusts their weights to eliminate this contribution. This process is repeated several times for all training vectors, until a norm of the error drops below a set value, at which point the training is complete.

In the present network, the activation function of the hidden layer nodes was tangent-sigmoid. For the output layer a linear activation function was used. The output domains for both functions were $[-1, 1]$. The actual system inputs and outputs were scaled to lie in the interval $[-1, 1]$. The MLP was trained with an average of 200 exemplars for each domain. The training process had 8000 epochs. Figure 4 presents the training history of the neural network during the first 6000 epochs. The plot presents the sum-squared error of the training data after each training epoch.

From our experience with seven-hole probe calibrations, typically the prediction of the roll angle is the most challenging. Figure 5 presents a comparison between the predicted and the actual roll angle for several test points that did not belong to the training exemplars. Most of the test points were predicted with good accuracy, with about 50 percent of them having errors of less than 1 deg. However, about 20 percent of the test points exhibit deviations between 3 and 6 deg. For evaluating the performance of the techniques presented here, we set calibration accuracy standards similar to those typically expected, although not always achieved, by polynomial calibration: (a) error in the flow-angle prediction of 0.25 to 0.5 deg, typically, and never exceeding 2 deg for cone angles up to 70 deg, (b) error in the velocity magnitude prediction not exceeding 3 percent and typically in the 1 percent neighborhood, for the calibration and testing velocity range (20 ft/s to 90 ft/s). The neural network did not seem to meet these standards for the entire calibration domain. In an attempt to assist the MLP in identifying the system, we used the product of the two inputs as an additional input to the system. This increases the dimension of the input space and generally assists the universal approximator in finding a nonlinear mapping. In the specific system, the improvement was marginal.

The previous discussion, however, should by no means indicate that there is no ANN that could meet the set standards for the entire calibration domain. The fact that in this first, unoptimized effort, the ANN performance came close to the performance of well-established techniques, indicates, to the authors at least, that further development of the ANN approach should be pursued. Suggested improvements are discussed below. It is likely that the selected ANN architecture is still not optimal, although several configurations were tried. Since all the rules for selecting the parameters of a MLP (such as number and size of layers, learning rate, etc.) are heuristic, it is hard to describe a consistent way of selecting the network architecture

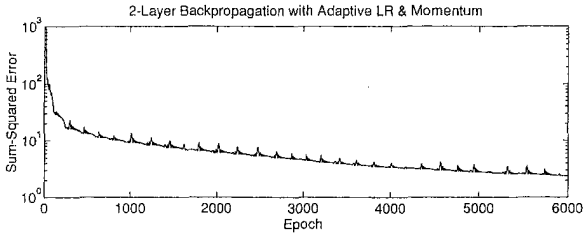

Fig. 4 Training history of the neural network

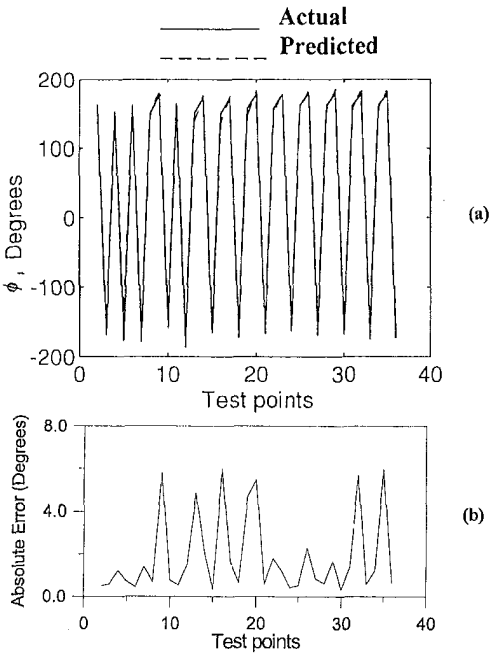

Fig. 5 Seven-hole probe roll angle prediction by the ANN: (a) predicted versus actual roll angle, (b) prediction error

with the optimum performance. In other words, when one is constructing the network, one decides on the system's parameters, for example, how many hidden layers and how many nodes per layer to use, mainly guided by one's own previous experience with similar problems and networks. If such experience does not exist, one has to resort to experimentation with different network architectures until the desired performance is achieved. To overcome this tedious task, network self-optimization techniques can be implemented. One of the traditional handicaps of multi-layer perceptrons is that the system often gets trapped in local minima (rather than the global minimum) which prohibits the network from successfully identifying the system, even if training continues for many epochs. Usually, this problem is remedied by using momentum during learning (Freeman and Skapura, 1992), or reinitializing the system weights to different values. Also, as previously mentioned, the same activation function was used for all the nodes in one layer, although the type of activation function could vary from layer to layer. Additionally, a limited base of activation functions was available at the time of this study. Significant network performance could be achieved by allowing each node to have its own activation function (i.e. two nodes in the same layer can have different activation functions), selected from a more diverse base. Since the submission of the present paper, our group has implemented the previous (and other) improvements and the results will be discussed in a different paper.

Fuzzy Logic Approach

Figure 6 presents a schematic of the basic configuration of the fuzzy logic systems we used in this work. The fuzzy rule

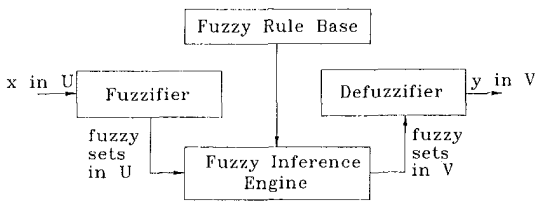

Fig. 6 Fuzzy-logic calibrator configuration

base consists of a collection of fuzzy IF-THEN rules in the following form:

$$R^{(l)}: \text{IF } x_1 \text{ is } F_1^l \text{ and } \ldots \text{ and } x_n \text{ is } F_n^l \text{ THEN } y \text{ is } G^l \quad (8)$$

where F_i^l and G^l are fuzzy sets, $\mathbf{x} = (x_1, \ldots, x_n)^T$, y are the input and output linguistic variables, respectively, and $l = 1, \ldots, M$ with M being the number of rules.

However, in engineering systems inputs and outputs are real-valued variables in crisp sets and not linguistic variables in fuzzy sets. The conversion from the former to the latter and vice-versa is achieved through the fuzzifier and defuzzifier respectively. The fuzzy inference engine is the heart of the system and maps the fuzzy inputs to the fuzzy outputs employing the rules from the fuzzy rule base. In our approach, we used center average defuzzifier, product-inference rule, singleton fuzzifier, and Gaussian membership functions. Then the fuzzy system reduces to:

$$S(\mathbf{x}) = \frac{\sum_{l=1}^{M} \underline{y}^l \left[\prod_{i=1}^{n} \alpha_i^l \exp\left(- \left(\frac{x_i - \underline{x}_i^l}{\sigma_i^l} \right)^2 \right) \right]}{\sum_{l=1}^{M} \left[\prod_{i=1}^{n} a_i^l \exp\left(- \left(\frac{x_i - \underline{x}_i^l}{\sigma_i^l} \right)^2 \right) \right]} \quad (9)$$

with $\mathbf{x} = (x_1, \ldots, x_n)^T \in U$. We state here the following Universal Approximation Theorem (Kosko 1992, Wang 1994). For any given real and continuous function $H(\mathbf{x})$ on a compact set $U \in R^n$ and arbitrary $\epsilon > 0$ there exists a fuzzy logic system $S(\mathbf{x})$ in the form of (9) such that

$$\sup_{\mathbf{x} \in U} |S(\mathbf{x}) - H(\mathbf{x})| \leq \epsilon \quad (10)$$

The above theorem guarantees the existence of an accurate approximator-interpolator to our calibration data.

In our first approach a fuzzy logic system was formulated using a table-lookup scheme (Wang, 1994) after a fuzzy rule base was derived from our calibration data. We developed an algorithm in C^{++} that implements a fuzzy rule base for any n-input, k-output system. The number of fuzzy regions per domain of antecedent and consequent (output) is adjustable and so is the choice of membership function. In a different approach, instead of using a table lookup method we used the crisp calibration data as the rules for the FLS. In a traditional fuzzy logic system the input and output domains are divided in fuzzy sets with their boundaries and centers determined heuristically. The rules are then formed by combining input sets with output sets

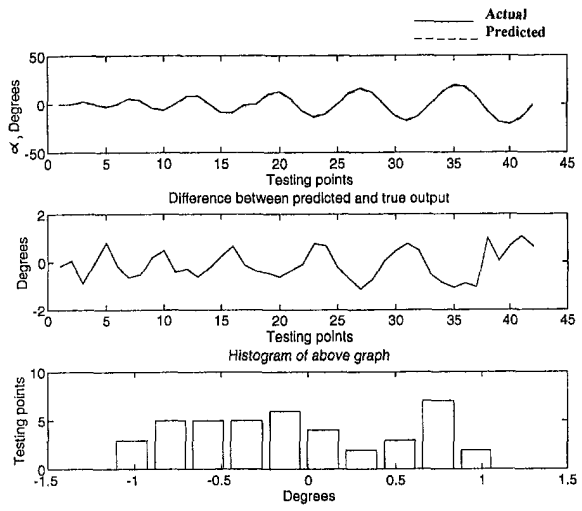

Fig. 7 FLS prediction of the pitch angle for domain 1 of the seven-hole probe

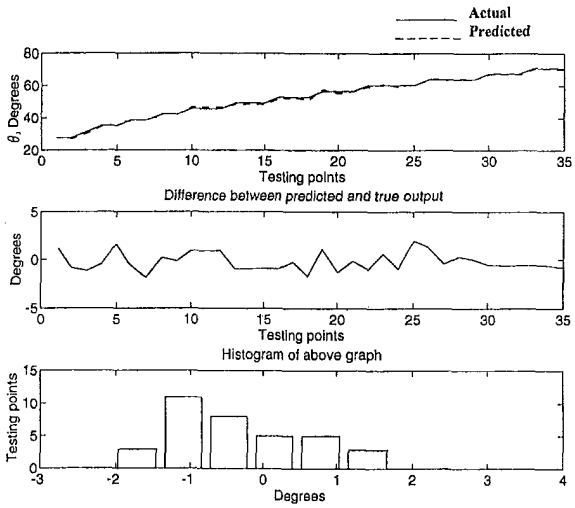

Fig. 8 FLS prediction of the cone angle for domain 6 of the seven-hole probe

in the form of IF-THEN statements. This heuristic approach to a problem for which only "crisp" data is available inherently introduces inaccuracies. Instead of resorting to such methods we initialized the centers of the input and output fuzzy sets to the actual calibration data. We observed significant improvement when this method was used instead of a table-lookup scheme. It should be noted here that this approach along with (9) is equivalent to the Probabilistic General Regression (Specht, 1991) of S on $\mathbf{x}$. However, relation (9) was arrived at with certain choices of deffuzzifier, inference rule, fuzzifier and membership function. If, for example, instead of product-inference rule we had chosen min or max inference rule, or instead of Gaussian we had chosen triangular membership function, relation (9) would be different and, thus, not equivalent to general regression.

Since we had 200 rules (calibration data points) for each domain, defuzzifying becomes a computationally intensive task. To increase the speed of the FLS, the defuzzifier determines, for each new input it is presented with, which rules (out of 200) are the most relevant. Then, it uses only those rules for calculating a crisp output. What determines the importance of each rule is the Euclidean distance of the input vector (B_c, B_r) of each rule from the new input vector. One of the merits of this specific metric is its ease of computation. To select only a limited number of rules, a threshold is used which determines how small a specific rule's distance from the input vector has to be for this rule to be considered important. This method provides speed improvement while not affecting system performance since rules with large distances have very small contribution to the calculation of the crisp output. Since we are using Gaussian membership functions, the membership value of a rule with a large Euclidean distance is practically zero. The results of the fuzzy approximator were significantly better compared to the neural network system. The FLS system requires no pre-processing of the data, no training, and its parameters have physical meaning making them easier to adjust and initialize.

Figure 7 presents a comparison between the predicted, by the fuzzy calibrator, and the actual pitch angle for several test points in domain 1 ($\theta < 22$ deg). A very good agreement can be observed. In the top graph, the solid line represents the actual data and the dashed line represents the predicted values. The middle graph presents the difference between the predicted and the actual values. The lower graph presents the histogram of the error. As it is seen there, the absolute error is never larger than 1.1 deg with more than 50 percent of the test points having

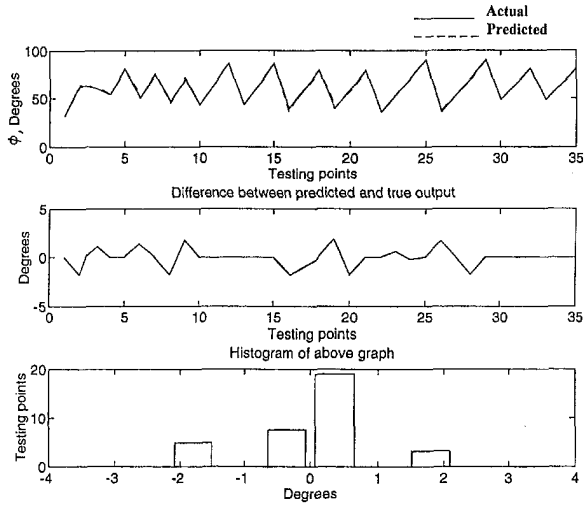

Fig. 9 FLS prediction of the roll angle for domain 6 of the seven-hole probe

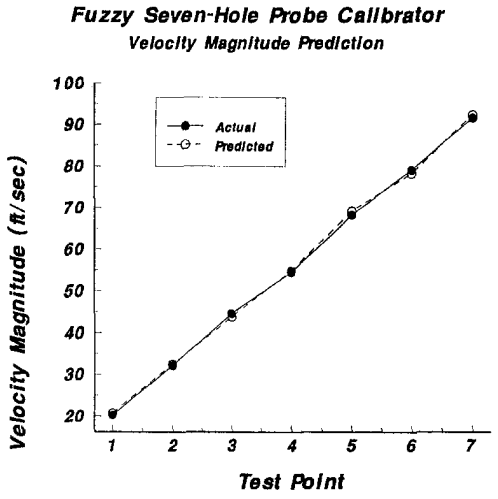

Fig. 11 FLS prediction of the velocity magnitude for the seven-hole probe

an absolute error less than 0.5 deg. The top plot in Fig. 7, as well as in subsequent similar figures, allows the reader to relate the magnitude of the error to the magnitude of the predicted quantity. For example, in Fig. 7, the combination of the top plot with the error plot (middle plot) reveals the fact that in the case of the pitch angle prediction, the error magnitude becomes larger as the pitch angle magnitude increases. The yaw angle is predicted with similar accuracy: the absolute error is always less than 1 deg with about 70 percent of the absolute error values being less than 0.5 deg.

Figures 8 and 9 present comparisons between actual and predicted values for the cone (θ) and roll (ϕ) angles in domain 6. From figure 8 it can be seen that cone angle values as high as 70° are predicted accurately. The comparisons for domain 6 presented above are in fact "worst case" comparisons. In Fig. 10 we arbitrarily collected test data from all the domains (2 through 7) and plotted the actual and the predicted values of the roll angle ϕ. In the top graph the high prediction accuracy and the large ϕ range combined, yield totally overlapping solid and dashed lines. From the histogram graph it can be seen that more than half of the absolute error values are below 0.3°.

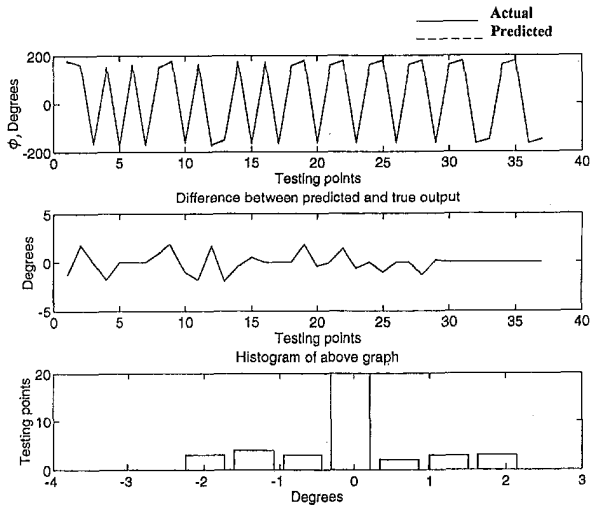

Fig. 10 FLS prediction of the roll angle for domains 2 through 7 of the seven-hole probe

Lastly, Fig. 11 presents the performance of the FLS calibrator in terms of velocity magnitude prediction accuracy. The maximum error does not exceed 3 percent.

Conclusions

The theory and techniques of neural networks and fuzzy logic were employed in the formulation of calibration methods for the seven-hole probe. Although it was originally expected that Artificial Neural Networks (ANN) would perform better than Fuzzy Logic Systems (FLS), it was found out that the reverse was true, at least in this first attempt to apply these techniques to the calibration of the seven-hole probe.

Several possible improvements to the ANN approached were discussed. During the neural-network calibration, and in the search for an optimal network architecture, an inherent handicap of conventional multi-layer perceptrons was repeatedly witnessed. Decisions about the MLP architecture were made heuristically, without the guidance of a unified design methodology. A trial-and-error design procedure, guided by some heuristic rules derived from previous experience, is a lengthy iterative process that keeps humans in the loop as the decision-makers regarding network architecture changes. The need for a self-optimizing, multilayer perceptron was obvious.

Although, traditionally, fuzzy logic has been viewed as a technique for quantitatively representing vague information, it was proven to accurately deal with "crisp" data as well. The fuzzy-logic calibration techniques introduced here feature very good accuracy for a wide range of flow conditions.

References

Fan, X., Herbert, T., and Haritonidis, J. H., 1995, "Transition Control with Neural Networks," AIAA Paper No. 95-0674, Reno, NV, Jan.

Freeman, J. A., and Skapura, D. M., 1992, "Neural Networks Algorithms, Applications, and Programming Techniques," Addison-Wesley.

Kosko, B., 1986, "Neural Networks and Fuzzy Systems," Prentice Hall, New Jersey, 1992.

McClelland, J., and Rumelhart, D., *Parallel Distributed Processing, Volumes 1 and 2*, MIT Press, Cambridge, MA.

McMillen, R. L., Steck, J. E., and Rokhsaz, K., 1995, "Application of an Artificial Neural Network as a Flight Test Data Estimator," AIAA Paper No. 95-0561, Reno, Nevada, Jan.

Rediniotis, O. K., 1992, "The Transient Development of Vortices Over a Delta Wing," Doctoral Dissertation, VPI & SU, Oct.

Rediniotis, O. K., Hoang, N. T., and Telionis, D. P., 1993, "The Seven-Hole Probe: Its Calibration and Use," (invited paper) Forum on Instructional Fluid Dynamics Experiments, Vol. 152, pp. 21–26, June.

Rediniotis, O. K., 1994, "A Computer-Controlled, Precision Pressure Stan-

dard," presented at the *ASCE Symposium on Fundamentals and Advancements in Hydraulic Measurements and Experimentation,* Buffalo, NY, Aug. 1994.

Schreck, S. J., Faller, W. E., and Luttges, M. W., 1993, "Neural Network Prediction of Three-Dimensional Unsteady Separated Flow Fields," AIAA Paper No. 93-3426-CP, Monterey, CA, Aug.

Schreck, S. J., and Faller, W. E., 1995, "Encoding of Three-Dimensional Unsteady Separated Flow Field Dynamics in Neural Network Architectures," AIAA Paper No. 95-0103, Reno, Nevada, Jan.

Specht, D. F., 1991, "A General Regression Neural Network," IEEE Trans. on Neural Networks, Vol. 2, No. 6, pp. 568–576.

Wang, L.-X., 1994, "Adaptive Fuzzy Systems and Control, Design and Stability Analysis," Prentice Hall, NJ.

Werbos, P. J., 1974, "Beyond Regression: New Tools for Prediction and Analysis in the Behavioral Sciences," PhD Dissertation, Harvard University.

Zilliac, G. G., 1989, "Calibration of Seven-Hole Pressure Probes for Use in Fluid Flows with Large Angularity," NASA TM 102200, Dec.

Wing Section Optimization for Supersonic Viscous Flow

Cem C. Item
Former Graduate Research Assistant.
Mem. ASME

Oktay Baysal
Eminent Scholar and Professor.
Fellow ASME

Department of Aerospace Engineering,
Old Dominion University,
Norfolk, VA 23529-0247

To improve the performance of a highly swept supersonic wing, it is desirable to have an automated design method that also includes a higher fidelity to the flow physics. With this impetus, an aerodynamic optimization methodology incorporating the thin-layer Navier-Stokes equations and sensitivity analysis had previously been developed. Prior to embarking upon the full wing design task, the present investigation concentrated on the identification of effective optimization problem formulations and testing the feasibility of the employed methodology, by defining two-dimensional test cases. Starting with two distinctly different initial airfoils, two independent optimizations resulted in shapes with similar features: cambered, parabolic profiles with sharp leading- and trailing-edges. Secondly, an outboard wing section normal to the subsonic portion of the leading edge, which had a high normal angle-of attack, was considered. The optimization resulted in a shape with twist and camber that eliminated the adverse pressure gradient, hence, exploiting the leading-edge thrust. The wing section shapes obtained in all the test cases included the features predicted by previous studies. This was considered as a strong indication that the flow field analyses and sensitivity coefficients were computed and provided to the present gradient-based optimizer correctly. Also, from the results of the present study, effective optimization problem formulations could be deduced to start a full wing shape optimization.

Introduction

Studies initiated by NASA have identified a growing long-range transport market for a new supersonic airliner. This recent interest in a High Speed Civil Transport (HSCT) has led to renewed research studies for enhanced supersonic configurations. Improving the cruise efficiency of such an aircraft, which can be enhanced by optimizing its wing sections, is vital for its economical viability and environmental acceptability. In the past, several methods have been implemented to obtain the most suitable supersonic profiles. While linearized theory was used to develop the basic concepts, other advanced theories were studied to introduce the non-linear effects, and the critical role of the viscosity for highly swept wings was recognized. Therefore, the present objective is the introduction of the viscous nature of the flow to the supersonic wing design and performing the design process in an automated manner.

Reviewing the designs with linear theory (Drougge, 1965), or second-order theory (Miele and Lusty, 1965), or optimizations with shock-expansion theory (Dutt and Sreekanth, 1979), the following may be concluded: 1) when a thickness constraint is imposed, the optimum shape is a double-wedge profile, whereas using an area constraint leads to a parabolic profile; 2) linear theory results give symmetric profiles with respect to the mid-chord; 3) non-linear effects lead to a slight shift in the maximum thickness location in the flow direction; 4) for all the cases, the maximum thickness location is around the mid-chord, and the leading- and trailing-edges are sharp.

The next step in the wing section optimization has been the introduction of the three-dimensional effects of the flow. Among the significant studies are the conical full potential approach of Pittman (1987) and the modified linearized theory of Mann and Carlson (1994). Recently, three-dimensional inviscid optimizations were performed by Reuther et al. (1992), Burgreen and Baysal (1996), and Pandya and Baysal (1997a). Currently, viscous wing shape optimizations are under investigation (Pandya and Baysal, 1997b).

From this brief survey, it was deduced that as increasingly higher order flow equations were used in the design process, the more supersonic flow physics was introduced to the formulation, which led to more efficient wing shapes. Secondly, as more complex theories were implemented, the design process became prohibitively cumbersome, hence a need for an automated and efficient design methodology was identified.

As an example of how the viscous nature of the flow may affect the wing-section design, one may investigate the leading-edge thrust phenomenon. As indicated by Kulfan and Sigalla (1978) as well as Mann and Carlson (1994), supersonic wing performance is critically dependent upon the development of the leading-edge thrust. This thrust is realized when the leading-edge is subsonic and it is caused by the flow expanding around the leading-edge from the lower-surface stagnation point. This results in a very high suction pressure, a subsequent steep adverse pressure gradient near the leading-edge of the upper surface, and a possible flow separation (Fig. 1). When a separation occurs, the boundary layer leaves the wing surface along a swept separation line and rolls up into a region of concentrated vorticity, which is swept back over the surface of the wing. The formation of the leading-edge vortex affects the lift, pitching moment, and drag on a highly swept wing.

A wing designed to achieve a finite load distribution along the leading-edge is cambered and twisted such that the leading-edges of the wing align with the local flow direction. The attachment line lies along the leading-edge and the expansion over the upper surface is greatly reduced, thereby, eliminating the strong adverse pressure gradient near the leading-edge (Fig. 1). The thrust force on a cambered airfoil is achieved by the action of the reduced expansion pressure on the relatively large *shoulder* area of the airfoil. Also note that, in the analyses of separated flows around swept leading-edge wings, it has been found useful to correlate the data in terms of conditions normal to the leading-edge. The normal angle-of-attack (α_n) is appreciably higher than the wing angle-of-attack (α) for a highly swept wing.

After reviewing the status of the current and past research on supersonic wing design, it was deemed desirable to have an automated design methodology. The development of such a methodology had been initiated by Baysal and Eleshaky (1991, 1992). The present investigation was aimed at achieving the

Contributed by the Fluids Engineering Division for publication in the JOURNAL OF FLUIDS ENGINEERING. Manuscript received by the Fluids Engineering Division February 12, 1996; revised manuscript received October 15, 1997. Associate Technical Editor: M. Sindir.

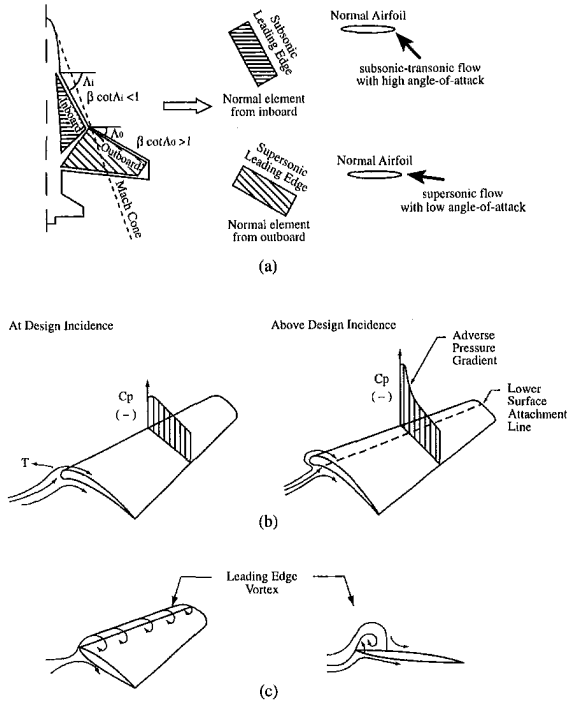

Fig. 1 Leading-edge thrust phenomenon: (*a*) schematic showing a highly swept, cranked-delta wing; (*b*) pressure coefficient distribution along a normal airfoil (inboard) at and above design incidence; (*c*) leading-edge vortex formation

following objectives using only two-dimensional simulations for the sake of cost-effectiveness: 1) perform a supersonic wing section optimization considering the viscous effects of the flow, and investigate possible nontraditional optimum profiles; 2) study an automated optimization leading to designs favoring the leading-edge thrust; 3) suggest initial designs and optimization problem formulations for future, detailed, three-dimensional, viscous, supersonic wing designs; 4) establish the present design method's capability in handling diverse test cases for such problems.

On Methodology

The present aerodynamic design optimization methodology which couples computational fluid dynamics analysis via sensitivity analysis was introduced by Baysal and Elashaky (1992). Its implementation is detailed by Item (1995), so only a brief description is included below. The constrained and gradient-based optimization, as coded in the ADS program (Vanderplaats, 1985), was used and loosely referred to as the optimizer herein. The method of feasible directions for constrained minimization was selected as the optimization technique. The step size, that is, the incremental change in the design variables along the search direction, was kept constant for a better search of the expected nonlinear design space. The univariate searches were concluded by selecting the last design as the best design prior to a constraint violation. The present surface definitions were based on the Bezier-Bernstein parameterization (Burgreen et al., 1994).

The flow field analysis and the evaluation of the objective and the constraints were obtained by solving the thin-layer Navier-Stokes equations. They are solved by an implicit, finite-volume, upwind-biased, approximately factored algorithm (Thomas et al., 1990). The inviscid fluxes were discretized using a flux-vector splitting and MUSCL approach, but the viscous terms were centrally differenced. Initial conditions were chosen to be the free stream conditions. On the airfoil surface, the no-slip, impermeable, and adiabatic conditions were imposed. In the farfield, characteristic boundary conditions were implemented. Since all the cases were computed on multiblock grids, additional interface boundary conditions were needed within the computational domain, where one-to-one correspondence between two sets of cells on either side was forced to ensure the flux continuity. The method was formally up to third-order accurate spatially and first-order accurate temporally.

Regridding en route to the optimized shape was completed using the *flexible grid* approach (Burgreen et al., 1994). Note that during the regridding, grid lines of the same family may inadvertently cross each other due to the inadequate grid parameters or undesirable inflexion points on the surface. In turn, this may cause the computed volume of the corresponding cell to be negative, which will be referred to as the *negative volume problem* herein.

Sensitivity analysis is the quasi-analytical determination of the sensitivity coefficients, which are the derivatives of the objective and the constraints with respect to the design variables (Baysal and Eleshaky, 1991). The adjoint variable method was used to obtain these coefficients. To reduce the computer memory requirements, the sensitivity analysis with domain decomposition technique (SADD), introduced by Eleshaky and Baysal (1994), was employed.

The present study utilized the computer code ADOS, aerodynamic design optimization using sensitivities, (Eleshaky and Baysal, 1997), which included the aforementioned three modules, namely, the flow analysis, the optimizer, and the sensitivity analysis. To perform a shape optimization using ADOS, the user should perform the following preparatory tasks: 1) determine the design variables for the initial geometry, which are the Bezier control points of Bezier-Bernstein definition of the surface (Burgreen et al., 1994); 2) modify the subroutines which require changes based on the particular problem at hand (case dependent subroutines); 3) obtain the initial grid; 4) obtain the converged flow solution; 5) set up the optimization problem with the initial values of the constraints, side constraints, and the step size. The last task plays a pivotal role in determining an optimized shape, and it will be discussed further through the present illustrative cases.

Airfoil Optimization in Purely Supersonic Flow

The first problem (Case 1) was formulated to obtain the optimum airfoil shape for maximum lift-to-drag ratio (cruise efficiency), subject to a maximum allowable drag while attaining a minimum lift. The initial airfoil's thickness-to-chord ratio was selected to be small in order to be able to compare the present results with those from the linearized theory. Then, two optimizations were performed, each starting with a completely different initial profile, so that upon a comparison of the optimized shapes, an assessment could be made for the optimality. Thus, Case 1a was set up for a NACA 0004 airfoil in Mach 2.4 flow with an angle-of-attack of 4.5-deg and a Reynolds number of 2 million. In Case 1b, a biconvex profile with a maximum thickness-to-chord ratio of 4 per cent was optimized under the same flow conditions as in Case 1a.

For both cases, the domains were decomposed into 4 blocks to reduce the memory required for the flow and sensitivity analyses. In order to locate the shocks and other flow characteristics for the given problem, a preliminary 165 × 35 C-type grid was generated with a circular outer boundary surrounding the leading-edge of the profile. Observing the computer flow field, a second grid was created, with equal number of cells but with the outer boundary moved in to be just a few cells upstream of the bow shock. The distance from the leading edge and the trailing edge to the outer boundary was one-half chord and three chords, respectively. This grid was clustered normal to the airfoil surface to capture the boundary layer, and further clustered where the shocks were expected. Block boundaries were at the leading and trailing-edges of the profile (Item, 1995).

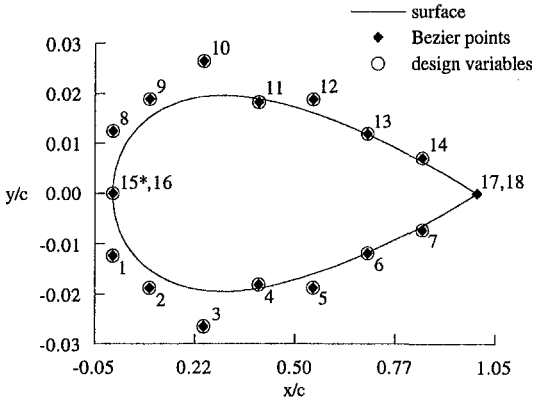

Fig. 2 Initial geometry and surface representation of NACA 0004 Airfoil (*used in Case 2 only)

To parameterize the airfoil, 9 Bezier points were used for the upper surface and another nine Bezier points were for the lower surface (Fig. 2). The leading- and trailing-edge Bezier points from each surface were fixed to avoid the conceivable crossing of the surfaces and to fix the angle-of-attack during the optimization. Hence, 14 design variables were allowed to modify the profiles. The side constraints were imposed rather liberally resulting in a rather large design space. The side constraints for both the upper and the lower surface Bezier points were set to 0.5 and −0.5 of the normalized chord length, respectively, while the Bezier points next to the leading edge (1st and 8th) were not permitted to move into the opposite region. This type of set up was critical in mitigating the negative volume problems in grid regeneration during optimization process.

Starting With a NACA 0004 Airfoil. The geometric constraints were imposed on the trailing-edge angle (`teang`) as well as the maximum thickness (`tmax`) to avoid converging to trivial and non-practical shapes, such as, a flat plate airfoil. Although the thickness was constrained, the `tmax` location, `xtmax`, along the chord was not. This permitted the optimizer to determine the maximum thickness location freely along the chord, which turned out to be a vital flexibility of the design process.

The convergence criterion (three consecutive iterations with a maximum absolute change of 0.001 in the objective function) was met after 49 optimization iterations, which included 6 gradient updates (each with a sensitivity analysis and a flow analysis) and 43 univariate searches (only flow analysis updates). This required 2.18 CPU hours and 12.6 Megawords of memory on a Cray Y-MP computer. Each of the sensitivity analyses required 126.5 CPU seconds while each of the flow analyses required 107.6 CPU seconds. A flow analysis was deemed converged when the L_2-norm of the residual was of 10e-6 order of magnitude. The path to the optimized profile, as sampled in Fig. 3, can be interpreted as follows. As the initial design was in the infeasible domain, during the initial 14 univariate searches, the optimizer sought a search direction to satisfy the given lift constraint, by lowering the upper surface to further incline the bow shock over the upper surface while cambering the lower surface to further compress the flow. Then, the optimizer determined another search direction to reduce the now increased drag value. As the thickness constraint became active, the optimizer further shifted the maximum thickness location along the chord which, in fact, decreased the drag even further. The optimized shape had a slightly thicker parabolic profile with sharp leading and trailing edges. The maximum thickness lied near but not at the mid-chord (`xtmax` = 0.4304).

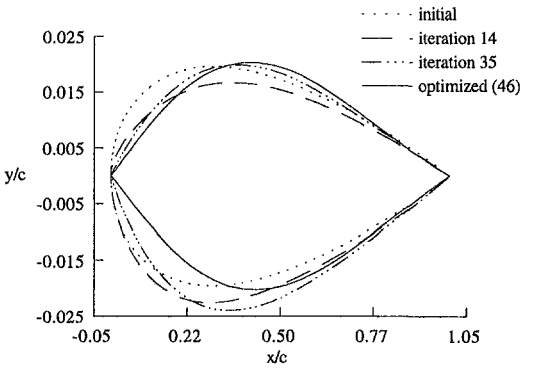

Fig. 3 Surface history for Case 1a (supersonic leading edge)

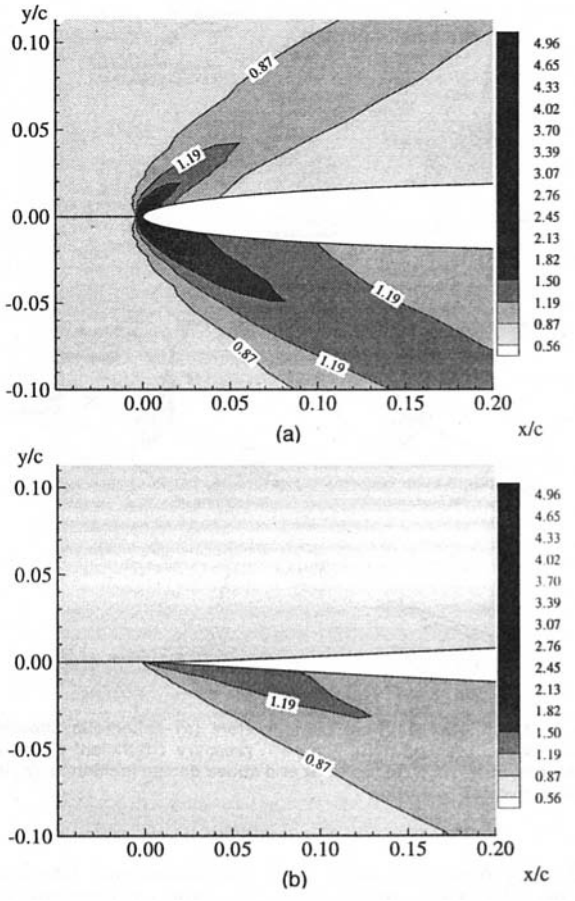

Fig. 4 Normalized pressure contours around the leading edge for Case 1a: (*a*) initial profile; (*b*) final profile

It was observed that near the leading edge, the large compression on the lower surface was largely reduced, and the expansion on the upper surface was slightly increased. A comparison of the initial and final flow fields can be made through their normalized pressure contours presented in Fig. 4. The initial flow field showed the detached bow shock weakening as it inclined around the leading edge. As the leading edge angle was reduced to decrease the wave drag, the leading edge shock angle was also reduced so it became attached, hence much weakened in its strength. The changes in the flow properties are shown in Table 1. The increase in the lift-to-drag ratio was achieved primarily by decreasing the drag. Also, the pressure drag ($C_{d,p}$) contributed more than the skin-friction drag ($C_{d,s}$) to the total drag decrease.

Comparing the optimized shape with the linear (Drougge, 1965), the nonlinear (Miele and Lusty, 1965), and the shock expansion theory (Dutt and Sreekanth, 1979) designs, a good agreement was observed: 1) maximum thickness around mid-

Table 1 Optimization results from Case 1a (supersonic leading edge)

	Initial	Constraint	Optimized	Change
C_l/C_d	4.9444	-	7.9054	+59.88%
C_l	0.1431	≥ 0.1460 V	0.1460	+2.03%
C_d	0.0289	≤ 0.0300 I	0.0185	-35.99%
$C_{d,p}$	0.0263	-	0.0157	-40.30%
$C_{d,s}$	0.0026	-	0.0028	+7.69%
TE angle	0.0942	≥ 0.0170 I	0.0796	-15.50%
tmax	0.0391	≥ 0.0390 A	0.0405	+3.58%
xtmax	0.3074	-	0.4303	0.1229

A: active I: inactive V: violated (All with respect to their initial values)

chord; 2) sharp leading and trailing edges; 3) only slightly cambered. Note that, unlike all the cited prior investigations, which had sharp edged profiles as their initial designs, the present case started with a blunt edge, and automatically converged to a sharp leading edge profile. Therefore, it was deemed that the function evaluations via the flow analyses and the gradients via the sensitivity analyses, were accurately provided to the optimizer, resulting in the effective search directions that led to the optimized profile.

Starting With a Biconvex Airfoil. In Case 1b, the optimizer started with an initial design which was aerodynamically much more efficient than the previous blunt leading-edge case. Two new constraints were introduced into the optimization process. A minimum profile area (area) was specified to replace the maximum thickness (tmax) constraint (commonly used in the prior supersonic optimization studies). After witnessing the decreasing trend of the leading edge angle in Case 1a, a constraint was imposed on the minimum leading edge angle.

Since the selection of the initial shape and the constraints was pivotal in attaining a fast convergence to an optimal shape, several variations in the problem definition were tried, where the profile area and the thickness constraint were examined interchangeably (Fig. 5). Different combinations of starts with violated and active constraints for the initial design were used to examine several search directions. Note that the result from the tmax > 0.039 formulation coincides with the initial shape. Basically, the optimizer always tried to reduce the thickness of the profile within the limits of the geometric constraints. As it can be deduced from Figs. 3 and 5, the main difference in the optimized shapes obtained from the two cases (Cases 1a and 1b) is the location of the maximum thickness, xtmax. The optimizer did not shift the tmax exactly to the mid-chord in Case 1a, while in Case 1b, it achieved the objective by reducing tmax without shifting xtmax from the mid-chord. This aspect of the present results was verified by Fiecke (1979): when

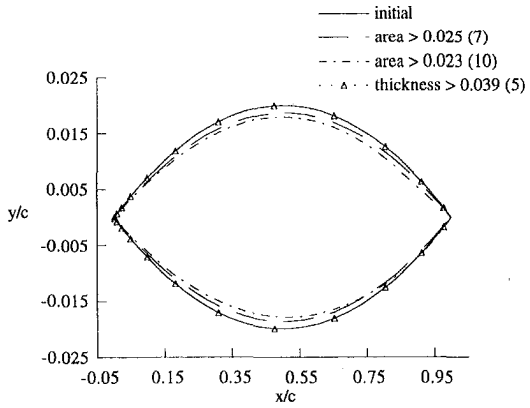

Fig. 5 Optimized shapes obtained in Case 1b (supersonic leading edge) using various area or thickness constraints. The number of optimization iterations are indicated parenthetically.

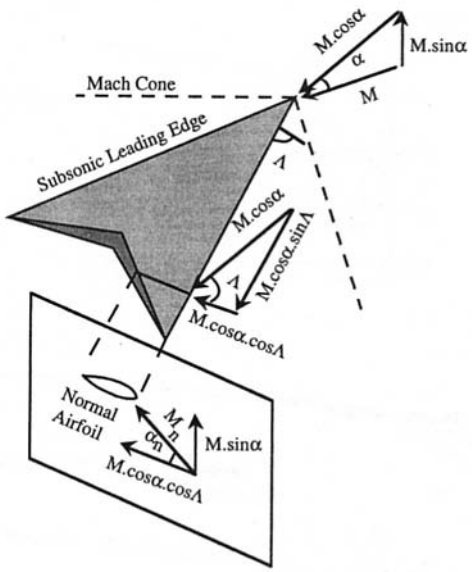

Fig. 6 Schematic showing the simplification of a 3-D wing problem to an assumed equivalent 2-D problem

xtmax was away from the mid-chord, any slight change in xtmax caused a dramatic change in the wave drag; on the other hand, around the mid-chord, wave drag was almost insensitive to the variation in xtmax. Hence, further confidence was achieved in the present optimizations through comparisons with Fiecke's studies on supersonic wing sections.

Airfoil Optimization With Inferred Leading-Edge Thrust Increase

As discussed in the Introduction section, the flow is vulnerable to separation near the leading edge of a highly swept supersonic wing, where the normal Mach number (M_n) is subsonic and the normal angle-of-attack (α_n) is high. In order to study this phenomenon by two-dimensional means for cost-effectiveness, the normal section in the middle of the right half-span (Fig. 6) was chosen, where the wing root and wing tip effects were expected to be minimal. Consequently, the spanwise flow and the related upwash were omitted. Then, an effective normal angle-of-attack was estimated from geometric arguments (Fig. 6). Note that the main issue in this study was the reduction of the circumstances which set the stage for the flow separation. That is, the optimizer should automatically detect the adverse pressure gradients due to extensive expansion around the leading-edge, hence improve the cruise efficiency. Thus, positioning the stagnation point on the lower surface then expanding the flow around the leading edge was deemed sufficient to examine the problem for the arguments set forth for the present study.

A NACA 0004 airfoil was selected as the initial normal section. Then, starting with an arbitrarily picked Mach number (M) of 2.45, an angle-of-attack (α) of 3.5-deg, and a sweep angle (Λ) of 69.7-deg, the normal Mach number (M_n) and the normal angle-of-attack (α_n) were computed to be 0.85 and 10-deg, respectively. The Reynolds number was chosen to be one million based on the chord length. A C-type grid with 125 × 33 cells was generated. The outer boundary was pushed eight chord lengths from the surface to accommodate the transonic flow problem at hand. The domain was again decomposed into 4 blocks.

As predicted by the steady-state solution, the flow characteristics of the initial section were as initially desired: the stagnation point at the lower surface resulting in a very low pressure bubble near the leading-edge. Although the flow did not separate on the upper surface, a threshold for the separation was clearly

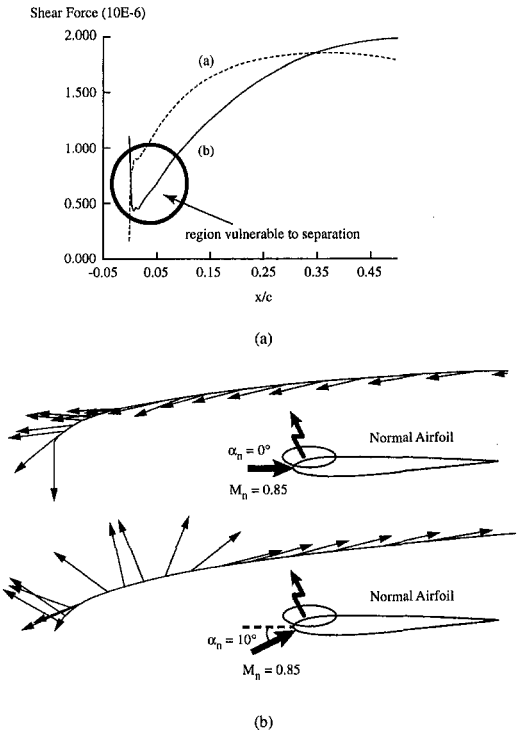

Fig. 7 Effect of normal angle of attack on the separation vulnerability. Comparison of, (*a*) shear force distributions, (*b*) pressure gradient distributions.

achieved. This was loosely called the separation vulnerability herein, and demonstrated through the distributions of the shear force and the pressure gradient along the surface (Fig. 7). To establish a reference point, the shear force distribution of the zero angle-of-attack flow was superimposed. In the 10-deg case, the shear force on the upper surface sharply plunged to almost zero from its initial value at the leading edge, whereas in the 0-deg case, it continuously increased from its minimum value at the leading-edge (stagnation point). Comparing the pressure gradients of these flows further explained the separation vulnerability; the gradient became an adverse one as the airfoil was pitched from zero to 10-deg angle of attack (Fig. 7).

The objective function was again selected as the lift-to-drag ratio. The constraints were set as a maximum allowable drag while attaining a specified minimum lift. The geometric constraints were posed as the minimum values for the trailing-edge angle (`teang`) and the thickness (`tmax`). The Bezier-Bernstein surface representation shown in Fig. 2 was again implemented in this case. In addition to the 14 Bezier points selected as design variables, another design variable was needed to give the profile the freedom to align itself with the local flow direction. Thus, the fifteenth design variable was chosen as the Bezier point at the leading-edge. This flexibility allowed for twist as well as additional camber to the profile. The upper and lower side constraints were chosen to be -0.1 and 0.1, respectively, for all the design variables except for the fifteenth design point, which was given a smaller design space. Further details are given by Item (1995).

It should be noted that the side constraint definitions and grid quality are two important factors for getting a smooth optimization surface modification. For inviscid grids, there usually is ample width of a cell to accommodate the surface perturbation without distorting the integrity of a nearby cell. This, however, may not be the case with highly clustered viscous grids, necessitating some additional care in generating the initial grid. The same may be true for the regridding during the shape evolution. For example, it helped to modify the original flexible grid approach (Burgreen et al., 1994), so that both ends of a given grid line normal to the surface were allowed to move.

The convergence criterion was satisfied after 36 optimization iterations, which included 5 gradient updates and 31 univariate searches. This required 1.53 CPU hours and 10.8 Megawords of memory on a Cray Y-MP computer. Each of the sensitivity analyses required 80.1 CPU seconds while each of the flow analyses required 84.8 CPU seconds. The surface evolution for this case is shown in Fig. 8. The optimizer evaluated the first search direction based on the objective function and all but the trailing-edge angle constraint. The leading-edge started to shift downward to align the upper surface with the oncoming flow, while the curvature of the lower surface near the trailing edge was changed to further compress the flow. As the thickness constraint became active, the optimizer thickened the profile without changing `xtmax` along the chord. The optimized shape was a slightly thicker section with a negative twist and supercritical (Burgreen and Baysal, 1994, and Lacasse and Baysal, 1994) tendencies as far as the lower surface camber. It was seen from the pressure distribution (Fig. 9), that the high suction region on the upper surface was reduced by the drooped leading-edge. The compression on the lower surface near the trailing-edge was also increased. By and large, this shape is in agreement with the wing sections obtained by Mann and Carlson (1994) and Carlson et al. (1996).

Comparing the normalized pressure distributions for the initial and optimized shapes (Fig. 10), the following observations were made. For both geometries, the flow along the upper surface was supersonic, which adjusted to the freestream conditions and compressed through a trailing-edge shock. The low pressure bubble on the upper surface of the initial geometry, resulting from the high expansion around the leading-edge, was totally eliminated after the optimization. The negative twist and camber of the optimized shape led to a rather gradual expansion. Also, on the lower surface, the high pressure region was further extended to the trailing edge point resulting in increased lift. The initial and final values of the objective function and the constraints are listed comparatively in Table 2. As the result of the shape optimization, the lift and the cruise efficiency were both increased and the total drag was decreased.

Conclusions

A recently developed aerodynamic design optimization methodology was applied and tested for its feasibility in producing viscous, supersonic wing sections. The slightly cambered, parabolic profiles with sharp leading and trailing edges obtained (in Cases 1a and 1b) were in good agreement with the sections obtained by prior investigations. When a sharp edged section was used as the initial design (Case 1b), no considerable change in the profile was observed (reduced tmax without shifting xtmax). Despite the fact that the starting designs were vastly different, the final shapes obtained from the two independent shape optimizations (in Cases 1a and 1b) were similar in most

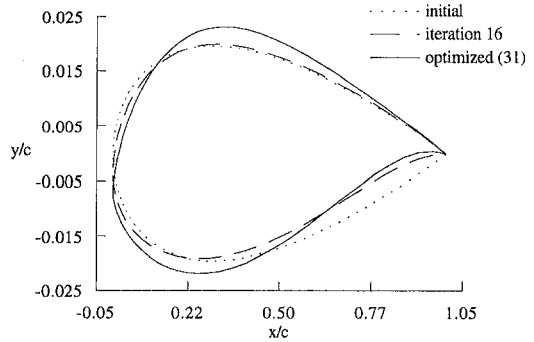

Fig. 8 Surface history for Case 2 (subsonic leading edge)

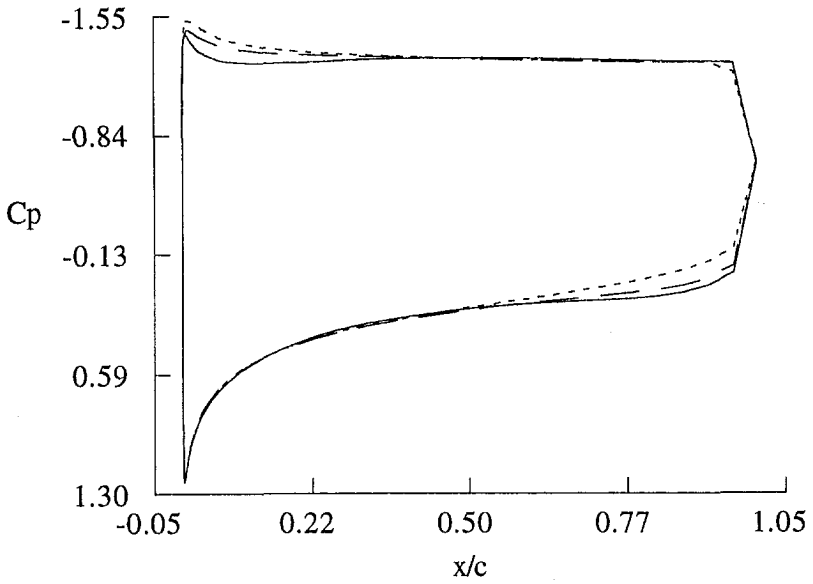

Fig. 9 Pressure coefficient history for Case 2 (subsonic leading edge). Legend shown in Fig. 8.

of their salient features. This was considered as a strong indication that the analysis and gradient information were accurately fed into the optimizer, and the final shapes were optimal.

As a result of a successful optimization problem formulation in Case 2, the optimizer drooped the leading edge and changed the curvature on the lower surface near the trailing edge. This trend was verified by the previous nonautomated design approaches, where the flow separation at the subsonic leading edge of a highly swept supersonic wing was also avoided by introducing a twist and a camber near the leading edge (by drooping the leading edge to reduce the adverse pressure gradient along the upper surface). The distinguishing merit of the present result, however, was the fact that it was achieved by an automated methodology without the intervention of an aerodynamicist having a priori knowledge of the expected flowfield.

On the other hand, the present study also demonstrated the possible difficulties in solving such optimization problems and rendered the opportunity to devise some remedies. It was observed that, when the viscous effects were included in the design process, the grid quality and the side constraint definitions had accentuated importance. The results obtained so far showed that the present design methodology was robust and would potentially be a good candidate to obtain aerodynamically efficient wing shapes. Subsequently, a three-dimensional, viscous, supersonic wing shape optimization has been pursued by Pandya and Baysal (1997b).

Table 2 Optimization results from Case 2 (subsonic leading edge)

	Initial	Constraint	Optimized	Change
C_l/C_d	5.3144	-	5.5869	+5.13%
C_l	1.5102	≥ 1.500 A	1.5326	+1.48%
C_d	0.2842	≤ 0.286 A	0.2743	-3.48%
$C_{d,p}$	0.2782	-	0.2684	-3.52%
$C_{d,s}$	0.0059	-	0.0060	+1.69%
TE angle	0.0910	≥ 0.035 I	0.0358	-60.66%
tmax	0.0391	≥ 0.039 A	0.0445	+13.81%
xtmax	0.2857	-	0.2857	0.00%

A: active I: inactive (All with respect to their initial values)

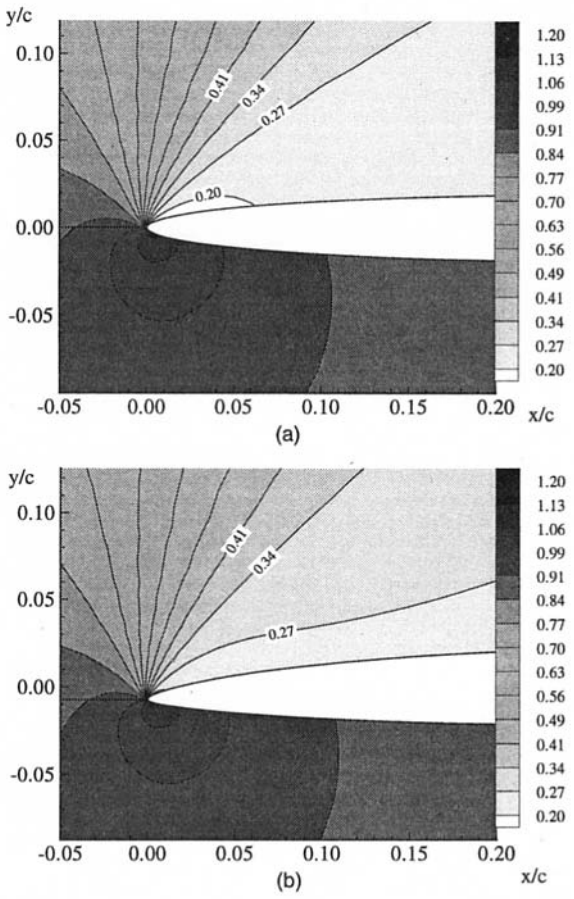

Fig. 10 Normalized pressure contours around the leading edge for Case 2 (subsonic leading edge): (*a*) initial profile; (*b*) final profile

Acknowledgment

This research was supported by NASA Langley Research Center under Grant NAG-1-1576. The technical monitor was Dr. J. M. Luckring.

References

Baysal, O., and Eleshaky, M. E., 1991, "Aerodynamic Sensitivity Analysis Methods for the Compressible Euler Equations," ASME JOURNAL OF FLUIDS ENGINEERING, Vol. 113, pp. 681–688.

Baysal, O., and Eleshaky, M. E., 1992, "Aerodynamic Design Optimization Using Sensitivity Analysis and Computational Fluid Dynamics," *AIAA Journal,* Vol. 30, No. 3, pp. 718, 725.

Burgreen, G. W., and Baysal, O., 1994, "Aerodynamic Shape Optimization Using Preconditioned Conjugate Gradient Methods," *AIAA Journal,* Vol. 32, No. 11, pp. 2145–2152.

Burgreen, G. W., and Baysal, O., 1996, "Three-Dimensional Aerodynamic Shape Optimization Using Discrete Sensitivity Analysis," *AIAA Journal,* Vol. 34, No. 9, pp. 1761–1770.

Burgreen, G. W., Baysal, O., and Eleshaky, M. E., 1994, "Improving the Efficiency of Aerodynamic Shape Optimization Procedures," *AIAA Journal,* Vol. 32, No. 1, pp. 69–76.

Carlson H. W., McElroy, M. O., Lessard, W. B., and McCullers, L. A., 1996, "Improved Method for Prediction of Attainable Wing Leading Edge Thrust," NASA TP-3557, National Aeronautics and Space Administration, Washington, D.C.

Drougge, G., 1965, "Two-Dimensional Wings of Minimum Pressure Drag," *Theory of Optimum Aerodynamic Shapes,* Chapter 5, Miele A., ed., Academic Press, New York/London.

Dutt, H. N. V., and Sreekanth, A. K., 1979, "Design of Supersonic Airfoils by Numerical Optimization," *Computer Methods in Applied Mechanics and Engineering,* No. 19, pp. 417–427.

Eleshaky, M. E., and Baysal, O., 1994, "Discrete Aerodynamic Sensitivity Analysis on Decomposed Computational Domains," *Journal of Computers and Fluids,* Vol. 23, No. 4, pp. 595–611.

Eleshaky, M. E., and Baysal, O., 1997, "Shape Optimizing Nacelle Near Flat-Plate Wing Using Multiblock Sensitivity Analysis," *Journal of Aircraft,* Vol. 35, No. 1, pp. 33–38.

Fiecke, D., 1979, *Aerodynamics of the Airplane,* Schlichting, H., Truckenbrodt, E., Ramm, H. J., eds., McGraw-Hill, pp. 242–243.

Kulfan, R. M., and Sigalla, A., 1978, "Real Flow Limitations in Supersonic Airplane Design," AIAA Paper 78-147.

Item, C. C., 1995, "Wing-Section Optimization for Supersonic Viscous Flow," M.S. thesis, Aerospace Engineering Department, Old Dominion University, Norfolk, VA.

Lacasse, J. M., and Baysal, O., 1994, "Shape Optimization of Single- and Multi-Element Airfoils on Blocked Grids," AIAA Paper 94-4273 CP, *Proceedings of 5th AIAA/USAF/NASA/ISSMO Multidisciplinary Analysis and Optimization Conference,* Panama City, FL, pp. 108–116. To appear in *Inverse Problems in Engineering.*

Mann, M. J., and Carlson, H. W., 1994, "Aerodynamic Design of Supersonic Cruise Wings with a Calibrated Linearized Theory," *Journal of Aircraft,* Vol. 31, No. 1, pp. 35–41.

Miele, A., and Lusty, A. H., 1965, "Second-order Theory for Optimum Two-Dimensional Wings," *Theory of Optimum Aerodynamic Shapes,* Chapter 9, Miele, A., ed., Academic Press, New York/London.

Pandya, M. J., and Baysal, O., 1997a, "Gradient-Based Aerodynamic Shape Optimization Using ADI Method for Large-Scale Problems," *Journal of Aircraft,* Vol. 34, No. 3, pp. 346–352.

Pandya, M. J., and Baysal, O., 1997b, "3D Viscous ADI Algorithm and Strategies for Shape Optimization," Paper No. 97-1853 CP, *Proceedings of AIAA 13th CFD Conference,* Snowmass, CO, pp. 217–226.

Pittman, L. J., 1987, "Supersonic Airfoil Optimization," *Journal of Aircraft,* Vol. 24, No. 12, pp. 873–879.

Reuther, J., Cliff, S. E., Hicks, R. M., and van Dam, C. P., 1992, "Practical Design Optimization of Wing-Body Configurations using the Euler Equations," AIAA Paper 92-2633.

Thomas, J. L., Krist, S. T., and Anderson, W. K., 1990, "Navier-Stokes Computations of Vortical Flows Over Low Aspect Ratio Wings," *AIAA Journal,* Vol. 28, No. 2, pp. 205–215.

Vanderplaats, G. N., 1985, "ADS-A FORTRAN Program for Automated Design Synthesis," NASA CR-177985, National Aeronautics and Space Administration, Washington, D.C.

Combustors for Micro-Gas Turbine Engines

Ian A. Waitz
Associate Professor,
Massachusetts Institute of Technology,
Gas Turbine Laboratory,
Cambridge, MA 02139

Gautam Gauba
Consultant,
Arthur D. Little Inc.,
Cambridge, MA 02140

Yang-Sheng Tzeng
Graduate Research Assistant,
Massachusetts Institute of Technology,
Gas Turbine Laboratory,
Cambridge, MA 02139

The development of a hydrogen-air microcombustor is described. The combustor is intended for use in a 1 mm² inlet area, micro-gas turbine engine. While the size of the device poses several difficulties, it also provides new and unique opportunities. The combustion concept investigated is based upon introducing hydrogen and premixing it with air upstream of the combustor. The wide flammability limits of hydrogen-air mixtures and the use of refractory ceramics enable combustion at lean conditions, obviating the need for both a combustor dilution zone and combustor wall cooling. The entire combustion process is carried out at temperatures below the limitations set by material properties, resulting in a significant reduction of complexity when compared to larger-scale gas turbine combustors. A feasibility study with initial design analyses is presented, followed by experimental results from 0.13 cm³ silicon carbide and steel microcombustors. The combustors were operated for tens of hours, and produced the requisite heat release for a microengine application over a range of fuel-air ratios, inlet temperatures, and pressures up to four atmospheres. Issues of flame stability, heat transfer, ignition and mixing are addressed. A discussion of requirements for catalytic processes for hydrocarbon fuels is also presented.

1 Introduction

Micromachining of silicon and refractory ceramics is enabling the development of a new class of miniature devices including micromotors, microvalves, pressure transducers, microaccelerometers, and numerous others (Bryzek et al., 1994). Arguably one of the most challenging and innovative endeavors being pursued in this area is the development of microscale turbomachines as described by Epstein et al. (1995). These devices include micromotor compressors, micro-turbine generators, micro-gas turbines, microrefrigerators, and micro-rocket engines. Several of these heat engine applications require conversion of chemical energy to kinetic and thermal energy, and thus it is necessary to develop combustion strategies suitable for use in these miniature devices.

The objective of this paper is to elucidate many of the challenges and opportunities associated with combustion in small volumes, and to offer possible strategies for microcombustion systems. Following a brief overview of micro-gas turbine technology in Section 1.1, the specific challenges and opportunities for microcombustor development are discussed in Section 1.2. Two viable microcombustion alternatives are presented in Section 2: the first based upon hydrogen-air combustion (Section 2.2.1), and the second upon a catalytic hydrocarbon-air reaction (Section 2.2.2). Results from experiments in a full-scale microcombustor are presented in Section 3 to provide a first proof-of-concept demonstration. The paper ends in Section 4 with a summary, conclusions and recommendations for future research.

1.1 Overview of Microengine Technology. The primary motivation for the work described in this paper is the development of micro-gas turbine generators capable of producing 10-100 watts of electrical power while occupying less than 1 cm³ and consuming approximately 7 grams of jet fuel per hour. If such a device is successfully developed, it will possess an energy density 10 times that available from the best existing batteries. Feasibility studies, preliminary designs, and performance estimates have been discussed in detail by Epstein et al. (1995) and Groshenry (1995). In this section, we present only a short review of the technology in order to establish the design goals and constraints for a microcombustor.

Microengine technology has been enabled by the advent of micromachining processes for refractory, structural ceramics such as silicon nitride (Si_3N_4) and silicon carbide (SiC). These materials have excellent mechanical, thermal, and chemical properties for hostile environment applications, and indeed have been the focus of several development efforts for larger-scale devices (Nakazawa et al., 1996; Measley and Smyth, 1996; Tanaka et al., 1996). Components manufactured from these materials can survive uncooled operation at temperatures as high as 1750 K (Tanaka et al., 1996; The Carborundum Company, 1989). Therefore, use of these materials for a micro-gas turbine engine insures sufficient power per unit air flow to allow for useful power output despite the fact that individual component performances are likely to be below those of larger machines. Further, millimeter-size parts can be fabricated with 1–2 micron tolerances using micromachining processes (Juan et al., 1996), providing a dimension-to-tolerance ratio that is competitive with larger-scale turbomachinery components. Micromachined parts however, are typically limited to extrusions of two-dimensional shapes, thus the geometries are somewhat rudimentary when compared to their larger counterparts.

An example of a micro-gas turbine design is shown in Fig. 1. The overall dimensions of the device are roughly 1 cm in diameter and 3 mm in height. This design is the result of a preliminary analysis for an engine geometry and layout that are compatible with individual component characteristics and constraints of micromachining technology. Thus the design embodies trade-offs between power output requirements, cycle parameters, material limitations, physical dimensions and manufacturing processes. The device consists of a radial flow compressor and a radial flow turbine mounted on the same shaft and separated by a combustor. An integral electrostatic induction generator is located on the top face of the compressor shroud. The combustor is the largest component of the engine.

The characteristics of the micro-gas turbine are summarized in Table 1; the device is a factor of 500 smaller than conventional gas turbine engines. Preliminary analyses by Epstein et al. (1995) suggest that such a machine operating at a tip speed of 500 m/s, with a compressor pressure ratio of 4.5:1 and a

Contributed by the Fluids Engineering Division for publication in the JOURNAL OF FLUIDS ENGINEERING. Manuscript received by the Fluids Engineering Division October 14, 1996; revised manuscript received September 11, 1997. Associate Technical Editor: Wing-Fai Ng.

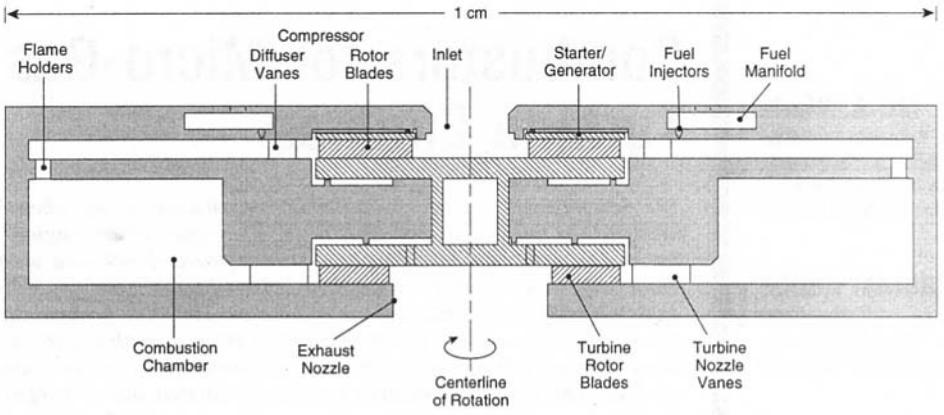

Fig. 1 Schematic of a micro-gas turbine and electrical generator

turbine inlet temperature of 1600 K, may be capable of producing 10-20 watts for a canonical inlet area of 1 mm^2.

The overall goal is to develop a complete microengine system that is contained within a volume on the order of 1 cm^3. Before such a device can be realized however, many difficulties must be overcome. Micro-gas turbines and other applications of this technology are not simply scaled-down larger machines. The small size and constraints on fabrication and testing pose many challenges: the surface area-to-volume ratio is increased, viscous effects are more important, time-scales are shorter, and the range of three-dimensional shapes that can be fabricated is limited. All of these effects either directly or indirectly impact the selection and development of appropriate combustion strategies for a microengine.

1.2 Challenges and Opportunities for Microcombustor Development. The functional requirements of a microcombustor are similar to those of a typical gas turbine combustor. Primarily, chemical energy must be converted into thermal and kinetic energy with high efficiency and low total pressure loss. In addition, there are requirements for introduction and mixing of fuel and oxidizer, reliable and smooth ignition, wide flammability limits so the flame stays lit over a range of operating conditions, low pollutant emissions, and freedom from combustion instabilities. Likewise, the principal constraints on microcombustor design mirror those of the larger-sized counterpart, including the maintenance of low-stressed, cooled structures, minimal weight, and an overall shape and size that are compatible with the rest of the engine layout.

A comparison between design parameters of a conventional gas turbine combustor and those of a microcombustor are shown in Table 2. The parameters listed for the conventional combustor are representative of a modern 30:1 pressure ratio gas turbine engine. The estimates cited for the microcombustor were obtained by making conservative assumptions about achievable performance and size of a microengine operating with a total pressure ratio of 4.5:1. Compared to the larger-scale device, the size of the microcombustor has been reduced by a factor of 100 and the volume by over 6 orders of magnitude. The space heating rate is 10 times larger than that of current technology aircraft gas turbine combustors.

The differences between design parameters listed in Table 2 for the micro and conventional applications are largely due to the reduction in scale, but are also influenced by the relative size of the combustor with respect to the engine, the cycle pressure ratio, and material temperature limitations. These effects are discussed in greater detail in the following sections.

1.2.1 Shorter Residence Time for Mixing and Combustion. The most significant and technically challenging aspect of a microcombustor is its limited residence time. If the dimensions of a conventional engine were to be reduced by a factor of 500, while maintaining the same mass flow rate per unit area, then the flow residence time within the combustor would be approximately 0.05–0.1 ms. This is on the same order as the characteristic chemical kinetic time scale for hydrocarbon-air reactions (0.01–0.1 ms). Thus for the microengine, it will be necessary to increase the relative size of the combustor compared to the engine.

The required increase in relative combustor size can be approximated using a simplified scaling for combustor residence time given by Kerrebrock (1992)

$$\tau_{res} \propto \frac{L \cdot (A_b/A_2) \cdot \pi_c^{1/\gamma}}{\dot{m}/A_2} \tag{1}$$

Nomenclature

A_2 = compressor flow area
A_b = combustor cross-sectional area
A_c, A_h = pre-exponential factors for reaction rates
A_s = surface area [m^2]
C_p = specific heat at constant pressure [J/kg·K]
d_h = hydraulic diameter [m]
Da_c = catalytic Damkohler number
Da_h = homogeneous Damkohler number
E'' = rate of energy/heat flux [W]
$\dot{E}$ = rate of energy/heat generation [W]
h = convective heat transfer coefficient [W/m^2·K]
J_D = mass transport number
J_H = heat transport number
k = thermal conductivity [W/m·K]
L = length [m]
$\dot{m}_a$ = air flow rate [kg/s]
$\dot{m}_f$ = fuel flow rate [kg/s]
Nu_d = Nusselt number based on diameter
$\dot{Q}$ = volumetric rate of energy/heat generation [W/m^3]
Q_f = fuel heating value [J/kg]
Re_d = Reynolds number based on diameter
T = flow temperature [K]
T_w = wall temperature [K]
T_{T3} = compressor exit temperature [K]
T_{T4} = turbine inlet temperature [K]
V_o = reference velocity [m/s]
Vol = volume [m^3]
α = mass transfer coefficient [m/s]
η = combustor efficiency
π_c = compressor pressure ratio
γ = ratio of specific heats
ρ_o = reference density [kg/m^3]
τ_{res} = combustor residence time
ϕ = equivalence ratio

Table 1 Performance estimates for a micro-gas turbine engine

Type	Single spool turbojet/turbogenerator
fuel	H_2
recuperator	No
engine weight	1 g
inlet area	1 mm^2
air flow rate	0.2 g/s
pressure ratio	4.5:1
turbine inlet temperature	1600 K
power output (electrical)	10–20 W
thrust (as turbojet)	0.1~0.2 N
fuel consumption	7 g/hr
specific fuel consumption	0.45 kg/kW · hr
thrust/wt	20:1
energy/air flow	84 J/g

Note that either the length or the area of the microcombustor must be enlarged by a factor of 4 solely to account for the reduced pressure ratio of the cycle (4.5:1 compared to 30:1 for the conventional application), for fixed mass flow per unit area. It will require a further ten-fold increase in either microcombustor length or area to raise the combustor residence time by a factor of 10. This will result in a residence time of 0.5 to 1 ms which is several times larger than the chemical time scale. Therefore, if a full-sized engine is scaled down by a factor of 500, the volume of the microcombustion chamber must grow relative to the engine by a factor of approximately 40 to provide sufficient residence time for complete reaction. Even after this factor of 40 increase, the entire microengine can still be contained in less than 1 cm^3 volume.

Note, however, that the residence time in conventional gas turbine combustors is not driven primarily by the reaction rate. Rather it is governed by requirements for fuel-air mixing as well as dilution with air to reduce the flow temperature and meet efficiency and emissions requirements. Indeed, of the typical 5–8 ms combustor residence time in a conventional gas turbine, approximately 3–5 ms is devoted to fuel vaporization and mixing, and about 2–3 ms to mixing of dilution air (Dodds and Bahr, 1990; Lefebvre, 1983). Thus if conventional combustion strategies are adopted for the microengine application, augmenting the fuel-air mixing rate will be necessary.

1.2.2 Heat Losses Due to the High Surface-to-Volume Ratio. Energy loss due to heat transfer at the walls of the combustion chamber is typically neglected in the design of conventional gas turbine engines. However, for the combustor designs presented in Table 2, the surface area-to-volume ratio, which is proportional to the inverse of the hydraulic diameter, increases from 3–5 m^{-1} for the large-scale combustor to 500 m^{-1} for the microcombustor, and thus heat transfer losses may pose a significant problem.

The effects of surface heat loss on combustion have been investigated in several studies. In premixed gases, flame extinction occurs when the amount of heat liberated by combustion, minus the heat transferred from the gas, no longer exceeds the amount needed to ignite the mixture (Dodds and Bahr, 1990; Ballal and Lefebvre, 1979). Studies of premixed combustion in flame tubes (Zeldovich et al., 1990; Zamaschikov, 1995) have shown that if the inner diameter of a flame tube is less than some critical size, heat transfer from the flame front to the tube wall quenches the reaction. Below this critical diameter, a combustion wave can only be stabilized through external heating of the tube wall.

For a combustor, the ratio of surface heat transfer losses to total heat released in the combustion process can be written as

$$\frac{E''}{\dot{E}} = \frac{A_s h(T - T_w)}{Vol \cdot \dot{Q}} \tag{2}$$

For given fuel, equivalence ratio, inlet temperature, and pressure, the energy per unit volume released in the combustion process, $\dot{Q}$, is constant. Since the dependence of Nusselt number on Reynolds number differs between the flow regimes of a conventional combustor and a microcombustor, the turbulent flow case, which is more sensitive to Reynolds number

$$\mathrm{Nu}_d \propto \sqrt[5]{\mathrm{Re}_d^4} \tag{3}$$

is adopted for both flow conditions. As a result, the convective heat transfer coefficient

$$h = \frac{k \cdot \mathrm{Nu}_d}{d_h} \tag{4}$$

is inversely proportional to the fifth root of the hydraulic diameter. Finally, if the temperature difference between the wall and the flow is assumed to be roughly equal for the two combustors, then the ratio of heat lost to that generated would scale with the hydraulic diameter as follows:

$$\frac{E''}{\dot{E}} \propto \frac{1}{d_h^{1.2}} \tag{5}$$

The hydraulic diameter of the microcombustor is on the order of 2 mm, several hundred times smaller than that of a conventional gas turbine combustor. Thus the ratio of heat lost to heat generated will be about 2 orders of magnitude greater than that of typical combustors. This is likely to influence the performance of a microcombustor in two ways: 1) typical large-scale combustor efficiencies of greater than 99.9 percent may not be feasible due to the significant surface heat transfer losses, and 2) flammability limits are likely to be affected because of flame quenching.

1.2.3 Use of Refractory Structural Ceramics. A noteworthy item listed in Table 2 is the maximum material temperature allowable for each application: 1200 K for uncooled structures in current gas turbines, and approximately 1600 K for the structural refractory ceramics targeted for use in micro-gas turbine engines. The increase in operating temperature projected for the microengine structure alleviates some of the requirements for combustor wall cooling.

Fracture failure has generally hindered the use of refractory ceramics for large-scale applications. Parts with larger volumes statistically entail flaws that are greater in quantity, larger in size, and deeper in location (Scott, 1979). Failure of ceramic

Table 2 Comparison between conventional and microcombustors

Design requirement (sea level takeoff)	Conventional combustor	Microcombustor
length	0.3 m	0.003 m
volume	6×10^{-2} m^3	4×10^{-8} m^3
cross-sectional area	0.2 m^2	4×10^{-5} m^2
inlet total pressure	30 atm	4.5 atm
intlet total temperature	800 K	500 K
mass flow	55 kg/s	20×10^{-4} kg/s
average flow speed	40–60 m/s	6 m/s
residence time	5–8 ms	0.5 ms
efficiency	>99.5%	>99.5%
combustor pressure ratio	>0.95	>0.95
exit temperature	1800 K	1500 K
allowable wall temperature	1200 K	1600 K
space heating rate (kW/m^3/atm)	3.8×10^4	3.3×10^5

parts typically occurs through propagation of existing material imperfections, but this is less of a concern for microengines because of the small component size. Quality control and refinement during manufacturing can be more readily applied to reduce inherent flaws, so the structural capabilities of these high temperature refractory ceramics can be more fully realized.

2 Combustors for Microengines

Before discussing the proposed combustion strategies for microengines, it is instructive to review the physical basis for the combustion scheme that is currently employed in most gas turbine applications.

2.1 Combustion in Large-Scale Engines. The enthalpy rise requirement of a gas turbine combustor is set by the cycle pressure ratio, properties of the working fluid and the fuel, and material limitations. A balance of these influences is described by the equation

$$\frac{\dot{m}_f}{\dot{m}_a} = \frac{C_p}{Q_f}(T_{T4} - T_{T3}) \tag{6}$$

an expression of the first law of thermodynamics. The required fuel-air ratio is a function of the combustor inlet temperature (T_{T3}), which is set by the compressor pressure ratio, the combustor exit temperature (T_{T4}), which is typically set by maximum material temperature limits downstream of the combustor, and properties of the fuel and air (Q_f, and C_p, respectively). For gas turbine applications, the fuel-air ratio mandated by these constraints typically falls between 0.015 and 0.045 over the operating range of the engine. This proportion may also be expressed as an equivalence ratio

$$\phi = \frac{\dot{m}_f/\dot{m}_a}{(\dot{m}_f/\dot{m}_a)_{\text{stoichiometric}}} \tag{7}$$

which would then range between 0.21 and 0.63.

The combustion strategies employed in current combustors are set to a large extent by the fact that most hydrocarbon-air mixtures will not burn at equivalence ratios less than approximately 0.5. The restrictive flammability range mandates a two-zone combustion scheme: a primary zone with relatively high equivalence ratio, which also implies high temperatures beyond material limits, and a secondary or dilution zone where additional air is supplied to reduce the mixture temperature to fall within material limits. The dilution zone is also the region where pollution processes are of critical concern. These factors lead to a residence time requirement of between 5 and 8 ms which is relatively independent of the physical size of the engine.

2.2 Combustion Strategies for Microengines. Turning to a discussion of the microcombustor applications, the strategies presented are based upon three general concepts: 1) increasing the size of the combustor relative to the engine to increase residence time, 2) premixing, and 3) lean burning. Removal of fuel-air mixing from the combustion chamber is driven by the severe residence time requirements for the micro application, and the realization that a large part of the residence time in current combustors is devoted to mixing. However, if the reactants are mixed upstream of the combustor, then the stability benefits of a near stoichiometric primary zone are lost. Two alternatives for offsetting this difficulty and achieving stable burning at low equivalence ratios are the use of hydrogen fuel, and the use of hydrocarbons with the assistance of surface catalysis. Concepts based upon these ideas are discussed in Sections 2.2.1 and 2.2.2, respectively.

2.2.1 Lean Burning Hydrogen-Air System. Hydrogen is an ideal fuel in many respects. Table 3 compares selected fuel properties of hydrogen with a typical hydrocarbon. Hydrogen has a greater heating value, more rapid rate of vaporization, faster diffusion velocity, shorter reaction time, a significantly higher flame speed, wider burning limits, lower ignition energy, and radiates less heat to its surroundings. Most importantly, the broad flammability limits remove requirements for a relatively rich primary burning zone followed by a dilution zone as is often necessary for hydrocarbon fuels. For a hydrogen-air reaction to provide a turbine inlet temperature of 1600 K, the required equivalence ratio of 0.34 (assuming no surface heat loss) falls well above the lean flammability limit of $\phi = 0.1$.

Table 3 Comparison of selected microengine fuels (winter, 1990)

Fuel property*	Hydrogen/ air mixture	Hydrocarbon/ air mixture
nominal composition	H_2	$CH_{1.8}$
fuel specific heating value (kJ/g)	120	42.8
diffusion velcoity (cm/s)	2	0.2
flammability limits (% by volume)	4–75	0.6–4
vaporization rate w/o burning (cm/min)	2.5–5	0.05–0.5
minimum ignition energy (mJ)	0.02	0.25
autoignition temperature (K)	858	500
characteristic reaction time at 5 atm (s)	$1 \times 10^{6-}$	1×10^{5}
flame propagation velocity (cm/s)	300	20
stoichiometric adiabatic flame temperature (K)	2318	2200
fraction of thermal energy radiated (%)	17–25	30–42

*(in air at STP, unless otherwise specified).

Although the diffusion speed of hydrogen in air is an order of magnitude greater than that of a hydrocarbon fuel, providing adequate fuel-air mixing is still a critical requirement. Requisite mixing can be achieved if the hydrogen gas is introduced well upstream of the combustor, possibly even upstream of the compressor. Similar lean, premixed, prevaporized combustors have been developed for hydrocarbon fuels for larger-scale gas turbines to meet low-emissions requirements. Two significant difficulties have been identified in studies of these combustors: lean blowout, and flashback or autoignition at high inlet temperatures (Grieb and Simon, 1990). For the current application, lean blowout is not a concern because of the wide flammability limits for hydrogen-air mixtures. Further, at the low operating pressure of 4.5 atm projected for a micro-gas turbine engine, the combustor inlet temperature is around 500 K, which is below the autoignition temperature for a hydrogen-air mixture. Therefore, introduction and premixing of hydrogen well upstream of the combustor is feasible in a microengine to enable nearly complete mixing of fuel and air.

Adoption of a lean, premixed hydrogen system also results in a significant reduction in complexity because of the higher operating temperatures allowed for the microengine's materials. Transpiration and film-cooling are used in conventional gas turbine combustors to maintain the combustor liner below material temperature limits. However, as discussed in Section 1.2.3, the ceramic materials intended for use in microturbomachinery have a distinct thermal advantage over the materials currently used in gas turbines, and are expected to withstand local wall temperatures in the vicinity of 1600 K. Thus a lean burning hydrogen-air system not only obviates the need for a dilution zone, but also removes any requirement for combustor wall cooling. A turbine inlet temperature of 1500 K permits the entire combustion process to be carried out without exceeding material limits.

While storage requirements currently prohibit the use of hydrogen in commercial aircraft, several studies (Winter, 1990) support its use as a fuel for future transport aircraft. For micro-gas turbines, the use of hydrogen fuel is not necessarily viewed as an endpoint, but rather as a first step to enable the realization of a workable microscale device. This hydrogen-air system is the subject of the experimental development efforts described in Section 3.

2.2.2 Catalytic Hydrocarbon-Air Combustion. To achieve stable, lean combustion with a hydrocarbon fuel, catalytic processes must be employed. During the last 30 years, catalysts have been investigated both for augmenting primary heat releasing reactions in gas turbines and for post-combustion treatment of pollutant emissions in aircraft, automobiles, and power generation applications. The focus here will be on situations where catalytic reactions are used to promote the primary combustion reactions.

Overview of Catalytic Combustion. The principal advantage of using catalysts for primary combustion reactions is their ability to sustain reactions for hydrocarbon-air mixtures that are well below the lean flammability limit for homogeneous gaseous combustion. Indeed, combustion of JP-4 at equivalence ratios as low as 0.1 has been reported (Rosfjord, 1976). This is attractive for large-scale applications because the extended lean flammability limit allows combustion to proceed at relatively low temperatures providing the potential for a factor of 100 decrease in emissions of nitrogen oxides.

Catalytic combustors typically employ proprietary platinum- and palladium-based catalysts on monolithic, parallel channel, substrates. Silicon carbide is a leading substrate material. The residence times in the catalyst bed are typically 5 to 30 ms for tubes with hydraulic diameters on the order of 1 to 4 mm. For combustor inlet temperatures ranging from 650 K to 900 K, combustion efficiencies of greater than 99.5 percent have been reported over a range of fuel-air equivalence ratios that result in adiabatic flame temperatures between 1100 K and 1800 K (e.g., Wampler et al., 1976; Mori et al., 1987).

The important technology limiters for catalytic gas turbine combustors are two-fold. First, the minimum operating temperature of approximately 600 K rules out use of catalysts for combustor inlet conditions corresponding to idle and low power cruise operation. Second, the maximum temperature limit of around 1800 K, set by catalyst and substrate thermal degradation, does not allow use for hydrocarbon mixtures with equivalence ratios greater than around 0.6. In practical devices these limits are offset by using preburners, pilot flames, fuel and air staging, and a variety of other hybrid catalytic/homogeneous combustion concepts.

The reacting flow processes within the catalytic bed are complicated, and a brief review of these is necessary to understand how the processes scale with combustor size. The following discussion is based on descriptions given by Groppo et al. (1993), Rosfjord (1976), and Pfefferle (1978). Consider preheated, premixed air and fuel as it passes through a long channel with catalytic surfaces. Reactants are absorbed by the catalyst, surface reactions occur, and then the products are desorbed and along with heat are transported into the flow by diffusion. Three different regions exist in the channel. Region I: Near the inlet of the channel, the fuel conversion is controlled by the kinetics of the heterogeneous reaction at the surface of the catalyst. The bulk gas temperatures are typically too low to support homogeneous combustion. This region of the flow usually extends for a distance of less than five tube diameters. Region II: As the near-wall gas and substrate temperatures rise, the heterogeneous reaction rates increase. The reaction rates increase to an extent that the fuel conversion is no longer controlled by the surface reaction rate, but rather by the rate at which new gas phase reactants are transported to the surface. Pfefferle (1978) notes that, for any reasonably active catalyst at temperatures above 800 K, the catalytic reaction at the wall will be limited solely by the rate of mass transfer. This diffusion limited region extends for 10–100 tube diameters in typical catalytic combustors. Region III: Further downstream, as heat continues to diffuse into the bulk gas flow, thermal ignition of homogeneous or gas phase reactions occurs. These homogeneous reactions are initiated at bulk gas temperatures in the range of 1200–1300 K (Pfefferle, 1978) which is far below the value of 1600 K, the minimum adiabatic flame temperature typically associated with mixtures at the lean flammability limit.

Cerkanowicz, Cole, and Stevens (1977) present several dimensionless groups that are useful for scaling the performance of catalytic combustors. The reaction in Region I is primarily dependent on the catalytic Damkohler number, Da_c, the ratio of residence time to the characteristic heterogeneous reaction time:

$$\mathrm{Da}_c = \left(\frac{L}{V_o}\right)\left(\frac{A_c e^{-E_c/RT_o}}{d_h}\right) \tag{8}$$

Because of the dependence of the reaction rate on surface area, $\mathrm{Da}_c \propto 1/d_h$ for fixed residence time. The transition from Region I to Region II, and the progression of the reaction in Region II are expected to scale with the mass transport number which is the ratio of the characteristic residence time of the gas in the reactor to the mass transport time

$$J_D = \left(\frac{L}{V_o}\right)\left(\frac{\alpha}{d_h}\right) \tag{9}$$

and the heat transfer number

$$J_H = \left(\frac{L}{V_o}\right)\left(\frac{k}{\rho_o C_p}\frac{1}{d_h}\right) \tag{10}$$

which is the ratio of the residence time of the gas to the characteristic heat transfer time. Both the heat and mass transfer scale inversely with the hydraulic diameter, and thus both are favored as the size of the tube is decreased, as is the overall progression to the homogeneous reaction region. Finally in Region III the process scales with the homogeneous Damkohler number, Da_h the ratio of gas residence time to the homogeneous reaction time.

$$\mathrm{Da}_h = \left(\frac{L}{V_o}\right)\left(\frac{A_h[\,\mathrm{fuel}\,]^a[O_2]^b e^{-E_h/RT_o}}{[\,\mathrm{fuel}\,]_o}\right) \tag{11}$$

For fixed residence time, Da_h is independent of the scale of the device.

Application to Microengines. Based on the preceding discussion of performance and scaling of catalytic combustion systems, the following conclusions can be drawn with respect to a microengine application. The size of the combustor relative to the engine can be increased to obtain a factor of 10 increase in residence time, as was proposed for the hydrogen system. However, the resultant residence time, at 0.5 ms, will still be an order of magnitude less than that in any successfully demonstrated catalytic combustion systems. Second, the combustor inlet temperature of 460 to 500 K in the microengine application is below the 600 K limit required for catalytic ignition. We will discuss each of these challenges in turn, beginning with the low residence time.

The reduced residence time is largely offset by the favorable effects associated with the high surface area-to-volume ratio of the microcombustor, including order of magnitude increases in both the heterogeneous Damkohler number and the nondimensional heat and mass transfer rates that are the primary controlling parameters for the rate of reaction in the system. This suggests that catalytic combustion of hydrocarbons can be completed for flow residence times on the order of 1 ms if the hydraulic diameter of the flow path is reduced by an order of magnitude from larger-scale applications. For the microengine application then, the catalytic flow passages should be approximately 100 microns in diameter. Manginell et al. (1996) have used chemical vapor deposition technology to apply platinum

catalysts to micromachined polysilicon, providing proof that miniature catalytic elements can be microfabricated.

The second problem mentioned above was that the combustor inlet temperature was too low to support catalytic ignition. However, the experimental results presented in Section 3.4 suggest that, for the current configuration, enough heat transfer may be occurring between the combustor and the compressor exit flow passage to overcome this difficulty. If not, a recuperator can be employed. A recuperator is a heat exchanger used to transfer waste heat in the turbine exhaust to the compressor exit flow prior to its entrance into the combustor. Recuperated cycles can provide significantly higher thermal efficiency for low pressure ratio engines because of the relatively large difference in temperature between the combustor exit flow and the turbine exhaust. For the microengine with a 4.5:1 pressure ratio, the compressor exit flow will be approximately 460 K and the turbine exhaust approximately 1200 K, so heat exchangers with efficiencies as low as 20% will allow catalytic combustor operation. A typical heat exchanger efficiency reported in the literature for 50 kW automotive gas turbine applications is about 90% (AlliedSignal Aerospace Company, 1988; Allison Gas Turbine Division, 1988), suggesting that sufficient heat exchanger efficiency can be attained to enable catalytic combustion of hydrocarbons.

The envisioned configuration for a recuperated, catalytic hydrocarbon combustion system is shown in Fig. 2. The compressor exit flow exchanges heat with the engine exhaust before passing into a catalytic combustor. The catalytic combustor is in the form of a radial labyrinth. An additional benefit of such a system is that a large fraction of the heat lost from the walls of the combustion chamber can be retained in the cycle thus improving the overall efficiency of the chemical to thermal energy conversion process. The primary drawback of this system is its geometrical complexity, which may pose a significant challenge to existing microfabrication technology.

3 Hydrogen-Air Microcombustor Experiments and Simulations

A microcombustor test rig was developed to study combustion phenomena for microengine applications. The apparatus and diagnostics are described in Sections 3.1 and 3.2, respectively. Numerical simulations of the flowfield are presented in Section 3.3, followed by initial experimental results for lean, premixed hydrogen-air combustion in Section 3.4.

3.1 Apparatus. A schematic of the model microcombustor is presented in Figure 3. As depicted in the figure, the model consists of a series of plates stacked on top of each other. The hydrogen-air mixture is introduced into the dump combustor through a ring of holes in the combustor inlet plate. After combustion, the flow exits axially. This differs from the flow in the microengine shown in Fig. 1 where the combustion products exit radially into the turbine. Two model microcombustors were constructed, one of silicon carbide, which is the proposed material for the micro-gas turbine, and the other of steel, which allowed easier addition of diagnostics since it was less troublesome to machine. The volume of both combustors was approximately 0.13 cm^3. Likewise, two combustor inlet plates were

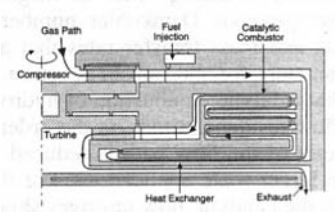

Fig. 2 Schematic of a recuperated microengine with a catalytic combustor for burning hydrocarbon fuels

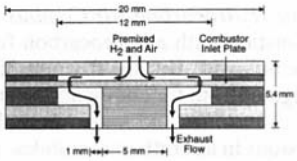

Fig. 3 Schematic of the model microcombustor

manufactured, a 0.4 mm thick steel piece with 24 combustor inlet holes of 0.4 mm diameter around a circle of 5 mm radius, and a 0.5 mm thick silicon carbide plate with 40 inlet holes of 0.38 mm diameter also around a circle of 5 mm radius. The large backward facing area of the inlet plates was designed to set up recirculation zones to provide flameholding.

The apparatus for holding the microcombustor is shown in Fig. 4. The microcombustor plates are held together in compression by a spring. This modular design permits replacement of plates to simplify the task of conducting parametric studies for various geometric configurations. The residence time for the microcombustor flow can be adjusted by adding or removing plates, thereby changing the flowpath length and combustor volume. The downstream side of the combustor is supported by a clear quartz tube to allow limited visual access to the combustor exit flow field. The entire combustor rig is housed in a water-cooled pressure chamber to enable testing at elevated pressures. Visual access is provided by a quartz window.

3.2 Diagnostics and Ignition. Due to the small size and restrictive geometry of the microcombustor, diagnostics for the combusting flow were difficult to apply. Two diagnostic techniques were used: 0.25 mm type K thermocouples and an ionization probe. Temperature measurements included inlet and exit flow temperature, combustion chamber temperature, and combustor wall temperature. The ionization probe was used for evaluating whether a flame existed within the microcombustor. A schematic of the steel combustor illustrating the location of some of the thermocouples, the ion probe, as well as an ignitor, is presented in Fig. 5. For the silicon carbide microcombustor, only a single thermocouple and an ignitor were used. Both the thermocouple and the ignitor were introduced axially into the exit of the combustion chamber. Additional details of these measurement techniques and the ignition procedure are discussed below.

Generally, the temperature indicated by a thermocouple probe is not the same as the gas temperature because of the energy exchange between the thermocouple probe and the surrounding environments. In steady-state, the temperature attained by the probe is a net result of convective energy transfer from the surrounding gas, radiative energy flux to the cooler walls, and

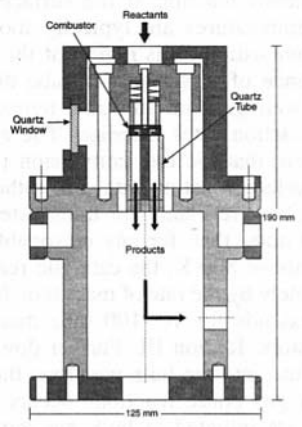

Fig. 4 Schematic of the microcombustor testing facility

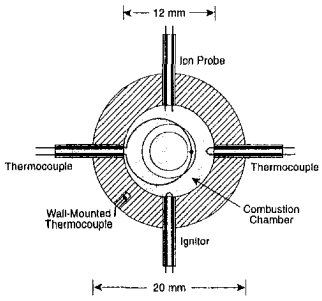

Fig. 5 Microcombustor diagnostics and ignitor layout

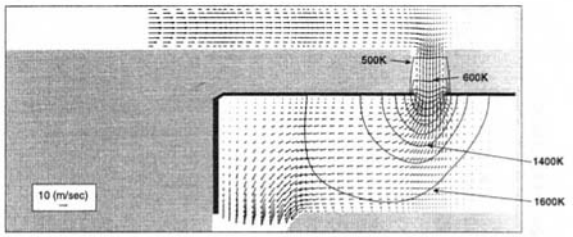

Fig. 6 Results of a numerical simulation showing temperature and velocity fields for the microcombustor for $\phi = 0.4$, $T_{in} = 450$ K, $P_{in} = 1$ atm, and $\dot{m} = 0.045$ g/s

conduction along the wires away from the thermocouple junction. Corrections for these effects must be made to obtain accurate temperature measurements (see, for example, Bradley and Matthews, 1968). For most applications, the length of thermocouple wire exposed to the flow is long enough, and the gradients along the wire are small enough, so that conduction losses are small. However, for the microcombustor, the length of thermocouple wire that protrudes into the flow is limited to only a few millimeters by the scale of the device. Further, the large temperature gradients within the combustion chamber imply unusually high uncertainties in flow temperature measurements due to conduction losses. These uncertainties were aggravated by lack of knowledge of the interior temperature field and additional inaccuracies introduced by the combustor wall measurements. Finally, since radiation corrections require the use of surrounding surface temperatures, they are also impacted by inaccuracies in the combustor wall temperature measurements. Because of these accumulated errors, the estimated uncertainty of the temperature measurements is about ±100 K.

An ionization probe was used to provide a secondary indication of the presence of a flame within the combustion chamber. The underlying concepts of ion probes are discussed in several references (Smy, 1976; Calcote, 1963; Travers and Williams, 1965; Zsak, 1993). The probe consisted of two platinum electrodes separated by an air gap. The two electrodes were maintained at a fixed electrical potential difference. When ionized radicals associated with the combustion zone were present, a current was induced across the air gap, and this was manifest as a change in voltage across a resistance placed in series with the probe.

Ignition of the microcombustor was achieved by resistance heating of a 0.2 mm platinum wire. The ignitor consumed approximately 50 watts of power. Ignition usually occurred in a matter of seconds, but was sensitive to wire location. Ignition occurred more readily if the ignitor was positioned toward the center of the combustion chamber; however, the wires would only survive one test in this position. Moving the ignitor closer to the combustor wall substantially increased its lifetime. As with other experiments reported in the literature (Lewis and von Elbe, 1987) catalysis on the heated platinum may have played a role in the ignition behavior. This will be investigated in future tests.

3.3 CFD Simulations of the Microcombustor. Before presenting experimental results, we illustrate the general features of the flowfield in the microcombustor using results from two-dimensional reacting flow simulations. These simulations were carried out using ALLSPD (Chen et al., 1995), a Navier-Stokes solver incorporating finite-rate chemical kinetics. The code has been validated by personnel at NASA Lewis Research Center (ALLSPD, 1995) for laminar reacting flows like those expected in the microcombustor. A hydrogen-air chemistry model with 9 species and 18 reaction mechanisms was used in the current study. The simulations were conducted for a $\phi = 0.4$ hydrogen-air mixture flowing at a rate of 0.045 g/s. The mixture was specified an inlet temperature of 450 K at atmospheric pressure, to provide a comparison with the microcombustor experiments.

The velocity and temperature fields are shown in Figure 6. Flameholding is seen to occur in the immediate vicinity downstream of the combustor inlet plate hole. The maximum flowfield temperature is 1650 K. The location of the maximum temperatures indicates that there is sufficient time for reactions to be completed well within the current combustor volume of 0.13 cm^3. This conclusion is supported by the results obtained in the experiments, which are discussed in the following section.

3.4 Preliminary Experimental Results. Tests of both the steel and silicon carbide combustors were completed for the two combustor inlet plates described in Section 3.1. Equivalence ratios between 0.4 and 1.0 were tested with mass flow rates from 0.045 g/s to 0.2 g/s for combustor pressures of 1 to 4.5 atmospheres respectively, such that the combustor residence time was maintained at approximately 0.5 ms. These conditions were chosen to correspond to typical microengine operating parameters. All of the tests were carried out by varying the equivalence ratio from $\phi = 1.0$ down to $\phi = 0.4$ in increments of 0.1, and then back up to $\phi = 1.0$ in increments of 0.1. Stable combustion was observed for both the silicon carbide combustor and the steel combustor over the full range of equivalence ratios tested.

Internal temperature measurements obtained with the steel microcombustor are shown in Fig. 7 over a range of hydrogen-air equivalence ratios at atmospheric pressure. The flow rate for the case shown was 0.045 g/s. The measurements have been corrected for radiation and conduction errors, however the uncertainty in these measurements is expected to be ±100 K due to inadequate knowledge of thermal gradients within the combustion chamber as described in Section 3.2. The magnitude of each of the corrections is shown on the plot along with the raw temperature measurement. Also included in the figure are the estimated adiabatic flame temperatures over the range of equiva-

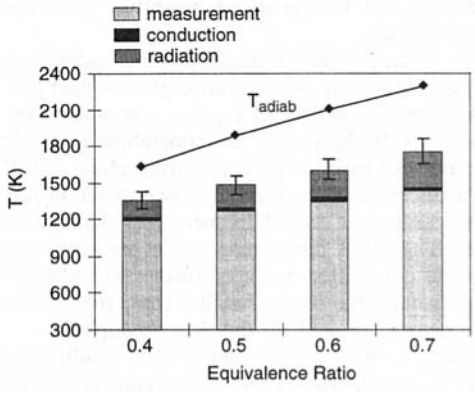

Fig. 7 Exit gas temperatures measured in the hydrogen-air microcombustor

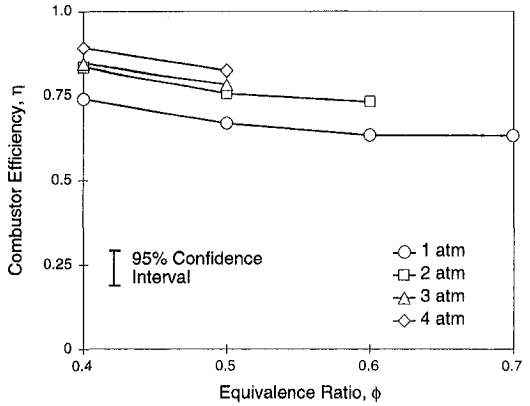

Fig. 8 Combustor efficiency for the microcombustor over a range of pressures and equivalence ratios

lence ratios based on the measured inlet air temperatures. Lack of any visible indication of a flame at the combustor exit (even when the hydrogen was seeded with five percent methane to increase the chemiluminescence) suggests that the combustion efficiency was near one. However, the combustor efficiency was reduced due to heat transfer losses as is suggested by the difference between the corrected temperatures and the adiabatic flame temperatures. This difference increased with increasing equivalence ratio as is expected.

The overall combustor efficiencies associated with these temperature differences fall between 0.7 and 0.9 and are shown plotted in Fig. 8 for the range of equivalence ratios and pressures tested. Results are not presented for many of the higher pressure and equivalence ratio conditions because the associated high temperatures generally resulted in failure of the fine wire thermocouple probes. The combustor efficiency variation with pressure is consistent with the variation in heat transfer coefficients with pressure and flow rate. In sum, despite the low combustor efficiency, both the steel and silicon carbide microcombustors were operated for tens of hours and throughout produced the requisite heat release necessary to support the various heat engine applications that are currently envisioned.

Other observations from these preliminary tests include:

1) The ionization probe indicated the presence of a flame within the combustor over the full range of flow rates tested for equivalence ratios between 0.4 and 1.0. The observed voltage was found to increase with increasing equivalence ratio.
2) At constant flow rate, the choice of the combustor inlet plate did not significantly affect the temperatures measured, probably indicating similar flameholding characteristics, and thus similar temperature fields for the two geometries.
3) The microcombustor plates became sufficiently hot to glow red at equivalence ratios greater than 0.5, and the heat transfer to the inlet gases was significant (on the order of 50 K to 100 K temperature rise). Typically, combustor wall temperatures were about 750 K.
4) The thermocouples located at two different radii within the combustor sensed temperatures that differed by as much as 180 K due to large radial temperature gradients in the combustor. Lack of further knowledge of these gradients is the source for the large errors in conduction corrections quoted for the thermocouples.
5) During some low equivalence ratio conditions, hysteresis in the thermocouple measurements of 200 K was observed suggesting that flameholding did not always occur at the same location within the microcombustor.

4 Summary and Conclusions

Microengines and other miniature thermal devices pose unique challenges and opportunities for combustion in small volumes. The principal difficulties are associated with the limited residence times, and heat transfer losses due to the high surface area-to-volume ratio. Two viable combustion alternatives for microengines were presented in the paper, one that takes advantage of the wide flammability limits of hydrogen-air mixtures, and a second that involves surface catalysis of a hydrocarbon fuel. Both options require an order of magnitude increase in the size of the combustor relative to the engine, and premixing the fuel and the oxidizer to decrease residence time requirements within the combustor. Both combustion strategies also represent significant reductions in complexity from typical gas turbine systems by the removal of requirements for a primary combustion zone where temperatures exceed the material limits.

Preliminary test results from 0.13 cm^3 silicon carbide and steel microcombustors were presented for inlet pressures between 1 and 4 atm. Stable and complete combustion of hydrogen and air was achieved over the full range of equivalence ratios required for a microengine application. Combustor efficiencies between 0.7 and 0.9 were obtained. The low combustor efficiencies were largely a result of heat transfer losses from the walls of the combustor. The experiments provide a first proof-of-concept demonstration for the hydrogen-air system, and suggest that combustion in small volumes for microengine applications is feasible.

The work presented in this paper also highlights the need for significant additional research to more carefully understand flow behavior within the microcombustor. This research would be aided by the development of miniature diagnostic techniques for these flows. Experimental and computational work is continuing with the focus on issues of hydrogen injection and mixing, ignition, catalytic combustion of hydrocarbon fuels, and determination of oxidation rates for silicon carbide in the post-combustion gas environment. A parallel experimental effort is also ongoing using a miniature flame tube apparatus. The flame tube will be used to provide measurements to help validate reacting flow simulations and finite element heat transfer models.

Acknowledgments

We first recognize and thank Professor Alan H. Epstein, both for conceiving and pursuing the concept of microengines, and for being a constant source of encouragement and ingenuity. In addition, we thank the members of the MIT microengines team: Kuo-Shen Chen, Eric Esteve, Luc Frechette, Chuang-Chia Lin, Amitav Mehra, Steve Nagle, Ed Piekos, G. Ananthasuresh, Arturo Ayon, Fredric Ehrich, Stuart Jacobson, Choon Tan, Kenneth Breuer, Mark Drela, Jeffrey Lang, Martin Schmidt, Stephen Senturia, and Mark Spearing, for all they have taught us. The skill and assistance of Viktor Dubrowski, Mariano Hellwig, and James Letendre made the apparatus used in this study possible. We are grateful to Diana Park for superb editing and graphics, and to Holly Anderson for shouldering many of the administrative burdens.

This work was largely supported by the Army Research Office through Grant DAAH04-95-1-0093. We greatly appreciate the interest and encouragement of the technical monitor, Dr. Richard Paur. We also thank the MIT Lincoln Laboratory for providing support for the initial feasibility studies.

References

AlliedSignal Aerospace Company, 1998, "Advanced Gas Turbine AGT Technology Development Project," Final Report to NASA Lewis Research Center, DOE/NASA 0167-12, Mar.

Allison Gas Turbine Division, 1985, "Advanced Gas Turbine AGT Technology Project," Final Report to NASA Lewis Research Center, DOE/NASA 0168-11, Aug.

ALLSPD Demonstration Workshop, Personal Communication, 1995.

Ballal, D. R., and Lefebvre, A. H., 1979, "Weak Extinction Limits of Turbulent Flowing Mixtures," *Journal of Engineering for Power,* Vol. 101, No. 3.

Bradley, D., and Matthews, K. J., 1968, "Measurement of High Gas Temperatures with Fine Wire Thermocouples," *Journal of Mechanical Engineering Science,* Vol. 10, No. 4.

Bryzek, J., Peterson, K., and McCulley, W., 1994, "Micromachines on the March," *IEEE Spectrum,* Vol. 31, No. 5, May.

Calcote, H. F., 1963, "Ion and Electron Profiles in Flames," *Ninth Symposium (International) on Combustion,* The Combustion Institute.

Cerkanowicz, A. E., Cole, R. B., and Stevens, J. G., 1977, "Catalytic Combustion Modeling; Comparisons with Experimental Data," ASME Paper 77-GT-85, Mar.

Chen, K-H., Duncan, B., Fricker, D., Lee, J., and Quealy, A., 1995, ALLSPD-3D, Version 1.0, Internal Fluid Mechanics Division, NASA Lewis Research Center, Nov.

Dodds, W. J., and Bahr, D. W., 1990, "Combustion System Design," *Design of Modern Gas Turbine Combustors,* Mellor, A. M. (Editor), Academic Press Limited.

Epstein, A. H., Groshenry, C., Haldeman, C. W., Schmidt, M. A., Senturia, S. D., Tan, C. S., Waitz, I. A., and Wong, J., 1995, "Microjet Engines," Final Technical Report to MIT Lincoln Laboratory, Massachusetts Institute of Technology.

Grieb, H., and Simon, B., 1990, "Pollutant Emissions of Existing and Future Engines for Commercial Aircrafts," Air Traffic and the Environment—Background, Tendencies and Potential Global Effects, *Proc. of the DLR International Colloquium,* Bonn, Germany, U. Schumann (Ed.), Springer-Verlag.

Groppo, G., Tronconi, E., and Forzatti, P., 1993, "Modelling of Catalytic Combustors for Gas Turbine Applications," *Catalysis Today,* Vol. 17, Elsevier Science Publishers B. V., Amsterdam, pp. 237–250.

Groshenry, C., 1995, "Preliminary Study of a Micro-Gas Turbine Engine," S.M. thesis, Massachusetts Institute of Technology, May.

Juan, W-H., Pang, S. W., 1996, "Released Si Microstructures Fabricated by Deep Etching and Shallow Diffusion," *Journal of Microelectromechanical Systems,* Vol. 5, No. 1, Mar.

Kerrebrock, J. L., 1992, *Aircraft Engines and Gas Turbines,* 2nd ed., MIT Press.

Lefebvre, A. H., 1983, *Gas Turbine Combustion,* Hemisphere Publishing Corporation.

Manginell, R. P., Smith, J. H., Ricco, A. J., Moreno, D. J., Hughes, R. C., Huber, R. J., and Senturia, S. D., 1996, "Selective, Pulsed CVD of Platinum on Microfilament Gas Sensors," Solid State Sensor and Actuator Workshop, Hilton Head, South Carolina, June.

Measley, M. L., and Smyth, J. R., 1996, "Ceramic Gas Turbine Technology Development," ASME paper 96-GT-367.

Mori, K., Kitajima, J., Kajita, S., and Ichihara, S., 1987, "Development of a Catalytic Combustor for Small Gas Turbines," ASME Paper 87-GT-62, May-June.

Nakazawa, N., Ogita, H., Takahashi, M., Yoshizawa, T., and Mori, Y., 1996, "Radial Turbine Development for the 100 kW Automotive Ceramic Gas Turbine," ASME paper 96-GT-366.

Pfefferle, W. C., 1978, "The Catalytic Combustor: An Approach to Cleaner Combustion," *AIAA J. Energy,* Vol. 2, May-June.

Rosfjord, T. J., 1976, "Catalytic Combustors for Gas Turbine Engines," AIAA Paper 76-46, Jan.

Scott, W. D., 1979, "Statistics of the Strength of Brittle Materials," *Design with Brittle Materials,* Mueller, J. I., Kobayashi, A. S., Scott, W. D. (Editors), University of Washington.

Smy, P. R., 1976, "The Use of Langmuir Probes in the Study of High Pressure Plasmas," *Advances in Physics,* Vol. 25, No. 5.

Tanaka, K., Tsuruzono, S., Kubo, T., and Yoshida, M., 1996, "Development and Fabrication of Ceramic Gas Turbine Components," ASME paper 96-GT-446.

The Carborundum Company, 1989, "Physical Properties of Hexoloy® SA Silicon Carbide—Technical Data," The Carborundum Company, November 10.

Travers, B., and Williams, H., 1965, "The Use of Electrical Probes in Flame Plasmas," Tenth Symposium (International) on Combustion, The Combustion Institute.

Wampler, F. B., Clark, D. W., and Gaines, F. A., 1976, "Catalytic Combustion of C_3H_8 on Pt Coated Monolith," *Combustion Science and Technology,* Vol. 14, pp. 25–31.

Winter, C.-J., 1990, "Hydrogen Technologies for Future Aircraft," Air Traffic and the Environment—Background, Tendencies, and Potential Global Atmospheric Effects, *Proc. of the DLR International Colloquium,* Bonn, Germany, U. Schumann (Editor), Springer-Verlag.

Zamaschikov, V. V., 1995, "Combustion of Gases in Thin-Walled Small-Diameter Tubes," *Combustion, Explosion, and Shock Waves,* Vol. 31, No. 1, Jan.-Feb.

Zeldovich, Y. B., Barenblatt, G. I., Librovich, V. B., et al., 1990, *Mathematical Theory of Combustion and Explosion.*

Zsak, T. W., 1993, "An Investigation of the Reacting Vortex Structures Associated with Pulse Combustion," Ph.D. thesis, California Institute of Technology.

D. V. Pence
Assistant Professor,
Department of Mechanical Engineering and Applied Mechanics,
University of Rhode Island,
92 Upper College Road,
Kingston, RI 02881

D. E. Beasley
Professor,
Department of Mechanical Engineering,
Clemson University
Box 340921,
Clemson, SC 29634

Multi-Fractal Signal Simulation of Local Instantaneous Pressure in a Bubbling Gas-Fluidized Bed—Part 1: Signal Simulation

Introduction

The purpose of this paper, in two parts, is to (1) determine the fractal characteristics of time-series pressure data from a gas-fluidized bed, (2) evaluate the possibility of using the Weierstrass-Mandelbrot (WM) function to simulate the fractal and dynamic characteristics of such pressure data, (3) refine the method of signal simulation introduced by Humphrey et al. (1992) for turbulence data, and (4) to investigate the nonlinear, fractal, and physical phenomena of pressure in a fluidized bed as a function of angular position around a cylinder, location in the bed, and the fluidization ratio. The present paper, Part 1, (*a*) provides evidence that pressure signals from a bubbling fluidized bed are fractal, and delineates the range of scales over which these signals are fractal, (*b*) demonstrates that simulated signals have statistical measures essentially identical to experimental signals, and (*c*) relates parameters of the WM function to the physics of pressure fluctuations in fluidized beds. In addition, a refinement to the method of simulation employed by Humphrey et al. (1992) is proposed that employs the method presented by Higuchi (1988) to identify the fractal dimension and upper scaling frequency. Also, a direct means of specifying the amplitude of the fractal component of the signal results from using the peak-to-peak pressure of the experimental signal. Part 2 is devoted to assessing the nonlinear characteristics of the simulation and relating the physics to chaos measures.

Signal simulation has been widely employed for a variety of control and forecasting applications, and the limitations are clear. However, in many situations fractal signals can be simulated with little or no knowledge of the underlying physics, and such simulations are not entirely without value. As far as is known, the fractal analysis of time series data has not yet resulted in a true physical model.

Hydrodynamics and transport processes in fluidized systems are fundamentally a result of the interaction of dispersed phases, having unique flow and stability characteristics. In a gas-solid fluidized bed operating in the bubbling regime, pressure fluctuations result from the complex hydrodynamics associated with the interaction of the emulsion and bubble phases. At a surface, the emulsion phase is continually replaced with bubble phase, a phenomenon known as surface renewal; this surface renewal also contributes to fluctuations in pressure. Numerous fluidized bed combustor designs employ horizontal tube banks as heat exchange surfaces; therefore, the geometry examined in the present study is a horizontal cylinder. An experimental fluidized bed facility was designed to acquire local instantaneous pressure at the surface of a horizontal cylinder and at the wall of the test section.

Several investigators have examined instantaneous pressure and pressure drop in a variety of fluidized systems, describing both statistical and physical aspects of these pressure variations. The most relevant investigation to the present study was performed by Baskakov et al. (1986). In their study, the physical basis for pressure fluctuations in fluidized beds was described, and the time series was found to be directly related to the fluidized height of the particles, a definitive length scale of the bed. More recently, Fan et al. (1990 and 1995) found that the time series of three-phase and liquid-solid fluidized beds exhibited fractal characteristics.

Fluidized systems have also been analyzed using chaos analysis techniques, which provide information regarding the dynamic nature of the system from a multi-dimensional, phase space perspective. The results of these analyses, using instantaneous measurements of heat flux (Pence et al., 1995), and pressure and void fraction (van der Stappen et al., 1993; Skrzycke et al., 1993; Schouten and van den Bleek 1992; Fuller et al., 1993; Daw and Halow, 1991; and Daw et al., 1990) indicate behavior consistent with low-dimensional, deterministic chaos.

The Weierstrass-Mandelbrot (WM) function is a geometric progression of frequencies that can be employed to represent the fractal or scale-independent nature of a signal. In the present context, the object whose fractal nature is examined is the time series itself. A fractal signal displays self-similarity or self-affinity over a scaling range in the time domain. Using appropriate constraints, the fractal or multi-fractal component of a signal can be simulated using the multi-fractal WM function. Successful application of the multi-fractal WM function to simulate the scale-independent characteristics of turbulence was performed by Humphrey et al. (1992). This fractal component was superimposed on a nonfractal, or scale-dependent, component yielding a simulated signal that yielded correct forms for the energy and dissipation spectra. The multi-fractal simulations are based on the work of Berry and Lewis (1980) for a single fractal.

Humphrey et al. (1992) established the nonfractal parameters for signal simulation by examining the power spectrum of a measured signal, and the fractal parameters using both the power-law scaling behavior of the power spectrum and the fractal dimension of the signal. Independent assessments of the scaling law and fractal dimension were made, and the relation between these two values, which was first identified by Mandelbrot (1977), was verified. A refinement of the method employed by Humphrey et al. (1992) is proposed and implemented in the present paper. An important parameter of the WM function is the scaling factor, H_j, which is directly related to the fractal

Contributed by the Fluids Engineering Division for publication in the JOURNAL OF FLUIDS ENGINEERING. Manuscript received by the Fluids Engineering Division June 5, 1995; revised manuscript received October 15, 1997. Associate Technical Editor: O. C. Jones.

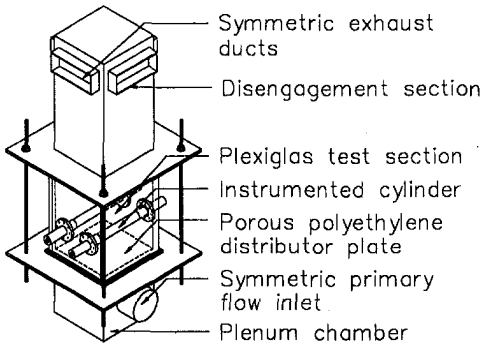

Fig. 1 Experimental facility

dimension of the signal, as discussed by Berry and Lewis (1980) and Humphrey et al. (1992). In the present paper, the method of Higuchi (1988) is used to quantify the fractal dimension of the signal in the time domain and to provide the upper frequency limit in the WM function. The WM function is subsequently employed to simulate the pressure fluctuations observed at the surface of a submerged horizontal cylinder and at the wall of a bubbling gas-fluidized bed.

Experimental Facilities and Measurements

An experimental fluidized bed facility, as shown in Fig. 1, was designed to accommodate two submerged horizontal cylinders. The cylinders, 3.8 cm diameter, were positioned with their axes 15 cm above a porous polyethylene distributor plate and with a center-to-center distance of 18 cm. Each cylinder was instrumented with a 0.3 cm diameter pressure tap that could be rotated to any angular position around the cylinder. Employing two horizontal cylinders created symmetry in the system and provided a means of assessing fluidization uniformity and signal repeatability. A similar tap was located in the wall of the facility at a height above the distributor plate corresponding to the stagnation point of the cylinders.

All pressure taps were connected to Omega model PX162-027D5V pressure transducers with a 1–6 Volt range corresponding to 0–6.9 kPa (gage). Local pressures were measured relative to atmosphere. The transducers were calibrated using a digital micro-manometer as a standard, yielding an uncertainty of 40 Pa in the pressure level and an uncertainty of 4 percent in the pressure fluctuations. A total of 16,500 data points were acquired for each signal at a sample rate of 500 Hz using a 12-bit Metrabyte data acquisition system.

The choice of a porous distributor plate with nominal pore size of 40 microns provided uniform flow distribution and bubbling, and removed distributor plate design as an extraneous variable in the hydrodynamics. The cross sectional flow area of the distributor plate was 930 cm^2. The facility was charged to a slumped bed height of 30.5 cm with spherical glass particles. A monosize particle distribution of 345 μm belonging to Geldart's group B particles (Geldart, 1973) was used as the particulate media. Manufacturer specifications reported the density and sphericity to be 2.5 g/cm and 85 percent, respectively. The experimental value of minimum fluidization velocity was found to be 0.086 m/s. Pressure drop curves used for determining minimum fluidization velocity along with visual observations confirmed that the porous distributor yielded uniform fluidization. Operation of the fluidized bed was limited to the bubbling flow regime with fluidization velocity ratios, U/U_{mf}, of 1.2 and 1.5 reported in the present study. Instantaneous measurements of pressure at the wall of the test section and at angular positions on the cylinder corresponding to 0, 90, and 180 degrees relative

Nomenclature

A_i = amplitude of nonfractal component, i (Pa)
A_j = amplitude of fractal component, j
b = constant base of cyclic frequency (defined in Eq. (2))
D_j = local fractal dimension estimate of jth fractal (defined in Eq. (3) and Eq. (5))
$E(f)$ = power spectrum of pressure signal $(Pa)^2/Hz$
f = frequency (Hz)
f_i = frequency of non-fractal component (Hz)
f_p = natural frequency of gravitational pressure fluctuations (Hz)
$f_{1,j}$ = lowest frequency associated with fractal j (Hz)
$f_{2,j}$ = highest frequency associated with fractal j (Hz)
g = gravitational acceleration (9.81 m/s^2)
G_j = slope of jth fractal on log-log power spectrum
H = Hurst exponent
H_j = scaling factor of jth component of multi-fractal
i = summation index for nonfractal contribution of signal (Eq. (9)) and in Higuchi method (Eq. (8))
j = summation index for fractal contribution of signal (Eq. (1))
k = number of nonfractal components
L_o = bed height at minimum fluidization (m)
$L_m(\tau)$ = length of curve in time domain
$\langle L_m(\tau)\rangle$ = average length of curve in time domain
m = index in Higuchi method (Eq. (7))
M = number of fractal components composing multi-fractal contribution
n = summation index for cyclic frequency calculations
$n_{1,j}$ = lower limit of frequency equivalent for cyclic frequency calculations of jth fractal
$n_{2,j}$ = upper limit of frequency equivalent for cyclic frequency calculations of jth fractal
N = number of points in time series used for calculation purposes
$p(t)$ = experimental instantaneous pressure signal (Pa)
$p_f(t)$ = fractal (scale-independent) contribution to simulated signal (Pa)
$p_{nf}(t)$ = nonfractal (scale-dependent) contribution to simulated signal (Pa)
$p_s(t)$ = simulated instantaneous pressure signal (Pa)
RMS = root-mean-square
t = time (s)
T = length of time series (s)
U = superficial fluidization velocity (m/s)
U_{mf} = minimum fluidization velocity (m/s)
U/U_{mf} = fluidization velocity ratio
X = time series
X_τ^m = decimated time series (defined in Eq. (7))
γ = mean signal width (ms)
θ = angular position of sensor (degrees)
τ = integer time interval in Higuchi method (Eq. (7) and Eq. (8))
τ_c = characteristic time (ms)
ω = cyclic frequency of fractal component (see Eq. (2)) (rad/s)
ω_i = cyclic frequency of nonfractal component (rad/s)

Subscripts

e = experimental signal
s = simulated signal

to the stagnation point were examined in the present work. The 0 and 90 degree angular positions correspond to the lower half of the cylinder where surface renewal characteristics have been extensively documented.

Signal Simulation and Analysis

Opportunity exists for simulation of time-series representations of physical variables exhibiting one or more fractal dimensions using the multi-fractal Weierstrass-Mandelbrot function. The Weierstrass-Mandelbrot (WM) function is a geometric progression of frequencies defined by

$$p_f(t) = \sum_{j=1}^{M} A_j \sum_{n=n_{1,j}}^{n_{2,j}} \frac{\sin(\omega t)}{\omega^{H_j}} \tag{1}$$

where $p_f(t)$ represents the fractal or scale-independent contribution of time variations of a simulated signal, and t represents time. Each fractal, j, is valid over a defined, non-overlapping range of frequencies and has an associated constant amplitude, A_j. The range of frequencies is specified by the summation index n in Eq. (1) which varies from $n_{1,j}$ to $n_{2,j}$. The cyclic frequency, ω, is defined according to

$$\omega = b^n \tag{2}$$

and H_j, the scaling factor, is related to the fractal dimension of the signal, D_j, and the slope of the logarithmic power spectrum, G_j, according to

$$H_j = 2 - D_j = -\left[\frac{G_j + 1}{2}\right] \tag{3}$$

Humphrey et al. (1992) reports this relationship between G_j, the scaling factor, and the fractal dimension for multi-fractal simulations. In the present study, the relationship between the scaling factor and the fractal dimension is used in specifying H_j. The density of the spectrum is determined by the value of parameter b. For the WM simulated signal to be fractal, i.e., continuous and nondifferentiable with self-affinity, constraints on H_j and b must be met. The values of H_j and b remain constant for each value of j, and must lie between 0 and 1, and be greater than 1, respectively. The summation of multiple fractals remains fractal provided the constraints on b and H_j are maintained. The constraints on H_j are equivalent to limits between -3 and -1 for G_j over the range of the scale-independent frequencies. The approach used here for determining this frequency range and the scaling factor will be described in subsequent paragraphs.

Defined in frequency space, the continuous power spectrum is defined by

$$E(f) = \frac{1}{T}\left|\int_0^T p(t)\exp(i2\pi ft)dt\right|^2 \tag{4}$$

where T is the length of the data set and $p(t)$ represents a time-dependent pressure signal. First stated by Mandelbrot (1977), the local fractal dimension, D_j, is related to the slope of the power spectrum, G_j, according to

$$D_j = \frac{G_j + 5}{2} \tag{5}$$

Multi-fractals, characterized by more than one distinct slope of the logarithmic power spectrum, do not follow a single power law over all time scales. As an example, for a multi-fractal of degree two there exists two distinct linear regions, each having slopes between -3 and -1. Each dimension, or slope, is associated with a range of frequencies, and for simulation purposes the two slopes meet at a common frequency to avoid any discontinuity in the power spectrum of the signal. The amplitudes of the two fractal components, A_1 and A_2, are related according to

$$\frac{A_2}{A_1} = \omega^{(G_1 - G_2)/2} \tag{6}$$

where ω represents the cyclic frequency common to both fractals, i.e., n equal to $n_{2,1}$ and $n_{1,2}$ (Humphrey et al., 1992).

A means of rationally determining values of the parameters in the WM function is required for signal simulation. Employing the relationship between the fractal dimension, the power law index, and the scaling factor stated in Eq. (3), an estimate of the fractal dimension allows determination of both G_j and H_j. Burlaga and Klein (1986) presented a method that calculated the fractal dimension from the length of the curve of the time series; an alternative method for calculating the length of the fractal curve was proposed by Higuchi (1988). In the present work, the fractal dimension of the signal is calculated using the method of Higuchi (1988, see also Higuchi, 1990). This method provides an indication of the fractal dimension(s) of the signal and the upper limit(s) of the frequency range(s) over which these fractal dimension(s) are an appropriate description of the signal. The method for estimating the fractal dimension(s) relies on the scaling behavior of the length of the fractal curve with the time scale. Briefly, a specific number of time series are constructed from the measured time series, X, as

$$X_\tau^m \rightarrow X(m), X(m+\tau), X(m+2\tau), \ldots, X\left(m + \left[\frac{N-m}{\tau}\right]\tau\right) \quad m = 1, 2, \ldots, \tau \tag{7}$$

Here m is simply an index representing the starting time, and τ is an integer time interval. The time interval is varied, and for each value of τ this process yields τ new time series. In effect, the sample rate is systematically reduced as the time series is decimated using increasing values of τ. For each resulting time series the length of the curve is calculated from

$$L_m(\tau) = \left\{\left[\sum_{i=1}^{[N-m/\tau]} |X(m+i\tau) - X(m+(i-1)\tau)|\right] \times \frac{N-1}{\left[\frac{N-m}{\tau}\right]\tau}\right\}\frac{1}{\tau} \tag{8}$$

The average curve length, $\langle L_m(\tau)\rangle$, determined from averaging the lengths of the decimated time series for each τ, is plotted as a function of τ on logarithmic axes. The scaling behavior of this curve length is shown in Fig. 2 for a measured pressure signal. In measured data, the power law index or the fractal dimension will not be constant over all time scales. As clearly described by Higuchi (1988), the slopes on this plot represent dimension estimates. In Fig. 2, two distinct linear regions are observed. For the range of ln (τ) between 0 and 3.5, the slope

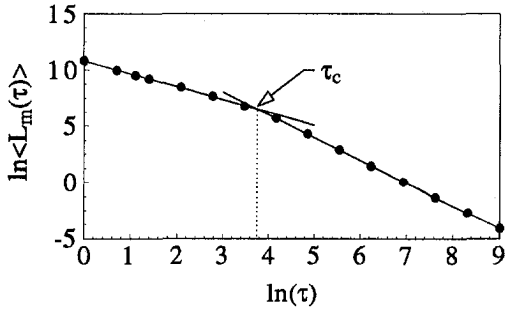

Fig. 2 Scaling relationship from Higuchi method

on the scaling curve is equal to -1.22 ± 0.01, i.e., $D_1 = 1.22$. Over this range of time scales, scaling is valid and the curve exhibits self-affinity. For values of ln (τ) greater than 4, the slope is equal to -2.00 ± 0.01, i.e., $D_2 = 2.00$. The curve is no longer fractal for time scales in this region. The point on the figure of ln $\langle L_m(\tau) \rangle$ versus ln (τ) where the two linear regions meet is known as the characteristic time, τ_c. The characteristic time suggests a maximum sample frequency, $f_{2,1}$, for which the signal remains fractal. For all experimental signals in the present investigation, only one fractal region was identified on the scaling curves; therefore, $M = 1$ in Eq. (1).

A simulated pressure signal, $p_s(t)$, consists of a fractal and non-fractal contribution which are superimposed. These two contributions represent the scale-independent and scale-dependent contributions, respectively. The scale-dependent contribution is non-universal and will change with the relevant scales, such as physical dimensions. Based on the number of significant peaks in the power spectrum not uniquely characterized by the scale-independent contributions, the scale-dependent contribution may consist of a number of terms:

$$p_{nf}(t) = \sum_{i=1}^{k} A_i \cos(\omega_i t) \tag{9}$$

The amplitudes of the non-fractal components, A_i, are determined directly from the amplitude spectrum at the various ω_i. For the present work, the non-fractal or scale-dependent contribution of the simulated pressure signal is represented by a single term characterizing the natural frequency of the bed; therefore, $k = 1$ in Eq. (9). Using Eq. (1) and Eq. (9) in conjunction with

$$p_s(t) = p_f(t) + p_{nf}(t) \tag{10}$$

allowed for a pressure signal to be simulated.

The natural frequency of the gravitational pressure fluctuations in a fluidized bed can be determined from measured pressure data, and can also be predicted from (Baskakov et al., 1986)

$$f_p = \frac{1}{\pi}\sqrt{\left(\frac{g}{L_o}\right)} \tag{11}$$

For the operating conditions in the present facility, the natural frequency of the bed was determined both from Eq. (11) and experimentally to be 1.8 Hz. The amplitude corresponding to 1.8 Hz on the amplitude spectrum of the experimental signal provides the additional input, A_i, required for Eq. (9).

Results and Discussion

The pressure signals analyzed in the present study are representative of bubbling fluidized bed behavior for Group B particles. To determine the parametric dependence of these characteristics on various operating conditions, several pressure signals were investigated. Bubble hydrodynamics and surface renewal phenomena are well documented for the lower half of a horizontal cylinder immersed in a gas-fluidized bed operating at low U/U_{mf}. Signals acquired at 0 and 90 degree positions relative to the stagnation point correspond to this region of the cylinder. Signals at 180 degrees from the stagnation point experienced no surface renewal. For the present study, signals were examined for fluidization ratios of 1.2 and 1.5 with the cylinder pressure tap positioned at 0, 90 and 180 degrees and with a pressure tap located in the wall of the test section.

Figure 3 shows measured time variations in pressure; the mean of the signal has been offset to zero. This signal was acquired at a fluidization ratio of 1.2 with the pressure tap located 90 degrees from the stagnation point. The dimension, D_1, determined from the Higuchi method for this signal is 1.22, yielding values of -2.56 and 0.78 for G_1 and H_1, respectively.

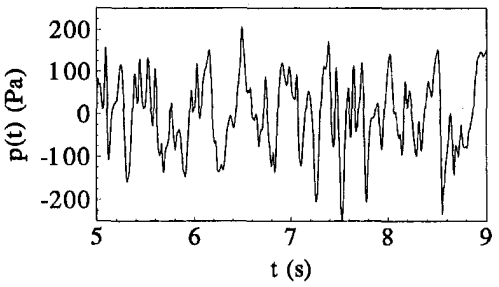

Fig. 3 Experimental signal corresponding to $U/U_{mf} = 1.2$ at the 90 degree position (mean offset to zero)

The scaling curve for this particular signal is shown in Fig. 2. The value of τ_c was determined to be 53 ms which corresponds to a maximum frequency, $f_{2,1}$, of 18.8 Hz. In Fig. 4, the log-log power spectrum of the signal in Fig. 3, a power law behavior is observed in the frequency range between 4 Hz and 18.8 Hz. Using a linear regression analysis, the slope of this region on the logarithmic power spectrum was equal, within the data uncertainty, to that determined from the fractal dimension. The consistency between the slope G_1 and D_1 helped to confirm the validity of employing 4 Hz as the lower frequency, $f_{l,1}$, in the simulation process.

The sensitivity of the signal simulation process to the parameters of the WM function yields insight into the consistency of the relationships between the fractal characteristics of the measured signal and the WM function. The precision error in the slope of the scaling region in Fig. 2 is ± 0.01. A change of this magnitude in the simulation process yields a change of approximately 5 percent in the RMS of the simulated signal. This is comparable with the 35 percent change in RMS observed for a change of ± 0.10 in D_1. Further details regarding the sensitivity of the simulation process to changes in H_1 are provided in Part 2 of this paper.

It was necessary to establish a value for the amplitude of the single fractal component of the simulated signal. The values for this amplitude and the other signal simulation parameters are strongly coupled; thus, it was desired to establish a value of the amplitude that accurately represented the signal characteristics when used with the value of H_1 determined from the fractal dimension of the curve. It was found that using the peak-to-peak value of the experimental signal as the fractal amplitude yielded excellent simulations. Determination of b, the remaining parameter in the WM model, was accomplished by parametric studies comparing measured and simulated pressure signals (Eq. 10). The quality of the simulation was judged using the statistical and dynamic quantities of the signal. It should be noted that it was ultimately possible to use a single value of b for each operating condition. Further investigations of the dynamic quantities are discussed in Part 2 of this paper.

The value of b that best replicated the frequency distribution of the fluctuating phenomena of the experimental signal in Fig.

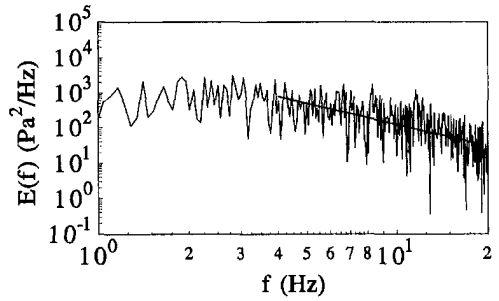

Fig. 4 Power spectrum of experimental signal in Fig. 3 ($G_1 = -2.28$, $H_1 = 0.64$)

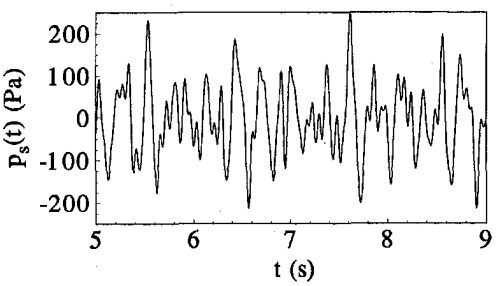

Fig. 5 Simulated signal based on parameter values from Fig. 4 (U/U_{mf} = 1.2 and 90 degrees)

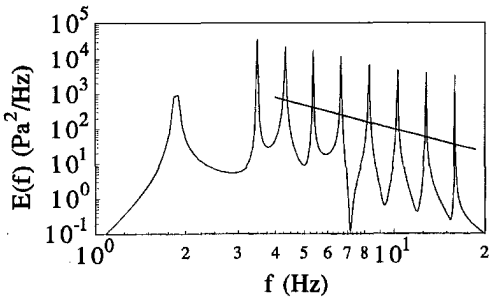

Fig. 6 Power spectrum of simulated signal in Fig. 5 (G_1 = −2.28, H_1 = 0.64)

3 was found, by visual, statistical, and dynamical comparison with the measured data, to be 1.245. Figure 5 shows the simulated signal corresponding to the experimental signal in Fig. 3. Information required to simulate the pressure signal in Fig. 5, which includes both scale-dependent and scale-independent contributions, is shown in Table 1. The local fractal dimension and the slope of the power spectrum are also provided in Table 1. Figure 6 shows the power spectrum of the simulated signal in Fig. 5.

Because the parameters of the fractal signal simulation process are derived in part from the power spectrum of the measured signal, it is reasonable to expect that the simulated signal will reproduce the frequency characteristics of the measured data. However, the definition of frequency in Eq. (1) and Eq. (2) is such that the value of b can have a considerable impact on the simulated signal. For example, given a fixed range of frequencies, an increase in b yields a smaller range of the index n, and therefore, fewer frequencies composing the fractal. The influence of b on the simulation process and the statistical and dynamic measures is addressed in greater detail in Part 2 of this paper.

In the present paper, signal simulation will be examined qualitatively through comparison of the power spectra and quantitatively through use of root-mean-square (RMS) assessments of both the experimental and simulated signals. Additional measures of the signal characteristics can be derived from the physical basis of the largest scale pressure fluctuations. Consider the occurrence of a large rise or drop in pressure, associated with bubble dynamics in the bed. It is desired to have the simulated signal correctly model the time that the pressure remains near its maximum or minimum values. A method for determining the mean signal width, which provides a means of assessing the time duration of the minimum and maximum regions of pressure, is described. The procedure takes advantage of the characteristic positive and negative crossings of the mean value observed in the signal. In the present case, signal width is measured as the duration of a positive pressure occurrence, thus the time between a positive crossing of the mean and a negative crossing of the mean represents one positive pressure occurrence. The average of all such occurrences will be termed the mean signal width, γ.

The mean signal width and root-mean-square value of the simulated signal were compared with those of the experimental signal. The results are tabulated in Table 2. Mean signal widths for the experimental and simulated signals corresponding to U/U_{mf} = 1.2 and θ = 90 degrees were found to be 74 ms and 77 ms, respectively. The RMS value of 85.0 Pa for the simulated signal is within 3 percent of the RMS value of 87.4 Pa determined from the experimental signal. Maximum and minimum values of pressure also showed excellent agreement between the experimental signal and simulated signal. Each assessment was performed using a data set consisting of 16,384 points, a length found to yield a stationary signal.

It is desired to simulate and examine signals acquired under different operating conditions and at different angular positions and locations throughout the bed. Shown in Fig. 7 is a pressure signal acquired at the wall of the test section with the bed operating at U/U_{mf} = 1.2. The values employed in the simulation of the signal shown in Fig. 8 are provided in Table 1. Once again, the value of b that provided the best simulation of the experimental signal was equal to 1.245. Values of γ and RMS for the simulated signal are within five percent of those values determined for the experimental data. A comparison of the RMS and mean signal widths of the simulated signal with those of the experimental signal show excellent agreement for each case identified in Table 2.

For both fluidization ratios, 1.2 and 1.5, the pressure tap in the wall of the test section experienced alternating bubble and emulsion phase interactions. Likewise, when the cylinder pressure tap was positioned at the 0 and 90 degree positions, it experienced surface renewal, whereas it remained under a stagnant cap of particles when in the 180 degree position. Although, for a fixed fluidization ratio, some tap locations experienced surface renewal while others did not, the same value of b was found to best reproduce the characteristics of the experimental signal. For instance, b = 1.245 was employed to simulate all signals acquired with U/U_{mf} = 1.2, and b = 1.230 was used for simulating data at U/U_{mf} = 1.5. The fact that b remained constant for a fixed fluidization ratio is of interest considering the surface renewal phenomenon varies considerably as a function of angular position around the cylinder and at different locations in the test section. In summary, b appears to be a

Table 1 Input values used to simulate the pressure signals ($f_i = f_1$ = 1.8 Hz)

U/U_{mf} (—)	θ (degs)	A_i (Pa)	b (—)	A_j (Pa)	$f_{1,1}$ (Hz)	$f_{2,1}$ (Hz)	H_1 (—)	D_1 (—)	G_1 (—)
1.2	0	12.3	1.245	600	4.5	20.8	0.73	1.27	−2.46
1.2	90	16.3	1.245	725	4.0	18.8	0.78	1.22	−2.56
1.2	180	17.8	1.245	465	2.5	11.6	0.85	1.15	−2.70
1.2	wall	5.5	1.245	150	2.5	11.0	0.77	1.23	−2.54
1.5	0	7.6	1.230	500	4.0	19.4	0.81	1.19	−2.62
1.5	90	24.5	1.230	620	3.0	15.0	0.85	1.15	−2.70
1.5	180	10.0	1.230	300	2.0	12.0	0.85	1.15	−2.70
1.5	wall	4.0	1.230	110	2.5	9.8	0.71	1.29	−2.42

function of fluidization velocity, but independent of local hydrodynamic conditions.

Of particular interest in comparing the signals obtained at a fixed fluidization ratio is the density of the pressure fluctuations. In the present context, the density of the fluctuations provides a qualitative assessment of the number of times the pressure signal crosses the mean. Although variations in the fluctuating nature of the experimental pressure signals in Fig. 5 and Fig. 8 are evident, both signals were simulated using the same value of b. Variations in the mean signal width are also noted in Table 2 for fixed values of b. Three aspects of the signal simulation that may contribute to these variations for a constant value of b are discussed. First, as was pointed out by Berry and Lewis (1980), if all other parameters are kept constant, including b, an increase in H_j results in an increase in the mean signal width of the simulated signal. Second, decreases in the frequency range $f_{2,1}-f_{1,1}$ also result in increases in γ. Similarly, decreases in $f_{1,1}$ result in increased values of γ. Simulation of data at the wall was performed with the smallest range of frequencies. For the aforementioned reasons, it is possible to simulate signals that display significantly different fluctuations using the same value of b. In a parallel study on signal simulation of local instantaneous heat transfer (Pence and Beasley, 1995), the parameter b was also found to be independent of angular position of the cylinder, as long as the heat flux probe was experiencing surface renewal. Obviously, fluctuations in the heat transfer coefficient are more dependent upon the surface renewal phenomenon than are pressure fluctuations.

The best simulations, as judged both from statistical and dynamical measures, resulted from employing the following. For the nonfractal contribution, a single term based on the natural frequency of the bed was employed. For the fractal contribution,

1. fractal dimension estimates and upper bound frequency contributions were determined from Higuchi's method (Higuchi, 1988),
2. the lower bound frequency was determined from the power spectrum,
3. the amplitude of the fractal was found from the experimental signal itself, and
4. a constant value of b, which was found to be independent of the fluidization velocity, was used.

Sensitivity analyses of H_1, b, $n_{1,1}$, and $n_{2,1}$ based on statistical measures were performed. A change of ± 0.10 in H_1 resulted in 30 to 40 percent changes in RMS_s, and an average 6 percent change in γ_s. Changes on the order of ± 0.01 in the parameter b were found to yield an average change of 10 percent in both RMS_s and γ_s. Because of the integer restrictions on n in Eq. (2) and the truncating nature of the algorithm employed for simulation purposes, slight variations in the range of frequencies, while holding all other parameters constant, did not necessarily result in variations of $n_{1,1}$ and $n_{2,1}$. Under such limiting conditions, changes in the frequency range would yield no change in the simulated signal. For instance, for a value of b equal to 1.245, changing $f_{1,1}$ from 4 Hz to 3.5 Hz yields no change in $n_{1,1}$; rather, both frequencies yield an integer value of 14 for $n_{1,1}$. For this reason, increases and reductions in $n_{1,1}$ and $n_{2,1}$ were investigated. Changes of ± 1 in $n_{1,1}$, the lower bound of the frequency range, resulted in an average change of 15 percent in both RMS_s and γ_s. On the other hand, changing $n_{2,1}$ by ± 1 yielded negligible changes in statistical measures while yielding significant changes in the Kolmogorov entropy. A more comprehensive evaluation of the effect of perturbing the aforementioned parameters on the Kolmogorov entropy is provided in Part 2 of the paper.

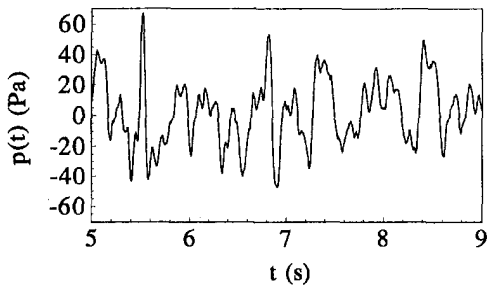

Fig. 7 Experimental signal corresponding to $U/U_{mf} = 1.2$ at the wall tap (mean offset to zero)

The signal simulations presented here provide a basis for further investigation of the fractal nature of pressure and hydrodynamics in bubbling fluidized systems. While the simulations are promising, no definitive connection with the physics has been achieved. Previous studies of single fractal time-series data suggest some directions for relating fractal aspects of time-series data to physical phenomena. Feder (1988) describes Hurst's rescaled range (R/S) analysis, which has a basis in the physics of water reservoirs and wave phenomena, and describes a characteristic termed persistence. Persistence is a measure of positive correlation in time-series data over consecutive increments of time (an increase in the signal is likely to be followed by another increase). The Hurst exponent, H, is a measure of persistence, having a value of 0.5 for random signals, greater than 0.5 for persistent signals, and less than 0.5 for antipersistent signals.

Consider the results presented in Table 1 for H_j, in light of the equivalence of H_j and the Hurst exponent. For each signal investigated, the Hurst exponent is greater than 0.5, suggesting persistent behavior. Kwon et al. (1994) also found H values greater than 0.5 in three phase fluidized beds, and found H to decrease with increasing gas flow rate and to increase with increasing liquid flow rate. With the exception of the wall pressure data, Table 1 displays an increase in H_j with increasing gas flow rate. In general, an increase in H_j is also observed with increasing angular position around the cylinder. Further investigation regarding Hurst exponents is warranted.

Table 2 Comparison between experimental and simulated signals

U/U_{mf} (—)	θ (degs)	γ_e (ms)	γ_s (ms)	RMS_e (Pa)	RMS_s (Pa)
1.2	0	59	60	73.9	71.5
1.2	90	74	77	87.4	85.0
1.2	180	128	122	62.4	62.2
1.2	wall	122	117	24.8	25.4
1.5	0	64	68	58.6	52.6
1.5	90	97	97	71.7	68.6
1.5	180	115	126	45.4	46.5
1.5	wall	111	115	18.5	21.3

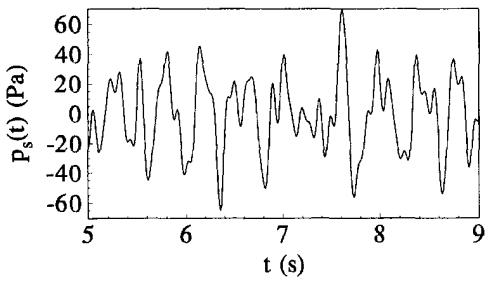

Fig. 8 Simulated signal corresponding to signal in Fig. 7 ($U/U_{mf} = 1.2$ and wall tap)

Conclusions

Signals representing local instantaneous pressure in a bubbling gas-fluidized bed were simulated. Signal simulation was accomplished by superimposing the scale-dependent contribution of pressure fluctuations, determined from the natural frequency of the bed, onto the scale-independent contribution. The scale-independent, or fractal, contribution was simulated using the Weierstrass-Mandelbrot function and parameters determined from measured time-series data. The method of signal simulation employed by Humphrey et al. (1992) is refined in the present paper by using the method of Higuchi (1988) to determine the scaling factor and upper frequency limit in the Weierstrass-Mandelbrot function. The peak-to-peak value of the experimental pressure signal was used as input for the amplitude of the fractal contribution in the simulation process. Fractal dimension estimates showed single fractal characteristics for all pressure data investigated. Average signal widths and root-mean-square values suggest that the statistical characteristics of the experimental signal can be accurately reproduced in the simulated signal. A dynamic, or chaotic, assessment of the simulation process is provided in Part 2 of this paper.

The value of the frequency parameter, b, used in the Weierstrass-Mandelbrot function remained constant for each fluidization ratio. These results strongly suggest that b, which is related to frequency distribution, may be related to the fluidization ratio, and may be independent of both angular and planar location in the regions of similar fluidization conditions. Increases in angular position and increases in flow rate generally demonstrated an increase in persistence. No clear relation between the physics and frequency range of the signal simulation was found, perhaps limiting the use of the signal simulation for scale up modeling. However, the simulated signals have suggested there may be relationships between fractal dimensions and both surface renewal phenomena and particle motion.

Acknowledgments

Thanks are extended to Manufacturing and Technology Conversion International, Inc. and the South Carolina Energy Research and Development Center for partial funding of the experimental work. Support from the Department of Mechanical Engineering is gratefully acknowledged. Thanks are also extended to Dr. James A. Liburdy for bringing the WM function to our attention, and to Mr. M. Cory Postle for his invaluable assistance in the laboratory.

References

Baskakov, A. P., Tuponogov, V. G., and Filippovsky, N. F., 1986, "A Study of Pressure Fluctuations in a Bubbling Fluidized Bed," *Powder Technology,* Vol. 45, pp. 113–117.

Berry, M. V., and Lewis, Z. V., 1980, "On the Weierstrass-Mandelbrot Fractal Function," *Proc. R. Soc. Lond. A,* Vol. 370, pp. 459–484.

Burlaga, L. F., and Klein, L. W., 1986, "Fractal Structure of the Interplanetary Magnetic Field," *J. Geophys. Res.,* Vol. 91, pp. 347.

Daw, C. S. and Halow, J. S., 1991, "Characterization of Voidage and Pressure Signals from Fluidized Beds Using Deterministic Chaos Theory," *Proceedings of the 11th International Conference on Fluidized Bed Combustion,* Montreal, Vol. 2, pp. 777–786.

Daw, C. S., Lawkins, W. F., Downing, D. J., and Clapp, N. E. Jr., 1990, "Chaotic Characteristics of a Complex Gas-Solids Flow," *Physical Review A,* Vol. 41, No. 2, pp. 1179–1181.

Fan, L. T., Kang, Y., Yashima, M., and Neogi, D., 1995, "Stochastic Behavior of Fluidized Particles in a Liquid-Solid Fluidized Bed," *Chem. Eng. Comm.,* Vol. 135, pp. 147–160.

Fan, L. T., Neogi, D., Yashima, M., and Nassar, R., 1990, "Stochastic Analysis of a Three-Phase Fluidized Bed: Fractal Approach," *AIChE Journal,* Vol. 36, No. 10, pp. 1529–1535.

Feder, J., 1988, *Fractals,* Plenum Press, New York, pp. 149–199.

Fuller, T. A., Flynn, T. J., Daw, C. S., and Halow, J. S., 1993, "Interpretation of Pilot-Scale, Fluidized Bed Behavior using Chaotic Time Series Analysis," *Proceedings of the 12th International Conference on Fluidized Bed Combustion,* San Diego, ASME, Vol. 1, pp. 126–140.

Geldart, D., 1973, "Types of Fluidization," *Powder Technology,* Vol. 7, pp. 285–292.

Higuchi, T., 1988, "Approach to an Irregular Time Series on the Basis of the Fractal Theory," *Physica D,* Vol. 31, pp. 277–283.

Higuchi, T., 1990, "Relationship between the Fractal Dimension and the Power Law Index for a Time Series: A Numerical Investigation," *Physica D,* Vol. 46, pp. 254–264.

Humphrey, J. A. C., Schuler, C. A., and Rubinsky, B., 1992, "On the Use of the Weierstrass-Mandelbrot Function to Describe the Fractal Component of Turbulent Velocity," *Fluid Dynamics Research,* Vol. 9, pp. 81–95.

Kwon, H. W., Kang, Y., Kim, S. D., Yashima, M., and Fan, L. T., 1994, "Bubble-Chord Length and Pressure Fluctuations in Three-Phase Fluidized Beds," *Ind. Eng. Chem. Res.,* Vol. 33, pp. 1852–1857.

Mandelbrot, B. B., 1977, *Fractals: Form, Chance and Dimension,* Freeman, San Francisco.

Pence, D. V., and Beasley, D. E., 1995, "Multi-Fractal Signal Simulation of Local, Instantaneous Heat Transfer in a Bubbling Gas Fluidized Bed," *Proceedings of the 30th National Heat Transfer Conference,* Portland, OR, ASME HTD-Vol. 309, pp. 73–82.

Pence, D. V., Beasley, D. E., and Riester, J. B., 1995, "Deterministic Chaotic Behavior of Heat Transfer in Gas-fluidized Beds," ASME *Journal of Heat Transfer,* Vol. 117, No. 2, pp. 465–472.

Schouten, J. C. and van den Bleek, C. M., 1992, "Chaotic Hydrodynamics of Fluidization: Consequences for Scaling and Modeling of Fluid Bed Reactors," *A.I.Ch.E. Symposium Series,* Vol. 88, No. 289, pp. 70–84.

Skrzycke, D. P., Nguyen, K., and Daw, C. S., 1993, "Characterization of the Fluidization Behavior of Different Solid Types Based on Chaotic Time Series Analysis of Pressure Signals," *Proceedings of the 12th International Conference on Fluidized Bed Combustion,* San Diego, Vol. 1, pp. 155–166.

van der Stappen, M. L. M., Schouten, J. C., and van den Bleek, C. M., 1993, "Application of Deterministic Chaos Theory in Understanding the Fluid Dynamic Behavior of Gas-Solids Fluidization," *Fluid-Particle Processes: Fundamentals and Applications,* A.I.Ch.E. Symposium Series, Vol. 296, pp. 91–102.

D. V. Pence
Assistant Professor,
Department of Mechanical Engineering and
Applied Mechanics,
University of Rhode Island,
92 Upper College Road,
Kingston, RI 02881

D. E. Beasley
Professor,
Department of Mechanical Engineering,
Clemson University,
Box 340921,
Clemson, SC 29634

Multi-Fractal Signal Simulation of Local Instantaneous Pressure in a Bubbling Gas-Fluidized Bed—Part 2: Chaos Assessment

Introduction

The purpose of this paper, in two parts, is to (1) determine the fractal characteristics of time-series pressure data from a gas-fluidized bed, (2) evaluate the possibility of using the Weierstrass-Mandelbrot (WM) function to simulate the fractal and dynamic characteristics of such pressure data, (3) refine the method of signal simulation introduced by Humphrey et al. (1992) for turbulence data, and (4) to investigate the nonlinear, fractal, and physical phenomena of pressure in a fluidized bed as a function of angular position around a cylinder, location in the bed, and the fluidization ratio. In Part 1, the time series data was found to be singularly fractal over a well-defined scale or range of frequencies. In addition, the simulation method employed by Humphrey et al. (1992) was made somewhat less subjective by employing the method of Higuchi (1988) to determine the upper frequency range in the WM function. The method of Higuchi (1988) was also used to compute the fractal dimension of the time series, from which the scaling factor was determined. Also in Part 1, the simulation method was shown to replicate the statistical characteristics of the time-series data with a high degree of fidelity, and the frequency parameter in the WM function was found to be dependent upon the fluidization velocity. The present paper, Part 2, is specifically devoted to (a) assessing the nonlinear dynamical, or chaotic, characteristics of the simulated data, and (b) relating chaos measures to physical phenomena as a function of operating conditions.

Recently, fluidized systems have been analyzed from the perspective of chaos signal analysis using instantaneous time-series measurements of physical quantities. The results of these analyses for heat flux traces (Pence et al., 1995), and pressure and void fraction traces (van der Stappen et al., 1993; Skrzycke et al., 1993; Schouten and van den Bleek, 1992; Fuller et al., 1993; Daw and Halow, 1991; and Daw et al., 1990), indicate behavior consistent with low-dimensional deterministic chaos. As such, there exists the possibility that the complex behavior observed in fluidized systems may be described through relatively simple mathematical functions, or even controlled as has been the case for several nonlinear systems. For example, Pence and Beasley (1997) have recently demonstrated chaos suppression in pulse-stabilized fluidization.

In the work of Humphrey et al. (1992), the Weierstrass-Mandelbrot (WM) function, a geometric progression of frequencies, was employed to simulated the irregularity in a turbulent velocity time series. The Weierstrass-Mandelbrot (WM) function, used to simulate the scale-independent or fractal characteristics of turbulence, successfully yielded correct forms for the energy and dissipation spectra. Superposition of the simulated fractal contribution and a deterministic, scale-dependent contribution yielded signals that exhibited characteristics similar to those of the experimental signals. The multi-fractal simulations of Humphrey et al. (1992) were based on the work of Berry and Lewis (1980) for a single fractal. Turbulence data, like fluidized bed data, have also been investigated using chaos analysis techniques (Bergé et al., 1984). Therefore, it is logical that fluidized bed data may in fact be fractal and, similar to the investigation of Humphrey et al. (1992), the WM function may provide a means for simulating fluidized bed pressure data for applications in scale up and modeling.

A clear distinction is necessary in the present context between the fractal geometry of the WM function, and the fractal dimension of an attractor in phase space. Briefly, chaotic dynamical systems exhibit phase-space attractors that have fractal dimensions in phase space, and thus are termed "strange attractors." On the other hand, fractal or multi-fractal signals, such as fractal Brownian motion, yield fractal dimensions when examined as geometrical objects, for example, a plot of $p(t)$ versus t.

Previous studies of single fractal time-series data suggest some directions for relating fractal aspects of time-series data to physical phenomena. Feder (1988) describes Hurst's rescaled range (R/S) analysis, which has a basis in the physics of water reservoirs and wave phenomena, and describes a quantitative measure termed persistence. Persistence is a measure of positive correlation in time-series data over consecutive increments of time, i.e. an increase in the signal is likely to be followed by another increase. The Hurst exponent, H, is a quantitative measure of persistence, having a value of 0.5 for random signals, greater than 0.5 for persistent signals, and less than 0.5 for antipersistent signals. Fan et al. (1993) used rescaled range (R/S) analysis to examine the fractal nature of liquid-solid fluidized beds; the pressure fluctuations in liquid-solid fluidized beds are amenable to this analysis procedure, and show behavior consistent with persistent fractal Brownian motion. In a subsequent paper (Kwon et al., 1994), Hurst exponents were used as a correlating variable for bubble chord length in three-phase fluidized beds.

It is the purpose of this part of the two-part paper to examine chaos measures for experimentally measured and simulated time-series data that represent pressure in a bubbling gas-fluidized bed. In Part 1 of this paper, the experimental facility in which pressure was measured was described. Briefly, an experimental fluidized bed facility was designed to accommodate two submerged horizontal cylinders. The cylinders, 3.8 cm in diameter, were positioned with their axes 15 cm above a porous polyethylene distributor plate and with a center-to-center distance of 18 cm. Each cylinder was instrumented with a 3 mm

Contributed by the Fluids Engineering Division for publication in the JOURNAL OF FLUIDS ENGINEERING. Manuscript received by the Fluids Engineering Division June 5, 1995; revised manuscript received October 15, 1997. Associate Technical Editor: O. C. Jones.

diameter pressure tap that could be rotated to any angular position on the cylinder. A similar tap was located in the wall of the facility at a height above the distributor plate corresponding to the stagnation point of the cylinders.

A porous distributor plate with a nominal pore size of 40 microns and cross sectional flow area of 930 cm^2 provided uniform flow distribution and bubbling. The facility was charged with a monosize particle distribution of 345 μm spherical glass particles. The experimental value of minimum fluidization velocity was found to be 0.086 m/s. Operation of the fluidized bed was limited to the bubbling flow regime, with fluidization velocity ratios, U/U_{mf}, of 1.2 and 1.5 reported in the present study. Angular positions of the pressure tap on the cylinder corresponding to 0, 90 and 180 degrees relative to the stagnation point were examined in the present work. The 0 and 90 degree angular positions correspond to the lower half of the cylinder where surface renewal characteristics are best documented.

All pressure taps were connected to Omega model PX162-027D5V pressure transducers with a 1–6 Volt range corresponding to 0–6.9 kPa (gage). Local pressures were measured relative to atmosphere. The transducers were calibrated using a digital micro-manometer as a standard, yielding an uncertainty of 40 Pa in the pressure level and an uncertainty of 4 percent in the pressure fluctuations. A total of 16,500 data points were acquired for each signal at a sample rate of 500 Hz using a 12 bit Metrabyte data acquisition system.

Signal Simulation and Analysis

Signal Simulation. The multi-fractal Weierstrass-Mandelbrot (WM) function, used to simulate the signals under analysis in the present paper, is a geometric progression of frequencies defined by

$$p_f(t) = \sum_{j=1}^{M} A_j \sum_{n=n_{1,j}}^{n_{2,j}} \frac{\sin(\omega t)}{\omega^{H_j}} \tag{1}$$

where $p_f(t)$ represents the fractal or scale-independent contribution of time variations in pressure of a generated signal. For the experimental pressure signals investigated in the present work, the scaling curve (Higuchi, 1988) indicated one scaling region. This is consistent with the experimental power spectra which exhibited a single slope, which is indicative of only one fractal component, over the entire scaling region.

In Part 1 of this paper, pressure signals were simulated by linearly superposing the fractal contribution of Eq. (1) on a nonfractal or scale-dependent contribution, defined by

$$p_{nf}(t) = \sum_{i=1}^{k} A_i \cos(\omega_i t) \tag{2}$$

The resulting signals were found to accurately reflect the statistical nature of the experimental signals. Further details regarding the simulation process are available in Part 1.

Chaos Analysis. An assessment of the signal simulation from a statistical viewpoint is outlined in Part 1 of this paper. Here the examination of the simulated signals focuses on the nonlinear dynamical quantities. Techniques for the analysis of chaotic time series data are applied to both the experimental and simulated signals to provide a comparison of both quantitative and qualitative measures of chaos. Specifically, minimum embedding dimension and Kolmogorov entropy will be evaluated. These measures result from the construction of an attractor in phase space. Minimum embedding dimensions and 2-D phase portraits of an attractor provide qualitative assessments of chaos. Kolmogorov entropy estimates provide a quantitative analysis of the degree of chaotic behavior represented by the resulting attractor.

According to Takens' embedding theorem (Takens, 1981), a single measurement time series contains sufficient information regarding the system dynamics to reconstruct a state vector, and through time-delay embedding to reconstruct an attractor in phase space. Evidence of chaotic behavior in nonlinear signals requires estimates of invariant probability measures. By definition, these invariant measures will be the same in the reconstructed space, if properly embedded in phase space, as those evaluated from a state space evolution of the attractor. If the signal is embedded in too small of a dimension, however, the trajectory will not be truly unfolded and the invariant measures of the reconstructed attractor will not be representative of the underlying dynamics. Abarbanel and Kennel (1993) distinguish between the minimum embedding dimension and the dynamical dimension. The latter quantity represents the actual number of degrees of freedom representative of the dynamic state of the system and is an invariant measure of the system dynamics.

Nomenclature

A_i = amplitude of nonfractal component, i (Pa)
A_j = amplitude of fractal component, j
b = constant base of cyclic frequency; frequency parameter
D_j = local fractal dimension estimate of jth fractal, determined using Higuchi method (Higuchi, 1988)
$f_{1,j}$ = lowest frequency associated with fractal j (Hz)
$f_{2,j}$ = highest frequency associated with fractal j (Hz)
G_j = slope of jth fractal on log-log power spectrum [$G_j = 2D_j - 5$]
H = Hurst exponent
H_j = scaling factor of jth component of multi-fractal [$H_j = 2.0 - D_j$]
i = summation index for nonfractal contribution of signal (Eq. (2))
j = summation index for fractal contribution of signal (Eq. (1))
k = number of nonfractal components
K = Kolmogorov entropy estimate (bits/s)
M = number of fractals composing multi-fractal
n = summation index for cyclic frequency calculations
$n_{1,j}$ = lower limit of frequency equivalent for cyclic frequency calculations of jth fractal
$n_{2,j}$ = upper limit of frequency equivalent for cyclic frequency calculations of jth fractal
$p(t)$ = experimental instantaneous pressure signal (Pa)
$p_f(t)$ = fractal (scale-independent) contribution to simulated signal (Pa)
$p_{nf}(t)$ = nonfractal (scale-dependent) contribution to simulated signal (Pa)
$p_s(t)$ = simulated instantaneous pressure signal (Pa) [$p_s(t) = p_f(t) + p_{nf}(t)$]
t = time (s)
U = superficial fluidization velocity (m/s)
U_{mf} = minimum fluidization velocity (m/s)
U/U_{mf} = fluidization velocity ratio
δ = minimum embedding dimension
θ = angular position of sensor (degrees)
ω = cyclic frequency of fractal component (rad/s) [$\omega = b^n$]
ω_i = cyclic frequency of nonfractal component (rad/s)

Subscripts

e = experimental signal
s = simulated signal

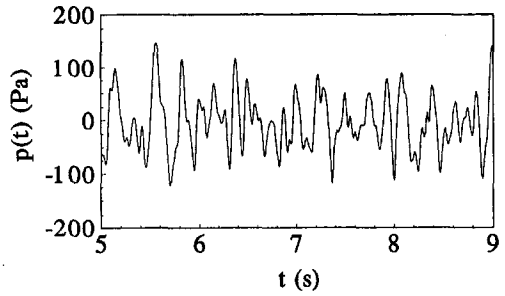

Fig. 1 Experimental signal (U/U_{mf} = 1.5, θ = 0 degrees – mean offset to zero)

This is the minimum dimension the attractor occupies in state space. A consequence of the nonlinear transformation from state space to phase space coordinates results in global folding of the attractor and a minimum embedding dimension that may be greater than the dynamical dimension.

The method of false nearest neighbors is employed here to determine an appropriate minimum embedding dimension for reconstruction of a phase space attractor. The method of false nearest neighbors by Kennel et al. (1992) identifies neighboring points. These neighbors are identified as false nearest neighbors if the nearest neighbors identified in m-dimensional space are no longer nearest neighbors when the signal is embedded in m + 1-dimensional space. The minimum dimension required to essentially eliminate these false nearest neighbors and unfold the attractor is identified as the minimum embedding dimension. In the present study, the distance between neighbors is taken as the Euclidian norm in the phase space, although other measures are possible. In addition, Kennel et al. (1992) established criteria to ensure that nearest neighbors are actually close in comparison to the scale of the attractor. To eliminate any time dependence that may result in a random signal producing a finite minimum embedding dimension, the suggestion made by Fredkin and Rice (1995) is employed. They suggest eliminating a fixed number of consecutive points in time away from the point under investigation when evaluating the nearest neighbors. We employ the time delay from mutual information, explained in detail below, for this fixed number of points.

The time delay necessary to construct a phase space trajectory from a discrete, noise free signal can in principle be chosen arbitrarily (Takens, 1981). However, this is not the case for noise distorted data. Fraser and Swinney (1986) suggest using the first minimum of the mutual information function as the time delay. This time ensures a high level of independence between coordinates in phase space; however, other time delays are also acceptable. Mutual information is based on entropy as defined in information theory, and upon the concept of uncertainty. Uncertainties associated with measurements are dependent upon the probabilities of certain outcomes. Mutual information is a quantitative measure of the amount that knowledge of a given measurement reduces the uncertainty of a future measurement.

A conclusive indicator of chaotic behavior is the metric entropy, which can be reasonably estimated from the Kolmogorov entropy. The Kolmogorov entropy represents the rate of memory loss of the system dynamics, or in other words, represents the average rate of divergence, as time progresses, of two points initially on different orbits of a trajectory and in close proximity. Purely periodic signals show no loss of memory and yield Kolmogorov entropy values equal to zero. On the other hand, random signals are completely unpredictable yielding infinite values of Kolmogorov entropy. For a signal to be considered chaotic in nature, its Kolmogorov entropy must be finite and positive.

Results and Discussion

The pressure signals analyzed in the present study are representative of bubbling fluidized bed behavior for Group B particles (Geldart, 1973). For systems where the fluidizing medium and the particles have much different densities, density wave instabilities create local pockets of very high void fraction termed bubbles. Such a system is appropriately termed a self-excited nonlinear system. Instantaneous traces of pressure provide the basis for investigating the chaotic nature of the underlying dynamics and the fractal characteristics of pressure signals. To determine the parametric dependence of these characteristics on various operating conditions, several pressure signals were investigated. Bubble hydrodynamics and surface renewal phenomena are well documented for the lower half of a horizontal cylinder immersed in a gas-fluidized bed operating at low U/U_{mf}. Signals acquired at 0 and 90 degree positions relative to the stagnation point correspond to this region of the cylinder. Signals at 180 degrees from the stagnation point experienced no surface renewal for either of the fluidization ratios, 1.2 and 1.5, examined in the present study. The fact that the fluidization conditions vary as a function of angular position around the cylinder and location within the bed will be addressed in light of the simulation process and the nonlinear analysis.

Consider representative experimental and simulated signals, as shown in Fig. 1 and Fig. 2. Figure 1 shows time variations in pressure, with the mean of the signal offset to zero, for an experimental signal with U/U_{mf} equal to 1.5 and the pressure tap located at the stagnation point of the cylinder. The signal in Fig. 2 was simulated using the WM model along with information obtained from the experimental power and amplitude spectra, and the fractal dimension determined from Higuchi's method (Higuchi, 1988).

As described in Part 1, the fractal dimension, D_j, is related to the slope of the scaling region on the logarithmic power spectrum, G_j, and the scaling factor, H_j, a parameter employed in the WM function. These values are provided in Table 1 for all operating conditions investigated in the present study. All reported fractal dimensions are between 1.5 and 2.0, which, in agreement with the results of Berry and Lewis (1980), yield smooth fractal signals. However, of particular interest is the apparent dependence of G_j, H_j, and D_j on the angular position, θ, of the pressure tap on the cylinder. In general, as noted from Table 1 for a fixed fluidization ratio, there is a decrease in D_j with increasing θ. Decreases in D_j correspond to increases in H_j. As was pointed out by Berry and Lewis (1980), keeping all other parameters constant, including b, an increase in H_j results in a larger mean signal width in the simulated signal. This trend was illustrated in Table 2 of Part 1. Also evident from Table 1 is that for a fixed fluidization ratio all signals were simulated with the same value of b. Figure 2 and Fig. 4 are the simulated data for U/U_{mf} = 1.5 at θ = 0 and θ = 180, respectively. The observed increases in mean signal width with increasing values of θ result from increases in the scaling factor as well as decreases in the frequency range and $f_{1,1}$.

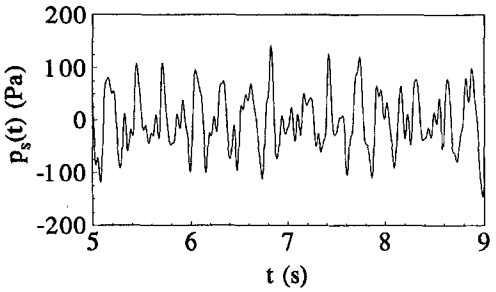

Fig. 2 Simulated signal (U/U_{mf} = 1.5, θ = 0 degrees)

Table 1 Input values used to simulate fractal component of several signals

U/U_{mf} (—)	θ (degs)	A_i (Pa)	b (—)	A^j (Pa)	$f_{1,1}$ (Hz)	$f_{2,1}$ (Hz)	G_1 (—)	H_1 (—)	D_1 (—)
1.2	0	12.3	1.245	600	4.5	20.8	−2.46	0.73	1.27
1.2	90	16.3	1.245	725	4.0	18.8	−2.56	0.78	1.22
1.2	180	17.8	1.245	465	2.5	11.6	−2.70	0.85	1.15
1.2	wall	5.5	1.245	150	2.5	11.0	−2.54	0.77	1.23
1.5	0	7.6	1.230	500	4.0	19.4	−2.62	0.81	1.19
1.5	90	24.5	1.230	620	3.0	15.0	−2.70	0.85	1.15
1.5	180	10.0	1.230	300	2.0	12.0	−2.70	0.85	1.15
1.5	wall	4.0	1.230	110	2.5	9.8	−2.42	0.71	1.29

Consider the results presented in Table 1 for H_j, in light of the equivalence of H_j and the Hurst exponent, H. For each signal investigated the Hurst exponent is greater than 0.5, suggesting persistent behavior. Kwon et al. (1994) also found H values greater than 0.5 in three phase fluidized beds, and found H to decrease with increasing gas flow rate and to increase with increasing liquid flow rate. With the exception of the wall pressure data, Table 1 shows an increase in H_j with increasing gas flow rate. An increase in H_j is also observed, in general, for increasing angular positions on the surface of the cylinder. Further investigation regarding Hurst exponents is warranted.

Chaos analysis techniques are based on an attractor constructed in phase space through time delay embedding. Table 2 provides the minimum embedding dimensions, δ_e and δ_s, for the experimental and simulated signals, respectively. For both the experimental and simulated signal with $U/U_{mf} = 1.5$ and $\theta = 180$ degrees, Fig. 3 and Fig. 4, respectively, the percentage of false nearest neighbors drops below one percent when the embedding dimension is increased from 5 to 6, suggesting a minimum embedding dimension of 5 for both signals. For the entire range of operating conditions, the minimum embedding dimensions for the simulated signals are identical to their respective experimental signals. Although the minimum embedding dimension may be larger than the dynamical dimension, the minimum embedding dimension does provide an indication of the number of active degrees of freedom in a nonlinear system. The consistency between the simulated and experimental values suggests that the chaotic nature of the simulated and measured signals may not be fundamentally different.

Phase space portraits using the numerical derivative of the signal provide a means of qualitatively assessing the agreement between the dynamic characteristics of the experimental and simulated data, and are consistent with those reconstructed using time-delay embedding for the present signals. Phase portraits for the experimental and simulated signals at 180 degrees for a fluidization ratio of 1.5 are shown in Fig. 5 and Fig. 6, respectively. These figures qualitatively illustrate the large-scale divergence of the orbits on the trajectories. The general pattern formed by the phase trajectories clearly show similar character-

Table 2 Dynamic comparison between experimental and simulated signals

U/U_{mf} (—)	θ (degs)	δ_e (—)	δ_s (—)	K_e (bits/s)	K_s (bits/s)
1.2	0	5	5	62	49
1.2	90	5	5	45	38
1.2	180	5	5	27	24
1.2	wall	5	5	23	24
1.5	0	5	5	43	43
1.5	90	5	5	35	32
1.5	180	5	5	28	20
1.5	wall	5	5	32	20

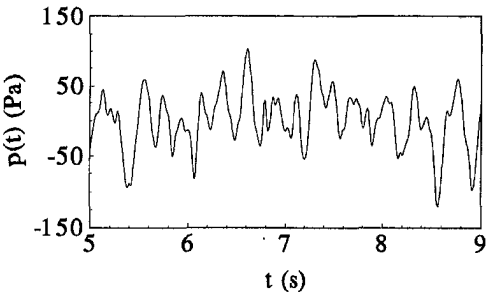

Fig. 3 Experimental signal ($U/U_{mf} = 1.5$, $\theta = 180$ degrees − mean offset to zero)

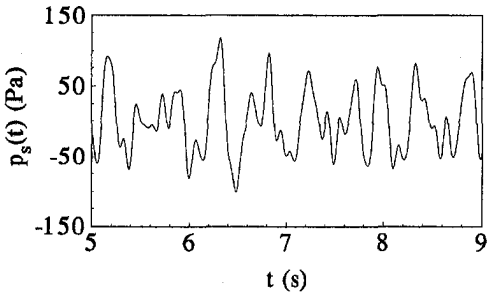

Fig. 4 Simulated signal ($U/U_{mf} = 1.5$, $\theta = 180$ degrees)

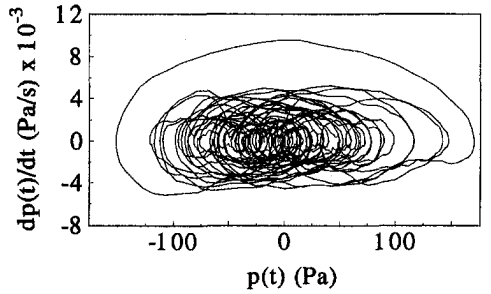

Fig. 5 Experimental signal phase trajectory ($U/U_{mf} = 1.5$, $\theta = 180$ degrees)

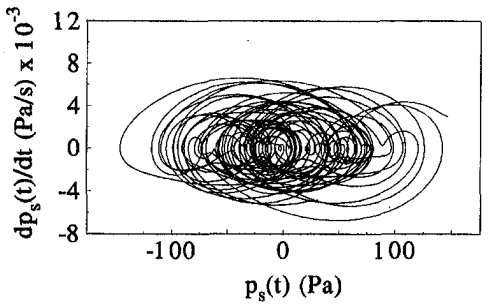

Fig. 6 Simulated signal phase trajectory ($U/U_{mf} = 1.5$, $\theta = 180$ degrees)

istics, and the minimum and maximum of both the signal and the signal derivatives are consistent between the experimental and simulated data. Experimental data used for purposes of phase space visualization were filtered with a 5 point moving average. However, data were not filtered for computing the root-mean-square, mean signal widths, power spectra, mutual information, minimum embedding dimension, or entropy.

In the commercially available software package, RRChaos, used to assess the Kolmogorov entropy, the embedding dimension and time delay used for embedding purposes were determined from the average number of points per cycle (see Schouten et al., 1994). A correlation integral code based on the work of Grassberger and Procaccia (1983) and written by the authors was used to confirm the results of RRChaos. In the author's code, the attractors were constructed using time delays determined from mutual information (Fraser and Swinney, 1986) and minimum embedding dimensions (Kennel and Abarbanel, 1993). Time correlated data were removed from the analysis using the method recommended by Theiler (1986).

Kolmogorov entropy provides an indication of the average rate of divergence of orbits on a phase space trajectory. In the present investigation, infinity corresponded to 6,500 bits/sec. All values of K_e and K_s tabulated in Table 2, which range from 20 to 62 bits/sec, are positive and finite. These results suggest that both the experimental and simulated signals exhibit characteristics consistent with chaos. The average difference between K_e and K_s is approximately 15 percent suggesting that the dynamical nature of the experimental signal was adequately reconstructed in the simulated signal. Uncertainty levels in these estimates of entropy are limited to 5 percent. This value is based on the statistical variance of repeated estimates of K and on a one percent level of uncertainty employed in the maximum likelihood approach of RRChaos. In a trend similar to that identified in Table 1 for D_j, entropy decreases with increasing angular position.

Details regarding the sensitivity of H_1, b, $n_{1,1}$ and $n_{1,2}$ based on statistical characteristics of the signals were described previously in Part 1 of this paper. In the present paper, sensitivity analyses of H_1, b, $n_{1,1}$ and $n_{1,2}$ based on the dynamic measure K_s were performed. The results suggest that changes in $n_{2,1}$, although not significantly affecting the statistical characteristics of the signals, had a pronounced affect on estimates of the Kolmogorov entropy. For instance, an average 20 percent change in K_s was observed as a result of changing $n_{2,1}$ by as little as ± 1. Small variations in $n_{1,1}$, on the order ± 1, resulted in an average variation in K_s of 8 percent. Small perturbations of ± 0.010 in b yielded an average change in K_s of 13 percent. Results of the sensitivity analysis are provided in Table 3 for the signal acquired with $U/U_{mf} = 1.2$ and $\theta = 90$ degrees.

The independence of b on the hydrodynamic or surface renewal phenomenon is investigated in light of the signal simulation process. For the signal acquired with $U/U_{mf} = 1.2$ and $\theta = 90$ degrees, $b = 1.100$ and $b = 1.900$ were employed in the WM function instead of $b = 1.245$, and RMS_s, γ_s, and K_s were assessed. The results are tabulated in Table 4. Maintaining a fixed frequency range from 4 Hz to 18.8 Hz, these changes in b result in a considerable change in both the index range, $n_{1,1}$ to $n_{2,1}$, and the RMS_s values. For $b = 1.900$, the signal was simulated with only three frequencies composing the fractal contribution, i.e. $n = 5$, 6, and 7. The entropy estimate for this signal, 3 bits/sec, suggests a highly ordered signal. This result is intuitively inconsistent with the complexity of the experimental signal, which yielded a value of K_e equal to 45 bits/s. Decreasing b from 1.245 to 1.100 did not significantly alter K_s or γ_s. However, an increase in RMS_s for $b = 1.100$ is quite apparent. The coupled nature of the various simulation parameters resulted in $b = 1.245$ for the best simulation of the experimental data, both from a statistical and dynamic perspective. Visually, the signals simulated with $b = 1.100$ and $b = 1.900$ were significantly different from that simulated using a b of 1.245.

Table 3 Sensitivity analysis of representative pressure signal ($U/U_{mf} = 1.2$, $\theta = 90$ degrees)

	b	H_1	$n_{1,1}$	$n_{2,1}$	RMS_s (Pa)	γ_s (ms)	K_s (bits/s)
simulation value	1.235				79.6	75	42
	1.245				85.0	77	38
	1.255				77.1	70	42
simulation value		0.68			120.0	73	39
		0.78			85.0	77	38
		0.88			60.6	84	36
simulation value			13		101.1	91	35
			14		85.0	77	38
			15		70.9	68	41
simulation value				20	83.2	85	17
				21	85.0	77	38
				22	85.8	70	23

Table 4 Influence of frequency parameter on statistical and dynamic measures ($U/U_{mf} = 1.2$, $\theta = 90$ degrees)

b	$n_{1,1}$	$n_{1,2}$	RMS_s	γ_s	K_s
1.100	33	50	116.0	70	35
1.245	14	21	85.0	77	38
1.900	5	7	52.7	84	3

The best simulations, as judged both from statistical and dynamical measures, resulted from employing the following. For the nonfractal contribution, a single term based on the natural frequency of the bed was employed. For the fractal contribution,

1. fractal dimension estimates and upper bound frequency contributions were determined from Higuchi's method (Higuchi, 1988),
2. the lower bound frequency was determined from the power spectrum,
3. the amplitude of the fractal was found from the experimental signal itself, and
4. a constant value of b, which was found to be independent of the fluidization velocity, was used.

The fidelity of the simulation process relied on simulating both the statistical and dynamic characteristics of the experiment pressure data. In Part 1 of the paper, the mean signal width, which increased with angular position, appeared to be related to the fractal dimension of the signal and to the Hurst exponent. In this part of the paper, the degree of chaotic behavior was found to decrease with increasing angular position. However, a more clearly delineated relation between the physics and fractal parameters is clearly warranted.

Conclusions

The statistical assessment of the simulated signals and the signal simulation process were discussed in Part 1 of this paper. In the present paper, signals representing local instantaneous pressure in a bubbling gas-fluidized bed simulated using the multi-fractal Weierstrass-Mandelbrot (WM) function were evaluated for dynamical consistency with their experimental counterparts using false nearest neighbors and Kolmogorov entropy estimates. A comparative chaos analysis demonstrated that the nonlinear characteristics of the experimental signals were replicated in the simulated signals. Minimum embedding dimensions, consistently reported to be 5, were identical between experimental and simulated signals suggesting that the dynamical characteristics of the two signals were not significantly different. Positive finite entropy values were found to exhibit similar angular trends between experimental and simulated data, with the level of entropy, or degree of chaotic behav-

ior, lessening with increasing angular position. These latter results suggest that the nonlinear nature of the hydrodynamics may be most complex at the stagnation point and least complex in the stagnant cap of particles. The results presented here provide a basis for further investigation of the fractal and chaotic nature of pressure and hydrodynamics in bubbling fluidized systems. While the simulations are promising, no definitive connection with the physics has been achieved.

Acknowledgments

Thanks are extended to Manufacturing and Technology Conversion International, Inc. and the South Carolina Energy Research and Development Center for partial funding of the experimental work. Support from the Department of Mechanical Engineering is gratefully acknowledged. Thanks are also extended to Dr. James A. Liburdy for bringing the WM function to our attention, and to Mr. M. Cory Postle for his invaluable assistance in the laboratory.

References

Abarbanel, H. D. I., and Kennel, M. B., 1993, "Local False Nearest Neighbors and Dynamical Dimensions from Observed Chaotic Data," *Physical Review E,* Vol. 47, No. 5, pp. 3057–3068.

Bergé, P., Pomeau, Y., and Vidal, C., 1984, *Order within Chaos,* Wiley, New York.

Berry, M. V., and Lewis, Z. V., 1980, "On the Weierstrass-Mandelbrot Fractal Function," *Proc. R. Soc. Lond. A,* Vol. 370, pp. 459–484.

Daw, C. S., and Halow, J. S., 1991, "Characterization of Voidage and Pressure Signals from Fluidized Beds Using Deterministic Chaos Theory," *Proceedings of the 11th International Conference on Fluidized Bed Combustion,* Montreal, Vol. 2, pp. 777–786.

Daw, C. S., Lawkins, W. F., Downing, D. J., and Clapp, N. E. Jr., 1990, "Chaotic Characteristics of a Complex Gas-Solids Flow," *Physical Review A,* Vol. 41, No. 2, pp. 1179–1181.

Fan, L. T., Kang, Y., Neogi, D., and Yashima, M., 1993, "Fractal Analysis of Fluidized Particle Behavior in Liquid-Solid Fluidized Beds," *AIChE Journal,* Vol. 39, No. 3, pp. 513–517.

Feder, J., 1988, *Fractals,* Plenum Press, New York, pp. 149–199.

Fraser, A. M., and Swinney, H. L., 1986, "Independent Coordinates for Strange Attractors from Mutual Information," *Physical Review A,* Vol. 33, No. 2, pp. 1134–1140.

Fredkin, D. R., and Rice, J. A., 1995, "Method of False Nearest Neighbors: A Cautionary Note," *Physical Review E,* Vol. 51, No. 4, pp. 2950–2954.

Fuller, T. A., Flynn, T. J., Daw, C. S., and Halow, J. S., 1993, "Interpretation of Pilot-Scale, Fluidized Bed Behavior using Chaotic Time Series Analysis," *Proceedings of the 12th International Conference on Fluidized Bed Combustion,* San Diego, CA, Vol. 1, pp. 126–140.

Geldart, D., 1973, "Types of Fluidization," *Powder Technology,* Vol. 7, pp. 285–292.

Grassberger, P., and Procaccia, I., 1983, "Estimation of the Kolmogorov Entropy from a Chaotic Signal," *Physical Review A,* Vol. 28, No. 4, pp. 2591–2593.

Higuchi, T., 1988, "Approach to an Irregular Time Series on the Basis of the Fractal Theory," *Physica D,* Vol. 31, pp. 277–283.

Humphrey, J. A. C., Schuler, C. A., and Rubinsky, B., 1992, "On the Use of the Weierstrass-Mandelbrot Function to Describe the Fractal Component of Turbulent Velocity," *Fluid Dynamics Research,* Vol. 9, pp. 81–95.

Kennel, M. B., Brown, R., and Abarbanel, H. D. I., 1992, "Determining Embedding Dimension for Phase-Space Reconstruction Using a Geometrical Construction," *Physical Review A,* Vol. 45, No. 6, pp. 3403–3411.

Kwon, H. W., Kang, Y., Kim, S. D., Yashima, M., and Fan, L. T., 1994, "Bubble-Chord Length and Pressure Fluctuations in Three-Phase Fluidized Beds," *Ind. Eng. Chem. Res.,* Vol. 33, pp. 1852–1857.

Pence, D. V., and D. E. Beasley, "Chaos Suppression in Gas-Solid Fluidization," *Proceedings of the 32nd National Heat Transfer Conference,* Baltimore, MD, ASME HTD-Vol. 350, pp. 175–182.

Pence, D. V., Beasley, D. E., and Riester, J. B., 1995, "Deterministic Chaotic Behavior of Heat Transfer in Gas-fluidized Beds," ASME *J. Heat Transfer,* Vol. 117, No. 2, pp. 465–472.

Schouten, J. C., and van den Bleek, C. M., 1992, "Chaotic Hydrodynamics of Fluidization: Consequences for Scaling and Modeling of Fluid Bed Reactors," *A.I.Ch.E. Symposium Series,* Vol. 88, No. 289, pp. 70–84.

Schouten, J. C., Takens, F., and van den Bleek, C. M., 1994, "Maximum-Likelihood Estimation of the Entropy of an Attractor," *Physical Review E,* Vol. 49, No. 1, pp. 126–129.

Skrzycke, D. P., Nguyen, K., and Daw, C. S., 1993, "Characterization of the Fluidization Behavior of Different Solid Types Based on Chaotic Time Series Analysis of Pressure Signals," *Proceedings of the 12th International Conference on Fluidized Bed Combustion,* San Diego, Vol. 1, pp. 155–166.

Takens, F., 1981, "Detecting Strange Attractors in Turbulence," *Lecture Notes in Mathematics,* Vol. 898, Rand, D. A., and Young, L. S., eds., Springer-Verlag, Berlin, pp. 366–381.

Theiler, J., 1986, "Spurious Dimension from Correlation Algorithms Applied to Limited Time-Series Data," *Physical Review A,* Vol. 34, No. 3, pp. 2427–2432.

van der Stappen, M. L. M., Schouten, J. C., and van den Bleek, C. M., 1993, "Application of Deterministic Chaos Theory in Understanding the Fluid Dynamic Behavior of Gas-Solids Fluidization," *Fluid-Particle Processes: Fundamentals and Applications, A.I.Ch.E. Symposium Series,* Vol. 296, pp. 91–102.

Numerical Modeling of Non-Newtonian Fluid Flow in a Porous Medium Using a Three-Dimensional Periodic Array

Masahiko Inoue
Graduate Student.

Akira Nakayama
Professor.

Department of Mechanical Engineering,
Shizuoka University,
3-5-1 Johoku, Hamamatsu, 432 Japan

Three-dimensional numerical experiments have been conducted to investigate the viscous and porous inertia effects on the pressure drop in a non-Newtonian fluid flow through a porous medium. A collection of cubes placed in a region of infinite extent has been proposed as a three-dimensional model of microscopic porous structure. A full set of three-dimensional momentum equations is treated along with the continuity equation at a pore scale, so as to simulate a flow through an infinite number of obstacles arranged in a regular pattern. The microscopic numerical results, thus obtained, are processed to extract the macroscopic relationship between the pressure gradient-mass flow rate. The modified permeability determined by reading the intercept value in the plot showing the dimensionless pressure gradient versus Reynolds number closely follows Christopher and Middleman's formula based on a hydraulic radius concept. Upon comparing the results based on the two- and three-dimensional models, it has been found that only the three-dimensional model can capture the porous inertia effects on the pressure drop, correctly. The resulting expression for the porous inertia possesses the same functional form as Ergun's, but its level is found to be only one third of Ergun's.

Introduction

A number of industrially important fluids including fossil fuels, which may saturate underground beds, exhibit non-Newtonian fluid behavior. Naturally, the understanding of non-Newtonian flows through porous media represents interesting challenges in geophysical systems, chemical reactor design, certain separation processes, polymer engineering or in petroleum production. Many of inelastic non-Newtonian fluid flows encountered in such engineering processes are known to follow the so-called "power-law model" in which the pressure drop is in proportion to power function of the mass flow rate. Darcy's law for such power-law fluid flows in porous media was first proposed by Christopher and Middleman (1965) and Dharmadhikari and Kale (1985). The model was used to attack the problem of free convection of non-Newtonian fluid from a vertical plate in a porous medium by Chen and Chen (1988) and the corresponding problem of mixed convection by Wang et al. (1990). Later, dealing with free convection from an arbitrary body shape in a non-Newtonian fluid saturated porous medium, Nakayama and Koyama (1991) introduced the modified permeability to unify the two distinct expressions proposed by Christopher and Middleman (1965) and Dharmadhikari and Kale (1985). Since Darcy's law accounts only for a balance of the viscous force and pressure drop, it fails to describe the flow inertia effects on the pressure drop, which become significant when the Reynolds number is high. Shenoy (1993) introduced a non-Newtonian version of the Forchheimer-extension of Darcy's law to investigate various aspects associated with convective flows in power-law fluid saturated porous media. Nakayama and Shenoy (1993) pointed out that the inertial drag force is independent of a particular stress-strain relationship, such that the same inertial drag expression as the Newtonian one should be used for all cases of non-Newtonian fluids. This point, however, has not been substantiated experimentally nor numerically. A comprehensive review on non-Newtonian fluid flow and heat transfer in porous media may be found in Shenoy (1994).

Detailed flow field inside a microscopic structure in a porous medium may numerically be investigated using a periodic array, rather than treating complex porous media in reality. Such numerical (or analytical-numerical) attempts were made by Eidsath et al. (1983), Coulaud et al. (1988), Sahraoui and Kaviany (1991), Larson and Higdon (1989), Kuwahara et al. (1994), Nakayama et al. (1995) and many others. However, all assume that the fluids within porous media are Newtonian. To the best of the authors' knowledge, no numerical investigations on the microscopic flow field of non-Newtonian fluid flows in porous media have been reported so far.

The present study has been conducted to model non-Newtonian power-law fluid flows passing through porous media numerically, using a periodic array. An infinite number of obstacles placed periodically in an infinite space are proposed to simulate microscopic porous structures. A full set of the three-dimensional momentum equations with the power-law strain rate-shear stress relationship are numerically treated at a pore-scale. The resulting microscopic results are processed to extract the macroscopic pressure gradient-Darcian velocity relationship purely from a theoretical basis. The resulting expression is compared against the Darcy law with the Christopher and Middleman formula and its Forchheimer modification.

Numerical Model and Boundary Conditions

We consider a macroscopically uniform flow, meandering through an infinite number of cubes placed in a regular fashion in an infinite space, as shown in Fig. 1(a). Only one structural unit of $H \times H \times H$, as shown in Fig. 1(b) can be taken as a calculation domain in consideration of the geometric periodicity. The direction of the microscopically uniform flow is expressed in terms of (θ, ϕ) as illustrated in Fig. 1(c) such that

Contributed by the Fluids Engineering Division for publication in the JOURNAL OF FLUIDS ENGINEERING. Manuscript received by the Fluids Engineering Division July 31, 1996; revised manuscript received August 4, 1997. Associate Technical Editor: O. C. Jones.

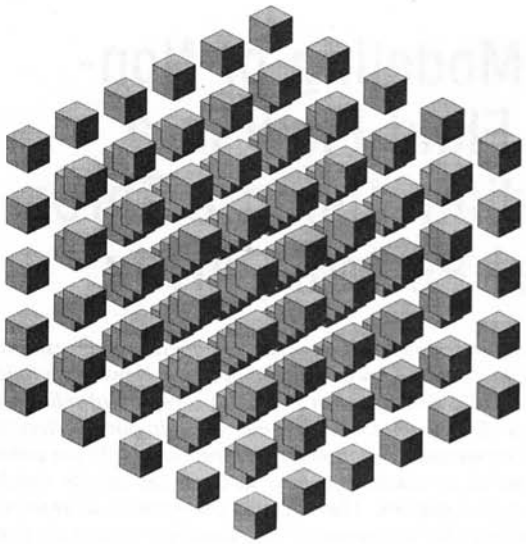

Fig. 1(a)

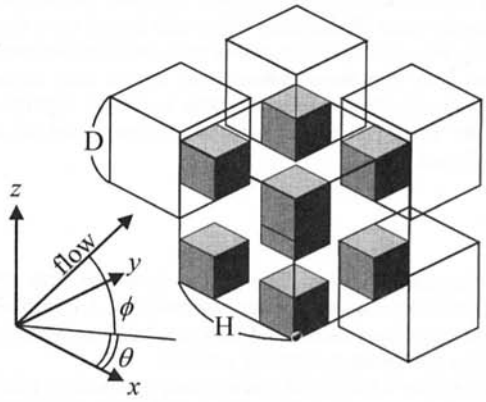

Fig. 1(b)

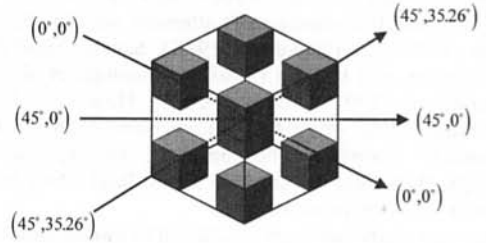

Fig. 1(c)

Fig. 1 Numerical model: (*a*) arrangement of cubes, (*b*) structural unit, (*c*) typical flow directions

$$\langle \mathbf{u} \rangle = |\langle \mathbf{u} \rangle| (\cos\theta \cos\phi \mathbf{i} + \sin\theta \cos\phi \mathbf{j} + \sin\phi \mathbf{k}) \quad (1)$$

where $\langle\ \rangle$ indicates a volume averaged quantity. In other words, $|\langle \mathbf{u} \rangle|$ is the apparent velocity or Darcian velocity. The porosity may be varied by changing the ratio of the size of cube D to the unit cell size H as

$$\epsilon = 1 - \left(\frac{D}{H}\right)^3 \quad (2)$$

The governing equations, namely, the continuity and momentum equations for the steady incompressible non-Newtonian fluid flows are given by

$$\frac{\partial u_j}{\partial x_j} = 0 \quad (3)$$

$$\rho \frac{\partial}{\partial x_j}(u_j u_i) = -\frac{\partial p}{\partial x_i} + \frac{\partial}{\partial x_j}\left(\mu_{ap}\left(\frac{\partial u_i}{\partial x_j} + \frac{\partial u_j}{\partial x_i}\right)\right) \quad (4)$$

where

$$\mu_{ap} = \mu^* \Phi^{(n-1)/2} \quad \text{for} \quad \Phi^{1/2} \geq \frac{|\langle \mathbf{u} \rangle|}{H}$$

$$\mu_{ap} = \mu^* \left(\frac{|\langle \mathbf{u} \rangle|}{H}\right)^{n-1} \quad \text{for} \quad \Phi^{1/2} \leq \frac{|\langle \mathbf{u} \rangle|}{H} \quad (5)$$

and

$$\Phi = \frac{\partial u_k}{\partial x_l}\left(\frac{\partial u_k}{\partial x_l} + \frac{\partial u_l}{\partial x_k}\right) \quad (6)$$

We employ the constitutive Eq. (5) such that the Ostwald-de Waele model, the so-called, "power-law model," holds, when the apparent viscosity μ_{ap} is less than a threshold value, namely, $\mu^*(|\langle \mathbf{u} \rangle|/H)^{n-1}$ where μ^* is the consistency index. Otherwise, the fluid is Newtonian with μ_{ap} set to the threshold value, so as to account for the fact that all fluids behave like Newtonian, when the strain rate is sufficiently small (see Fig. 2). Preliminary calculations on laminar flows in ducts revealed that the constitutive Eq. (5) leads to the profiles which are almost exact for the cases of fully developed flows. Many of inelastic non-Newtonian fluids encountered in chemical engineering processes are known to follow this empirical power-law model.

The boundary and periodic constraints are given by

$$\mathbf{u} = \mathbf{0} \quad \text{at the wall} \quad (7)$$

and

$$\mathbf{u}|_{x=0} = \mathbf{u}|_{x=H}$$

$$\mathbf{u}|_{y=0} = \mathbf{u}|_{y=H}$$

$$\mathbf{u}|_{z=0} = \mathbf{u}|_{z=H} \quad (8)$$

Nomenclature

b = Forchheimer constant
D = size of cube
H = size of structural unit
$\mathbf{i}, \mathbf{j}, \mathbf{k}$ = unit vectors in the x, y and z directions
K^* = modified permeability
n = power-law index
$\mathbf{u}$ = velocity vector
p = microscopic pressure
Re_H = Reynolds number based on H and the macroscopically uniform velocity
s = coordinate set along the macroscopic flow direction
x, y, z = Cartesian coordinates
θ, ϕ = macroscopic flow angles
ϵ = porosity
μ_{ap} = apparent viscosity
μ^* = fluid consistency
ρ = density
Φ = dissipation function

Special Symbols

$\langle\ \rangle$ = volume average
$|\ |$ = absolute value

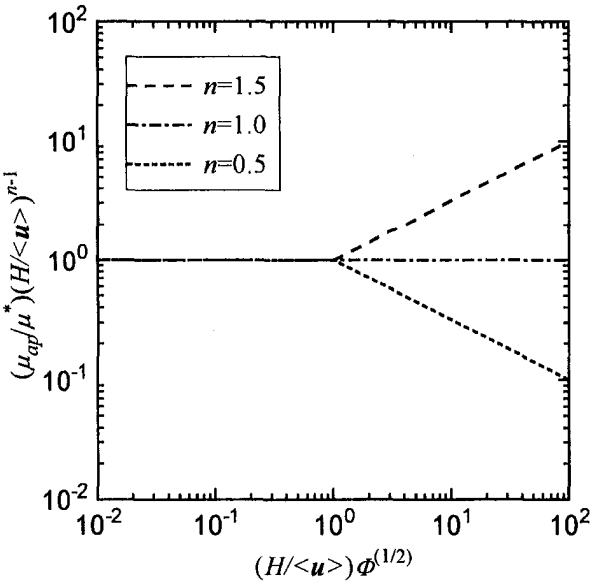

Fig. 2 Apparent viscosity

$$\int_0^H \int_0^H udydz|_{x=0} = \int_0^H \int_0^H udydz|_{x=H} = H^2|\langle \mathbf{u}\rangle| \cos\theta \sin\phi$$

$$\int_0^H \int_0^H vdzdx|_{y=0} = \int_0^H \int_0^H vdzdx|_{y=H} = H^2|\langle \mathbf{u}\rangle| \sin\theta \cos\phi$$

$$\int_0^H \int_0^H wdxdy|_{z=0} = \int_0^H \int_0^H wdxdy|_{z=H} = H^2|\langle \mathbf{u}\rangle| \sin\phi \quad (9)$$

to describe a macroscopically uniform flow in the direction given by the set of angles (θ, ϕ).

We shall define the Reynolds number based on the Darcian velocity and the size of the structural unit as

$$\mathrm{Re}_H = \frac{\rho|\langle \mathbf{u}\rangle|^{2-n}H^n}{\mu^*} \quad (10)$$

Method of Computation

Discretization is carried out by integrating the governing equations over an elementary control volume. The SIMPLE algorithm for the pressure-velocity coupling, as proposed by Patankar and Spalding (1972), is adopted to correct the pressure and velocity fields. Fully implicit scheme is adopted with the hybrid differencing scheme for the advection terms.

Computation starts with arbitrary initial velocity distribution inside the calculation domain. First, the three momentum equations are solved, and the velocity field, thus estimated, is corrected by solving the pressure correction equation derived from the discretized continuity equation, such that the velocity fields fulfills the continuity principle. The details of the numerical procedure may be found in Patankar (1980) and Nakayama (1995). The sequence is repeated until the maximum change in each variable normalized by appropriate references during an iteration becomes less than a prescribed value, 10^{-5}. All computations were carried out for one structural unit using the computer system HP-UX A 9000/7000 with a grid system 50 $\times$ 50 $\times$ 50, which were proven to produce sufficiently accurate results, comparing the results with those based on a finer grid system.

Results and Discussion

Determination of Modified Permeability. The gradient of the intrinsic average pressure $\langle p\rangle^f$ may readily be evaluated using the microscopic results as

$$-\frac{d\langle p\rangle^f}{ds} = \frac{\cos\theta\cos\phi}{H(H^2-D^2)}\int_{A^f}\int (p|_{x=0} - p|_{x=H})dydz + \frac{\sin\theta\cos\phi}{H(H^2-D^2)}\int_{A^f}\int (p|_{y=0} - p|_{y=H})dzdx + \frac{\sin\phi}{H(H^2-D^2)}\int_{A^f}\int (p|_{z=0} - p|_{z=H})dxdy \quad (11)$$

where **S** is the coordinate taken in the macroscopic flow direction, whereas $A^f (=H^2 - D^2)$ is the cross-sectional area of the flow passage. The Forchheimer modification of Darcy's law for the power-law fluids may be written as

$$-\frac{d\langle p\rangle^f}{ds} = \frac{\mu^*}{K^*}|\langle \mathbf{u}\rangle|^n + \rho b|\langle \mathbf{u}\rangle|^2 \quad (12a)$$

or, in dimensionless form, as

$$-\frac{d\langle p\rangle^f}{ds}\frac{H}{\rho|\langle \mathbf{u}\rangle|^2}\mathrm{Re}_H = \frac{H^{n+1}}{K^*} + bH\,\mathrm{Re}_H \quad (12b)$$

Thus, the modified permeability $K^*[m^{n+1}]$ and the Forchheimer constant $b[1/m]$ may readily be determined by fitting the numerical results of the macroscopic pressure gradient against Eq. (12b). Typical pressure gradient results are plotted against the Reynolds number in Fig. 3 for the case of $\epsilon = 0.488$, $(\theta, \phi) = (45°, 35.26°)$ and $n = 0.5$, 1.0 and 1.5. It is clearly seen that the dimensionless pressure gradient stays constant for the low Reynolds number range, where the viscous force dominates, and then increases steeply for the high Reynolds number range, where the porous inertial contribution becomes predominant. All three curves merge together as increasing the Reynolds number, which substantiates the assumption made by Nakayama and Shenoy (1993), namely, that the inertial drag force is independent of a particular stress-strain relationship, so that the same inertial drag expression as the Newtonian one can be used for all cases of non-Newtonian fluids.

The modified permeability K^* may be determined by reading the intercept on the ordinate axis in the figure. The permeability, thus obtained for three distinct flow angles $(\theta, \phi) = (0°, 0°)$, $(45°, 0°)$, $(45°, 35.26°)$ with $\epsilon = 0.488$, are plotted in Fig. 4, for $n = 0.5$, 1.0 and 1.5. The figure shows that the modified permeability K^* is virtually independent of the macroscopic flow direction. This suggests that the average mean shear rate within a unit cell for the case of low Reynolds number, is fairly insensitive to the macroscopic flow direction, despite that the velocity field within a unit cell changes markedly with the flow direction. Thus, we expect the dimensionless permeability to be function of the porosity ϵ and power-law index n.

Figure 5 shows the effects of the porosity ϵ and power-law index n on the dimensionless permeability. The lines generated from Christopher and Middleman's formula based on a simple

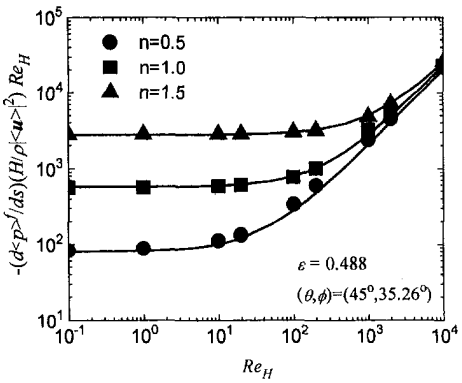

Fig. 3 Effect of Reynolds number on pressure gradient

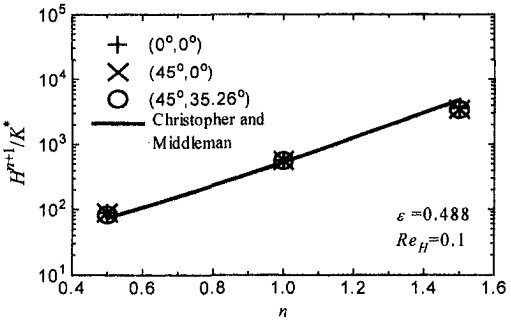

Fig. 4 Effects of flow angle and power-law index n on permeability

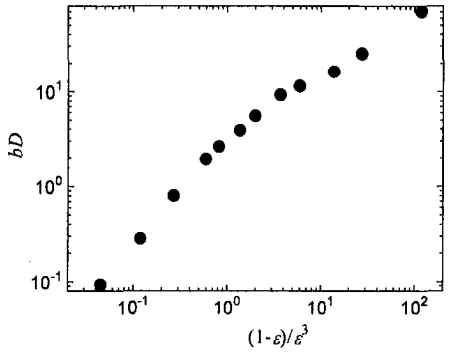

Fig. 6 Forchheimer constant based on two-dimensional model

hydraulic radius concept are also indicated in the same figure, where the abscissa variable is chosen following their formula:

$$K^* = \frac{6}{25}\left(\frac{n\epsilon}{1+3n}\right)^n\left(\frac{\epsilon D}{3(1-\epsilon)}\right)^{1+n}$$

$$= \frac{6}{25}\left(\frac{n}{1+3n}\right)^n\left(\frac{H}{3}\right)^{1+n}\frac{\epsilon^{1+2n}}{(1-\epsilon)^{2(1+n)/3}} \qquad (13)$$

It is interesting to note that the numerical results essentially follow the Christopher and Middleman's formula, which suggests that the permeability for a collection of cubes of size D is nearly the same as that of packed bed of spheres of diameter D, under the same porosity.

Determination of Forchheimer Constant. The Forchheimer constant b may be determined by fitting the numerical results obtained at high Reynolds numbers with Eq. (12b). Preliminary calculations were performed using the two-dimensional numerical model of square cylinders, proposed in the previous study (Kuwahara et al. 1994), to investigate the porous inertial contribution. Figure 6 shows a typical variation of the Forchheimer constant b predicted using the two-dimensional numerical model of square cylinders. The abscissa variable is chosen anticipating that Ergun's functional form (1952) for the Forchheimer term should hold, whether or not the fluid is Newtonian:

$$b = 1.75\,\frac{(1-\epsilon)}{\epsilon^3}\,\frac{1}{D}\,:\ \text{Ergun} \qquad (14)$$

However, no proportional relationship between b and $(1-\epsilon)/\epsilon^3$ can be seen from these two-dimensional results. The three-dimensional results on the Forchheimer constant b are presented for three different flow directions in Fig. 7 in a similar fashion. Figure clearly shows that the three-dimensional results possess the same functional relationship $b \propto (1-\epsilon)/\epsilon^3$ as in Ergun's formula. The multiplicative constant, however, is indeterminable, since it is rather sensitive to the macroscopic flow direction, as shown in the figure. In reality, a fluid particle travels through a porous medium, changing its direction freely. Thus, any numerical model based on periodic structures seem to have its limitation for simulating such random flow motions. For the first approximation, we may average the multiplicative constant for the Forchheimer constant over the flow angles as

$$\frac{4}{\pi\tan^{-1}(1/\sqrt{2})}\int_0^{\tan^{-1}(1/\sqrt{2})}\int_0^{\pi/4} bD\left(\frac{\epsilon^3}{1-\epsilon}\right)d\theta d\phi \cong 0.5$$

such that

$$b \approx 0.5\,\frac{(1-\epsilon)}{\epsilon^3}\,\frac{1}{D}\,:\ \text{Present model} \qquad (15)$$

The predicted multiplicative constant 0.5 is about one third the Ergun multiplicative constant, 1.75. In order to make a realistic prediction for the porous inertial effects, irregularity of porous structures, along with possible flow unsteadiness, must be taken into full consideration. An attempt by Martys (1994), using model random porous media, is noteworthy. However, the model is limited to the Darcy newtonian flow regime. The unsteady term, sometimes used in the extension to Darcy's law is somewhat controversial. A series of unsteady flow calculations, which are underway, may shed some light on the issue.

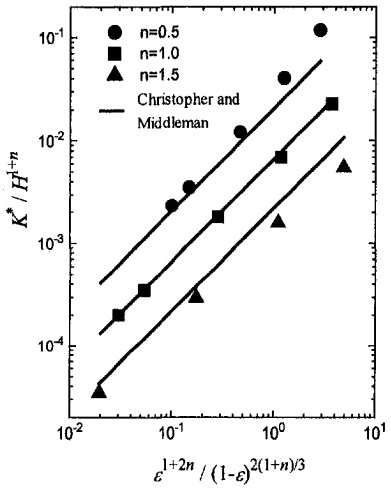

Fig. 5 Effects of porosity ϵ and power-law index n on permeability

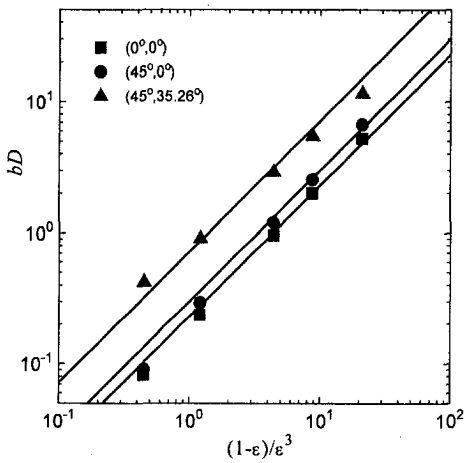

Fig. 7 Forchheimer constant based on three-dimensional model

Conclusions

A collection of cubes placed in a region of infinite extent has been proposed as a three-dimensional model of microscopic porous structure. Exhaustive numerical calculations were carried out to investigate the viscous and porous inertia effects on the pressure drop in a non-Newtonian fluid flow through a porous medium. A full set of three-dimensional momentum equations is treated along with the continuity equation at a pore scale, so as to simulate a flow through an infinite number of obstacles arranged in a regular pattern. The modified permeability determined by reading the intercept in the dimensionless pressure gradient versus Reynolds number plot closely follows Christopher and Middleman's formula for packed beds of spheres based on a hydraulic radius concept, leading to an interesting conclusion that the permeability for a collection of cubes of size D is nearly the same as that of packed beds of spheres of diameter D, under the same porosity. Upon comparing the results based on the two- and three-dimensional models, it has been found that only the three-dimensional model can capture the porous inertia effects on the pressure drop, correctly. The resulting expression possesses the same functional form as Ergun's formula, but its level is found much less than Ergun's.

References

Chen, H. T., and Chen, C. K., 1988, "Free Convection of Non-Newtonian Fluids Along a Vertical Plate Embedded in a Porous Medium," ASME *Journal of Heat Transfer,* Vol. 110, pp. 257–260.

Christopher, R. H., and Middleman, S., 1965, "Power-law Flow Through a Packed Tube," *Industrial Engineering Chemical Fundamentals,* Vol. 4, pp. 422–426.

Coulaud, O., Morel, P., and Caltagirone, J. P., 1988, "Numerical Modeling of Nonlinear Effects in Laminar Flow Through a Porous Medium," *Journal of Fluid Mech.,* Vol. 190, pp. 393–407.

Dharmadhikari, R. V., and Kale, D. D., 1985, "Flow of Non-Newtonian Fluids Through Porous Media," *Chemical Engineering Science,* Vol. 40, pp. 527–529.

Eidsath, A., Carbonell, R. G., Whitaker, S. and Herrmann, L. R., 1983, "Dispersion in Pulsed Systems, III Comparison Between Theory and Experiments in Packed Beds," *Chemical Engineering Science,* Vol. 38, pp. 1803–1816.

Ergun, S., 1952, "Fluid Flow Through Packed Columns," *Chemical Engineering Progress,* Vol. 48, pp. 89–94.

Kuwahara, F., Nakayama, A. and Koyama, H., 1994, "Numerical Modeling of Heat and Fluid Flow in a Porous Medium," *Proceedings of International Heat Transfer Conference,* Vol. 5, pp. 309–314.

Larson, R. E. and Higdon, J. J. L., 1989, "A Periodic Grain Consolidation Model of Porous Media," *Physics of Fluids,* Vol. A1, pp. 38–46.

Nakayama, A., 1995, "PC-Aided Numerical Heat Transfer and Convective Flow," CRC Press, Boca Raton.

Nakayama, A., and Koyama, H., 1991, "Buoyancy-Induced Flow of Non-Newtonian Fluids Over a Non-Isothermal Body of Arbitrary Shape in a Fluid-Saturated Porous Medium," *Applied Scientific Research,* Vol. 48, pp. 55–70.

Nakayama, A., Kuwahara, F., Kawamura, Y., and Koyama, H., 1995, "Three-Dimensional Numerical Simulation of Flow Through a Microscopic Porous Structure," *Proceedings of ASME/JSME Thermal Engineering Conference,* Vol. 3, pp. 313–318.

Nakayama, A. and Shenoy, A. V., 1993, "Non-Darcy Forced Convective Heat Transfer in a Channel Embedded in a Non-Newtonian Inelastic Fluid-Saturated Porous Medium," *Canadian Journal of Chemical Engineering,* Vol. 71, pp. 168–173.

Patankar, S. V., 1980, *Numerical Heat Transfer and Fluid Flow,* Hemisphere, Washington, D.C.

Patankar, S. V., and Spalding, D. B., 1972, "A Calculation Procedure for Heat, Mass and Momentum Transfer in Three-Dimensional Parabolic Flows," *International Journal of Heat and Mass Transfer,* Vol. 15, pp. 1787–1806.

Sahraoui, M., and Kaviany, M., 1991, "Slip and No-Slip Boundary Condition at Interface of Porous, Plain Media," *Proceedings of ASME/JSME Thermal Engineering Conference,* Vol. 4, pp. 273–286.

Shenoy, A. V., 1933, "Darcy-Forchheimer Natural, Forced and Mixed Convection Heat Transfer in Non-Newtonian Power-Law Fluid Saturated Porous Media," *Transport of Porous Media,* Vol. 11, pp. 219–241.

Shenoy, A. V., 1994, "Non-Newtonian Fluid Heat Transfer in Porous Media," *Advances in Heat Transfer,* Vol. 24, pp. 101–190.

Wang, C., Tu, C., and Zhang, X., 1990, "Mixed Convection of Non-Newtonian Fluids from a Vertical Plate Embedded in a Porous Medium," *Acta Mechanica Sincia,* Vol. 6, pp. 214–220. 55–70.

Turbulent Friction Factor for Two-Phase: Air-Powerlaw Fluid Flows Through Horizontal Tubes

B. K. Rao
Associate Professor,
College of Engineering,
Idaho State University,
Pocatello, Idaho 83209.
Mem. ASME

Turbulent experimental friction factors for air and power-law fluid flows through a horizontal tube are reported. The power-law fluids studied were aqueous solutions of Carbopol® (at concentrations 1000 and 2000 wppm). The two-phase friction factors were correlated in terms of the generalized Reynolds number (Re). Over a range of the Re* from 6000 to 80,000, the simpler homogeneous model is accurate enough for engineering prediction of turbulent friction factor for air and power-law fluid flows through straight tubes.*

I Introduction

The designer's key interests in adiabatic two-phase flows are in the void fraction and pressure drop, which are related to fluid properties, flowrates, and configuration of the equipment.

For given flows of the two phases in a given channel, the gas-liquid interfacial distribution can take several possible forms resulting in various flow patterns. The pressure drop relationships are sensitive to the flow patterns. A variety of methods have been proposed for the determination of flow patterns in horizontal flows (Baker, 1954; Bell et al., 1969; Collier, 1972; Dsarasov et al., 1974; Fiori and Bergles, 1966; Hewitt, 1978; Kutateladze, 1973; Reimann and John, 1978; Sakaguchi et al., 1979; Scott, 1963; Taitel and Dukler, 1976) based on the dimension-less quantities K, F, T, X, λ, and Ψ.

The immense volume of literature on gas-liquid horizontal flows and flow patterns deals with air-water mixtures (in tubes up to 5 cm diameter). To represent the effects of various system parameters, alternative flow maps (Schicht, 1969; Al-Sheikh et al., 1970; Mandhane et al., 1974; Fisher and Yu, 1975) have been developed. Notable studies on flow transitions are those of Wallis and Dobson (1973), Gardner (1977), and Kubie (1979). However, none of the above represents all the appropriate transitions in terms of a single set of parameters. Some analytical models are available to describe the two-phase flows: the homogeneous model, separated-flow model, drift-flux model etc. (Wallis, 1969). The homogeneous model reduces the homogeneous density and void fraction to the following:

$$\epsilon = x/[x + (1 - x)\rho_g/\rho_l] \tag{1}$$

$$\rho_{TP} = \epsilon\rho_g + (1 - \epsilon)\rho_l \tag{2}$$

The most widely used two-phase viscosity (μ_{TP}) is that due to McAdams et al. (1942):

$$1/\mu_{TP} = x/\mu_g + (1 - x)/\mu_l \tag{3}$$

In spite of its little general applicability to design problems, the homogeneous model is still the most widely accepted in design practice for predicting two-phase pressure drop.

Separated Flow Model is based on the assumption that the two phases can have different velocities. The Lockhart-Martinelli (1949) correlation for frictional pressure drop in two-phase Newtonian flows is:

$$(\phi_l)^2 = 1 + C/X + 1/X^2 \tag{4}$$

$$(\phi_g)^2 = 1 + CX + X^2 \tag{5}$$

where C is a dimensionless parameter whose value depends on the nature of the phase-alone flows. In spite of its deficiencies, most technical calculations are still done using the method of Lockhart-Martinelli.

II Non-Newtonian Fluids

NonNewtonian fluids such as food products and petrochemicals are frequently encountered in these process industries. Knowledge of the hydrodynamic behavior of these rheologically complex fluids is essential to an improved design of the equipment handling such fluids. Some excellent references on non-Newtonian flows are: Bird et al. (1960), Middleman (1968), Skelland (1967), and Wilkinson (1960).

The simplest mathematical model that describes the flow behavior of a non-Newtonian fluid is:

$$\tau = K'\dot{\gamma}^n \tag{6}$$

The most commonly used Reynolds numbers for nonNewtonian flows are:

$$\mathrm{Re}_a = 4\dot{m}/\pi D\eta \tag{7}$$

$$\mathrm{Re}^* = \rho v^{2-n} D_h^n/\{K'[(a + bn)/n]^n 8^{n-1}\} \tag{8}$$

For circular tubes, the values of a and b in Eq. (8) are $\frac{1}{4}$ and $\frac{3}{4}$, respectively (Kozicki, 1966). The turbulent friction factor for power-law fluid flows through straight tubes are well predicted by Dodge-Metzner's (1959) as well as Yoo's (1974) correlations:

$$1/\sqrt{f} = (4/n^{3/4}) \log [\mathrm{Re}^* f^{1-1/2n}] - 0.4/n^{1.2} \tag{9}$$

$$f = 0.0791 n^{0.675} (\mathrm{Re}^*)^{-1/4} \tag{10}$$

The turbulent friction factor for power-law fluids, at any fixed Re*, decreases with decreasing n value. This experimental investigation is undertaken to study the friction factor for two-phase: air and power-law fluid flows in horizontal tubes.

III Experimental Setup and Procedure

The schematic of the flow loop is shown in Fig. 1. The test section (0.025 m diameter and 11 m long) is opaque. The power-law fluids studied were aqueous solutions of Carbopol® 934 (produced by B. F. Goodrich, Inc). Distilled water was used as a Newtonian solvent. The test fluid concentrations em-

Contributed by the Fluids Engineering Division for publication in the JOURNAL OF FLUIDS ENGINEERING. Manuscript received by the Fluids Engineering Division June 27, 1996; revised manuscript received July 11, 1997. Associate Technical Editor: O. C. Jones.

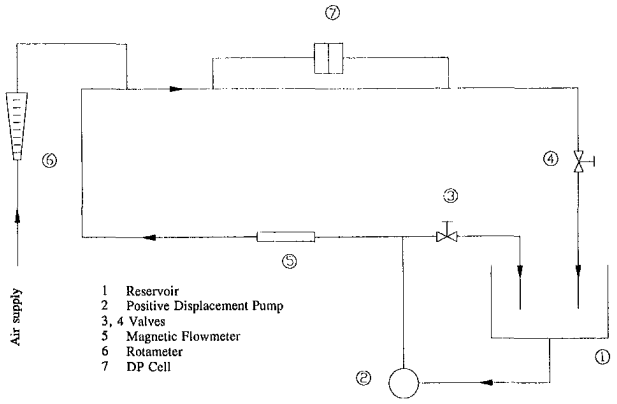

Fig. 1 Schematic of flow loop

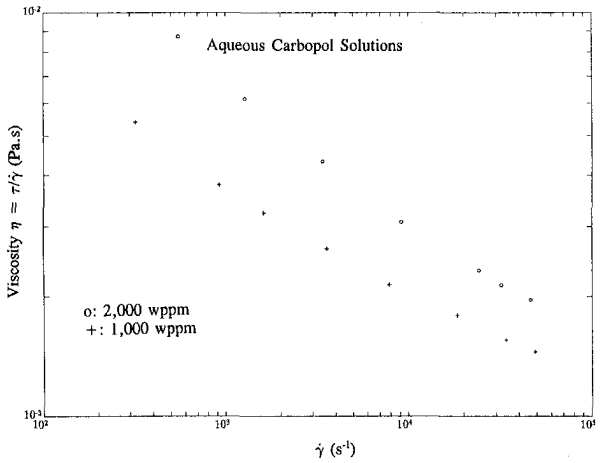

Fig. 2 Characteristic curves for Carbopol

ployed were 1000 and 2000 ppm (by weight). In order to obtain lower values of n, Carbopol solutions were neutralized by adding sodium hydroxide solution until the pH value reached about 7.4.

Air was injected at about 15 diameters downstream of the tube entrance. The flow rates of liquid and air were varied from 0 to 4.2×10^{-3} m^3/s and 0 to 1.2×10^{-3} m^3/s, respectively. The pressure drop values measured between taps at 250 and 300 diameters from the entrance were used to calculate the friction factor.

The steady-shear viscometric data ($\dot{\gamma}$ and τ) were obtained at room temperature (18°C) using a Bohlin rheogoniometer, a Brookfield viscometer, and a capillary viscometer. The following regression equation was obtained and the rheological constants were calculated:

$$\ln \tau = a_0 + a_l \ln \dot{\gamma} + a_2(\ln \dot{\gamma})^2 \quad (11)$$

$$n = a_l + 2a_2(\ln \dot{\gamma}) \quad (12)$$

$$K' = \exp[a_0 - a_2(\ln \dot{\gamma})^2] \quad (13)$$

The characteristic curves are shown in Fig. 2. The test fluid viscosity was measured before and after each run to monitor the polymer degradation. The variation in viscosity was within ±2 percent.

IV Results and Discussion

The observed hydrodynamic entrance length for two-phase flows in this study is about 65 diameters. Based on the gas-Newtonian flow regimes (cited in Section I) in terms of K, F, T, and X (not shown here), the present data are in the plug flow region.

The present two-phase friction factors shown as a function of the Re_{TP}^* in Fig. 3 are well predicted by Eq. (9). From Fig.

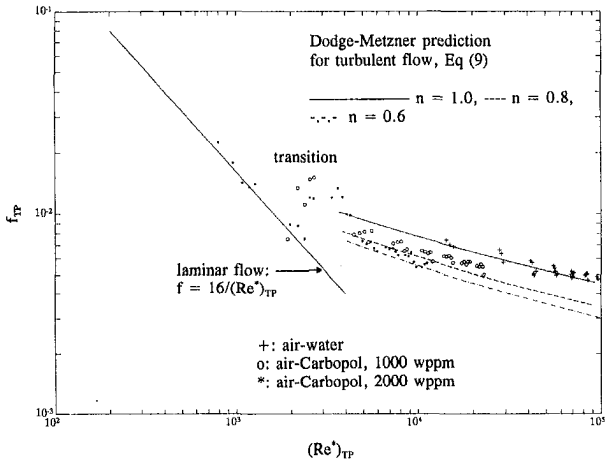

Fig. 3 Experimental fully developed friction factors as a function of the two-phase Reynolds number, Re_{TP}^*, for turbulent flow of air-power law fluid flows through a horizontal tube. Comparison with Dodge-Metzner prediction

Nomenclature

A_c = cross-sectional area of tube [m^2]
D = tube inside diameter [m]
K' = consistency index of power-law fluid [N s^n/m^2]
L = distance between pressure taps [m]
$\dot{m}$ = mass flow rate [kg/s]
$\dot{Q}$ = volume flow rate = $\dot{m}/\rho$ [m^3/s]
v = superficial velocity = $\dot{Q}/A_c$ [m/s]
v_{TP} = 2-phase velocity = $\dot{m}_l/(A_c\rho_{TP})$
z = axial distance [m]
μ = viscosity [Pa.s]
$\dot{\gamma}$ = shear rate [1/s]
η = $\tau/\dot{\gamma}$, apparent viscosity [Pa.s]
ν = kinematic viscosity [m^2/s]
ρ = density of fluid [kg/m^3]
σ = surface tension [N/m]
τ_w = wall shear stress, $\Delta pD/(4L)$ [Pa]
$(dp/dz)_g = 32\, f_g \dot{m}^2 x^2/\rho\pi^2 D^5$
$(dp/dz)_l = 32\, f_l \dot{m}^2 (1-x)^2/\rho\pi^2 D^5$

Dimensionless Quantities

ϵ = void fraction
$\lambda = [(\rho_g/\rho_a)(\rho_l/\rho_w)]^{1/2}$
$\Psi = (\sigma_w/\sigma)[(\mu_l/\mu_w)(\rho_w/\rho_l)]^{1/3}$
$\phi_g = [(dp/dz)_{TP}/(dp/dz)_g]^{1/2}$
$\phi_l = [(dp/dz)_{TP}/(dp/dz)_l]^{1/2}$
f = Fanning friction factor = $2\tau_w/(\rho v^2)$
$f_{TP} = (\Delta p/\Delta z)D^5\pi^2\rho/(32\dot{m}^2)$
$F = [(\rho_g/(\rho_l - \rho_g))/(Dg)]^{1/2} v_g$
$K^2 = F^2\,\mathrm{Re}_l$
n = power-law exponent
Re = Reynolds number = $4\dot{m}/(\pi D\mu)$
$\mathrm{Re}_l = Dv_l/\nu_l = 4\dot{m}(1-x)/(\pi D\mu_l)$
$\mathrm{Re}_g = 4\dot{m}x/(\pi D\mu_g)$
$\mathrm{Re}_{TP} = 4\dot{m}/(\pi D\mu_{TP})$
$T^2 = (\Delta p/\Delta z)_l/[(\rho_l - \rho_g)g]$
x = mass quality = $\dot{m}_g/(\dot{m}_g + \dot{m}_l)$
$X^2 = \Delta p_l/\Delta p_g$

Suffixes

a, g, l, w = air, gas, liquid, water
m, p = measured, predicted
TP = two-phase
w = at the wall

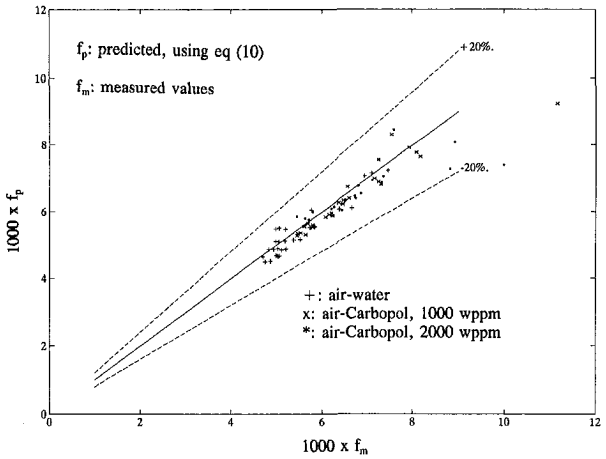

Fig. 4 Comparison of measured friction factors with friction factors predicted by Eq. (10)

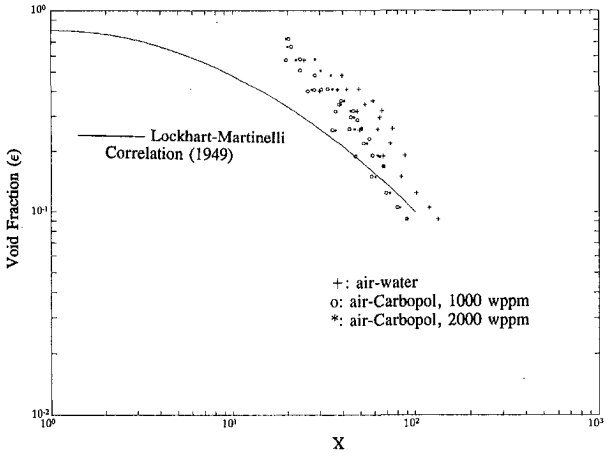

Fig. 6 Void fraction, ϵ, as a function of the Martinelli parameter, X

3 it can be seen that the f_{TP} for air-power-law fluids decreases with decreasing n, at any fixed value of Re^*_{TP}. The average n values for the 1000 and 2000 wppm Carbopol solutions employed in this study are 0.74 and 0.65, respectively.

The measured f_{TP} for air-water and air-powerlaw fluids and the predicted, using Eq. (10), are shown in Fig. 4. The present experimental data are within ±20 percent of the prediction.

The estimated uncertainties, using the root-sum-square method, in the friction factors and Reynolds numbers reported in this study are ±5 and ±3 percent, respectively.

The frictional pressure drop multipliers, ϕ_l and ϕ_g, are shown as a function of X in Fig. 5. In this study, the liquid phase flowing alone in the channel was turbulent and the gas phase flowing alone was laminar. Under such conditions, the value of C in Eqs. (4) and (5) for gas-Newtonian liquid flows is equal to 10 (Chisholm, 1967). Equations (4), (5) predicted the present air-powerlaw fluid multipliers with reasonable accuracy.

The void fraction is shown as a function of the Martinelli parameter, X in Fig. 6. The present two-phase experimental data are underpredicted by the correlation of Lockhart-Martinelli (1949).

V Conclusions

(1) The present two-phase data are in the plug flow region.

(2) Air-power-law fluids exhibit lower friction factor compared to that of air-Newtonian solvent, at any fixed Re*. The turbulent f_{TP} decreases with decreasing n value.

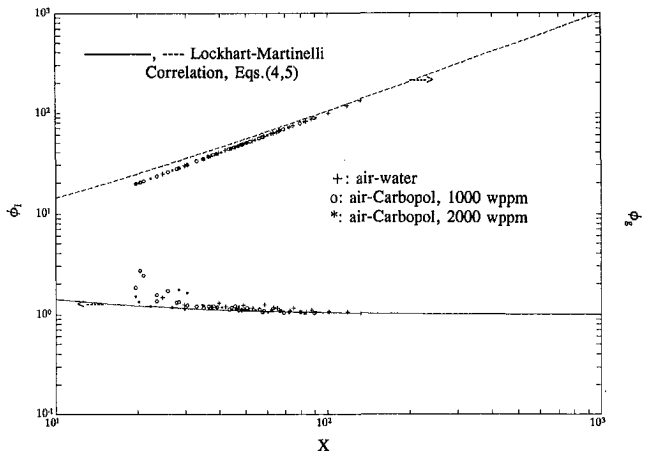

Fig. 5 Frictional pressure drop multipliers, ϕ_l and ϕ_g, as a function of the Martinelli parameter, X

(3) Both Eqs. (9) and (10) predict the fully developed turbulent friction factor in straight tubes for the two-phase: air-water and air-powerlaw fluids.

(4) The homogeneous model (simple and at best semi-empirical) is adequate for engineering prediction of two-phase pressure drop for air-powerlaw fluids.

(5) At atmospheric pressure, Lockhart-Martinelli correlation holds for predicting the two-phase pressure drop for air-water, as well as air-power-law fluid turbulent flows in horizontal tubes. Lockhart-Martinelli correlation underestimates the void fraction for air-powerlaw fluids.

Acknowledgments

Help received from Dennis Norton in data collection is appreciated. Miles Whiting and Terry Snarr helped in the fabrication and instrumentation.

References

Al-Sheikh, J. N. et al., 1970, "Prediction of Flow Patterns in Horizontal Two-phase Type Flow," *Canadian Journal of Chemical Engineering,* Vol. 48, pp. 21–29.

Baker, O., 1954, "Simultaneous Flow of Oil and Gas," *Oil and Gas Journal,* Vol. 53, p. 185.

Bell, K. J. et al., 1969, "Interpretation of Horizontal In-tube Condensation Heat Transfer Correlations with a Two-phase Flow Regime Map," *Chemical Engineering Progress Symposium Series 66,* pp. 150–163.

Bird, R. B. et al., 1960, *Dynamics of Polymeric Liquids,* Vol. 1, Wiley, New York.

Chisholm, D., 1967, "A Theoretical Basis for the Lockhart-Martinelli Correlation for Two-phase Flow," *International Journal of Heat and Mass Transfer,* Vol. 10, pp. 1767–1778.

Cho, Y. I., and Hartnett, J. P., 1982, "NonNewtonian Fluids in Circular Pipe Flow," *Advances in Heat Transfer,* Vol. 15, pp. 59–141.

Collier, J. G., 1972, *Convective Boiling and Condensation,* McGraw-Hill, NY.

Dodge, D. W., and Metzner, A. B., 1959, "Turbulent Flow of Non-Newtonian Systems," *American Institute of Chemical Engineering Journal,* Vol. 5, pp. 189–204.

Dsarasov, Y. I. et al., 1974, "Experimental Study of Relation between Heat and Mass Transfer Characteristics in Evaporating Channels," *Proceedings 5th International Heat Transfer Conference,* Tokyo, B5.3 4, pp. 195–199.

Fiori, M. P. and Bergles, A. F., 1966, "A Study of Boiling Water Flow Regimes at Low Pressure," M. I. T. Report 3582-40.

Fisher, S. A., and Yu, S. K. W., 1975, "Dryout in Serpentine Evaporators," *International Journal of Multiphase Flow,* Vol. 1, pp. 771–791.

Gardner, G. C., 1977, "Motion of Miscible and Immiscible Fluids in Closed Horizontal and Vertical Ducts," *International Journal of Multiphase Flow,* Vol. 3, pp. 305–318.

Hewitt, G. F., 1978, *Measurement of Two Phase Flow Parameters,* Academic Press, New York, NY.

Kozicki, W. et al., 1966, "Non-Newtonian Flow in Ducts of Arbitrary Cross-sectional Shape," *Chemical Engineering Science,* Vol. 21, pp. 665–679.

Kozicki, W., and Tiu, C., 1971, "Improved Parametric Characterization of Flow Geometries," *Canadian Journal of Chemical Engineering,* Vol. 49, pp. 562–569.

Kubie, J., 1979, "The Presence of Slug Flow in Horizontal Two-phase Flow," *International Journal of Multiphase Flow,* Vol. 5, pp. 327–339.

Kutateladze, S. S., 1972, "Elements of Hydrodynamics of Gas-liquid System," *Fluid Mechanics Soviet Research,* Vol. 1, pp. 29–50.

Lockhart, R. W., and Martinelli, R. C., 1949, "Proposed Correlation of Data for Isothermal Two-phase, Two-component Flow in Pipes," *Chemical Engineering Progress,* Vol. 45, pp. 39–48.

Mandhane, J. M. et al., 1974, "A Flow Pattern Map for Gas-liquid Flow in Horizontal Pipes," *International Journal of Multiphase Flow,* Vol. 1, pp. 537–553.

McAdams, W. H. et al., 1942, "Vapourisation inside Horizontal Tubes, 2: Benzene-oil mixtures," *Trans. ASME* Vol. 64, pp. 193–200.

Middleman, S., 1968, *The Flow of High Polymers,* Wiley, New York.

Reimann, J., and John, H., 1978, "Measurements of the Phase Distribution in Horizontal Air-water and Steam-water Flow," *CNSI Meeting on Transient Two-Phase Flow,* Paris.

Sakaguchi, T. et al., 1979, "Flow Regime Maps for Developing Steady Air-water Two-phase Flow in Horizontal Tubes," *Mem. Fac. Eng. Kobe Univ.,* Vol. 25, pp. 191–202.

Schicht, H. H., 1969, "Flow Patterns for Adiabatic Two-phase Flow of Water and Air within a Horizontal Tube," *Verfahrenstechnik,* Vol. 3, pp. 153–161.

Scott, D. S., 1963, "Properties of Co-current Gas-liquid Flow," *Advances in Chemical Engineering,* Vol. 4, pp. 199–277, Academic Press, New York, NY.

Skelland, A. H. P., 1967, *NonNewtonian Flow and Heat Transfer,* Wiley, New York.

Taitel, Y., and Dukler, A. E., 1976, "A Model for Predicting Flow Regime Transitions in Horizontal and near Horizontal Gas-liquid Flow," *American Institute of Chemical Engineering Journal,* Vol. 22, pp. 47–55.

Wallis, G. B., 1969, "One-dimensional Two-phase Flow, McGraw-Hill, New York.

Wallis, G. B., and Dobson, J. E., 1973, "The Onset of Slugging in Horizontal Stratified Air-water Flow," *International Journal of Multiphase Flow,* Vol. 1, pp. 173–193.

Wilkinson, W. L., 1960, *NonNewtonian Fluids,* Pergamon Press, Oxford, UK.

Yoo, S. S., 1974, "Heat Transfer and Friction Factors for Non-Newtonian Fluids in Turbulent Pipe Flow," PhD thesis, University of Illinois, Chicago.

G. P. Xu
Graduate Student.

K. W. Tou
Associate Professor.

C. P. Tso
Associate Professor.

School of Mechanical and Production Engineering, Nanyang Technological University, Singapore 639798

Two-Phase Void Fraction and Pressure Drop in Horizontal Crossflow Across a Tube Bundle

Void fraction and friction pressure drop measurements were made for an adiabatic, horizontal two-phase flow of air-water, air-oil across a horizontal in-line, 5 × 20 tube bundle with pitch-to-diameter ratio, P/D, of 1.28. For both air-water and air-oil flow, the experimental results showed that the average void fraction were less than the values predicted by a homogenous flow model, but were well correlated with the Martinelli parameter X_{tt} and liquid-only Froude number Fr_{LO}. The two-phase friction multiplier data exhibited an effect of flow pattern and mass velocity, and they could be well-correlated with the Martinelli parameter.

Introduction

It has been estimated that more than 50 percent of all heat exchanger employed in process industries involved two-phase flow on the shell-side, such as condensers, reboilers, and steam generators. Paralleled flow through a tube bundle, whether the flow is inside the tubes or outside the tubes, has been studied extensively. However, the hydrodynamics for flows across the shell-side of a tube bundle have only recently been studied in detail (Jensen, 1989).

Void Fraction. Butterworth (1975) had shown that a number of the more commonly used void fraction equations for tube flows may be represented by the following relationship:

$$\frac{1-\alpha}{\alpha} = A\left(\frac{1-x}{x}\right)^p \left(\frac{\rho_G}{\rho_L}\right)^q \left(\frac{\mu_L}{\mu_G}\right)^r \tag{1}$$

The factors A, p, q, r, were shown to assume varying numerical values depending on which particular model was under consideration.

For vertical upflow across a horizontal tube bundle, at early stage, Kondo and Nakajima (1980) investigated the air-water two-phase flow void fraction measurements, but their correlation can not be generally applied because of the very low mass velocities used to generate the data. Recently, Schrage et al. (1988) tested air-water in a square in-line tube bundle with $P/D = 1.3$. The data were correlated by applying a mass velocity correction factor in terms of a Froude number to the homogeneous void fraction. Dowlati et al. (1988, 1990, 1992a) using gamma densitometry, measured void fractions in staggered and in-line tube bundles with different pitch-to-diameter ratios (i.e., 1.26, 1.30, 1.75). They also found that the void fraction was a function of the mass flux and were able to correlate all their data using the Wallis parameter. Dowlati et al. (1992b) applied the drift flux model to predict the bundle-average void fraction data tested earlier by Dowlati et al. (1990). Void fraction measurements have been taken for vertical up-and-down two-phase flow of air-water mixtures across an in-line tube bundle by Xu (1992). They found that their data and others' data (Schrage et al., 1988; Dowlati et al., 1990) were well-correlated in terms of the Martinelli parameter X_{tt} and liquid-only Froude number Fr_{LO}.

For horizontal crossflow, Grant and Chisholm (1979) have developed an expression of the void fraction for stratified flow in a horizontal tube bundle with $P/D = 1.25$ and an equilateral triangular layout. The authors stated that their correlation represented the data well at low qualities and underestimated the data at high qualities. Grant et al. (1984), Chisholm (1988) extend their previous work to other flow patterns by making use of the "quick-closing valve" method in both a model and full-size industrial heat exchangers. The predicting method they developed gave the correct trend with quality, but overestimated the effect of mass velocity.

All of the tube bundles that had been investigated are staggered in horizontal flow, the liquid phase being water. There are no published data on void fraction for horizontal crossflow across an in-line tube bundle, especially, with air-oil mixtures.

Two-Phase Friction Multiplier. In comparison to the work that has been done on shell-side void fraction, there has been much attention given to the two-phase friction multiplier. In practice, many investigators have used a Martinelli-type model to represent the two-phase friction multiplier φ_L^2 as follows:

$$\varphi_L^2 = \frac{\Delta p_{TP}^F}{\Delta p_L^F} = 1 + \frac{C}{X_{tt}} + \frac{1}{X_{tt}^2} \tag{2}$$

where $X_{tt} = ((1-x)/x)^{0.9}(\rho_G/\rho_L)^{0.5}(\mu_L/\mu_G)^{0.1}$.

Δp_{TP}^F is the two-phase flow friction pressure drop and Δp_L^F is the liquid phase only friction pressure drop, respectively. For the shell-side, after critically reviewing both two-phase friction multiplier data and models (Diehl, 1957; Diehl et al., 1958; Grant et al., 1972, 1974), Ishihara et al. (1980) fitted Eq. (2) to their total 458 sets of data and obtained a value of 8 for the C factor. This predicted the shear-controlled flow data for $X_{tt} < 0.2$ with good results. However, for $X_{tt} > 0.2$ deviations between the data and the predictions were quite large. They concluded that to improve the correlation, flow patterns should be taken into account when evaluating the C factor.

For vertical upflow, Schrage et al. (1988) and Dowlati et al. (1988) have presented results for two-phase air-water flow in in-line tube bundles. Schrage et al. (1988), on the other hand, found that a C value of 8 over-predicted their friction pressure drop data and furthermore suggested dependence of C on flow patterns. Dowlati et al. (1990, 1992a) had investigated the effect of P/D ratio (1.3, 1.75) on the two-phase friction multiplier for square in-line and staggered tube bundles, respectively. They also applied the form of Eq. (2) to correlated their two-phase friction multiplier for air-water mixtures.

Contributed by the Fluids Engineering Division for publication in the JOURNAL OF FLUIDS ENGINEERING. Manuscript received by the Fluids Engineering Division November 7, 1995; revised manuscript received July 24, 1997. Associate Technical Editor: O. C. Jones.

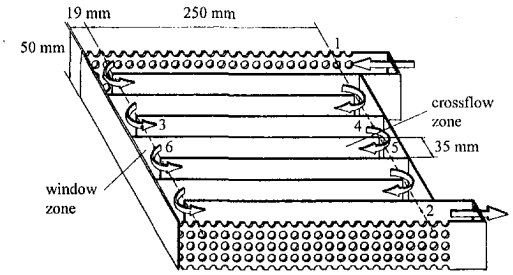

Fig. 1 Experimental heat exchanger

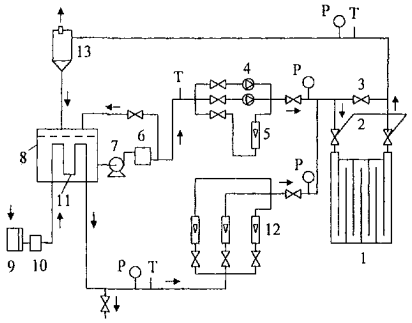

1. Experimental heat exchanger
2. A pair of quick closing valves
3. Bypass
4. Liquid turbine flow meter
5. Liquid rotameter
6. Liquid surge tank
7. Liquid pump
8. Liquid tank
9. Air compressor
10. Air surge tank
11. Air cooler
12. Air rotameter
13. Gas liquid separator
P — Pressure gauge
T — Mercury thermometer

Fig. 2 Schematic of flow loop

The effect of flow direction (upflow and downflow) on the two-phase friction multiplier had been investigated by Xu (1992) recently. They found that the C in Eq. (2) depended on the Wallis parameter and the ratio of the mass velocity of gas phase to the mass velocity of liquid phase.

It is noted that only the data of Grant et al. (1974) had been published for horizontal crossflow in a staggered tube bundle. Not only are there very little work performed on horizontal crossflow across an in-line tube bundle, but also the liquid phase has not been extended to oil.

Scope of Present Study. In the present work, void fraction and two-phase pressure drop have been measured for air-water, air-oil two-phase flow across a horizontal tube bundle with $P/D = 1.28$. The data are compared with the results of previous work, and new correlations for bundle average void fraction and two-phase friction multiplier are proposed.

Experimental Apparatus and Procedure

The experimental data in this paper were obtained from the model heat exchanger shown in Fig. 1. It has a rectangular shell made of Plexiglas measuring 280 mm long by 250 mm high by 50 mm wide. The test section containing the tube bundle model was fitted with 20 rows of 9.79 mm diameter tubes with three full rods and two half rods in each row in the crossflow zone. The two half rods were used to reduce bypass leakage and minimize wall effects. The in-line, square array had a pitch-to-diameter ratio of 1.28. There was no clearance between baffles and tubes. A total of seven segmental baffles were employed to give eight passes on the shell-side.

Pressure tapping points were located between the baffles and level with the baffle cut-edges at both ends. Pressure drop in the test section was measured with four U-tube manometers, which were modified so that each could be inclined from a vertical position at various degrees for improved accuracy when pressure drops were less than 2 kPa. The points 3 and 4, 5 and 6 in crossflow zones were used to measure the pressure drop as shown in Fig. 1.

A diagram of the flow loop is shown in Fig. 2. The air flow rates were measured with rotameters, and the liquid flow rates were measured with turbine flow meters at the higher flow rates and with rotameters at the lower flow rates. All flow meters were calibrated prior to the experiments. The pressure level in the air flowmeter was measured with a Bourdon tube pressure gauge. The temperature of air in the air flowmeter and the air-water or air-oil mixtures were measured with mercury thermometers. Compressed air was injected into the liquid through a porous tube and it mixed with the liquid phase in the mixing chamber. The gas-liquid mixtures then entered the experimental heat exchanger.

The flow patterns were observed by visualization for a wide range of flow rates of liquid and gas at inlet crossflow zone and outlet crossflow zone, respectively. A pair of quick closing valves located at the entrance zone and exit zone were used to obtain volume-average void fraction. The valves can be closed simultaneously by moving a single handle connected through linkages to both valves. The closing time was estimated to be less than 0.5 second. When the pair of valves was being closed, the bypass valve (item 3) was opened. The levels of the liquid were measured after 5 minutes. Tests of void fraction and pressure drop were run so that the total mass velocity was fixed as the quality was increased.

Uncertainties for the majority of the experimental data as estimated through a propagation of error analysis are shown in Table 1. However, at low velocities of gas and liquid, low qualities and mass velocities, the uncertainties in single-phase friction factor f, void fraction α, and two-phase friction multiplier φ_L^2 could be substantially greater than those values in Table 1. The nominal range of experimental conditions covered in this investigation were:

Quality: $10^{-3} < x < 0.68$

Nomenclature

C = C factor, Eq. (2)
C_1, C_2, C_3 = coefficients, Eq. (16)
C_4 = coefficient, Eq. (19)
D = tube outdiameter, m
$\mathrm{Fr}_{LO} = G^2/(\rho_L^2 gD)$, liquid-only Froude number
G = mass velocity based on minimum flow area, kg/m^{2}s
g = gravitational constant, m/s^2
m = exponent in Blasius-type equation
n = coefficient, Eq. (19)
N = number of tube rows
Δp = pressure drop, Pa
P = pitch, m
Re = GD/μ, Reynolds number
U = velocity, m/s
x = quality
α = void fraction
μ = dynamic viscosity, N·s/m
ρ = density, kg/m^3
φ^2 = two-phase friction multiplier
X_{tt} = Martinelli parameter

Subscripts

exp = experimental data
F = friction
G = gas phase only
L = liquid phase only
o = oil
pre = prediction
TP = two-phase flow
w = water

Table 1 Estimated uncertainties in the data

Parameters	f	Re	G	α	x	X_{tt}	Fr_{LO}	φ_L^2
Uncertainty	±6%	±3%	±3%	±2%	±5%	±5%	±6%	±8%

Mass velocity: $37 < G < 658$ kg/m^2·s
Pressure: $1 < p < 2$ atm
Temperature: $t = 25$°C
Viscosity: $\mu_w = 0.8 \times 10^{-3}$ N·s/m, $\mu_o = 2.6 \times 10^{-3}$ N·s/m, $\mu_g = 1.85 \times 10^{-5}$ N·s/m
Density: $\rho_w = 1000$ kg/m^3, $\rho_o = 810$ kg/m^3, $\rho_g = 1.2 \sim 1.7$ kg/m^3

where x is the quality (fraction of gas mass velocity); G is the total mass velocity based on minimum flow area in the crossflow zone.

Results and Analysis

Single-Phase Friction Factor. Single-phase pressure drop tests were taken separately with water, air, and oil as a check on the experimental apparatus and procedures, and to assist in obtaining the two-phase results. The experimental data cover a range of Reynolds number from 2×10^2 to 2×10^4. These data were compared with the ESDU (1979) and HEDH (1983) correlations as shown in Fig. 3, and there was close agreement between the data and correlations. To accurately represent the single-phase friction factor, a three-part Blasius-type friction factor model was used to correlate the data as:

$$f = 4.05\ \mathrm{Re}^{-0.55} \quad (\mathrm{Re} \le 10^3) \tag{3}$$

$$f = 0.08\ \mathrm{Re}^{0.048} \quad (10^3 < \mathrm{Re} \le 10^4) \tag{4}$$

$$f = 0.774\ \mathrm{Re}^{-0.196} \quad (\mathrm{Re} > 10^4) \tag{5}$$

where $f = (\rho \Delta p_F / 2NG^2)$, Δp_F is friction pressure drop, and $N = 20$ is the number of tube rows in the crossflow zone. The above equations are able to correlate the corresponding sets of data with a standard deviation of ±7.2 percent. The single-phase pressure drop were calculated from those correlations for calculation of two-phase friction multipliers.

Void Fraction. The experimental results of void fraction in horizontal flow across a horizontal tube bundle for air-water and air-oil are shown in Fig. 4(a) and Fig. 4(b), respectively. In comparison with the predictions by the homogeneous flow model, the measured void fractions were significantly lower in horizontal flow. For $x < 0.1$, a strong mass velocity effect was observed. At a given quality, higher void fraction was obtained with increasing mass velocity. Similar results have also been reported by Schrage et al. (1988), Dowlati et al. (1988, 1990, 1992a) and Xu (1992) in vertical flow across horizontal tube bundles.

At low mass velocity, the effect of buoyancy is significant especially at low qualities. The flow visualization revealed that at low mass velocity and low quality, the flow pattern is stratified flow. At high mass velocity and quality $x < 0.1$, the turbulence in the liquid phase helps in mixing the gas-liquid two-phase, with the gas phase uniformly distributed in the form of discrete bubbles in a continuous liquid phase, and a more homogeneous mixture is obtained.

When the quality $x > 0.1$, the mass velocity has little effect on the void fraction. The difference between the void fraction data and the predictions by the homogeneous model is decreased as the quality increases. Because the flow pattern has become annular flow, the tube wall and the inside wall of the shell are covered by an annular liquid film, with some liquid entrained as droplets in the gas phase. The degree of mixing increases and the slip is reduced. Therefore the void fraction data is closer to the homogeneous model at higher qualities.

The poor agreement between the homogeneous model and the data indicates that the homogeneous flow model is not applicable. Thus, the separated flow model must be used. The method of Lockhart and Martinelli (1949), developed from the separated flow model, is one of the most popular and simplest procedures for calculating two-phase pressure drop and void fraction (Johannessen, 1972). The following equations are derived in the present analysis with this method for tube-side flow.

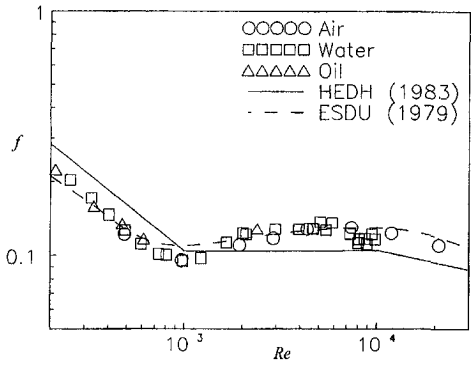

Fig. 3 Comparison of single-phase friction factor data

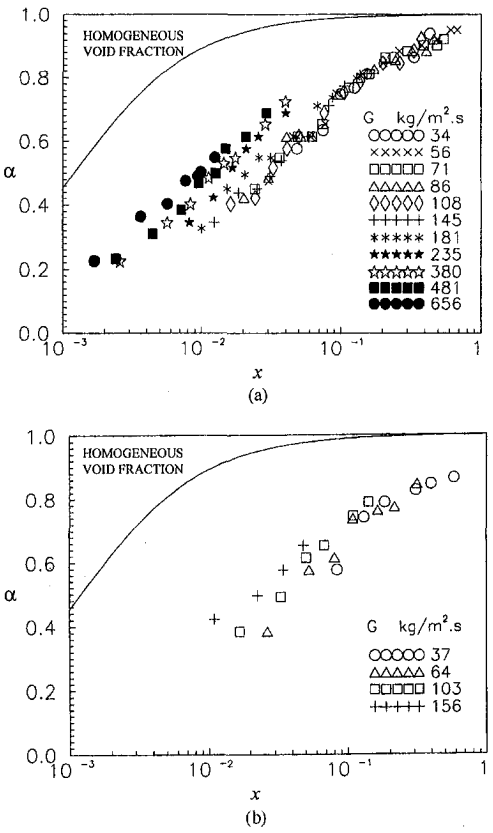

Fig. 4 Void fraction data and mass velocity effect. (*a*) Air-water; (*b*) air-oil

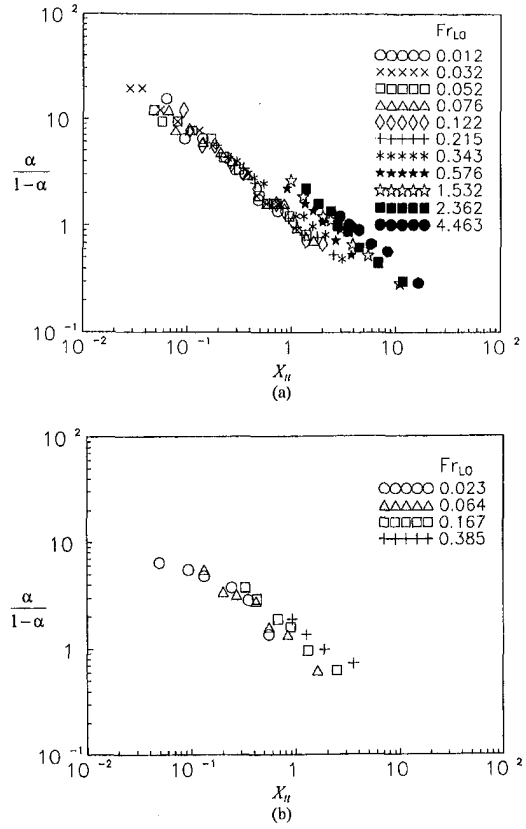

Fig. 5 Variation of void fraction with Martinelli parameter. (*a*) Air-water; (*b*) air-oil

$$(\Delta p/\Delta L)_G = (\Delta p/\Delta L)_L \tag{6}$$

$$(\Delta p/\Delta L)_G = f_G \rho_G U_G^2/(2D_G) \tag{7}$$

$$(\Delta p/\Delta L)_L = f_L \rho_L U_L^2/(2D_L) \tag{8}$$

$$f_G = C'/\mathrm{Re}_G^m = C'\mu_G^m/(\rho_G U_G D_G)^m \tag{9}$$

$$f_L = C'/\mathrm{Re}_L^m = C'\mu_L^m/(\rho_L U_L D_L)^m \tag{10}$$

$$A_G/A_L = \alpha/(1-\alpha) = BD_G^2/D_L^2 \tag{11}$$

$$\frac{U_G}{U_L} = \frac{x}{1-x}\,\frac{1-\alpha}{\alpha}\,\frac{\rho_L}{\rho_G} \tag{12}$$

Here $\Delta p/\Delta L$ is the friction pressure drop per unit length, f is the friction factor, U is the actual average velocity, D is the hydraulic diameter for the phase, A is the flow area for the particular phase, C' is a numerical constant, B is a geometric parameter related to the liquid-gas interfacial characteristics as defined in Eq. (11).

The following equation is obtained by substituting Eq. (9) into (7) and (10) into (8), and then substituting (7) and (8) into (6):

$$\left(\frac{\rho_G}{\rho_L}\right)^{1-m}\left(\frac{U_G}{U_L}\right)^{2-m}\left(\frac{\mu_G}{\mu_L}\right)^{m}\left(\frac{D_G}{D_L}\right)^{-1-m} = 1 \tag{13}$$

From Eqs. (11), (12), and (13), one has

$$\frac{\alpha}{1-\alpha} = B^{(1+m)/(5-m)}\left[\left(\frac{\mu_G}{\mu_L}\right)^{(m/2)}\left(\frac{\rho_L}{\rho_G}\right)^{0.5} \times \left(\frac{x}{1-x}\right)^{(2-m)/2}\right]^{2/(2.5-0.5m)} \tag{14}$$

where m is the Blasius exponent which is assumed to have a value of $m = 0.2$ in this study. This is because this value had been used in the shell-side studies by other investigators such as Ishihara et al. (1980), Schrage et al. (1988), Dowlati et al. (1990), and Xu (1992). Equation (14) then simplifies to

$$\frac{\alpha}{1-\alpha} = B^{0.25} X_{tt}^{-0.833} \tag{15}$$

It is of interest to note at this point that the analytical solution of the Lockhart and Martinelli flow model gives some theoretical justifications to the Butterworth (1975) form of void fraction correlation as given by Eq. (1). Although the above expression is derived for two-phase flow in tube-side, in this work, Eq. (15) is tested against the data sets in shell-side. The mass velocity effect is also evident, when $\alpha/(1-\alpha)$ is plotted against the Martinelli parameter X_{tt} as shown in Fig. 5. Liquid-only Froude number Fr_{LO}, is introduced, resulting in:

$$\frac{\alpha}{1-\alpha} = C_1 \mathrm{Fr}_{LO}^{C_2} X_{tt}^{-C_3} \tag{16}$$

where $\mathrm{Fr}_{LO} = G^2/(\rho_L^2 gD)$. The constants $C_1 = 1.95$, $C_2 = 0.18$, and $C_3 = 0.833$ give the best overall fit for both air-water and air-oil mixtures as shown in Fig. 6. A comparison of the void fraction models with the adiabatic data resulted in an average absolute deviation of 4.77 percent between the value calculated by using the correlation and the experimental data.

Attempts were made to compare the correlation for horizontal flow. Initially, 9 sets of data from Grant et al. (1979), which were obtained in the equilateral triangular layout $P/D = 1.25$ bundle using a pair of quick-closing plate valves, are found to fit very well as shown in Fig. 7. The average absolute deviation is 7.30 percent. Subsequently, 37 sets of data from Grant et al. (1984) obtained from a model and full-size industrial heat exchangers with staggered tube bundles are used. Their data are also fitted well by Eq. (16), with the average absolute

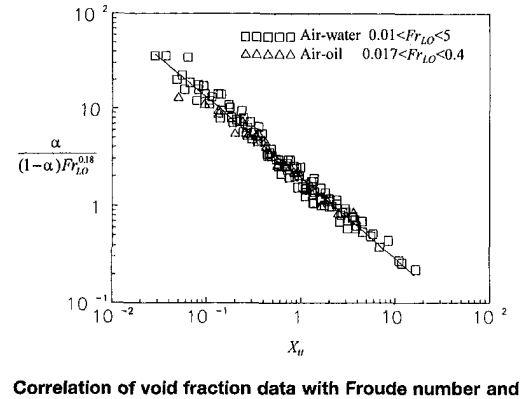

Fig. 6 Correlation of void fraction data with Froude number and Martinelli parameter

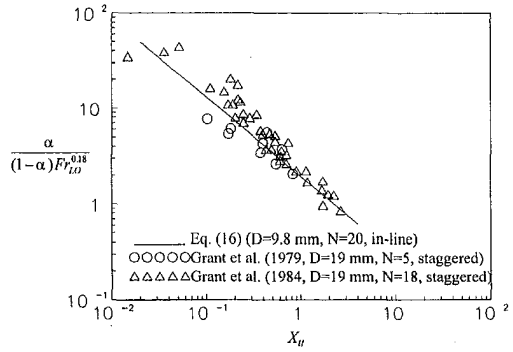

Fig. 7 Comparison of the correlation with the void fraction data of Grant et al. (1979, 1984)

deviation being 6.0 percent. It can been seen that the present model could predict well for void fraction data with different gas-liquid mixtures (air-water, air-oil), different layout of tube bundles (staggered (Grant et al., 1979, 1984), in-line), different row numbers (5 (Grant et al., 1979), 18 (Grant et al., 1984), 20), and different outside diameters of tubes (19.1 mm (Grant et al., 1979, 1984), 9.8 mm).

Two-Phase Friction Multiplier. The two-phase friction multiplier is computed based on

$$\varphi_L^2 = \frac{\Delta p_{TP}^F}{\Delta p_L^F} = \frac{\rho_L \Delta p_{TP}^F}{2 f_L [G(1-x)]^2 N} \tag{17}$$

For air-water two-phase flow, the two-phase friction multiplier data are plotted against the Martinelli parameter in Fig. 8(*a*). Mass velocity effect is observed when $X_{tt} > 0.2$, and the value of two-phase friction multiplier decreased with decreasing mass velocity at a given value of X_{tt}. Mass velocity effect is not obvious when $X_{tt} < 0.2$. These findings are similar to those obtained by Dowlati et al. (1990) and Xu (1992) for vertical flow. Effects of mass velocity in horizontal flow are not so strong as in vertical flow, and the present data of two-phase friction multiplier are much lower than the results obtained by Dowlati et al. (1990) and Xu (1992) in vertical flow. These are likely due to the change in flow patterns. The results of flow pattern in the vertical flow are obtained from Grant and Chisholm (1979) and Xu (1992). When $X_{tt} < 0.2$, almost all the data fall into the annular flow pattern. The characteristics of annular flow in horizontal direction are similar with those in the vertical upflow. The flow direction has little effect on the two-phase friction multiplier. When $X_{tt} > 0.2$, the flow pattern in the horizontal flow becomes stratified. In the vertical upflow, when the flow pattern is churn flow or intermittent flow, the

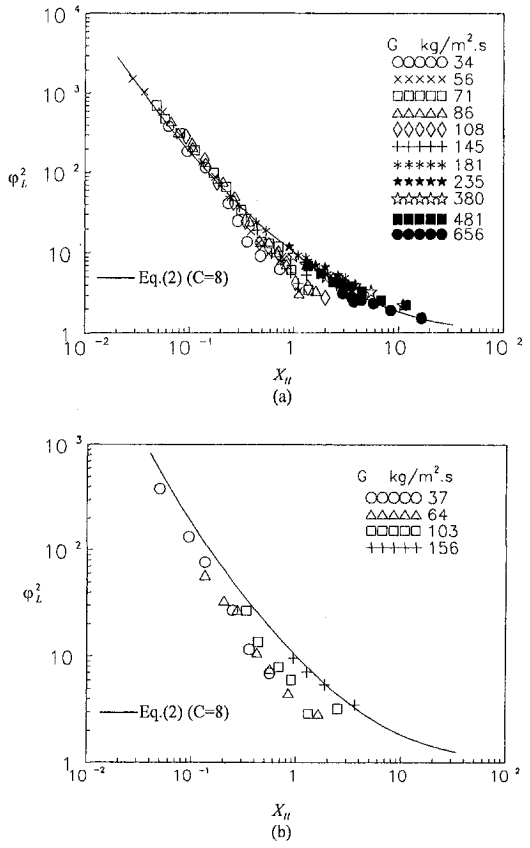

Fig. 8 Liquid-only two-phase friction multiplier data and Martinelli parameter. (*a*) Air-water; (*b*) air-oil.

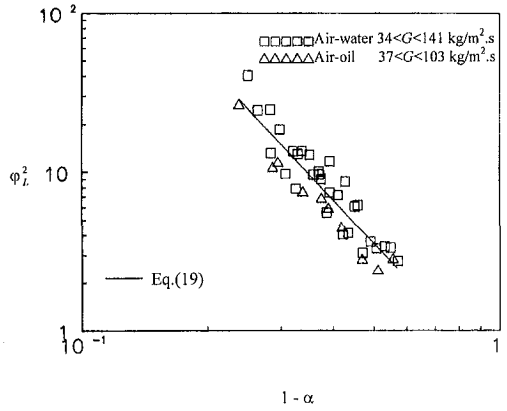

Fig. 9 Correlation of liquid-only two-phase friction multiplier data for stratified flow

liquid-gas interfacial shear stress is affected by mass velocity strongly. The two-phase friction multiplier in the vertical flow is higher than that in the horizontal flow.

Although the data of the present study have the same trend as predicted by Eq. (2), the use of $C = 8$ as suggested by Ishihara et al. (1980) did not result in a good representation of all the data. An average absolute deviation between the predictions and the experimental data is 22.7 percent. This could be attributed to the fact that the effects of the flow patterns in the shell-side have not been taken into consideration. Wang et al. (1992) noticed annular flow, bubbly flow, intermittent flow, stratified-annular flow, smooth-stratified flow, and wavy-stratified flow for air-water two-phase flow in the same heat exchanger model. The flow pattern could be determined by using the correlations proposed by Wang et al. (1992). When the flow patterns are annular flow, bubbly flow, intermittent flow and stratified-annular flow, the data are fitted well using $C = 8$, with the average absolute deviation between the predictions and the experimental data being reduced to 14.6 percent.

The data for air-oil two-phase are shown in Fig. 8(*b*). The majority of data are below the curve with $C = 8$. The mass velocity also affected the two-phase friction multiplier. It should be noted that the Reynolds number of oil for all the data are smaller than 10^3. However, when $X_{tt} < 0.2$, the two-phase friction multiplier of air-oil mixtures are lower than that of air-water. The measured data of two-phase pressure drop for air-oil mixtures are higher than that of air-water two-phase at the same mass velocity and Martinelli parameters, but the pressure drop of single liquid phase of oil are much lower, compared to water at $Re_L < 10^3$. This is due to the fact that the viscosity of oil is higher than the viscosity of water. The effect of the viscosity of liquid phase on the two-phase pressure drop is not as strong as the single-phase pressure drop at $Re_L < 10^3$, because there is slip between the gas and liquid phase.

In applying Eq. (2) to predict the air-oil two-phase friction multiplier for $G < 150$ kg/m^{2}s, it was found that the value of $C = 2.4$ resulted in a better prediction of the measured data. It is interesting to note that $C = 8$ in Eq. (2) is also seen to best fit the friction multiplier data of air-oil mixtures for $G = 156$ kg/m^{2}s as shown in Fig. 8(*b*).

For smooth-stratified flow and wavy-stratified flow, the two-phase flow is affected by gravity. Two-phase friction multiplier are correlated well with void fraction or liquid fraction as shown in Fig. 9. If there is no interfacial shear between the two phases, the following correlation was proposed by Wallis (1969):

$$\varphi_L^2 = 1/(1-\alpha)^2 \tag{18}$$

In view of the fact that there is a slip between gas and liquid phase, the similar correlation between friction and liquid fraction was used by Chisholm (1983) as follows:

$$\varphi_L^2 = C_4/(1 - \alpha)^n \quad (19)$$

The constants $C_4 = 0.507$, $n = 2.811$, correlated the present data of two-phase friction multiplier well for the flow patterns, with α being calculated by Eq. (16). Predictions from this equation differ from the experimental data of stratified flow by an average error of 16.7 percent.

Conclusions

Air-water and air-oil two-phase void fraction and friction pressure drop data are obtained for horizontal flow across a horizontal, in-line tube bundle with $P/D = 1.28$. The main findings from the experiments are:

1. The tube bundle average void fractions are smaller than the values predicted by a homogeneous flow model, and show a mass velocity effect as $x < 0.1$. A semi-emprical equation for the prediction of void fraction in shell-side is proposed and derived in terms of Fr_{LO} and X_{tt}.
2. For both air-water and air-oil two-phase flow, the data are correlated well by Eq. (16). The correlation is also in good agreement with the data of Grant et al. (1979, 1984) obtained with different number of tube rows and layout of tube bundles.
3. The two-phase friction multiplier data could be correlated well in terms of the Martinelli parameter. The effects of flow pattern on the two-phase friction multiplier have been considered. For annular flow, bubbly flow, intermittent flow and stratified-annular flow, $C = 8$ in Eq. (2) is recommended. For other flow patterns, the data are correlated well in terms of liquid fraction.
4. The effect of viscosity on the two-phase friction multiplier has been studied, and it is found that air-oil two-phase friction multiplier data are lower than that of air-water on the shell-side.

Acknowledgment

The authors acknowledge the availability of data obtained from the model heat exchanger in Xi'an Jiaotong University, P.R. China.

References

Butterworth, D., 1975, "A Comparison of Some Void-Fraction Relationships for Co-Current Gas-Liquid Flow," *International Journal of Multiphase Flow,* Vol. 1, pp. 845–850.

Chisholm, D., 1983, *Two-Phase Flow in Pipelines and Heat Exchangers,* Godwin, London.

Chisholm, D., 1988, *Heat Exchanger Technology,* Elsevier Applied Science, pp. 55–74.

Diehl, J. E., 1957, "Calculate Condenser Pressure Drop," *Petrol Refiner,* Vol. 36, No. 10, pp. 147–153.

Diehl, J. E., and Unruh, C. H., 1958, "Two-Phase Pressure Drop for Horizontal Crossflow Through Tube Banks," ASME Paper No. 58-HT-20.

Dowlati, R., Kawaji, M., and Chan, A. M. C., 1988, "Void Fraction and Friction Pressure Drop in Two-Phase Flow Across a Horizontal Tube Bundle," *AIChE Symposium Series,* Vol. 184, No. 263, pp. 126–132.

Dowlati, R., Kawaji, M., and Chan, A. M. C., 1990, "Pitch-to-Diameter Effect on Two-Phase Flow Across an In-Line Tube Bundle," *AIChE Journal,* Vol. 36, No. 5, pp. 765–772.

Dowlati, R., Chan, A. M. C., and Kawaji, M., 1992a, "Hydrodynamics of Two-Phase Flow Across Horizontal In-Line and Staggered Rod Bundle," ASME JOURNAL OF FLUIDS ENGINEERING, Vol. 114, pp. 450–456.

Dowlati, R., Kawaji, M., Chisholm, D., and Chan, A. M. C., 1992b, "Void Fraction Prediction in Two-Phase Flow Across a Tube Bundle," *AIChE Journal,* Vol. 38, No. 4, pp. 619–622.

ESDU, 1979, "Crossflow Pressure Loss Over Banks of Plain Tubes in Square and Triangular Arrays Including Effects of Flow Direction," Item No. 79034, Eng. Sci. Data Unit, London.

Grant, I. D. R., and Murry, I., 1972, "Pressure Drop on the Shell-Side of a Segmentally Baffled Shell-and-Tube Heat Exchanger with Vertical Two-Phase Flow," NEL Report No. 500, National Engineering Laboratory, East Killbride, Glasgow.

Grant, I. D. R., and Murry, I., 1974, "Pressure Drop on the Shell-Side of a Segmentally Baffled Shell-and-Tube Heat Exchanger with Horizontal Two-Phase Flow," NEL Report No. 560, National Engineering Laboratory, East Killbride, Glasgow.

Grant, I. D. R., and Chisholm, D., 1979, "Two-Phase Flow on the Shell-Side of a Segmentally Baffled Shell-and-Tube Heat Exchanger," ASME *Journal of Heat Transfer,* Vol. 101, No. 1, pp. 38–42.

Grant, I. D. R., Cotchin, C. D., and Henry, J. A. R., 1984, "Submergence in Baffled Shell-and-Tube Heat Exchangers," *First UK National Conference on Heat Transfer,* Pergamon Press, Oxford, pp. 673–683.

HEDH, 1983, *Heat Exchanger Design Handbook,* Hemisphere, New York.

Ishihara, K., and Palen, J. W., and Taborck, J., 1980, "Critical Review of Correlations for Predicting Two-Phase Flow Pressure Drop Across Tube Banks," *Heat Transfer Engineering,* Vol. 1, No. 3, pp. 23–33.

Jensen, M. K., 1989, "Plenary Lecture: Advances in Shell-Side Boiling and Two-Phase Flow," ASME HTD-Vol. 108, pp. 1–11.

Johannessen, T., 1972, "A Theoretical Solution of The Lockhart and Martinelli Flow Model for Calculating Two-Phase Flow Pressure Drop and Hold Up," *International Journal of Heat and Mass Transfer,* Vol. 15, pp. 1443–1449.

Kondo, M., and Nakajima, K. I., 1980, "Experimental Investigation of Air-Water Two-Phase Upflow Across Horizontal Tube Bundles. Part-1 Flow Pattern and Void Fraction," *Bulletin of the JSME,* Vol. 23, No. 177, pp. 385–393.

Lockhart, R. W., and Martinelli, R. C., 1949, "Proposed Correlation of Data for Isothermal Two-Phase, Two-Component Flow in Pipes," *Chemical Engineering Progress,* Vol. 45, No. 1, pp. 39–48.

Schrage, D. S., Hsu, J. -T., and Jensen, M. K., 1988, "Two-Phase Pressure Drop in Vertical Crossflow Across a Horizontal Tube Bundle," *AIChE Journal,* Vol. 34, No. 1, pp. 107–115.

Wallis, G. B., 1969, *One Dimensional Two-Phase Flow,* McGraw-Hill, New York.

Wang, Q. J., Xu, G. P., and Yang, X. Q., 1992, "Two-Phase Flow Patterns and Their Transitions on the Shell-Side of a Segmentally Baffled Shell-and-Tube Heat Exchanger—Vertically-Cut Segmentally Baffles," *Joint Conference of 3rd International Symposium on Heat Transfer and 5th International Symposium on Transport Phenomena,* pp. 930–935.

Xu, G. P., 1992, "Experimental Research on the Shell-Side Two-Phase Flow Characteristics," M.E. thesis, Xi'an Jiaotong University, P. R. China.

Effects of Particulate Diffusion on the Compressible Boundary-Layer Flow of a Two-Phase Suspension Over a Horizontal Surface

Ali J. Chamkha
Associate Professor,
Department of Mechanical and Industrial Engineering,
Kuwait University,
P.O. Box 5969
Safat, 13060-Kuwait

The problem of steady, laminar, compressible flow and heat transfer of a particulate suspension past a semi-infinite horizontal flat surface is formulated and solved numerically using an implicit finite-difference scheme. The mathematical formulation of the governing equations is based on the Eulerian description familiar from fluid mechanics where both phases are treated as two separate interacting continua. These equations account for Brownian diffusion which is important when the particle phase consists of very tiny particles and allow for a general power-law fluid-phase viscosity-temperature and particle-phase diffusion-temperature relations. Obtained flow and heat transfer results are illustrated graphically to show interesting features of this type of flow.

Introduction

Boundary-layer flow and heat transfer have been the subject and of interest of many investigators for many years due to its direct application in many industries such as the aerospace, automotive, and petroleum industries. Other possible applications include fluidized beds and environmental pollutant motions, gas purification, dust collection, aerodynamic ablation, transport processes, and conveying of powdered materials. This type of problems is often complex due to the nature of the coupled nonlinear equations governing the behavior of the flow and heat transfer characteristics. There has been considerable work done on incompressible and compressible boundary-layer flow through and over many different geometries for a single-phase system (Stewartson, 1974, and Kuerti, 1951). The high possibility of the presence of solid particles in the fluid due to different processes, led to the consideration and analysis of two-phase systems. Modeling of two-phase particulate suspensions can be accomplished in two main ways. The first way is by assuming that both the fluid and the particles suspended in it behave as two interacting continua and can exchange momentum and heat transfer (Marble, 1970, and Ishii, 1975). This approach of representing the particle phase by continuous variables (similar to the fluid phase) is limited to problems of dilute dispersed systems. These consist of multiphase systems in the form of suspensions of particulates in predominating continuous fluid media (Soo, 1989). The second approach is by treating the fluid phase as a continuum while the particle phase is governed by the kinetic theory (Berlemont et al., 1990).

The presence of a second phase (like solid particles) adds more complexity to the problem and the equations governing it. The present work considers a fundamental problem in two-phase flow. This problem is that of steady, laminar, compressible, boundary-layer flow of a fluid-particle suspension over a semi-infinite horizontal flat surface or plate. The particle phase is assumed to consist of very tiny particles which allow for Brownian motion of particles. This leads to the consideration of the effects of particulate diffusion. Special cases of the present problem have been considered earlier by Singleton (1965) and Wang and Glass (1988). Both references obtained asymptotic solutions using the series expansion method. In addition, Wang and Glass (1988) reported numerical solutions based on the finite-difference methodology. Recently, Chamkha (1996) generalized the problem considered by Singleton (1965) and Wang and Glass (1988) for a dense suspension where particle-phase viscous effects are of importance. Review of the extensive work on the incompressible version of the present problem is available in the works of Osiptsov (1980), Prabha and Jain (1982), Datta and Mishra (1982), Chamkha and Peddieson (1989, 1992), and Chamkha (1994). A major conclusion of the work on the incompressible problem is that when the original dusty-gas model (a model meant for the description of particulate suspension having small particulate volume fraction and excludes particulate viscous and diffusive effects) discussed by Marble (1970) is used, a singularity (where the particle-phase density at the plate surface becomes infinite) exists. In contrast with this conclusion, the work of Chamkha (1996) has shown that for a compressible boundary-layer flow of a dense particulate suspension, a particle-free zone is formed somewhere downstream of the leading edge of the plate.

The presence of a particle-phase diffusivity in the dusty-gas model has shown to provide smoothing effects and is capable of removing the singularity predicted in the incompressible problem (Chamkha and Peddieson, 1989 and Chamkha, 1994). The present work investigates whether the inclusion of particle-phase diffusion effects in the dusty-gas model have the same influence on the compressible problem. Namely, the smoothing of the sharp peak in the particle-phase wall density predicted by Chamkha (1996). The fluid-phase dynamic viscosity, thermal conductivity, and particle-phase diffusivity are represented by general power-law functions of the fluid-phase temperature or the particle-phase temperature. The interaction between the phases is limited to drag and heat transfer. The particles are assumed very small and of spherical shape and their volume fraction is assumed small. Furthermore, the particle Reynolds number is assumed to be less than unity.

Governing Equations

Consider a steady, laminar, two-dimensional, boundary-layer flow of a two-phase particulate suspension bounded by

Contributed by the Fluids Engineering Division for publication in the JOURNAL OF FLUIDS ENGINEERING. Manuscript received by the Fluids Engineering Division October 5, 1995; revised manuscript received October 9, 1997. Associate Technical Editor: D. E. Stock.

a semi-infinite space in the x, y plane with a flat plate at zero angle of attack placed at $y = 0$. The flow is a uniform stream in the x-direction parallel to the plate. Far above the plate, both phases are in equilibrium. The governing equations for this investigation are based on the balance laws of mass, linear momentum, and energy for both phases. The boundary-layer form of these equations for the present problem can be written as

$$\frac{\partial(\rho u)}{\partial x} + \frac{\partial(\rho v)}{\partial y} = 0 \tag{1}$$

$$\rho\left(u\frac{\partial u}{\partial x} + v\frac{\partial u}{\partial y}\right) = \frac{\partial}{\partial y}\left(\mu\frac{\partial u}{\partial y}\right) + \rho_p N(u_p - u) \tag{2}$$

$$\rho c\left(u\frac{\partial T}{\partial x} + v\frac{\partial T}{\partial y}\right) = \frac{\partial}{\partial y}\left(k\frac{\partial T}{\partial y}\right) + \mu\left(\frac{\partial u}{\partial y}\right)^2 + \rho_p N(u_p - u)^2 + \rho_p c_p N_T(T_p - T) \tag{3}$$

$$P = \rho RT \tag{4}$$

$$\frac{\partial}{\partial x}(\rho_p u_p) + \frac{\partial}{\partial y}(\rho_p v_p) = \frac{\partial}{\partial y}\left(D_p\frac{\partial \rho_p}{\partial y}\right) \tag{5}$$

$$\rho_p\left(u_p\frac{\partial u_p}{\partial x} + v_p\frac{\partial u_p}{\partial y}\right) = \rho_p N(u - u_p) \tag{6}$$

$$\rho_p\left(u_p\frac{\partial v_p}{\partial x} + v_p\frac{\partial v_p}{\partial y}\right) = \rho_p N(v - v_p) \tag{7}$$

$$\rho_p c_p\left(u_p\frac{\partial T_p}{\partial x} + v_p\frac{\partial T_p}{\partial y}\right) = \rho_p c_p N_T(T - T_p) \tag{8}$$

where x and y are the distances along and normal to the plate, respectively. ρ, u, v, P, and T are the fluid-phase density, x-component of velocity, y-component of velocity, pressure, and temperature, respectively. μ, c, k, and R are the fluid-phase dynamic viscosity, specific heat, thermal conductivity, and gas constant, respectively. D_p is the particle-phase diffusivity. The subscript p refers to the same variable for the particle phase. $N = 18\mu/(\rho_s d^2)$ and $N_T = 12k/(\rho_s d^2 c_p)$ (where ρ_s and d are the density for the particle material and the particle diameter, respectively) are the momentum and temperature transfer coefficients, respectively.

Equation (4) assumes that the fluid phase is treated as an ideal gas. This equation is needed to render the problem determinant. The hydrodynamic and thermal coupling between the phases is accounted for by the interphase drag force and the interphase heat transfer. Other interphase mechanisms such as the virtual mass force (Zuber, 1964), the shear lift force (Saffman, 1965), and the spin-lift force (Rubinow and Keller, 1961) are neglected compared to the drag force. This is feasible when the particle Reynolds number is assumed to be small (Apazidis, 1985). Equation (5) for the particle-phase balance of mass is often used for flows with chemical reactions and mass generation processes. An alternative way to incorporate the particle-phase diffusivity is through the particle-phase momentum equation. However, since the present formulation has worked well for the incompressible problem (Chamkha and Peddieson, 1989), it is adopted in the present work.

Following Wang and Glass (1988), assume that

$$\Gamma = \frac{\mu}{\mu_\infty} = \left(\frac{T}{T_\infty}\right)^\omega \quad (0.5 \le \omega \le 1.0) \tag{9}$$

where ω is a fluid-phase power index coefficient and μ_∞ and T_∞ are the free-stream fluid-phase dynamic viscosity and temperature, respectively. Singleton (1965) employed $\omega = 0.5$ in his work on this problem.

In the absence of fundamental knowledge on how the particle-phase diffusivity varies with temperature (if so), it will be assumed without loss of generality that

$$D_p^* = \frac{D_p}{D_{p\infty}} = \left(\frac{T_p}{T_\infty}\right)^{\omega_p} \quad (0.5 \le \omega_p \le 1.0) \tag{10}$$

where ω_p is a particle-phase power index coefficient and $D_{p\infty}$ is the free-stream particle-phase diffusion, respectively. For convenience and simplicity, both the fluid and the particle phases will be assumed to have the same power index coefficient such that $\omega_p = \omega$. When ω and ω_p were varied separately, very similar results were predicted. For this reason and to cut down on the number of figures to be reported subsequently, they were assumed to be equal.

A set of boundary conditions suggested by the physics of the problem to be employed to solve the governing equations given previously are as follows:

$$u(x, 0) = 0, \quad v(x, 0) = 0, \quad T(x, 0) = T_w,$$

$$\frac{\partial \rho_p}{\partial y}(x, 0) = 0, \quad v_p(x, 0) = 0$$

$$u(x, \infty) = U_\infty, \quad u_p(x, \infty) = U_\infty,$$

$$v_p(x, \infty) = v(x, \infty), \quad T(x, \infty) = T_\infty$$

$$T_p(x, \infty) = T_\infty, \quad \rho(x, \infty) = \rho_\infty, \quad \rho_p(x, \infty) = \beta\rho_\infty \tag{11 a-l}$$

where ρ_∞, U_∞, T_w, and β are the free-stream fluid-phase density, free-stream velocity, wall temperature, and the mass loading ratio of particles, respectively. Equations ($11a$–c) indicate that the fluid phase exhibits a no slip condition at the plate surface, no suction or injection condition, and is maintained at a uniform temperature T_w at the wall, respectively. Equations ($11d$, e) suggest that both the particle-phase normal variation of density and the normal velocity vanish at the plate surface, respectively. The rest of Eqs. (11) are matching conditions for both phases far above the plate and they indicate that both phases are in equilibrium with the free-stream conditions.

In the present work, a convenient set of modified Blasius transformations (similar to that employed previously by Chamkha and Peddieson (1994) converts the problem from semi-infinite in x ($0 \le x < \infty$) to finite in ξ ($0 \le \xi \le 1$) and eliminates the problems related to the singularities associated with the leading edge of the plate. In that it allows exact solution of the equations at the leading edge of the plate ($\xi = 0$) instead of assuming initial profiles of the dependent variables to start off the solution procedure as done previously by Wang and Glass (1988). This set of transformations is as follows

$$x = U_\infty\xi/(N(1 - \xi)), \quad y = U_\infty/(N\,\mathrm{Re}_\infty^{1/2})(2\xi/(1 - \xi))^{1/2}\eta$$

$$u = U_\infty F, \quad v = U_\infty((1 - \xi)/(2\xi))^{1/2}(G + \eta F)/\mathrm{Re}_\infty^{1/2}$$

$$u_p = U_\infty F_p, \quad v_p = U_\infty((1 - \xi)/(2\xi))^{1/2}(G_p + \eta F_p)/\mathrm{Re}_\infty^{1/2}$$

$$T = T_\infty H, \quad T_p = T_\infty H_p, \quad \rho = \rho_\infty Q, \quad \rho_p = \beta\rho_\infty Q_p$$

$$\mu = \mu_\infty\Gamma, \quad \delta = D_{p\infty}\rho_\infty/\mu_\infty, \quad \mathrm{Pr} = \mu c/k, \quad Ec = U_\infty^2/(cT_\infty)$$

$$\gamma = c/c_p, \quad \mathrm{Re}_\infty = \rho_\infty U_\infty^2/(N\mu_\infty) \tag{12}$$

Substituting Eqs. (12) (with $\beta = 1$ as done by Wang and Glass, 1988) along with Eqs. (9) and (10) into Eqs. (1) through (8) transforms the problem to

$$\frac{\partial(QG)}{\partial\eta} + QF + 2\xi(1-\xi)\frac{\partial(QF)}{\partial\xi} = 0 \quad (13)$$

$$\Gamma\frac{\partial^2 F}{\partial\eta^2} + \left(\frac{d\Gamma}{dH}\frac{\partial H}{\partial\eta} - QG\right)\frac{\partial F}{\partial\eta} - \frac{2\xi}{1-\xi}\left((1-\xi)^2 QF\frac{\partial F}{\partial\xi} - Q_p\Gamma(F_p - F)\right) = 0 \quad (14)$$

$$\Gamma\frac{\partial^2 H}{\partial\eta^2} + \left(\frac{d\Gamma}{dH}\frac{\partial H}{\partial\eta} - \mathrm{Pr}QG\right)\frac{\partial H}{\partial\eta} - 2\xi(1-\xi)\,\mathrm{Pr}QF\frac{\partial H}{\partial\xi} + \mathrm{Pr}Ec\Gamma\left(\frac{\partial F}{\partial\eta}\right)^2 + \left(\frac{2\xi}{1-\xi}\right) \times \left(\mathrm{Pr}Ec\Gamma Q_p(F_p - F)^2 + \frac{2\Gamma Q_p}{3}(H_p - H)\right) = 0 \quad (15)$$

$$QH = 1 \quad (16)$$

$$\delta D_p^*\frac{\partial^2 Q_p}{\partial\eta^2} + \left(\delta\frac{dD_p^*}{dH_p}\frac{\partial H_p}{\partial\eta} - G_p\right)\frac{\partial Q_p}{\partial\eta} - \left(F_p + \frac{\partial G_p}{\partial\eta}\right)Q_p - 2\xi(1-\xi)\frac{\partial(Q_pF_p)}{\partial\xi} = 0 \quad (17)$$

$$G_p\frac{\partial F_p}{\partial\eta} + \left(\frac{2\xi}{1-\xi}\right) \times \left(\Gamma(F_p - F) + (1-\xi)^2 F_p\frac{\partial F_p}{\partial\xi}\right) = 0 \quad (18)$$

$$G_p\frac{\partial G_p}{\partial\eta} + \eta G_p\frac{\partial F_p}{\partial\eta} - \eta F_p^2 + \left(\frac{2\xi}{1-\xi}\right)\left((1-\xi)^2 F_p\frac{\partial}{\partial\xi}(G_p + \eta F_p) + \Gamma(G_p - G + \eta(F_p - F))\right) = 0 \quad (19)$$

$$G_p\frac{\partial H_p}{\partial\eta} + \left(\frac{2\xi}{1-\xi}\right) \times \left((1-\xi)^2 F_p\frac{\partial H_p}{\partial\xi} + \frac{2\Gamma\gamma}{3\,\mathrm{Pr}}(H_p - H)\right) = 0 \quad (20)$$

The dimensionless boundary and matching conditions become

$$F(\xi, 0) = 0, \quad G(\xi, 0) = 0, \quad H(\xi, 0) = t_0$$

$$\frac{\partial Q_p}{\partial\eta}(\xi, 0) = 0, \quad G_p(\xi, 0) = 0, \quad F(\xi, \infty) = 1$$

$$F_p(\xi, \infty) = 1, \quad G_p(\xi, \infty) = G(\xi, \infty), \quad H(\xi, \infty) = 1$$

$$H_p(\xi, \infty) = 1, \quad Q(\xi, \infty) = 1, \quad Q_p(\xi, \infty) = 1 \quad (21)$$

where $t_0 = T_w/T_\infty$ is a dimensionless fluid-phase surface temperature.

Of special practical significance for this type of flow are the fluid-phase displacement thickness Δ, the particle-phase displacement thickness Δ_p, the fluid-phase skin-friction coefficient C, and the wall heat transfer coefficient q_w. These physical parameters are defined in dimensionless form as

$$\Delta(\xi) = \int_0^\infty (1 - QF)d\eta, \quad \Delta_p(\xi) = \int_0^\infty (1 - Q_pF_p)d\eta$$

$$C(\xi) = \Gamma(\xi, 0)\frac{\partial F}{\partial\eta}(\xi, 0), \quad q_w(\xi) = \frac{\Gamma(\xi, 0)}{Ec\ \mathrm{Pr}}\frac{\partial H}{\partial\eta}(\xi, 0) \quad (22)$$

Results and Discussion

Equations (13) through (21) exhibit no self-similar solution and must be solved numerically. In this section, some representative numerical results are reported to elucidate the behavior of the flow and heat transfer aspects of the problem under consideration. These results are computed using an iterative, implicit, tri-diagonal second-order accurate, finite-difference method similar to that discussed by Blottner (1970) and Patankar (1980).

All first-order derivatives with respect to ξ are replaced by three-point backward difference formulas. Three-point central difference quotients are also employed to discretize all second-order differential equations with respect to η. First-order differential equations are discretized using the trapezoidal rule. A two-dimensional domain is divided into 1001 nodes in the ξ direction and 195 nodes in the η direction in which the governing equations are solved. Very small step sizes are used in the region close to the wall where significant changes in the dependent variables occur and these step sizes are gradually increased as the distance above the plate is increased. However, constant small step sizes are used in the ξ direction. After many numerical experimentations, it was decided to use an initial step size of 0.001 with a growth factor of 1.03 in the η direction, and a constant step size of 0.001 in the ξ direction. Smaller step sizes than these produced no significant changes in results. The governing equations are then converted into sets of linear algebraic equations and solved by iteration at each line of constant ξ using the Thomas' algorithm (Blottner, 1970). A convergence criterion based on the difference between the current and the previous iterations was employed. It required that the difference be 10^{-5} in the present work.

Many numerical experimentations were performed by altering the step sizes in both directions to ensure accuracy of the results and to assess grid independence. For example, when $\Delta\eta_1$ was set to 0.01 instead 0.001, an average error of about 8 percent was observed in the results with the maximum error being close to $\xi = 1$. Also, when $\Delta\eta_1$ was equated to 0.0001 no significant changes of results were observed. For this reason $\Delta\eta_1 = 0.001$ was chosen and employed in producing the numerical results. The flow and heat transfer parameter are not as sensitive to $\Delta\xi$ as they are sensitive to $\Delta\eta_1$. For this reason, a constant step size was used in the ξ direction. The sensitivity analysis of the results to changes in $\Delta\xi$ was also performed. For instance, when $\Delta\xi$ was set to 0.01, an average deviation of 5 percent from the results with $\Delta\xi = 0.001$. Smaller values of $\Delta\xi$ than 0.01 produced no changes in the results and, therefore, $\Delta\xi$ was set to 0.001 in all the produced results. Two types of convergence criterion were tried. One was based on the percentage error between the previous and the current iterations and the other was based on their difference. Since we are not dealing with very small numbers, the convergence criterion based on the difference between the previous and current iterations was employed in the present study. No convergence problems were encountered even with the small value of 10^{-5} used in this work. Equations (13) through (20) were solved for G, F, H, Q, Q_p, F_p, G_p, and H_p, respectively.

Many numerical computations were performed and a parametric study illustrating the influence of the various parameters on the solution was done throughout the course of this work. Only a small representative portion of the results obtained is presented in Figs. 1 through 10.

Figures 1 and 2 illustrate the development of the fluid-phase displacement thickness Δ and the particle-phase displacement

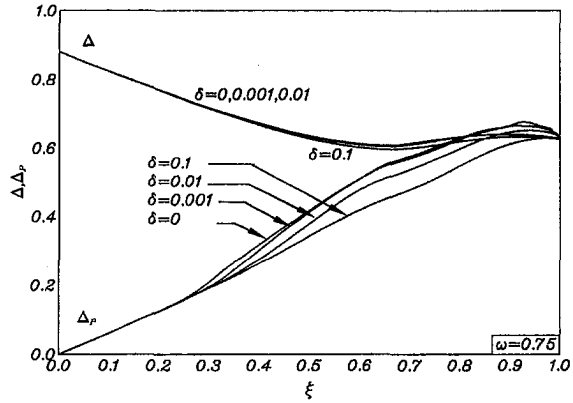

Fig. 1 Fluid and particle-phase displacement thicknesses profiles

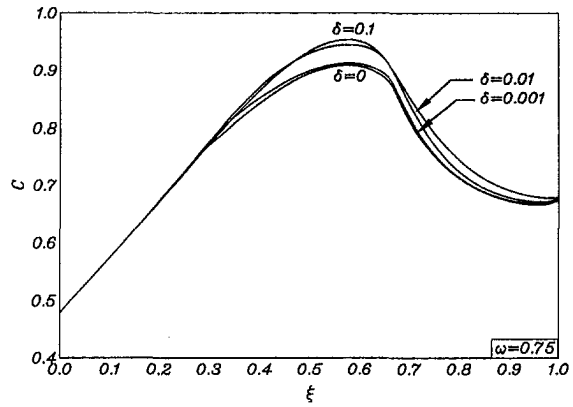

Fig. 2 Fluid-phase skin friction coefficient profiles

thickness Δ_p, and the fluid-phase skin-friction coefficient C along the plate's axial or tangential distance ξ for various inverse Schmidt's number δ, respectively. The four values of δ used to produce the numerical results are representative of nondiffusive suspensions ($\delta = 0$), small to moderate diffusive particulate phase ($\delta = 0.001$, 0.01) such as powdered gas flow and relatively high diffusive suspension such as smoke in air flow. Physically speaking, at the leading edge of the plate, a frozen flow condition exists where both phases move independently. As a result, the drag force between the phases is maximum. As the flow moves downstream of the plate's leading edge, the momentum exchange mechanism through the drag force increases causing Δ to decrease and Δ_p to increase until an equilibrium condition where both the fluid and the particle phases move together is reached at $\xi = 1$. However, the values of C tend to increase to a peak and then decrease to the equilibrium value. This behavior in Δ, Δ_p, and C are clearly depicted in Figs. 1 and 2. Furthermore, as the inverse Schmidt's number δ increases, a slight reduction in Δ, and a noticeable decrease in Δ_p and an increase in C are predicted as seen in Figs. 1 and 2.

Figures 3 and 4 present representative profiles for the particle-phase tangential velocity and density at the wall for various inverse Schmidt's numbers δ, respectively. At $\xi = 0$, the particle phase experiences a perfect slip condition at the wall with a uniform density distribution. As ξ increases and the interaction between the phases takes place, the drag force begins to decrease. As a result, the particle-phase wall tangential velocity $F_p(\xi, 0)$ starts to decrease and the particle-phase wall density $Q_p(\xi, 0)$ starts to increase slightly until equilibrium between the phases at the plate surface occurs. At this wall equilibrium position ($\xi = 0.67$), $F_p(\xi, 0)$ vanishes and $Q_p(\xi, 0)$ becomes maximum. This type of behavior was predicted in analysis of the incompressible version of the present problem where $Q_p(\xi, 0)$ became infinite (suggesting the presence of a singularity) when $F_p(\xi, 0)$ vanished (Osiptsov, 1980; Datta and Mishra, 1982; and Chamkha and Peddieson, 1989). However, in this problem continuous nonsingular solution exists in the whole computational domain. This is because as the particle phase continues to adjust with the fluid phase, its wall density begins to decrease until complete equilibrium between the phases is attained at $\xi = 1$. These behaviors in $F_p(\xi, 0)$ and $Q_p(\xi, 0)$ are clearly illustrated in Figs. 3 and 4, respectively. The effect of particulate diffusion is limited to spreading the particles away from the wall causing a significant reduction in the peak values of $Q_p(\xi, 0)$ without affecting the wall velocities of the particles as shown in Figs. 3 and 4. This problem serves as a special example of how a small change in the mathematical model (by addition of particulate diffusion in this case) produces a significant change in results.

In Fig. 5, the wall heat transfer coefficient q_w is presented along the plate for various values of δ. It is seen from this figure that q_w increases to a peak existing in the vicinity of $\xi = 0.67$ where $Q_p(\xi, 0)$ is maximum and then decreases to a limiting value at the equilibrium condition existing between the phases at $\xi = 1$. It is also seen that for $\delta = 0$ (nondiffusive particle phase) a sharp peak in q_w (corresponding to a sharp peak in $Q_p(\xi, 0)$) exists and this peak flattens out as δ increases as predicted for the profiles of $Q_p(\xi, 0)$. This suggests that the energy transfer between the phases increases as the density of the particles increases which, in turn, augments the wall heat transfer as depicted in Fig. 5. While ω was set to 0.75 in Figs. 1 through 5, similar trends are observed for other values of ω.

Figures 6 through 10 show the influence of the power index coefficient ω on the flow and heat transfer properties reported

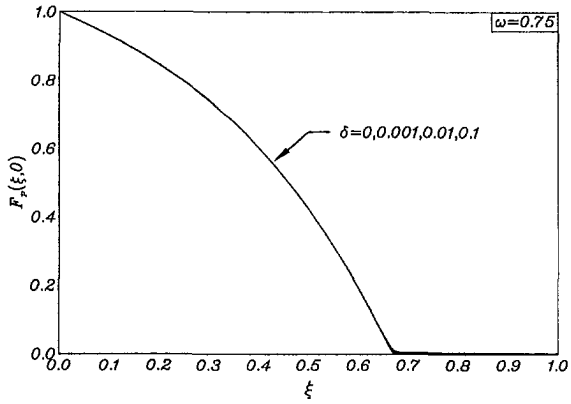

Fig. 3 Wall particle-phase tangential velocity profiles

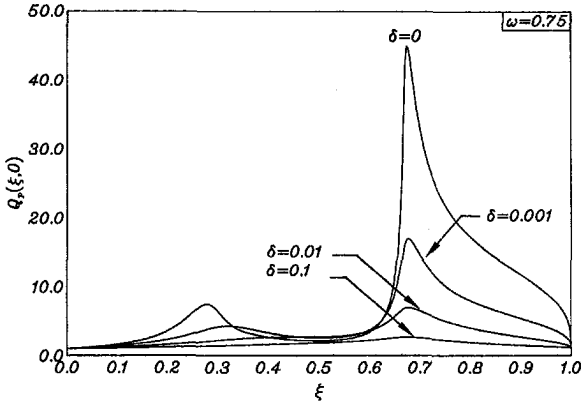

Fig. 4 Wall particle-phase density profiles

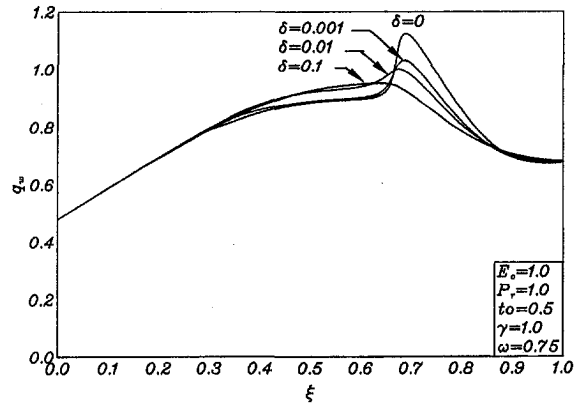

Fig. 5 Wall heat transfer coefficient profiles

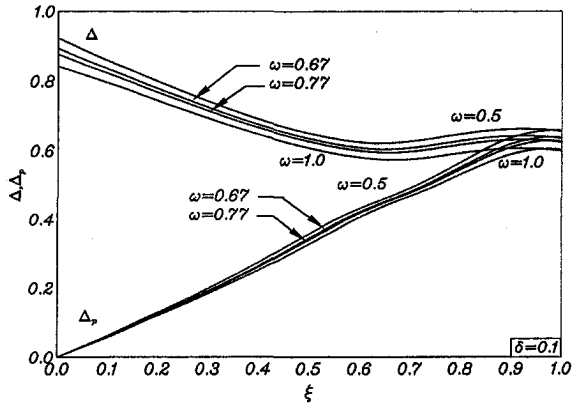

Fig. 6 Fluid and particle-phase displacement thicknesses profiles

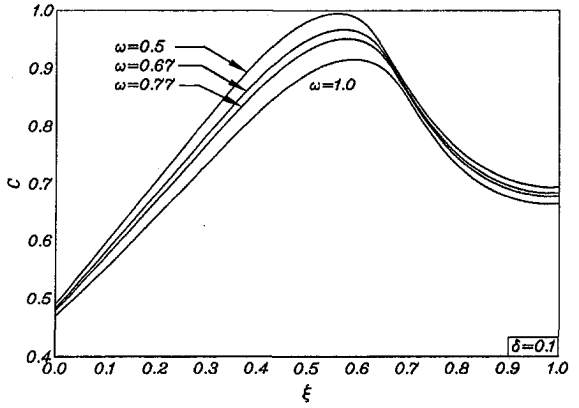

Fig. 7 Fluid-phase skin friction coefficient profiles

in Figs. 1 through 5, respectively. In general, increasing ω has a tendency to decrease the domain of viscous effects along the plate causing both Δ and Δ_p to decrease as clearly depicted in Fig. 6. The fluid-phase skin-friction coefficient C is related to the fluid wall viscosity which is dependent on the fluid-phase wall temperature (a constant value of 0.5 in this case) raised to the power index ω. Thus, increasing ω causes a decrease in C as shown in Fig. 7. In addition, as ω is increased, higher particle-phase wall tangential velocities are predicted which delay the approach to a no slip condition far downstream. This, in turn, causes the peak in $Q_p(\xi, 0)$ discussed earlier to move downstream with a reduced value. These phenomena are due to the fact that the effect of the particle-phase diffusion increases as ω increases and they are clearly depicted in Figs. 8 and 9. Finally, similar to the skin-friction coefficient C, the wall heat transfer coefficient q_w is directly proportional to the wall fluid viscosity. Therefore, increasing ω results in decreasing q_w for the reasons discussed earlier. These reductions in q_w as ω increases are apparent in Fig. 10.

The results associated with $\delta = 0$ (diffusionless theory) were put in terms of their primitive untransformed variables and compared with those reported by Wang and Glass (1988) and were found to be in good agreement. Furthermore, additional favorable comparisons were performed with the incompressible results reported by Chamkha and Peddieson (1989) and Chamkha (1994). In the absence of reported experimental results on the problem considered in this paper, and inspite of the favorable

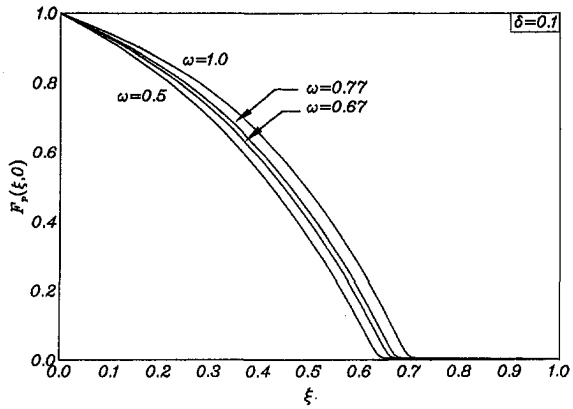

Fig. 8 Wall particle-phase tangential velocity profiles

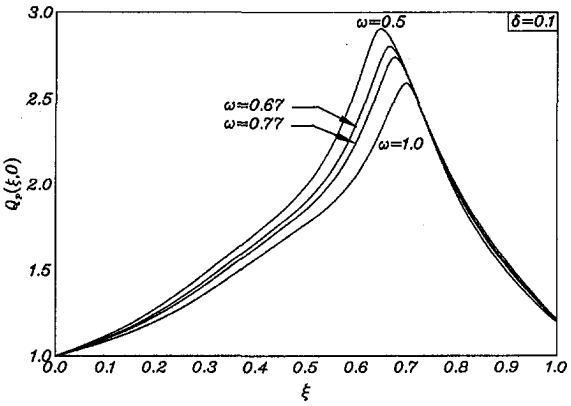

Fig. 9 Wall particle-phase density profiles

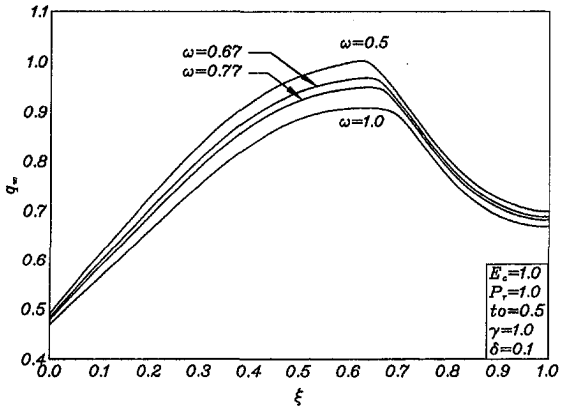

Fig. 10 Wall heat transfer coefficient profiles

comparisons made (which lend confidence in the numerical procedure), it is difficult to be certain that the interesting phenomena predicted in this work and the work reported previously (Chamkha, 1996) are physically possible. This is difficult to evaluate because of the contrast that these results offer when a small change in the mathematical model occurs. Therefore, it is highly recommended that experimental investigation of this problem be undertaken. The present and the previously reported results (Chamkha, 1996) can serve as a stimulus for this investigation by identifying a special phenomenon to look for.

Conclusion

In the present work, a two-phase (particle-fluid) theory based on the continuum approach modified to include particle-phase diffusion effects is formulated and applied to the problem of steady, laminar, compressible boundary-layer flow over a semi-infinite flat plate. General power-law viscosity- and diffusion-temperature relations are utilized. An implicit numerical scheme based on the tri-diagonal finite-difference methodology is employed in the solution of the governing equations. The predicted results show that the presence of the particulate diffusion in the model is capable of reducing significant wall heat transfer and particle concentration occurring at the plate surface somewhere downstream of the leading edge. Also, in contrast with the incompressible version of the problem (where a singularity in the particle-phase wall density is predicted for a diffusionless theory), nonsingular continuous solutions were obtained throughout the computational region. Favorable comparisons with previously published numerical results are performed which serve as a check on the correctness of the reported results. It is hoped that experimental investigations on this problem be undertaken to verify the physical validity of the predictions.

Acknowledgment

The author wishes to acknowledge and thank the Research Administration of Kuwait University for funding this project under grant No. EPM-079. Also, special thanks are due to Engineer Khalil Khanafer for producing the graphs used in this paper.

References

Apazidis, N., 1985, "On Two-Dimensional Laminar Flows of a Particulate Suspension in the Presence of Gravity Field," *International Journal of Multiphase Flow,* Vol. 11, pp. 657–698.

Berlemont, A., Desjonqueres, P., and Gouesbet, G., 1990, "Particle Lagrangian Simulation in Turbulent Flows," *International Journal of Multiphase Flow,* Vol. 16, pp. 19–34.

Blottner, F. G., 1970, "Finite-Difference Methods of Solution of the Boundary-Layer Equations," *AIAA Journal,* Vol. 8, pp. 193–205.

Chamkha, A. J., and Peddieson, J., 1994, "Boundary-Layer Theory of a Particulate Suspension with Finite Volume Fraction," ASME JOURNAL OF FLUIDS ENGINEERING, Vol. 116, pp. 147–153.

Chamkha, A. J., and Peddieson, J., 1992, "Singular Behavior in Boundary-Layer Flow of a Dusty Gas," *AIAA Journal,* Vol. 30, pp. 2966–2968.

Chamkha, A. J., and Peddieson, J., 1989, "Boundary-Layer Flow of a Particle-Fluid Suspension Past a Flat Plate," *Developments in Mechanics,* Vol., 15, pp. 315–316.

Chamkha, A. J., 1996, "Compressible Dusty-Gas Boundary-Layer Flow Over a Flat Surface," ASME JOURNAL OF FLUIDS ENGINEERING, Vol. 118, pp. 179–185.

Chamkha, A. J., 1994, "Effects of Particulate Diffusion on the Thermal Flat Plate Boundary Layer of a Two-Phase Suspension," ASME *Journal of Heat Transfer,* Vol. 116, pp. 236–239.

Datta, N., and Mishra, S. K., 1982, "Boundary Layer Flow of a Dusty Fluid Over a Semi-Infinite Flat Plate," *Acta Mechanica,* Vol. 42, pp. 71–83.

Ishii, M., 1975, *Thermo-Fluid Dynamic Theory of Two-Phase Flow,* Eyrolles, Paris.

Kuerti, G., 1951, "The Laminar Boundary Layer in Compressible Flow," *Advances in Applied Mechanics II,* pp. 21–92.

Marble, F. E., 1970, "Dynamics of Dusty Gases," *Annual Review of Fluid Mechanics,* Vol. 2, pp. 297–446.

Osiptsov, A. N., 1980, "Structure of the Laminar Boundary Layer of a Disperse Medium on a Flat Plate," *Fluid Dynamics,* Vol. 15, pp. 512–517.

Patankar, S. V., 1980, *Numerical Heat Transfer and Fluid Flow,* McGraw-Hill, New York.

Prabha, S., and Jain, A. C., 1980, "On the Use of Compatibility Conditions in the Solution of Gas Particulate Boundary Layer Equations," *Applied Scientific Research,* Vol. 36, pp. 81–91.

Rubinow, S. I., and Keller, J. B., 1961, "The Transverse Force on a Spinning Sphere Moving in a Viscous Fluid," *Journal of Fluid Mechanics,* Vol. 11, pp. 447–459.

Saffman, P. G., 1965, "The Lift on a Small Sphere in a Slow Shear Flow," *Journal of Fluid Mechanics,* Vol. 22, pp. 385–400.

Singleton, R. E., 1965, "The Compressible Gas-Solid Particle Flow Over a Semi-Infinite Flat Plate," *Zamp,* Vol. 16, pp. 421–449.

Soo, S. L., 1989, *Particulates and Continuum Multiphase Fluid Dynamics,* Hemisphere Publishing, New York.

Stewartson, K., 1974, "Multistructured Boundary Layers on Flat Plates and Related Bodies," *Advances in Applied Mechanics 14,* Academic Press, New York, pp. 146–239.

Wang, B. Y., and Glass, I. I., 1988, "Compressible Laminar Boundary-Layer Flows of a Dusty Gas Over a Semi-Infinite Flat Plate," *Journal of Fluid Mechanics,* Vol. 186, pp. 223–241.

Zuber, N., 1964, "On the Dispersed Two-Phase Flow in a Laminar Flow Region," *Chemical Engineering Science,* Vol. 19, pp. 897–917.

Pressure Drop and Heat Transfer of Magnetohydrodynamic Annular Two-Phase Flow in Rectangular Channel

H. Kumamaru
Associate Professor,
Machine and Engineering Workshop.

Y. Fujiwara
Professor,
Department of Mechanical Engineering,
Himeji Institute of Technology
2167 Shosha, Himeji,
Hyogo, 671-22, JAPAN

An annular two-phase flow model has been proposed to predict the pressure drop and heat transfer of magnetohydrodynamic (MHD) gas-liquid metal two-phase flow in a rectangular channel for the case of high void fraction. The model for a rectangular channel, in which the applied magnetic field is perpendicular to the short side of the channel cross-section, nearly predicts Inoue et al.'s experimental data on the MHD pressure drop. For fusion reactor conditions, the model shows calculated results that the MHD pressure drop for two-phase flow can be lowered to 10 percent of that of the single-phase liquid flow and the heat transfer coefficient can be increased by a factor of two or more over that of the single-phase liquid flow.

Introduction

In a fusion reactor, a high-temperature reacting plasma is magnetically confined and produces the majority of its reaction energy as high-energy neutrons. These neutrons are absorbed in a lithium bearing blanket, producing a great amount of heat and tritium which will be used as fuel. Several methods have been proposed for cooling this lithium blanket and for using the heat for the generation of electric power; for example, cooling by high-pressure helium gas, high-pressure water and liquid metal. However, it is considered that liquid-metal cooling is required for a fusion reactor of a commercial scale.

The cooling by liquid-metal single-phase flow passing through the confining magnetic field has a serious problem of a large magnetohydrodynamic (MHD) pressure drop which requires a large pumping power. In order to solve this problem, the use of gas-liquid metal (two-component) two-phase flow or liquid-metal boiling two-phase flow has been proposed in expectation of the decrease in effective electrical conductivity of fluid.

For two-phase flow in a rectangular channel, Thome (1964) reported by performing experiments on gas-liquid metal two-phase flow and developing a homogeneous two-phase flow model that the MHD pressure drop of two-phase flow is nearly equal to and a little higher than that of single-phase flow, for the same liquid flow rate and the same magnetic field, in the cases of low and medium void fractions. Also, for two-phase flow in a rectangular channel, Owen et al. (1976) proposed a separated two-phase flow (annular two-phase flow) model, together with a homogeneous flow model, and showed that the two-phase flow pressure drop cannot be lowered below the single-phase flow pressure drop. However, Inoue et al. (1987) showed by performing experiments on gas-liquid metal two-phase flow that the two-phase flow pressure drop becomes ~10 percent of the single-phase flow pressure drop in a rectangular channel for the case of high void fraction.

In this paper, therefore, separated flow (annular flow) models for a rectangular channel have been developed in order to propose a flow model which can predict Inoue et al.'s experimental data on the MHD pressure drop. Also, in this paper, the heat transfer from the channel walls to gas-liquid metal two-phase flow has been calculated based on the proposed flow models in order to estimate the improvement of heat transfer in the two-phase flow comparing with that in the single-phase liquid flow.

Finally, in this paper, the MHD pressure drop and heat transfer of gas-liquid metal two-phase flow for fusion reactor conditions have been calculated by the proposed flow and heat transfer models and have been compared with those of single-phase liquid flow.

Theoretical Models on MHD Pressure Drop

For a rectangular channel, an annular two-phase flow model has been considered in this paper. In the model, the liquid flow is assumed to be laminar due to large electromagnetic damping force. Also, it is assumed that the gas-liquid interface is smooth and there is no liquid entrainment from liquid phase to gas phase.

Model 1. As shown in Fig. 1, Model 1 assumes an annular flow pattern in which there are liquid continua adjacent to channel walls while in the center of the channel there is a gas continuum. The applied uniform magnetic field is directed perpendicularly to the long side of the channel cross-section. The flow is in the direction of z-axis, as shown by vector representation in Fig. 1. This model is basically the same as Owen et al.'s model (1976). Typical paths of induced current for two-phase flow and corresponding single-phase liquid flow are shown in Fig. 2(a). The solution is assumed to be dependent only on the y coordinate. This is completely true if the extent of the x direction is infinite, i.e. the flow channel is infinite parallel plates. Owen et al. (1976) solved this problem numerically by considering the thinning of liquid film due to heat input from the channel walls, simulating boiling two-phase flow, but not calculating the heat transfer coefficient. Also, they neglected the viscous effect in the liquid film in calculating the MHD pressure drop (see the last term in Eq. (5)). The problem without the thinning of the liquid film, corresponding to two-component two-phase flow, but considering the viscous effect, is solved analytically in this paper.

The motion of a conducting liquid under a magnetic field is described by the momentum equation including the Lorentz force (electromagnetic force) term ($\mathbf{J} \times \mathbf{B}$) and Ohm's law (Thome, 1964). They are, respectively, expressed by

Contributed by the Fluids Engineering Division for publication in the JOURNAL OF FLUIDS ENGINEERING. Manuscript received by the Fluids Engineering Division October 15, 1996; revised manuscript received September 11, 1997. Associate Technical Editor: P. R. Bandyopadhyay.

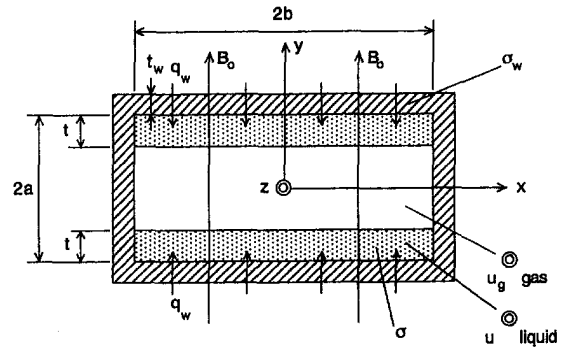

Fig. 1 Annular flow in magnetic field perpendicular to channel long-side; Model 1

$$\rho(\mathbf{u}\cdot\nabla)\mathbf{u} = -\nabla p + \eta\nabla^2\mathbf{u} + \mathbf{J}\times\mathbf{B}, \tag{1}$$

$$\mathbf{J} = \sigma(\mathbf{E} + \mathbf{u}\times\mathbf{B}). \tag{2}$$

Maxwell's equations are unnecessary for the present one-dimensional problem. In the present problem, $\mathbf{u}$ and $-\nabla p$ have only a z component, $\mathbf{B}$ only a y component, and $\mathbf{J}$ and $\mathbf{E}$ only an x component.

The total induced current in the x direction within the liquid is obtained by integration of Eq. (2) (note that E in the x direction is constant since there is no current in the y direction):

$$\bar{J}t = \int_{a-t}^{a} \sigma(E - uB_o)dy = t\sigma E - \sigma\int_{a-t}^{a} udyB_o$$

$$= t\sigma E - t\sigma\bar{u}B_o,$$

where $\bar{u}$ is the average liquid velocity. The plus and minus signs correspond to the positive and negative direction of y-axis, respectively. The total current in the x direction within the wall is given by $\bar{J}_w t_w = t_w\sigma_w E$. Since the net current in the x direction must be zero, $t\sigma(E - \bar{u}B_o) + t_w\sigma_w E = 0$. From this equation,

$$E = \frac{\bar{u}B_o}{1 + t_w\sigma_w/t\sigma} = \frac{\bar{u}B_o}{1 + \phi/(1-\alpha)},$$

where

$$\phi = \frac{t_w\sigma_w}{a\sigma}, \tag{3}$$

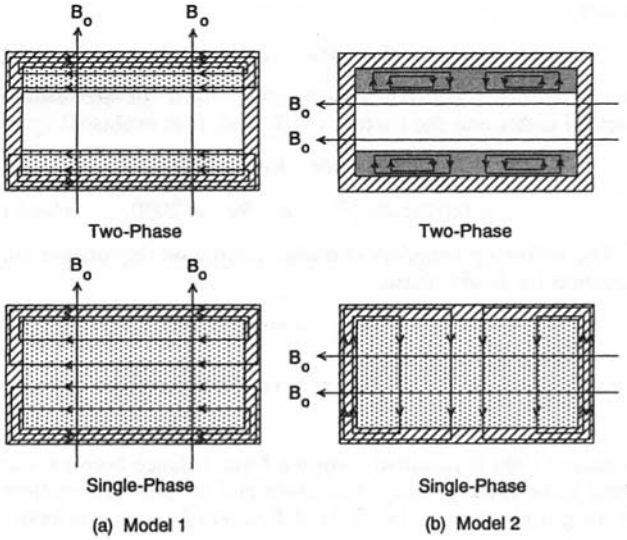

Fig. 2 Induced electric current paths in Model 1 and Model 2

is the wall conductivity number, and

$$\alpha = (a - t)/a, \tag{4}$$

is the void fraction. By substituting the above expression for E in Ohm's law, Eq. (2),

$$J = \frac{\sigma\bar{u}B_o}{1 + \phi/(1-\alpha)} - \sigma uB_o.$$

From this equation, the momentum equation for liquid phase, Eq. (1), becomes

$$-\frac{\partial p}{\partial z} + \frac{\sigma\bar{u}B_o^2}{1 + \phi/(1-\alpha)} - \sigma uB_o^2 + \eta\frac{\partial^2 u}{\partial y^2} = 0. \tag{5}$$

The Lorentz force, the sum of second and third terms, acts in the direction opposite to the flow, i.e., the negative direction of z-axis, resulting in the increase in the pressure gradient.

For the gas phase with a large gas-to-liquid relative velocity, the pressure gradient is evaluated for a flow channel with a width of $2a-2t$ by

$$-\frac{\partial p}{\partial z} = 4f\frac{1}{d_h}\frac{\rho_g\bar{u}_g^2}{2}, \tag{6}$$

Nomenclature

bold-faced = vector
bar ($\bar{}$) = average
a = half width of short side of channel
b = half width of long side of channel
B = magnetic field
B_o = applied magnetic field
C_p = specific heat
d_h = hydraulic equivalent diameter
E = induced electric field
f = friction coefficient
Ha = Hartmann number
J = induced current
k = thermal conductivity
Nu = Nusselt number
p = pressure
P = Poiseuille number
P' = Eq. (20)
Pr = Prandtl number
q = heat flux
Re = Reynolds number
RNU_M = Nusselt number ratio
RPD_M = pressure drop ratio
t = thickness, or $t = T - T_w$
t_b = bulk temperature for t
T = temperature
u = local velocity
u^* = $u/\bar{u}$, nondimensional local velocity
x, y, z = coordinate
x^* = x/a, y^* = y/a, nondimensional coordinate
α = void fraction
ϕ, ϕ' = conductivity number
η = viscosity
ρ = density
σ = electrical conductivity
τ_I = shear stress at gas-liquid interface

Subscripts

no subscript = liquid phase
g = gas phase
o = superficial velocity, or based on superficial velocity
SP = single-phase
TP = two-phase
w = wall

where

$$d_h = 4(a - t), \tag{7}$$

is the hydraulic equivalent diameter, defined for the infinite parallel plates and the friction coefficient, f, is evaluated by

$$f = 16/\mathrm{Re}_g \quad \text{for} \quad \mathrm{Re}_g \le 2000;$$

$$f = 0.0791/\mathrm{Re}_g^{0.25} \quad \text{for} \quad \mathrm{Re}_g \ge 2000. \tag{8a,b}$$

The following boundary conditions apply on the momentum equation for liquid phase.

$$y = a: \quad u = 0;$$

$$y = a - t: \quad -\eta \frac{\partial u}{\partial y} = \tau_I = (a - t)\left(-\frac{\partial p}{\partial z}\right). \tag{9a,b}$$

Equation (9b) is obtained from the force balance between the shear force at the gas-liquid interface and the pressure gradient in the gas-phase flow. From the definition of average velocity,

$$\bar{u} = \frac{1}{t}\int_{a-t}^{a} u dy. \tag{10}$$

By introducing nondimensional variables $u^* = u/\bar{u}$ and $y^* = y/a$, and Hartmann number $\mathrm{Ha} = B_o a\sqrt{\sigma/\eta}$ and Poiseuille number $\mathrm{P} = (-\partial p/\partial z)(a^2/\eta\bar{u})$, Eqs. (5), (9$a$, b), (6), (8a, b), and (10) are, respectively, rewritten in nondimensional form by the equations

$$\mathrm{P} + \frac{\mathrm{Ha}^2}{1 + \phi/(1 - \alpha)} - \mathrm{Ha}^2 u^* + \frac{\partial^2 u^*}{\partial y^{*2}} = 0, \tag{11}$$

$$y^* = 1: \quad u^* = 0; \quad y^* = \alpha: \quad -\frac{\partial u^*}{\partial y^*} = \alpha P, \tag{12a,b}$$

$$\mathrm{P} = f\frac{\mathrm{Re}_{go}^2}{\mathrm{Re}_o}\frac{\rho}{\rho_g}\left(\frac{\eta_g}{\eta}\right)^2\frac{1 - \alpha}{\alpha^3}\frac{1}{8}, \tag{13}$$

$$f = 16/\mathrm{Re}_{go} \quad \text{for} \quad \mathrm{Re}_{go} \le 2000;$$

$$f = 0.0791/\mathrm{Re}_{go}^{0.25} \quad \text{for} \quad \mathrm{Re}_{go} \ge 2000, \tag{14a,b}$$

$$1 = \frac{1}{1 - \alpha}\int_{\alpha}^{1} u^* dy^*. \tag{15}$$

The Reynolds numbers, based on both real velocities and superficial velocities, are defined by using the hydraulic equivalent diameters for the infinite parallel plates:

$$\bar{u} = \bar{u}_o/(1 - \alpha), \quad \bar{u}_g = \bar{u}_{go}/\alpha, \tag{16a,b}$$

$$\mathrm{Re} = \rho\bar{u}4t/\eta, \quad \mathrm{Re}_g = \rho_g\bar{u}_g 4(a - t)/\eta_g, \tag{17a,b}$$

$$\mathrm{Re}_o = \rho\bar{u}_o 4a/\eta\,(=\mathrm{Re}), \quad \mathrm{Re}_{go} = \rho_g\bar{u}_{go}4a/\eta_g\,(=\mathrm{Re}_g). \tag{18a,b}$$

The solution of Eq. (11) under boundary conditions (12a) and (12b) becomes

$$u^* = \frac{\dfrac{\alpha \mathrm{P}}{\mathrm{Ha}}\,\mathrm{sh}\{\mathrm{Ha}\,(1 - y^*)\} - \dfrac{\mathrm{P}'}{\mathrm{Ha}^2}\,\mathrm{ch}\{\mathrm{Ha}\,(y^* - \alpha)\}}{\mathrm{ch}\{\mathrm{Ha}\,(1 - \alpha)\}} + \frac{\mathrm{P}'}{\mathrm{Ha}^2}, \tag{19}$$

where

$$\mathrm{P}' = \mathrm{P} + \frac{\mathrm{Ha}^2}{1 + \phi/(1 - \alpha)}. \tag{20}$$

and symbols "sh" and "ch" represent hyperbolic sine and cosine, respectively.

By substituting Eq. (19) in Eq. (15), the friction pressure drop in nondimensional form, i.e., the Poiseuille number, results in

$$\mathrm{P} = \frac{\mathrm{Ha}^2}{1 + \phi/(1 - \alpha)} \times \frac{\mathrm{Ha}\,\phi\,\mathrm{ch}\{\mathrm{Ha}\,(1 - \alpha)\} + \mathrm{sh}\{\mathrm{Ha}\,(1 - \alpha)\}}{\mathrm{Ha}\,[\mathrm{ch}\{\mathrm{Ha}\,(1 - \alpha)\} - \alpha] - \mathrm{sh}\{\mathrm{Ha}\,(1 - \alpha)\}}. \tag{21}$$

For large Hartmann numbers, Eq. (21) becomes

$$\mathrm{P} = \mathrm{Ha}^2\left\{\frac{\phi}{1 + \phi/(1 - \alpha)} + \frac{1}{\mathrm{Ha}}\frac{1 + \phi}{1 + \phi/(1 - \alpha)}\right\}. \tag{22}$$

When α approaches zero (corresponding to single-phase liquid flow), the limits of Eqs. (21) and (22) become, respectively,

$$\mathrm{P} = \frac{\mathrm{Ha}^2}{1 + \phi}\frac{\mathrm{Ha}\,\phi\,\mathrm{ch}\,\mathrm{Ha} + \mathrm{sh}\,\mathrm{Ha}}{\mathrm{Ha}\,\mathrm{ch}\,\mathrm{Ha} - \mathrm{sh}\,\mathrm{Ha}}, \tag{23}$$

$$\mathrm{P} = \mathrm{Ha}^2\left(\frac{\phi}{1 + \phi} + \frac{1}{\mathrm{Ha}}\right). \tag{24}$$

These equations agree with expressions on the classical Hartmann flow for single-phase liquid (Thome, 1964).

From Eqs. (22) and (24), for large Ha, the friction pressure drop ratio (termed the friction factor multiplier in some cases), defined for the same liquid flow rate and the same magnetic field as the two-phase pressure drop divided by the single-phase liquid pressure drop, is expressed as

$$\mathrm{RPD}_M = \left(-\frac{\partial p}{\partial z}\right)_{TP}\Big/\left(-\frac{\partial p}{\partial z}\right)_{SP} = \frac{\mathrm{P}_{TP}}{\mathrm{P}_{SP}}\frac{1}{1 - \alpha} = \left\{\frac{\phi/(1 - \alpha)}{1 + \phi/(1 - \alpha)} + \frac{1}{\mathrm{Ha}}\frac{1/(1 - \alpha) + \phi/(1 - \alpha)}{1 + \phi/(1 - \alpha)}\right\}\Big/\left(\frac{\phi}{1 + \phi} + \frac{1}{\mathrm{Ha}}\right). \tag{25}$$

The void fraction, α, can be calculated by setting that Eq. (22) is equal to Eq. (13). This means that the void fraction is automatically determined so that the pressure drops of the liquid phase and gas phase become equal and the boundary condition at the liquid-gas interface is satisfied. The calculation of the void fraction is performed numerically in this study, whereas the cubic equation for void fraction can be solved analytically.

Model 2. Model 2, shown in Fig. 3, is the same as Model 1; however, the applied uniform magnetic field is directed perpendicularly to the short side of the channel cross-section. Typical paths of induced current for two-phase flow and corresponding single-phase liquid flow are shown in Fig. 2(b).

In Model 2, one side of the liquid film is in contact with the gas core, i.e., nonconducting medium, and the thickness of the channel wall perpendicular to the magnetic field, t_w, is considerably smaller than the half width of the channel parallel to the magnetic field, b. Hence, induced current paths are considered to be nearly equivalent to those for liquid flow in a channel with insulating (nonconducting) walls perpendicular to the magnetic field (Lielausis, 1975). From the above consideration, the same equations as for Model 1 hold for Model 2 except that coordinate y and y^* are replaced by x and x^*, respectively, and conductivity number ϕ is set zero. The resulting expression on P for large Ha becomes

$$\mathrm{P} = \mathrm{Ha}. \tag{22'}$$

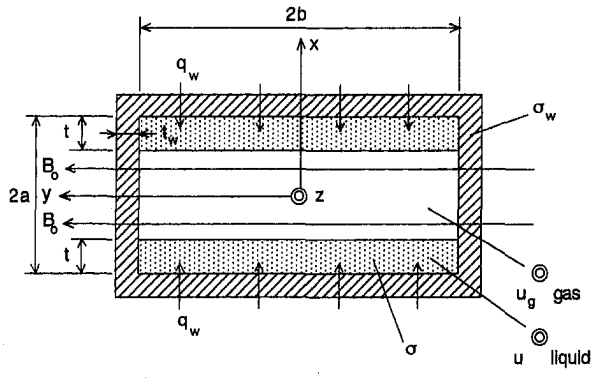

Fig. 3 Annular flow in magnetic field perpendicular to channel short-side; Model 2

In the single-phase flow of this model, current paths return through the channel walls as was the case of Model 1. For large Ha, therefore, Eq. (24) holds except that ϕ is replaced by ϕ':

$$\mathrm{P} = \mathrm{Ha}^2 \left(\frac{\phi'}{1 + \phi'} + \frac{1}{\mathrm{Ha}} \right), \tag{24'}$$

$$\phi' = \frac{t_w \sigma_w}{b\sigma}. \tag{3'}$$

The pressure drop ratio for large Ha becomes

$$\mathrm{RPD}_M = \left(-\frac{\partial p}{\partial z} \right)_{TP} \Big/ \left(-\frac{\partial p}{\partial z} \right)_{SP} = \left(\frac{1}{\mathrm{Ha}} \frac{1}{1 - \alpha} \right) \Big/ \left(\frac{\phi'}{1 + \phi'} + \frac{1}{\mathrm{Ha}} \right). \tag{25'}$$

Theoretical Models on Heat Transfer

In most conceptual designs of the fusion reactor blanket, lithium is used as liquid-metal coolant since it also serves as fuel-breeding material. In such designs, a considerable amount of heat is generated in coolant liquid itself, and the rest of heat is produced in structural material and neutron moderator-reflector such as stainless steel (Stewart and Sze, 1977). In this paper, therefore, only the heat transfer from channel walls to coolant fluid is treated since the heat generated internally in the coolant by mainly nuclear reaction and partly Joule heating is carried by the coolant itself.

Model 1. By neglecting the internal heat generation for the present one-dimensional problem, the energy equation for liquid phase with a constant heat flux from long-side channel walls for Model 1 shown in Fig. 1 can be simplified to

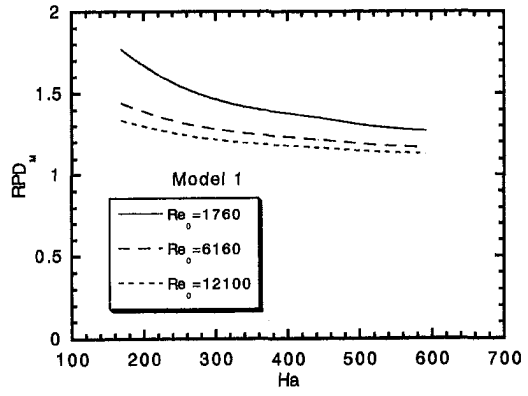

Fig. 4 Pressure drop ratios for Model 1

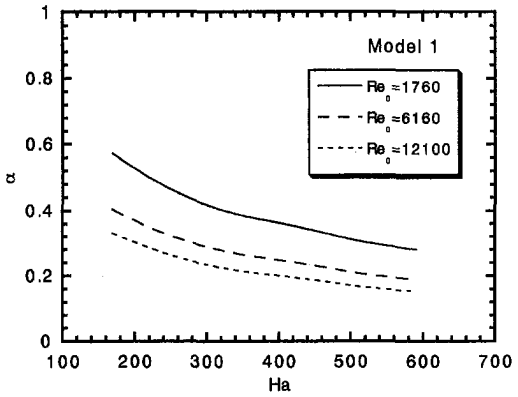

Fig. 5 Void fractions for Model 1

$$\rho C_p u \frac{\partial T}{\partial z} = k \frac{\partial^2 T}{\partial y^2}. \tag{26}$$

The boundary conditions are

$$y = a: \quad T = T_w; \quad y = a - t: \quad \frac{\partial T}{\partial y} = 0. \tag{27a,b}$$

Equation (27b) is derived based on the assumption that no heat flow exists from liquid-phase to gas-phase by neglecting heat capacity of gas as heat transfer medium.

By introducing variable $t = T - T_w$, and nondimensional variables $u^* = u/\bar{u}$, $y^* = y/a$ and $z^* = z/a$, Eqs. (26) and (27a, b) are, respectively, rewritten by the equations

$$\frac{\partial^2 t}{\partial y^{*2}} = \frac{\mathrm{Re}_o \, \mathrm{Pr}}{4(1 - \alpha)} \frac{\partial T}{\partial z^*} u^*, \tag{28}$$

$$y^* = 1: \quad t = 0; \quad y^* = \alpha: \quad \frac{\partial t}{\partial y^*} = 0. \tag{29a,b}$$

Considering $\partial T/\partial z^*$ is constant because of constant wall heat flux, the solution of Eq. (28) with boundary conditions Eqs. (29a) and (29b) becomes

$$t = \frac{\mathrm{Re}_o \, \mathrm{Pr}}{4(1 - \alpha)} \frac{\partial T}{\partial z^*} \left[\frac{\alpha \mathrm{P}}{\mathrm{Ha}^3} \frac{\mathrm{sh}\{\mathrm{Ha}\,(1 - y^*)\}}{\mathrm{ch}\{\mathrm{Ha}\,(1 - \alpha)\}} - \frac{\mathrm{P}'}{\mathrm{Ha}^4} \frac{\mathrm{ch}\{\mathrm{Ha}\,(y^* - \alpha)\}}{\mathrm{ch}\{\mathrm{Ha}\,(1 - \alpha)\}} + \frac{\mathrm{P}'}{2\,\mathrm{Ha}^2} y^{*2} + \frac{\alpha}{\mathrm{Ha}^2} (\mathrm{P} - \mathrm{P}') y^* - \frac{\alpha \mathrm{P}}{\mathrm{Ha}^2} + \frac{\mathrm{P}'}{\mathrm{Ha}^4} + \frac{\mathrm{P}'}{\mathrm{Ha}^2} \left(\alpha - \frac{1}{2} \right) \right]. \tag{30}$$

By using Eq. (30), a calculation on the heat transfer coefficient in nondimensional form, i.e. the Nusselt number, results in

$$\mathrm{Nu} = \frac{h \cdot a}{k} = \frac{-\partial T/\partial y^*|_{y^*=1}}{t_b} = \frac{A}{B}$$

$$A = -\frac{\alpha(1 - \alpha)\,\mathrm{P}}{\mathrm{Ha}^2 \,\mathrm{ch}\{\mathrm{Ha}\,(1 - \alpha)\}} - \frac{1 - \alpha}{\mathrm{Ha}^3} \mathrm{P}' \frac{\mathrm{sh}\{\mathrm{Ha}\,(1 - \alpha)\}}{\mathrm{ch}\{\mathrm{Ha}\,(1 - \alpha)\}} + \frac{\alpha(1 - \alpha)\,\mathrm{P}}{\mathrm{Ha}^2} + \frac{(1 - \alpha)^2}{\mathrm{Ha}^2} \mathrm{P}'$$

$$B = -\frac{\alpha^2 P^2}{2\,Ha^5}\left[\frac{sh\{Ha\,(1-\alpha)\}}{ch\{Ha\,(1-\alpha)\}} - \frac{Ha\,(1-\alpha)}{ch^2\{Ha\,(1-\alpha)\}}\right]$$

$$+\frac{P'^2}{2\,Ha^7}\left[\begin{array}{c}(Ha^2+1)\dfrac{sh\{Ha\,(1-\alpha)\}}{ch\{Ha\,(1-\alpha)\}} - 2\,Ha \\ +\dfrac{2\,Ha\,\alpha}{ch\{Ha\,(1-\alpha)\}} - \dfrac{Ha\,(1-\alpha)}{ch^2\{Ha\,(1-\alpha)\}}\end{array}\right]$$

$$+\frac{\alpha\,P\,P'}{Ha^6}\frac{1}{ch^2\{Ha\,(1-\alpha)\}}\left[\begin{array}{c}sh\{Ha\,(1+\alpha)\}\{sh\,Ha\,ch\,Ha - sh(Ha\,\alpha)ch(Ha\,\alpha)\} \\ +Ha\,(1-\alpha)sh\{Ha\,(1-\alpha)\} \\ -\{sh^2\,Ha - sh^2(Ha\,\alpha)\}ch\{Ha\,(1+\alpha)\}\end{array}\right]$$

$$-\frac{\alpha\,P\,P'}{2\,Ha^6}\left[(Ha^2\,\alpha^2+2) + \frac{2\,Ha\,\alpha sh\{Ha\,(1-\alpha)\}}{ch\{Ha\,(1-\alpha)\}} - \frac{Ha^2+2}{ch\{Ha\,(1-\alpha)\}}\right]$$

$$+\left(\frac{\alpha^2 P}{Ha^3} - \frac{1}{1+\phi/(1-\alpha)}\right)\left[Ha\,\alpha + \frac{sh\{Ha\,(1-\alpha)\}}{ch\{Ha\,(1-\alpha)\}} - \frac{Ha}{ch\{Ha\,(1-\alpha)\}}\right]$$

$$+\left(\frac{\alpha\,P\,P'}{Ha^6} - \frac{\alpha\,P'^2}{Ha^6}\right)\left[Ha\,\frac{sh\{Ha\,(1-\alpha)\}}{ch\{Ha\,(1-\alpha)\}} - 1 + \frac{1}{ch\{Ha\,(1-\alpha)\}}\right]$$

$$-\left\{\frac{2\alpha\,P\,P'}{Ha^6} - \frac{\alpha^2 P^2}{Ha^4} + \frac{\alpha\,P\,P'}{Ha^4}\left(\alpha - \frac{1}{2}\right)\right\}\left[1 - \frac{1}{ch\{Ha\,(1-\alpha)\}}\right]$$

$$+\left\{\frac{2\,P'^2}{Ha^7} - \frac{\alpha\,P\,P'}{Ha^5} + \frac{P'^2}{Ha^5}\left(\alpha - \frac{1}{2}\right)\right\}\frac{sh\{Ha\,(1-\alpha)\}}{ch\{Ha\,(1-\alpha)\}} - \frac{P'^2}{6\,Ha^4}(1-\alpha^3)$$

$$-\left(\frac{\alpha\,P\,P'}{2\,Ha^4} - \frac{\alpha\,P'^2}{2\,Ha^4}\right)(1-\alpha^2) + \left\{\frac{\alpha\,P\,P'}{Ha^4} - \frac{P'^2}{Ha^6} - \frac{P'^2}{Ha^4}\left(\alpha - \frac{1}{2}\right)\right\}(1-\alpha). \quad (31)$$

For large Ha, Eq. (31) becomes

$$Nu = A'/B'$$

$$A' = 3(1-\alpha)^2\{1 + \phi/(1-\alpha)\}^2$$

$$B' = (1-\alpha^3)\phi^2 + (2 - 3\alpha + \alpha^3)\phi + (1-\alpha)^3 + (1/Ha)\{(2 - 4.5\alpha^2 - 2\alpha^3)\phi^2 + (4 - 3\alpha - \alpha^3)\phi + (2 - 3\alpha + \alpha^3)\}. \quad (32)$$

When α approaches zero (corresponding to single-phase liquid flow), the limit of Eq. (32) becomes

$$Nu = 3/(1 + 2/Ha). \quad (33)$$

The expression on the limit of Eq. (31) as α approaches zero, corresponding to Eq. (23) for the case of Poiseuille number, is omitted on account of the limited space. The reader, however, can easily derive the expression by setting $\alpha = 0$ in Eq. (31).

From Eqs. (32) and (33), for large Ha, the Nusselt number ratio (equal to the heat transfer coefficient ratio), defined for the same liquid flow rate and the same magnetic field as the Nusselt number for two-phase flow divided by that for single-phase flow, is expressed as

$$RNU_M = Nu_{TP}/Nu_{SP} = \text{Eq. (32)/Eq. (33)}. \quad (34)$$

Model 2. For Model 2 shown in Fig. 3, the same equations as for Model 1 hold except that coordinate y and y^* are replaced by x and x^*, respectively, and conductivity number ϕ is set zero, as was the case in the calculation of Poiseuille number. The resulting expression on P for large Ha becomes

$$Nu = \frac{3(1-\alpha)^2}{(1-\alpha)^3 + (1/Ha)(2 - 3\alpha + \alpha^3)}, \quad (35)$$

The Nusselt number ratio is given by

$$RNU_M = Nu_{TP}/Nu_{SP} = \text{Eq. (35)/Eq. (33)}. \quad (36)$$

Calculated Results

Inoue et al. (1987) performed experiments on MHD pressure drop and heat transfer for helium-lithium two-phase flow at a temperature and a pressure of 623 K and 0.2 MPa, respectively, flowing with $\bar{u}_o$ = 0.0805, 0.282, 0.553 m/s and $\bar{u}_{go}$ = 180 m/s through a horizontal channel with a = 0.005 m, b = 0.02 m and t_w = 0.005 m under transverse magnetic fields of B_o = 0.4 ~ 1.4 T. The peculiarity of their experiments is that the applied magnetic field is perpendicular to the short side of the channel cross-section as was the case of Model 2. In this paper, therefore, pressure drop ratios obtained from their experiments are compared with those calculated by Model 2. However, heat transfer data in their experiments are expressed by the ratio of heat transfer coefficient of two-phase flow with a magnetic field to that without a magnetic field. Hence, comparison of their heat transfer data with calculated values by the present model is difficult since the heat transfer coefficients for two-component annular two-phase flow without a magnetic field are not presented in their paper.

A few experiments on MHD pressure drop have been performed in a rectangular channel in which the magnetic field is perpendicular to the long side of the channel cross-section as was the case of Model 1 (Thome, 1964; Saito et al., 1989).

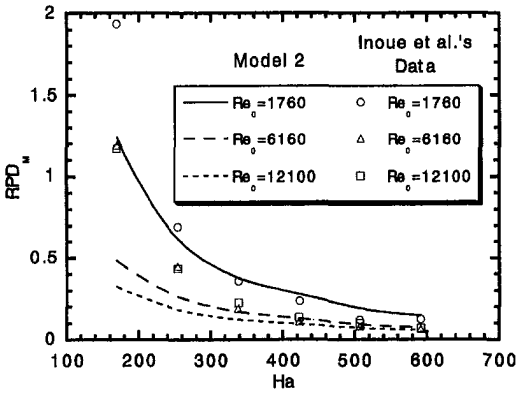

Fig. 6 Pressure drop ratios for Model 2 including comparison with Inoue et al's data

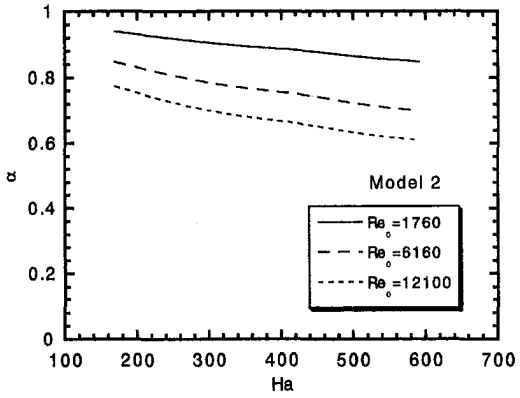

Fig. 7 Void fractions for Model 2

However, these experiments have been performed for the case of low or medium void fraction, showing that the pressure drop ratio is nearly equal to or a little higher than 1.0. No experimental data have been obtained for the case of high void fraction corresponding to the flow pattern shown in Model 1; hence, calculated results by Model 1 cannot be directly compare with experimental data. In this paper, however, calculated results by Model 1 are presented for the same geometry and experimental conditions as those in Inoue et al's experiments, except that the magnetic field is perpendicular to the long side of the channel cross-section, in order to compare Model 1 and Model 2.

Figures 4 and 5 show pressure drop ratios RPD_M and void fractions α, respectively, calculated by Model 1, in which the magnetic field is perpendicular to the long side of the channel cross-section, for the cases of Re_o = 1760, 6160, 12100, Re_{go} = 16700, $(\rho/\rho_g)(\eta_g/\eta)^2$ = 17.2, ϕ = 0.32, ϕ' = 0.080 and Ha = 169 ~ 592 simulating the conditions in Inoue et al.'s experiments. The void fractions shown in Fig. 5 are rather low compared with those expected for the annular flow, approximately greater than 0.7 (JSME, 1989). The reason may be that a large electromagnetic force by interaction between induced current and applied magnetic field decreases the liquid velocity, resulting in a large slip ratio (of the gas velocity to liquid velocity) and hence a small void fraction. Therefore, the annular flow pattern scarcely appears in the situation of Model 1, since the superficial gas velocity $\bar{u}_{go}$ = 180 m/s is considered to be sufficiently large.

Furthermore, Model 1 always gives pressure drop ratios greater than 1.0. This can be proved from Eq. (25) by replacing 1 in the denominator by $1 - \alpha$. This result agrees with that of Owen's calculation (1976) based on an annular flow model. The reason may be that the effect of the decrease in the film thickness of conducting liquid, which would decrease induced currents, cannot compensate for the effect of the increase in the average liquid velocity. Points to which attention should be paid are that experiments are usually performed in the situation of Model 1 since the gap width between pole faces of a magnet is quite small.

Figures 6 and 7 show pressure drop ratios RPD_M and void fractions α, respectively, calculated by Model 2, in which the magnetic field is perpendicular to the short side of the channel cross-section, for the same cases as for Figs. 4 and 5, exactly simulating the conditions in Inoue et al.'s experiments. The void fractions shown in Fig. 7 are high enough to realize the annular flow, i.e., approximately greater than 0.7 (JSME, 1989). The reason may be that comparing with Model 1, a smaller electromagnetic force due to a smaller induced current, as explained later, gives a larger liquid velocity, resulting in a smaller slip ratio and hence a larger void fraction. Even for a horizontal flow, the annular flow would appear rather than the stratified flow in the conditions studied in these figures, judging from experimental data on flow pattern in horizontal two-phase flow without a magnetic field (JSME, 1989) and in vertical liquid-metal two-phase flow with a magnetic field in a circular pipe (Michiyoshi et al., 1986).

Model 2 gives pressure drop ratios smaller than 1.0 except for the region of lower Hartmann numbers, as shown in Fig. 6. This is because the gas core functions as a nonconducting medium and interrupts induced currents. The pressure drop ratios calculated by Model 2 nearly agree with Inoue et al.'s experimental data except for the regions of lower Hartmann numbers and higher Reynolds numbers. The disagreement between calculated and experimental data increases with decreasing Hartmann number and increasing Reynolds number. The reason may be that phenomena of wave formation at the gas-liquid interface and liquid entrainment from the liquid-phase to the gas-phase, which are not taken into account in the present models, cannot be disregarded for smaller Hartmann numbers and higher Reynolds numbers. The wave formation and the liquid entrainment may have effects to increase the pressure drop of two-phase flow through increases in interfacial drag and gas-phase pressure drop, respectively.

Figure 8 shows Nusselt number ratios RNU_M calculated by Model 1, in which the magnetic field is perpendicular to the long side of the channel cross-section, for the same case as for Figs. 4 and 5. Model 1 always gives Nusselt number ratios greater than 1.0 for large Hartmann numbers. This can be proved by dividing the denominator and numerator of Eq. (34) by $(1 - \alpha)^2$ and performing a short calculation. For reference, the

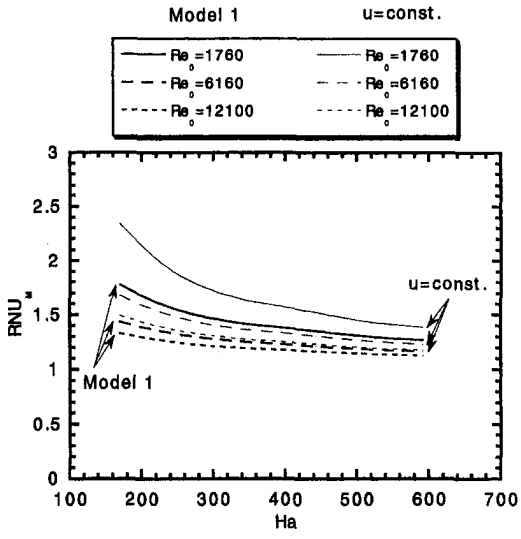

Fig. 8 Nusselt number ratios for Model 1

Nusselt number ratios estimated for constant liquid velocities ($RNU_M = 1/(1 - \alpha)$), i.e. the ratios of Nusselt number for two-phase flow with a constant liquid velocity ($Nu = 3/(1 - \alpha)$) to that for single-phase liquid flow with a constant velocity ($Nu = 3$), are also presented in Fig. 8. For large Hartmann numbers, the liquid velocity is nearly constant except for the regions very close to the wall and gas-liquid interface. The Nusselt number ratios by Model 1 roughly agree with those for constant liquid velocities. This means that the increases in the Nusselt number for two-phase flow compared with that for single-phase flow, calculated by Model 1, are mainly caused by the increases in the (real) liquid velocity for two-phase flow ($\bar{u} = \bar{u}_o/(1 - \alpha)$) compared with that for single-phase liquid flow ($\bar{u} = \bar{u}_o$).

Figure 9 shows Nusselt number ratios RNU_M calculated by Model 2, in which the magnetic field is perpendicular to the short side of the channel cross-section, for the same case as for Figs. 6 and 7. Model 2 always gives Nusselt number ratios greater than 1.0 for large Hartmann numbers. This can be proved by dividing the denominator and numerator of Eq. (36) by $(1 - \alpha)^2$. For reference, the Nusselt number ratios estimated for constant liquid velocities ($RNU_M = 1/(1 - \alpha)$) are also presented in Fig. 9. The Nusselt number ratios by Model 2 roughly agree with those for constant liquid velocities, as was the case of Model 1.

Table 1 presents void fractions α, pressure drop ratios RPD_M and Nusselt number ratios RNU_M calculated by Model 1 and Model 2 for fusion reactor conditions, i.e. $Re_o = 10^4$ and 10^5, $Re_{go} = 5 \times 10^5$, $(\rho/\rho_g)(\eta_g/\eta)^2 = 4.0$, $\phi = 0.02$, $\phi' = 0.01$, and $Ha = 10^4$. These values for the nondimensional parameters correspond roughly to helium-lithium fluid system at average fluid temperature and pressure of 650 K and 1 MPa, respectively, flowing with $\bar{u}_o = 0.05$ m/s and 0.5 m/s, and $\bar{u}_{go} = 100$ m/s through channels with $a = 0.05$ m, $b = 0.1$ m and $t_w = 0.0025$ m under a transverse magnetic field of $B_o = 5$ T, determined with reference to a conceptual design of fusion reactor (UW Study Group, 1975; Stewart and Sze, 1977). Model 1, in which the magnetic field is perpendicular to the long side of the channel cross-section, cannot give pressure drop ratios lower than 1.0, as was the case for the experimental conditions mentioned above.

Model 2, in which the magnetic field is perpendicular to the short side of the channel cross-section, predicts pressure drop ratios lower than ~0.1. Model 2 also gives Nusselt number ratios higher than ~2.0. This means that the MHD pressure drop for two-phase flow can be lowered to 10% of that of the single-phase liquid flow and the Nusselt number for two-phase flow can be increased by a factor of two or more over that of single-phase liquid flow, for the same liquid flow rate and the same magnetic field, under fusion reactor conditions.

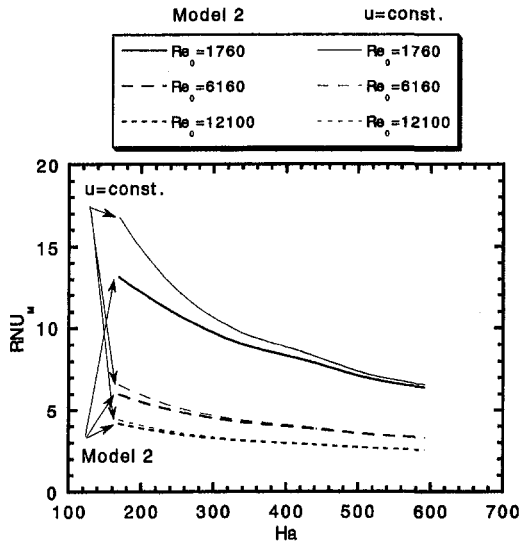

Fig. 9 Nusselt number ratios for Model 2

Table 1 Pressure drop ratios and Nusselt number ratios for fusion reactor conditions

	Model 1		Model 2	
ϕ	0.02		—	
ϕ'	—		0.01	
Re_{go}	5×10^5		5×10^5	
Re_o	10^4	10^5	10^4	10^5
α	0.243	0.119	0.840	0.551
RPD_M	1.31	1.13	0.0625	0.0222
RNU_M	1.31	1.13	6.24	2.22
(RNU_M*)	(1.32)	(1.13)	(6.25)	(2.22)

* The Nusselt number ratio obtained for flows with a constant velocity.

The existence of liquid film on heated wall surface under high heat flux conditions should be estimated by the critical heat flux (CHF). However, no experimental data exist on the CHF of both two-component and boiling two-phase flow with a magnetic field, and theoretical investigation on the CHF for such conditions is also difficult to perform. Therefore, this problem should be investigated experimentally in future. However, since a considerable amount of heat is generated in coolant liquid (lithium) itself as was stated previously, the CHF condition would not occur in annular flow pattern with the same liquid flow rate as that in adopted in conceptual designs of a fusion reactor.

Conclusions

An annular two-phase flow model has been proposed to predict the pressure drop and heat transfer of MHD gas-liquid metal two-phase flow in a rectangular channel for the case of high void fraction. Except for the region of lower Hartmann numbers, the proposed model for a rectangular channel, in which the applied magnetic field is perpendicularly to the short side of the channel cross-section, nearly predicts Inoue et al.'s experimental data on MHD pressure drop, which showed that the pressure drop ratio takes values considerably lower than 1.0 in most cases.

This model predicts for fusion reactor conditions that the pressure drop ratio becomes lower than ~0.1 and the Nusselt number ratio takes values higher than ~2.0. This means that the MHD pressure drop for two-phase flow can be lowered to 10 percent of that of the single-phase liquid flow, and the heat transfer coefficient for two-phase flow can be increased by a factor of two or more over that of the single-phase liquid flow, for the same liquid flow rate and the same magnetic field.

References

Inoue, A., Aritomi, M., Takahashi, M., Narita, Y., Yano, T., and Matsuzaki, M., 1987, "Studies on MHD Pressure Drop and Heat Transfer of Helium-Lithium Annular-Mist Flow in a Transverse Magnetic Field," *JSME International Journal*, Vol. 30, No. 267, pp. 1768–1775.

Japan Society of Mechanical Engineers (JSME), 1989, *Handbook of Gas-Liquid Two-Phase Flow Technology*, (in Japanese), Chap. 12, Corona Publishing Co., Ltd..

Lielausis, O., 1975, "Liquid Metal Magnetohydrodynamics," *Atomic Energy Review*, Vol. 13, pp. 527–581.

Michiyoshi, I., Serizawa, A., Takahashi, O., Gakuhari, K., and Ida, T., 1986, "Heat Transfer and Hydraulics of Liquid Metal-Gas Two-Phase Magnetohydrodynamic Flow," *Proc. 8th Int. Heat Transfer Conf.*, San Francisco, USA, Vol. 5, pp. 2391–2396.

Owen, R. G., Hunt, J. C. R., and Collier, J. G., 1976, "Magnetohydrodynamic Pressure Drop in Ducted Two-Phase Flows," *Int. J. Multiphase Flow*, Vol. 3, pp. 23–33.

Saito, M., Inoue, S., and Fujii-e, Y., 1978, "Gas-Liquid Slip Ratio and MHD Pressure Drop in Two-Phase Liquid Metal Flow in Strong Magnetic Field," *J. Nucl. Sci. Technol.*, Vol. 15, No. 7, pp. 476–489.

Stewart, W. E. and Sze, D. K., 1977, "Transport Problems in Lithium Cooling of Tokamak Reactors," *AIChE Symposium Series*, Vol. 73, No. 168, pp. 56–62.

Thome, R. J., 1964, "Effect of a Transverse Magnetic Field on Vertical Two-Phase Flow through a Rectangular Channel," Argonne National Laboratory Report ANL-6854.

University of Wisconsin Fusion Feasibility Study Group (UW Study Group), 1975, "UWMAK-I, A Wisconsin Toroidal Fusion Reactor Design," University of Wisconsin Fusion Design Memo UWFDM-68, Vol. 2.

Flow Visualization in Bubbly Two-Phase Hydraulic Jump

Michele Mossa
PhD, Dipartimento di Ingegneria delle Acque-Politecnico di Bari, Via E. Orabona, 4-70125 Bari, Italy

Umberto Tolve
Researcher, Tecnopolis CSATA Novus Ortus, Km 3 str. Prov.le Casamassima-70010 Valenzano-Bari, Italy

The present study investigates bubbly two-phase flow in a hydraulic jump using a flow visualization technique. Bubbly two-phase flow is encountered in many engineering problems; however, mainly because of experimental difficulties, little is known on the internal structure of these flows, although such knowledge is clearly essential to a thorough understanding of the mass transfer between the two component phases. In the past, some authors measured the distribution of void ratio in a hydraulic jump using hot-film anemometry. Nowadays this interesting technique may be improved using a flow visualization technique, which enables one to obtain the percentage of air across each vertical section of the jump. This is possible by evaluating the gray levels of the first principal axes of transformed images starting from RGB images. The experiments considered the phenomenon of air concentration in a hydraulic jump, which was studied and analyzed using image processing techniques, aimed at obtaining reliable quantitative measurements. To achieve this, the processing system was planned and tested at the hardware level and a procedure for managing the processing was set up. The calibration curve was obtained using the McCorquodale and Khalifa law (1983). The results permit the visualization of flow structures and the estimation of air concentration of the flow along all the jump and to show the position in which the air concentration reaches the maximum value versus time.

1 Introduction

Bubbly two-phase flow is encountered in many branches of engineering, but little information is available on the internal structure of these flows, although this knowledge is clearly essential to understanding the mass transfer processes. As known, a hydraulic jump is a transition from supercritical to subcritical flow in an open channel. This transition is characterized by the formation of a surface roller, which is responsible for visible air entrainment, intense turbulence, and dissipation of kinetic flow energy. These are the reasons why the hydraulic jump is used as an energy dissipator and is suited for aeration purposes.

The aim of the processing is to determine the relative measurements of air concentration in a hydraulic jump. Flow visualization techniques are among the most intuitive methods of analyzing flows. It differs from other experimental methods in that it renders certain properties of a flow field directly accessible to visual perception (Merzkirch, 1988; Yang, 1989).

Each physical process analysis is always improved if it can be observed. This is obvious for a fluid-mechanical process where a fluid is flowing in a channel or around a solid obstacle. By observing such a flow pattern, which can be stationary or variable with time, one gets information about the whole development of the flow. Flow visualization techniques provide information about the complete flow field under investigation without physically interfering with the fluid flow. In contrast, a single flow-measuring instrument, such as pressure or temperature probes, provides data for one point in the flow field only and may disturb the fluid flow to a certain degree.

There are several reasons for studying a hydraulic jump (for example, most stilling basins are designed on the basis of small scale model tests). The Froude number is generally used for scaling data. However, as McCorquodale and Khalifa (1983) suggested, the relative effects of viscosity, entrained air, and entrance boundary layers are significantly different in the model and prototype. The same authors showed that the size of the air bubbles and the detention time for air in the jump do not follow the Froude similarity. An adequate mathematical model of the internal flow in the hydraulic jump could be used to predict prototype cavitation potentials, and to simulate mixing and aeration characteristics of the jump. However, a mathematical model needs calibration using laboratory data. Rajaratnam (1976) studied the hydraulic jump as a wall jet; Rouse et al. (1958) studied the internal flow in the hydraulic jump by using an air model to simulate the expanding flow in the jump which enabled them to measure velocities and turbulence characteristics which are otherwise difficult to obtain in a two-phase flow such as a hydraulic jump.

For a hydraulic jump formed in a rectangular channel of constant width, a generally accepted view is that a high velocity jet flows along the bed, diffusing as a plane turbulent wall jet under a longitudinal adverse piezometric pressure gradient with an aerated recirculating roller on the top (Rajaratnam, 1976). Many experimental observations on the hydraulic jump (Long et al., 1991; Habib et al., 1994) look at the large scale eddy features of the roller. The hydraulic jump may also be interpreted as a mixing or shear layer with associated coherent structures (Hoyt and Sellin, 1989). All these studies show the kinematics of the roller and all features of the jump.

As shown by Habib et al. (1994), it is evident that the surface roller in the upper part of the hydraulic jump is made up of several vortices, with their sizes increasing from the toe to the downstream end. These vortices move downstream and grow by vortex pairing. The growth and downstream travel of these vortices cause a water spill which runs down the slope causing the upstream toe movement. This means that it is possible to define a pulsation frequency of the jump toe. The results obtained by Long et al. (1991) concerning the flow structure in the roller zone confirm the existence of periodic toe fluctuations of the hydraulic jump.

Habib et al. (1994) also analyzed the velocity components downstream of a hydraulic jump using a Laser Doppler Anemometer (LDA) system. The measurements were taken in terms of velocity profiles at some downstream sections of the jump. A Fourier analysis was performed for the fluctuating velocities. The amplitude spectrum showed higher values in the frequency bandwidth which included the pulsation frequency of the jump

Contributed by the Fluids Engineering Division for publication in the JOURNAL OF FLUIDS ENGINEERING. Manuscript received by the Fluids Engineering Division November 1, 1996; revised manuscript received August 25, 1997. Associate Technical Editor: O. C. Jones.

toe. The fluctuations of the jump influences the turbulent velocity components within the jump and the downstream reach of the roller zone.

All these analyses confirm that the features of a hydraulic jump are unsteady or oscillating and that the formulae which enable the calculation of air concentration, values of pressure beneath hydraulic jump stilling basins, etc. are valid on the average. A better comprehension of the jump cannot neglect these oscillating phenomena.

The values of C_0, defined as the depth averaged air fraction at a particular section along the jump, can be estimated using the law of McCorquodale and Khalifa (1983) employing Rajaratnam's experimental data:

$$C_0 = 0.066F_1^{1.35}\frac{x}{L_j}\ ;\ x < 8Y_1 \tag{1}$$

$$C_0 = 0.0115F_1^{1.35}\left(1 - \frac{x}{1.6}\right)\ ;\ x \geq 8Y_1 \tag{2}$$

where Y_1 is the initial depth of the hydraulic jump, L_j is the jump length, x is the horizontal distance from the mean jump toe position and F_1 is the inflow Froude number, defined as $V_1/(gY_1)^{0.5}$, where V_1 is the inflow mean velocity and g is the acceleration due to gravity.

On this subject, Resch et al. (1974) proposed to analyze the void ratio in a hydraulic jump using a hot-film anemometer with conical probes. They showed that the turbulence signals in a bubbly two-phase fluid is different than in homogeneous one. It means that it is possible to define a critical fluctuation threshold of the hot-film anemometer signal. For fluctuations greater than the threshold level, the signal was designated as originating in the gaseous phase and was interpreted as identifying an air bubble; fluctuations less than the threshold level were classified as representing turbulence of the liquid phase. The void ratio α was expressed in terms of exposure time, i.e.,

$$\alpha = \frac{T_G}{T_G + T_L} \tag{3}$$

in which T_G is the total time spent by the probe in the gaseous phase and T_L is the total time spent by the probe in the liquid phase. Of course this technique requires definition of an appropriate signal threshold to distinguish between phases. It is clear that these measurements are rather sensitive to changes in fluctuation threshold.

2 Experimental Setup

The experiments were carried out at the laboratory of the Water Engineering Department of Bari Polytechnic, in a 24.40-m-long channel made of plexiglas having a rectangular section 40 cm wide and 50 cm deep. Water was fed from an upstream reservoir with a maximum charge of 90 cm equipped with a stilling grid and a lateral weir which maintains a constant head upstream of a movable gate mounted at the upstream end of the flume. This gate was made of plexiglas and allows the passage of different discharges with different corresponding upstream flow depths.

Another movable gate was constructed at the downstream end of the flume to control the downstream flow depth and the position and type of the formed hydraulic jump. The flume was supplied through a steel pipe by a tank of the laboratory hydraulic circuit. The flow rate was measured by means of a triangular weir. The tailwater depth was measured by a hydrometer with a decimal vernier gauge (absolute error ± 0.0001 m). The detailed scheme of the flume is shown in Fig. 1.

The image acquisition system was comprised of a video camera with a $\frac{1}{2}$ in. Charge-Coupled Device (CCD) reproducing a resolution of 200,000 pixel. The camera was mounted in such a way to frame the frontal part of the hydraulic jump, and is linked to an analog storage system and is connected to a monitor. The video camera was positioned so as to focus closely on the hydraulic jump region. In order to get high-quality images much time was spent to improve the system layout so as to obtain the most correct intensity and quality of illumination reducing the reflections or shadows from other object.

Essentially, the image acquisition system also includes a live video image decoder and a frame-grabbing apparatus. The decoder is a Video Live (VL) EISA expansion Card which places live video images in a window on the monitor of a HP 9000/735 workstation. The expansion card is cabled between the graphics card and the monitor of the workstation. The VL cable intercepts the graphics card signal and routes it to the VL card where the image is overlaid; then, it returns the combined signal to the monitor cable, which carries it to the monitor. The con-

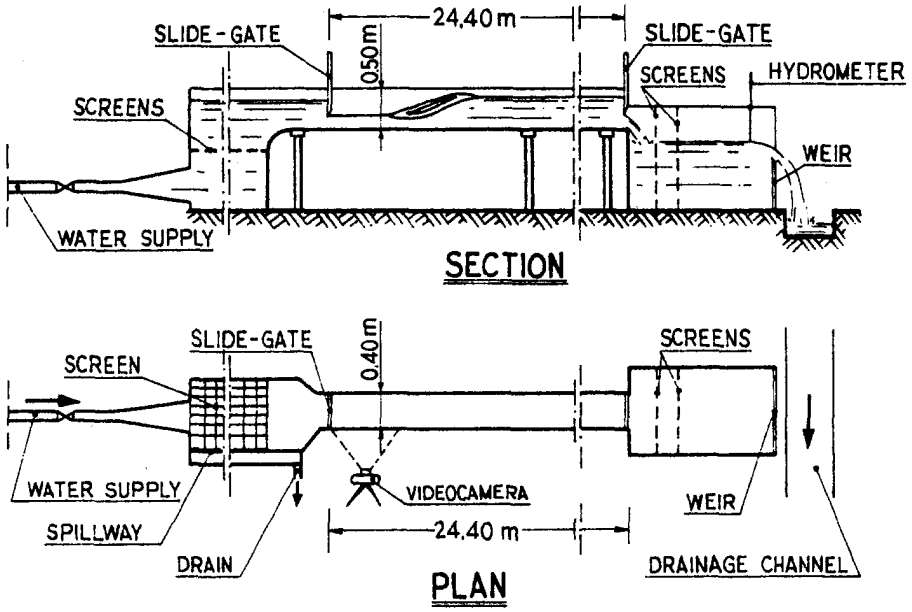

Fig. 1 Detailed scheme of the channel

Fig. 2(*a*) First principal component image of jump zone

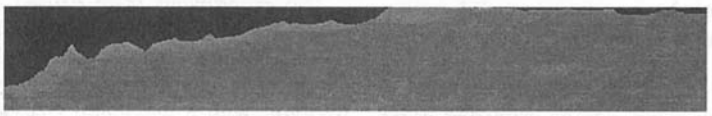

Fig. 2(*b*) Second principal component image of jump zone

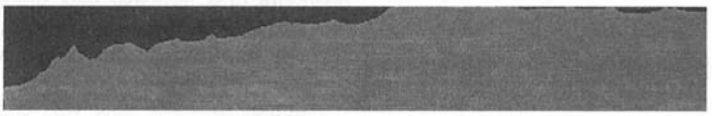

Fig. 2(*c*) Third principal component image of jump zone

tents of the VL frame buffer are mixed with the workstation graphics subsystem frame buffer on a pixel by pixel basis. The VL card accepts inputs from three types of video sources: S-Video, Composite and RGB. However, only one source may be active at given time. The card is capable of decoding NTSC, PAL, and SECAM video signals playing them at full speed (25 frame per seconds in PAL/SECAM or 30 in NTSC) in a monitor window (768 × 576 pixels in PAL/SECAM or 640 × 480 in NTSC), using 24-bit color.

For the aims of this study a PAL system VCR was used. The VL card and the coupled software running on the workstation utilized the X Video Extension protocol for X Window environment to provide a frame-grab utility. It allows one to capture and save either individual or a series of images, using 24-bit color. The professional features of the VCR were used to display a snapshot at a useful time interval (greater or equal to 0.04 sec). The images grabbed to memory, using the VL frame-grab utility, can be saved to a TIFF or JPEG industry standard graphics format file through the calls that the VL software makes to HP image integration library. According to the needs of this study, a TIFF format was used.

To evaluate the errors related to the use of the camera, some panels with uniform colors have been installed on the zone near to the hydraulic jump. The shooting referred to a zone which included the hydraulic jump and the panels as well. The analysis of RGB components carried out on each pixel of the panels zone of each frame showed that their values varied in time with a maximum value of rms equal to 21 (expressed in gray levels). The video camera was equipped with a polarizing filter to reduce reflection. Particular attention was given to avoid shadow zones. To this aim, we verified that the RGB components of the panels images were sufficiently uniform on the whole development. The best results were obtained using intense diffused light.

3 Image Processing Procedure

The processing was aimed at determining both the variation in time of air concentration and its mean value. Once the relevant frames for each jump to be analyzed were chosen, the images were processed by cutting the jump zone and transforming the RGB color bands in the principal axes.

As already stated, a single image was grabbed and each of the three eight bit converters transformed the signal relating to one of the three colors (red, green, and blue) into 256 levels of gray. This produced 16,777,216 levels of gray per pixel. The digital RGB information was processed in order to obtain the principal axes components.

It is well known that the quality of the features of an image is critical for a good analysis. If two features of an image are correlated, generally the second one does not give further information. The assumption that many features would provide the best solution is incorrect due to the fact that many features could be correlated. Particularly, the correlation of the RGB data of an image can be studied with statistical methods (Buchlin et al., 1988; Gonzales and Wintz, 1987; Jahne, 1991; Jain, 1989).

The important quantity is the cross covariance of the gray levels m_k and m_l of two bands (the kth and the lth respectively) of an image

$$C_{kl} = \overline{(m_k - \overline{m_k})(m_l - \overline{m_l})} \tag{4}$$

The cross covariance is zero if both bounds are uncorrelated. With p color bands it is possible to form a symmetric matrix with coefficients C_{kl}, i.e., the covariance matrix

$$C = \begin{cases} C_{11} & C_{12} & \cdots & C_{1p} \\ C_{12} & C_{22} & \cdots & C_{2p} \\ \cdots & & & \\ C_{1p} & C_{2p} & \cdots & C_{pp} \end{cases} \tag{5}$$

The diagonal elements of the covariance matrix contain the variances of the p bands (three bands, i.e., RGB, in this study) while the off-diagonal elements constitute the cross covariances. As in every symmetric matrix, the covariance matrix can be diagonalized. This procedure is called the principal axes transform. The principal component analysis is often used as a method of data compression. It allows redundant bands to be compacted into few ones. The data of principal component bands are uncorrelated, independent, and often more interpretable than the source data. The principal components are linear combinations of the RGB components and are defined by the eigenvectors of the RGB covariance matrix. The corresponding eigenvalues are the variances. The best new bands show the largest variances; bands with low variances are not of much help in analyzing the image and can be omitted.

Figures 2(*a*), 2(*b*), and 2(*c*) show, respectively, the first, the second, and the third typical principal component images of cut jump zone of the RGB image. The eigenvalues of the corresponding RGB covariance matrix are 3497.95 (98.97%), 26.09 (0.74%) and 10.37 (0.29%), respectively. These magnitudes are nearly equal for each frame used for concentration analyses. It is clear that much information is controlled by the first principal component image, which was used in what follows.

Figures 3(*a*), 3(*b*), and 3(*c*) show the histograms of the principal component images of Figs. 2(*a*), 2(*b*), and 2(*c*), respectively. These histograms confirm that only the first principal component can be used in order to analyze the air concentration in a hydraulic jump. The histograms of the second and third principal component images are typical of a Gaussian noise, confirmed by the Kolmogorov fitting test.

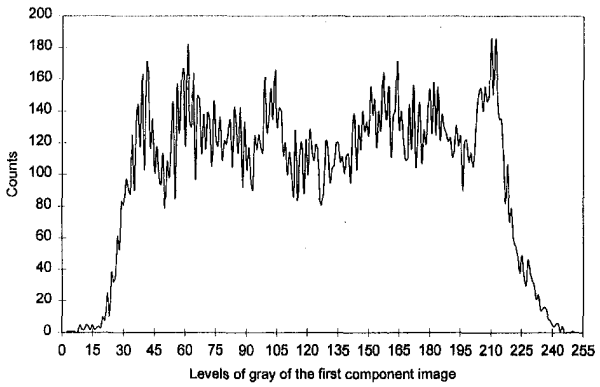

Fig. 3(*a*) Histogram of the image of Fig. 2(*a*)

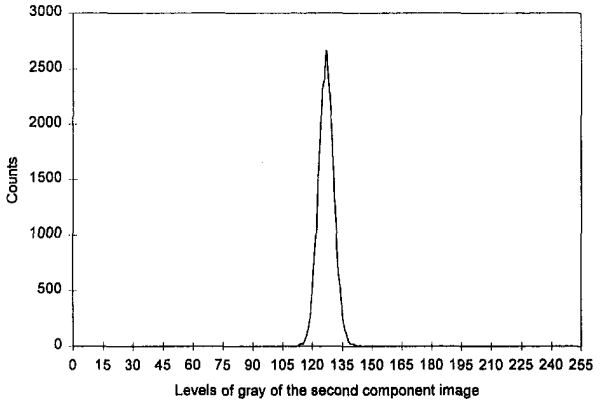

Fig. 3(*b*) Histogram of the image of Fig. 2(*b*)

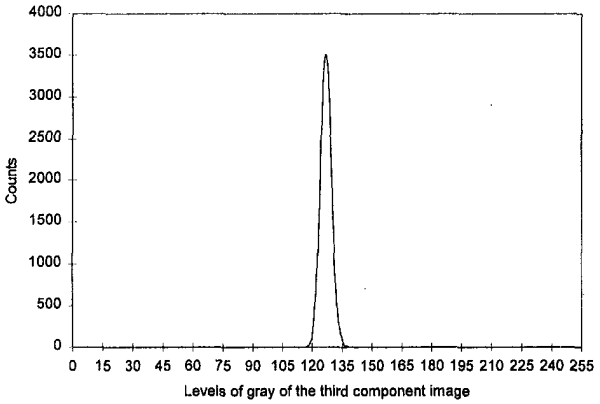

Fig. 3(*c*) Histogram of the image of Fig. 2(*c*)

Table 1 The hydraulic jumps of this study

No	Y_1 [m]	L_j [m]	Re	F_1
1	0.0202	1.0	58000	6.45
2	0.0185	1.0	57769	7.33
3	0.0201	1.0	57301	6.42

4 Test Results

The tests were carried out for three configurations of the hydraulic jump, whose features are reported in Table 1, where $\mathrm{Re} = V_1 Y_1/\nu$ is the Reynolds number and ν is the water kinematic viscosity. All these jumps are characterized by undeveloped inflow.

For the sake of brevity, only the results of jump no. 3 will be reported; this jump is the same one analyzed by Habib et al. (1994). The period of its toe fluctuations (as described in Section 1) was about 1.5 s. During this period, ten snapshots were chosen. The jump region of each image was cut and the principal axes transform procedure was applied. The eigenvectors of RGB covariance matrix were equal for all the cut images.

This procedure gave the first principal component images for which the 8-bit gray levels represent a scale of air concentration. The 256 gray levels of the first principal component images were divided into six regularly spaced intervals. Each interval was characterized by the mean value, used in a color map of gray scale. The results are reported in Figs. $4(a)-4(l)$, where time is expressed in minutes, seconds and hundredths of second from the shooting start. These pictures show, in a color map, the qualitative evolution of air concentration of jump no. 3 during the time period of interest (the lighter the color, the greater the concentration).

From these figures it is possible to see the variation in time of the roller region in which the maximum air concentration is available. An iron frame which supports the vertical channel wall is also visible. In the present study the wall support was not eliminated to highlight that possible discontinuities are absolutely visible. In Figs. $4(a)-4(l)$ a pattern of growing, whirling, pairing and intersecting vortex can be observed.

It is interesting to analyze the roller dynamics. In some pictures two regions are clearly visible with the greatest air concentration. This occurs when the largest vortex breaks down causing the water to spill. In other pictures only one region with the greatest air concentration is present, as evidence of the mutual influence of two neighbouring vortices which merge into a larger one. During this period, when the toe of the hydraulic jump was at its most upstream location, the surface roller of the jump appeared to be made up of several vortices with only the single, largest vortex located near the air-water interface. Then, two neighbouring vortices, because of their rotation and mutual influence, tended to get deformed and eventually merge into a larger one. The effect of the pairing was a remarkable shifting of the location of the jump toe. At this moment the front portion of the jump surface was much steeper and the largest formed vortex appeared to break down causing the water to spill producing two regions with great air concentration. The spilling water flows downstream on the steep water surface causing the toe to drift back in the upstream direction.

The variation in time of the air concentration is in tune with the toe fluctuations of the hydraulic jump (Habib et al., 1994), the fluctuating pressures beneath jump stilling basins (Gioia et al., 1979; Di Santo et al., 1994), and the fluctuating velocities just downstream of the jump, where a transition region may be recognized (Razavan, 1967 and 1971).

Figure 5 shows the depth averaged air concentrations of jump no. 3 versus x/L_j. They are evaluated using the depth-means of gray levels of the first principal component images showed in Figs. $4(a)$ to $4(l)$. Equations (1) and (2), whose diagram is plotted in Fig. 6, may be used for calibration. Of course, Eqs. (1) and (2) represent a fitting of the experimental data, with a discontinuity at x equal to $8Y_1$; it means that these equations are a simplification of the phenomenon. For jump no. 3 the maximum value of C_0 is 0.13 and it should correspond to the maximum gray level value of Fig. 5 (i.e. 200).

If the two lines of Eqs. (1) and (2) are blended using a curve, the maximum value of C_0 becomes smaller than 0.13 and occurs at x/L_j between 0.2 and 0.3 in accordance with the results of Fig. 5.

5 Conclusions

The technological evolution in the flow visualization techniques, together with the analogous evolution of electronic components for processing video signals, provide increasingly powerful tools at low costs. The present paper reports a methodology to analyze the air concentration in a hydraulic jump through image processing. The investigation undertaken leads to the following conclusions:

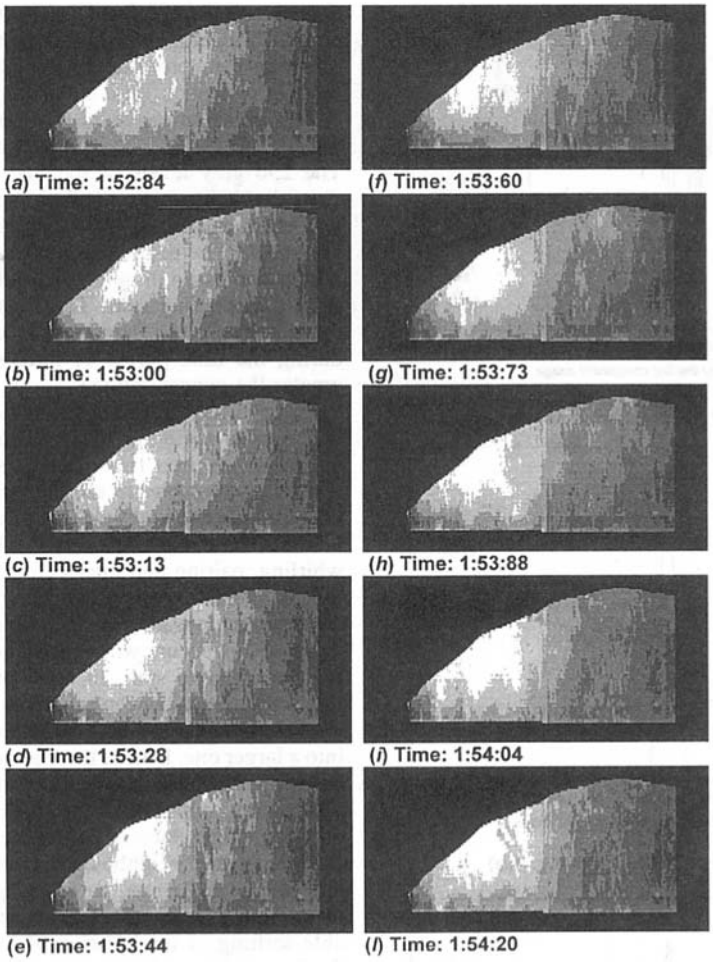

Fig. 4 Jump no. 3 of Table 1 (distorted length scale). (*a*) Time: 1:52:84; (*b*) Time: 1:53:00; (*c*) Time: 1:53:13; (*d*) Time: 1:53:28; (*e*) Time: 1:53:44; (*f*) Time: 1:53:60; (*g*) Time: 1:53:73; (*h*) Time: 1:53:88; (*i*) Time: 1:54:04; (*l*) Time: 1:54:20

- the technique proposed allows the evaluation of air concentration in a hydraulic jump without interfering with the flow;
- unlike the other techniques existing in literature, it is possible to evaluate the concentration in an entire region of the flow;
- the images obtained permit one to visualize the coherent structures of turbulence. Some jump pictures show the existence of two regions with the greatest air concentration when the largest vortex breaks down causing the water to spill; in other figures only one region with a great air concentration is present because of merging of two neighbouring vortices into a larger one.

Acknowledgments

The authors are grateful to Prof. Antonio F. Petrillo, Director of the Water Engineering Department of Bari Polytechnic, and Dr. Luigi Borriello and Dr. Francesco P. Murgolo, of Tecnopolis CSATA Novus Ortus, for their invaluable support.

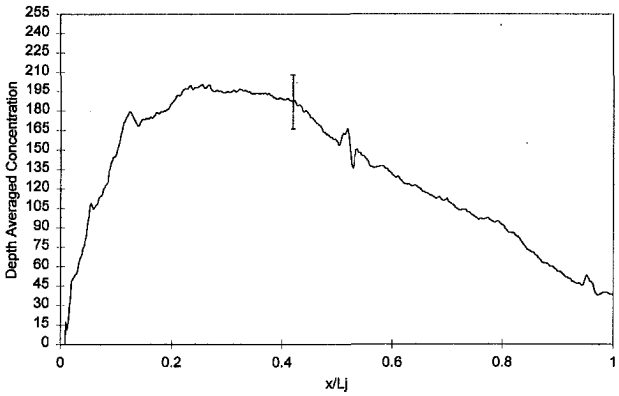

Fig. 5 Depth averaged air concentration of jump no. 3 in gray levels

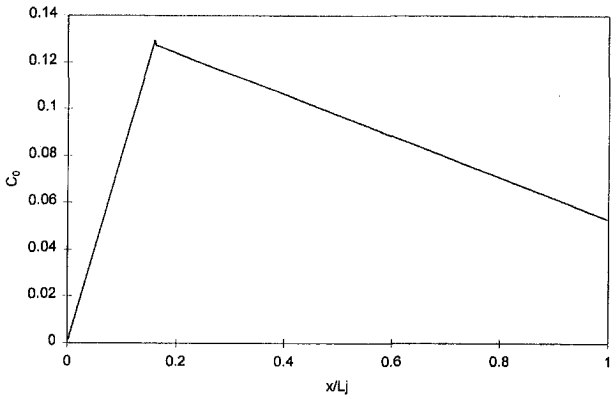

Fig. 6 Diagram of Eqs. (1) and (2) for jump no. 3

References

Buchlin J. M., Moraitis C. S., and Riethmuller M. L., 1988, *Digital Image Processing in Fluid Dynamics—Discharge and Velocity Measurements,* Muller Ed., Balkema Rotterdam.

Di Santo A., Petrillo A., and Piccinni A. F., 1994, "Lining Stability in Hydraulic Jump Stilling Basins," *Modelling Testing & Monitoring for Hydro Powerplants,* organized by The International Journal on Hydropower & Dams, Budapest, Hungary, pp. 319–329.

Gioia G., Petrillo A., and Vitale A., 1979, "Indagine sperimentale sulle sollecitazioni al fondo del risalto idraulico," *Idrotecnica,* No. 5, pp. 183–194.

Gonzales R. C., and Wintz P., 1987, *Digital Image Processing,* Addison-Wesley, Reading Ma.

Habib E., Mossa M., and Petrillo A., 1994, "Scour Downstream of Hydraulic Jump," *Modelling Testing & Monitoring for Hydro Powerplants,* organized by The International Journal of Hydropower & Dams, Budapest, Hungary, pp. 591–602.

Hoyt J. W., and Sellin R. H. J., 1989, "Hydraulic Jump as 'Mixing Layer'," ASCE, *Journal of Hydraulic Engineering,* Vol. 115, No. 12, pp. 1607–1614.

Jahne B., 1991, *Digital Image Processing—Concepts, Algorithms, and Scientific Applications,* Springer-Verlag, USA.

Jain A. K., 1989, *Fundamentals of Digital Image Processing,* Prentice-Hall International Editions, USA.

Long D., Rajaratnam N., Steffler P. M., and Smy P. R., 1991, "Structure of Flow in Hydraulic Jumps," *Journal of Hydraulic Research, IAHR,* Vol. 29, No. 2, pp. 207–218.

McCorquodale J. A., and Khalifa A., 1983, "Internal Flow in Hydraulic Jumps," ASCE, *Journal of the Hydraulics Division,* Vol. 109, No. 5, pp. 684–701.

Merzkirch W., 1988, *Methods of Flow Visualization—Discharge and Velocity Measurements,* Muller Ed., Balkema, Rotterdam.

Rajaratnam N., 1965, "The Hydraulic Jump as a Wall Jet," *ASCE, Journal of the Hydraulics Division,* Vol. 91, No. HY5, pp. 107–132.

Rajaratnam N., 1976, *Turbulents Jets,* Elsevier Scientific Co., New York, N.Y..

Rajaratnam N., and Subramanya K., 1968, "Profile of the Hydraulic Jump," ASCE, *Journal of the Hydraulics Division,* Vol. 94, No. HY3, pp. 663–673.

Razavan E., 1967, "Resultats de l'etude du movement macroturbulent en aval du ressaut hydraulique," 12th Congress of IAHR, Fort Collins, Vol. 2, paper B4.

Razavan E., 1971, "L'influence de la haute turbulence sur l'entrainement des alluvions," 14th Congress of IAHR, Paris, Vol. 3, paper C3.

Resch F. J., Leutheusser H. J., and Alemu S., 1974, "Bubbly two-phase flow in hydraulic jump," ASCE, *Journal of the Hydraulics Division,* Vol. 100, No. HY1, pp. 137–149.

Rouse H., Siao T. T., and Nagaratnam R., 1958, "Turbulence characteristics of the hydraulic jump," ASCE, *Journal of the Hydraulics Division,* Vol. 84, No. HY1, Proc. Paper 1528, pp. 1528-1 to 1528-30.

Yang W., 1989, *Handbook of Flow Visualization,* Taylor & Francis, Hemisphere Publishing Corporation.

One-Dimensional Bubbly Cavitating Flows Through a Converging-Diverging Nozzle

Yi-Chun Wang
Assistant Professor,
Department of Mechanical Engineering,
National Cheng Kung University,
Tainan 701, Taiwan

C. E. Brennen
Professor,
Mail Code: 104-44
Department of Mechanical Engineering
California Institute of Technology,
Pasadena, CA 91125

A nonbarotropic continuum bubbly mixture model is used to study the one-dimensional cavitating flow through a converging-diverging nozzle. The nonlinear dynamics of the cavitation bubbles are modeled by the Rayleigh-Plesset equation. Analytical results show that the bubble/bubble interaction through the hydrodynamics of the surrounding liquid has important effects on this confined flow field. One clear interaction effect is the Bernoulli effect caused by the growing and collapsing bubbles in the nozzle. It is found that the characteristics of the flow change dramatically even when the upstream void fraction is very small. Two different flow regimes are found from the steady state solutions and are termed: quasi-steady and quasi-unsteady. The former is characterized by large spatial fluctuations downstream of the throat which are induced by the pulsations of the cavitation bubbles. The quasi-unsteady solutions correspond to flashing flow. Bifurcation occurs as the flow transitions from one regime to the other. An analytical expression for the critical bubble size at the bifurcation is obtained. Physical reasons for this quasi-static instability are also discussed.

Introduction

One-dimensional bubbly liquid flows in ducts and nozzles represent one of the simplest confined gas-liquid flows. This is an important problem by itself in many engineering applications, but has not, previously, been studied in the context of cavitation bubble/bubble interactions. The nozzle flow is also a useful model of any cavitating flow in which a low pressure region causes the flow to accelerate, for example, the cavitating flow on the suction surface of a hydrofoil. Therefore, study of the one-dimensional accelerating flow with bubble cavitation effects may have value in building up fully nonlinear solutions for practical three-dimensional flows.

In some bubbly flows it is possible to establish a barotropic relation, $p = f(\rho)$, which assumes that the fluid pressure is the function of fluid density only. This implies that all effects caused by bubble content are disregarded except for the compressibility and that the bubbly mixture can be regarded effectively as a single-phase compressible fluid. Tangren et al. (1949) first addressed the barotropic nozzle flow of a two-phase mixture. A summary of this subject can be found, for example, in Brennen (1995). In many practical flows, however, the barotropic criterion is not met. In the present context, the hydrodynamic effects of the flow acceleration cause the bubbles to cavitate and then the flow deceleration makes them collapse. Under these circumstances, the fluid is not barotropic and, as we shall see, the growth and collapse of cavitating bubbles can dramatically change or destabilize the flow.

The flow model used here is a nonlinear continuum bubbly mixture model coupled with the Rayleigh-Plesset equation for the bubble dynamics. This model was first proposed by van Wijngaarden (1968, 1972) and has been used for studying steady and transient shock wave propagation in bubbly liquids without the acceleration of the mean flow (see, for example, Noordzij and van Wijngaarden, 1974; Kameda and Matsumoto, 1995). Ishii et al. (1993) proposed a bubbly flow model and used it to study steady flows through a converging-diverging nozzle. However, by assuming that the gas pressure inside the bubbles is equal to the ambient fluid pressure, they neglected the bubble radial dynamics (as represented by the Rayleigh-Plesset equation) which are dominant mechanisms in a cavitating flow. Morioka and Matsui (1980) and Morioka and Toma (1984) investigated the acoustic dispersion relation for a flowing bubbly liquid using van Wijngaarden's model and Toma and Morioka (1986) examined characteristics of different acoustic modes in flowing bubbly liquid using the same model. Toma et al. (1988) conducted experiments with bubbly liquid flows in a converging-diverging nozzle and recorded the temporal fluctuation characteristics of this kind of flow. However, fully nonlinear solutions of the accelerating bubbly flows with bubble cavitation effects have not, previously, been obtained. The purpose of the present work is to examine what effects bubble dynamics can have on the flow structure.

Basic Equations

Referring to Fig. 1, consider a one-dimensional converging-diverging nozzle with length L and cross-sectional area $A(x)$. The flow direction is in positive x direction and the inlet of the nozzle is located at $x = 0$. The variables in all the figures and equations are non-dimensionalized using the upstream conditions (denoted by subscript s) and the liquid density, ρ_L^*. All quantities with superscript * represent dimensional values. For example, $\eta = \eta^* R_s^{*3}$ is the non-dimensional bubble population per unit liquid volume, where R_s^* is upstream bubble radius.

The continuity and momentum equations of the bubbly flow (references d'Agostino and Brennen, 1983, 1989; Wang, 1996) have the forms

$$\frac{\partial}{\partial t}[(1-\alpha)A] + \frac{\partial}{\partial x}[(1-\alpha)uA] = 0 \tag{1}$$

$$\frac{\partial u}{\partial t} + u\frac{\partial u}{\partial x} = -\frac{1}{2(1-\alpha)}\frac{\partial C_P}{\partial x} \tag{2}$$

where $\alpha(x, t)$, the bubble void fraction, is related to the bubble radius, $R(x, t)$, by $\alpha(x, t) = 4/3\pi\eta R^3(x, t)/[1 + 4/3\pi\eta R^3(x, t)]$, $u(x, t)$ is the fluid velocity, $C_P(x, t) = (p^*(x, t) -$

Contributed by the Fluids Engineering Division for publication in the JOURNAL OF FLUIDS ENGINEERING. Manuscript received by the Fluids Engineering Division October 28, 1996; revised manuscript received May 6, 1997. Associate Technical Editor: J. Katz.

$p_s^*)/1/2\rho_L^* u_s^{*2}$ is the fluid pressure coefficient, $p^*(x, t)$ is the fluid pressure, p_s^* is the upstream fluid pressure, and u_s^* is the upstream fluid velocity. The liquid has been assumed to be incompressible and the relative motion between the phases has been ignored. Friction between the fluid and the duct wall is also neglected. It is assumed that the upstream bubble population per unit volume of liquid is piecewise uniform and that there is no coalescence or break-up of bubbles in the flow. Since relative motion and the mass of liquid vaporized or condensed are neglected, it follows that η remains both constant and piecewise uniform in the flow. The nondimensional fluid density has been approximated by $\rho \approx (1 - \alpha)$ in (1) and (2) since the liquid density is very much larger than the vapor density. The interactions of the bubbles with the flow are modeled by the Rayleigh-Plesset equation (Knapp et al., 1970; Plesset and Prosperetti, 1977) which connects the local fluid pressure coefficient, C_P, to the bubble radius, R:

$$R\frac{D^2R}{Dt^2} + \frac{3}{2}\left(\frac{DR}{Dt}\right)^2 + \frac{\sigma}{2}(1 - R^{-3k}) + \frac{4}{\mathrm{Re}}\frac{1}{R}\frac{DR}{Dt} + \frac{2}{\mathrm{We}}(R^{-1} - R^{-3k}) + \frac{1}{2}C_P = 0 \quad (3)$$

where $D/Dt = \partial/\partial t + u\partial/\partial x$ is the Lagrangian derivative, $\sigma = (p_s^* - p_V^*)/1/2\rho_L^* u_s^{*2}$ is the cavitation number and p_V^* is the partial pressure of vapor inside the bubble. The partial pressure of noncondensable gas (it is assumed the mass of gas inside each bubble is constant) does not appear explicitly in (3) because the upstream equilibrium condition has been employed to eliminate this quantity. It has also been assumed that the noncondensable gas inside the bubbles behaves polytropically with an index k. If $k = 1$, a constant bubble temperature is implied and $k = \gamma$, the ratio of specific heats of the gas, would model adiabatic behavior. We define a Reynolds number, $\mathrm{Re} = \rho_L^* u_s^* R_s^*/\mu_E^*$ where μ_E^* is the effective viscosity of liquid which incorporates the various bubble damping mechanisms, namely acoustic, thermal, and viscous damping, described by Chapman and Plesset (1971). We also define a Weber number, $\mathrm{We} = \rho_L^* u_s^{*2} R_s^*/S^*$ where S^* is the surface tension of the liquid.

Equations (1), (2), and (3) represent a simple model of one-dimensional flowing bubbly fluid with nonlinear bubble dynamics. Previous investigations have examined the dispersion and stability properties of this model in the linear regimes (see, for example, Biesheuvel and van Wijngaarden, 1984; Morioka and Matsui, 1980; Morioka and Toma, 1984; Toma and Morioka, 1986; Toma et al., 1988). These results helped to identify the propagation modes and the dispersion characteristics of the acoustic waves in a flowing bubbly liquid. However, if the flow is accelerating, simple linearization of the equations of motion is impossible since the mean flow quantities are changing rapidly with both space and time. Analyses of the dynamics of this model then become significantly more complicated and new phenomena may be manifest due to the coupling of flow acceleration and bubble dynamics.

Steady-State Solutions

Only steady flows are considered in the present work. It is assumed that (1), (2), and (3) have steady-state solutions for a constant mass flow rate with upstream conditions denoted by p_s^*, u_s^*, and $\rho_s^* \approx \rho_L^*(1 - \alpha_s) = \rho_L^*/(1 + 4/3\pi\eta^* R_s^{*3})$ where α_s is the upstream void fraction. After dropping all the partial time derivative terms, the governing equations become a system of ordinary differential equations with one independent variable, x:

$$(1 - \alpha)uA = (1 - \alpha_s) = \text{constant} \quad (4)$$

$$u\frac{du}{dx} = -\frac{1}{2(1 - \alpha)}\frac{dC_P}{dx} \quad (5)$$

$$R\left(u^2\frac{d^2R}{dx^2} + u\frac{du}{dx}\frac{dR}{dx}\right) + \frac{3u^2}{2}\left(\frac{dR}{dx}\right)^2 + \frac{4}{\mathrm{Re}}\frac{u}{R}\frac{dR}{dx} + \frac{2}{\mathrm{We}}\left(\frac{1}{R} - \frac{1}{R^{3k}}\right) + \frac{\sigma}{2}\left(1 - \frac{1}{R^{3k}}\right) + \frac{1}{2}C_P = 0 \quad (6)$$

The initial or upstream conditions are given by:

$$R(x = 0) = 1, \quad u(x = 0) = 1, \quad C_P(x = 0) = 0 \quad (7)$$

We choose to examine a simple nozzle, $A(x)$, such that

$$A(x) = \begin{cases} \left\{1 - \frac{1}{2}C_{PMIN}\left[1 - \cos\left(\frac{2\pi x}{L}\right)\right]\right\}^{-1/2}; & 0 \le x \le L \\ 1; \quad x < 0 \text{ and } x > L \end{cases} \quad (8)$$

Nomenclature

A = dimensionless cross-sectional area of nozzle, A^*/A_s^*
A^* = cross-sectional area of nozzle
A_s^* = upstream cross-sectional area of nozzle
C_P = fluid pressure coefficient, $(p^* - p_s^*)/1/2\rho_L^* u_s^{*2}$
C_{Pc} = critical pressure coefficient at which flashing occurs
$C_{P\,MIN}$ = minimum pressure coefficient at throat for pure liquid nozzle flow
L = dimensionless length of the nozzle, L^*/R_s^*
L^* = length of the nozzle
R = dimensionless bubble radius, R^*/R_s^*
R_c = dimensionless critical bubble radius at which flashing occurs
R_s^* = upstream bubble radius
Re = Reynolds number, $\rho_L^* u_s^* R_s^*/\mu_E^*$
S^* = surface tension of the liquid
We = Weber number, $\rho_L^* u_s^{*2} R_s^*/S^*$
k = polytropic index for the gas inside the bubbles
p^* = fluid pressure
p_s^* = upstream pressure
p_V^* = vapor pressure
t = dimensionless time, $t^* u_s^*/R_s^*$
t^* = time
u = dimensionless fluid velocity, u^*/u_s^*
u^* = fluid velocity
u_s^* = upstream fluid velocity
x = dimensionless Eulerian coordinate, x^*/R_s^*
x^* = Eulerian coordinate
α = void fraction of the bubbly fluid
α_b = upstream void fraction at which flashing occurs
α_s = upstream void fraction
η = dimensionless bubble population per unit liquid volume, $\eta^* R_s^{*3}$
η^* = bubble population per unit liquid volume
γ = ratio of specific heats of the gas inside the bubbles
μ_E^* = effective dynamic viscosity of the liquid
ρ = dimensionless fluid density
ρ_L^* = density of the liquid
ρ_s^* = upstream fluid density
σ = cavitation number, $(p_s^* - p_V^*)/1/2\rho_L^* u_s^{*2}$

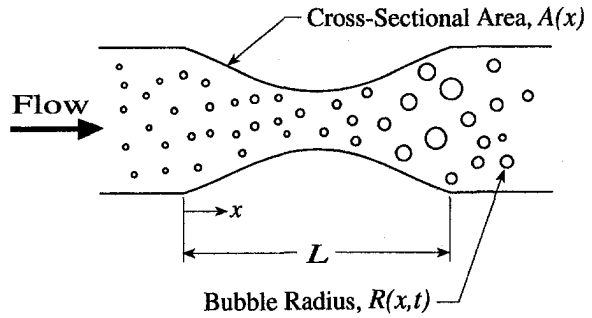

Fig. 1 Notation for bubbly liquid flow in a converging-diverging nozzle

This profile will produce a simple sinusoidal pressure distribution in the case of incompressible flow with the minimum pressure coefficient, C_{PMIN}, located at the nozzle throat, $x = L/2$. The value of $-C_{PMIN}$ relative to the cavitation number, σ, represents the intensity of tension in the flow. If $-C_{PMIN}$ is greater than the cavitation number, σ, the minimum fluid pressure experienced by the individual bubbles will be lower than vapor pressure and the bubbles will cavitate.

Results and Discussion

A fourth-order Runge-Kutta scheme was used to integrate Eqs. (5) and (6). The following flow conditions were chosen to illustrate the computational results. A bubbly fluid, composed of air bubbles ($k = 1.4$) of upstream radius $R_s^* = 100$ μm in water at 20°C ($\rho_L^* = 1000$ kg/m^3, $\mu_L^* = 0.001$ Ns/m^2, $S^* = 0.073$ N/m) flows with $u_s^* = 10$ m/s through a nozzle with profile given by Eq. (8); the nondimensional length of the nozzle is $L = 500$. The minimum pressure coefficient, C_{PMIN}, for the pure liquid flow is chosen as -1. The upstream cavitation number, σ, is set at 0.8, smaller than $-C_{PMIN}$ so that cavitation will occur. The Reynolds number, Re, based on the upstream fluid velocity, the upstream bubble radius, the liquid density, and the effective liquid viscosity is taken as 33. An effective liquid viscosity, $\mu_E^* = 0.03$ Ns/m^2, is used in place of actual liquid viscosity to incorporate the various bubble damping mechanisms (Chapman and Plesset, 1971). Five different upstream void fractions, α_s, of the order of 10^{-6} are used in the computation and the results are shown in Figs. 2 to 5.

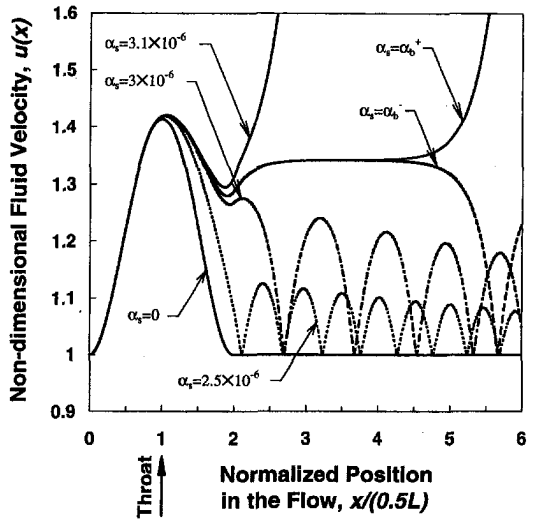

Fig. 2 The nondimensional fluid velocity distribution as a function of the normalized position in the flow for five different upstream void fractions. Labels of $\alpha_s = \alpha_b^-$ and $\alpha_s = \alpha_b^+$ correspond to α_s just below and above the critical value $\alpha_b \approx 3.045 \times 10^{-6}$. The dimensionless length of the nozzle, L, is 500 with the throat located at $0.5L$. Other parameters are $\sigma = 0.8$, $C_{PMIN} = -1.0$, Re = 33, and We = 137.

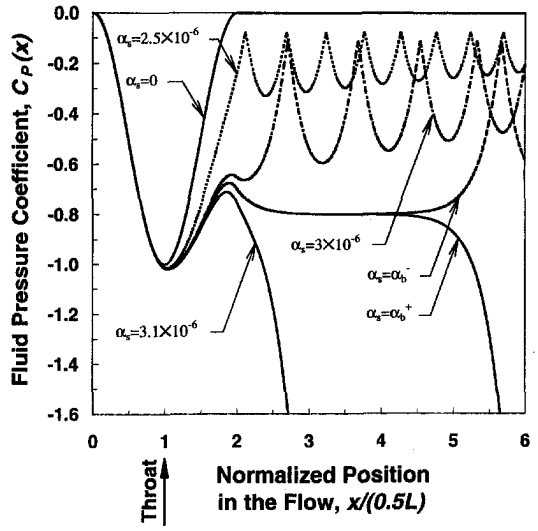

Fig. 3 The fluid pressure coefficient corresponding to Fig. 2

Figure 2 illustrates the fluid velocity. The case of $\alpha_s = 0$ corresponds to the incompressible pure liquid flow. It is notable that even for an upstream void fraction as small as 2.5×10^{-6}, the characteristics of the flow are radically changed from the case without bubbles. Radial pulsation of bubbles results in the downstream fluctuations of the flow. The amplitude of the velocity fluctuation downstream of the nozzle is about ten percent of that of the incompressible flow in this case. As α_s increases further, the amplitude as well as the wavelength of the fluctuations increase. However, the velocity does eventually return to the upstream value due to the bubble damping. In other words, the flow is still "quasi-statically stable." However, as α_s increases to a critical value, α_b (about 3.045×10^{-6} in the present calculation), a bifurcation occurs. The velocity increases dramatically and the flow becomes "quasi-statically unstable." The physical picture of this instability is quite simple: Growth of the cavitation bubbles increases the fluid velocity according to the mass conservation of the flow. The increase of the velocity then causes the fluid pressure to decrease due to the Bernoulli effect. The decrease of the pressure is fed back

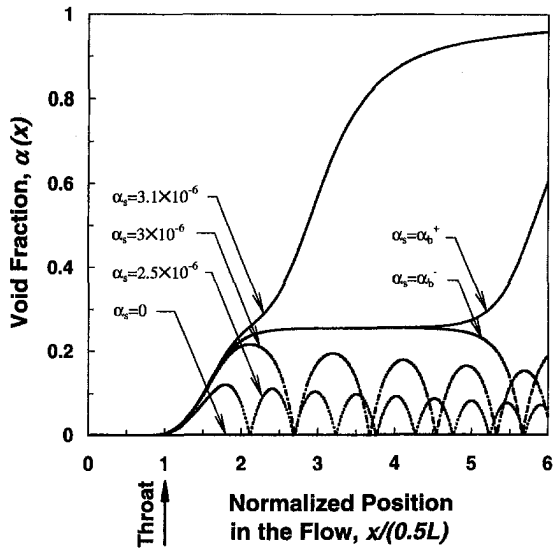

Fig. 4 The void fraction distribution corresponding to Fig. 2

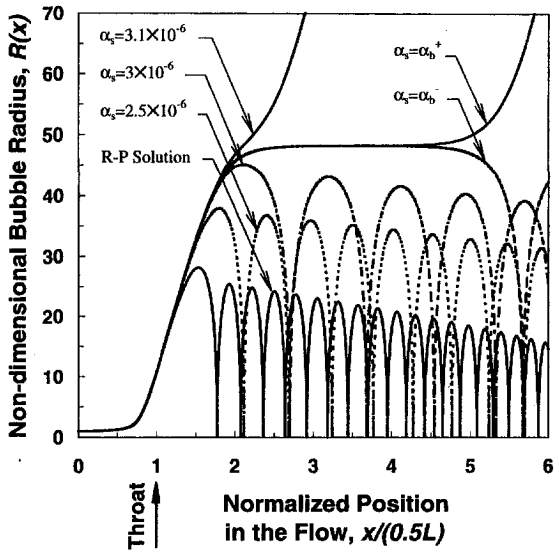

Fig. 5 The nondimensional bubble radius distribution corresponding to Fig. 2. R-P solution represents the solution from the Rayleigh-Plesset equation.

to the Rayleigh-Plesset dynamics and results in more bubble growth.

The corresponding variations in the fluid pressure coefficient are shown in figure 3. In addition to the two different flow regimes, another important feature in the quasi-statically stable flow is the typical frequency associated with the downstream periodicity. This "ringing" will result in acoustic radiation at frequencies corresponding to this wavelength. How this ring frequency relates to the upstream flow conditions remains to be studied. Furthermore, it should be noticed that there is a pressure loss downstream; the fluid pressure does not return to the upstream value except in the case of the pure liquid flow. The only damping mechanism in the present model is due to the bubble damping. Since the viscosity of wall and slip motion between bubbles and liquid are all neglected, the pressure loss is caused by the radial motion of bubbles and represents the "cavitation loss."

Figure 4 illustrates the void fraction distribution in the flow. When the flow becomes quasi-statically unstable, the bubble void fraction, $\alpha(x)$, quickly approaches unity. This means that the flow is flashing to vapor. Moreover we should emphasize that when α becomes large, our model equations, which are limited to flows with small void fraction (for the limitation of void fraction in the present model, see d'Agostino and Brennen, 1989), lose their validity.

Figure 5 indicates the non-dimensional bubble radius distribution in the flow. Due to time lag during the bubble growth phase, bubbles reach the maximum size after passing the nozzle throat. With increase in the upstream void fraction, the maximum size of the bubbles increases and is shifted further downstream. The bubbles grow without bound after reaching the critical radius, R_c, at which flashing begins. Note that R_c is dependent on the cavitation number and the upstream void fraction. An analytical expression for R_c can be found as follows. From figure 5 we note that dR/dx and d^2R/dx^2 both vanish at $R = R_c$. Substitution of these conditions into (6) gives

$$\frac{2}{\mathrm{We}}(R_c^{-1} - R_c^{-3k}) + \frac{\sigma}{2}(1 - R_c^{-3k}) + \frac{1}{2}C_{Pc} = 0 \qquad (9)$$

Here C_{Pc} can be found by integrating (4) and (5) by putting $A = 1$ (assuming that the flow exits the nozzle into a length of constant area duct downstream of the nozzle):

$$C_{Pc} = -\frac{24\pi\eta R_c^3}{(3 + 4\pi\eta)^2}\left(1 - \frac{1}{R_c^3}\right) \qquad (10)$$

Since $R_c \gg 1$, all the higher order terms ($1/R_c^{3k}$ in (9) and $1/R_c^3$ in (10)) can be neglected. After combining these two equations, one can write

$$R_c^4 - \frac{\sigma}{2\alpha_b(1 - \alpha_b)}R_c - \frac{2}{\alpha_b(1 - \alpha_b)\ \mathrm{We}} = 0 \qquad (11)$$

in which $4/3\pi\eta = \alpha_b/(1 - \alpha_b)$ has been used. The third term in (11) can be neglected because, in addition to $R_c \gg 1$, practical values for 2/We are about an order of magnitude less than the values of $\sigma/2$ in the second term. Thus, finally we have:

$$R_c = \left[\frac{\sigma}{2\alpha_b(1 - \alpha_b)}\right]^{1/3} \approx \left[\frac{\sigma}{2\alpha_b}\right]^{1/3} \qquad (12)$$

If $R > R_c$, the flow becomes quasi-statically unstable and flashes. In the cases presented here $(\sigma/2\alpha_b)^{1/3} \approx 51$. With known R_c, the expressions for the critical pressure coefficient can be obtained from (10):

$$C_{Pc} = 2\alpha_b(1 - \alpha_b) - \sigma \approx -\sigma \qquad (13)$$

Concluding Remarks

Steady cavitating bubbly flows through a converging-diverging nozzle have been examined in the present paper. It was found that the nonlinear bubble dynamics coupled with the equations of motion of the bubbly fluid strongly affect the structure of the flow even for very small bubble populations. Two different flow regimes, distinguished by the parameter $R_c = (\sigma/2\alpha_b)^{1/3}$, (where σ is the cavitation number of the flow and α_b is the upstream void fraction at which the bifurcation occurs) are revealed in the steady state solutions. The flow becomes quasi-statically unstable and flashes to vapor if the radius of the cavitating bubbles is greater than R_c. In this circumstance, the growth of bubbles increases the fluid velocity due to mass conservation of the flow. The velocity increase then causes the fluid pressure to decrease according to the momentum equation. The decrease of the pressure is fed back to the Rayleigh-Plesset equation and results in further bubble growth. In this case the velocity and void fraction of the fluid increase and the pressure coefficient of the flow decreases significantly below the upstream values and the flow flashes to vapor. On the other hand, if the bubbles do not grow beyond R_c, the flow is quasi-statically stable and is characterized by large amplitude spatial fluctuations downstream of the throat.

Finally, we should note that the present work analyzes a simplified internal bubbly flow model with bubble cavitation effects only. Other possible nonequilibrium factors in a real flow, such as thermal nonequilibrium between the phases and nuclei number density distribution in the flow, are excluded. Direct comparison between the present work and previous experimental data are therefore limited. However, the present results show that bubble cavitation may contribute to the void development and downstream oscillation of a bubbly flow in a drastic way.

Acknowledgments

The authors are very grateful for the support for this research provided by National Science Council, Taiwan, R.O.C., under Contract NSC86-2621-E006-039-T and by the Office of Naval Research under Contract N00014-91-J-1295.

References

Biesheuvel, A., and van Wijngaarden, L., 1984, "Two Phase Flow Equations for a Dilute Dispersion of Gas Bubbles in Liquid," *Journal of Fluid Mechanics*, Vol. 148, pp. 301–318.

Brennen, C. E., 1995, *Cavitation and Bubble Dynamics,* Oxford University Press, New York.

Chapman, R. B., and Plesset, M. S., 1971, "Thermal Effects in the Free Oscillation of Gas Bubbles," ASME *Journal of Basic Engineering,* Vol. 93, pp. 373–376.

d'Agostino, L., and Brennen, C. E., 1983, "On the Acoustical Dynamics of Bubble Clouds," ASME *Cavitation and Multiphase Flow Forum,* Houston, TX, pp. 72–75.

d'Agostino, L., and Brennen, C. E., 1989, "Linearized Dynamics of Spherical Bubble Clouds," *Journal of Fluid Mechanics,* Vol. 199, pp. 155–176.

Ishii, R., Umeda, Y., Murata, S., and Shishido, N., 1993, "Bubbly Flows Through a Converging-Diverging Nozzle," *Physics of Fluids A,* Vol. 5(7), pp. 1630–1643.

Kameda, M., and Matsumoto, Y., 1995, "Structure of Shock Waves in a Liquid Containing Gas Bubbles," IUTAM *Symposium on Waves in Liquid/Gas and Liquid/Vapour Two-Phase Systems,* pp. 117–126.

Knapp, R. T., Daily, J. W., and Hammitt, F. G., 1970, *Cavitation,* McGraw Hill, New York.

Morioka, S., and Matsui, G., 1980, "Mechanism and Effect of Dispersion and Dissipation in Nozzle Flows of Bubbly Liquid," *Proceedings of 1st Asian Congress on Fluid Mechanics,* Bangalore, India, A54.

Morioka, S., and Toma, T., 1984, "Stability of Two-Phase Liquid Metal MHD Channel Flows," *Progress in Astronautics & Aeronautics,* Vol. 100, pp. 317.

Noordzij, L., and van Wijngaarden, L., 1974, "Relaxation Effects, Caused by Relative Motion, on Shock Waves in Gas-Bubble/Liquid Mixtures," *Journal of Fluid Mechanics,* Vol. 66, pp. 115–143.

Plesset, M. S., and Prosperetti, A., 1977, "Bubble Dynamics and Cavitation," *Annual Review of Fluid Mechanics,* Vol. 9, pp. 145–185.

Tangren, R. F., Dodge, C. H., and Seifert, H. S., 1949, "Compressibility Effects in Two-Phase Flow," *Journal of Applied Physics,* Vol. 20(7), pp. 637–645.

Toma, T., and Morioka, S., 1986, "Acoustic Waves Forced in Flowing Bubbly Liquid," *Journal of the Physical Society of Japan,* Vol. 55(2), pp. 512–520.

Toma, T., Yoshino, K., and Morioka, S., 1988, "Fluctuation Characteristics of Bubbly Liquid Flow in Converging-Diverging Nozzle," *Fluid Dynamics Research,* Vol. 2, pp. 217–228.

van Wijngaarden, L., 1968, "On the Equations of Motion for Mixtures of Liquid and Gas Bubbles," *Journal of Fluid Mechanics,* Vol. 33, pp. 465–474.

van Wijngaarden, L., 1972, "One-Dimensional Flow of Liquids Containing Small Gas Bubbles," *Annual Review of Fluid Mechanics,* Vol. 4, pp. 369–396.

Wang, Y.-C., 1996, "Shock Waves in Bubbly Cavitating Flows," Ph.D. thesis, California Institute of Technology, Pasadena, California.

Influence of the Nuclei on the Cavitation Inception for Different Types of Cavitation on Ship Propellers

B. Gindroz
International Business Manager,
Senior Scientist,
Bassin d'Essais des Carènes,
27400 Val de Reuil, France

M. L. Billet
Senior Scientist,
Applied Research Laboratory,
The Pennsylvania State University,
State College, PA 16804

In order to relate nuclei size distributions with inception cavitation in cavitation facilities, a test program was conducted at the Grand Tunnel Hydrodynamique (GTH) of the Bassin d'Essais des Carènes. The GTH, which has a complete air control system including dissolved gas and nuclei (microbubbles) control, offers the opportunity to answer this question. The tests were conducted on the three 34 mm diameter propellers used by Kuiper (1981), each of these propellers being characterized by a different cavitation type: bubble, sheet and vortex cavitation. The water nuclei content correspond to strong degassed water (maximum tension), low injection of medium size nuclei (medium tension-low content), large injection of medium size nuclei (medium tension-high content) and large injection of large nuclei (minimum tension). By injecting medium size nuclei for a low content and a high content, we can examine the influence of the number of nuclei on the cavitation inception characteristic. During all the tests, the dissolved air content was kept constant. The GTH on-line Cavitation Nuclei Counter (Centerbody Venturi) was used to measure both the water nuclei distribution and the liquid tension. Comparisons are made with the calibrated Centerbody Venturi, a Phases Doppler Particles Analyzer (PDPA) and Holographic measurements.

Introduction

For engineers, cavitation means performance degradation, noise generation, vibration and material erosion. These effects are generally unacceptable. For this reason, the prediction of cavitation occurance becomes a major engineering problem. Numerous research has been carried out to attempt to identify, understand, predict and control the physical mechanism leading to cavitation inception. Rood (1991) in his paper entitled "Mechanisms of Cavitation Inception," makes a precise review of research progress during the last twenty years. He underlines that the scaling laws to predict the full-scale cavitation behavior from the model tests, are based on empirical rules, defined on a correlation between measurements at model scale and observations of full-scale characteristics. The need to better understand the scale phenomena and to develop physical prediction laws has led to focus studies on real fluid characteristics. Indeed, for an engineer, the purpose of any model scale test is the accurate prediction of the full-scale behavior.

Experimental observations have shown the persistance of microbubbles in a real fluid. These free microbubbles or nuclei have been found to be a major parameter in the cavitation inception process. According to the study of Billet (1985) and Gindroz et al. (1990), natural waters such as rivers and oceans contain free microbubbles.

The influence of the nuclei on the cavitation behavior has been written in numerous publications, such as those from Billet on the different types of cavitation (1984, 1985, 1986), from Kuiper on ship propellers (1978, 1979, 1982, 1985), from Gindroz on turbines and nuclei measuring techniques (1986, 1988, 1990, 1991), from Gowing on nuclei measurements (1982, 1987), from Lecoffre on nuclei measuring techniques (1976, 1979, 1982, 1986), and from Shen (1986, 1989).

To summarize all these studies, the nuclei distribution of the water is a major parameter in cavitation inception and development. More particularly, we must be able to measure and to change the nuclei content in a facility, when performing cavitation tests on a model, in order to understand the influence.

Rood in his review (1991), underlines the fact that different facilities are characterized by different nuclei distributions, corresponding to the hydrodynamic configuration of each facility. The nuclei spectrum is affected by the whole nuclei time history through the facility. The use of a deaerator to remove air and a resorber to dissolve the small nuclei can change significantly the spectrum. Moreover, the nuclei distribution depends strongly on the operation conditions.

Several previous studies were conducted with the objectives to correlate nuclei concentration with air content in the facilities (see Peterson, 1972). But the relationship between total air content, dissolved air content and nuclei distributions is not well defined. There are several experimentally determined rules for a few facilities, but, they are not applicable to others.

Gowing et al. (1982) and Lecoffre (1987) stated that it is necessary to control both the dissolved air and the free air, when performing cavitation tests on models. Thus, the best method is to degass and inject nuclei.

To do a study on the influence of the nuclei distribution on the cavitation behavior, it is necessary to use a facility in which both dissolved air content and nuclei can be controlled. This means, the dissolved air content and the nuclei spectra must be constant during the whole cavitation test. This is only possible when a facility is equipped with a downstream tank with gravity bubbles separators and a large resorber, to ensure that the generated microbubbles will not recirculate through the facility (see Avellan et al., 1987 and Lecoffre et al., 1987). Then, by injecting a proper nuclei distribution, it is possible to guarantee a constant spectrum.

Contributed by the Fluids Engineering Division for publication in the JOURNAL OF FLUIDS ENGINEERING. Manuscript received by the Fluids Engineering Division August 21, 1995; revised manuscript received December 4, 1996. Associate Technical Editor: J. Katz.

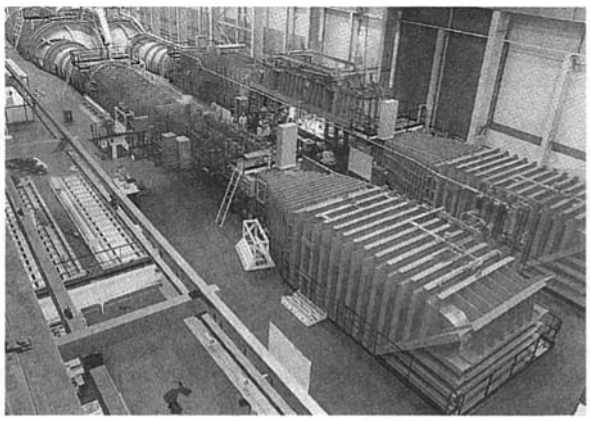

Fig. 1 General view of the Grand Tunnel Hydrodynamique (GTH)

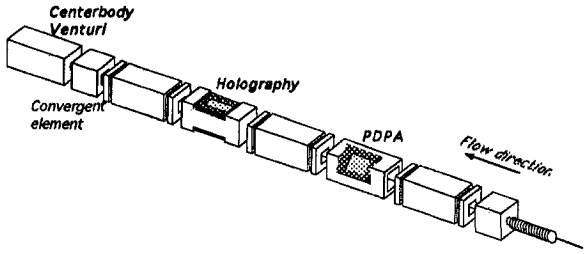

Fig. 2 In-line installation for comparative nuclei measurements

Proposed Study

The 19th ITTC recommanded that experiments be conducted to relate nuclei size measurements and cavitation susceptibility measurements to various types of propellers cavitation inception in a cavitation facility. The Grand Tunnel Hydrodynamique (GTH) of the Bassin d'Essais des Carènes (Figure 1), which has a complete air control system including dissolved gas and nuclei (microbubbles) control, offers the opportunity to answer this question. In addition, the GTH on-line Cavitation Susceptibility Meter (CSM) should allow to quantify precisely the number and the dimension (tension) of the test water nuclei.

The Cavitation Susceptibility Meter (Centerbody Venturi) was calibrated by comparing its results with Phases Doppler Particles Analyzer (PDPA from Aerometrics) and Holographic measurements. These comparisons were conducted for different nuclei contents, corresponding to degassed water without nuclei injection and with three different nuclei injections. The three measuring techniques were installed in-line (along a by-pass from the GTH) to ensure the same water sampling characteristics (Fig. 2).

As the inception of cavitation is very sensitive to nuclei distribution, joint tests were conducted by the 20th ITTC and the Bassin d'Essais des Carènes to quantify the importance of microbubbles on the inception of three cavitation types: leading edge sheet, bubble and tip vortex cavitation. These tests were conducted at the GTH on three 34 mm diameter propellers used by Kuiper (1981), each of these propellers being characterized by a different cavitation type: bubble, sheet and vortex cavitation. Four different nuclei distributions were generated: degassed water (maximum water tension), injection of a low amount of medium size nuclei (medium tension, low number), injection of a high number of medium size nuclei (medium tension, high number), and injection of a large amount of large size nuclei (minimum tension). Due to the unique design of the GTH, the injected nuclei distributions can be fully controlled during the complete test.

For a given propeller, the global hydrodynamic parameters of the tunnel fix the absolute pressure distribution, and, more particularly, the lowest pressure value. Then, with a precise nuclei distribution measurement, we should be able to correlate the inception cavitation with the tension corresponding to the largest nuclei containing in the test water.

Initially, Cavitation Inception values were determined by visual observation. In parallel, performances measurements, basic acoustic measurements, photographs and video recording are made.

Results about the influence of the water nuclei distribution (water tension) on the cavitation inception index and the desinent cavitation index are presented. Moreover, the influence of the cavitation development on the acoustic level is presented, by comparing acoustic spectra.

Experimental Setup

The test facility utilized for this wide study and all the instruments for measuring cavitation characteristics on propellers are briefly presented.

Test Facility: GTH. This experimental study was conducted in the French largest cavitation tunnel for naval hydrodynamic research, known as GTH, Grand Tunnel Hydrodynamique, with a 2 MW power supply (see Lecoffre and Chantrel, 1987). This facility has two parallel test sections: a free surface one (that can be closed) with a section of 2 m × 1,35 m by 10 m long, and a closed one with a section of 1,14 m square by 6 m long. The maximum flow velocities are respectively 12 m/s and 20 m/s. The GTH downstream tank, used to remove the air produced in or injected into the test section, can remove air from dispersions with void fractions up to less than 20 percent. No bubbles larger than 100 μm pass through the downstream tank, even at the maximum flow rate. Bubbles smaller than 100 μm are dissolved through the GTH, mainly in the resorber, 30 m long and 5 m in diameter, before they reach the test section.

The 250 kW shaft propeller driving system can be set either in one shaft configuration or in double shaft configuration. The maximum rate of revolution is 5000 rd/min, the maximum thrust is 500 daN and the maximum torque is 50 m daN.

The GTH is equipped with two Laser Doppler Velocimeters, a 2-D and a 3-D, for accurate velocity measurements in the test section.

Nuclei Control. The GTH is a unique facility to do such a study, because of a complete air control system, including dissolved gas and microbubbles control, that enables the control of the nuclei in the test section. Details of this system are described by Lecoffre et al. (1987).

Nomenclature

J = advance ratio (−)
P = pressure (N/m^2)
P_v = vapor pressure (N/m^2)
R = radius (m)
T = water tension (N/m^2)
V = flow velocity (m/s)
γ = gas-liquid surface tension (N/m)
Γ = ratio of the specific heats of the gas inside a bubble (−)
σ = cavitation number (−)

Subscripts

d = desinent value
i = incipient value
CR = critical value
CSM = cavitation susceptibility meter (centerbody Venturi)
HOLO = holography
PDPA = phases doppler particles analyzer

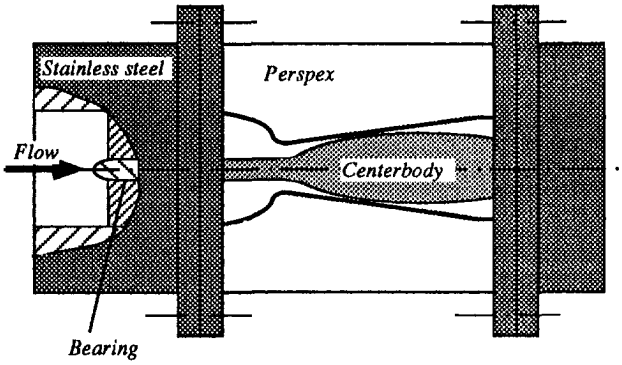

Fig. 3 Principle of a Centerbody Venturi

Cavitation nuclei can be injected into the upstream vertical tunnel leg from the contraction to have a uniform nuclei seeding in the test section. This is achieved by a rapid expansion of high pressure saturated water through a series of injectors. The nuclei generators are built on the following principle: a gaseous cavitation is produced at the outlet of the injectors and, by adjusting the downstream pressure recovery time, which governs the diffusive process of nuclei growth, it is possible to provide nuclei of different diameters. The high pressure air saturated water is obtained in a separate vessel.

The nuclei generators lie on a 600 × 600 mm grid on the upstream vertical tunnel leg from the contraction. They can produce either a homogeneous nuclei concentration in the test section or a distribution with an increased concentration at the center of the test section, where the propeller is located. By changing the number of generators in function, it is possible to generate different nuclei contents, and by changing the pressure feeding the injectors, it is possible to generate different sizes of nuclei.

The GTH is equipped in-line with a Centerbody Venturi, to measure the nuclei distribution. In this Cavitation Susceptibility Meter (CSM) (Fig. 3), the flow is accelerated through a restricted area, bound by a central conical body and a cone diffuser, in order to promote the explosive growth of the nuclei. Then, in the region where the pressure increases, the activated nuclei collapse. The number of activated nuclei is obtained by counting the number of collapse pulses. By setting a controlled lower pressure—under the vapor pressure—in the restricted section of the venturi, all the nuclei characterized by a critical pressure higher than this lower value will be activated. The critical pressure of a nuclei corresponds to its limit of stability. By changing the flow rate through the Centerbody Venturi, the lowest controlled pressure can be adjusted, in order to change the critical pressure range of activated nuclei, so that a cumulative nuclei distribution can be determined. For further details, Lavigne (1991) discusses the principle.

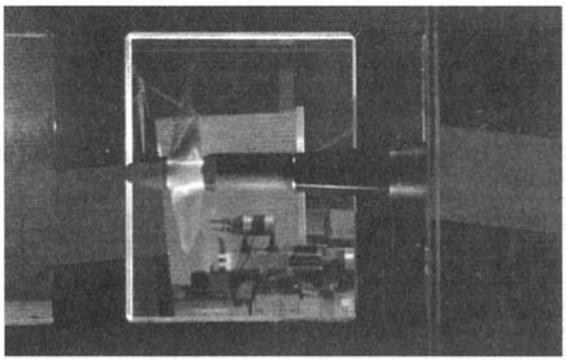

Fig. 4 Propeller mounted in open water configuration in the test section

Table 1 Propeller cavitation test conditions

Cavitation type	Advance ratio	Flow velocity (m/s)
Bubble	$J = 0.60$	$V = 6.0$
Sheet	$J = 0.55$	$V = 6.0$
Tip Vortex	$J = 0.55$	$V = 4.0$

Air Control. The air content is controlled with two measuring techniques: a polarographic method for the oxygen content and a Van Slyke method for the air content. The level is fixed before the start of the test.

Acoustic. For the usual acoustic measurements, the GTH is equipped with hydrophones plug flush mounted on the bottom of the test section. A calibration of this system was done before the test.

Visualization. The GTH is equipped with CCD Video cameras and high speed cameras. Stroboscopic light (3 × 200 W), synchronized with the frequency of the shaft revolution is utilized as light supply.

Models of Propellers. Depending on the loading of the propeller blades, different types of cavitation can occur. Thus, Kuiper (1981) designed three different propellers, exhibiting three types of cavitation at the design condition: bubble cavitation (Propeller B), sheet cavitation (Propeller S) and tip vortex cavitation (Propeller V). These three propellers of Kuiper are used in this study. They have four blades and a diameter of 34 cm.

Measurements

Preliminary measurements were conducted, to calibrate the Centerbody Venturi. The main problem is to determine precisely the pressure distribution through the Venturi and more particularly its minimum value, which defines the characteristic tension or dimension of the smallest detected nuclei. An attempt to qualify the Cavitation Nuclei Counter (Centerbody Venturi) was held, by measuring velocity profiles through the instrument, using a LDV method, and by running a 3-D Navier-Stokes code. A precise agreement was found. This first step determined the pressure distribution through the Nuclei Counter. For further details, see Gindroz (1992) and Billard, Dupont and Gindroz (1992).

Then, preliminary tests are conducted to not only calibrate the Centerbody Venturi, the Phases Doppler Particles Analyzer and Holography, but also to select appropriate nuclei distributions/liquid tensions for the propeller cavitation tests. The three measuring techniques are installed in-line along a by-pass to ensure each system sampled the same water (see Figure 2). The new perspex in-line comparative installation has been designed with optimal conditions for each technique and with optical glass windows, treated (air-glass and glass-water) for the wave length of the Laser rays used during the experiments. The length of the by-pass is chosen to correspond to the elapsed time from the intake of the sample tube to the test propeller.

The PDPA is placed the most upstream of the nuclei instruments along the in-line comparative installation to prevent any

Table 2 Water tension conditions

Case N^o	Water tension type
1	Maximum tension
2	Medium tension, low nuclei concentration
3	Medium tension, high nuclei concentration
4	Minimum tension

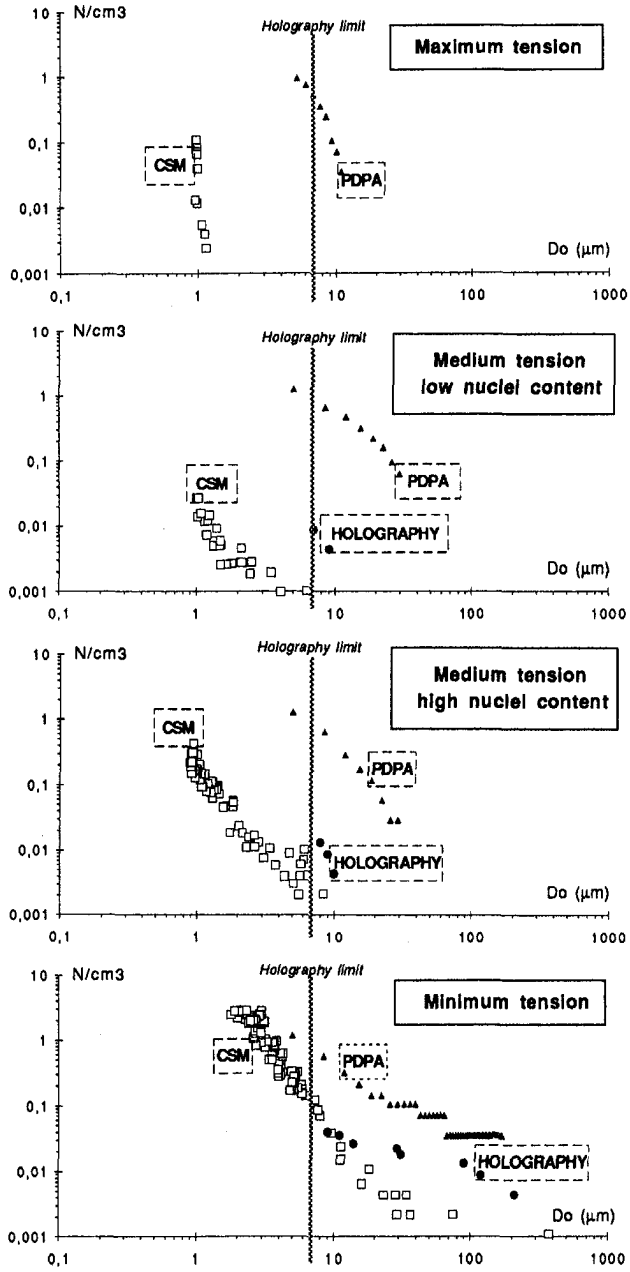

Fig. 5 Nuclei distributions measured during the tests on the B propeller (bubble cavitation)

vertical migration of larger bubbles by buoyancy from skewing the PDPA results.

Due to the quality of the optical glass windows and the dimensions of the in-line installation, the size limitation for accurate measurements with the holography technique is as low as 7 μm.

After the selection of appropriate nuclei distributions, nuclei measurements are made in parallel with the cavitation inception tests, to insure the injection of a proper nuclei spectrum.

For this study, the propellers are mounted in open water configuration in the test section (Fig. 4).

The test conditions are chosen close to the design condition of each propeller, to have only one type of cavitation at the inception. The flow velocities correspond to the maximum admissible load of the propellers blades.

Table 1 summarizes the propeller cavitation test conditions.

The cavitation inception data are obtained for four values of liquid tension/nuclei distribution, at a constant dissolved oxygen level of 30 percent. These conditions are summarized in Table 2.

Table 3 Water tension from the different nuclei measurement techniques

Propeller B (Bubble cavitation)

Water tension type	T_{CSM} (mbar)	T_{HOLO} (mbar)	T_{PDPA} (mbar)
1: Maximum	1092	>140	70
2: Med./low nuclei cont.	114	99	24
3: Med./high nuclei cont.	99	90	24
4: Minimum	1,3	1,7	2,5

Propeller V (Vortex cavitation)

Water tension type	T_{CSM} (mbar)	T_{HOLO} (mbar)	T_{PDPA} (mbar)
1: Maximum	909	>140	87
2: Med./low nuclei cont.	114	88	20
3: Med./high nuclei cont.	78	52	15
4: Minimum	2,5	3,1	3,2

Propeller S (Sheet cavitation)

Water tension type	T_{CSM} (mbar)	T_{HOLO} (mbar)	T_{PDPA} (mbar)
1: Maximum	993	>140	87
2: Med./low nuclei cont.	99	80	34
3: Med./high nuclei cont.	—	—	—
4: Minimum	2,5	3,7	4,1

The liquid tensions of the water for cases 2 and 3 are similar although the number of nuclei differs by an order of magnitude.

The determination of the cavitation inception or desinence is made visually. Rood, in his review on the Mechanisms of Cavitation Inception (1991), underlines the difficulty to objectively define cavitation Inception. He writes that "a scientific definition of cavitation inception could be the initial rapid growth of vapor—and gas-filled bubbles." But, "an engineering definition applies when cavitation inception is determined indirectly through visual or acoustic techniques, in which case a notion of events per unit time is often required." Then, as visual determination can depend strongly on the observer and his own criteria to quantify cavitation inception, only the decision from the usual operator of the GTH is taken into account. Cavitation inception index and desinence index are determined three times for each tension condition, in order to have an idea on the precision and the repeatability of the results, based on the operator criteria.

Acoustic spectra are measured on a 100 kHz range filtered at 3 kHz, for several cavitation development conditions: free of cavitation, at cavitation inception and for a larger development of cavitation. There are not used to detect cavitation inception.

In parallel, to the cavitation inception data and nuclei/tension measurements, photographs and videos are taken.

Results

The results consist of cavitation index for inception and desinent cavitation for each propeller, with corresponding nuclei

Table 4 Incipient/desinent cavitation numbers for the B propeller

Propeller B (Bubble cavitation)

Water tension type	σ_i (—)	σ_d (—)
1: Maximum	0.86 ± 0.01	0.86 ± 0.01
2: Medium/low nuclei content	3.10 ± 0.04	3.36 ± 0.02
3: Medium/high nuclei content	3.45 ± 0.05	3.65 ± 0.06
4: Minimum	3.62 ± 0.02	3.74 ± 0.01

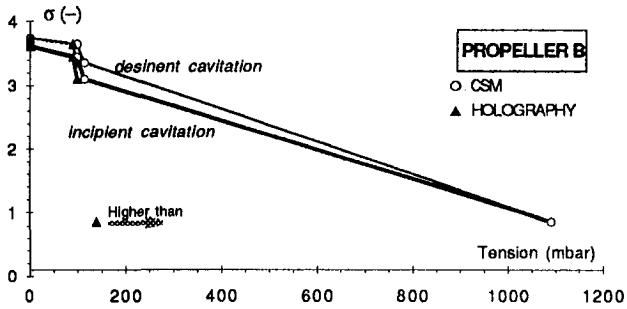

Fig. 6 Evolution of the cavitation numbers with the water tension (propeller B)

distributions measured with different techniques, and with characteristic acoustic spectra.

Nuclei Distributions. As discussed previously, an extensive calibration of the Centerbody Venturi was done in order to determine precisely the pressure distribution through the venturi and more particularly the minimum pressure that determines the tension corresponding to the smallest detected nuclei. All microbubbles with an internal critical pressure higher than the lowest value in the Venturi (P_{min}) will cavitate. By varying the flow rate, it is possible to change the lowest pressure value in the Venturi (P_{min}). As the smallest detected nuclei depends on this minimum pressure, it is possible to determine the cumulative nuclei distribution as a function of the critical pressure or the critical radius. The relationship between the critical pressure and the critical radius comes from static equilibrium and is given by

$$R_{CR} = -\frac{3\Gamma - 1}{3\Gamma} \cdot \frac{2\gamma}{P_{CR} - P_V}$$

where Γ is the ratio of the specific heats of the gas inside the bubble, γ is the gas-liquid surface tension and P_V is the liquid vapor pressure.

The nuclei dimension, determined with the Centerbody Venturi, corresponds to the critical value. To compare this value with the results from the other measuring techniques, the nuclei size is calculated upstream of the instrument, using a quasi-static evolution with the pressure level. As a control, a numerical resolution of the Rayleigh-Plesset equation (dynamic evolution of a nuclei in a variable pressure field), shows that the quasi-static approximation gives correct results in this case.

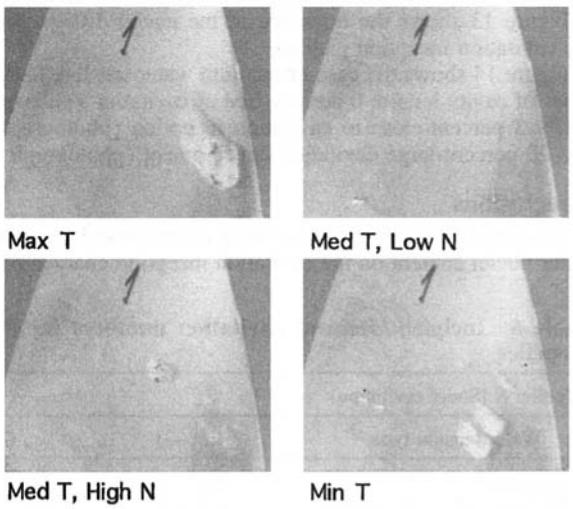

Fig. 7 Cavitation inception patterns

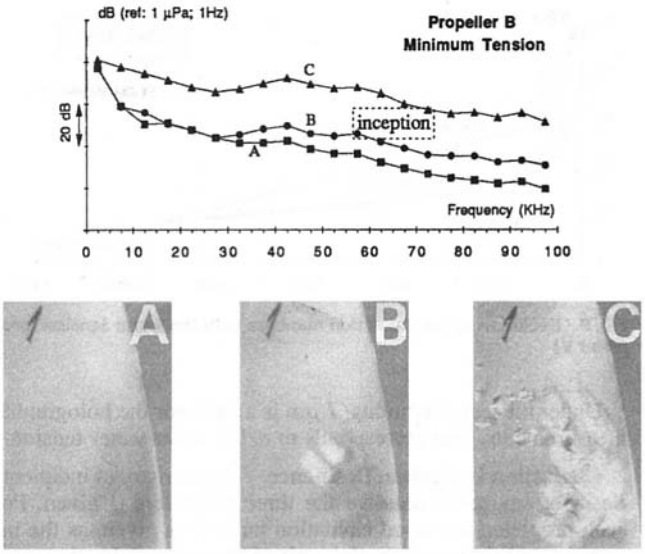

Fig. 8 Acoustic spectra for three cavitation conditions

From these microbubble distributions the critical liquid tension can be defined as

$$T = P_V - P_{CR}$$

where T is the liquid tension, P_V is the liquid vapor pressure and P_{CR} is the critical pressure of the largest microbubble.

For the Centerbody Venturi each measurement corresponds to a mean value based on a 10 seconds acquisition period or 100 detected bubbles. All the measurements for the PDPA where performed with the same photomultiplier voltage because preliminary tests showed it to have a significant influence on the number of small nuclei measured. For the holography, at first it was planned to use an automatic system to analyze the holograms; however, all the analyses were done manually due to the few bubbles present.

All the nuclei distributions are measured during the propeller cavitation inception tests, with the three techniques mounted in-line. The spectra are kept constant during each test. The repeatability to obtain similar liquid tensions for each propeller test is very good in spite of different reference pressures in the test section.

Figure 5 represents the four typical nuclei spectra. The uncertainty on the measurements is ±7 mbar for the Centerbody Venturi, ±2 μm for holography and ±2.5 μm for PDPA.

The comparison between distributions measured by the Centerbody Venturi, the PDPA and Holography gives the following remarks: in each case the PDPA has a higher number of bubbles above 10 μm than holography and holography has a higher number than the CSM. In all cases, each measurement technique predicts similar trends as the microbubble distributions are varied. Absolute comparisons of liquid tension and critical microbubble size between CSM and holography are very good.

Table 3 represents the water tension from the different techniques.

Table 5 Incipient/desinent cavitation numbers for the V propeller

Propeller V (Vortex cavitation)		
Water tension type	σ_i (—)	σ_d (—)
1: Maximum	8,8 ± 0.1	9,0 ± 0.0
2: Medium/low nuclei content	12,7 ± 0.2	19,0 ± 0.6
3: Medium/high nuclei content	17,0 ± 1.2	24,5 ± 0.2
4: Minimum	21,3 ± 0.6	30,2 ± 0.7

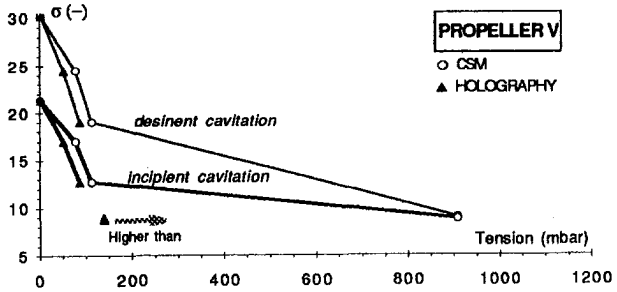

Fig. 9 Evolution of the cavitation numbers with the water tension (propeller V)

Under the test conditions, 7 μm is a limit for the holographic measurements, that corresponds to a 140 mbar water tension.

Cavitation Inception/Desinence. A summary of incipient/desinent cavitation data for the three propellers is given. For each propeller, averaged cavitation number is given, as the inception and desinence is determined three times by the same operator. The sensitivity of inception to liquid tension/nuclei distribution is different for each type of propeller cavitation.

Propeller B (Bubble Cavitation). The B Propeller was designed to generate bubble cavitation. Table 4 summarizes the incipient/desinent cavitation numbers, corresponding to the different water tensions.

Figure 6 represents the evolution of the cavitation numbers (σ_i, σ_d) with the water tension measured by the Centerbody Venturi and by holography. The uncertainty is within ± 7 mbar.

Figure 7 shows the influence of the nuclei distribution on the cavitation inception patterns.

During the tests, basic acoustic measurements are performed. The results are represented in Power Spectral Density, referred to 1 μPa and 1 Hz, with 20 values along the x-axis, corresponding to a mean value on every 5 kHz band width. The uncertainty is a typical $\pm 1\frac{1}{2}$ dB.

Figure 8 shows the case of minimum water tension, for three cavitation conditions: free of cavitation (photograph A), cavitation inception (photograph B) and larger cavitation development (photograph C).

Propeller V (Vortex Cavitation). The V Propeller was designed to generate tip vortex cavitation. Table 5 summarizes the incipient/desinent cavitation numbers, corresponding to the different water tensions.

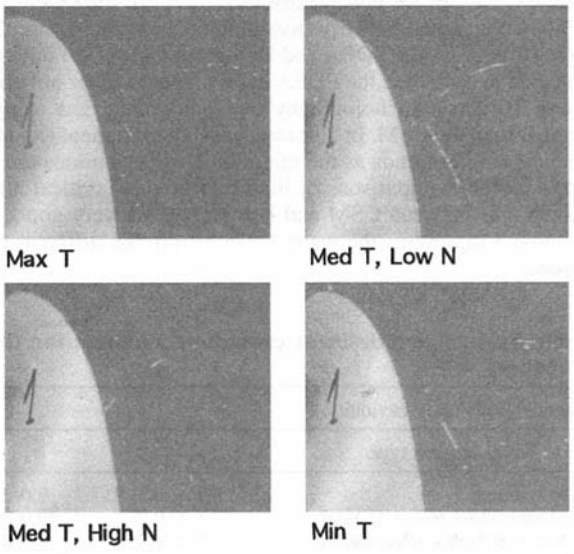

Fig. 10 Cavitation inception patterns

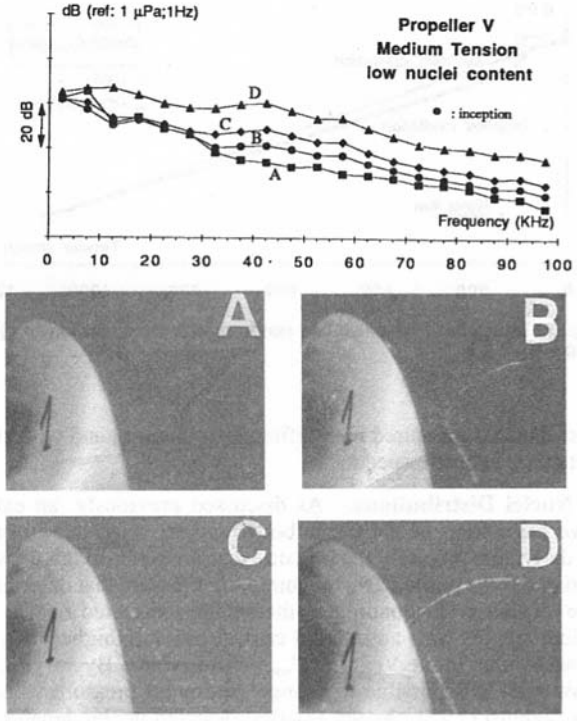

Fig. 11 Acoustic spectra for four cavitation conditions

Figure 9 represents the evolution of the cavitation numbers (σ_i, σ_d) with the water tension measured by the Centerbody Venturi and by holography. The uncertainty is within ± 7 mbar.

Figure 10 shows the influence of the nuclei distribution on the cavitation inception patterns.

Figure 11 shows the case of medium water tension, for four cavitation conditions: free of cavitation (photograph A), cavitation inception (photograph B), permanent vortex (photograph C) and attached tip vortex (photograph D).

Propeller S (Sheet Cavitation). The S Propeller was designed to generate sheet cavitation. For this propeller (S), the tests are performed with three water conditions: Maximum tension, medium tension with low nuclei content, and minimum tension.

Table 6 summarizes the incipient/desinent cavitation numbers, corresponding to the different water tensions.

Figure 12 represents the evolution of the cavitation numbers (σ_i, σ_d) with the water tension measured by the Centerbody Venturi and by holography. The uncertainty is within ± 7 mbar.

Figure 13 shows the influence of the nuclei distribution on the cavitation inception patterns.

Figure 14 shows the case of medium water tension, for three cases of cavity length: 0 percent-free of cavitation (photograph A), <3 percent-close to cavitation inception (photograph B) and 20 percent-large cavitation development (photograph C).

Conclusions

The purpose of this study was to examine the influence of the water nuclei content on the cavitation inception characteristics.

Table 6 Incipient/desinent cavitation numbers for the S propeller

Propeller S (Sheet cavitation)		
Water tension type	σ_i (—)	σ_d (—)
1: Maximum	11,6 ± 0.2	12,3 ± 0.2
2: Medium/low nuclei content	11,8 ± 0.1	12,5 ± 0.1
3: Minimum	11,9 ± 0.0	12,6 ± 0.1

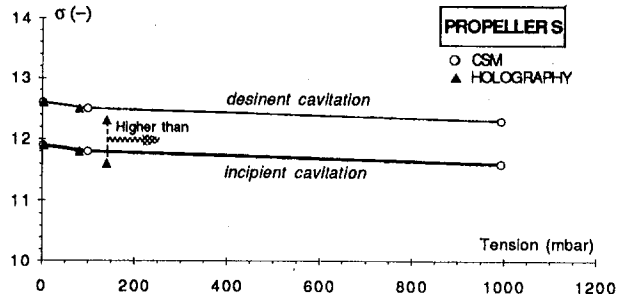

Fig. 12 Evolution of the cavitation numbers with the water tension (propeller S)

When determining cavitation inception, the water tension corresponding to the bigger nuclei in the water must be known with precision, as it governs the whole process. Some of the initial results are summarized in the 20th ITTC Cavitation Committee Report. The following summarizes the important conclusions.

Nuclei Measurements. During the tests, the repeatability to obtain similar liquid tensions for each propeller test was very good in spite of different reference pressures in the test section. In all cases, each measurement technique predicted similar trends as the nuclei distributions were varied. Absolute comparisons of liquid tension and critical microbubble size between CSM and Holography are very good in most cases.

The PDPA is very easy to run and allows quasi-real time measurements of the nuclei content and their velocity. Nevertheless, the problem of the Phases Doppler Anemometer amplification setting and the size of the control volume for measurements remains relevant. An in-situ calibration of the effective control volume function of the photomultiplier voltage is required.

Holography is still a reference technique in granulometry, but it presents a major disadvantage due to the long analyzing time of the holograms.

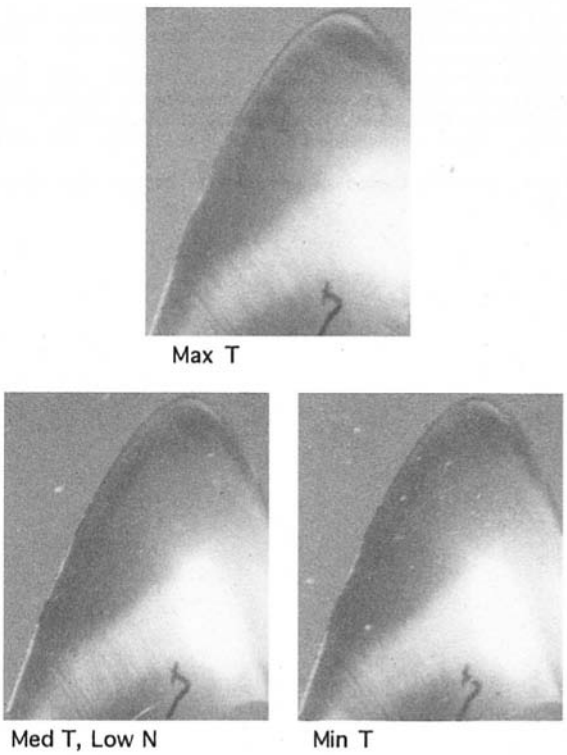

Fig. 13 Cavitation inception patterns

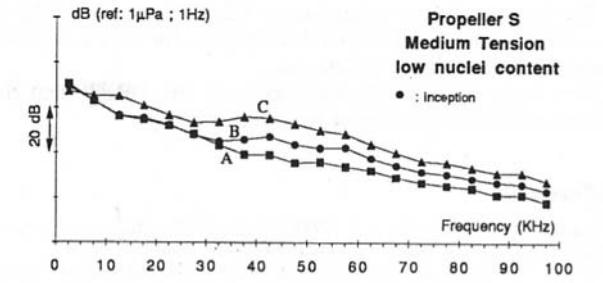

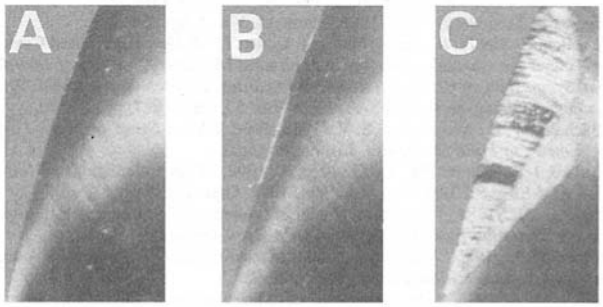

Fig. 14 Acoustic spectra for three cavitation conditions

After an extensive calibration in order to determine precisely the lowest pressure value inside the instrument, that defines correctly the characteristics of the detected nuclei, the Centerbody Venturi is used as a precise nuclei counter. This technique has a major advantage, as it detects only particles governing the cavitation developments (cavitation nuclei). Moreover, it analyzes in real time the quasi-total volume of the water sample by-passed from the main flow of a test rig.

Nuclei Distribution-Cavitation Inception/Desinence. These tests clearly demonstrate the direct influence of the nuclei distribution on the cavitation inception/desinence characteristics on propeller cavitation. For the sheet cavitation propeller (S), little change in inception characteristic values with a large increase in liquid tension was found. However, bubble cavitation (B) and tip vortex cavitation (V) propellers are very sensitive to the nuclei distributions. The inception/desinent cavitation numbers decreases significantly with increasing the liquid tension. The sensitivity of inception to nuclei distribution (water tension) is different for each type of propeller cavitation. The maximum reduction in cavitation index with increased water tension is respectively 76 percent for bubble cavitation, 59 percent for tip vortex cavitation and 3 percent for sheet cavitation. The sensitivity of desinence is respectively 77 percent for bubble cavitation, 70 percent for tip vortex cavitation and 2 percent for sheet cavitation. For the sheet cavitation case, there is no apparent nuclei effect on the incipient/desinent cavitation characteristics.

It is of major interest to continue to study precisely the role of the nuclei in the inception process for the different types of cavitation. The determination of cavitation inception scale effects can not be complete without accurate measurements of liquid tension/nuclei distributions.

Acknowledgments

The authors wish to acknowledge all the colleagues from the Bassin d'Essais des Carènes and from the 20th ITTC Cavitation Committee, as also Mr. Gowing from DTMB and Dr. Rood from ONR for participating actively in the GTH tests, Miss Luquet and Mr. Royer from the Institut Franco-Allemand de Recherches de Saint-Louis, for the holographic measurements, Mr. Stanislas, Mr. Geiler and Mr. Bernard from the Institut de Mécanique des Fluides de Lille, for the holograms analysis, and Mister Bauché, who represents Aerometrics France, for the PDPA measurements.

The authors wish to acknowledge Mr. Bliaux and Mr. Fournier from the Bassin d'Essais des Carènes, for all the acoustic measurements and post-treatments.

This work is supported financially by the DRET, that the authors wish to acknowledge more particularly.

References

Arndt, R. E. A., and Keller, A. P., 1992, "Water Quality Effects on Cavitation Inception in a Trailing Vortex," *Journal of Fluid Mechanics.*

Avellan, F., Gindroz, B., Henry, P., Bachmann, P., Vullioud, G., and Wegner, M., 1986, "Influence de la chute d'essai et de la nucléation sur les performances en cavitation des modèles de turbines Francis," *Proc. of 13th I.A.H.R. Symp. on Progress in Technology,* Sept. 1986, Montreal, Vol. 1, pp. 2-1, 2-15.

Avellan, F., Henry, P., and Ryhming, I. L., 1987, "A New High Speed Cavitation Tunnel for Cavitation Studies in Hydraulic Machinery," *Proc. of International Symposium on Cavitation Research Facilities and Techniques,* ASME Winter annual Meeting, Boston (USA), FED: Vol. 57, Dec. 1987, pp. 49–60.

Bachalo, W. D., and Sankar, S. V., 1988, *Proc. 4th Int. Symp. on Appl. Laser Anemometry to Fluid Mechanics,* Lisbon, Portugal.

Billard, J-Y., Dupont, Ph., and Gindroz, B., 1992, "Flow Calculations in Venturies," *FDI-FIDAP Users Congress,* Sept. 1992, Germany.

Billet, M. L., 1984, "Cavitation Nuclei Measurements," *International Symposium on Cavitation Inception,* ASME WAM, New Orleans.

Billet, M. L., 1985, "Cavitation Nuclei Measurements—A Review," *Cavitation and Multiphase Flow Forum,* 1985, ASME.

Billet, M. L., 1986, "The Importance and Measurement of Cavitation Nuclei," *Advancements in Aerodynamics,* Fluid Mechanics and Hydraulics, Minneapolis.

Brennen, C. E., and Kuhn de Chizelle, Y., 1992, "Cavitation Nuclei Concentrations and Event Rates," Internal Report, CALTEC, Pasadena, California, July 1992.

Gindroz, B., Avellan, F., and Henry, P., 1988, "Similarity Rules of Cavitation Tests: The Case of the Francis Turbine," *Proc. of 14th I.A.H.R. Symp. on Progress within Large and High-Specific Energy Units,* June 1988, Trondheim, vol. 2, Session L, pp. 755–766.

Gindroz, B., and Avellan, F., 1988, "Règles de similitude dans les essais de cavitation," *XX^{èmes} journées de l'Hydraulique,* SHF, avril 1989, Lyon, Rapport I.18, pp. 1–8.

Gindroz, B., Henry, P., and Avellan, F., 1990, "Similarity of cavitation inception in Francis turbine," *Proc. of 15h I.A.H.R. Symp.,* Sept., Belgrade, Yugoslavia.

Gindroz, B., Avellan, F., and Henry, P., 1990, "Guide lines for performing cavitation tests," *Proc. of 15h I.A.H.R. Symp.,* Sept., Belgrade, Yugoslavia.

Gindroz, B., 1991, "Lois de similitude dans les essais de cavitation des turbines Francis," PhD. dissertation, Lausanne, Ecole Polytechnique Fédérale.

Gindroz, B., and Briançon-Marjollet, L., 1992, "Experimental Comparison Between Different Techniques of Cavitation Nuclei Measurements," *2nd International Symposium on Propeller and Cavitation,* Sept., Hangzhou, China.

Gindroz, B., 1992, "Qualification of a Centerbody Cavitation Nuclei Counter Using Optical Techniques," *Proc. of 16h I.A.H.R. Symp.,* Sept., São Paulo, Brazil.

Gowing, S., and Shen, Y. T., 1982, "The Role of Microbubbles on Cavitation Inception on Head Forms," David Taylor Research Center Report.

Gowing, S., and Shen, Y. T., 1987, "Cavitation Susceptibilities in Ocean Waters," David Taylor Research Center Report DTNSRDC-SHD-1241-01, Aug.

Gréhan, G., Gouesbet, G., Naqwi, A., Durst, F., "Evaluation of Phase Doppler System using Generalized Lorenz-Mie Theory," *Multiphase Flow,* Tsukuba, Japan, Sept. 1991.

Henry, P., Lecoffre, Y., and Larroze, P. Y., 1980, "Effets d'Echelle en Cavitation," IAHR 10th, Tokyo.

Keller, A. P., 1984, "Scale Effects at Beginning Cavitation Applied to Submerged Bodies," *Int. Symp. on Cavitation Inception.*

Kuiper, G., 1978, "Cavitation Scale Effects—A Case Study," *International Shipbuilding Progress,* Vol. 25.

Kuiper, G., 1979, "Some Experiments With Distinguished Types of Cavitation on Ship Propellers," *International Symposium on Cavitation Inception,* ASME WAM, New York.

Kuiper, G., 1981, "Cavitation Inception on Ship Propellers Models," Ph.D. Dissertation, Wageningen, The Netherlands.

Kuiper, G., 1982, "Some Experiments With Distinguished Types of Cavitation on Ship Propellers," JOURNAL OF FLUIDS ENGINEERING, Vol. 104.

Kuiper, G., 1985, "Reflections on Cavitation Inception," *Cavitation and Multiphase Flow Forum,* ASME.

Lavigne, S., and Noe, Ph., 1988, "Venturi à ogive centrale," *Rapport d'essais,* R. 21.025.

Lavigne, S., 1991, "Le Venturi analyseur de germes," *Journées DRET Cavitation,* Arcueil.

Lavigne, S., 1991, "Le Venturi analyseur de germes," *Journées DRET Cavitation,* Arcueil.

Lecoffre, Y., 1976, "Contrôle de la nucléation d'une eau en moyens d'essais," *IAHR 8th Symposium,* Leningrad.

Lecoffre, Y., 1979, "Cavitation Tests and Nuclei Control," ASME WAM, New York.

Lecoffre, Y., Marcoz, J., and Valibouse, B., 1982, "Aspects pratiques du contrôle de germes de cavitation en moyens d'essais," *IAHR 11th Symposium,* Amsterdam.

Lecoffre, Y., 1986, "Méthodes pratiques de contrôle de la teneur en air libre et dissous dans les moyens d'essais," *IAHR 13th Symposium,* Montréal.

Lecoffre, Y., Chantrel, P., and Teiller, J., 1987, "Le Grand Tunnel Hydrodynamique," ASME WAM, Boston.

Liu, Z., and Brennen, C. E., 1992, "Cavitation Nuclei Measurements and Population Dynamics," Internal Report, CALTEC, Pasadena, California, July 1992.

Meyer, R. S., Billet, M. L., and Holl, J. W., 1992, "Free Stream Nuclei and Travelling-Bubble Cavitation," *Journal of Fluid Mechanics,* Vol. 114, Dec.

Pendleton, J. D., "Mie and Refraction Theory Comparison for Particle Sizing with the Laser Velocimeter," *Applied Optics,* Vol. 21, pp. 684–688, 1982.

Rood, E. P., 1991, "Review-Mechanisms of Cavitation Inception," ASME JOURNAL OF FLUID ENGINEERING, June, Vol. 113.

Royer, H., 1974, "Une application de la micro-holographie ultra-rapide," *Nouvelle Revue Opt.,* 5–87.

Royer, H., Lecoq, P., and Ramseyer, E., 1981, "Application of holography to bubble chamber visualization," *Optical Communication,* 37–84.

Sankar, S. V., and Bachalo, W. D., "Response characteristics of the phase Doppler particle analyzer for sizing spherical particles larger than the light wavelength," *Applied Optics,* 30, Vol. 12, 1991.

Shen, Y. T., Gowing, S., and Pierce, R., 1984, "Cavitation Susceptibility Measurements by a Venturi," International Symposium on Cavitation Inception, ASME WAM, New Orleans.

Shen, Y. T., Gowing, S., and Eckstein, B., 1986, "Cavitation Susceptibility Measurements of Ocean, Lake and Laboratory Water," David Taylor Research Center Report No. 86/019.

Shen, Y. T., and Dimotakis, P. E., 1989, "Viscous and Nuclei Effects on Hydrodynamic Loadings and Cavitation of a NACA66 (MOD) Foil Section," JOURNAL OF FLUID ENGINEERING, Vol. 111.

Tanger, H., Strechwall, H., Weitendorf, E.-A., and Mills, L., 1992, "Recent Investigations of the Free Air Content and its Influence on Cavitation and Propeller-Exited Pressure Fluctuations," ISPC, Hamburg, Germany, June.

19 ITTC, "Report of Cavitation Committee," 12–22 Sept. 1990, Madrid, Spain.

20 ITTC, "Report of Cavitation Committee," 19–24 Sept. 1993, San Francisco, CA.

Shuji Hattori
Associate Professor,
Department of Mechanical Engineering,
Fukui University,
9-1 Bunkyo 3-Chome,
Fukui 910, Japan

Hiroyuki Mori
Engineer,
Development Section,
Steel Casting & Forging Plant, Takasago,
Takasago Works,
Kobe Steel Ltd.,
2-3-1, Shimahama, Arai-Cho,
Takasago-Shi, Hyogo-Ken,
676, Japan

Tsunenori Okada
Professor Emeritus,
Department of Mechanical Engineering,
Fukui University,
9-1 Bunkyo 3-Chome,
Fukui 910, Japan

Quantitative Evaluation of Cavitation Erosion

In order to evaluate the quantitative cavitation-erosion resistance of materials, a pressure-detector-installed specimen was developed, which can measure both the impact load produced by cavitation bubble collapse and the volume loss simultaneously. Test specimens (pressure-detection rod) used were nine kinds of metals and were exposed to vibratory cavitation. A linear relation was obtained for all materials between the accumulated impact energy ΣFi^2 calculated from the distribution of impact loads and the volume loss, independent of test conditions. Impact energy accumulated during the incubation period and the energy for a unit material removal in steady-state period were obtained from the relation. These values are very important concerning quantitative erosion resistance evaluation. That is, when the distribution of impact loads is acquired for different cavitation conditions, the volume loss can be estimated. This idea was applied to the venturi cavitation erosion. The experimental results for venturi test corresponds well with the prediction using these impact energy values. It was concluded that the quantitative impact energy values of materials can be determined independent of the apparatus and the test condition by using the newly developed pressure-detector-installed specimen.

1 Introduction

In order to evaluate the cavitation-erosion resistance of materials, a quantitative relation between bubble collapse pressure and erosion should be clarified. However, it is very difficult to measure the magnitude and frequency of many impact loads produced by bubble collapse, because cavitation impact act on minute area of the surface in a very short time. The authors have developed the pressure detector and the data acquisition system to measure bubble collapse impact loads, and have obtained the distribution of impact loads in vibratory (Okada et al., 1989) and in venturi device (Iwai et al., 1990). By corresponding the distribution of impact loads to that of size of indents on the specimen surface, a critical impact load to create an indent was estimated to be 5.5 N, 6.7 N, and 11.0 N for Al, Cu, and SUS304, respectively (Okada et al., 1995). Moreover, it was found that the plastic energy needed to form an indent dynamically is about ten times larger than that for static indentation (Okada et al., 1994). De and Hammitt (1982) reported that a linear relation can be obtained between the acoustic power caused by cavitation bubble collapse and the erosion power obtained by volume loss for aluminum specimen. However, it left unclear whether other materials follow the similar linear relation and the accuracy of their experimental results would not necessarily be good, because bubble collapse pressure and the damage was measured separately.

In this study, a test specimen installing pressure detector was built to estimate the cavitation-erosion resistance quantitatively. The specimen was exposed to vibratory cavitation to measure impact loads and volume loss simultaneously. A new method was proposed to evaluate the quantitative erosion resistance of various materials using the pressure-detector-installed specimen.

2 Test Specimen

Figure 1 shows a pressure-detector-installed specimen which can measure both the impact loads produced by cavitation bubble collapse and the resulted volume loss. A pressure-sensitive piezoelectric ceramic disk with a chemical composition of $PbTiO_3 \cdot PbZrO_3$ had 3 mm diameter and 0.25 mm thickness, and was made by MURATA Co., Ltd. The resonance frequency was 8 MHz. The ceramic disk was sandwiched with electrically conductive adhesives between a 20 mm length pressure detection rod and a 15 mm length pressure reflection rod. Equalizing the diameter of pressure detection and reflection rods has an advantage in preventing dissipation of the pressure waves. However, since the different materials were used between the detection and reflection rods, there was the possibility of the wave interference between the original wave and the reflected wave from their boundary. A steel ball drop test showed that no interference occurs, when a length of detection rod is more than 13 mm (Mori et al., 1996). Therefore, the length was determined to be 20 mm in this study. The diameters of both rods were selected 3 mm to reduce the probability of measuring several impact load at the same time. Epoxy resin agent was used to full in the space between the part of pressure detector and the acrylic resin pipe for vibration-proof, water-proof and the protection from the breakage of ceramic disk. The materials of test specimen (detection rod) were pure aluminum and pure copper for fcc lattice, pure iron and S15 C carbon steel (equivalent to AISI 1015 steel) for bcc lattice, pure zinc and pure titanium for hcp lattice, and aluminum alloys A2017, A5052, A7075 (equivalent to ISO Al-Cu 4 MgSi(A), ASTM 5052 and ASTM 7075, respectively). Chemical compositions and mechanical properties of these materials are listed in Tables 1 and 2, respectively. The test surface of specimen was polished with emery paper and then was buff finished. The reflection rod was pure copper different from material of detection rod.

3 Calibration of the Pressure Detector

Each detector was calibrated by a steel ball drop test after setting up. A steel ball (3.19 mm in diameter with a mass of 1.30×10^{-4} kg) was dropped from heights of 50, 100, and 150 mm. Figure 2 shows the output signal of the detector recorded with a digital storage oscilloscope. The time interval $\Delta t(s)$ of impact load and output voltage V were measured from Fig. 2

Contributed by the Fluids Engineering Division for publication in the JOURNAL OF FLUIDS ENGINEERING. Manuscript received by the Fluids Engineering Division October 10, 1996; revised manuscript received September 11, 1997. Associate Technical Editor: Jong H. Kim.

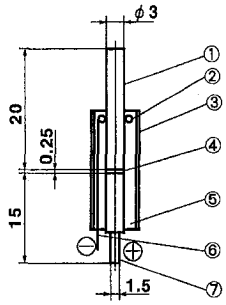

Fig. 1 Pressure-detector-installed specimen

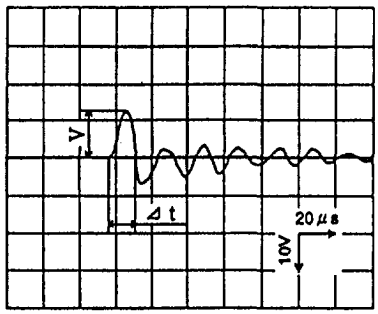

Fig. 2 Output signal of detector produced by a steel ball drop (Al specimen)

Table 1 Chemical compositions of materials tested (wt. %)

	Si	Fe	Cu	Mn	Mg	Cr	Zn	Ti	Al
Al	0.09	0.14	0.01	0.01	0.01	0	0.01	0.01	99.72
Cu			99.96						

	C	Si	Mn	P	S	Pb	Fe
Fe	0.007	0.25	0.24	0.007	0.007	0.08	99.41
S15C	0.15	0.25	0.47	0.015	0.015		99.1

	Al	Cu	Pb	Cd	Fe	N	O	H	Zn	Tl
Zn	0.2~0.7	<0.007	<0.22	0.003 ~0.14	<0.014				BAL	
Tl					<0.25	<0.05	<0.20	<0.015		BAL

	Si	Fe	Cu	Mn	Mg	Cr	Zn	Ti	Al
A2017	0.61	0.32	4.18	0.70	0.54	0.034	0.194		BAL
A5052	0.09	0.24	0.03	0.07	2.6	0.21	0.01		BAL
A7075	0.10	0.21	1.3	0.02	2.4	0.13	5.8	0.03	BAL

Table 2 Physical and mechanical properties of samples

Metal	Crystal lattice	Density kg/m^3	Modulus of longitudinal elasticity E GPa	Acoustic impedance Z N·s/m^3	Tensile strength σ_B MPa	Elongation δ %	Vickers hardness HV
Al	fcc	2.71×10^3	71	13.9×10^6	125	25	33
Cu	fcc	8.96×10^3	129	34.0×10^6	326	14	100
Fe	bcc	7.87×10^3	206	40.3×10^6	343	29	130
S15C	bcc	7.87×10^3	206	40.3×10^6	388	44	151
Zn	hcp	7.14×10^3	93	25.8×10^6	235	4	59
Tl	hcp	4.49×10^3	116	22.8×10^6	500	26	200
A2017	fcc	2.70×10^3	71	13.8×10^6	454	19	136
A5052	fcc	2.70×10^3	69	13.6×10^6	233	33	65
A7075	fcc	2.70×10^3	71	13.8×10^6	540	12	166

and then impact loads F_0 were calculated by the laws of conservation of energy and momentum as follows,

$$F_0(N) = m(1+e)v_0/\Delta t = 5.77\times10^{-4}(1+e)\times\sqrt{h_0}/\Delta t \quad (1)$$

where m is the mass of the steel ball (kg), e is the rebound restitution coefficient, v_0 is the impact velocity (m/s), and h_0 is the potential height (m). The restitution coefficients were determined by the measurements of the rebound height of the steel ball using a high-speed video camera.

The calibration equation of impact load $F_0(N)$ against output voltage V (volt) was obtained as

$$F_0(N) = A\cdot V \quad (A\text{: coefficient}) \quad (2)$$

The results of steel ball drop tests and the calibration equations of each detector are listed in Table 3.

On the other hand, the relation between applied force and output voltage can be represented as follows according to the characteristic of piezoelectric ceramics,

$$F(N) = 1/g_{33}\cdot s/t\cdot \mathrm{V}(V) \quad (3)$$

where g_{33} is the potential output coefficient (22×10^{-3}V·m/N), s is the area of the piezoelectric ceramics (7.069×10^{-6}m^2) and t is the thickness of the piezoelectric ceramics (0.25×10^{-3} m).

By substituting the characteristic value,

$$F = A'\cdot V \quad (A' = 1.29) \quad (4)$$

The coefficient A in Eq. (2) obtained from a steel ball drop test as reported in table 3 differs from the coefficient A' in Eq. (4).

Nomenclature

A = impact load versus output voltage correlation coefficient obtained from a steel ball drop test
A' = impact load versus output voltage correlation coefficient calculated from characteristic of piezoelectric ceramics
A_0 = double amplitude (peak to peak) of vibrating disk
c = sound velocity in the test liquid (ion-exchanged water)
e = rebound restitution coefficient
E = impact energy
F_0 = impact load produced by a steel ball drop test
F = impact load produced by cavitation
Fi = impact load with the intensities more than 0.6 N produced by cavitation
g_{33} = potential output coefficient of piezoelectric ceramics
h = distance between the specimen surface and the vibrating disk
m = mass of the steel ball
p = compression stress at piezoelectric ceramics produced by a steel ball drop test
p_0 = stress wave passing through the detection rod
s = area of the piezoelectric ceramics
t = thickness of piezoelectric ceramics
V = output voltage of piezoelectric ceramics
v = throat velocity of venturi
v_0 = impact velocity for a steel ball drop test
Z_1 = acoustic impedance of the detection rod
Z_2 = acoustic impedance of the electric ceramics
Z_3 = acoustic impedance of the reflection rod
$\alpha_2 = (Z_3 - Z_1)/(Z_2 + Z_3)$
$\beta_1 = 2Z_2/(Z_2 + Z_1)$
ρ = test liquid density (ion-exchanged water)
σ = cavitation number
Δt = time interval of impact load
ΣFi^2 = equivalent value to impact energy

Table 3 Calibration values obtained by a steel ball drop test (Uncertainty in coefficient is ±10 percent)

Material	Potential height mm	Restitution coefficient	Time interval of impact load μs	Output voltage of detector V Volt	Calibration equation
Al	50.0	0.40	15.5	8.9	F_0=0.91V
	100.0		14.6	12.9	
	150.0		15.8	15.9	
Cu	50.0	0.58	10.1	12.4	F_0=1.30V
	100.0		10.0	18.0	
	150.0		10.2	23.9	
Fe	50.0	0.63	9.2	13.7	F_0=1.41V
	100.0		9.1	19.5	
	150.0		9.0	24.5	
S15C	50.0	0.63	9.3	11.1	F_0=1.31V
	100.0		9.1	15.9	
	150.0		9.2	18.8	
Zn	50.0	0.50	15.0	7.6	F_0=1.22V
	100.0		13.2	12.5	
	150.0		13.8	14.7	
Ti	50.0	0.71	13.6	11.7	F_0=1.12V
	100.0		11.9	18.9	
	150.0		11.8	23.6	
A2017	50.0	0.66	11.7	8.8	F_0=0.88V
	100.0		11.6	14.0	
	150.0		11.7	17.6	
A5052	50.0	0.46	13.1	7.2	F_0=0.82V
	100.0		13.4	11.2	
	150.0		13.0	12.4	
A7075	50.0	0.75	11.8	8.2	F_0=0.86V
	100.0		12.3	12.4	
	150.0		11.4	15.2	

This is because the various materials were used for erosion specimen as detection rod, while copper rod was used as the reflection rod, and the transmission or reflection of stress waves at its interface changes with detection rod material. Therefore, when the impact load with the same intensity is applied to the specimen surface, the output voltage is different. After the stress wave p_0 passes through the detection rod, the compression stress p at piezoelectric ceramics is given by (Chatani, 1989),

$$p = \beta_1/(1 - \alpha_2) \times p_0 \tag{5}$$

$$\beta_1 = 2Z_2/(Z_2 + Z_1)$$

$$\alpha_2 = (Z_3 - Z_1)/(Z_2 + Z_3)$$

where Z_1, Z_2, Z_3 are the acoustic impedance of the detection rod, the piezoelectric ceramics and the copper rod, respectively. This shows that the pressure p is $\beta_1/(1 - \alpha_2)$ times p_0 depending on the combination of the detection and reflection rods. Assuming that the impact load F_0 acts on the detection rod and the

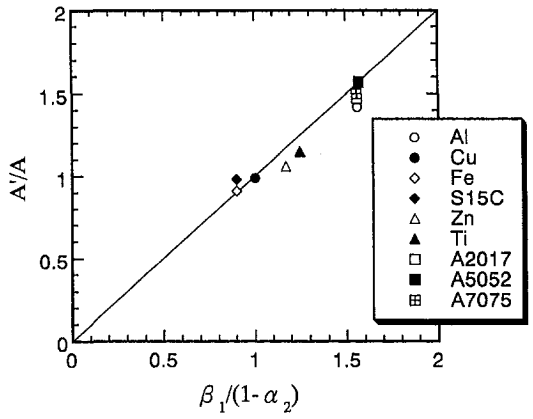

Fig. 3 Relation between $\beta_1/(1 - \alpha_2)$ and A'/A

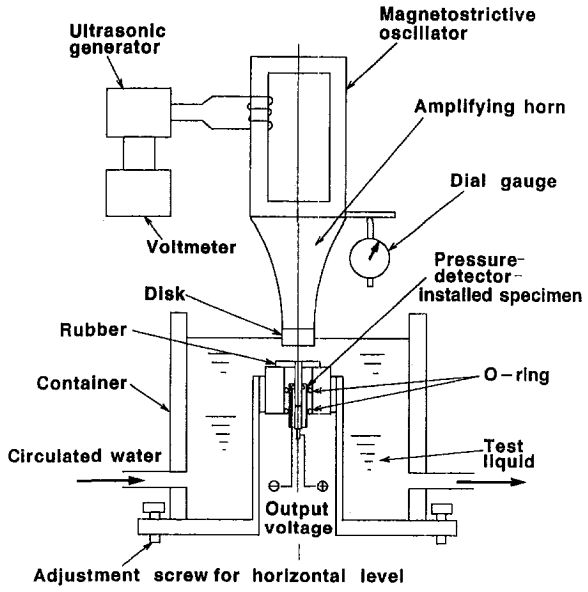

Fig. 4 Schematic of vibratory cavitation erosion test

force F is detected from the piezoelectric ceramics, F_0 and F are proportional to p_0 and p, respectively. Equation (5) is given by

$$F = \beta_1/(1 - \alpha_2) \times F_0 \tag{6}$$

From Eqs. (2), (4), and (6), the coefficient A is expressed as

$$A = A'/\{\beta_1/(1 - \alpha_2)\}, \tag{7}$$

or

$$A'/A = \beta_1/(1 - \alpha_2). \tag{8}$$

Figure 3 shows the relation between calculated values of the right term in Eq. (8) and the experimental values of ratio A'/A. Datapoints can be expressed by a straight line with some scatter. The scatter should be brought by the adhesive condition on the piezoelectric ceramics. Consequently, each detector was calibrated using the equation acquired from each steel ball drop test as listed in Table 3 in order to be sure precisely, and thus the differences among the detectors were excluded as much as possible.

4 Cavitation Erosion Test

Figure 4 shows the magnetostrictive vibratory device used for the cavitation test. The vibrating disk of stainless steel with a diameter of 16 mm was screwed into amplifying horn of magnetostrictive oscillator in close proximity to a newly developed test specimen. The specimen was inserted into a 3 mm diameter hole of rubber plate and was fixed flush with the surface to keep bubbles uniformly on the specimen. The specimen was exposed to cavitation to measure the impact load. At the same time, the specimen was weighted by a precision balance (sensitivity: 0.01 mg) after being maintained for evaporation in a vacuum chamber for 10 min during periodic interruptions of the test. The horn frequency was 19.5 kHz. The test liquid was ion-exchanged water which was kept at 25 ± 1°C.

5 Signal Treatment and Data Acquisition System

Figure 5 shows a block diagram of the signal treatment and data acquisition system. The circuit consists of a high-pass filter (50 kHz), a peak holder, an A/D converter and a PC98 microcomputer with large memory.

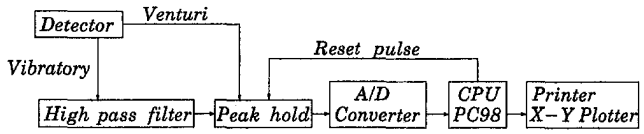

Fig. 5 Block diagram of data acquisition system

Figure 6(a) is a pressure signal wave showing the output of the detector recorded directly by a digital storage oscilloscope in a vibratory device. The output signals exhibit a number of hydrodynamic pressure waves which correspond to the frequency of horn vibration 19.5 kHz. By removing the 19.5 kHz signal through a high pass filter, the pulses from impact loads were obtained as shown in Fig. 6(b). The sampling interval of the peak hold circuit was set at 100 μs because the resonance frequency of the oscillating horn was 19.5 kHz. Figure 6(c) shows a wave of peaks which was held before the arrival of the reset pulses. Thus, the maxima of the impact load over about two periods were digitalyzed after A/D conversion of peak hold waves and then analyzed by a microcomputer.

6 Distribution of Impact Loads

Table 4 shows the distribution of impact loads measured on the Al specimen exposed to cavitation for 5 min at a double amplitude (peak to peak) A_0 of 50 μm and a distance h of 1 mm from the vibrating disk. Since the sampling interval was set at 100 μs, the counted number was 3×10^6 for 5 min. The total number of impact loads more than 0.6 N is 5.7×10^5, and the ratio to the counted number is 19 percent. The value of 0.6 N corresponds to the noise level of electric signal. Thus, it is considered that the probability of measuring several impact loads at the same time is very small.

Figure 7 shows the distribution of impact loads which was measured for various materials. The distributions are very similar for all materials except Fe. This allows to suggest that impact loads were measured accurately independent of material. The reduced number of impact load on Fe specimen can be attributed to the condition of the surface finish and the parallelism between the specimen surface and the vibrating disk.

Table 4 Distribution of impact loads (Al specimen, t = 5 min; Uncertainty in count is ±10 percent)

F(N)	Counts	F(N)	Counts	F(N)	Counts
0	2,428,320	5.0	3,343	10.0	13
0.6	233,449	5.6	1,566	10.6	4
1.2	147,347	6.2	821	11.2	4
1.8	88,568	6.8	401	11.8	4
2.4	48,881	7.4	182	12.4	2
3.2	26,573	8.0	99	13.0	0
3.8	13,592	8.6	40	13.6	0
4.4	6,769	9.4	22	14.2	0

On the other hand, the impact energy E exerted on the surface is calculated from the impact load F using the following expression (De and Hammitt, 1982):

$$E = (\Delta t/\rho c)F^2 \tag{9}$$

where c is the sound velocity in the liquid, ρ is the liquid density and Δt is the time interval of impact load. If the time interval of impact load is assumed to be constant independent of load intensity, the impact energy becomes proportional to the square of impact load. Various impact loads are exerted on the detector surface (erosion test surface) with diameter 3 mm and the impact energy is expressed as

$$E \propto \Sigma Fi^2 \tag{10}$$

where Fi is the impact load with the intensities more than 0.6 N (noise level) detected in the acquisition system. The contribution of impact loads lower than 0.6 N to the impact energy is about 5 percent.

Figure 8 shows an example of the variation in accumulated impact energy ΣFi^2 recorded using an Al specimen. The energy increases first proportionally with exposure time in the early stage, then slowly beyond $\Sigma Fi^2 = 1.5 \times 10^7$. These variations imply the energy vs. time to show the convex curve. Similar trends were observed for Cu and Zn, but the impact energy increased at a constant rate for Fe, S15C, Ti, and Al alloys. This means that the eroded surface was roughened by exposure to cavitation for soft metals such as Al, Cu, and Zn and the

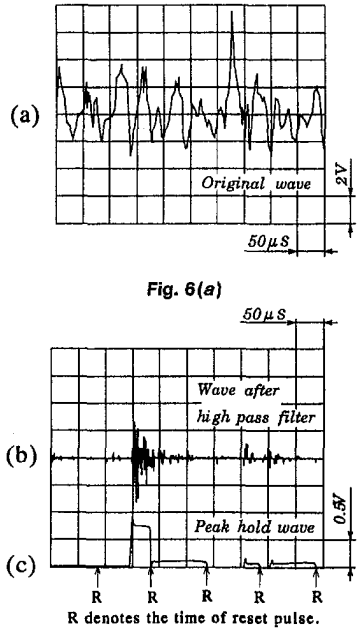

Fig. 6(a)

Fig. 6(b, c)

Fig. 6 Original wave from detector (a), and signal-treated wave (b and c) for cavitation test

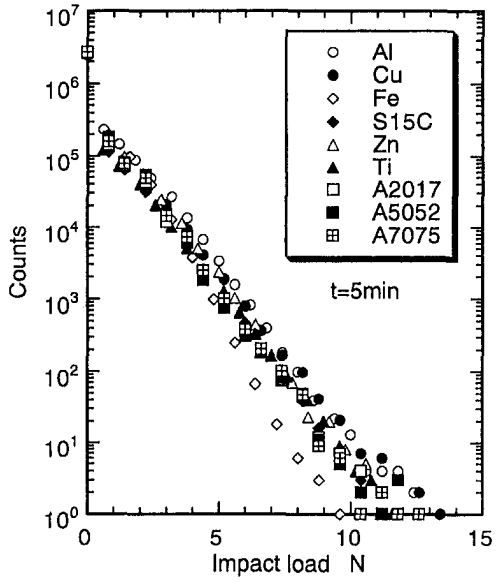

Fig. 7 Distribution of impact loads in vibratory cavitation apparatus (Uncertainty in count is ±10 percent)

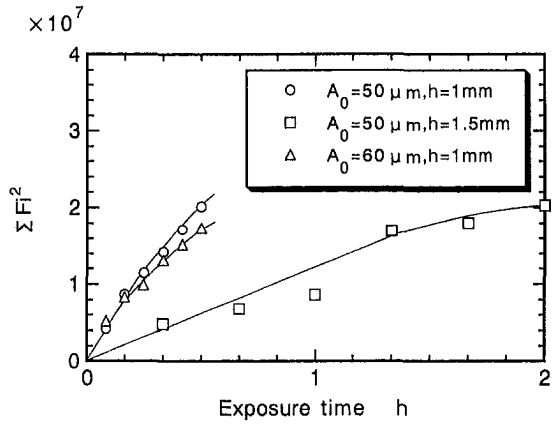

Fig. 8 Accumulated impact energy curves (Al specimen; Uncertainty in ΣFi^2 is ±10 percent)

frequency of impact loads was decreased due to the fixed bubbles at the bottom of the unevenness (Endo et al., 1968). In Fig. 8, the impact energy at $A_0 = 60$ μm is smaller than that at $A_0 = 50$ μm. This is not surprising because the diameter of the specimen was small as 3 mm, far from the regular test specimen with the diameter of 15.9 mm (ASTM Standards, 1989).

7 Volume Loss

Cavitation erosion was evaluated in terms of the volume loss, which is obtained from weight loss of the pressure-detector-installed specimen divided by the density of the specimen material. Figure 9 shows an example of the volume loss curves of Al specimen. The volume loss increases proportionally with exposure time in the early stage, followed by an increase at a slower rate, which is consistent with the variation in energy as shown in Fig. 8. The volume loss at $A_0 = 60$ μm is lower than that at $A_0 = 50$ μm, similarly to the impact energy curves.

8 Relation Between Impact Energy and Volume Loss

Figure 10(a) shows the direct relation between the cumulative ΣFi^2 and the cumulative volume loss of Al and Cu (fcc lattice metals). The lines were drawn by least-square method and the data can be expressed by two straight lines. This means that, when materials are subjected to a certain amount of the ΣFi^2, the cumulative volume loss is independent of test condition such as amplitude of vibration and the distance between the horn and the specimen. The cumulative volume loss is pro-

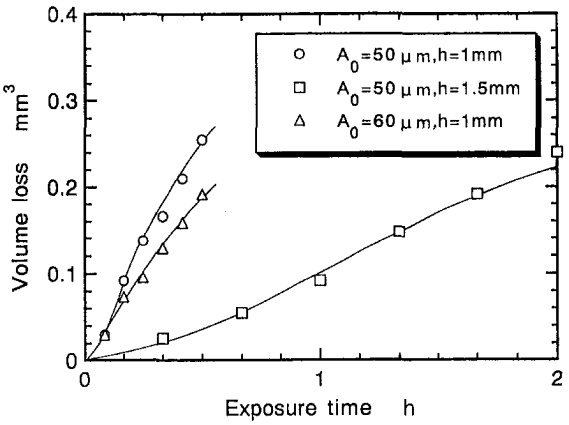

Fig. 9 Volume loss curves (Al specimen; Uncertainty in volume loss is ±10 percent)

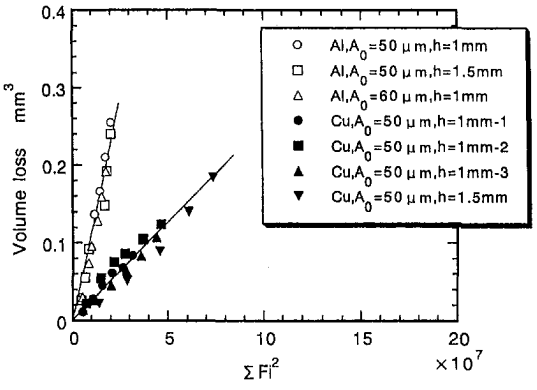

Fig. 10(a)

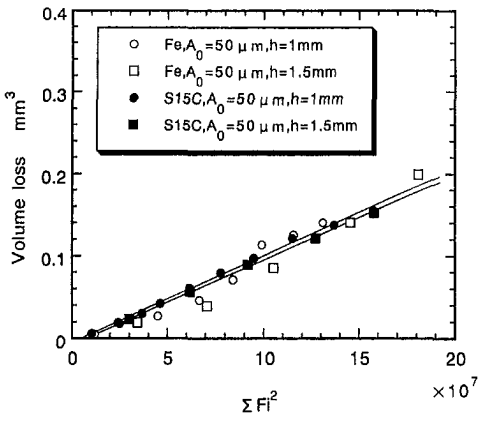

Fig. 10(b)

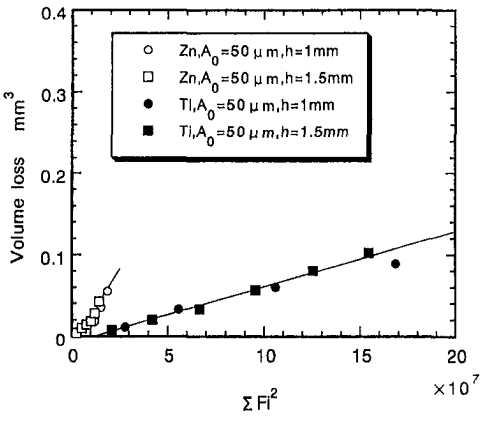

Fig. 10(c)

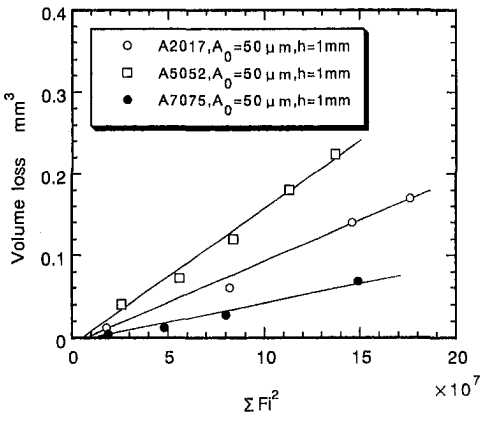

Fig. 10(d)

Fig. 10 Relation between impact energy and volume loss (Uncertainty is ±10 percent)

Table 5 Quantitative impact energy values associated with the erosion resistance of various materials (Uncertainty is ±10 percent)

	ΣFi^2 for incubation period $\times 10^7$	ΣFi^2 for a unit volume loss in steady-state period $\times 10^9$ mm^{-3}
Al	0.20	0.08
Cu	0.40	0.37
Fe	0.85	0.91
S15C	0.90	0.91
Zn	0.35	0.30
Ti	1.70	1.46
A2017	1.20	1.06
A5052	0.80	0.62
A7075	1.90	2.00

portional to impact energy as reported previously by De and Hammitt (1982).

Figure 10(b) shows the results of Fe and S15C (bcc lattice metals). Since the Vickers hardness of both materials are very similar, the straight lines obtained by least squares method are almost the same. Moreover, it can be seen that the straight lines intersect the abscissa with same incubation. The presence of incubation period coincides with our previous result (Iwai et al., 1989), i.e., some amount of plastic deformation occurs before material removal at the beginning of cavitation erosion. Figures 10(c) and (d) show the results of Zn and Ti (hcp lattice structure) and Al alloys, respectively. For all these materials, a linear relation between impact energy and volume loss was obtained independent of test conditions.

9 Quantitative Evaluation for Erosion Resistance of Materials

Impact energy (ΣFi^2) accumulated during the incubation period was obtained from the intersection between the experimental line and the abscissa, and ΣFi^2 for a unit material removal in steady-state period was obtained from the slope of straight lines in Fig. 10(a) to (d). These quantitative impact energy values are listed in Table 5.

Similar measurements were performed in a venturi cavitation apparatus. The surface of the test specimen was fixed flush with the wall of venturi as shown in Fig. 11. The impact load and volume loss were measured at the position of 45.5 mm apart from the throat end at the conditions of throat velocity of 25 m/s or 30 m/s and cavitation number of 0.68. Figure 12 shows an example of the distribution of impact load produced in venturi, and compared to vibratory cavitation (a dashed line). Although the distribution curves differ according to the apparatus, the number of large impact loads decreases exponentially in both cases. When the impact loads for the venturi test are compared with those of vibratory test, the total number of impact is smaller but the number of large impact loads is much larger. The relation between impact energy and volume loss is plotted in Fig. 13. The lines are drawn using the data of Al and Cu in Table 5. The experimental results corresponds well with the data obtained from vibratory test.

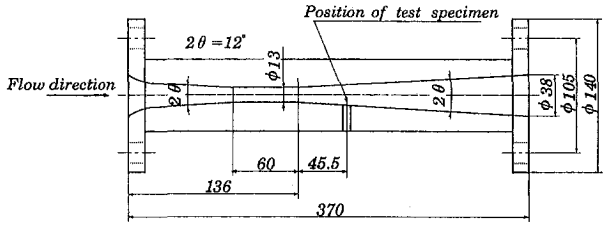

Fig. 11 Venturi test device

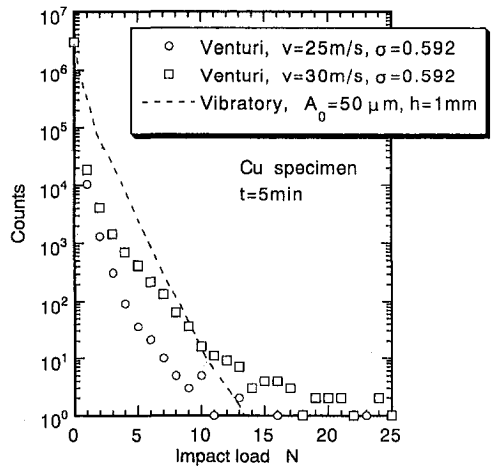

Fig. 12 Distribution of impact loads in venturi (Uncertainty in count is ±10 percent)

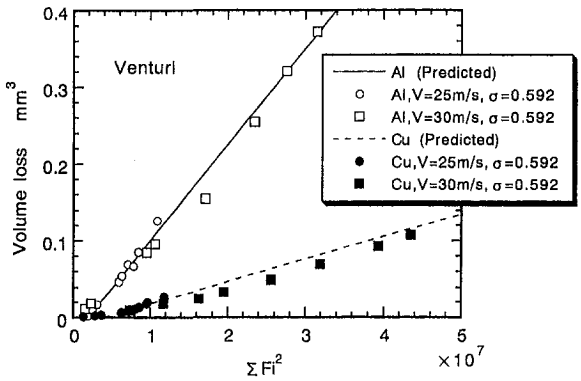

Fig. 13 Relation between impact energy and volume loss (Venturi test, fcc metals; Uncertainty is ±10 percent)

Concludingly, the impact load and the volume loss can be measured simultaneously by using the newly developed pressure-detector-installed specimen. The impact energy for incubation period termination and a unit volume loss in steady-state period can be obtained irrespective of the apparatus and the test conditions. This means that, if the distribution of impact load is obtained in the focussed cavitation device, the incubation period and the volume loss can be predicted from these impact energies.

10 Conclusions

A new pressure-detector-installed specimen can measure impact loads and related volume loss. Vibratory test was carried out by using a new type of specimen and was compared with venturi test. The following conclusions can be drawn.

(1) A linear relationship was obtained between the accumulated summation of squares of impact loads (equivalent to the impact energy) and the cumulative volume loss of the material of test conditions.

(2) At the beginning of the test, an incubation period of erosion was observed when hardly any volume loss occurs. In steady-state period, volume loss increases proportionally with the impact energy ΣFi^2.

(3) ΣFi^2 for incubation period and ΣFi^2 for a unit volume loss in steady-state period were indicated as quantitative impact energy values and characteristic of materials.

(4) These ΣFi^2 obtained from the vibratory cavitation shows a good agreement with the results obtained from the venturi apparatus.

References

Annual Book of ASTM Standards G32-92, 1992, "Standard Test Method for Cavitation Erosion Using Vibratory Apparatus," pp. 110–123.

Chatani, A., 1989, "Shogeki kyodo sekkei (3)," *Science of Machine,* Vol. 41, No. 7, pp. 856–860.

De, M. K., and Hammitt, F. G., 1982, "New Method for Monitoring and Correlating Cavitation Noise to Erosion Capability," *Trans.* ASME, Vol. 104, pp. 434–442.

Endo, K., Okada, T., and Nakashima, M., 1968, "Erosion of Bearing Alloys in Oil Film," *Bulletin of JSME,* Vol. 11, No. 45, pp. 536–544.

Iwai, Y., Okada, T., and Mori, H., 1990, "An Experimental Investigation of Cavitation Bubble Collapse Pressures and Erosion Pits in a Flowing System," *Cavitation and Multiphase Flow Forum-1990,* ASME FED Vol. 98, pp. 127–132.

Iwai, Y., Okada, T., and Tanaka, S., 1989, "A Study of Cavitation Bubble Collapse Pressures and Erosion Part 2: Estimation of Erosion From the Distribution of Bubble Collapse Pressures," *Wear,* Vol. 133, pp. 233–243.

Mori, H., Shibata, K., Hattori, S., and Okada, T., 1996, "Cavitation Erosion Based on the Propagation of Stress Waves (Result of 3-Layer Damping Materials)," *JSME,* Vol. 62, No. 600, pp. 1820–1826.

Okada, T., Iwai, Y., and Awazu, K., 1989, "A Study of Cavitation Bubble Collapse Pressures and Erosion Part 1: A Method for Measurement of Collapse Pressures," *Wear,* Vol. 133, pp. 219–232.

Okada, T., Iwai, Y., Hattori, S., and Tanimura, N., 1994, "Relation between Impact Load and the Damage produced by Cavitation Bubble Collapse," *Wear,* Vol. 184, pp. 231–239.

Emmanuel Etasse
PhD Student, Institut de Mécanique des Fluides, Toulouse, UMR CNRS/INP-UPS 5502, France

Charles Meneveau
Professor, Department of Mechanical Engineering, The Johns Hopkins University, Baltimore, MD 21218

Thierry Poinsot
Research Director, Centre Européen de Recherche et de Formation Avancée en Calcul Scientifique, 42 Av. G. Coriolis, 31057, Toulouse, France

Simple Stochastic Model for Particle Dispersion Including Inertia, Trajectory-Crossing, and Continuity Effects

An eddy-lifetime, stochastic Lagrangian model for particle dispersion in weakly laden turbulent flows is proposed, in which the interaction time-scale between particles and turbulent eddies is parametrized so as to include several physical effects. It takes into account particle inertia, crossing-trajectory effect, the possible difference in lateral and longitudinal dispersion, and some Reynolds number effects. The parametrization is based on previous results, from a theoretical dispersion model in isotropic turbulence using the trajectory-velocity independence and Gaussian approximations, as well as from Large-Eddy-Simulation. Simple fits are introduced to efficiently capture the main results from these prior studies, allowing practical implementation within the context of $k - \epsilon$ engineering codes. Results from simulations using the proposed approach are compared with experimental data of dispersion in decaying isotropic turbulence.

1 Introduction

Within the context of Reynolds-averaged Navier-Stokes (RANS) simulations of turbulent flows, two approaches for dealing with transport of a dispersed phase are commonplace: (i) the Eulerian two-fluid method and (ii) the Lagrangian particle transport method. The latter consists of explicitly solving the equation of motion of a sample of particles as they follow the mean fluid motion, while accounting for additional turbulent transport by randomly perturbing their trajectories using properties of the turbulence obtained from e.g., the $k - \epsilon$ parametrization. This approach has been used for a number of years (Yuu et al., 1978; Gosman and Ioannides, 1981; Shuen et al., 1983, etc..), especially for applications in combustion, sprays, etc.., and will be the focus of the present work.

The essence of stochastic Lagrangian dispersion modeling is to follow particle trajectories $\mathbf{x}_p(t)$,

$$\frac{d^2\mathbf{x}_p}{dt^2} = \frac{d\mathbf{v}}{dt} = \frac{\mathbf{u} - \mathbf{v}}{\tau_p} + \mathbf{g}. \tag{1}$$

Here τ_p is the response time of the particle, $\mathbf{u}$ and $\mathbf{v}$ are the fluid and particle velocities, respectively, and $\mathbf{g}$ is the gravitational acceleration. (For many applications involving solid particles in fluids, or liquid droplets in gases, other forces may typically be neglected.) The fluid velocity $\mathbf{u}$ is given by the sum of the mean fluid velocity and a stochastic component. The variance of the stochastic component is selected based on the turbulent kinetic energy, as computed in the $k - \epsilon$ parametrization. If $\mathbf{r}$ is a random vector with Gaussian distribution of zero mean and unit variance, equal in each direction, one writes

$$\mathbf{u} = \bar{\mathbf{u}} + \sqrt{(2/3)k}\,\mathbf{r}. \tag{2}$$

The random component of the fluid velocity seen by the particle is updated at time intervals δt, equal to twice the assumed time of interaction of a particle with a typical large-scale eddy. In most practical implementations, the so-called "eddy-lifetime model" is used. There, δt is given by the smallest between the eddy lifetime (T_e) and the time (T_c) it takes the particle to cross the large-scale eddy (due to relative mean velocities, i.e. trajectory crossing effect),

$$\delta t = 2 \min (T_e, T_c). \tag{3}$$

The factor 2 ensures the equality between the integral time-scale of the model and the postulated interaction time, since the stochastic process generates a linear autocorrelation function.

The particle dispersion resulting from such a random walk is described by a dispersion coefficient in each direction α:

$$D_{\alpha\alpha} = \frac{1}{2}\frac{d\langle x_\alpha^2 \rangle}{dt} = \langle v_\alpha^2 \rangle \int_0^t R_{\alpha\alpha}(t')dt', \tag{4}$$

where v_α is the fluctuating particle velocity in the α direction, and $R_{\alpha\alpha}(t')$ is the Lagrangian autocorrelation function of particle velocities (no summation over α's).

At long times, the dispersion coefficient is simply $D_{\alpha\alpha} = \langle v_\alpha^2 \rangle \tau_{L\alpha}^p$, where $\tau_{L\alpha}^p$ is the Lagrangian autocorrelation time of the particle velocities in direction α. When the particle follows a linear relaxation equation (neglecting the non-linearity when τ_p depends on Reynolds number), the dispersion characteristics of particle and fluid can be related (Tchen, 1947). Among others, this implies that in the long-time limit, the particle dispersion coefficient can be expressed in terms of fluid properties (expressed along the particle's trajectory) as $D_{\alpha\alpha} = \langle u_\alpha^2 \rangle \tau_{L\alpha}^f$, where $\tau_{L\alpha}^f$ is the Lagrangian integral time of fluid velocity as seen along the particle trajectory. $\langle u_\alpha^2 \rangle$ is the variance of fluid velocity, also as sampled along the actual particle trajectory. Therefore, in the simulated case using the random-walk model described above, the resulting long-time dispersion coefficient can be evaluated, and gives

$$D_{\alpha\alpha} = \frac{2}{3}k\frac{\delta t}{2}. \tag{5}$$

We have used the fact that the integral time-scale of a random process of fluid-velocity regeneration after δt (and random time-origin) is $\delta t/2$, and that the fluid's velocity variance is expressed as $2k/3$ (assumed constant).

Contributed by the Fluids Engineering Division for publication in the JOURNAL OF FLUIDS ENGINEERING. Manuscript received by the Fluids Engineering Division March 5, 1996; revised manuscript received October 9, 1997. Associate Technical Editor: D. E. Stock.

However, when δt is given by Eq. (3), several physical effects are not represented: (*a*) As τ_p increases, and approaches or exceeds the eddy turn-over or eddy-crossing time, the particle motion is known to become less responsive to the turbulence, and the Lagrangian integral time-scale increases. This leads to increased dispersion. Since δt does not depend on τ_p in the limit of low trajectory crossing, this effect is not accounted for in the standard approach. (*b*) As the mean relative velocity increases, particles have less time to interact with the eddies, and the effective agitation seen by the particles should weaken—leading to a decrease of dispersion coefficient. While this effect is accounted for in Eq. (3) through the dependence of T_c on relative velocity, it involves an abrupt transition due to the min operation. This transition is in practice smoothed out once an ensemble of many particles and fluctuating relative velocities is considered. Physically, however, the smooth crossover occurs due to a different mechanism: The existence of a range of turbulent eddy-sizes which will have different effects on the particles, and operate at different time-scales. Depending on the value of τ_p and relative velocity, the particle may still be responsive to the slower (larger) eddies in the spectrum, but be oblivious to the faster ones due to its inertia and/or trajectory crossing. (*c*) Another effect which a model should strive to reproduce (and which Eq. (3) does not accomodate) is that for large trajectory crossing effect, the dispersion in the directions transverse to the relative velocity is less than that in the longitudinal direction (Csanady, 1963).

In order to allow Lagrangian simulations to reproduce some of these effects, a number of more sophisticated stochastic models have been proposed in the past. Their main ingredient (see e.g., Berlemont et al., 1990; Zhou and Leschziner, 1991) is that the random fluid velocity is updated much more frequently than on a time-scale given by the large-scales of turbulence. In such a way, the particle can be subjected to random fluid motion occurring at a variety of time-scales and may respond to them accordingly. Another method, in which the fluid velocity is not directly given by random numbers but by the solution of a stochastic differential (Langevin) equation, has been proposed by Haworth and Pope (1987). Langevin models have been found desirable in order to satisfy "thermodynamic" constraints in the tracer-limit ($\tau_p \to 0$). The problem is to ensure that initially homogeneous particle distributions should not concentrate in certain regions, a problem that may occur in stochastic models if the mean-flow is inhomogeneous (see also Sawford, 1984; MacInnes and Bracco, 1992; Pope, 1987). Another advantage of Langevin models is their ability to reproduce consistently some inertial-range properties.

Similar to the work of Huang et al. (1993), the motivation of the present work is to include several features, such as particle inertia, crossing trajectory, and continuity effects into dispersion models, within as practical a framework as possible. To this end, we wish to maintain the essential feature of the standard "eddy-lifetime" approach, namely that random velocity perturbations are updated only at time-intervals dictated by large-scale turbulence variables, and not more often. This allows the use of relatively large time-steps when tracking the particles. However, we propose to choose the value of the time-intervals δt by using more realistic considerations than those leading to Eq. (3).

Huang et al. (1993) employ the analysis of Wang and Stock (1993) to prescribe interaction time and length scales (see also the review article by Stock, 1996). Recently, Graham (1996) has extended existing eddy-lifetime models by including additional discrete "if-statements" in the algortithms to mimic inertia, trajectory crossing and continuity effects. As explained below, the proposed approach differs from these efforts, mainly in the theoretical foundations based on which δt is selected.

2 Approach

An important parameter for particle dispersion is the Stokes number $S_p = \tau_p/\tau_L^f$, the ratio of τ_p, the particle response-time, to τ_L^f, the standard Lagrangian integral time of the fluid. Following Mei et al. (1991), instead of S_p, we employ a parameter bounded between 0 and 1, defined as

$$\gamma = \frac{S_p}{1 + S_p}. \tag{6}$$

Another important parameter is the slip number χ_r, the ratio of slip-velocity between phases ΔU and turbulence fluctuating (rms) velocity u'

$$\chi_r = \frac{\Delta U}{u'} = \frac{|\bar{\mathbf{u}} - \bar{\mathbf{v}}|}{\sqrt{(2/3)k}}. \tag{7}$$

Other parameters are the turbulence Reynolds number $\mathrm{Re} = (u' L_{11}/\nu)$ and the ratio of particle diameter to longitudinal integral scale, d_p/L_{11}. Since dispersion is dominated by large scales of turbulence, the usual expectation is that the effect of Reynolds number and d_p/L_{11} are relatively small. However, recent work by Mei and Adrian (1995) shows that turbulence Reynolds number can have a significant effect when going from low to moderate Reynolds numbers. We assume that the effect of particle-Reynolds number is already included in the value of τ_p. Naturally, if the particle loading is high, one expects turbulence modulation to occur, and then the number of relevant parameters and mechanisms increases considerably. Here we only consider one-way coupling, valid for low mass loading.

Thus, at this stage we assume that the dispersion coefficient depends on γ and χ_r. For convenience, this dispersion coefficient is made dimensionless with the fluid diffusivity,

$$D^*_{\alpha\alpha}(\gamma, \chi_r) = \frac{D_{\alpha\alpha}(\gamma, \chi_r)}{D_{\alpha\alpha}(0, 0)} = \frac{D_{\alpha\alpha}(\gamma, \chi_r)}{(2/3)k\tau_L^f}. \tag{8}$$

In Sections 3 and 4, we review previous theoretical and numerical results, in isotropic turbulence, where the dependence of dispersion coefficient $D^*_{\alpha\alpha}$ on γ and χ_r is explicitly found. Once the $D^*_{\alpha\alpha}$-value is known as function of the two parameters γ and χ_r, our proposed method regenerates the random velocity fluctuations in the α direction, at every δt_α, where

$$\delta t_\alpha = 2\,\frac{D_{\alpha\alpha}(\gamma, \chi_r)}{(2/3)k} = 2D^*_{\alpha\alpha}(\gamma, \chi_r)\tau_L^f. \tag{9}$$

From Eq. (5) we see that, by construction, this choice ensures that a stochastic, Lagrangian, simulation of dispersion in homogeneous turbulence will yield the same long-time dispersion coefficients as those of the previous analyses.

In order to apply Eq. (9), one must know the fluid Lagrangian integral time-scale τ_L^f. In the context of two-equation turbulence simulation, τ_L^f must be expressed as function of k and ϵ. While on dimensional grounds we have

$$\tau_L^f = \beta_1 \frac{k}{\epsilon}, \tag{10}$$

the numerical value of β_1 depends strongly on the details of the spatio-temporal structure of the largest eddies in the spectrum, and is thus not universal. In fact, as Mei and Adrian (1995) have shown recently, at low to moderate Reynolds numbers β_1 may also depend on Reynolds number. Given our constraint of working within the $k - \epsilon$ model, we have no choice but to use an empirical expression for β_1 and to keep in mind its lack of universality.

A related parameter that shall be found to be of relevance to this problem is the ratio of Lagrangian to the eddy turnover time scale L_{11}/u',

$$\beta_2 = \frac{\tau_L^f}{(L_{11}/u')}. \tag{11}$$

The following fit is consistent with experimental data of Sato

and Yamamoto (1987), as well as with an asymptotic result at large Reynolds number derived by Yakhot and Orszag (1986):

$$\beta_2(R_\lambda) = 0.33(1 + \exp[-(R_\lambda/40)^4]). \quad (12)$$

Here $R_\lambda = u'\lambda/\nu$ is the Taylor-scale Reynolds number. The dissipation ϵ and the Taylor micro-scale λ are related (Tennekes and Lumley, 1972) by

$$\epsilon = 15\nu u'^2/\lambda^2, \quad (13)$$

which leads to

$$R_\lambda = 2.6\,\frac{k}{\sqrt{\nu\epsilon}}. \quad (14)$$

As pointed out by Mei and Adrian (1995), for fixed k and ϵ the trend in Eq. (12) is that the fluid diffusivity (or τ_L^f) increases as the Reynolds number decreases, because the relative effect of the largest eddies (which govern transport) becomes more dominant at low Re.

In order to find β_1, L_{11} must be expressed as function of k and ϵ. We employ the standard relation

$$L_{11} = C_L\,\frac{k^{3/2}}{\epsilon}, \quad (15)$$

where C_L is a coefficient of order ~0.5. Finally, we obtain

$$\beta_1(R_\lambda) = 0.40C_L(1 + \exp[-(R_\lambda/40)^4]). \quad (16)$$

The precise value of the coefficient C_L will be selected by comparisons with experimental data of dispersion in isotropic turbulence, in Section 5.

3 Statistical Theory of Mei et al.

In this section, we present results from a theoretical analysis that is general enough to include the three effects that we wish to reproduce in simplified stochastic simulations. An analytically appealing approach for particle dispersion in random flows has been developed by Pismen and Nir (1978), Reeks (1977), and more recently, simplified and further examined by Mei et al. (1991).

The approach uses the relation (via a transfer function, (Tchen, 1947)) between velocity spectra of particles and fluid, as seen along particle trajectories. The latter is expressed as Fourier transform of the fluid's Eulerian velocity spatio-temporal correlation function. The argument for the spatial displacement in this expression combines both the deterministic drift motion (crossing trajectory) and random displacements of the particle. These random displacements are related to the particle's velocity correlation function, a step that is used to close the set of equations. The main approximation made is the so-called "independence approximation," due to Corrsin (1959), which states that the above-mentioned random displacement vector may be assumed to be statistically independent of *individual* Fourier modes of the fluid velocity. Another assumption is that the velocity field is a Gaussian variable, an assumption needed to evaluate expected values of exponentials of the random displacement vector. Finally, in order to perform the calculations, a Eulerian spectrum $\Phi_{ij}(\mathbf{k}, \tau)$ of the fluid velocity must be prescribed.

Mei et al. (1991) show that using a Gaussian spectrum of the form

$$\Phi_{ij}(\mathbf{k}, \tau) = \frac{16}{(2\pi)^{3/2}}\,k^2 e^{-2k^2}\left(\delta_{ij} - \frac{k_i k_j}{k^2}\right)e^{-(1/2)\tau^2}, \quad (17)$$

separable in space and time, further simplifies the approach, because an integration over wavenumbers can be done analytically. The remaining equations are solved iteratively. Once the Lagrangian particle-velocity spectrum is known, the long-time dispersion coefficient can be evaluated.

The results of Mei et al. (1991) are now presented. In the units of the spectrum in Eq. (17), $L_{11} = \sqrt{2\pi}$, and the velocity variance is $u'^2 = (1/3)\int \Phi_{ii}(\mathbf{k}, 0)d^3\mathbf{k} = 1$. The value for fluid dispersion resulting from Mei et al. (1991)'s calculations is $D_{11}(0, 0) = 0.913$. Since $u' = 1$, and $D_{11}(0, 0) = u'^2\tau_L^f$, the Lagrangian integral time-scale of the fluid, is $\tau_L^f = 0.913$, in the units of Mei et al. (1991). Then, the parameter S_p can be evaluated as follows:

$$S_p = \frac{\tau_p}{\tau_L^f} = \frac{1}{0.913}\,\tau_p, \quad (18)$$

where τ_p^{-1} was called β in Mei et al. (1991). The parameter χ_r (called λ in Mei et al. (1991)) does not need rescaling. Finally, the results are tabulated in Tables 1 and 2 and, for $\gamma = 0.523$, are displayed as circles in Fig. 1.

A convenient fit, consistent with the Csanady form (Csanady, 1963) at large χ_r, is given by

$$D^*_{\alpha\alpha}(\gamma, \chi_r) = \frac{1 + 0.35\gamma^2\exp(-0.128\chi_r^2)}{\sqrt{1 + (C_\alpha\beta_2\chi_r)^2}}, \quad (19)$$

where $C_1 = 1$ for dispersion in the direction of mean relative velocity, and $C_2 = C_3 = 2$ for dispersion in the transverse directions. We use the high Reynolds number limit of Eq. (12) $\beta_2 = 0.33$, since with this value a better fit is obtained than by using $\beta_2 = 0.913/\sqrt{2\pi} \approx 0.364$. Figure 1 shows the fit for the case $\gamma = 0.523$, compared to Mei et al.'s calculations.

For the sake of comparison, in Fig. 1 we also show dimensionless dispersion coefficients that arise from some earlier parameterizations. The dotted line is the model of Shuen et al. (1983), who took T_e in Eq. (3) as $T_e = \tau_L^f = \beta_1 k/\epsilon$ (with $\beta_1 = C_\mu^{3/4}\sqrt{3/2}$), and the crossing time as $T_c = -\tau_p \ln[1 - L_e/(\tau_p\Delta U)]$, with $L_e = \tau_L^f\sqrt{2k/3}$. In terms of variables used here, D^* becomes $D^*_{\mathrm{SCF}} = \min\{1, \ln[1 - (1 - \gamma)/(\beta_2\chi_r\gamma)]^{\gamma/(\gamma-1)}\}$. The dashed line is the model of Wang and Stock (1993) as used by Huang et al. (1993). They propose $T_e = \tau_L^f\beta_2^{-1}[1 - 0.644/(1 + St)^{0.4(1+0.01St)}]$, with $\beta_2 = 0.356$ and $St = \beta_2\gamma/(1 - \gamma)$ (their factor 2 is already included in Eq. (3)). The crossing time is given by $T_c = L_e/\Delta U$, with an angular dependence of L_e to account for the continuity effect. For the longitudinal direction, $T_c/\tau_L^f = L_e/(\tau_L^f\Delta U) = 1/(\beta_2\chi_r)$

Table 1 Nondimensional dispersion coefficient $D^*_{11}(\gamma, \chi_r)$ from theoretical analysis by Mei et al. (1991)

γ	0.064	0.214	0.523	0.8456	0.9910
$\chi_r = 0$	1.0001	1.0136	1.0880	1.2400	1.3527
$\chi_r = 0.5$	0.9877	1.0010	1.0732	1.2146	1.3143
$\chi_r = 1$	0.9522	0.9651	1.0311	1.1471	1.2157
$\chi_r = 2$	0.8345	0.8460	0.8915	0.9463	0.9663
$\chi_r = 3$	0.7009	0.7096	0.7352	0.7551	0.7599
$\chi_r = 4$	0.5852	0.5915	0.6049	0.6120	0.6132
$\chi_r = 5$	0.4948	0.4993	0.5063	0.5091	0.5095

Table 2 Nondimensional dispersion coefficient $D^*_{22}(\gamma, \chi_r)$ from theoretical analysis by Mei et al. (1991)

γ	0.064	0.214	0.523	0.8456	0.9910
$\chi_r = 0$	1.0001	1.0136	1.0880	1.2400	1.3527
$\chi_r = 0.5$	0.9735	0.9863	1.0550	1.1870	1.2764
$\chi_r = 1$	0.9006	0.9116	0.9656	1.0526	1.0961
$\chi_r = 2$	0.6900	0.6961	0.7157	0.7279	0.7265
$\chi_r = 3$	0.5019	0.5043	0.5064	0.5014	0.4977
$\chi_r = 4$	0.3758	0.3765	0.3745	0.3702	0.3684
$\chi_r = 5$	0.2955	0.2956	0.2934	0.2909	0.2901

(we have included a factor of 2 to make their model conform to the Csanady limit at high χ_r). In terms of variables used here, D^* becomes $D^*_{WS} = \min\{0.356^{-1}(1 - 0.644/[1 + 0.356\gamma/(1-\gamma)]^{0.4[1+0.00356\gamma/(1-\gamma)]}), 1/(\beta_2\chi_r)\}$.

Figure 1 illustrates that there are similarities and some differences among the models. At large χ_r, all display the Csanady limit. At low χ_r, the Shuen et al. model does not include the inertia effect, while the Wang and Stock model gives larger diffusivities in the limit of very large particle inertia, mainly because of the larger value specified for the ratio of Eulerian to Lagrangian integral time scale. An important distinction between the Shuen et al. and Wang and Stock models with the formulation of Mei et al. is that in the former two, χ_r is based on the fluctuating relative velocity instead of the mean relative velocity. Thus, the curves in Fig. 1 must be understood to hold for a given realization of the velocity fluctuation. To obtain the effective dispersion, one must average over velocity fluctuations which will significantly smooth the sharp step, and should reduce the difference between the Wang and Stock model with Mei et al.'s calculations.

4 Large-Eddy-Simulation of Deutsch

The theoretical analyses of Mei et al. and Wang and Stock reviewed in the previous section are based on several key assumptions. In order to complement the analysis with another option, and to ascertain a range of sensitivity to possible parametrizations, we also consider results by Deutsch (1992), who used forced Large-Eddy-Simulation to numerically evaluate dispersion of diverse types of particles in isotropic turbulence. The forcing was done so that the 3D radial energy spectrum is constant at all times. We shall employ his results concerning simulation THI3, which is a 64^3 modes case, with the following relevant hydrodynamic parameters (from Deutch's (1992) Table 1.1): Root-mean-square fluid velocity $u' = 0.3$ m/s ($k = 0.135$ m^2/s^2), integral longitudinal scale $L_{11} = 7.7 \times 10^{-3}$ m, rate of dissipation $\epsilon = 6.17$ m^2/s^3 and eddy turnover time-scale $L_{11}/u' = 0.026$ s. Also, the Lagrangian integral scale is $\tau^f_L = 0.0233$ s (Table 3.1b, Deutsch (1992)), hence $\beta_2 \sim 0.9$ for the simulation. For the case of zero trajectory crossing, six different particles are considered (all are heavy and thus the drag-force is the dominant momentum exchange mechanism). For $\chi_r = 0$, all $D_{\alpha\alpha}$ are equal in the different directions.

From Table 6.2 (Deutsch, 1992), we obtain the dispersion coefficient, and normalize it by $u'^2\tau^f_L$. The values are shown

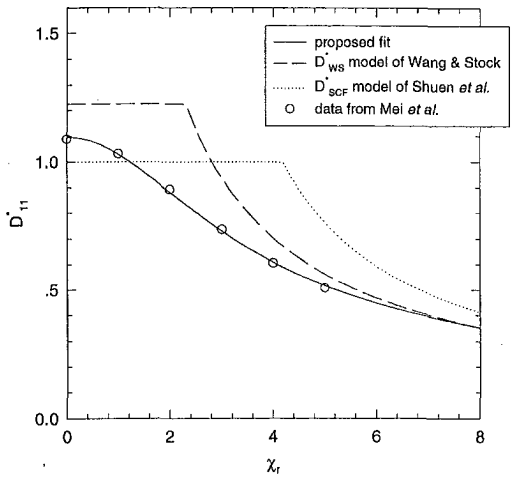

Fig. 1 Circles: Longitudinal dispersion coefficient $D^*_{11}(\gamma, \chi_r)$ for $\gamma = 0.523$ as function of χ_r, as obtained from Mei et al.'s (1991) analysis. Solid line: proposed fit. Dotted line: model of Shuen et al. (1983). Dashed line: model of Wang and Stock (1993). In implementations of the latter two models χ_r should be based on the fluctuating relative velocity, which should lead to a smoothing of the curve's sharp transition.

Table 3 Nondimensional dispersion coefficients from LES by Deutsch (1992)

γ	χ_r	D^*_{11}	D^*_{22}
0.0082	0	1.02	1.02
0.068	0	1.14	1.14
0.22	0	1.20	1.20
0.37	0	1.13	1.13
0.37	0.45	0.91	0.84
0.37	0.88	0.76	0.58
0.48	0	1.05	1.05
0.48	0.68	0.84	0.68
0.48	1.32	0.68	0.42
0.68	0	1.04	1.04
0.68	1.51	0.60	0.37
0.68	2.78	0.38	0.22

in Table 3. We notice that the dispersion behavior is non-monotonic. First, at increasing particle inertia, the dispersion coefficient increases. This behavior has also been observed by others and is thought to be due to increased particle correlation time. However, according to the LES results of Deutsch, after a peak is reached, the dispersion decreases again with increasing particle inertia. For the cases with trajectory crossing, three particle sizes are considered, (a) for $S_p \sim 0.59$, (b) for $S_p \sim 0.9$, and $S_p \sim 2.0$.

The next goal is to find a convenient fit. Taking into account that for large χ_r we wish to, again, recover the Csanady limit, and that for zero χ_r we reproduce the non-monotonic behavior found in Deutsch (1992), a very good fit is

$$D^*_{\alpha\alpha}(\gamma, \chi_r) = \frac{1 + 3.5\gamma \exp[-6.4\gamma^2]}{\sqrt{1 + (C_\alpha\beta_2\chi_r)^2}}, \qquad (20)$$

with $\beta_2 = 0.9$, where $C_1 = 1$ for dispersion in the direction of relative mean velocity and $C_2 = C_3 = 2$ for the transverse directions.

It should be kept in mind that a well-known drawback of using forced simulations is that the forcing at large-scales directly affects the dispersion dynamics, since transport is dominated by the largest eddies. Decaying simulations, on the other hand, are difficult to employ for our use because the parameters change during the decay.

5 Application and Comparison With Experiment

Particle trajectories are obtained from integrating

$$\frac{d^2x_{p,i}}{dt^2} = \frac{\bar{u}_i + u'_i - v_i}{\tau_p} + g_i, \quad i = 1, 2, 3 \qquad (21)$$

in time. The relaxation time τ_p is based on the Stokes drag. In our case we use Runge-Kutta integration and, for stability reasons, a time-step smaller than the particle response time. The fluid mean velocity $\bar{u}_\alpha$ is obtained from a $k - \epsilon$ code. The random fluid perturbation seen by the particle, u'_α, is obtained according to Eq. (2) using the turbulent kinetic energy k. Then, the "interaction" time δt_α is obtained from Eq. (9), or

$$\delta t_\alpha = 0.8C_L(1 + \exp[-(R_\lambda/40)^4])D^*_{\alpha\alpha}(\gamma, \chi_r)\frac{k}{\epsilon},$$

where $D^*_{11}(\gamma, \chi_r)$ and $D^*_{22}(\gamma, \chi_r)$ are given by the fits of Eqs. (19) or (20). The two parameters γ and χ_r are defined by Eqs. (6) and (7). In effect, we obtain two times $\delta t_{\alpha=1}$ and $\delta t_{\alpha=2}$, which are the times between two consecutive generations of $u'_{\alpha=1}$ and $u'_{\alpha=2}$, the fluctuating velocities in longitudinal and transverse directions to the mean relative velocity, respectively. $u'_{\alpha=1}$ and $u'_{\alpha=2}$ are kept constant during these times.

In order to distinguish between the $\alpha = 1$ and $\alpha = 2$ directions, and to obtain χ_r, we consider two approaches: In the first, we define a local "mean particle velocity" $\bar{v}$, which is com-

puted by averaging over a set of neighboring particles contained in some predetermined Eulerian cell. Then, the random fluctuation $u'_{\alpha=1}$ is taken to be colinear to $\bar{\mathbf{v}}$, and $u'_{\alpha=2}$ is used to generate the random components in the plane perpendicular to $\bar{\mathbf{v}}$. This approach requires that enough particles be present in each cell to define meaningful averages. The second approach simply uses the instantaneous velocity of the particle to define the $\alpha = 1$ (and the perpendicular) direction, and to compute the slip number χ_r. Then, the computation of one trajectory is independent of the others. While this approach is simpler to implement in practice, the theoretical arguments leading to our parametrization of dispersion require, in principle, to use the mean drift velocities and not the instantaneous values. Especially for small mean drift velocities, where the fluctuating velocity dominates, this simpler approach may cause significant errors.

Next, simulations are compared with the classic Snyder and Lumley (1971) experiments on the dispersion of solid particles in decaying grid turbulence. The mean velocity of the flow is taken in the x_1 (vertical) direction, and is constant, equal to $\bar{u}_1|_0 = 6.55$ m/s. In the experiments, the turbulence-generating mesh's size is $M = 2.54$ cm. Fluid statistics are homogeneous in the x_2 and x_3 directions. The dispersion of particles in the x_2 and x_3 directions is computed starting from a downstream point at $x_1|_0/M = 68.4$. The turbulence characteristics at this location are $k_0 = 0.03\ \mathrm{m^2/s^2}$, and $\epsilon_0 = 0.139\ \mathrm{m^2/s^3}$. In this simple case, the mean fluid velocity is constant, $\bar{u}_1(x) = \bar{u}_1|_0$, while the kinetic energy and dissipation rate evolve with x_1 according to the standard $k - \epsilon$ equations, for decaying turbulence according to

$$k(\mathbf{x}) = k_0\left[1 + (C_{\epsilon 2} - 1)\frac{x_1 - x_1|_0}{\bar{u}_1|_0}\frac{\epsilon_0}{k_0}\right]^{-[1/(C_{\epsilon 2}-1)]} \quad (22)$$

$$\epsilon(\mathbf{x}) = \epsilon_0\left[1 + (C_{\epsilon 2} - 1)\frac{x_1 - x_1|_0}{\bar{u}_1|_0}\frac{\epsilon_0}{k_0}\right]^{-[C_{\epsilon 2}/(C_{\epsilon 2}-1)]} \quad (23)$$

with $C_{\epsilon 2} = 1.92$. We use this analytic solution to the $k - \epsilon$ equations since, for this flow, it is available.

For the dispersed phase, a sample consisting of 10^4 particles is released at $x_1|_0$. The initial particle velocity is set equal to the particle's terminal velocity. In order to evaluate $\bar{\mathbf{v}}$, the mean particle velocity required (in the first approach) to distinguish both longitudinal and lateral dispersion directions, we employ a $64 \times 1 \times 1$ grid and average the particle velocities falling into a given cell. The overall size of the discretized domain is $64\Delta x_1 = 3.8$ m in the streamwise direction, and $\Delta x_2 = \Delta x_3 = 0.3$ m in the spanwise directions. This typically provided about 2.10^3 particles in each cell (for the lightest particles, at the end of calculation). We checked that the mesh size and number of particles had negligible influence on the results. The independency of the results on number of particles was tested by changing this parameter over large factors: for example, increasing the number of particles from 10^3 up to 10^4 changes the particle dispersion by only about 2 percent. However, in this flow the particles' mean velocity is quite uniform. We expect that more particles may be needed when smaller meshes are involved, typically for complex geometry applications.

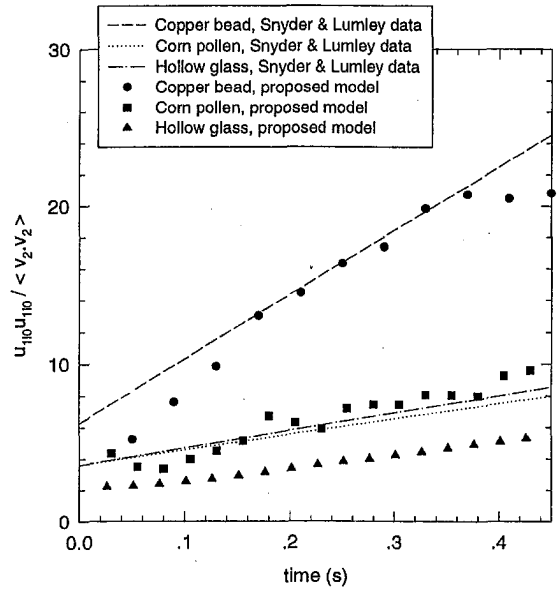

Fig. 2 Inverse lateral kinetic energy of particles, in decaying isotropic turbulence, as function of time. Lines: Fit through data by Snyder and Lumley (1971). Symbols: results from proposed random-walk model, using parametrization based on the calculation of Mei et al.

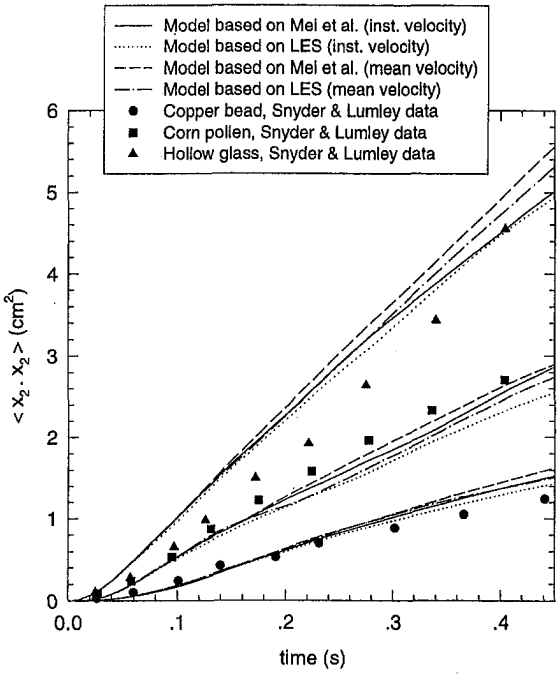

Fig. 3 Lateral dispersion of particles $\langle x_2^2(t) \rangle$ in decaying isotropic turbulence, as function of time. Symbols: measurements by Snyder and Lumley (1971). Lines: results from proposed random-walk model, using parametrizations from both theory and LES.

Figure 2 shows the computed lateral kinetic energy of particles, as compared to a fit through the Snyder and Lumley measurements. A good agreement is found, except for the lightest particle (hollow glass) for which the simulation does not match the experimental points and has about the same energy level as the fluid. Considering the fact that Snyder & Lumley mention that their measurement error for hollow glass particles may have lead to significant underestimation of their energy, we do not ascribe much significance to the discrepancy.

Figure 3 shows the computed lateral dispersion $\langle x_2^2(t) \rangle$, as function of downstream distance (or time $t = x_1/\bar{u}_1$), compared to the experimental results. A reasonable overall agreement is observed. Also, we find that the results from the theoretical and LES parametrizations differ very little. This is because in the parameter regime of this experiment, both approaches yield very similar dimensionless dispersion coefficients. Some discrepancy is observed between using the instantaneous particle velocity and the cell-averaged particle velocity, to determine χ_r and the longitudinal and transverse directions. As expected, using the instantaneous particle velocities yields slightly larger drift velocities, which causes the dispersion coefficient to fall slightly below that of the case using the particle's mean velocity.

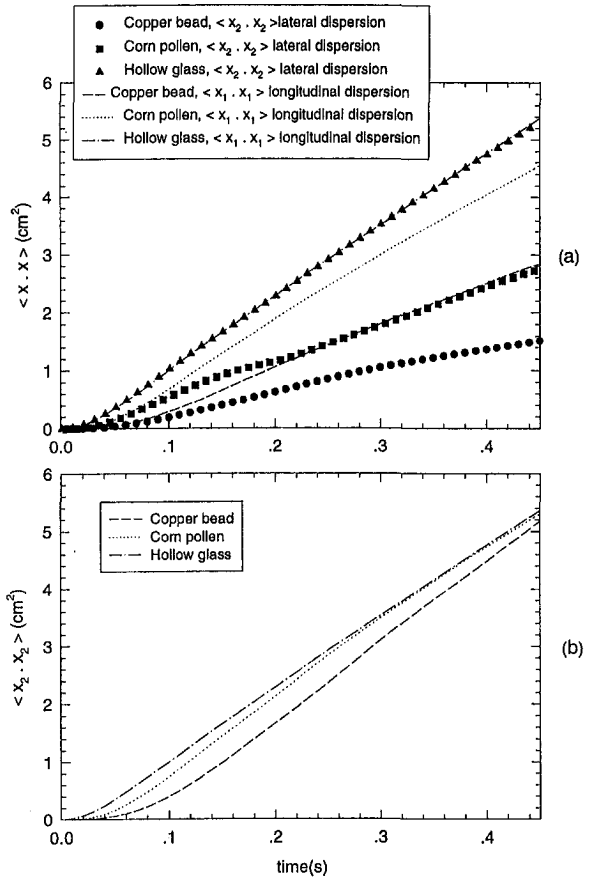

Fig. 4 (*a*) Comparison between lateral and longitudinal dispersion in decaying isotropic turbulence with slip, from proposed random walk model (local mean approach). (*b*) Lateral dispersion from proposed random walk model without slip, for different particle inertias (local mean approach).

These results were obtained by setting $C_L = 0.36$, which was arrived at after some experimentation. This value is about two times larger than the value of 0.15 used by Gosman & Ioannides (1984). With this value, the simulation yielded values of β_1 going from 0.159 up to 0.166, as time (or downstream distance) increases. For β_2, values between 0.360 and 0.377 were obtained. The Reynolds number R_λ varied from 49.7 down to 47.3. For reference, these values may be compared with the simulation of Luu et al. (1993), using a continuous Lagrangian model. In their simulation of the Snyder and Lumley experiment, they took values $\beta_1 = 0.16$ and $\beta_2 = 0.40$ in order to obtain good results. Ormancey (1984) took $\beta_1 = 0.21$ and $\beta_2 = 0.40$, in order to simulate the same experiment with a two-particles Lagrangian model. The fact that the present results show reasonable agreement with experimental data for three vastly different particle types, after adjusting only one free parameter, is encouraging.

In order to illustrate the new effects that are included in our simple random walk model, in Fig. 4(*a*) we exhibit the 'continuity effect' by comparing the dispersion in the direction of relative velocity, $\langle (x_1 - \langle x_1 \rangle)^2 \rangle$, with the weaker lateral dispersion $\langle x_2^2(t) \rangle$. As expected, the difference is more pronounced for the heavier particles, which have larger relative velocity. The effect of increasing particle inertia for the case of zero slip velocity ($\chi_r = 0$) is shown in Fig. 4(*b*). In this case we set $\mathbf{g} = 0$, and longitudinal and lateral dispersion are equivalent. As can be seen, at long times the heavier particles disperse more rapidly than the lighter ones (the slope in the curve is larger).

6 Conclusions

A simple procedure is proposed to include several effects into existing schemes for simulation of particle dispersion within two-equation turbulence modeling. The interaction time is selected using results of previous theoretical or LES analyses. Through simple parametrization of these results, we are able to include dependence on particle response time and trajectory crossing effect, as well as the continuity effect. Application to dispersion in decaying isotropic turbulence shows acceptable agreement with experimental data.

Limitations of the approach are the following: (*a*) The theoretical and LES results on which are parametrization is built refer to homogeneous isotropic turbulence. Errors may occur when the proposed approach is implemented in non-homogeneous environments (where k, ϵ and the relative velocities depend strongly on position and/or time), and where the fluid's real energy spectrum may be quite different from those assumed in the theoretical or LES studies. While errors may possibly be decreased by employing the local values of k, ϵ when evaluating Δt_α, one is still relying on a strong assumption of "quasi-equilibrium." (*b*) The approach is based on matching long-time dispersion properties of the random walk with that of the theory or LES. At short times (short with respect to the interaction time itself), e.g. just after release of particles into the flow, there is no guarantee that the random walk approach with prescribed interaction times will lead to accurate predictions of short-time particle dispersion. (*c*) Random-walk models of single non-interacting particles typically do not explicitly enforce the divergence-free condition for the particle velocity field, required in the limit $S_p = 0$ (fluid particles). Our version suffers from the same deficiency.

In spite of these limitations, the proposed approach allows to include in a practical fashion more detailed effects of particle dispersion in the context of eddy-lifetime modeling, which allows the use of large time steps. We point out that the approach may be extended to include other effects besides particle inertia and trajectory crossing. For instance, Mei and Adrian (1995) have repeated the calculation of Mei et al. (1991) using more general energy spectra, including Reynolds number effects. Such results could be incorporated by letting $D_{\alpha\alpha}$ depend also on Re. Furthermore, effects of Basset forces on particle-turbulence interaction could be included, by parameterizing the results of Mei et al. (1991) for the case of finite density ratio.

Acknowledgments

We wish to thank Prof. R. Mei for providing us with the tabulated results for D_{11} and D_{22}. CM would like to acknowledge the financial support and hospitality received at CERFACS during his visit.

References

Berlemont, A., Desjonqueres, D., and Gouesbet, G., 1990, "Particle Lagrangian Simulation in Turbulent Flows," *International Journal of Multiphase Flow*, Vol. 16, pp. 19–34.

Corrsin, S., 1959, "Progress Report on Some Turbulent Diffusion Research," *Advances in Geophysics*, Vol. 6, pp. 161.

Csanady., G. T, 1963, "Turbulent Diffusion of Heavy Particles in Atmosphere," *Journal of Atmospheric Sciences*, Vol. 20, pp. 201–208.

Deutsch, E., 1992, "Dispersion de particules dans une turbulence homogène isotrope stationnaire calculée par simulation numérique directe des grandes échelles," Ph.D., Electricité de France.

Gosman, A. D., and Ioannides, E., 1981, "Aspects of Computer Simulation of Liquid-Fuelled Combustors," *Journal of Energy*, Vol. 7, pp. 482–490.

Graham, D. I., 1996, "An Improved Eddy Interaction Model for Numerical Simulation of Turbulent Particles Dispersion," ASME JOURNAL OF FLUIDS ENGINEERING, Vol. 228, pp. 819–823.

Graham, D. I, and James, P. W., 1996, "Turbulent Dispersion of Particles Using Eddy Interaction Models," *International Journal of Multiphase Flow*, Vol. 22 (1), pp. 157–175.

Haworth, D., and Pope, S., 1987, "A Generalized Langevin Model for Turbulent Flows," *Physics of Fluids*, Vol 29, pp. 387–405.

Huang, X, Stock, D. E., and Wang, L. P., 1993, "Using the Monte-Carlo Process to Simulate Two-Dimensional Heavy Particles Dispersion," ASME/FED, *Gas-Solid Flows,* ASME FED-Vol. 166, pp. 1897–1913.

Luu, Q. Q., Fontaine, J. R., and Aubertin, G., 1993, "A Lagragian Model for Solid Particles in Turbulent Flows," *International Journal of Multiphase Flow,* Vol. 19, pp. 347–367.

MacInnes, J. M., and Bracco, F. V., 1992, "Stochastic Particle Dispersion Modeling and the Tracer-Particle Limit," *Physics of Fluids A,* Vol. 4, pp. 2809–2824.

Mei, R. W., Adrian, R. J., and Hanratty, T. J., 1991, "Particle Dispersion in Isotropic Turbulence Under Stokes Drag and Basset Force with Gravitational Settling," *Journal of Fluid Mechanics,* Vol. 225, pp. 481–495.

Mei, R. W., and Adrian, R. J., 1995, "Effect of Reynolds Number on Isotropic Turbulent Dispersion," ASME JOURNAL OF FLUIDS ENGINEERING, Vol. 117, pp. 402–409.

Ormancey, A., 1984, "Simulation du comportement de particules dans des ecoulements turbulent," Ph.D., Ecole Sup. Mines de Paris.

Pismen, L. M. and Nir, A., 1978, "On the Motion of Suspended Particles in Stationary Homogeneous Turbulence," *Journal of Fluid Mechanics,* Vol. 84, pp. 193–206.

Pope, S. B., 1987, "Consistency Conditions for Random-Walk Models of Turbulent Dispersion," *Physics of Fluids,* Vol. 30, pp. 2374–2379.

Reeks, M. W., 1977, "On the Dispersion of Small Particles Suspended in an Isotropic Turbulent Fluid," *Journal of Fluid Mechanics,* Vol. 83, pp. 529–546.

Sato, Y., and Yamamoto, K., 1987, "Lagrangian Measurement of Fluid-Particle Motion in an Isotropic Turbulent Field," *Journal of Fluid Mechanics,* Vol. 175, pp. 183–199.

Sawford, B. L., 1983, "The Basis for, and Some Limitations of, the Langevin Equation in Atmospheric Relative Dispersion Modelling," *Atmospheric Environment,* Vol. 18, pp. 2405.

Shuen, J.-S., Chen, L.-D., and Faeth, G. M., 1983, "Evaluation of a Stochastic Model of Particle Dispersion in a Turbulent Round Jet," *American Institute of Chemical Engineering Journal,* Vol. 29, pp. 167–170.

Snyder, W. H., and Lumley, J. L., 1971, "Some Measurements of Particle Velocity Auto-Correlation Functions in a Turbulent Flow," *Journal of Fluid Mechanics,* Vol. 48, pp. 41–71.

Stock, D. E., 1996, "Particle Dispersion in Flowing Gases—1994 Freeman Scholar Lecture," ASME JOURNAL OF FLUIDS ENGINEERING, Vol. 118, pp. 4–17.

Tchen, C. H., 1947, "Mean Value and Correlation Problems Connected with the Motion of Small Particles Suspended in a Turbulent Fluid," Ph.D., Delft Univ., The Hague.

Tennekes, H., and Lumley, J. L., 1972, *A First Course in Turbulence,* The MIT Press, Cambridge, MA.

Wang, L. P., and Stock, D. E., 1993, "Dispersion of Heavy Particles by Turbulent Motion," *Journal of Atmospheric Sciences,* Vol. 50 (13), pp. 1897–1913.

Yakhot, V., and Orszag, S., 1986, "Renormalization Group Analysis for Turbulence. I. Basic Theory," *Journal of Scientific Computing,* Vol. 1, pp. 3–51.

Yuu, S., Yasukouchi, N., Hirosawa, Y., and Jotaki, T., 1978, "Particle Turbulent Diffusion In a Dust Laden Round Jet," *American Institute of Chemical Engineering Journal,* Vol. 24, pp. 509.

Zhou, Q., and Leschziner, M. A., 1991, "A Time-Correlated Stochastic Model for Particle Dispersion in Anisotropic Turbulence," *8th Turbulent Shear Flow Symposium.*

Alternate Eddy Shedding Set Up by the Nonaxisymmetric Recirculation Zone at the Exhaust of a Cyclone Dust Separator

A. J. Griffiths
Senior Lecturer.

P. A. Yazdabadi
Researcher.

N. Syred
Professor,
Chair in Mechanical Engineering.

Division of Mechanical Engineering
and Energy Studies,
University of Wales, Cardiff,
P.O. Box 685, Cardiff,
United Kingdom, CF2 3TA

Two cyclone dust separators with geometric swirl numbers of 3.324 and 3.043 were used to analyze the motion of the complex three-dimensional time dependent motion set up in the free exhaust. A quantitative analysis of the flow was carried out, obtaining time dependent velocity measurements with the use of laser Doppler anemometry (L.D.A.) techniques. The investigations highlighted a eddy or vortex shedding mechanism in two distinct areas of the flow. This was in part caused by a reverse flow zone and a precessing vortex core within the exhaust region of the separator. Changes in the Reynolds number by a factor of 2 were observed to have no effect on the main characteristics of the flow. Some changes were seen in the flow structure with change in swirl number, particularly the size of the reverse flow zone and the position of the large engulfment vortices.

1 Introduction

The cyclone separator in its many forms is a device which has been the subject of numerous investigations. Until recently little was known about the complicated details of the cyclone flow because the object of a large portion of the previous investigations was only the measurement of the gross behavior of the cyclone (Shepard and Lapple, 1939; Kelsall, 1952; Smith, 1962). A large amount of experimental data exists on cyclone performance (Ter Linden, 1949; Stairmand, 1951; Boysan et al., 1983) which forms the basis of semi-empirical correlations on which current design practice is almost entirely based. Despite the wealth of performance data, detailed information with regard to the structure of the turbulent flow in cyclone separators is conspicuously lacking (Gupta, 1979), especially that associated with the exhaust flow.

In many process industries these devices are used in a continuous mode to improve product recovery and conversion within the process. These units are sited at the downstream end of the main reactor plant and are thus connected with a complex array of pipework. The complex flow patterns in the exhaust are in part responsible for induced vibration and in some instances catastrophic failure of the plant. Thus vibration can be triggered by the flow regime and regular fluid periodicity, especially at the exhaust region and can readily resonate with instabilities leading to unacceptably high amplitudes of vibration.

Few studies have endeavored to establish the similarities between the various types of instability phenomenon. Three main forms of instabilities can be found which can be summarized as:

1. chamber instabilities
2. system instabilities
3. intrinsic instabilities

Types 2 and 3 are usually found in combustion processes and are only stated for completeness. Chamber instabilities include acoustic, shock, and fluid dynamic types (Williams, 1993). Acoustic instabilities, such as Helmholtz and Organ Pipe, are characterized by the propagation of acoustic waves in the main chamber. Fluid dynamic instabilities are related to the establishment of certain flow patterns, especially that of the vortex shedding mechanism (Williams, 1993). The mechanism is also sensitive to pressure changes due to the acoustic oscillations. Coupling can take place with the net result of larger amplitude pressure oscillations and hence catastrophic failure of the mechanical system (Gupta et al., 1977; Claypole et al., 1986; Van der Akker et al., 1992).

The standard solution to a vibration problem is to absorb the vibrations after they are produced. Quarter wave damping tubes and noise absorbent lining materials are used quite extensively for this purpose. However, they only damp out the resultant oscillations and do not attack the underlying cause. Also extensive bracing of both cyclones and interconnecting pipework has been undertaken with limited success. However, the mode of vibration still remains.

This study has sought to further improve the understanding of the structure of the turbulent vortex flow at the exhaust of a cyclone dust separator. Specifically analyzed was the precessing vortex core and the action of two vortex shedding mechanisms set up in the axial/radial plane. A quantitative analysis of the flow was carried out, obtaining velocity measurements with the use of laser doppler anemometry (L.D.A.) techniques in a time dependent mode.

2 Flow Inside a Cyclone Separator

The flows inside a cyclone separator have been characterized in the literature and have normally been assumed to be rotationally symmetrical with the largest component being the tangential velocity (Reydon and Gavin, 1981; Rhode et al., 1983). Radial and axial components are always of a much lower level, but are very significant in terms of secondary flow patters and particle separation characteristics. This work will show that certainly in the exhaust nozzle these assumptions are erroneous.

2.1 Exhaust Flows From Cyclone Separators. Little attention has been paid in the literature to the flows at the exhaust of cyclone dust separators except to assume that the flow is of

Contributed by the Fluids Engineering Division for publication in the JOURNAL OF FLUIDS ENGINEERING. Manuscript received by the Fluids Engineering Division November 26, 1993; revised manuscript received August 4, 1987. Associate Technical Editor: D. E. Stock.

a Rankine vortex type superimposed on a mean flow in the axial direction. The radial tangential velocity profile is normally assumed to follow a law of form $w.r^n$ = constant where $0.5 < n < 0.8$ for cyclonic flows (Linoya, 1953).

It is now known that under many operating conditions the vortex flow in the exhaust can start to precess about the central axis of the system (Syred and Beer, 1972a; Syred and Beer, 1972b; Syred et al., 1973; Gouldin et al., 1984) forming a coherent structure called the precessing vortex core (P.V.C.) phenomena. Associated with the P.V.C. is a reversed flow zone, which is offset from the central axis, and also provides the feedback mechanism for the P.V.C. phenomena (Gupta, 1979; Chao et al., 1991; Yazdabadi et al., 1992).

The result of this type of flow regime, especially at the exhaust of a cyclone, is akin to a large out of balance mass of fluid/particles rotating at a high swirl velocity. Thus vibration may be encountered, caused, or initiated by the flow instability set up by the P.V.C. (Yazdabadi et al., 1994), and coupling may occur with acoustic instabilities.

In addition to the P.V.C., there is another associated instability found with vortex flows (Syred and Beer, 1972b; Syred et al., 1973) termed the axial/radial eddy. Water models have shown the existence of eddy shedding in the axial/radial direction from the exhaust nozzles of swirl burners, especially at high Reynolds numbers (Gupta, 1979). The P.V.C. phenomena normally dissipates by $L/D = 1$ (Syred et al., 1973) but the axial/radial eddy often persists up to $L/D = 10$ (Syred et al., 1973) with consequences for coupling with other system instabilities.

Most of the studies examining the presence of fluid flow instabilities contained within, or at the exhaust of vortex/swirling flow devices, have been concerned with the P.V.C. The study and characterization of eddy shedding in the axial radial plane has been limited, and usually only considered as an aside to the P.V.C.

2.2 Characterization of Swirling Flows and the P.V.C.

Swirling flows results from the application of a spiralling motion, to the flow swirl component, sometimes described as a tangential or azimuthal component imparted to the flow; for cyclones this is achieved by direct tangential entry into the chamber.

Previous studies have shown that the degree of swirl imparted to the flow has a large-scale effect on the flow field, growth, entrainment, and decay (Gupta, 1979). The degree of swirl is usually characterized by a swirl number, S, which is a nondimensional number representing axial flux of the swirl momentum divided by axial flux of axial momentum times the equivalent nozzle radius. The flow pattern in cyclones is extremely complicated and it is difficult to define one characteristic swirl number, because the axial flow rate is not constant. To overcome this problem, a geometric swirl number, Sg, has been defined based on the physical shape. Hence

$$Sg = \pi R_e \cdot R_o / A_t$$

Where

Sg = geometric swirl number
R_e = exhaust port radius
R_o = radius of the cyclone body
A_t = square inlet area (sometimes called throat area)

Most cyclone dust separators operate with swirl numbers >2 and thus if conditions are suitable (i.e., sudden expansion) a reverse flow zone and P.V.C. will develop at the exhaust. Even with long and often curved radius exhaust ductwork, vortex flow will persist for many diameters and give rise to the P.V.C. phenomena even at small junctions/discontinuities, etc. The frequency of the P.V.C. is then transmitted back through most of the ductwork into the swirl generator (or cyclone dust separator in this instance). It has been previously noticed via various flow visualization studies that associated with the P.V.C. phenomena are other types of coherent structures (Syred et al., 1973; Williams, 1993; Yazdabadi et al., 1994), these include an axial/radial eddy shed from the inside edge of the precessing vortex core/boundary of the recirculation zone and engulfment/entrainment eddies on the outside of the flow; these appear to be part of the mechanism which causes very high entrainment rates with swirling jets. This paper thus follows on from recent previous work which elucidated the P.V.C. phenomena in detail both experimentally and with models (Chao et al., 1991; Yazdabadi et al., 1992) in describing associated coherent structures and relating them to the P.V.C. phenomena.

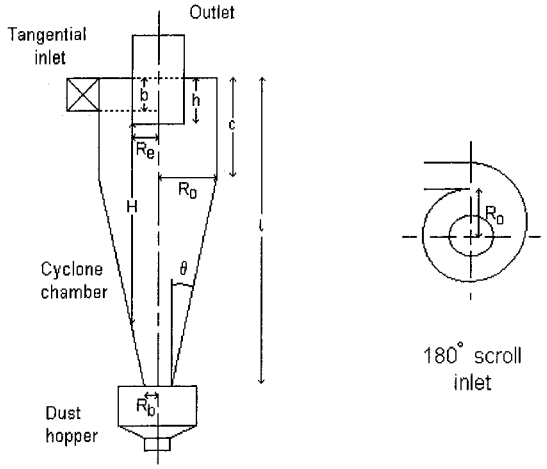

Fig. 1 Typical Defining Parameters for a cyclone

3 Experimental Analysis

Under examination were two separate laboratory scale cyclone dust separators with geometric swirl numbers of 3.043 and 3.324; these were both examined at two separate flowrates, thus creating four tests in total. A schematic diagram of a cyclone dust separator is shown in Fig. 1. Experiments were carried out to obtain a quantitative analysis of the flow by obtaining velocity measurements. These measurements were carried out by a Dantec dual beam or differential L.D.A. system operating in the back scatter mode. Seeding of the flow was carried out using smoke via a Rosco 4500 smoke system, operating with a Rosco fog fluid which provided smoke particles in the size range of 0.25 to 0.6 microns. The smoke system was attached the inlet air supply of the cyclone apparatus.

The optical arrangement employed a two-color system, using the blue and green lines of a Coherent Innova 70 series argon-ion laser. The single beam emitted by the laser was split into four separate beams, two in the green spectrum (λ = 514.5 nm) and two in the blue spectrum (λ = 488.0 nm). A plano convex lens (focal length of 600 mm) focused the beams into a single control volume producing two independent interference fringe patterns. This permitted the simultaneous measurement of two velocity components.

The laser probe incorporating both the light emitting and back-scatter receiving optics was mounted on a computer controlled, motor driven traversing unit. The laser beams were carefully aligned such that the control volume was located at the central axis of the exhaust of the cyclone under consideration. The closest distance the laser control volume could be brought to the cyclone exhaust was 2 mm for the cyclone with a geometric swirl number of 3.043 and 6 mm for the cyclone with a geometric swirl number of 3.324. These limitations arise from the configuration of the cyclone and the L.D.A. system.

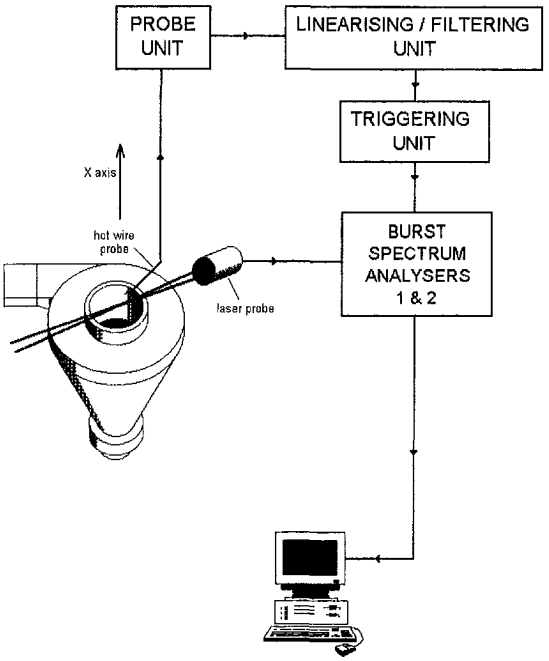

Fig. 2 Schematic diagram of the experimental setup

A hot-wire probe, utilizing linearizing and filtering equipment, was positioned (so as to be sensitive to tangential and radial velocities and insensitive to axial velocities) 90 degrees counter-clockwise from the line of the incoming light beams, close to the outer edge of the exhaust nozzle. A clear sinusoidal P.V.C. signal was obtained of regular frequency, as is well known in the literature (Syred et al., 1972a; Gupta et al., 1977). This was input into a triggering unit, which output a synchronized square wave, used to reset the L.D.A. time base after each cycle of the P.V.C. Figure 2 highlights the experimental configuration for the trigger system.

This meant that for a specific radial position the instantaneous velocity variations with time for several cycles of the P.V.C. could be superimposed over one another. These data were presented as a scatter diagram. Thus representative mean and r.m.s instantaneous rotating velocity values for an averaged single P.V.C. cycle could be produced. This is commonly termed phase averaging and is a technique derived from L.D.A. work in reciprocating engines.

The laser control volume was traversed from the center of the flow to beyond the extremities of the cyclone exhaust under consideration in the x direction. Velocity measurements for the axial and radial components were taken every 2 mm.

The acquired data was recorded on an IBM PC-AT compatible computer using Dantec, menu driven software. At the completion of each traverse the laser control volume was relocated at the centre of the system and elevated either 2 mm or 4 mm depending on the cyclone under test. The process was then repeated until the laser control volume was greater than half an exit diameter above the cyclone exhaust. At each measurement point axial and radial components of the flow were recorded,

Table 1 Experimental cyclones' operating conditions

Test no.	Sg	Re
1	3.324	20,000
2	3.324	11,850
3	3.043	40,910
4	3.043	24,240

(Reynolds numbers are based on average axial velocity in the exhaust nozzle.)

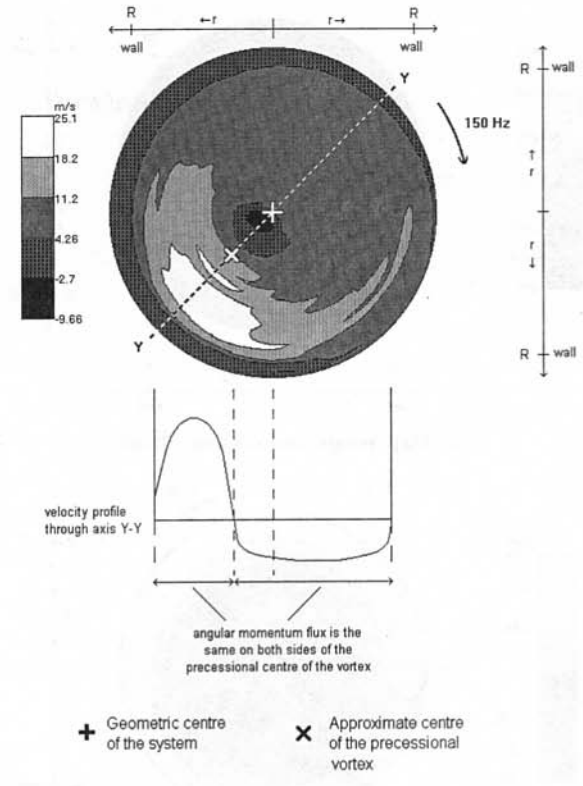

Fig. 3(*a*) Mean tangential velocities

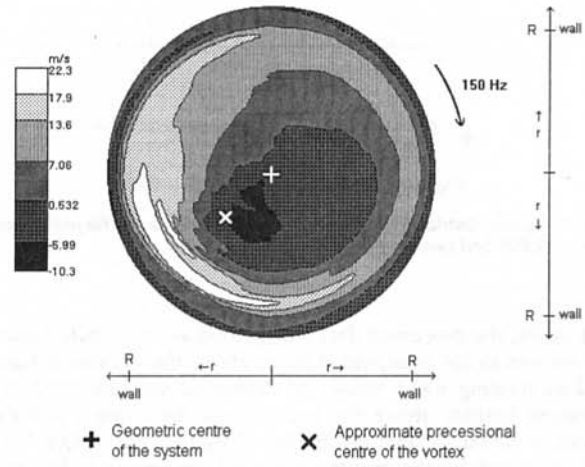

Fig. 3(*b*) Mean axial velocities

Fig. 3 Spatial distribution of rotating velocities at a Reynolds number = 28,500, geometric swirl number = 3.043 and height above exhaust = *D*/20

and the data were presented as a mean velocity time curve for a complete cycle of the P.V.C. From these data derivations of rotating mean axial and radial velocities were made by digitizing each velocity/time curve for a complete P.V.C. cycle. Sixteen identical radial paths, each separated by 22.5 degrees (i.e., one sixteenth of the period of rotation of the P.V.C. cycle) were chosen and velocity data tabulated as a function of radius.

During each trial 10,000 data points were recorded. The turbulence intensity levels were of the order 0.9. This required a minimum sample size of 1500 data points to ensure confidence limits of 99 with 5 percent error. At the trial data rate, confidence limits of 99 percent ensured a 1 percent error (Bates, 1979). Furthermore, the trial data rate gave an inaccuracy of less than 2 percent in the measured turbulence intensity (Bates, 1979). Thus giving a high degree of confidence of the recorded data.

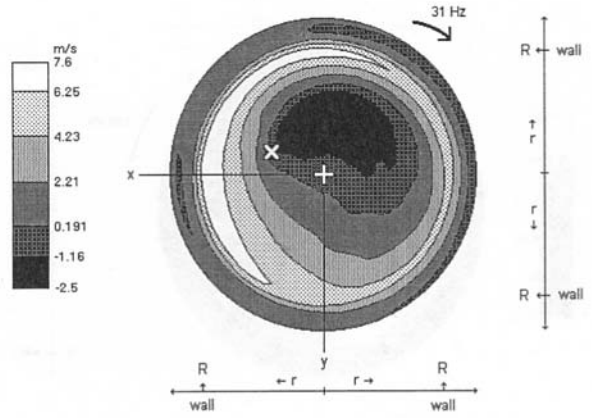

Fig. 4(*a*) Height from exhaust = *D*/20

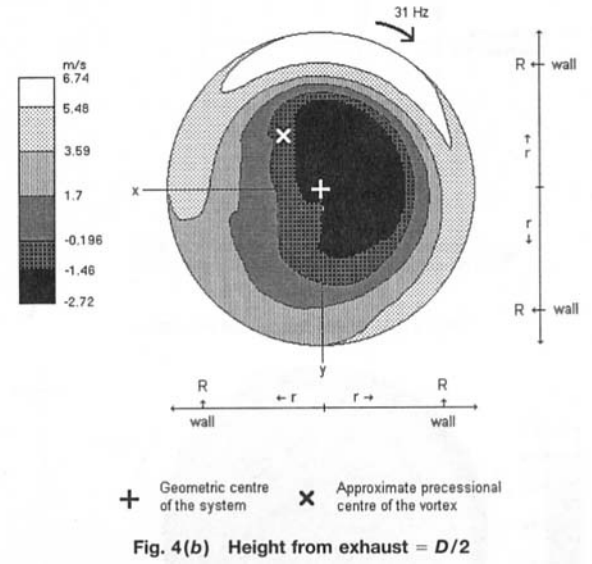

Fig. 4(*b*) Height from exhaust = *D*/2

Fig. 4 Spatial distribution of rotating axial velocities at a Reynolds number = 19,600 and geometric swirl number = 3.324

Finally, the processed data was plotted as axial/radial velocity vectors in the axial/radial plane above the cyclone exhaust, and as rotating mean axial and tangential velocity profiles at different heights above the cyclone exit by using a software package called "Quantitative Flow Visualisation" (Q.F.V.).

Unfortunately, the profiles produced are known to be prone to P.V.C. jitter causing slight changes in the trigger point from cycle to cycle. Obviously the size of the control volume (effectively 2 mm long) also affected the sharpness of the results (commonly called "broadening"). Accuracy of these rotating mean velocity measurements is estimated to be ±5 percent for velocities > 4 m/s, ±10 percent for velocities < 4 m/s (Kline and McClintok, 1953).

4 Preliminary Analysis of Results

The operating conditions of the cyclones are highlighted in Table 1 and as discussed in the last section, the flows at the exhaust nozzle of the two cyclone dust separators freely exhausting to atmosphere have been characterized. Mean axial and radial velocities for the two geometric swirl numbers at different heights above the cyclone exhaust are illustrated by the mean rotating tangential and axial velocity fields, Figs. 3(*a*) and 3(*b*). Figures 4 and 5 give more specific detail of rotating axial velocity fields for the two swirl numbers while Figs. 6 to 11 show axial/radial velocity vectors.

For each measurement point a mean phase averaged rotating velocity value for an average single P.V.C. cycle could be produced. The start of a cycle is indicated by the electronics, triggered by the hot wire signal. The resulting data can be processed and interpolated between the measured points to give among other data. Rotating mean phase averaged tangential, axial or radial velocity fields, Figs. 3, 4, and 5. Axial/radial velocity vector diagrams across a diameter at several sections corresponding to different times in the P.V.C. cycle or to different sections in an instantaneously stationary flow.

5 Discussion of Results

Figures 3(*a*) and 3(*b*) show the mean rotating tangential and axial velocity fields at the exhaust of the cyclone operating at Sg = 3.043 and Re = 28500 with a precessional frequency of 150 Hz. Figure 3(*a*) shows the main features of the rotating mean tangential velocity field. The geometric center of the system and approximate center of precession of the vortex have both been marked. This has been determined from the zero swirl or tangential velocity component within the flow and is inline with the peak flow regions. A region of negative tangential velocity can be observed between these two centers and this merely arises from the choice of coordinate center for the tangential velocity. When the precessional center of the vortex is used a tangential velocity profile, as shown in the bottom of Fig. 3(*a*), is produced with no negative velocities. Angular

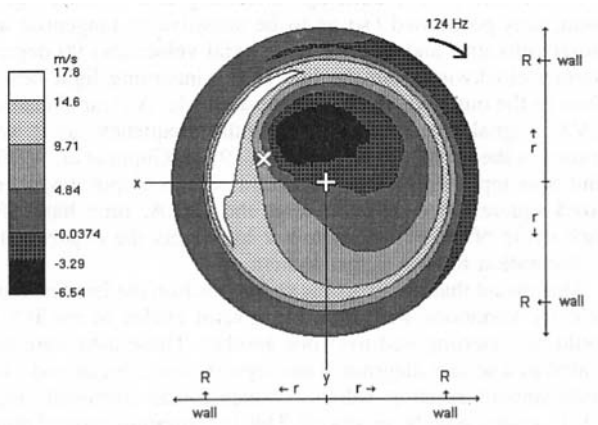

Fig. 5(*a*) Height above exhaust = *D*/25

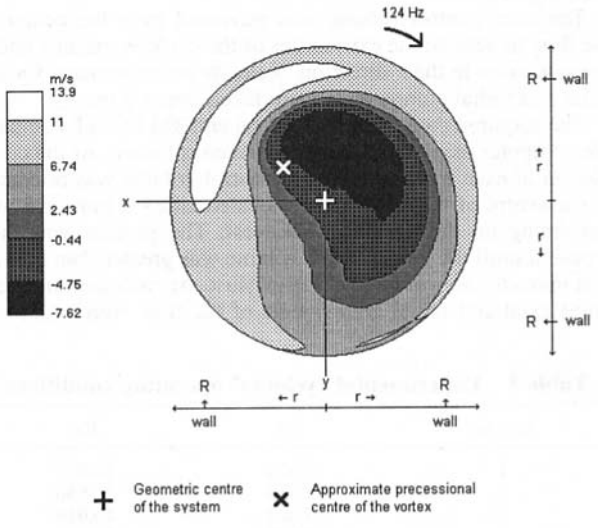

Fig. 5(*b*) Height above exhaust = *D*/2.8

Fig. 5 Spatial distribution of rotating axial velocities at a Reynolds number = 23,300 and geometric swirl number = 3.043

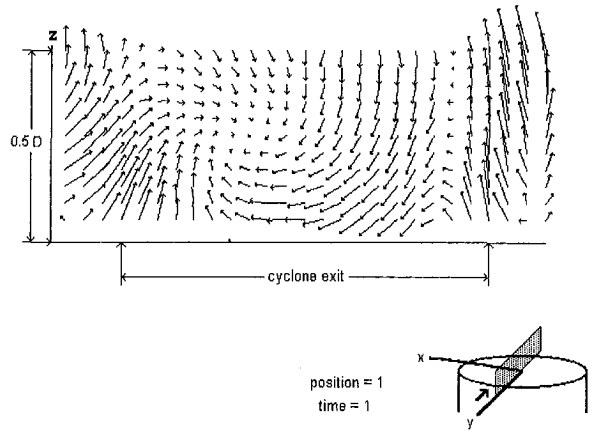

Fig. 6 Axial/radial velocity vectors at a Reynolds number = 19,600 and geometric swirl number = 3.324 (max. velocity = 6.99 m/s)

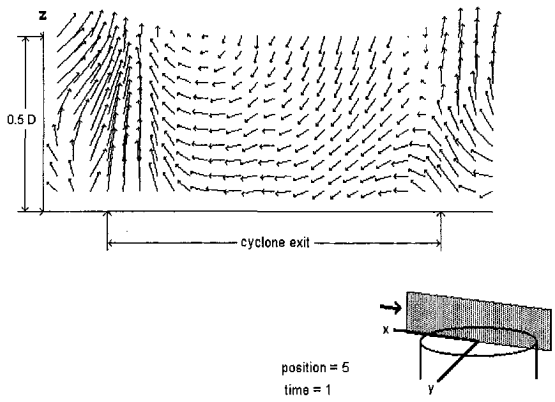

Fig. 8 Axial/radial velocity vectors at a Reynolds number = 19,600 and geometric swirl number = 3.324 (max. velocity = 7.77 m/s)

momentum flux balances, carried out on the diameter of the precessional center of the vortex, showed agreement within ±2 percent. The high tangential velocity levels produced between the precessional center of the vortex and the nearest wall merely arise due to considerations of angular momentum flux conservation, i.e., typical tangential velocity levels have increased from 10 m/s to up to 25 m/s. In effect, the swirling flow is accelerated as angular momentum flux is conserved by being squeezed through a narrow region between the precessional center of the vortex and the wall.

The formation of reverse flow zones in swirling flow is well known to be caused by (Linoya, 1953); (a) The formation of strong radial pressure gradients due to the term $(dp/dr) = -\rho(w^2/r)$ which give for cyclonic units operating at near atmospheric pressure sub atmospheric pressure levels on the axis; (b) axial decay of tangential velocity level (as occur at sudden enlargements etc. as in this work) which translates via the radial pressure gradient term in (a) above into negative axial pressure gradients which induce reverse axial flow.

Thus as the precessional center of the vortex is displaced from the geometric center it must also be assumed that the reverse flow zone will also be displaced and will also precess with the vortex. This indeed is the case for the corresponding rotating axial velocity field, Fig. 3(b). A large region of reverse flow now surrounds the precessional center of the vortex, although there is a wake effect with the reverse flow zone trailing behind the precessional center by up to 180 deg in a near elliptical form. The region of most intense reverse flow is, however, concentrated around the precessional center of the vortex. Again, the squeezing effect on the flow by the precessional center is clear, Fig. 3(b), as shown by the region of high forward axial velocity (up to 22 m/s) between the precessional center and the nearest wall.

Figures 4(a) and 4(b) show the effect of change of swirl number to 3.324 and height above the cyclone exhaust on the rotating axial fields. The P.V.C. frequency has changed considerably, dropping to 31 Hz, but the axial velocity fields show the same characteristics as Fig. 3(b). Close to the exhaust, Fig. 4(a) an area of reversed axial flow is observed off the geometric center coupled with a segment of relatively high axial velocity near to the cyclone exhaust wall extending over 180 deg. There is some evidence of the outer engulfment eddy as shown by the areas of reversed axial flow on the outer periphery of the diagram (obviously measurements did not extent far enough radially). Further downstream, Fig. 4(b), it is clear that the precessional motion of the vortex flow has developed considerably as shown by the enlarged area of reversed flow and the region of high velocity which is now concentrated over a smaller area whilst being located closer in an angular sense to the precessional center of the vortex. For a given radius the difference between maximum and minimum axial velocities is greater, Figs. 4(a) and 4(b). There is also evidence of twisting of the reverse flow zone in the θ direction by nearly 90 deg by comparison of their relative positions in Figs. 4(a) and 4(b).

Figure 5(a) and 5(b) show more data for the original swirl number of 3.043, but at a lower Reynolds number, Re = 23,300, as opposed to Re = 28,500 for Figs. 3(a) and 3(b). The precessional frequency has now altered to 124 Hz. The general characteristics of the flow are similar to those for Figs. 4(a) and 4(b).

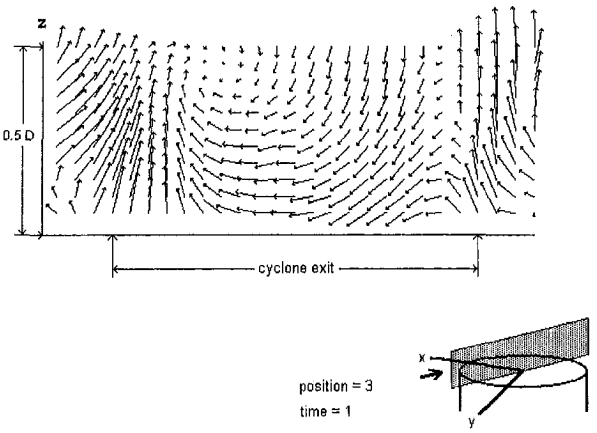

Fig. 7 Axial/radial velocity vectors at a Reynolds number = 19,600 and geometric swirl number = 3.324 (max. velocity = 6.97 m/s)

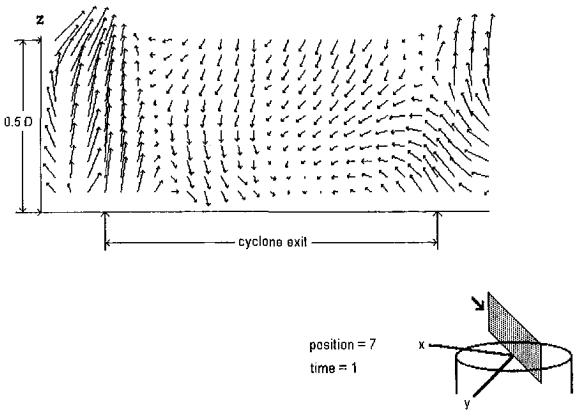

Fig. 9 Axial/radial velocity vectors at a Reynolds number = 19,600 and geometric swirl number = 3.324 (max. velocity = 7.46 m/s)

Again, at the lower section close to the exhaust, Fig. 5(*a*), there is clear evidence of the outer engulfment eddy as shown by the outside section of reversed axial flow. Again, close to the nozzle the precessional motion of the vortex has not properly developed, Fig. 5(*a*), as shown by the much larger reverse flow region at the greater height, Fig. 5(*b*). The relative location of the region of high axial velocity (or squeezed flow) is similar at the two heights. There again is some evidence of twisting of the reverse flow zone as shown by their relative displacement in the θ direction in Figs. 5(*a*) and 5(*b*). Increases of Reynolds numbers by 100 percent were observed to have little effect on the nondimensional flow characteristics.

The data generated over many trials have thus been used to generate the axial/radial velocity vector plots shown in Figs. 6 to 11. Figures 6 to 9 show axial/radial vectors across a diameter and for various planes in a Lagrangian time frame, i.e., each slice shows vectors at a different plane in an instantaneously stationary flow field. The development of the axial/radial eddy can be clearly seen from Figs. 6 to 9; it is obviously associated with the termination of the reverse flow zone and its interaction with the forward flow (i.e., Figs. 6 and 7) as the reverse flow zone is turned around by the forward flow. The structure shows evidence of being of helical shape, maybe becoming wrapped around the reverse flow zone. Figure 9 clearly shows in the bottom right the formation of a new eddy as the old eddy just disappears from the top left of the diagram.

The effect of lower a Reynolds number at the same position is clearly shown by comparing Figs. 6 and 10. The diagrams are very similar apart from the velocity levels.

Finally Fig. 11 shows the effect of increasing Reynolds number in the axial/radial plane for the same swirl number. It can be seen that the eddy formed is greatly influencing the velocity distribution in both the reversed flow and the entrained flow regions, as compared to Fig. 10. This can have a significant effect in the discharge characteristics further downstream.

6 Conclusions

It has now been demonstrated that in the free exhaust of a cyclone dust separator the reverse flow zone is not centralized, and is in fact precessing about the central axis of the system. This displacement causes acceleration of part of the flow as it is squeezed between the reverse flow zone and the wall of the cyclone exhaust.

Alternate eddy shedding or helical vortices have been clearly shown to exist both in the central region and on the outer periphery of the flow. It was observed that both probably followed a spiral or helical path as they leave the cyclone exhaust.

Both eddy shedding mechanisms are caused by the reverse flow zone being off set from the central axis of the system due to the presence of the P.V.C. Flow visualization clearly indicated that the axial/radial engulfment eddy found on the outer periphery of the flow was responsible for the high rates of flow entrainment on the outer periphery of the flow.

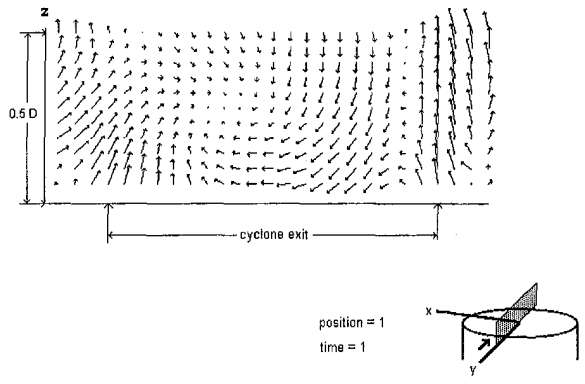

Fig. 10 Axial/radial velocity vectors at a Reynolds number = 11,600 and geometric swirl number = 3.324 (max. velocity = 4.38 m/s)

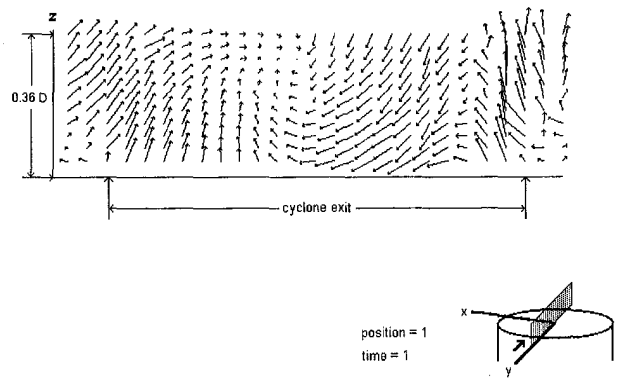

Fig. 11 Axial/radial velocity vectors at a Reynolds number = 23,300 and geometric swirl number = 3.324 (max. velocity = 14.70 m/s)

The presence of an eddy shedding mechanism in the central region of the flow was clearly demonstrated by the phase averaged L.D.A. measurements. This eddy appears to be associated with the termination of the bottom of the reverse flow zone and its interaction with some of the forward flow.

Phase averaging has been shown to be powerful in elucidating the complex flow mechanisms found in time dependent periodic flows.

Changes in the Reynolds number by a factor of 2 were observed to have no effect on the main characteristics of the flow. Some changes were seen in the flow structure with change in swirl number, particularly in the size of the reverse flow zone and the position of the large engulfment vortices.

This research has highlighted areas of high axial and tangential velocity components rotating at a frequency that is dependent on the physical parameters of cyclone. The complex nature of the flow structure can be seen as a concentration of an out-of-balance mass and therefore, has gone some way in explaining the induced nature of these vibrational instabilities.

References

Shepherd, C. B., Lapple, C. E., 1939, "Flow Pattern and Pressure Drop in Cyclone Dust Collectors," *Industrial and Engineering Chemistry,* Vol. 31, p. 972.

Kelsall, D. F., 1952, "A Study of the Motion of Solid Particles in a Hydraulic Cyclone," *Transactions of The Institution of Chemical Engineers,* Vol. 30, p. 87.

Smith, J. L., 1962, "An Experimental Study of the Vortex in a Cyclone Separator," *Trans.* ASME, Dec., pp. 602–608.

Ter Linden, A. J., 1949, "Investigation into Cyclone Dust Collectors," *Proceedings Institutions of Mechanical Engineers,* Vol. 160, pp. 233–251.

Stairmand, C. J., 1951, "The Design and Performance of Cyclone Separators," *Transactions of the Institution of Chemical Engineers,* Vol. 29, pp. 356–384.

Boysan, F., Ewan, B. C. R., Swithenbank, J., and Ayers, W. H., 1983, "Experimental and Theoretical Studies of Cyclone Separator Aerodynamics," 9th Powertech Conference, Birmingham, May, p. 9.

Gupta, A. K., 1979, "Combustion Instabilities in Swirling Flames," *Gas Warme International,* Vol. 28, Part 1, pp. 55–66.

Williams, J. M., 1993, "Investigations into the Precessing Vortex Core Phenomenon within Dust Separating Cyclones," Cardiff School of Engineering, Cardiff University of Wales, Internal Report no. 1772.

Gupta, A. K., Taylor, D. S., and Beer, J. M., 1977, "Investigation of Combustion Instabilities in Swirling Flows using Real Time LDV," *Proceedings of the Symposium on Turbulent Shear Flows,* Pennsylvania State University, Apr., p. 11.

Claypole, T. C., Evans, P., Hodge, J., and Syred, N., 1986, "The Influence of the P.V.C. on Velocity Measurements in Swirling Flows," *Proceedings of the 3rd International Symposium on Application of Laser Techniques to Fluid Mechanics,* Lisbon, Portugal, July, p. 6.

Van der Akker, T. L., and Liem, H. E. A., 1992, "LDV Measurements of the Turbulent Flow in Gas Cyclones," Kramers Laboratorium voor Fysische Technologie, Delft University of Technology, Prins Bernhardlaan 6, 2628 BW Delft, The Netherlands.

Reydon, R. F., and Gauvin, W. H., 1982, "Theoretical and Experimental Studies of Confined Vortex Flow," *Canadian Journal Chemical Engineering,* Vol. 59, pp. 14–23.

Rhode, D. L., Lilley, D. G., and McLaughlin, D. K., 1983, "Mean Flow in Axisymmetric Combustor Geometries with Swirl," *Journal of the American Institute of Aeronautics and Astronautics,* Vol. 21, No. 4, pp. 225–237.

Linoya, K., 1953, *Study of the Cyclone,* Memoirs of the Faculty of Engineering, Nagoya University, Vol. 5, 1953, p. 131.

Syred, N., and Beer, J. M., 1972a, "Effect of Combustion upon P.V.C.'s Generated by Swirl Combustors," *Fourteenth International Symposium on Combustion,* The Combustion Institute, PA, Aug. 20–25, p. 12.

Syred, N., and Beer, J. M., 1972b, "The Damping of Precessing Vortex Cores by Combustion in Swirl Generators," *Astronautica Acta,* Vol. 17, 4/5, pp. 783–802.

Syred, N., Hanby, V. I., and Gupta, A. K., 1973, "Resonant Instabilities Generated by Swirl Burners," *Journal of the Institute of Fuel,* Vol. 46, No. 387, pp. 402–407.

Gouldin, F. C., Halthore, R. N., and Vu, B. T., 1984, "Periodic Oscillations Observed in Swirling Flow with and without Combustion," *20th International Symposium on Combustion,* The Combustion Institute, pp. 269–276.

Chao, Y. C., Leu, J. H., Hung, Y. F., and Lin, C. K., 1991, "Downstream Boundary Effects on the Spectral Characteristics of a Swirling Flowfield," *Experiments in Fluids,* Vol. 10, pp. 341–348.

Yazdabadi, P. A., Griffiths, A. J., and Syred, N., 1992, "Axial and Tangential Velocity Components at the Exhaust end of a Highly Complex Flow Pattern generated by a Precessing Vortex Core," University of Wales College of Cardiff, Internal Report 1782.

Yazdabadi, P. A., Griffiths, A. J., and Syred, N., 1994, "Investigations into Precessing Vortex Core Phenomenon in Cyclone Dust Separators," Institution of Mechanical Engineers, Part E, *Journal of Process Engineering,* Vol. 208, pp. 147–154.

Bates, C. J., 1979, "The Use of Laser Doppler Anemometry for the study of Water Flow," PhD thesis, University of Wales, pp. 22–29.

Kline, S. J., and McClintok, I. A., 1953, "Describing Uncertainties in Single-Sample Experiments," *Mechanical Engineering,* Jan., pp. 3–8.

An Experimental Study of Swirling Flow Pneumatic Conveying System in a Vertical Pipeline

Hui Li
Assistant Professor,
Department of Mechanical Engineering,
Kagoshima University,
1-21-40 Korimoto, Kagoshima,
Japan

Yuji Tomita
Professor,
Department of Mechanical Engineering,
Kyushu Institute of Technology,
1-1 Sensuicho, Tobata, Kitakyushu,
Japan

A swirling flow is adopted for a vertical pneumatic conveying system to reduce conveying velocity, pipe wear, and particle degradation. An experimental study has addressed the characteristics of swirling flow pneumatic conveying (SFPC) for the total pressure drop, solid flow patterns, power consumption, and additional pressure drop. Polystyrene, polyethylene, and polyvinyl particles with mean diameters of 1.7, 3.1, and 4.3 mm, respectively, were transported as test particles in a vertical pipeline 12.2 m in height with an inside diameter of 80 mm. The initial swirl number was varied from 0.38 to 0.94, the mean air velocity was varied from 9 to 23 m/s, and the mass flow rate of the solids was varied from 0.3 to 1.25 kg/s. The minimum and critical air velocities decreased as much as 20 and 13 percent, respectively, when using SFPC. The total pressure drop and power consumption of SFPC are close to those of axial flow pneumatic conveying in the low air velocity range.

1 Introduction

Pneumatic conveying is an important operation in a significant number of industrial processes, such as in the transportation of materials from storage areas, in catalytic cracking in the petroleum industry, and in the production of synthetic fuels from coal in energy conversion systems. Conventional vertical pneumatic conveying, that is axial flow pneumatic conveying (AFPC), is frequently operated in the dilute-phase regime in the high air velocity region. Power consumption, pipe erosion, and particle degradation considerations dictate that the conveying velocity be held to a minimum. In the last thirty-five years, there has been increasing interest in dense-phase pneumatic conveying, and several commercial systems have been developed. Unfortunately, these systems require high pressure drops and have high initial costs. Furthermore, dense-phase pneumatic conveying may lead to unstable flows at low conveying velocities. These unstable flows often cause blockage and pipe vibration.

Recent work by Watanabe (1995) experimentally applied dense-phase pneumatic conveying in a spiral tube to avoid pipe blockage. To reduce power consumption, blockage, particle degradation, and pipe wear, this new swirling flow technique, called swirling flow pneumatic conveying (SFPC), was applied to horizontal pneumatic conveying by Li and Tomita (1996a). In the low velocity conveying range, SFPC was determined to be effective.

The purpose of this study is to apply SFPC to a vertical pipeline, experimentally investigating the characteristics of SFPC in terms of total pressure drop, solid flow patterns, power consumption, and the additional pressure drop.

2 Background

As described by Li and Tomita (1996a), the reasons swirling flow was applied successfully to horizontal pneumatic conveying are summarized as follows. (1) The swirling flow technique has a large kinetic energy to accelerate particles at the initial conveying stage. (2) Although the kinetic energy of the swirling flow decays along the pipeline, particles can safely be conveyed since the air velocity increases downstream due to the expanded air volume. Thus the swirling flow has a requisite kinetic energy distribution required to convey the particles along the pipeline. (3) The strength of the swirling flow can be adjusted to satisfy various needs. These advantages are also applicable to vertical pneumatic conveying.

Because the direction of gravity is parallel to the pipeline axis in vertical pneumatic conveying, the air velocity distribution in the pipe cross section plays an important role, which is different from horizontal pneumatic conveying. In vertical AFPC (axial flow pneumatic conveying), the velocities of particles and air near the wall are lower than those near the pipe axis. Thus the particle concentration is relatively high in the region of low air velocity near the wall (Li and Tomita, 1996b). If the air velocity decreases further, particles near the wall begin to drift, oscillate, and even move downward. This may result in pipeline blockage or unstable flow in the acceleration region. A higher air velocity is required to avoid this problem. However, this leads to a rise in the power consumption, particle degradation, and pipe wear.

If a swirling flow is utilized, the circumferential component of air velocity will force particles to the wall. Here the axial component of the air velocity of the swirling flow is larger than that of the axial flow (Li and Tomita, 1994), and the kinetic energy of the air can be used to accelerate particles sufficiently. Therefore, vertical SFPC has the potential to operate at lower air velocity than does vertical AFPC. The downstream air velocity distribution of SFPC approaches that of AFPC due to the decay of the swirl flow. For long conveying distances, which require a relatively high pressure drop, the air velocity increases downstream due to air expansion and the particles can safely be conveyed.

A vaned swirler, which is placed upstream the particle feeding point, is employed to minimize the pressure drop across the swirler. The swirl number S is used to evaluate the intensity of swirling flow and is defined by

$$S = \frac{2\pi\rho_a \int_0^R uwr^2 dr}{2\pi\rho_a R \int_0^R u^2 r dr}, \quad (1)$$

where u and w are the axial and circumferential components of

Contributed by the Fluids Engineering Division for publication in the JOURNAL OF FLUIDS ENGINEERING. Manuscript received by the Fluids Engineering Division October 30, 1996; revised manuscript received October 15, 1997. Associate Technical Editor: D. P. Telionis.

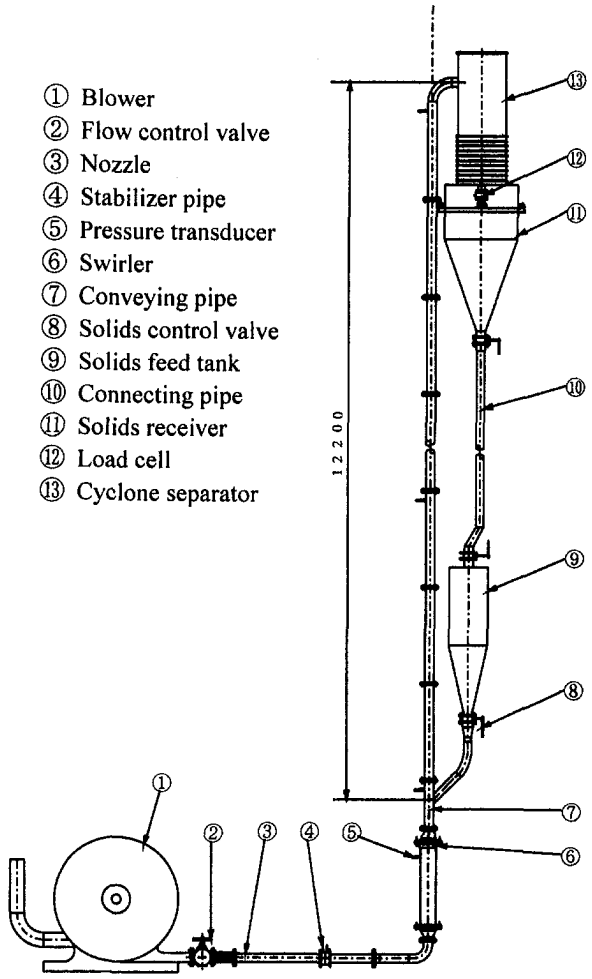

Fig. 1 Experimental equipment

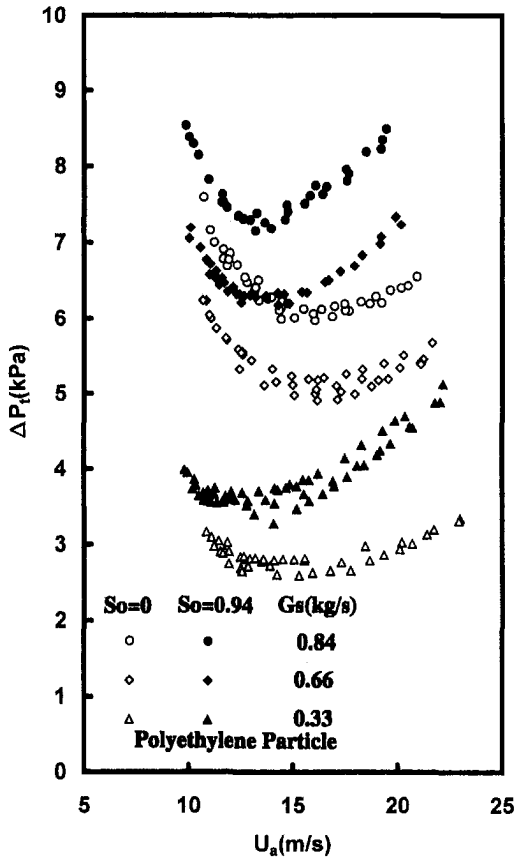

Fig. 2 Comparison of SFPC (S_0 = 0.94) and AFPC (S_0 = 0) in terms of total pressure drop for polyethylene particles (Uncertainty in Δp_t = ±12 percent, in U_a = ±8.9 percent, in G_s = ±8 percent)

the air velocities, respectively, R is the pipe radius, and ρ_a is the air density.

3 Experimental Apparatus and Procedure

Figure 1 shows the schematic diagram of the experimental apparatus, which is a positive pressure conveying system. The conveying pipeline consists of smooth acrylic tubes with an inside diameter of 80 mm and a height of about 12.2 m. Particles are fed by gravity from the solids feed tank into the conveying pipe inlet. These particles are introduced into the swirling flow produced by the vaned swirler. The air flow rate was measured by a calibrated quadrant flow nozzle. The solids mass flow rate was measured by a load cell. The wall pressures along the pipeline were measured by pressure transducers. Three different vaned swirlers were used. The initial swirl number S_0 was measured experimentally by Li and Tomita (1994). To study the characteristics of SFPC on different kinds of particles, we used polystyrene, polyethylene, and polyvinyl particles in this experiment. Their properties are given in Table 1. The mean air velocity U_a was varied from 9 to 23 m/s, the mass flow rate of solids

Table 1 Properties and dimensions for conveyed particles

Particle	Shape	Average diameter (mm)	Density (kg/m³)	Floating Velocity (m/s)
Polystyrene	Spherical	1.65	976	5.90
Polyethylene	Cylindrical	3.13	946	7.20
Polyvinyl	Discal	4.26	1419	8.24

G_s was varied from 0.3 to 1.25 kg/s, and the S_0 values examined were 0.38, 0.68, and 0.94. AFPC, a condition where S_0 is 0.0 (no swirl), was also included for comparison.

The estimated average uncertainties in this experiment were ±12 percent for the total pressure drop, ±8.9 percent for the mean air velocity, and ±8 percent for the solid mass flow rate.

4 Experimental Results and Discussion

We estimate the total pressure drop Δp_t using the same method as for the horizontal SFPC (Li and Tomita, 1996a), which includes the pressure drop due to the vaned swirler. This is given

$$\Delta p_t = \Delta p_s - \frac{1}{2}\rho_a\left[1 - \left(\frac{D}{D_0}\right)^4\right]U_a^2, \qquad (2)$$

where Δp_s represents the static pressure difference between the stabilizer pipe and the conveying pipe exit and the second term is the change in dynamic pressure between the stabilizer pipe and conveying pipe. The diameters of the conveying and stabilizer pipes are D and D_0, respectively.

In this study, the air velocity at the minimum total pressure drop is defined as the minimum velocity. The critical or choking velocity is defined as the air velocity at which strong pressure fluctuations appear. These pressure fluctuations are accompanied by flow instability, which makes it impossible to continuously convey particles. We measured the air flow rate at the threshold of instability. These two velocities (minimum velocity and critical or choking velocity) are of particular importance in the design of a pneumatic conveying system.

Figure 2 shows Δp_t versus U_a and G_s as parameters for polyethylene particles with S_0 = 0.0 and 0.94. The minimum and

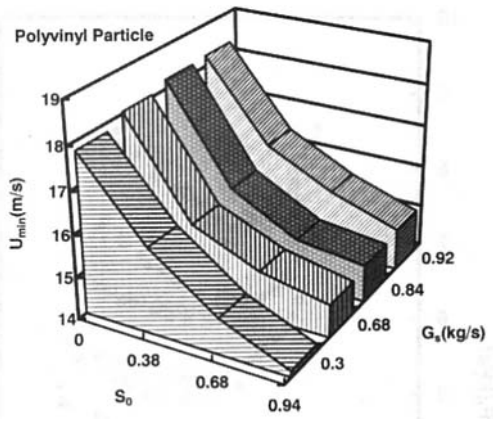

Fig. 3 Minimum velocity of swirling flow pneumatic conveying for conveyed polyvinyl particles (Uncertainty in U_{min} = ±8.9 percent, in G_s = ±8 percent)

critical velocities of SFPC are smaller than those of AFPC. As it does for AFPC, the pressure drop of SFPC first decreases and then rises below the minimum velocity, as the air velocity decreases. Comparing SFPC with AFPC, the Δp_t of SFPC approaches that of AFPC for U_a below the minimum velocity of SFPC, while the Δp_t for SFPC is higher than that for AFPC in the high air velocity region. It is significant that a lower conveying velocity can be realized by SFPC as compared with AFPC.

The minimum velocity is shown in Fig. 3 for the three types of particles tested. The minimum velocity decreases with an increasing S_0 and increases with G_s for a given S_0. Using SFPC, the minimum velocity can be decreased by 5 to 20 percent. For particles having a high floating velocity, the reduction of minimum velocity is apparently large.

Figure 4 shows the critical velocity for polystyrene particles, whose relation with S_0 and G_s is similar to that for the minimum velocity. Compared to AFPC, the maximum decrease of the critical velocity for SFPC is 13 percent for the swirl numbers examined.

The above results show that when using SFPC the conveying velocity can be decreased and the safe conveying velocity range can be extended, hence low rates of pipe wear and particle degradation are anticipated.

Flow patterns are important for examining the mechanism of pressure drop in vertical SFPC. In this section the flow patterns of polyethylene particles are examined by photographs of the acceleration region.

Particle flow pattern of AFPC changes for a constant mass flow rate of G_s = 0.84 kg/s when the air velocity is reduced

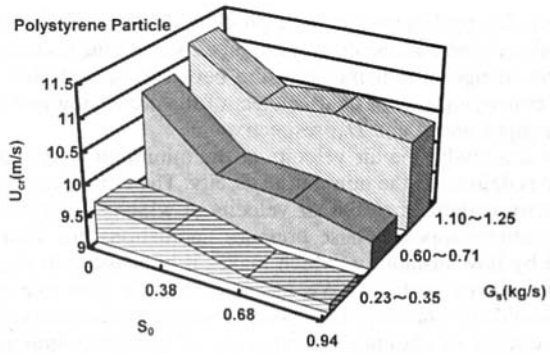

Fig. 4 Critical velocity of swirling flow pneumatic conveying for conveyed polystyrene particles (Uncertainty in U_{cr} = ±8.9 percent, in G_s = ±8 percent)

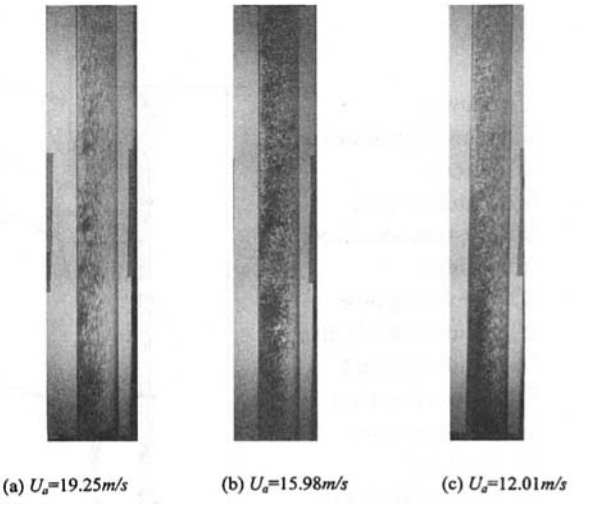

Fig. 5 Flow patterns of polyethylene particles for AFPC (G_s = 0.84 kg/s)

are shown in Fig. 5. When air velocity is high, as shown in Fig. 5(*a*) (U_a = 19.25 m/s), particles are transported in nearly uniform dispersed flow and the frictional pressure drop is significant. With a decreasing air velocity, shown in Fig. 5(*b*) (U_a = 15.98 m/s), particle clusters or packets gradually appear near the wall and the pressure drop due to the particles is essentially caused by the holdup of particles in the pipe. If the air velocity is further decreased, as shown in Fig. 5(*c*) (U_a = 12.01 m/s), particles appear to swirl, drift, and oscillate near the wall, while the particles being conveyed are mostly in the central region of pipe. This flow mode is unstable and a small variation of air velocity can result in a large pressure drop and flow instability. A further reduction of air velocity can lead to a choked flow mode.

Figures 6 and 7 show the change of particle flow patterns of SFPC with decreasing air velocity at a constant mass flow rate G_s = 0.84 kg/s when the initial swirl numbers S_0 are 0.38 and 0.68, respectively. At a high air velocity, a swirling flow pattern of particles is observed (Fig. 6(*a*)). It becomes strong (Fig. 7(*a*)) when the initial swirl number is increased. The frictional pressure drop is large in this flow mode. With a decrease in air velocity, the swirling flow pattern of particles weakens and approaches a dispersed flow (Figs. 6(*b*) and 7(*b*)). The particles are forced to the wall region by centrifugal force where

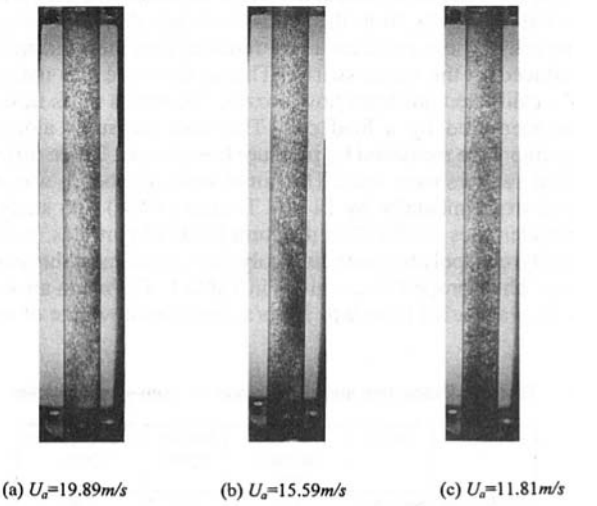

Fig. 6 Flow patterns of polyethylene particles for SFPC (S_0 = 0.38, G_s = 0.84 kg/s)

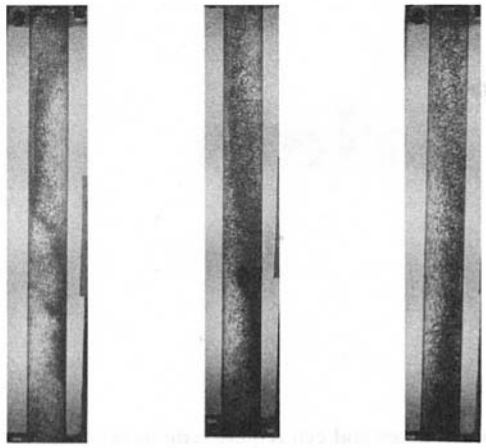

(a) U_a=19.53m/s (b) U_a=15.64m/s (c) U_a=12.16m/s

Fig. 7 Flow patterns of polyethylene particles for SFPC (S_0 = 0.68, G_s = 0.84 kg/s)

the axial velocity component of the swirling flow is larger than that of the axial flow. Thus, the particles remain suspended and particle clusters or packets do not appear, even at the lower air velocity (Figs. 6(*c*) and 7(*c*)). Therefore, the minimum and critical velocities of SFPC are lower than those of AFPC. Further, the total pressure drop for SFPC is almost the same as that for AFPC, but for SFPC it is obtained at a lower air velocity. Furthermore, because particles only remain suspended in AFPC at high velocity, the total pressure drop is lower than that of swirling particle flow in SFPC. The downstream particle flow pattern of SFPC approaches that of AFPC due to the decay of the swirling flow. Similar results are obtained for other kinds of particles.

We evaluate the power consumption by the coefficient of power consumption E defined by

$$E = \frac{\Delta p_t Q_a}{g G_s H} \tag{3}$$

where Q_a is the volumetric flow rate of air and g is the gravitational constant.

Figure 8 compares the E values of SFPC (S_0 = 0.94) and AFPC (S_0 = 0.00) against U_a and G_s as parameters for polyethylene particles. Although the E of SFPC is higher than that of AFPC in the high air velocity region, it approaches that of AFPC in the low air velocity region. The difference becomes small as the initial swirl number is decreased. This indicates

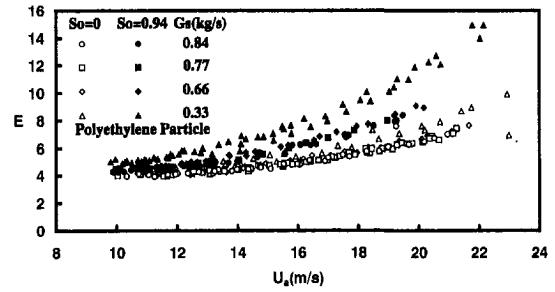

Fig. 8 Comparison of SFPC (S_0 = 0.94) and AFPC (S_0 = 0) power consumption coefficient for conveyed polyethylene particles (Uncertainty in E = ±13.11 percent, in U_a = ±8.9 percent)

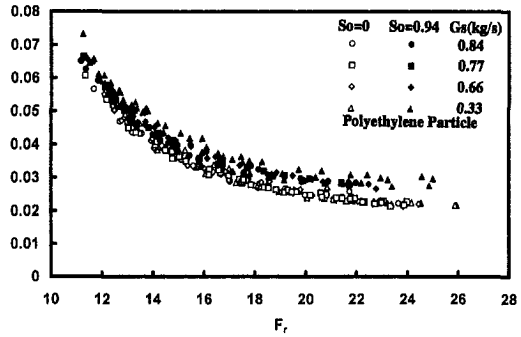

Fig. 9 Comparison of SFPC (S_0 = 0.94) and AFPC additional pressure drop coefficient for conveyed polyethylene particles (Uncertainty in λ_z = ±12 percent, in F_r = ±8.9 percent)

that SFPC can operate at the lower air velocity using almost the same power consumption as that of AFPC.

We define the total pressure drop Δp_t as

$$\Delta p_t = \Delta p_a + \Delta p_z, \tag{4}$$

where Δp_a is the total pressure drop of air alone including the pressure drop due to the vaned swirler and Δp_z is the additional pressure drop due to the particles. We define the additional pressure drop coefficient λ_z as (Barth, 1958)

$$\lambda_z = \frac{\Delta p_z}{m_t \dfrac{L}{D} \dfrac{\rho_a U_a^2}{2}}, \tag{5}$$

where m_t is the solids/air mass flow rate ratio given by $m_t = G_s/G_a$. In Fig. 9, the λ_z of polyethylene particles is plotted against the Froude number F_r defined as $F_r = U_a/\sqrt{gD}$ for SFPC (S_0 = 0.94) and AFPC with G_s as a parameter. It is noted that λ_z of SFPC is almost independent of G_s, which is different from horizontal SFPC (Li and Tomita, 1996a). The reason λ_z of SFPC is higher than that of AFPC for the high F_r is that the frequency of particle-wall collisions increases and the particle trajectories become long, due to the swirling motion of the particles, while λ_z of SFPC becomes almost the same as that of AFPC for the lower F_r.

5 Conclusions

In this investigation of a swirling flow pneumatic conveying (SFPC) of coarse particles in a vertical pipeline, we examined the total pressure drop and particle flow patterns. The results are summarized as follows.

(1) In the lower air velocity range, the pressure drop characteristics of SFPC approach those of axial flow pneumatic conveying (AFPC).

(2) The critical and minimum velocities decrease when using SFPC, up to 13 and 20 percent, respectively.

(3) Low rates of pipe wear and particle degradation are expected, since SFPC uses a lower conveying velocity.

References

Barth, W., 1958, "Stromungsvorgange beim Transport von Festteilchen und Flussigkeitsteilchen in Gasen," *Chemie-Ing Techn*, Vol. 30, pp. 171–180.

Li, H., and Tomita, Y., 1994, "Characteristics of Swirling Flow in a Circular Pipe," ASME JOURNAL OF FLUIDS ENGINEERING, Vol. 116, No. 2, pp. 370–373.

Li, H., and Tomita, Y., 1996a, "An Experimental Study of Swirling Flow Pneumatic Conveying System in a Horizontal Pipeline," ASME JOURNAL OF FLUIDS ENGINEERING, Vol. 118, No. 3, pp. 526–530.

Li, H., and Tomita, Y., 1996b, "A Numerical Simulation of Swirling Flow Pneumatic Conveying in a Vertical Pipeline," ASME FED-Vol. 239, pp. 503–508.

Watanabe, K., 1996, "Transport of Solids by Pipeline with Spiral Tube," ASME FED-Vol. 234, pp. 57–64.

Journal of Fluids Engineering

Technical Briefs

Refractive-Index-Matching Laser Velocimetry for Complex, Isothermal Flows

B. E. Thompson,[1] O. Bouchery,[1] and K. D. Lowney[1]

Refractive-Index-Matching Laser Velocimetry (RIMLV) obtains velocity distributions in flow through complex geometries. Laser velocimetry is used to measure the flow of a constant-temperature mixture that has the refractive index of acrylic models. This mixture can be used to obtain duct Reynolds numbers in the turbulent regime at moderate expense. Measurements can be obtained at desired locations, specifically inside complex models even if laser beams pass through multiple curved surfaces, which is advantageous when comparing measured and calculated results.

Background

Laser Doppler Velocimetry (LDV) measures velocity non-intrusively, however, its application is often limited in flows because of optical distortion associated with multiple and curved walls because light bends at any interface where the index of refraction changes. At these interfaces, some light intensity is lost to reflection and the remainder follows Snell's law and changes direction unless it is orthogonal to the interface. The consequences for LDV are that the position of the measurement volume is displaced or, more importantly, that measure velocities can be erroneous: fringe alignment and spacing can vary spatially and nonlinearly between measurement locations or within the measurement volume and this can results in erroneous measurement. Refraction can also alter the bisector angle formed by the two beams and change the conversion factor used to convert from frequency of scattered light intensity into velocity of the seed particle. It is also possible that the two laser beams will not intersect to form a measurement volume. Light scattered by seed particles also follows Snell's law so that high-intensity forward- or back-scattered light may be refracted away from the photodetector. This creates practical difficulties in alignment and focusing of the collection optics that increase measurement times and can require tedious optimization of the optics at almost every measurement location.

These problems are solved if the fluid and the solid have the same refractive index. Refractive-Index-Matching Laser Velocimetry (RIMLV) has been used in different forms, for example, Elphick et al. (1982), Dybbs and Edwards (1987), Park et al. (1989), and Longmire and Eaton (1992) and each with their own advantages and limitations. The present approach uses a low-viscosity mixture of organic solvents matched to the refractive index of acrylic. Thompson (1990) reports the use of this mixture in a variety of complex geometries including a Space Shuttle Main Engine (SSME) preburner LOX post, a scaled model of the SSME main Injector bowl (Thompson et al., 1992) a scaled model of a rotating SSME bearing cavity, a rotating impeller, an engine intake manifold, and two-phase flow in a coal combustor. It has also been applied to two-phase flows (Nouri et al., 1986 and Yianneskis et al., 1986), flow through ports of an internal combustion engine (Tindal et al., 1988), and flow in a centrifugal pump (Liu et al., 1994).

Refractive-Index-Matching Flow Circuit

The present Refractive-Index-Matching (RIM) fluid was a 65:35 mixture by volume of steam-distilled wood turpentine and 1,2,3,4-tetrahydronaphthalene. The concentrations were mixed to match the refractive index with that of the acrylic model. Properties of the mixture are shown on Table 1. Figure 1 shows a typical RIMLV flow circuit comprised of an acrylic model, a temperature-controlled reservoir, a centrifugal pump, a temperature sensor, piping, fittings, flexible hoses, valves and a flow-meter. The reservoir was a 55 gallon stainless steel drum with custom-made fittings welded on to accommodate piping connections with the pump, with return ducts from the flow circuit and the bypass flow, and with a refill vent. The RIM fluid was pumped through this circuit by a stainless steel centrifugal pump with Teflon-ceramic seals and an explosion-proof electric motor rated at 1.5 hp. This motor operated at a constant, continuous speed, and flow rate was adjusted with globe valves that created resistance and redirected a portion of the flow back into the reservoir via the bypass duct.

The RIM fluid was pumped from the reservoir in 30-mm ID Teflon-lined hosing with exterior stainless steel braiding. This flow passed through a mesh screen with 57 percent open-air ratio which was welded at the upstream entrance inside the pipe. The screen helped break-up any large vortices or secondary flows in the wake of the pump and bends in the flexible hose. Proceeding downstream, the flow went through a straight,

Table 1 Properties of the RIM fluid

Density	$\rho = 900\ \text{kg} \cdot \text{m}^{-3}$
Kinematic viscosity	$\nu = 1.54 \times 10^{-6}\ \text{m}^2 \cdot \text{s}^{-1}$
Refractive index at 32°C	$n = 1.489$

[1] Associate Professor, Graduate Student, and Graduate Student, respectively, Department of Mechanical Engineering, Aeronautical Engineering and Mechanics, Rensselaer Polytechnic Institute, Troy, NY 12180-3590.

Contributed by the Fluids Engineering Division of THE AMERICAN SOCIETY OF MECHANICAL ENGINEERS. Manuscript received by the Fluids Engineering Division December 9, 1994; revised manuscript received October 9, 1997. Associate Technical Editor: D. E. Stock.

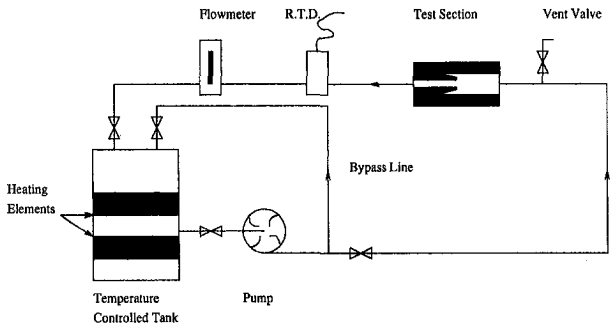

Fig. 1 Flow circuit for refractive index matching laser velocimetry

stainless steel pipe which had a length-to-diameter ratio of 30 so that the flow evolved into a fully-developed turbulent profile before entering the model. A small stainless steel valve was tapped in this pipe to vent air bubbles from the circuit and model. The piping was held in place for the model at four locations with one of these fittings placed immediately upstream of the model, and one immediately downstream in order to minimize stresses on the acrylic and thus extend model life as discussed below.

The model was clamped between two flanges that were welded onto the inlet and outlet pipes, respectively. These flanges were welded to a set of brackets that located the exterior face of the model and each flange had a circular slot into which a Teflon o-ring was fitted. The joints were leakproof and were as smooth and as continuous as possible to avoid unwanted flow disturbances. A major advantage of this connection technique is that no drilling or tapping of the model was required so that potential cracking of the model at thread roots and crazing near drill sites was avoided. Previous experiences with this RIM fluid found it caused crazing or cracking in regions with tensile stress on the acrylic. The present connection is compressive which, in combination with the annealing of the model discussed below, has resulted in no change in the optical condition of this model during over 60 months of service which is a much longer model lifetime than has been reported previously.

Temperature of the fluid was set to 32°C and maintained within 0.1°C with a temperature-control system that comprised a platinum resistance thermometer with stainless-steel compression fitting mounted in the outlet duct, an electronic temperature controller, a solid-state relay, and two external silicon rubber heating straps that were wrapped around the exterior of the reservoir. Flow rate was monitored with a stainless-steel, differential-pressure, flowmeter installed in the outlet pipe. All valves and fittings were made of stainless or carbon steel. Valves were sealed with either Teflon or Viton. A high temperature anti-galling sealant was successfully tested for tolerance to the mixture and subsequently used to leakproof all fittings.

Laser Velocimeter

A single-component Laser Doppler Velocimeter that was arranged in back-scatter mode with a 15-mW He-Ne laser and geometry described in Table 2, was mounted on a mechanism that traversed 350 mm in 1 mm/turn increments in axial, transverse and vertical directions. Seed particles added to the RIM fluid to follow the flow, were hollow acrylic spheres with an average diameter of 2 μm. Signals from the photodiode were processed with a counter and signal condition with low-frequency filters set to remove the pedestal of the Doppler burst and high-frequency limit filter set to maximize signal-to-noise ratio. Frequency validation was accomplished with a burst detector that was set to compare measurements for 10 and 16 cycles of the Doppler burst and accept those within 2 percent of each other. A microcomputer and data-acquisition system acquired these signals, and software calculated mean-flow and turbulence quantities and displayed probability distribution function. A digital oscilloscope was used to monitor the Doppler bursts that were accepted by the counter.

Table 2 LDV optics and measurement volume

Focal distance of the transmitting lens:	250 mm
Beam separation:	50 mm
Beam bisector half angle:	5.46 degrees
Diameter of laser beam entering the lens:	1.5 mm
Interfringe spacing:	5 μm
Measurement volume length inside the fluid:	2.1 mm
Measurement volume diameter:	0.13 mm

A Complex Flow Model

The present experiment demonstrates the benefits of RIMLV by measuring mean and fluctuating components of velocity in a model which closely replicates an actual submerged nozzle in a solid rocket motor at late burn times. Figure 2 shows the surfaces of this model are complex and curved, and there is a large annular recirculation region around the submerged part of the nozzle. An acrylic block was annealed at 420 K for twelve hours to alleviate residual stresses that could effect optical clarity and model life. This caused about 2 percent shrinkage. The block was then rough machined to within about 0.3 mm of its final dimensions, and annealed for a second time at 410 K for eleven hours. The model was then precision machined and polished to its final dimensions. Exterior walls of the model were machined flat and polished to simplify optical access. The Reynolds number based on the nozzle throat diameter was 2×10^6 in the Space Shuttle SRM compared to 4.6×10^4 in this model which is sufficiently high for turbulent flow in the experimentally-determined invariant range between 10^4 to 10^7 for SRM nozzle geometries (Waesche and Sargent, 1989).

RIMLV Measurements

RIMLV allowed optical access throughout the model. Figure 2 shows distributions of velocity that characterize flow patterns throughout the nozzle. To obtain these measurements, laser beams transmitted coherently through curved surfaces at the outer wall, the outer surface of the nozzle lip, and the inner nozzle surface, and at a variety of peculiar angles depending on the location of the measurement volume. Conventional approaches with LDV in water or air would have been frustrated trying to obtain both axial and radial components of velocity, and could not easily obtain the swirl component.

Figures 3 and 4 show axial and radial components of mean velocity obtained by traversing the LDV measurement volume to any desired location across the interior of the nozzle. Maximum uncertainties for 95 percent confidence in the mean veloci-

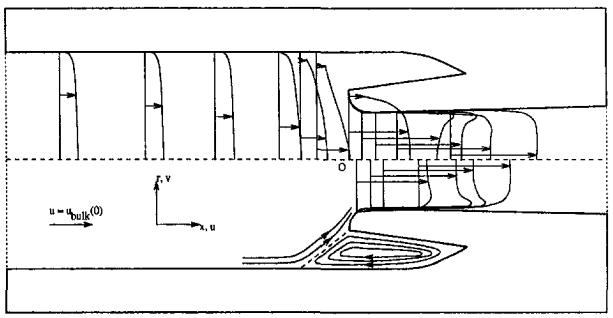

Fig. 2 Flow structure through the acrylic model. (The origin is on the centerline in the plane of the upstream lip of the submerged nozzle. The velocity scale is given in the figure.)

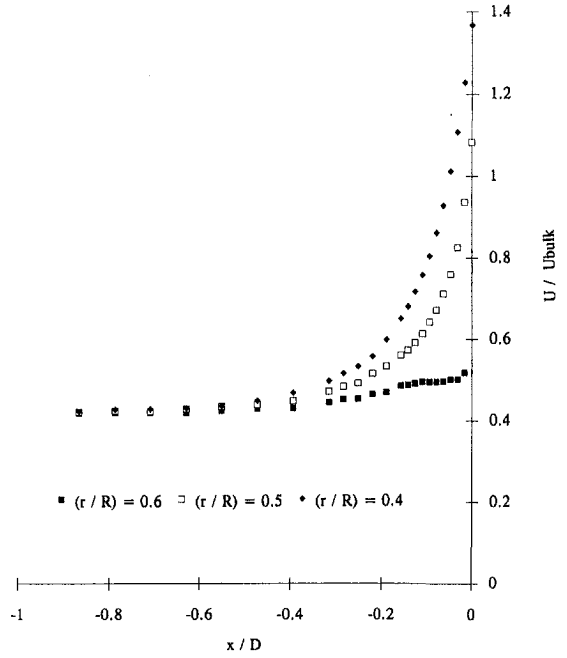

Fig. 3 Axial component of mean velocity upstream of the submerged nozzle. (Symbols are defined on the figure.)

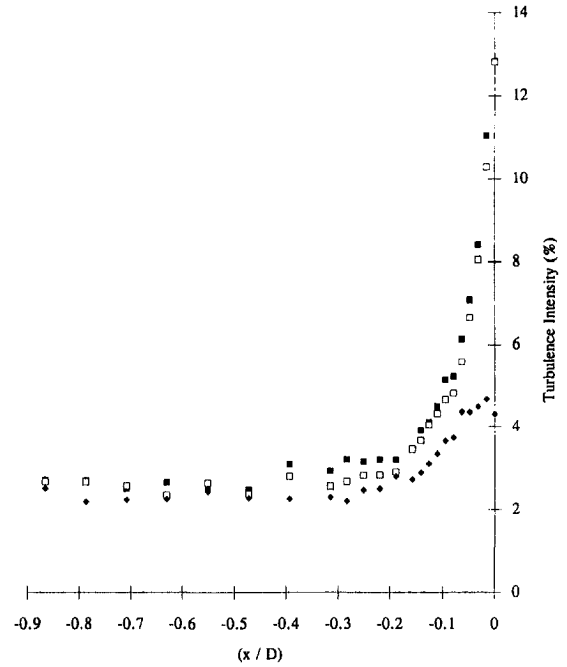

Fig. 5 Axial component of turbulence intensity upstream of the submerged nozzle. (Symbols are defined in Fig. 3.)

ties and turbulence intensities reported below, were less than 2 percent and 6 percent of the local values based on the optical characteristics of the RIM flow circuit and signal-processing instrumentation, and these were repeatable within less than 1 percent. Mean flow rate was monitored within 1 percent and the RIMLV measurement volume was positioned within 0.02 mm with a tridirectional, linear traversing mechanism. The swirl component of velocity was also obtained simply by rotating the RIMLV beams and its mean value was measured to be negligible throughout the present configuration. Figures 5 and 6 show distributions of axial and radial turbulence normal stresses, which are defined as the root-mean-square of velocity normalized with the bulk velocity at the origin. The magnitude of the turbulence intensities indicates laminarization effects associated with mean-flow acceleration were overwhelmed by turbulence production due to large shear stresses. For nozzle designers, these detailed measurements provide knowledge of the processes of energy exchange between the mean-flow and turbulence and thus the basic understanding for optimization of the lip contour to maximize rocket impulse and minimize losses. These results provide evidence that RIMLV simplifies the measurement of all three velocity components and allows positioning of the measurement volume wherever desired.

Concluding Remarks

RIMLV obtains nonintrusive measurements of velocity wherever desired in complex geometries. Previous problem of craz-

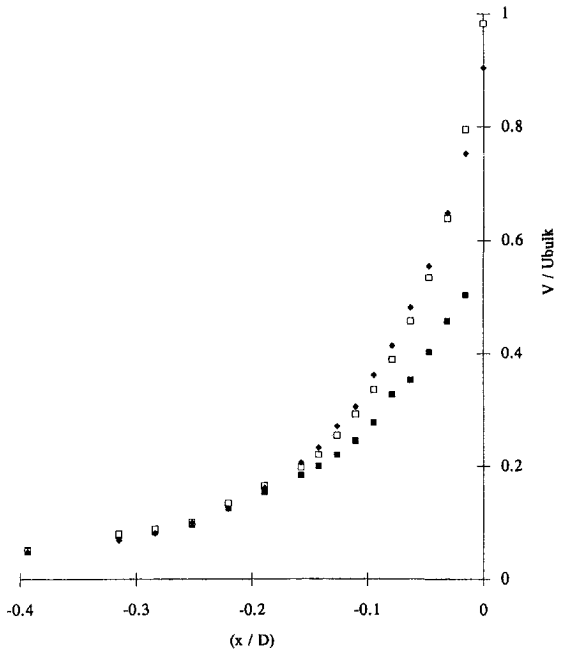

Fig. 4 Radial component of mean velocity upstream of the submerged nozzle. (Symbols are defined in Fig. 3.)

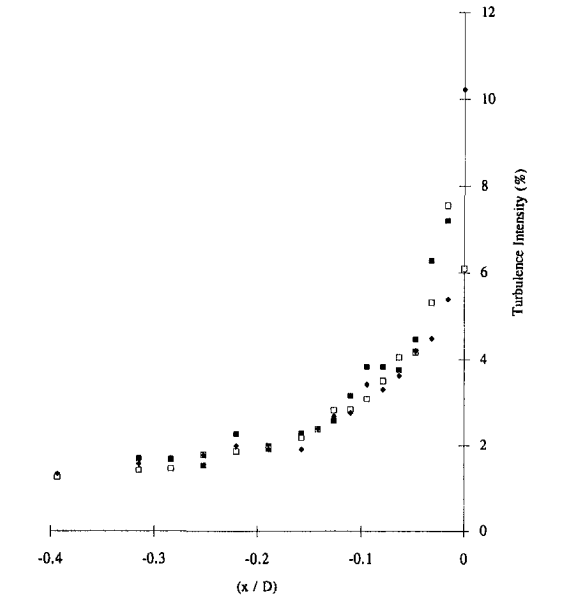

Fig. 6 Radial component of turbulence intensity upstream of the submerged nozzle. (Symbols are defined in Fig. 3.)

ing and cracking of acrylic models in this RIM fluid have been overcome with annealing and mounting strategies that have lead to practical model life. The present RIMLV approach avoids flow interference associated with probes, is not frustrated with the optical accessibility problems, and can be used to obtain high Reynolds numbers at reasonable cost.

References

Dybbs, A., and Edwards, R. V., 1987, "Refractive Index Matching for Difficult Situations," 2nd International Conference on Laser Anemometry—Advances and Applications, Paper I1, Sept.

Elphick, I. G., Martin, W. W., and Currie, I. G., 1982, "Application of LDA to High Reynolds Number Cross Flow," *Proceedings of the International Symposium on Application of Laser Anemometry to Fluid Mechanics,* Superior Technico, Lisbon, Portugal, July, pp. 15.1.1–15.1.12.

Longmire, E. K., and Eaton, J. K., 1992, "Structure of a Particle-Laden Round Jet," *Journal of Fluid Mechanics,* Vol. 236, pp. 217–257.

Liu, C. H., Vafidis, C., and Whitelaw, J. H., 1994, "Flow Characteristics of a Centrifugal Pump," ASME JOURNAL OF FLUIDS ENGINEERING, Vol. 116, June, pp. 303–309.

Nouri, J. M., Whitelaw, J. H., and Yianneskis, M., 1986, "Particle Motion and Turbulence in Dense Two-Phase Flows," *International Journal of Multiphase Flow,* Vol. 13, No. 6, pp. 729–739.

Park, J. T., Mannheimer, R. J., Grimley, T. A., and Morrow, T. B., 1989, "Pipe Flow Measurements of a Transparent Non-Newtonian Slurry," ASME JOURNAL OF FLUIDS ENGINEERING, Vol. 111, Sept., pp. 331–336.

Tindal, M. J., Cheung, R. S., and Yianneskis, M., 1988, "Velocity Characteristics of Steady Flows Through Engine Inlet Ports and Cylinders," Society of Automotive Engineers Paper 880383, Warrendale, PA, Feb.

Thompson, B. E., 1990, "Refractive-Index Matching Techniques in Complex Rocket-Engine Flow Configurations," Scientific Research Associates Report R89-900072-F, Glastonbury, Ct.

Thompson, B. E., Senaldi, J., Vafidis, C., Whitelaw, J. H., and McDonald, H., 1992, "Flow in a Model of the Space Shuttle Main Engine Main Injector Bowl," *Journal of Spacecraft and Rockets,* Vol. 29, Mar.–Apr., pp. 247–252.

Waesche, R. H. W., and Sargent, W. H., 1989, "Space Shuttle Solid Rocket Motor Aft-End Internal Flows," *Journal of Propulsion and Power,* Vol. 5, Nov.–Dec., pp. 650–656.

Flow Regime Identification in Horizontal Channels With Different Types of Rod Clusters

H. G. Lele,[1] S. K. Gupta,[1] and V. Venkat Raj[2]

1 Introduction

The presence of internals affects the flow pattern and flow stratification thresholds in horizontal geometry. Chang et al. (1985) have solved a particular case of concentric annulus geometry and Osamusali and Chang (1987) have extended it to 28 rod and 37 rod bundle geometry. In this paper, a model to determine the flow patterns in a horizontal channel with one or more cylindrical rods inside it is presented. The predictions of the model for 37 rod cluster are compared with the experimental results of Minato et al. (1990) and Osamusali et al. (1992). Flow regime maps for 19 rod bundles are presented in terms of dimensionless parameters, superficial velocities, mass flux, and quality.

2 Model Description

The model considers transition between five basic flow regimes in two-phase flow, viz. smooth stratified, wavy stratified, intermittent (slug and plug), annular with dispersed liquid, and dispersed bubble. The model calculates the equilibrium level and a set of independent dimensionless parameters taking into account internals present in the channel. The set of criteria used by Taitel and Dukler (1976) has been applied for the flow regime transitions.

The following assumptions have been made. (i) Wall resistance for liquid flow is similar to that in open channel flow; (ii) wall resistance for gas flow is similar to that in closed channel flow; (iii) friction coefficient for interfacial shear is same as that for wall gas shear. This assumption has been well established by Gazley (1949) for smooth stratified flow; (iv) Gas velocity is much larger than the interfacial velocity; (v) both the phases are turbulent and Blasius correlation is applicable; (vi) there are no subchannel effects. The flow regime structures are similar in pipe and bundle geometry; (vii) Eccentricity of rods does not influence the flow regime transition and equilibrium stratification level; (viii) Mass transfer between the phases is not considered; (ix) Effect of end plates and the length of the channel is not considered.

Since the condition of stratified flow is central to this analysis, a general relationship is developed for stratified flow. The development of general relationship for stratified flow involves momentum balance on each phase and computation of wall shear. Transformation of basic equations into dimensionless form is done by using reference variables such as D for length, D^2 for area and superficial velocities, u_l and u_g for liquid and vapor velocities, respectively. The dimensionless variables used for rod bundles are defined as follows:

$$\tilde{D} = \frac{d}{D}; \quad \tilde{Z} = \frac{Z}{D}; \quad \tilde{h}_{lr} = \frac{(\tilde{h}_l - \tilde{z})}{D}; \quad \tilde{h}_l = \frac{h_l}{D} \qquad (1)$$

The various symbols are explained in Fig. 1. The sign ~ on top denotes dimensionless variable.

The above-mentioned dimensionless parameters are used to obtain the various dimensionless quantities like wetted perimeters, areas, diameters and velocities for liquid and vapour phases and the interface. Presence of restriction affects these dimensionless quantities in different ways depending upon whether the restriction is covered, uncovered or partly covered with water. The detailed evaluation of these quantities is given below.

The formulation for a pipe without internals is similar to that described by Taitel and Dukler (1976). When internals are present, as a first step these quantities are evaluated assuming

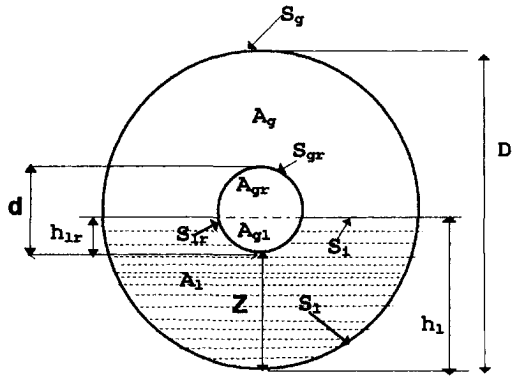

Fig. 1 A flow channel with internals

[1] Scientific Officer and Head respectively, Core Safety Studies Section, Reactor Safety Division, Bhaba Atomic Research Center, Mumbia 400085 India.

[2] Associate Director, Reactor Design and Development Group, Bhaba Atomic Research Center, Mumbia 400085, India.

Contributed by the Fluids Engineering Division of THE AMERICAN SOCIETY OF MECHANICAL ENGINEERS. Manuscript received by the Fluids Engineering Division March 26, 1996; revised manuscript received July 8, 1997. Associate Technical Editor: Jong H. Kim.

ing and cracking of acrylic models in this RIM fluid have been overcome with annealing and mounting strategies that have lead to practical model life. The present RIMLV approach avoids flow interference associated with probes, is not frustrated with the optical accessibility problems, and can be used to obtain high Reynolds numbers at reasonable cost.

References

Dybbs, A., and Edwards, R. V., 1987, "Refractive Index Matching for Difficult Situations," 2nd International Conference on Laser Anemometry—Advances and Applications, Paper I1, Sept.

Elphick, I. G., Martin, W. W., and Currie, I. G., 1982, "Application of LDA to High Reynolds Number Cross Flow," *Proceedings of the International Symposium on Application of Laser Anemometry to Fluid Mechanics,* Superior Technico, Lisbon, Portugal, July, pp. 15.1.1–15.1.12.

Longmire, E. K., and Eaton, J. K., 1992, "Structure of a Particle-Laden Round Jet," *Journal of Fluid Mechanics,* Vol. 236, pp. 217–257.

Liu, C. H., Vafidis, C., and Whitelaw, J. H., 1994, "Flow Characteristics of a Centrifugal Pump," ASME JOURNAL OF FLUIDS ENGINEERING, Vol. 116, June, pp. 303–309.

Nouri, J. M., Whitelaw, J. H., and Yianneskis, M., 1986, "Particle Motion and Turbulence in Dense Two-Phase Flows," *International Journal of Multiphase Flow,* Vol. 13, No. 6, pp. 729–739.

Park, J. T., Mannheimer, R. J., Grimley, T. A., and Morrow, T. B., 1989, "Pipe Flow Measurements of a Transparent Non-Newtonian Slurry," ASME JOURNAL OF FLUIDS ENGINEERING, Vol. 111, Sept., pp. 331–336.

Tindal, M. J., Cheung, R. S., and Yianneskis, M., 1988, "Velocity Characteristics of Steady Flows Through Engine Inlet Ports and Cylinders," Society of Automotive Engineers Paper 880383, Warrendale, PA, Feb.

Thompson, B. E., 1990, "Refractive-Index Matching Techniques in Complex Rocket-Engine Flow Configurations," Scientific Research Associates Report R89-900072-F, Glastonbury, Ct.

Thompson, B. E., Senaldi, J., Vafidis, C., Whitelaw, J. H., and McDonald, H., 1992, "Flow in a Model of the Space Shuttle Main Engine Main Injector Bowl," *Journal of Spacecraft and Rockets,* Vol. 29, Mar.–Apr., pp. 247–252.

Waesche, R. H. W., and Sargent, W. H., 1989, "Space Shuttle Solid Rocket Motor Aft-End Internal Flows," *Journal of Propulsion and Power,* Vol. 5, Nov.–Dec., pp. 650–656.

Flow Regime Identification in Horizontal Channels With Different Types of Rod Clusters

H. G. Lele,[1] S. K. Gupta,[1] and V. Venkat Raj[2]

1 Introduction

The presence of internals affects the flow pattern and flow stratification thresholds in horizontal geometry. Chang et al. (1985) have solved a particular case of concentric annulus geometry and Osamusali and Chang (1987) have extended it to 28 rod and 37 rod bundle geometry. In this paper, a model to determine the flow patterns in a horizontal channel with one or more cylindrical rods inside it is presented. The predictions of the model for 37 rod cluster are compared with the experimental results of Minato et al. (1990) and Osamusali et al. (1992). Flow regime maps for 19 rod bundles are presented in terms of dimensionless parameters, superficial velocities, mass flux, and quality.

2 Model Description

The model considers transition between five basic flow regimes in two-phase flow, viz. smooth stratified, wavy stratified, intermittent (slug and plug), annular with dispersed liquid, and dispersed bubble. The model calculates the equilibrium level and a set of independent dimensionless parameters taking into account internals present in the channel. The set of criteria used by Taitel and Dukler (1976) has been applied for the flow regime transitions.

The following assumptions have been made. (i) Wall resistance for liquid flow is similar to that in open channel flow; (ii) wall resistance for gas flow is similar to that in closed channel flow; (iii) friction coefficient for interfacial shear is same as that for wall gas shear. This assumption has been well established by Gazley (1949) for smooth stratified flow; (iv) Gas velocity is much larger than the interfacial velocity; (v) both the phases are turbulent and Blasius correlation is applicable; (vi) there are no subchannel effects. The flow regime structures are similar in pipe and bundle geometry; (vii) Eccentricity of rods does not influence the flow regime transition and equilibrium stratification level; (viii) Mass transfer between the phases is not considered; (ix) Effect of end plates and the length of the channel is not considered.

Since the condition of stratified flow is central to this analysis, a general relationship is developed for stratified flow. The development of general relationship for stratified flow involves momentum balance on each phase and computation of wall shear. Transformation of basic equations into dimensionless form is done by using reference variables such as D for length, D^2 for area and superficial velocities, u_l and u_g for liquid and vapor velocities, respectively. The dimensionless variables used for rod bundles are defined as follows:

$$\tilde{D} = \frac{d}{D}; \quad \tilde{Z} = \frac{Z}{D}; \quad \tilde{h}_{lr} = \frac{(\tilde{h}_l - \tilde{z})}{D}; \quad \tilde{h}_l = \frac{h_l}{D} \qquad (1)$$

The various symbols are explained in Fig. 1. The sign ~ on top denotes dimensionless variable.

The above-mentioned dimensionless parameters are used to obtain the various dimensionless quantities like wetted perimeters, areas, diameters and velocities for liquid and vapour phases and the interface. Presence of restriction affects these dimensionless quantities in different ways depending upon whether the restriction is covered, uncovered or partly covered with water. The detailed evaluation of these quantities is given below.

The formulation for a pipe without internals is similar to that described by Taitel and Dukler (1976). When internals are present, as a first step these quantities are evaluated assuming

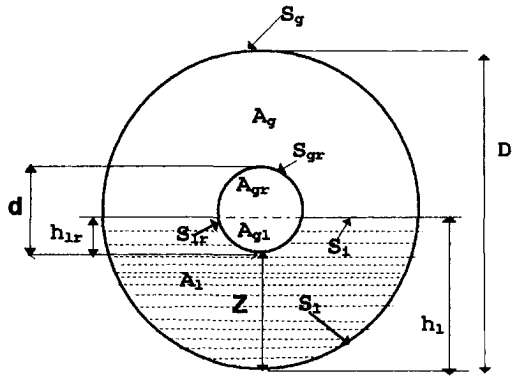

Fig. 1 A flow channel with internals

[1] Scientific Officer and Head respectively, Core Safety Studies Section, Reactor Safety Division, Bhaba Atomic Research Center, Mumbia 400085 India.

[2] Associate Director, Reactor Design and Development Group, Bhaba Atomic Research Center, Mumbia 400085, India.

Contributed by the Fluids Engineering Division of THE AMERICAN SOCIETY OF MECHANICAL ENGINEERS. Manuscript received by the Fluids Engineering Division March 26, 1996; revised manuscript received July 8, 1997. Associate Technical Editor: Jong H. Kim.

that there are no internals and then the effect of internals is calculated and appended to these quantities. The quantities related to an internal are evaluated assuming it as a cylindrical rod. At equilibrium level, when a rod is partially covered (see Fig. 1), its effect is evaluated as follows:

$$\tilde{A}_{lr} = 0.25[\pi - \cos^{-1}(2\,\tilde{h}_{lr} - 1) + (2\,\tilde{h}_{lr} - 1)\,[1 - (2\,\tilde{h}_{lr} - 1)^2]^{0.5}]$$

$$\tilde{A}_{gr} = 0.25[\cos^{-1}(2\,\tilde{h}_{lr} - 1) - (2\,\tilde{h}_{lr} - 1)\,[1 - (2\,\tilde{h}_{lr} - 1)^2]^{0.5}]$$

$$\tilde{S}_{lr} = \pi - \cos^{-1}(2\,\tilde{h}_{lr} - 1)$$

$$\tilde{S}_{gr} = \cos^{-1}(2\,\tilde{h}_{lr} - 1) \qquad (2)$$

where, A is the flow cross-sectional area, S is the perimeter, and subscripts gr and ir indicate gas in rod and interface in rod, respectively.

Under partially covered condition, for each rod, liquid and gas phase dimensionless areas reduce by factors D^2A_{lr} and D^2A_{gr} and liquid and gas phase wetted perimeters increase by factors $S_{lr}D$, and $S_{gr}D$ while the interfacial wetted perimeter reduces by a factor $S_{ir}D$. When the internals are fully submerged in water, the dimensionless quantities related to liquid phase will be affected depending upon the relative dimensions of the rod and pipe. When the internals are not covered by water, dimensionless quantities related to vapor phase get affected.

In the case of a channel with rod cluster, different rods can experience any one of the above mentioned 3 conditions at the same equilibrium level.

The transformation of the basic equations using the above-mentioned dimensionless quantities yields a relationship between the dimensionless Lockhart-Martinelli parameter X, inclination parameter YP and the parameters related to dimensionless equilibrium level h_l as follows:

$$X^2\left[(\tilde{u}_l\tilde{D}_l)^{-n}\tilde{u}_l^2\frac{\tilde{S}_l}{\tilde{A}_l}\right] - (\tilde{u}_g\tilde{D}_g)^{-m}\tilde{u}_g^2\left[\frac{\tilde{S}_l}{\tilde{A}_l} + \frac{\tilde{S}_g}{\tilde{A}_g} + \frac{\tilde{S}_i}{\tilde{A}_i}\right] - 4YP = 0 \qquad (3)$$

where, m and n are the indices in the Blasius correlation, u indicates velocity in x direction, X is Martinelli parameter and YP is inclination parameter. Subscripts g and i denote gas and liquid gas interface. X and YP are given by

$$X = \frac{\dfrac{4C_l}{D}\left(\dfrac{u_l^sD}{\nu_l}\right)^{-n}\dfrac{\rho_l u_l^{s^2}}{2}}{\dfrac{4C_g}{D}\left(\dfrac{u_g^sD}{\nu_g}\right)^{-n}\dfrac{\rho_g u_g^{s^2}}{2}} = \frac{\left(\dfrac{dP}{dx}\right)_l}{\left(\dfrac{dP}{dx}\right)_g}$$

$$YP = \frac{(\rho_l - \rho_g)g\sin\alpha}{\dfrac{4C_g}{D}\left(\dfrac{u_g^sD}{\nu_g}\right)^{-n}\dfrac{\rho_g u_g^{s^2}}{2}} = \frac{(\rho_l - \rho_g)g\sin\alpha}{\left(\dfrac{dP}{dx}\right)_g}$$

where C is a coefficient, g is acceleration due to gravity, α is pipe inclination angle, ρ is density, ν is kinematic viscosity and τ is shear stress. Subscript s is for superficial velocity.

The Kelvin-Helmholtz theory is applied in determining the transition between stratified and nonstratified flow regimes (Taitel and Dukler, 1976). The governing equations are as follows:

$$F^2\left[\frac{1}{C_2^2}\frac{\tilde{u}_g\tilde{d}A_l/\tilde{d}h_l}{\tilde{A}_g}\right] \geq 1 \qquad (4)$$

$$C_2 = 1.0 - \frac{h_l}{D}$$

$$\frac{\tilde{d}A_{lr}}{\tilde{d}h_{lr}} = \sqrt{1.-[2.\tilde{h}_{lr} - 1]^2}$$

$$\frac{\tilde{d}A_{ll}}{\tilde{d}h_l} = \sqrt{1.-[2.\tilde{h}_l - 1]^2}$$

$$\frac{\tilde{d}A_l}{\tilde{d}h_l} = \frac{\tilde{d}A_{ll}}{\tilde{d}h_l} - \frac{\tilde{d}A_{lr}}{\tilde{d}h_{lr}}(\tilde{D}^2) \qquad (5)$$

Froude number is computed as follows:

$$F = \sqrt{\frac{\rho_g}{(\rho_l - \rho_g)}}\frac{u_g^s}{\sqrt{Dg}} \qquad (6)$$

The criteria for transition between other flow regimes are similar to those described by Taitel and Dukler (1976), except that the evaluation of the transition dimensionless parameters is done using Eq. (2). The dimensionless parameters K and T for stratified wavy flow and dispersed bubble flow transition are given by

$$K = \left[\frac{\rho_g(u_g^s)^2\,u_l^s}{(\rho_l - \rho_g)g\nu_l}\right]^{0.5} \qquad (7)$$

$$T = \sqrt{\left[\frac{\dfrac{4C_l}{D}\left(\dfrac{u_l^sD}{\nu_l}\right)^{0.5}}{(\rho_l - \rho_g)g}\right]} \qquad (8)$$

3 Results and Discussion

Figure 2 shows the general flow regime map obtained for 220 Mwe PHWR coolant channel with and without rod bundle. The curve F gives the locus of F-X pairs which satisfy equation (4) and this transition results when the Bernoulli effect on the wave is greater than the gravity effect. Curve B locates the transition between annular flow and intermittent/dispersed bubble flow. This occurs at a constant value of X when h_l is 0.50 and indicates that the growing wave (i.e., increase in X) will have sufficient liquid to form a slug. Below this value, waves will be swept around a pipe to form an annular configuration. Curve K represents the transition between stratified smooth and stratified wavy flow. It is plotted in the K-X plane and locates K-X pairs that satisfy the criterion for transition to stratified smooth flow. Any value of K lower than the curve K will provide insufficient gas flow to cause wave formation. Curve T represents the transition between intermittent and dispersed bubble flow. It represents an identification of the condition where turbulent fluctuations in the liquid become equal to the

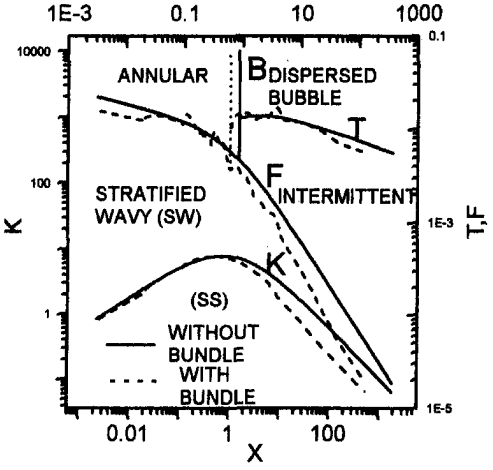

Fig. 2 Flow regime map—dimensionless plot for PHWR coolant channel

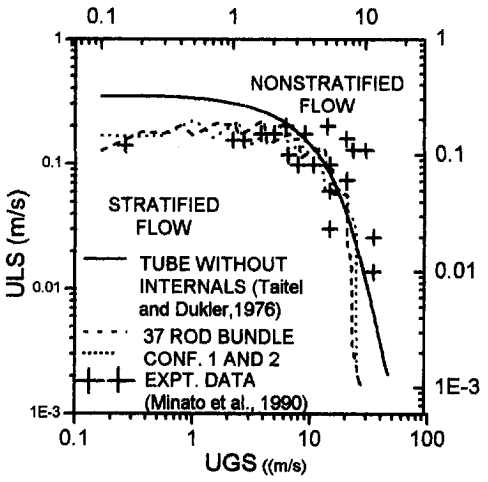

Fig. 3 Code validation using steam-water experimental data (37 rod bundle)

buoyant forces which tend to make the gas to rise to the top of the pipe. This curve gives the locus of T-X pairs which satisfy the criterion for transition to bubbly flow.

On comparison of the dotted and solid curves of Fig. 2, it is seen that the stratification curve F changes due to the presence of internals. The change depends upon the sensitivity of the Bernoulli forces, gravitational pull and the intensity of disturbance wave to the presence of rods. The relative position of the rod with respect to the level also has an influence. Curve B is the value of X corresponding to 50 percent level in a channel. The presence of the rod results in shifting of the line to the left. The influence of internals on the other curves, viz. K and T is also seen and this is due to the influence on various forces deciding these parameters, i.e., K and T.

Figure 3 shows a comparison of the experimental data of Minato et al. (1990) for a channel with 37 rod cluster with the predictions of the model described in this paper. The predictions based on Taitel and Dukler (1976) model for plain tube are also plotted in Fig. 3. It is clearly seen that the predictions of the present model, which considers the presence of internals, are closer to the experimental data. The effect of rod cluster orientation is also shown in Fig. 3. It is observed that the bundle orientation affects the stratification transition to some extent. Figure 4 shows a comparison of the steam-water experimental data of Osamusali et al. (1992) for a channel with 37 rod cluster, on the mass flux vs. quality plane, with the predictions of the model described in this paper. The predictions of the Flow regime Correlation of Osamusali et al. (1992) are also plotted in Fig. 4. It is clearly seen that both the models predict stratification fluxes of the same order. However the predictions of the present model cover the entire range of quality covered in the experiments of Osamusali et al. (1992).

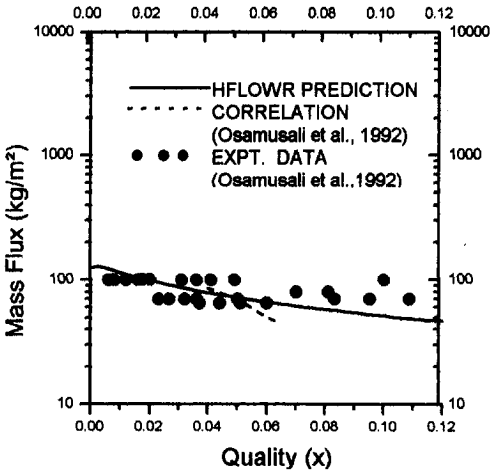

Fig. 4 Validation of HFLOWR with Osamusali's (1992) experimental data

References

Chang, J. S., Revanker, S. T., Raman, R., and Tran, F. B. P., 1985, "Application of EHD Technique to a Nuclear Power Plant Emergency Core Cooling System," *IEEE Trans. Industrial Applications,* Vol. 1A–21, No. 4, pp. 715–723.

Gazley, C., 1949, "Interfacial Shear and Stability in Two-phase Flow," Ph.D. thesis, Univ. Del., Newark.

Minato, A., Sawamura, O., Masao, W., and Ryuzo, M., 1990, "Stratified flow Conditions in a Horizontal Circular Tube Containing a Heated Rod Bundle," *Proceedings of International Topical Meeting on Safety of Thermal Reactors,* Portland, OR, pp. 517–521.

Osamusali, S. I., and Chang, J. S., 1987, "Regime-4 Code for the Prediction of Flow Regime Transitions in a Horizontal Pipe, Annulus and Rod Bundle Flow Under Gas-Liquid Two-Phase Flow," *Proc. 8th Annual Can. Nuclear Soc. Conference,* Saint John, NB.

Osamusali, S. I., Groeneveld, D. C., and Cheng, S. C., 1992, "Two-phase Flow Regimes and Onset of Flow Stratification in Horizontal 37 Rod Bundles," *Journal of Heat and Technology,* Vol. 10, No. 1–2.

Taitel, Y., and Dukler, A. E., 1976, "A Model For Predicting Flow Regime Transitions in Horizontal and Near Horizontal Gas-Liquid Flow," *AIChE Journal,* Vol. 22, No. 1, pp. 47–55.

Richardson's Annular Effect in Oscillating Laminar Duct Flows

A. Yakhot,[1] M. Arad,[1] and G. Ben-Dor[1]

An incompressible viscous fluid, which is forced to move under an oscillating pressure difference in a duct, has a number of characteristic properties. Some features of such a flow are similar to those occurring in the boundary layer on a body which performs reciprocating harmonic oscillations. This is an extension of the problem of the boundary layer when a viscous fluid is bounded by an infinite plane surface which executes a simple harmonic oscillation, with a frequency ω, in its own plane. The latter is the classic problem of the flow near an oscillating flat plate which was first studied by Stokes (see Schlichting, 1979). For this type of flow, transverse waves occur in a viscous fluid, with the velocity perpendicular to the direction of propagation. Stokes introduced a new length scale, the depth of penetration of the viscous wave, $\delta = (2\nu/\omega)^{1/2}$. The amplitude of the transverse waves is rapidly damped by the factor $\exp(-y/\delta)$ as one moves away from the solid surface whose oscillations generate the waves.

The motion of a viscous fluid in a duct caused by pressure gradient oscillations is also characterized by the depth of penetration of the viscous wave, $\delta = (2\nu/\omega)^{1/2}$. Let us choose h to be duct's characteristic dimension. The ratio h/δ is, for instance, the Reynolds number for the flow at hand. Introducing $\alpha = \delta^{-1} = (\omega/2\nu)^{1/2}$, we define the Reynolds number as $\alpha h = (\omega/2\nu)^{1/2}h$. In the case of high-frequency oscillations, where the Reynolds number, αh, is large, the viscous term can be neglected everywhere except in the very narrow layers near the

[1] Associate Professor, Graduate Student, and Professor, respectively, Pearlstone Center for Aeronautical Engineering Studies, Department of Mechanical Engineering, Ben-Gurion University of the Negev, Beersheva 84105, Israel.

Contributed by the Fluids Engineering Division of THE AMERICAN SOCIETY OF MECHANICAL ENGINEERS. Manuscript received by the Fluids Engineering Division February 7, 1997; revised manuscript received July 21, 1997. Associate Technical Editor: D. P. Telionis.

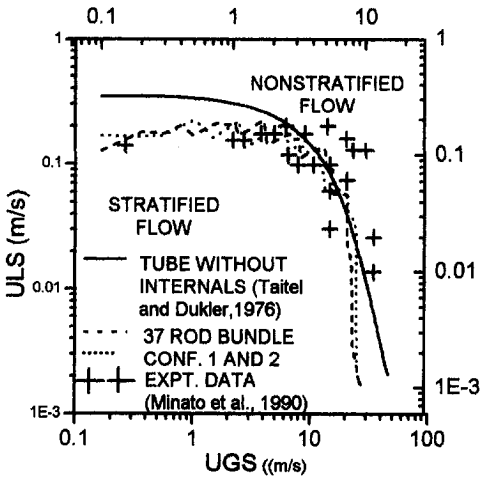

Fig. 3 Code validation using steam-water experimental data (37 rod bundle)

buoyant forces which tend to make the gas to rise to the top of the pipe. This curve gives the locus of T-X pairs which satisfy the criterion for transition to bubbly flow.

On comparison of the dotted and solid curves of Fig. 2, it is seen that the stratification curve F changes due to the presence of internals. The change depends upon the sensitivity of the Bernoulli forces, gravitational pull and the intensity of disturbance wave to the presence of rods. The relative position of the rod with respect to the level also has an influence. Curve B is the value of X corresponding to 50 percent level in a channel. The presence of the rod results in shifting of the line to the left. The influence of internals on the other curves, viz. K and T is also seen and this is due to the influence on various forces deciding these parameters, i.e., K and T.

Figure 3 shows a comparison of the experimental data of Minato et al. (1990) for a channel with 37 rod cluster with the predictions of the model described in this paper. The predictions based on Taitel and Dukler (1976) model for plain tube are also plotted in Fig. 3. It is clearly seen that the predictions of the present model, which considers the presence of internals, are closer to the experimental data. The effect of rod cluster orientation is also shown in Fig. 3. It is observed that the bundle orientation affects the stratification transition to some extent. Figure 4 shows a comparison of the steam-water experimental data of Osamusali et al. (1992) for a channel with 37 rod cluster, on the mass flux vs. quality plane, with the predictions of the model described in this paper. The predictions of the Flow regime Correlation of Osamusali et al. (1992) are also plotted in Fig. 4. It is clearly seen that both the models predict stratification fluxes of the same order. However the predictions of the present model cover the entire range of quality covered in the experiments of Osamusali et al. (1992).

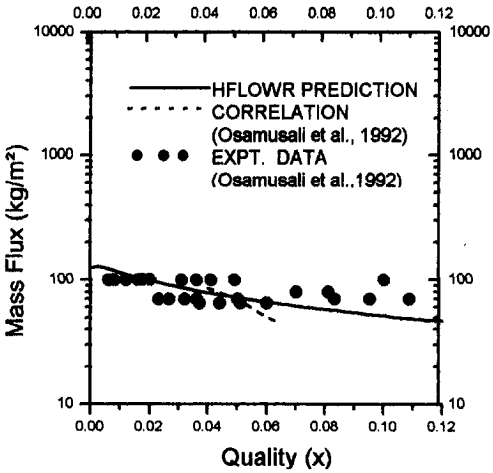

Fig. 4 Validation of HFLOWR with Osamusali's (1992) experimental data

References

Chang, J. S., Revanker, S. T., Raman, R., and Tran, F. B. P., 1985, "Application of EHD Technique to a Nuclear Power Plant Emergency Core Cooling System," *IEEE Trans. Industrial Applications,* Vol. 1A–21, No. 4, pp. 715–723.

Gazley, C., 1949, "Interfacial Shear and Stability in Two-phase Flow," Ph.D. thesis, Univ. Del., Newark.

Minato, A., Sawamura, O., Masao, W., and Ryuzo, M., 1990, "Stratified flow Conditions in a Horizontal Circular Tube Containing a Heated Rod Bundle," *Proceedings of International Topical Meeting on Safety of Thermal Reactors,* Portland, OR, pp. 517–521.

Osamusali, S. I., and Chang, J. S., 1987, "Regime-4 Code for the Prediction of Flow Regime Transitions in a Horizontal Pipe, Annulus and Rod Bundle Flow Under Gas-Liquid Two-Phase Flow," *Proc. 8th Annual Can. Nuclear Soc. Conference,* Saint John, NB.

Osamusali, S. I., Groeneveld, D. C., and Cheng, S. C., 1992, "Two-phase Flow Regimes and Onset of Flow Stratification in Horizontal 37 Rod Bundles," *Journal of Heat and Technology,* Vol. 10, No. 1–2.

Taitel, Y., and Dukler, A. E., 1976, "A Model For Predicting Flow Regime Transitions in Horizontal and Near Horizontal Gas-Liquid Flow," *AIChE Journal,* Vol. 22, No. 1, pp. 47–55.

Richardson's Annular Effect in Oscillating Laminar Duct Flows

A. Yakhot,[1] M. Arad,[1] and G. Ben-Dor[1]

An incompressible viscous fluid, which is forced to move under an oscillating pressure difference in a duct, has a number of characteristic properties. Some features of such a flow are similar to those occurring in the boundary layer on a body which performs reciprocating harmonic oscillations. This is an extension of the problem of the boundary layer when a viscous fluid is bounded by an infinite plane surface which executes a simple harmonic oscillation, with a frequency ω, in its own plane. The latter is the classic problem of the flow near an oscillating flat plate which was first studied by Stokes (see Schlichting, 1979). For this type of flow, transverse waves occur in a viscous fluid, with the velocity perpendicular to the direction of propagation. Stokes introduced a new length scale, the depth of penetration of the viscous wave, $\delta = (2\nu/\omega)^{1/2}$. The amplitude of the transverse waves is rapidly damped by the factor $\exp(-y/\delta)$ as one moves away from the solid surface whose oscillations generate the waves.

The motion of a viscous fluid in a duct caused by pressure gradient oscillations is also characterized by the depth of penetration of the viscous wave, $\delta = (2\nu/\omega)^{1/2}$. Let us choose h to be duct's characteristic dimension. The ratio h/δ is, for instance, the Reynolds number for the flow at hand. Introducing $\alpha = \delta^{-1} = (\omega/2\nu)^{1/2}$, we define the Reynolds number as $\alpha h = (\omega/2\nu)^{1/2}h$. In the case of high-frequency oscillations, where the Reynolds number, αh, is large, the viscous term can be neglected everywhere except in the very narrow layers near the

[1] Associate Professor, Graduate Student, and Professor, respectively, Pearlstone Center for Aeronautical Engineering Studies, Department of Mechanical Engineering, Ben-Gurion University of the Negev, Beersheva 84105, Israel.

Contributed by the Fluids Engineering Division of THE AMERICAN SOCIETY OF MECHANICAL ENGINEERS. Manuscript received by the Fluids Engineering Division February 7, 1997; revised manuscript received July 21, 1997. Associate Technical Editor: D. P. Telionis.

walls. The width of these layers is of the order of magnitude of the depth of penetration of the viscous wave, $\delta \propto (\nu/\omega)^{1/2}$.

We consider an incompressible liquid forced, under an oscillating pressure difference, to move in a duct of an arbitrary constant cross-sectional shape. We suppose that the motion is in the z-direction only, so that the velocity vector is $\mathbf{V} = [0, 0, u(x, y, t)]$. This means that the velocity is solely axial and, hence, the flow is fully developed. The governing equation is

$$\frac{\partial u}{\partial t} = \nu\nabla^2 u - \frac{1}{\rho}\frac{\partial p}{\partial z}, \quad \frac{\partial p}{\partial z} = -\frac{\gamma_p}{L}\cos(\omega t), \quad u|_\Gamma = 0 \quad (1)$$

where ∇^2 is the two-dimensional Laplacian operator, and Γ denotes the boundary of the duct. In Eq. (1), γ_p and ω are the amplitude and the frequency of the pressure difference oscillations, respectively.

A pure pulsating flow in a circular pipe driven by a periodic pressure difference was investigated experimentally by Richardson and Tyler (1929), and its exact analytic solution was obtained by Sexl (1930) and Uchida (1956). The nontrivial feature of this flow is that for very high values of the Reynolds number (very rapid oscillations) the time-mean velocity squared, $\overline{u^2}$, has a maximum, which occurs near the wall. Introducing the nondimensional distance from the wall $\eta = y(\omega/2\nu)^{1/2}$, it was found both experimentally and analytically, that the maximum occurs at $\eta = 2.28$. This effect is known as Richardson's "annular effect" (Schlichting, 1979; White, 1974). It should be noted that the physical meaning of the $\overline{u^2}$ could be associated with the turbulent kinetic energy, which for turbulent shear flows has a maximum near the wall. It is interesting that van Driest used the ideas of the Stokes flow near an oscillating plate to develop his famous turbulent viscosity damping factor (Van Driest, 1956). As far as for the annular effect for a turbulent oscillating flow in a pipe, it was not reported (Tu and Ramaprian, 1983).

We consider the asymptotic case of a very high-frequency flow in a duct with $\alpha h = (\omega/2\nu)^{1/2}h \gg 1$ (h is a characteristic length). We assume that the details of the duct geometry are negligible very close to the wall, and Eq. (1) reads

$$\frac{\partial u}{\partial t} = \frac{\gamma_p}{\rho L}\cos(\omega t) + \nu\frac{\partial^2 u}{\partial y^2}, \quad u = 0 \quad \text{at} \quad y = 0 \quad (2)$$

where y is a coordinate measured normal to the wall. If the duct boundary has any sharp corners, then it is natural to expect that very close to the corner this assumption is not valid. However, in the limiting case of high frequences at hand, the Stokes layer tends to zero and therefore the corner effects become negligible.

Substituting

$$u(y, t) = \frac{\gamma_p}{\rho L\omega}\sin(\omega t) + v(y, t) \quad (3)$$

reduces Eq. (2) to the famous Stokes second problem for $v(y, t)$ (Schlichting, 1979), viz.

$$\frac{\partial v}{\partial t} = \nu\frac{\partial^2 v}{\partial y^2}, \quad v = -\frac{\gamma_p}{\rho L\omega}\sin(\omega t) \quad \text{at} \quad y = 0 \quad (4)$$

Applying Stokes's solution for $v(y, t)$

$$v(y, t) = -\frac{\gamma_p}{\rho L\omega}\exp(-\eta)\sin(\omega t - \eta), \qquad \eta = y(\omega/2\nu)^{1/2} \quad (5)$$

the time-mean velocity squared can be derived from Eqs. (3) and (5). It reads

$$\frac{\overline{u^2}}{2(\gamma_p/\rho L\omega)^2} = 1 - 2\cos(\eta)\exp(-\eta) + \exp(-2\eta), \qquad \eta = y(\omega/2\nu)^{1/2} \quad (6)$$

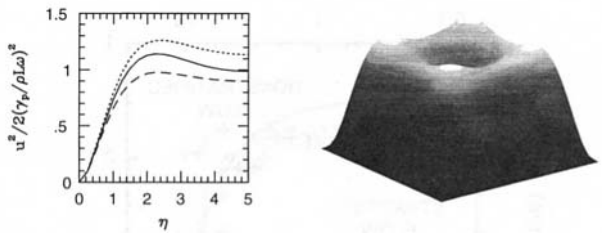

Fig. 1 Richardson's "annular effect" in a duct; $a/h = 1$, $\alpha h = 10$

The function on the right-hand side of Eq. (6) is the same as was obtained from the asymptotic near-wall high-frequency analysis of the oscillating flow in a circular pipe (Schlichting, 1979; White, 1974) and its maximum occurs at $\eta \approx 2.28$. Therefore, we conclude that Richardson's "annular effect" also takes place for high-frequency oscillating flows in ducts of arbitrary cross-sectional shapes.

In order to illustrate the near-wall effect described here, the problem defined by Eq. (1) was solved in a rectangular duct: $0 \le x \le a$, $0 \le y \le h$. It is convenient to use complex notation. Introducing a velocity function $f(x, y, t) = u(x, y, t) + iv(x, y, t)$, we rewrite Eq. (1) in the following form

$$\frac{\partial f}{\partial t} = \nu\nabla^2 f + \frac{\gamma_p}{\rho L}e^{-i\omega t}, \quad f|_\Gamma = 0 \quad (7)$$

when the velocity is the real part of the function $f(x, y, t)$, i.e., $u(x, y, t) = \Re\text{eal}[f(x, y, t)]$.

After substitution

$$f = \left(g + \frac{\gamma_p}{\rho L\omega}\right)ie^{-i\omega t}, \quad g(x, y) = U(x, y) + iV(x, y) \quad (8)$$

into Eq. (7) and decomposition the real and the imaginary parts, we have

$$\nabla^2 U - \frac{\omega}{\nu}V = 0, \quad U|_\Gamma = -\frac{\gamma_p}{\rho L\omega},$$

$$\nabla^2 V + \frac{\omega}{\nu}U = 0, \quad V|_\Gamma = 0 \quad (9)$$

The system of equations (9) has been solved numerically using a method based on a high-order-accurate discretization scheme recently developed by Arad et al. (1997). The calculations were performed for different aspect ratios (a/h) and frequencies (αh). Here we present the results for a square duct ($a = h$) and $\alpha h = (\omega/2\nu)^{1/2}h = 10$.

The plot of the time-mean velocity squared, $\overline{u^2}$, against the nondimensional distance from the wall $\eta = y(\omega/2\nu)^{1/2}$ at different locations (x/a) from the side wall, and the u^2-surface are shown in Fig. 1. The profile at the duct center-line ($x/a = 0.5$, solid line, Fig. 1) shows the near-wall Richardson's effect (about 13 per cent of the mean square velocity overshooting), and that the maximum of $\overline{u^2}$ occurs at $\eta \approx 2.28$. The "corner effect" is clearly seen from the velocity profiles at x-locations close to the side wall: $x/a = 0.25$ (short-dashed-line in Fig. 1) and $x/a = 0.125$ (dashed line in Fig. 1). As expected, close to the corner the effect attenuates.

In conclusion, it was shown analytically that Richardson's "annular effect", which was found in high-frequency oscillating flows in pipes, also takes place for oscillating flows in ducts of arbitrary cross-sectional shapes.

References

Arad, A., Yakhot, A., and Ben-Dor, G., 1997, "A Highly Accurate Numerical Solution of a Biharmonic Equation," *Numerical Methods for Partial Differential Equations*, Vol. 13, pp. 375–391.

Richardson, E. G., and Tyler, E., 1929, "The Transfer Velocity Gradient Near the Mouths of Pipes in which an Alternating or Continuous Flow of Air is Established," *Proceedings of Physics Society,* London, Vol. 42, pp. 1–15.

Schlichting, H., 1979, *Boundary-Layer Theory,* McGraw-Hill, New York.

Sexl, T., 1930, "Uber den von E. G. Richardson entdeckten Annulareffekt," *Zeitschrift fur Physik,* Vol. 61, p. 349.

Van Driest, E., 1956, "On Turbulent Flow Near a Wall," *Journal of Aeronautical Sciences,* Vol. 23, No. 11.

Tu, S. W., and Ramaprian, B. R., 1983, "Fully Developed Periodic Turbulent Pipe Flow. Parts 1 and 2," *Journal of Fluid Mechanics,* Vol. 137, pp. 31–81.

Uchida, C., 1956, "The Pulsating Viscous Flow Superposed on the Steady Motion of Incompressible Fluid in a Circular Pipe," *Zeitschrift fur Angewandte Mathematik und Physik,* Vol. 7, pp. 403–421.

White, F. M., 1974, *Viscous Fluid Flow,* McGraw-Hill, New York.

Asymptotic Flow Regimes in Pulsatile Flows of Bingham Plastics

K. J. Hammad[1,2] and G. C. Vradis[1]

1 Introduction

The internal unsteady flow of Bingham fluids is of importance to a number of industries. Of specific interest is pulsating flows of these fluids. Many pulsatile flows are naturally occurring phenomena, i.e., physiological flows such as the flow of blood in an artery. Additionally, handling, transporting, and processing of the aforementioned fluids are influenced by the pulsatile nature of either the pumping or the manufacturing process. Several studies have concentrated on the steady-state flow, with or without heat transfer, of Bingham fluids through pipes (see Vradis and Hammad, 1995; and Hammad and Vradis, 1996a). Earlier studies on the pulsating flows of Bingham fluids, such as those of Phan-Tien and Dudek (1982) and Kajiuchi and Saito (1984), have all shown that, at least within the narrow range of frequencies and Reynolds and yield numbers studied, pulsating the flow of a Bingham fluid through the imposition of a fluctuating pressure gradient over a nonzero mean value enhances the flow, i.e., the time averaged flow rate in a pulsating flow is higher than that corresponding to the steady state one at the same mean pressure gradient. However, the net power needed to pulsate the flow was found to be always greater than that required to maintain the enhanced flow rate in a steady-state manner. The amount of both the flow rate enhancement and the additional pumping power needed was shown to be dependent on the fluid's rheology parameter, i.e., the yield number, the Reynolds number, and the amplitude and the frequency of the pulsations (see Kajiuchi and Saito, 1984).

None of the previously mentioned studies conducted a comprehensive investigation of the effect of the imposed frequency and the Reynolds number on the flow rate enhancement and extra power requirement characteristics of pulsating flows of Bingham like fluids. The present work concentrates on studying the variations in the time averaged characteristics of the pulsating flow of a non-Newtonian Bingham plastic throughout a very wide range of the imposed nondimensional frequency and Reynolds number spectrums that allows the determination of all relevant flow regimes for this problem. The flow at any instant is considered periodically "fully-developed," thus rendering the problem two-dimensional. The fluid properties are assumed constant.

2 Governing Equations and Their Solution

The transient one-dimensional momentum conservation equation for inelastic and time-independent non-Newtonian fluids is (written nondimensional):

$$S\,\frac{\partial u}{\partial t} = -\frac{\partial p}{\partial x} + \frac{1}{\mathrm{Re}}\,\frac{1}{r}\,\frac{\partial}{\partial r}\left(\mu_{\mathrm{eff}} r\,\frac{\partial u}{\partial r}\right) \tag{1}$$

where:

$$\frac{\partial p}{\partial x} = \left(\frac{\partial p}{\partial x}\right)_{sfl}(1 + \epsilon \sin t) \tag{2}$$

Here $\mathrm{Re} = \rho d_w u_{sb}/\eta_p$ is the Reynolds number, $S = (1/2)(d_w f/u_{sb})$ is the Strouhal number, and the index sfl indicated steady, fully developed flow conditions. The velocity is nondimensionalized with respect to the bulk velocity u_{sb} of the corresponding steady flow. The "effective viscosity" concept has been utilized above in writing the governing equations. In the case of a Bingham fluid, the nondimensional effective viscosity μ_{eff} is given by (see Hammad and Vradis, 1996a):

$$\mu_{eff} = 1 + \frac{Y}{\sqrt{\frac{1}{2}D_{\mathrm{II}}}} \quad \text{for} \quad \tau_{\mathrm{II}} > 2\tau_y^2 \tag{3a}$$

$$\mu_{\mathrm{eff}} = \infty \quad \text{for} \quad \tau_{\mathrm{II}} \le 2\tau_y^2 \tag{3b}$$

Here $Y = \tau_y r_w/\eta_p u_{sb}$ is the yield number, τ_y is the yield stress, and D_{II} is the second invariant of the rate-of-deformation tensor, while τ_{II} is the second invariant of the stress tensor.

The flow is initialized assuming the steady state fully developed velocity distribution (for the corresponding yield number). Imposing the periodic pressure gradient, the solution eventually reaches a periodic state, which is the sought solution. The standard no-slip condition is imposed for the velocity on the pipe walls. The computational grid employed consisted of 100 points in the radial direction ($\Delta r = 0.01$) and a time step $\Delta t = 0.001$. Results obtained with a grid size and a time step half the above were identical with the ones presented here. For further details on the computational grid and the solution methodology of the governing equations, the reader is referred to Hammad and Vradis (1996b).

3 Results

For a fixed pulsation amplitude, in this case $\epsilon = 1$, the nondimensional formulation presented in Eqs. (1) and (2) results in velocity profiles that vary with the S*Re parameter and the yield number. Figures 1(*a*) and (*b*) show the bulk velocity evolution in one cycle for S*Re = 0.1 and 10, respectively, and for yield numbers of $Y = 1$, 10, and 100. The flow-wave form in the S*Re = 0.1 case follows closely that of the pressure gradient in the first half of the cycle without a noticeable phase shift. These are characteristics similar to those of a quasi-steady-state flow. However, in the second half of the cycle the bulk velocity drops to a zero value over a finite time interval of time. This is a unique characteristic of yield stress fluids, and occurs whenever the imposed pressure gradient drops below the critical value required to sustain a velocity gradient. As expected, the width of this zero bulk velocity time interval increases with the yield number. Increasing the S*Re parameter to 10, see Fig. 1(*b*), leads to an appreciable phase shift between the imposed pressure gradient and the resulting flow-wave form.

[1] Department of Mechanical, Aerospace and Manufacturing Engineering, Polytechnic University, Six Metrotech Center, Brooklyn, NY 11201. Professor Vradis is a Mem. ASME.

[2] Presently, Associate Research Scientist, Fluid Dynamics Group, Pacific Northwest Laboratory, Battelle Boulevard, P.O. Box 999, Richland, WA 99352.

Contributed by the Fluids Engineering Division of THE AMERICAN SOCIETY OF MECHANICAL ENGINEERS. Manuscript received by the Fluids Engineering Division September 1, 1996; revised manuscript received October 20, 1997. Associate Technical Editor: F. Giralt.

Richardson, E. G., and Tyler, E., 1929, "The Transfer Velocity Gradient Near the Mouths of Pipes in which an Alternating or Continuous Flow of Air is Established," *Proceedings of Physics Society,* London, Vol. 42, pp. 1–15.

Schlichting, H., 1979, *Boundary-Layer Theory,* McGraw-Hill, New York.

Sexl, T., 1930, "Uber den von E. G. Richardson entdeckten Annulareffekt," *Zeitschrift fur Physik,* Vol. 61, p. 349.

Van Driest, E., 1956, "On Turbulent Flow Near a Wall," *Journal of Aeronautical Sciences,* Vol. 23, No. 11.

Tu, S. W., and Ramaprian, B. R., 1983, "Fully Developed Periodic Turbulent Pipe Flow. Parts 1 and 2," *Journal of Fluid Mechanics,* Vol. 137, pp. 31–81.

Uchida, C., 1956, "The Pulsating Viscous Flow Superposed on the Steady Motion of Incompressible Fluid in a Circular Pipe," *Zeitschrift fur Angewandte Mathematik und Physik,* Vol. 7, pp. 403–421.

White, F. M., 1974, *Viscous Fluid Flow,* McGraw-Hill, New York.

Asymptotic Flow Regimes in Pulsatile Flows of Bingham Plastics

K. J. Hammad[1,2] and G. C. Vradis[1]

1 Introduction

The internal unsteady flow of Bingham fluids is of importance to a number of industries. Of specific interest is pulsating flows of these fluids. Many pulsatile flows are naturally occurring phenomena, i.e., physiological flows such as the flow of blood in an artery. Additionally, handling, transporting, and processing of the aforementioned fluids are influenced by the pulsatile nature of either the pumping or the manufacturing process. Several studies have concentrated on the steady-state flow, with or without heat transfer, of Bingham fluids through pipes (see Vradis and Hammad, 1995; and Hammad and Vradis, 1996a). Earlier studies on the pulsating flows of Bingham fluids, such as those of Phan-Tien and Dudek (1982) and Kajiuchi and Saito (1984), have all shown that, at least within the narrow range of frequencies and Reynolds and yield numbers studied, pulsating the flow of a Bingham fluid through the imposition of a fluctuating pressure gradient over a nonzero mean value enhances the flow, i.e., the time averaged flow rate in a pulsating flow is higher than that corresponding to the steady state one at the same mean pressure gradient. However, the net power needed to pulsate the flow was found to be always greater than that required to maintain the enhanced flow rate in a steady-state manner. The amount of both the flow rate enhancement and the additional pumping power needed was shown to be dependent on the fluid's rheology parameter, i.e., the yield number, the Reynolds number, and the amplitude and the frequency of the pulsations (see Kajiuchi and Saito, 1984).

None of the previously mentioned studies conducted a comprehensive investigation of the effect of the imposed frequency and the Reynolds number on the flow rate enhancement and extra power requirement characteristics of pulsating flows of Bingham like fluids. The present work concentrates on studying the variations in the time averaged characteristics of the pulsating flow of a non-Newtonian Bingham plastic throughout a very wide range of the imposed nondimensional frequency and Reynolds number spectrums that allows the determination of all relevant flow regimes for this problem. The flow at any instant is considered periodically "fully-developed," thus rendering the problem two-dimensional. The fluid properties are assumed constant.

2 Governing Equations and Their Solution

The transient one-dimensional momentum conservation equation for inelastic and time-independent non-Newtonian fluids is (written nondimensional):

$$S\,\frac{\partial u}{\partial t} = -\frac{\partial p}{\partial x} + \frac{1}{\mathrm{Re}}\,\frac{1}{r}\,\frac{\partial}{\partial r}\left(\mu_{\mathrm{eff}} r\,\frac{\partial u}{\partial r}\right) \tag{1}$$

where:

$$\frac{\partial p}{\partial x} = \left(\frac{\partial p}{\partial x}\right)_{sfl}(1 + \epsilon \sin t) \tag{2}$$

Here $\mathrm{Re} = \rho d_w u_{sb}/\eta_p$ is the Reynolds number, $S = (1/2)(d_w f/u_{sb})$ is the Strouhal number, and the index sfl indicated steady, fully developed flow conditions. The velocity is nondimensionalized with respect to the bulk velocity u_{sb} of the corresponding steady flow. The "effective viscosity" concept has been utilized above in writing the governing equations. In the case of a Bingham fluid, the nondimensional effective viscosity μ_{eff} is given by (see Hammad and Vradis, 1996a):

$$\mu_{eff} = 1 + \frac{Y}{\sqrt{\frac{1}{2}D_{\mathrm{II}}}} \quad \text{for} \quad \tau_{\mathrm{II}} > 2\tau_y^2 \tag{3a}$$

$$\mu_{\mathrm{eff}} = \infty \quad \text{for} \quad \tau_{\mathrm{II}} \le 2\tau_y^2 \tag{3b}$$

Here $Y = \tau_y r_w/\eta_p u_{sb}$ is the yield number, τ_y is the yield stress, and D_{II} is the second invariant of the rate-of-deformation tensor, while τ_{II} is the second invariant of the stress tensor.

The flow is initialized assuming the steady state fully developed velocity distribution (for the corresponding yield number). Imposing the periodic pressure gradient, the solution eventually reaches a periodic state, which is the sought solution. The standard no-slip condition is imposed for the velocity on the pipe walls. The computational grid employed consisted of 100 points in the radial direction ($\Delta r = 0.01$) and a time step $\Delta t = 0.001$. Results obtained with a grid size and a time step half the above were identical with the ones presented here. For further details on the computational grid and the solution methodology of the governing equations, the reader is referred to Hammad and Vradis (1996b).

3 Results

For a fixed pulsation amplitude, in this case $\epsilon = 1$, the nondimensional formulation presented in Eqs. (1) and (2) results in velocity profiles that vary with the S*Re parameter and the yield number. Figures 1(*a*) and (*b*) show the bulk velocity evolution in one cycle for S*Re = 0.1 and 10, respectively, and for yield numbers of $Y = 1$, 10, and 100. The flow-wave form in the S*Re = 0.1 case follows closely that of the pressure gradient in the first half of the cycle without a noticeable phase shift. These are characteristics similar to those of a quasi-steady-state flow. However, in the second half of the cycle the bulk velocity drops to a zero value over a finite time interval of time. This is a unique characteristic of yield stress fluids, and occurs whenever the imposed pressure gradient drops below the critical value required to sustain a velocity gradient. As expected, the width of this zero bulk velocity time interval increases with the yield number. Increasing the S*Re parameter to 10, see Fig. 1(*b*), leads to an appreciable phase shift between the imposed pressure gradient and the resulting flow-wave form.

[1] Department of Mechanical, Aerospace and Manufacturing Engineering, Polytechnic University, Six Metrotech Center, Brooklyn, NY 11201. Professor Vradis is a Mem. ASME.

[2] Presently, Associate Research Scientist, Fluid Dynamics Group, Pacific Northwest Laboratory, Battelle Boulevard, P.O. Box 999, Richland, WA 99352.

Contributed by the Fluids Engineering Division of THE AMERICAN SOCIETY OF MECHANICAL ENGINEERS. Manuscript received by the Fluids Engineering Division September 1, 1996; revised manuscript received October 20, 1997. Associate Technical Editor: F. Giralt.

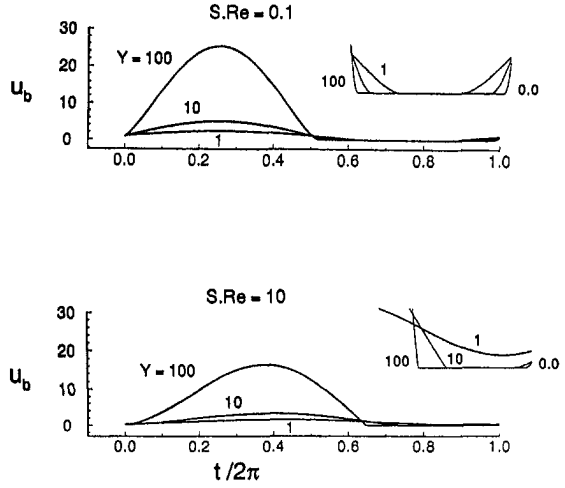

Fig. 1 Instantaneous bulk velocity for: (*a*) S*Re = 0.1 and (*b*) S*Re = 10

The phase shift angle between the pulsating pressure and the flow-wave is shown in Fig. 2 as a function of S*Re for yield numbers of $Y = 1$, 10, 100, and 1000. Since the "transfer of information" normal to the flow direction is faster for higher yield number fluids, the phase shift angle decreases with the yield number as shown in the figure. Additionally, asymptotic values of zero and 90 degrees, i.e., a quarter of the full cycle, are observed at the low and high ends of the frequency spectrum, respectively. At low S*Re numbers the viscous effects are dominant and the frequencies are low, therefore, the fluid has "enough time" to respond to the externally imposed changes and as a result the phase angle is very small. At the other end of the spectrum, high Re numbers and high frequencies result in strong inertia effects (that completely dominate negating the influence of the yield number) and lack of response time thus, the high phase angles between flow rate and the pressure gradient. The sensitivity of the phase shift to changes in the yield number is limited to the intermediate values of the studied S*Re range as shown in the figure. Returning back to Fig. 1(*b*), the result of this phase shift at a S*Re = 10 results in the appearance of the zero bulk velocity regime at about 0.65, the flow reappearing only at the very end of the period.

As mentioned earlier, pulsating the flow of a non-Newtonian fluid results in flow rates differing from the ones obtained under steady-state conditions. Shear-thinning behavior leads to flow rate enhancement while the contrary is true for a shear-thickening fluid (if the fluid's rheology is Newtonian, the obtained pulsatile flow rates are identical to those of the steady state). In addition to flow rate enhancement, the extra power requirements needed to establish such flows are of equal importance.

As seen in Figs. 3(*a*), (*b*), (*c*), and (*d*), the flow enhancement (defined as the percentage increase in the mean flow rate under pulsating flow conditions as it compares to the flow rate established under a steady pressure gradient equal to the mean pulsating pressure gradient) is maximum at the lowest S*Re value. Increasing S*Re results in a gradual initially, then sudden drop in the obtained flow rate followed by a sudden flattening of the profile and eventually a minimum and close to zero value at the highest S*Re value. This trend is observed for all yield numbers (1, 10, 100, and 1000). The intermediate flow regime, i.e., the one where the variations of the flow rates with the S*Re values are large, is narrower for smaller yield numbers and experiences a shift to the right as the yield number is increased. Additionally, large yield numbers are needed to bring about significant flow rate enhancement levels. This is consistent with similar results obtained by Kajiuchi and Saito (1984) for a different, rather limited, range of parameters.

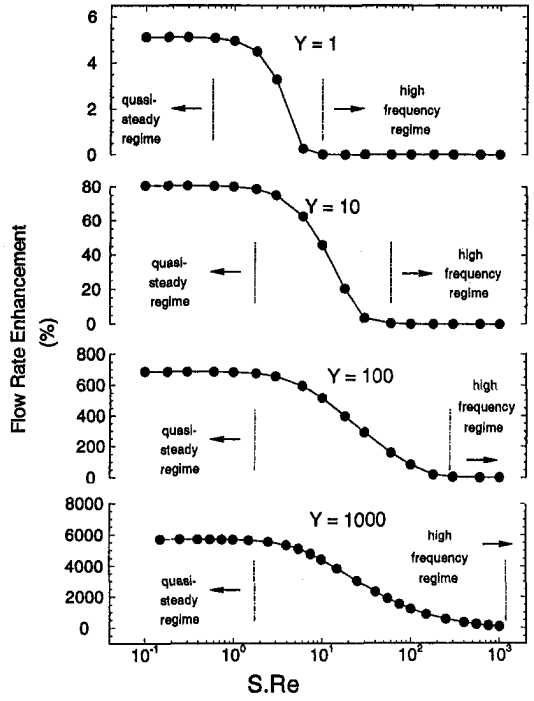

Fig. 3 Percentage of flow rate enhancement for $Y = 1$, 10, 100, and 1000

The flow enhancement in the case of a Bingham plastic is always accompanied with an increase in the power requirements necessary to sustain such a flow. This additional amount of power is shown in Fig. 4. The variation in the extra rate of work trend with both S*Re parameter and for all the studied yield numbers is similar to that of the flow rate enhancement. In the case of Newtonian fluids this extra work maximizes at low frequencies and asymptotically tends to zero at very high frequencies. The results in the present case of a Bingham fluid are consistent with those results in that the extra work needed is higher in the case of the lower frequency throughout the S*Re parameter and yield number ranges. Again, it should be emphasized here that for all values of the governing parameters the power required to maintain the pulsating flow is higher than that of steady-state flow.

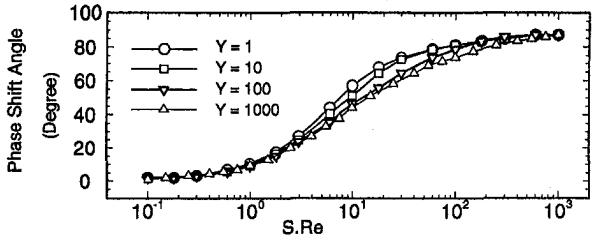

Fig. 2 Shift angle between pressure gradient and bulk velocity

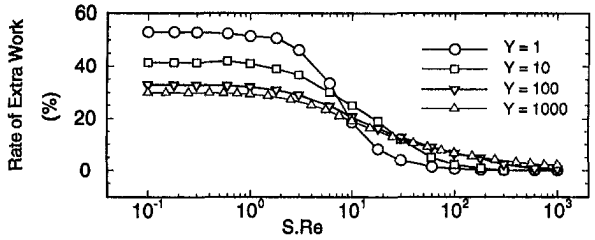

Fig. 4 Percentage of extra rate of work for $Y = 1$, 10, 100, and 1000

4 Conclusions

The present study has identified three distinct flow regimes associated with the axially fully-developed unsteady flow of a Bingham fluid through a circular pipe subjected to a time periodic pressure gradient. The first regime corresponds to low S*Re values and is identified as a quasi-steady-state regime whose time resolved characteristics are identical to those of the steady state conditions at the same instantaneous pressure gradient. In the second regime all flow characteristics are truly time dependent and varying continuously both with the S*Re and the yield number parameters, while in the third regime the time averaged flow characteristics are practically identical to the steady-state conditions.

References

Hammad, K. J., and Vradis, G. C., 1996a, "Creeping flow of a Bingham Plastic Through Axisymmetric Sudden Contractions with Viscous Dissipation," *International Journal of Heat and Mass Transfer,* Vol. 39(8), pp. 1555–1567.

Hammad, K. J., and Vradis, G. C., 1996b, "Viscous Dissipation and Heat Transfer in Pulsatile Flows of a Yield-Stress Fluid," *International Communications in Heat and Mass Transfer,* Vol. 23, No. 5, pp. 599–612.

Kajiuchi, T., and Saito, A., 1984, "Flow Enhancement of Laminar Pulsating Flow of Bingham Plastic Fluids," *Journal of Chemical Engineering of Japan,* Vol. 17(1), pp. 34–38.

Phan-Thien, N., and Dudek, J., 1982, "Pulsating Flow of a Plastic Fluid," *Nature,* Vol. 296, pp. 843–844.

Vradis, G. C., and Hammad, K. J., 1995, "Heat Transfer in Flows of Non-Newtonian Bingham Fluids Through Axisymmetric Sudden Expansions and Contractions," *Numerical Heat Transfer,* Part A, Vol. 28(3), pp. 339–353.

Laser Pointing Stability and Alignment Technique

Gerald L. Morrison[1] and Brian G. Wiedner[2]

Nomenclature

- a = laser beam $1/e^2$ intensity radius
- I = laser light intensity
- P = laser light power
- P_t = laser beam total power
- P' = $\partial P/\partial X$
- P'' = $\partial P^2/\partial X^2$
- r = radial distance from pinhole centerline
- R = radius of pinhole
- x = horizontal distance from pinhole centerline
- X = horizontal displacement of laser beam centerline from pinhole centerline
- y = vertical distance from pinhole centerline
- Y = vertical displacement of laser beam centerline from pinhole centerline
- θ = azimuthal angle measured counter-clockwise from the horizontal (x) axis
- ξ = radial distance from laser beam centerline

[1] Nelson-Jackson Professor, Texas A&M University, Mechanical Engineering Department, College Station, TX 77843-3123.

[2] Mechanical Engineer, Brown and Root Energy Services, 10200 Bellaire Blvd., Houston, TX 77072.

Contributed by the Fluids Engineering Division of THE AMERICAN SOCIETY OF MECHANICAL ENGINEERS. Manuscript received by the Fluids Engineering Division March 18, 1997; revised manuscript received September 11, 1997. Associate Technical Editor: P. W. Bearman.

Introduction

Optical systems for laser light can be very complex. For example, a six beam LDV system consisting of discrete optical components (not fiber optics) may use three colors from an argon-ion laser with each color beam split into two beams. These six beams pass through numerous optical components then cross at a single point in space that is usually 25 to 100 microns in diameter. Slight variations in the pitch and yaw of the laser beam exiting the laser as well a vertical and horizontal movement can result in the six beams not crossing. This variation in the laser beam orientation is very subtle and takes place over a period of hours or even days. Very complex optical systems which take days to align can be rendered useless since the laser beam has moved during the alignment. The laser beam orientation variation can also be costly in fiber optic systems. Some fiber optic LDV systems use a Bragg cell to split the beams, separate colors, and provide frequency shift to the various colors. This technique requires that there is a sizable distance between the Bragg cell and the individual fiber optic launchers for the beams to diverge sufficiently so that each can be deflected by a mirror into the fiber optic. The drift of the laser beam orientation can cause the beam to improperly enter or to entirely miss the fiber optic. If the laser is operating at a sufficiently high power, the end of the fiber optic can be burned. The fiber optic must then be cut and polished before it is usable again.

Laser Alignment Monitoring System

The solution devised in the Turbomachinery Laboratory to eliminate the problems encountered due to laser beam pointing stability consists of installing some extra optics between the laser output and the optical system being used. The purpose of these extra optics is to monitor and correct any variations in the laser beam orientation so that the optical system is always supplied a laser beam with the same pitch, yaw, and position. This system is in use on a 3-D LDV system and has made it possible to run the LDV without realigning the LDV optics for periods of months. We have even had the laser tube replaced and resumed full operation in less than 30 minutes after the laser technician left.

Figure 1 illustrates the additional optical components. The laser is offset from its original location and two mirrors are used to bounce the laser beam in a Z shaped path. The mirror mounts can pitch and yaw the mirror. By adjusting both mirrors it is possible to vertically and horizontally translate the laser beam as well as adjust the pitch and yaw of the laser beam. In order to monitor the beam orientation after these two mirrors, a low power beam must be split from the main laser beam. In the LDV system we use, there is a polarizing cube which dumps the portion of the laser beam with the wrong polarity. We used this beam to monitor the beam orientation. In other applications a 99:1 beam splitter cube could be employed to obtain the low power beam. The low power monitor beam is then split into

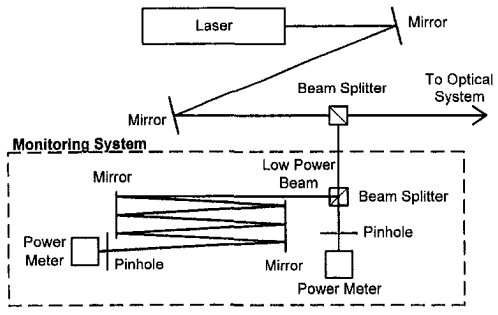

Fig. 1 Laser pointing stability monitoring and alignment system

4 Conclusions

The present study has identified three distinct flow regimes associated with the axially fully-developed unsteady flow of a Bingham fluid through a circular pipe subjected to a time periodic pressure gradient. The first regime corresponds to low S*Re values and is identified as a quasi-steady-state regime whose time resolved characteristics are identical to those of the steady state conditions at the same instantaneous pressure gradient. In the second regime all flow characteristics are truly time dependent and varying continuously both with the S*Re and the yield number parameters, while in the third regime the time averaged flow characteristics are practically identical to the steady-state conditions.

References

Hammad, K. J., and Vradis, G. C., 1996a, "Creeping flow of a Bingham Plastic Through Axisymmetric Sudden Contractions with Viscous Dissipation," *International Journal of Heat and Mass Transfer,* Vol. 39(8), pp. 1555–1567.

Hammad, K. J., and Vradis, G. C., 1996b, "Viscous Dissipation and Heat Transfer in Pulsatile Flows of a Yield-Stress Fluid," *International Communications in Heat and Mass Transfer,* Vol. 23, No. 5, pp. 599–612.

Kajiuchi, T., and Saito, A., 1984, "Flow Enhancement of Laminar Pulsating Flow of Bingham Plastic Fluids," *Journal of Chemical Engineering of Japan,* Vol. 17(1), pp. 34–38.

Phan-Thien, N., and Dudek, J., 1982, "Pulsating Flow of a Plastic Fluid," *Nature,* Vol. 296, pp. 843–844.

Vradis, G. C., and Hammad, K. J., 1995, "Heat Transfer in Flows of Non-Newtonian Bingham Fluids Through Axisymmetric Sudden Expansions and Contractions," *Numerical Heat Transfer,* Part A, Vol. 28(3), pp. 339–353.

Laser Pointing Stability and Alignment Technique

Gerald L. Morrison[1] and Brian G. Wiedner[2]

Nomenclature

- a = laser beam $1/e^2$ intensity radius
- I = laser light intensity
- P = laser light power
- P_t = laser beam total power
- P' = $\partial P/\partial X$
- P'' = $\partial P^2/\partial X^2$
- r = radial distance from pinhole centerline
- R = radius of pinhole
- x = horizontal distance from pinhole centerline
- X = horizontal displacement of laser beam centerline from pinhole centerline
- y = vertical distance from pinhole centerline
- Y = vertical displacement of laser beam centerline from pinhole centerline
- θ = azimuthal angle measured counter-clockwise from the horizontal (x) axis
- ξ = radial distance from laser beam centerline

[1] Nelson-Jackson Professor, Texas A&M University, Mechanical Engineering Department, College Station, TX 77843-3123.

[2] Mechanical Engineer, Brown and Root Energy Services, 10200 Bellaire Blvd., Houston, TX 77072.

Contributed by the Fluids Engineering Division of THE AMERICAN SOCIETY OF MECHANICAL ENGINEERS. Manuscript received by the Fluids Engineering Division March 18, 1997; revised manuscript received September 11, 1997. Associate Technical Editor: P. W. Bearman.

Introduction

Optical systems for laser light can be very complex. For example, a six beam LDV system consisting of discrete optical components (not fiber optics) may use three colors from an argon-ion laser with each color beam split into two beams. These six beams pass through numerous optical components then cross at a single point in space that is usually 25 to 100 microns in diameter. Slight variations in the pitch and yaw of the laser beam exiting the laser as well a vertical and horizontal movement can result in the six beams not crossing. This variation in the laser beam orientation is very subtle and takes place over a period of hours or even days. Very complex optical systems which take days to align can be rendered useless since the laser beam has moved during the alignment. The laser beam orientation variation can also be costly in fiber optic systems. Some fiber optic LDV systems use a Bragg cell to split the beams, separate colors, and provide frequency shift to the various colors. This technique requires that there is a sizable distance between the Bragg cell and the individual fiber optic launchers for the beams to diverge sufficiently so that each can be deflected by a mirror into the fiber optic. The drift of the laser beam orientation can cause the beam to improperly enter or to entirely miss the fiber optic. If the laser is operating at a sufficiently high power, the end of the fiber optic can be burned. The fiber optic must then be cut and polished before it is usable again.

Laser Alignment Monitoring System

The solution devised in the Turbomachinery Laboratory to eliminate the problems encountered due to laser beam pointing stability consists of installing some extra optics between the laser output and the optical system being used. The purpose of these extra optics is to monitor and correct any variations in the laser beam orientation so that the optical system is always supplied a laser beam with the same pitch, yaw, and position. This system is in use on a 3-D LDV system and has made it possible to run the LDV without realigning the LDV optics for periods of months. We have even had the laser tube replaced and resumed full operation in less than 30 minutes after the laser technician left.

Figure 1 illustrates the additional optical components. The laser is offset from its original location and two mirrors are used to bounce the laser beam in a Z shaped path. The mirror mounts can pitch and yaw the mirror. By adjusting both mirrors it is possible to vertically and horizontally translate the laser beam as well as adjust the pitch and yaw of the laser beam. In order to monitor the beam orientation after these two mirrors, a low power beam must be split from the main laser beam. In the LDV system we use, there is a polarizing cube which dumps the portion of the laser beam with the wrong polarity. We used this beam to monitor the beam orientation. In other applications a 99:1 beam splitter cube could be employed to obtain the low power beam. The low power monitor beam is then split into

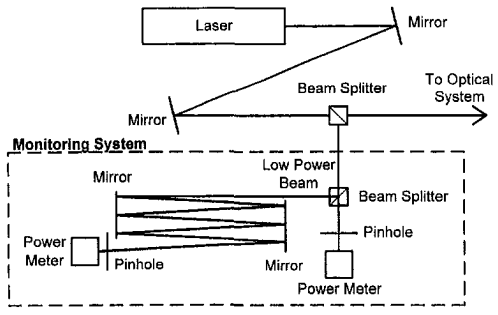

Fig. 1 Laser pointing stability monitoring and alignment system

two beams using a beam splitter. One beam terminates at a pinhole located close to the beam splitter. The second beam is folded upon itself several times using two mirrors to produce a beam path longer than ten meters which terminates at another pinhole.

The two mirrors on the main laser beam are adjusted so that the laser beam is entering the final optical system at the location and orientation required. The two pinholes on the monitoring system are then adjusted so that the laser beam is centered on each pinhole. From then on, as long as the laser beams are centered on the pinholes, the orientation of the main laser beam into the final optical system will be maintained.

The method employed to center the laser beam on a pinhole is performed in two steps. Coarse adjustments to the laser beam position are made by viewing the laser diffraction pattern produced by the pinhole-laser beam interaction. The diffraction of a beam centered on a pinhole will display concentric rings of light about the Airy disk. Fine adjustments to the laser beam position are then made by placing a power meter behind the pinhole and adjusting the pinhole or laser beam position to obtain the maximum power transmitted through the pinhole. The selection of the pinhole size which is most sensitive to the alignment process can help increase the accuracy of the alignment. In order to determine the optimum pinhole size the following analysis was performed.

The general equation for the Gaussian intensity distribution of a standard laser operating in the T_{oo} mode is given by:

$$I(\xi, a) = \frac{2P_t}{\pi a^2} e^{-2\xi^2/a^2}$$

In this equation, a is the $1/e^2$ intensity radius of the laser beam where the local intensity is 13.5 percent of the centerline intensity, ξ is the distance from the centerline of the laser beam, and P_t is the total power of the laser beam.

To analyze the power passing through a pinhole, the coordinate system shown in Figure 2 is used. Here r is the radial distance from the centerline of the pinhole and the centerline of the laser beam is located at coordinates (X, Y). The power of the light passing through a pinhole with radius R is then given by:

$$P(X, Y, a, R) = \int_0^R \int_0^{2\pi} I(\sqrt{(r\cos\theta - X)^2 + (r\sin\theta - Y)^2}, a) r d\theta dr$$

This expression was used to evaluate the effectiveness of different pinhole sizes for laser beam alignment. Figure 3 shows the power transmitted through a pinhole of various sizes for $Y = 0$ and X varying from 0 to $3a$. As expected the power level increases with increasing pinhole size until reaching the maximum of 1 at which point the power is constant near $X/a = 0$. This occurs when the entire beam is passing through the pinhole

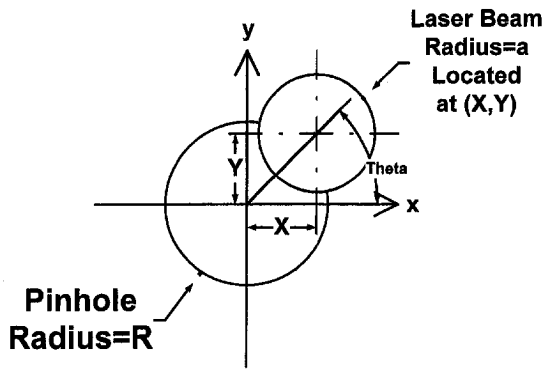

Fig. 2 Pinhole-laser beam coordinate system

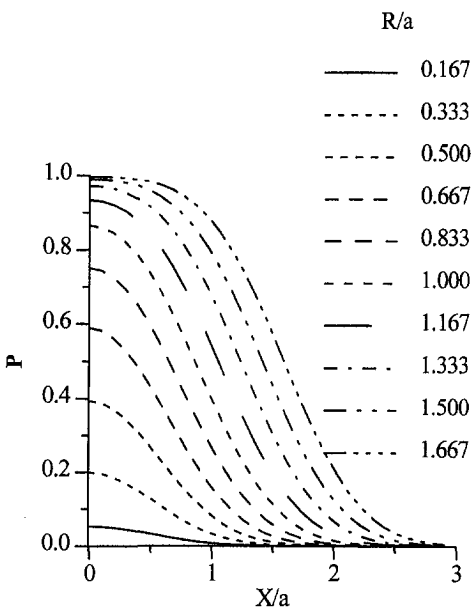

Fig. 3 Laser light power passing through a pinhole of varying size and location

and there is a dead band region where P is independent of X. These large sizes are unsuitable for laser beam positioning due to this dead band region.

The rate of change of P with X for $Y = 0$, $\partial P/\partial X = P'$, is shown in Fig. 4. P' is zero at $X = 0$ since that is the location of maximum laser beam power passing through the pinhole. The desired response to optimize the power meter's sensitivity to laser beam alignment is the maximum rate of change in P at $X = 0$ so that the laser light power meter will register the maximum variation with small displacements of the pinhole-laser beam orientation from the perfectly aligned case. This requires the largest rate of change in P' at the $X = 0$ position. This is somewhat observable from the slopes of the lines in Fig. 4. To better quantify the optimum pinhole size, $P'' = \partial^2 P/\partial X^2$ was evaluated at $X = 0$ and for $Y = 0$, $0.50a$, and $0.75a$. These results are shown in Figure 5 as a function of pinhole size. For the perfectly aligned case, $X = 0$ and $Y = 0$, the optimum pinhole size as indicated by the largest negative value of P'' is $0.71a$. As the centerline of the beam is displaced vertically further from the centerline of the pinhole, the opti-

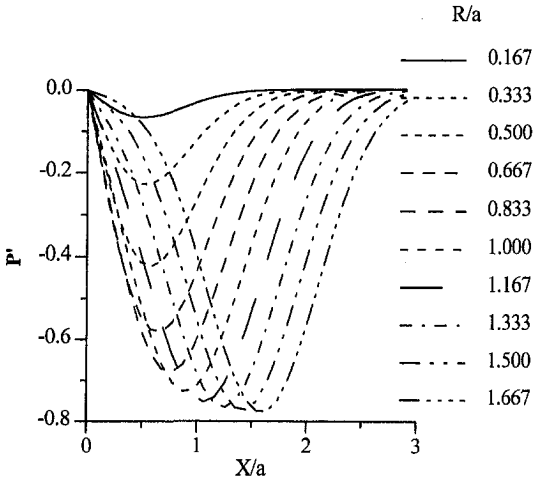

Fig. 4 $\partial P/\partial X$, rate of change in laser light power through a pinhole as a function of pinhole size and position

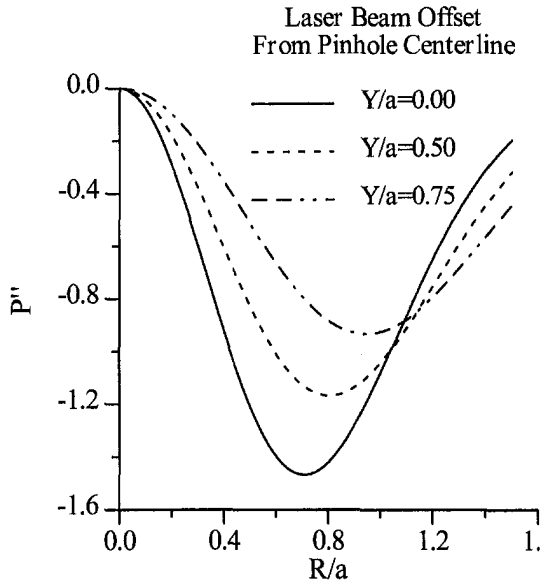

Fig. 5 $\partial^2 P/\partial X^2$ **evaluated at** $X = 0$**, varying pinhole size, and three different beam offsets from the pinhole centerline. The maximum absolute value represents the pinhole size most sensitive to changes in laser beam position.**

mum pinhole size increases to $0.80a$ at $Y = 0.50$ and $0.94a$ at $Y = 0.75$. However, since the desire is to have the most sensitivity in power variation at the perfectly aligned condition, the $0.71a$ value would be the most desirable.

Two other considerations are needed when using pinholes to align laser beams. First, if the laser beam is powerful enough the pinhole can warp due to the heating produced by the portion of the beam blocked. In our laboratory we use "high power" pinholes which help reduce the warpage. For the $0.71a$ sized pinhole, 63.5 percent of the laser beam power is passed through the hole when the pinhole and laser beam are perfectly aligned. The remaining 36.5 percent is absorbed by the pinhole. For the laser beam alignment monitoring system, this is not a problem since only a low power monitoring beam is split from the main beam. However, if using a pinhole to align the main laser beam in the primary optical system, the effects of the heating upon the pinhole must be monitored. This can be done by applying the beam to a room temperature pinhole with a power meter behind the pinhole. If the pinhole warps due to the laser beam power, the light power passing through the pinhole will change with time. We use a pinhole to align the six beams of the 3-D LDV system in our laboratory. In this case, the overall power of the six beams is sufficient to warp the pinhole. To overcome this problem, we block five of the beams so they do not reach the pinhole. The sixth beam is adjusted to pass through the pinhole. That beam is then blocked and another beam is adjusted. This procedure is repeated until all six beam are aligned with the pinhole. By using only one beam at a time the heating problem is avoided. In this manner, all six beams are aligned to intersect at a single spatial location.

The second consideration is that the diameter of the laser beam is not necessarily constant. The beam exiting the laser is not quite parallel, hence, the use of collimators to produce parallel light. Once the beam passes through a focusing lens the diameter decreases as it approaches the focal point. Therefore the pinhole diameter may vary depending on where in the optical system the laser beam is being positioned.

Conclusions

The use of pinholes to align and monitor laser beams has been presented along with an analysis for the selection of the optimum pinhole size. For a laser operating in the T_{oo} mode with a Gaussian beam intensity distribution, the pinhole most sensitive to laser beam-pinhole alignment has a radius that is 71 percent of the laser beam radius. A laser beam alignment/monitoring system which is placed between the laser output and the input to the user's optical system has been described. This system is used to monitor and adjust the pitch, yaw, horizontal translation and vertical translation of the laser beam so that the user's optical system will always have the same laser beam input. This can reduce realignment requirements in the user's system as well as prevent the burning of fiber optics where the laser light is introduced into the fiber optic. This system has greatly reduced the realignment requirements of a 3-D LDV system used in our laboratory.

Journal of Fluids Engineering

Book Review

Flow Around Circular Cylinders—Volume 1: Fundamentals, by M. M. Zdravkovich, Oxford Science Publications, 1997.

REVIEWED BY P. W. BEARMAN[1]

It can be argued that much of what we already know about fluid dynamics, and a great deal of what we still need to understand and predict, is present in the variety of phenomena generated by the flow around a circular cylinder. This simple body shape has challenged generations of experimentalists and latterly has proved to be an exacting test case for computationalists. Dr Zdravkovich has spent a lifetime studying flow around circular cylinders. His book is the most authoritative review of the subject to appear since the well known, but now outdated, study by Morkovin in 1964, entitled "Flow Around a Circular Cylinder; A Kaleidoscope of Challenging Fluid Phenomena."

The book is well organised, clearly presented and contains a wealth of information drawn from more than an estimated 1200 references. Volume 1 concentrates on fundamental aspects of flow around a circular cylinder and Volume 2, which is in preparation, will describe applications. In roughly the first third of the book the author presents in detail the various flow regimes experienced by the circular cylinder from low Reynolds number steady attached flow to very high Reynolds number postcritical flow. A lot of original material is reproduced, including a number of excellent flow visualisation photographs. The middle part is concerned with analytical and numerical solutions of flow around a circular cylinder, based on the Navier Stokes equations or on simplified models. The final third of the book is a compendium of influencing factors on circular cylinder flow: free stream turbulence, shear, compressibility, heat transfer, sound, cavitation and the effect of a non-Newtonian fluid.

This book is a major contribution to fluid dynamics and is thoroughly recommended to anybody interested in the flow around a circular cylinder. While there are a significant number of typographical errors this will not inhibit the reader's understanding or enjoyment. However, it is possible that there will be sections where the reader disagrees with the author's interpretation of flow phenomena or with the emphasis placed on certain aspects. For example, there could have been more on the application of hydrodynamic stability theory and the concepts of convective and absolute instability in cylinder flow. A fuller coverage of the control of circular cylinder flow might have been included. In the section on modelling I would have welcomed a more critical review of methods and perhaps some need not even have been presented. The application of CFD to circular cylinder flow is progressing rapidly and the book is not fully up to date in this area. However, one must acknowledge the enormous effort, spread over many years, that has gone into the preparation of this book. Recently the circular cylinder has found itself once more at the forefront of fluid dynamics research and in fast developing areas it is unreasonable to expect to have a book that is up to date in every detail.

This book will become the standard reference for the flow around a circular cylinder. I have already used it several times myself to check on the availability of data on certain aspects of circular cylinder flow. Without its help it might have taken me a lifetime to find them.

[1] Imperial College, London, United Kingdom.

